Nanometrology using Time-Resolved Fluorescence Techniques

Philip Yip

A thesis presented in partial fulfilment
of the requirements for the degree of
Doctor of Philosophy

Department of Physics, Photophysics Research Group
University of Strathclyde

HORIBA Scientific IBH

National Physical Laboratory
Biotechnology Group

HORIBA Scientific ISA

March 2016

This thesis is the result of the author's original research. It has been composed by the author and has not been previously submitted for examination which has lead to the award of a degree.

The copyright of this thesis belongs to the author under the terms of the United Kingdom Copyright Act as qualified by the University of Strathclyde regulation 3.50. Due acknowledgement must always be made for the use of the material contained in, or derived, from this thesis.

Signed: Date:

Acknowledgements

Abstract

This thesis looks at fluorescence techniques and their use for nanometrology applications. It has been primarily industrially linked with scientific instrument vendors Horiba Scientific IBH and Horiba Scientific ISA and examines the state of the art instrumentation taking the reader from grounds up from simple steady-state and time-resolved fluorescence spectroscopy techniques that are routinely used and newer more advanced techniques made possible but rapid developments in technology. Secondary industrial links are to NPL allowing the examination of the state of the art instrument in fluorescence microscopy an extension of fluorescence spectroscopy and this thesis likewise builds from simple to advanced microscopy techniques.

In the case of nanometrology well-established techniques in particular time-resolved fluorescence anisotropy, which overcomes the diffraction barrier by use of low concentrations and infers the average particle size of a homogeneous distribution by use of polarized light and Brownian motion are discussed. These applications are examined in conjunction to high concentration microscopy techniques such as direct Stochastic Optical Reconstruction Microscopy (dSTORM) High concentration heterogeneous techniques are better suited to most biological applications which involve the measurement of highly packed nanostructures. dSTORM requires use of specific chemical conditions and high laser power to enable stochastic blinking. A video of these stochastic blinks by use of a fast capture imaging CCD allows one to temporally resolve each single-molecule blinks and construct a single super-resolution image. The implication of these chemical conditions, high laser power and limitations even in today's state of the art CCDs need to be properly understood and any development in either but preferably all three will make this advanced microscopy technique more feasible. This work looks at the properties of some new probes for nanometrology however, the strict criteria required for successful dSTORM applications in particular leaves this work an open investigation.

List of Abbreviations

xxxx/yyy grating – grating blazed to optimise output at yyy nm and xxxx lines/mm.

xxxx/yyy double grating – double grating blazed to optimise output at yyy nm and xxxx lines/mm.

A – Signal from Auxiliary port, usually from a photodiode.

Ac – Corrected signal from Auxiliary port accounting for excitation wavelength correction factors and dark counts.

APS – 3-aminopropyl trimethoxysilane.

AFM – Atomic Force Microscopy.

Au_{xx} – xx number of atoms in a gold nanocluster.

Au_{xx}@BSA – xx number of atoms in a gold nanocluster encapsulated by Bovine Serum Albumin.

Au_{xx}@HSA – xx number of atoms in a gold nanocluster encapsulated by Human Serum Albumin.

Au_{xx}@GSH – xx number of atoms in a gold nanocluster encapsulated by Glutathione.

BPxxx/yy – Bandpass filter at xxx nm. Spectral Full width half maximum of yy nm.

BDR – Best Dynamic Range. Number of electrons per count setting which offers the best dynamic range for a Charged Coupled Device.

BSA – Bovine Serum Albumin

CCD – Charge Coupled Device.

CPS – Counts per second.

Cu_{xx} – xx number of atoms in a copper nanocluster.

Cu_{xx}@BSA – xx number of atoms in a copper nanocluster encapsulated by Bovine Serum Albumin.

DAEEM – Decay Associated Excitation Emission Matrix (not weighted by the decay time).

$DAEEM^W$ – Decay Associated Excitation Emission Matrix weighted by the decay time.

DAS – Decay Associated Spectra (not weighted by decay time). Emission unless otherwise stated.

DAS^W – Decay Associated Spectra weighted by decay time. Emission unless otherwise stated.

DDxxxD – DeltaDiode pulsed diode source at xxx nm peak wavelength. Maximum repetition rate = 20 MHz.

DDxxxD – DeltaDiode pulsed laser source at xxx nm peak wavelength. Maximum repetition rate = 100 MHz.

dSTORM – direct Stochastic Optical Reconstruction Microscopy.

EEM – Excitation Emission Matrix.

FCS – Fluorescence Correlation Spectroscopy.

FCCS – Fluorescence Cross-Correlation Spectroscopy.

FF – Front Face Geometry.

FITC – Fluorescein Isothiocyanate.

FITC- APS – Fluorescein Isothiocyanate coupled to 3-aminopropyl trimethoxysilane.

FLIM – Fluorescence Lifetime Imaging Microscopy.

FLCS – Fluorescence Lifetime Correlation Spectroscopy.

FWHM – Full Width at Half Maximum.

GSH – glutathione/

H – Polarizer orientation is horizontal 90°[1].

---

[1] When two polarizers are used. The first letter represents the orientation of the excitation polarizer and the second one represents the orientation of the emission polarizer.

HL – High Light. Number of electrons per count setting which accommodates the best setting for high light intensity when using a Charged Coupled Device.

HS – High Sensitivity. Number of electrons per count setting which accommodates the best setting for high sensitivity when using a Charged Coupled Device.

HSA – Human Serum Albumin

LPxxx – Long Pass filter at xxx nm.

M – Polarizer orientation is at the Magic Angle 54.7°[1].

MCorrect – Emission Wavelength correction factor for detector on S[2].

MCP – Multi-channel plate photomultiplier tube detector.

MCS – Multi-channel scaling.

N – No Polarizer present

NLxxxD – NanoLED pulsed diode at xxx nm peak wavelength. Maximum repetition rate = 1 MHz.

NLxxxL – NanoLED pulsed laser at xxx nm peak wavelength. Maximum repetition rate = 1 MHz.

NDx.x – Neutral Density filter x.x represents the grade.

NTA – Nanoparticle Tracking Analysis.

PARAFAC – Parallel Factor Analysis.

PMT – Photomultiplier Tube.

POPOP – 1,4-bis(5-phenyloxazol-2-yl) benzene

PT_{xx} – xx number of atoms in a platinum nanocluster.

$PT_{xx}@BSA$ – xx number of atoms in a Platinum nanocluster encapsulated by Bovine Serum Albumin.

R – Reference signal from excitation arm photodiode.

RA -Right Angle geometry.

Rc – Corrected reference accounting for excitation wavelength correction factors and dark counts.

S – Signal from emission arm. This is commonly the right arm when facing the fluorimeter[3].

Sc – Corrected signal accounting for emission wavelength correction factors and dark counts.

SIM – Structured Illumination Microscopy.

SLxxxD – SpectraLED diode at xxx nm peak wavelength.

SNR – Signal to Noise Ratio.

SNR_{FSD} – Signal to Noise Ratio First Standard Deviation.

SNR_{RMS} – Signal to Noise Ratio Root Mean Square.

SPxxx – Short Pass filter at xxx nm.

SS – Steady-State.

SSFA – Steady-State Fluorescence Anisotropy.

STED – Stimulated Emission Depletion Microscopy.

T – Signal from emission arm. This is commonly the right arm when facing the fluorimeter[3].

TAC – Time to Amplitude Convertor.

TCSPC – Time Correlated Single Photon Counting.

TCorrect – Emission Wavelength correction factor for detector on T2.

TDM – Time Domain Discriminator.

TR – Time Resolved

---

[2] If multiple detectors are mounted on S and T or multiple gratings used the names MCorrect and TCorrect will usually state, the grating, name of the detector and the emission arm.

[3] The first detector on the S emission arm is S1. In cases where there are multiple detectors mounted the first one will be called S1, the second S2 and the third S3. A similar nomenclature is used for the T emission arm.

TREEM – Time-Resolved Excitation Emission Matrix.
TRFA – Time-Resolved Fluorescence Anisotropy.
TRES – Time Resolved Emission Spectrum.
TRIZMA – 2-Amino-2-(hydroxymethyl)-1,3-propanediol.
Try-xxx – Trytophan amino acid at amino acid position xxx.
V – Polarizer orientation is vertical $0°^{1}$.
XCorrect – Excitation Wavelength correction factor.

List of Publications

Stewart H L, Yip P, Rosenberg M, Sørensen T J, Laursen B W, Knight A E and Birch D J S 2016 Nanoparticle metrology of silica colloids and super-resolution studies using the ADOTA fluorophore *Meas. Sci. Technol.* 27 045007

Birch D J S and Yip P 2014 Nanometrology *Fluorescence Spectroscopy and Microscopy: Methods and Protocols* Methods in Molecular Biology vol 1076, ed Y Engelborghs and A J W G Visser (Totowa, NJ: Humana Press) pp 279–302

Gracie K, Smith W E, Yip P, Sutter J U, Birch D J S, Graham D and Faulds K 2014 Interaction of fluorescent dyes with DNA an spermine using fluorescence spectroscopy. *Analyst* 139 3735–43

Wu Y, Stefl M, Olzyńska A, Hof M, Yahioglu G, Yip P, Casey D R, Ces O, Humpolíčková J and Kuimova M K 2013 Molecular rheometry: direct determination of viscosity in Lo and Ld lipid phases via fluorescence lifetime imaging. *Phys. Chem. Chem. Phys.* 15 14986–93

Yip P, Karolin J and Birch D J S 2012 Fluorescence anisotropy metrology of electrostatically and covalently labelled silica nanoparticles *Meas. Sci. Technol.* 23 084003

Conference Proceedings

Yip P, Hungerford G, Knight A, Chen Y and Birch D J S 2015 The Spectroscopy of Au_{25}@BSA Nanoclusters and their Application for dSTORM) *2015 FluoroFest* Presentation http://www.fluorofest.org/

Yip P, Knight A and Birch D J S 2015 Direct Stochastic Optical Reconstruction Microscopy *2015 SUPA Annual Meeting* 6 Minute Video

Yip P, Hungerford G, Knight A, Chen Y and Birch D J S 2014 The Spectroscopy of Au$_{25}$@BSA Nanoclusters and their Potential use as Probes for direct Stochastic Optical Reconstruction Microscopy (dSTORM) *2014 FluoroFest* Presentation http://www.fluorofest.org/

Yip P, Hungerford G, Knight A, Chen Y and Birch D J S 2014 The Potential Use of Au$_{25}$@BSA as Probes for direct Stochastic Optical Reconstruction Microscopy (dSTORM) *2014 SULSA Research Symposium Optical Imaging of Cells: From Single Molecules to Organelles* Poster

Yip P, Hungerford G, Knight A, Chen Y and Birch D J S 2014 The Investigation of the Fluorescence Profile of BSA Encapsulated Au$_{25}$ Nanoclusters as New Probes for Super Resolution Microscopy *Instruments & Methods for Biology and Medicine 2014* Presentation http://imbm.fbmi.cvut.cz/

Yip P, MacMilliam A, Knight A, Sutter J, Chen Y and Birch D J S 2013 Fluorescence Imaging of Single Gold Nanoclusters *Methods and Application in Fluorescence 2013* Poster http://www.maf13.org/

Yip P, Hungerford G, Knight A, McCalf D, Chen Y and Birch D J S 2013 A Nano-Toolbox for Biomolecular Fluorescence Imaging *2013 SUPA Physics and the Life Sciences* Poster http://www.supa.ac.uk/Research/PaLS/2013-PaLS-meeting

Yip P and Birch D J S 2011 Nanoparticle Metrology Using Covalently Labelled Fluorescence Probes *2012 PiMoP Prague Workshop on Photoinduced Molecular Processes* Presentation http://pimop2012.fjfi.cvut.cz/

Yip P, Hungerford G, Knight A, McCalf D, Chen Y and Birch D J S 2012 A Nano-Toolbox for Biomolecular Fluorescence Imaging *2012 SUPA Inspire Annual Meeting* Poster http://www.supa.ac.uk/inspire-annual-meeting/2012-inspire-annual-meeting

Yip P, Karolin J and Birch D J S 2011 Fluorescence Depolarisation of Covalently Labelled Silica Nanoparticles *2011 Nano Meets Spectroscopy* Poster

Yip P, Karolin J and Birch D J S 2011 A Nano-Toolbox for Biomolecular Fluorescence Imaging *2011 SUPA Inspire Annual Meeting* Poster http://www.supa.ac.uk/inspire-annual-meeting/2011-inspire-annual-meeting

Contents

1. Introduction

The work in this thesis looks at some of the latest developments in fluorescence techniques and fluorescence instrumentation. The application areas of fluorescence spectroscopy are incredibly diverse. As many biological components exhibit fluorescence [1] and organic components [2] have a unique excitation and emission profile the fluorescence excitation-emission matrixes may be used to detect any impurities as well as identify the impurity and concentration level via its excitation-emission profile [3]. The fluorescence profile from these biological components also plays an important in food science and as food ages the fluorescence profile which is greatly influenced by its chemical environment will change. Hence if the fluorescence profile of food is characterised for the foods lifecycle then future fluorescence measurements will be able to infer the quality of the food [4–6]. Fluorescence plays a key role for the encryption of documents; every passport or currency note has an embedded fluorescence/phosphorescence pattern which under normal light is not observed but under UV illumination can clearly be seen. Fraudulent documents can easily be identified as it is hard to replicate this pattern without the specialised printing technology and knowhow. More and more sophisticated fluorescence encryption and printing techniques are in demand [7,8]. Fluorescence techniques have potential applications in recycling as the high specificity of fluorescence techniques have the capability to identify different types of plastic flakes which are otherwise hard to distinguish from one another [9,10]. Fluorescence plays a key role in healthcare [11]. With carefully tailored systems, the sensitivity of fluorescence measurements can be taken advantage of and be utilised for specific analyte sensing [12,13]. A great deal of effort has been put into developing sugar specific sugar sensing in particular glucose [14–20]. Fluorescence spectroscopy of blood may be used as a diagnostic to detect disease [21] and the fluorescence profile of cells may be used for cell-sorting [22]. It is also possible to use fluorescence techniques for gas sensing for instance CO_2 [23] and O_2 [24]. Ion recognition and pH measurements are also possible with fluorescence [25–27] as well as viscosity measurements. By ingenuity of fluorescence measurement parameters including fluorophore, excitation wavelength, emission wavelength, polarization and time-scale of measurement [28] one can tune fluorescence techniques to measure and even visualise structures at nm resolution. Fluorescence spectroscopy and its extension fluorescence microscopy are already very well established techniques and widely used every day particular due to the high sensitivity of

fluorophores to their local environment. The most significant research area is that of the life sciences where basic fluorescence measurements are routinely used. Clearly all the application areas mentioned above can be incorporated into measurements of biological organisms. Analyte sensing in complex small μm, heterogeneous biological systems such as the cell requires a sensitive enough technique such as fluorescence [29]. Cellular viscosity measurements for example are made possible with a fluorescence molecular rotor which has a fluorescence lifetime dependant on the viscosity of the probes local environment [30]. A globally recognised application is the well-established area of DNA sequencing [31–36], in particular the Human Genome Project [37–39] which had led to a new era of medical breakthroughs. This project would not have been possible without the aid of fluorescence techniques and the associated rapid development of fluorescence instrumentation [40], fluorescent dyes with appropriate linkers [41] and techniques [42]. Although a vast deal of information has been collected within the life sciences, it can be said that there remain more questions than answers. One of the main difficulties is that in order to visualise biological structures one has to measure at a higher resolution i.e. measure at a nanoscale and the ultimate goal for biological imaging is to measure dynamically in nanoscale at x, y and z for a relatively large objects such as a human being. The last decade has seen a rapid development in fluorescence techniques and the beginning of the exciting frontier of super-resolution microscopy. Pioneering work has been carried out on gene regulation[43], actin filament assembly [44], self-organisation of the ecoli chemotaxis network and the investigation of a full embryo while its developing [45,46]. The main goal of nanometrology fluorescence measurements in the life sciences is to understand how biological organisms work and in cases don't work. This will allow for the development of new diagnostics and therapeutics as well as the development of new materials or nanomaterials.

The work in this thesis was done in conjunction to a fluorescence scientific instrument vendor HORIBA Scientific IBH and HORIBA Scientific ISA and a world renowned centre of nanometrology NPL Biotechnology Group and looks into the applications and developments of high end fluorescence techniques. The first chapter of this thesis will discuss the basic principles behind fluorescence and related phenomenon. The second chapter will build up an understanding of basic fluorescence measurements including system checks to more powerful advanced measurements that aren't yet fully established. There's still future scope for some of the techniques discussed. The third

chapter examines the use of time-resolved fluorescence anisotropy techniques for nanosizing objects down to 4 nm in radii however this technique has the limitation that a relatively simple system is required. The fourth chapter looks at the complicated spectroscopy and characterisation of Au_{25} nanoclusters which are a unique type of probe possessing a number of desired characteristics and the fifth chapter looks at the use of these probes for super-resolution microscopy. The last chapter is the conclusion.

1.1 Fluorescence Spectroscopy
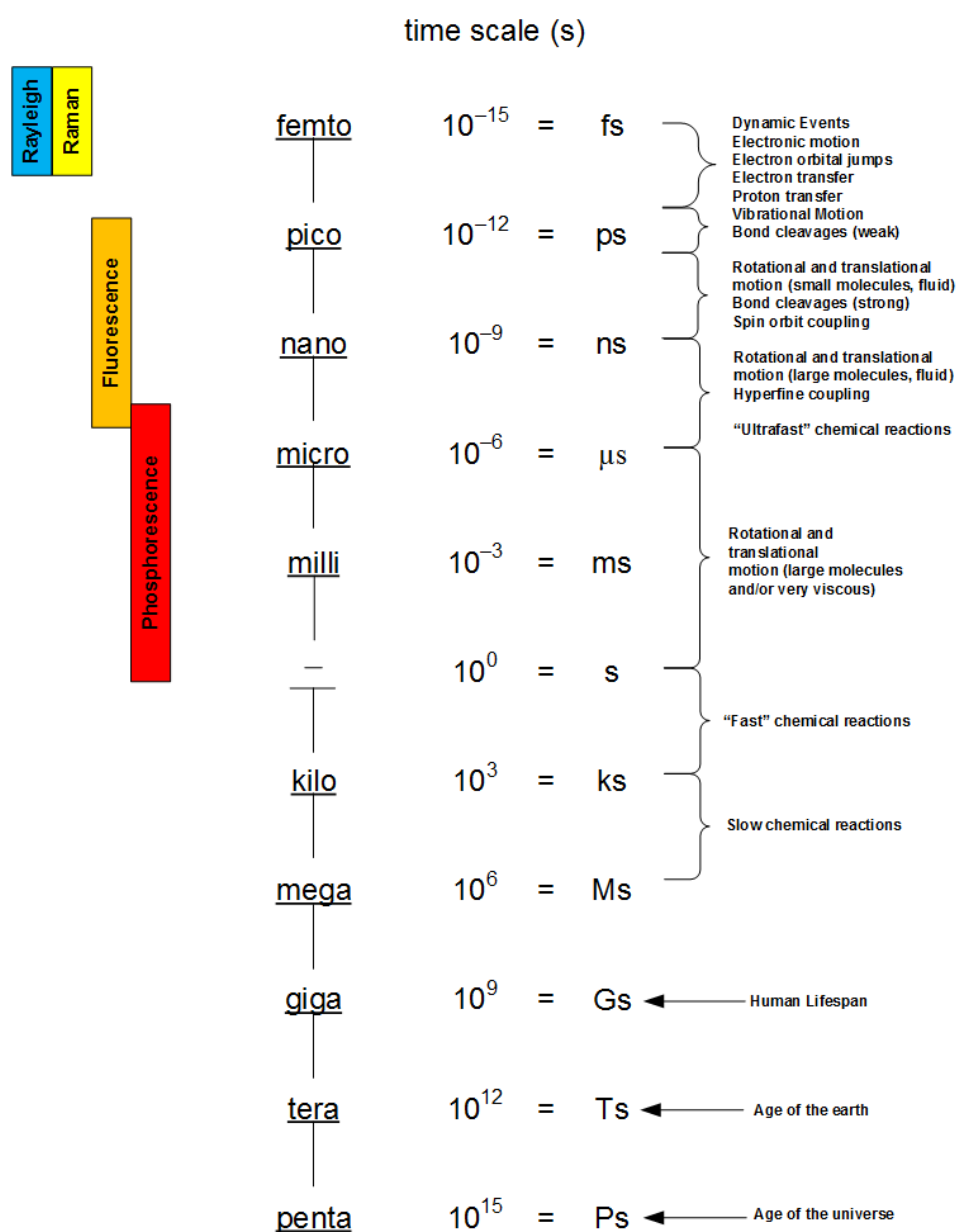
Figure 1: Time scale of emission processes with respect to chemical and atomic events. The time scales of emissive processes such as Raman, fluorescence and phosphorescence are on a suitable time-scale allowing investigation of these events.

This work focuses on luminescence spectroscopy, primarily fluorescence an emissive process on the ~ns time scale and secondary phosphorescence a longer-lived emissive process on the μs [47]. This work focuses primarily on the field of fluorescence and phosphorescence spectroscopy due to the very convenient time scale of these emissive processes comparable to underlying biological and chemical processes see **Figure 1** [40,48]. Fluorescence measurements in particular provide the sensitivity and correct timescales for studying and using reactions and kinetics needed across a wide range of disciplines. Fluorescence is a radiative emission process typically on the ≈ns time scale and phosphorescence is a radiative emission process on the ≈μs-ms time scale. Since the speed of light is 3×10^8 m s^{-1}, in 1 ns (1×10^{-9} s), light travels 30 cm.
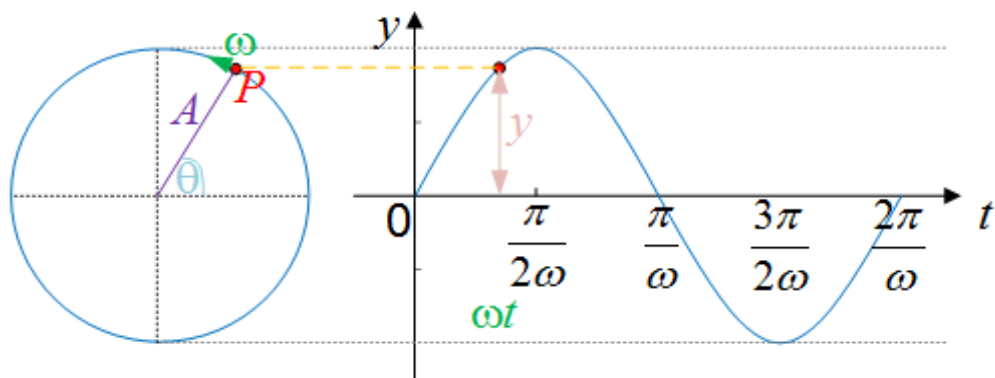
Figure 2: Schematic of an electron orbiting around a nucleus using a quantised radius which has the form $y = A\sin(\omega t)$.

Figure 3: Schematic of an electron orbiting around a nucleus at the quantised ground state. A photon of light can interact with the electron transferring energy to the electron taking it to the quantised first excited state.

The underlying processes of fluorescence spectroscopy will now be discussed. Spectroscopy is the investigation of the interaction of matter using electromagnetic radiation. **Figure 2** illustrates an ideal classical system, an electron orbiting around a nucleus where the energy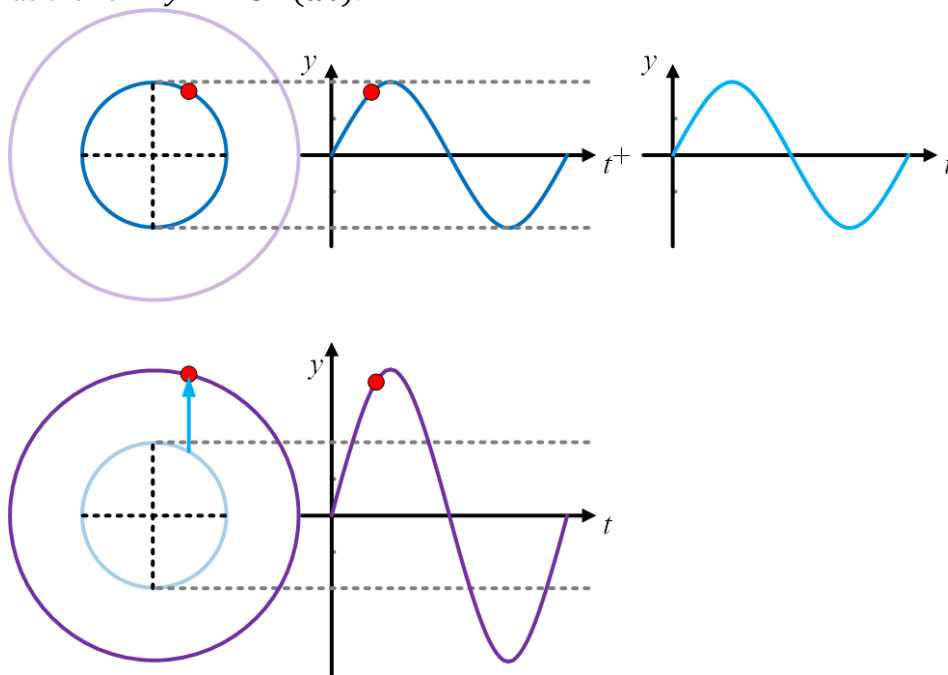 of each orbit is quantised. This motion has the form of a sine wave. In an atom or molecule, an electromagnetic wave (such as visible light) can induce an oscillating electric or magnetic moment. **Figure 3** a photon of light is equal in energy to the difference between the ground eigenstate Ψ_{i1} and the first excited eigenstate Ψ_j. A resonance interaction results in the transfer of energy to the electron allowing it to access a higher energy orbit. This is known as an electronic transition. The strength or probability of a transition depends on the overlap of the two waves (in this example both waves being sine waves) and also the phase of both waves (in this example both waves are in phase). In quantum mechanics the strength of a transition from Ψ_i to Ψ_j is given by $\left|\vec{M}_{ji}\right|^2$ where the transition dipole moment [49]:

$$\overline{M}_{ji} = \int \Psi_j \vec{\mu} \Psi_i dV \qquad (1)$$

The integration is performed over all space and $\vec{\mu}$ is the dipole moment operator, for a collection of charges this is the sum of each individual charge q_n multiplied by the distance of each individual charge r_n:

$$\vec{\mu} = \sum_n q_n r_n \qquad (2)$$

The mass of an electron is a thousandth of the mass of a proton or neutron hence the most probable vibronic transition is one which involves no change in the nuclear co-ordinates. This assumption is known as the Franck-Condon principle [50–53]. As a consequence, $\vec{M}_{ji}$ can be separated into electronic and vibrational components.

$$\overline{M}_{ji} = \int \Psi_{je} \vec{\mu} \Psi_{ie} dV \int \Psi_{jv} \vec{\mu} \Psi_{iv} dV \qquad (3)$$

Examining the vibrational part of $\vec{M}_{ji}$ separately the probability of an electronic transition from one vibrational energy to another will be more likely to occur if the vibrational wavefunctions of the two states overlap see **Figure 4**, these are known as Franck-Condon factors. Now consider a molecule in which only the vibrational mode is dominant, so that it approximates to a harmonic oscillation. The solutions of the simple harmonic oscillator are a fundamental problem in any quantum mechanics textbook. A state involving

electronic and vibrational energy is referred to as a vibronic state. Let the energy of the vibronic state be E_t. If the electronic energy of the ground state is E_e and the energy of the fundamental vibrational mode in the ground state is E_v then the total energy E_t:

$$E_t = E_e + \left(m + \frac{1}{2} \right) E_v \qquad (4)$$

where $m=0,1,2,\ldots$ is the vibrational quantum number. An electronic excited state is characterised by certain basic properties; its energy its multiplicity and its symmetry [53]. To reach an electronic state higher than the ground state the fluorophore (fluorescent species) must first absorb light energy. Once energy is absorbed because the nuclear co-ordinates are unchanged the vibronic energy of the excited state E_t':

$$E_t' = E_e' + \left(n + \frac{1}{2} \right) E_v' \qquad (5)$$

where $n=0,1,2,\ldots$, E_e' is the electronic energy in the excited state and E_v' is the energy of the fundamental vibrational mode in the excited electronic state.
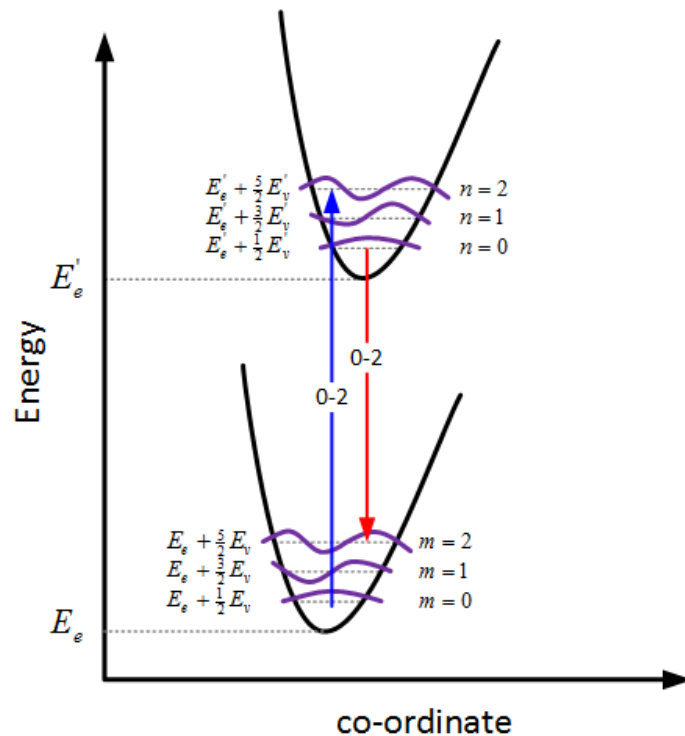

Figure 4: Illustration of the Franck-Condon principle alongside the assumption that the vibrational mode is dominant approximating to that of a simple harmonic oscillator. The purple curves denote the wavefunctions of each vibronic state. The intensity of lines is partially governed by the overlap of the vibrational wavefunctions denoted as purple lines

these are known as Franck Condon states. The blue absorption line 0-2 will give a strong band in the absorbance spectrum and the red emission line 0-2 will give a strong emission band in the emission spectrum because of the good overlap between the Franck Codon states. The absorption and emission lines are shown as straight lines as the assumption of no changes in the nuclear co-ordinates during vibronic transitions has been made.

If the ground state is in thermal equilibrium at absolute temperature T the fraction f_m of ground state molecules in a vibrationally excited state m is determined by the Boltzmann factor:

$$f_m = \exp\left(-\frac{mE_v}{kT}\right) \tag{6}$$

where k is Boltzmanns constant 1.38×10^{-23} J K^{-1}, T is the temperature in K and:

$$E_v \approx hc\left(\frac{1}{\lambda_1} - \frac{1}{\lambda_2}\right) \tag{7}$$

where $h=6.34\times10^{-34}$ J s is Planck's constant, $c\approx3\times10^8$ m s^{-1} is the speed of light and λ_1 is the first and λ_2 is the second emission maxima. In the case of Perylene **Figure 5** this is 436 nm and 465 nm respectively. At room temperature $T=298$ K then the probability distribution of molecules due to Maxwell-Boltzmann statistics are $f_1\approx0.0985$ % and $f_2\approx0.0001$ % respectively. Thus over 99 % of the molecules are in the zero-point vibrational level of energy i.e. for absorption $m=0$ thus 0-0, 0-1 and 0-2 absorption band are observed. Likewise for fluorescence emission any additional vibrational energy is quickly dissipated as heat and $n=0$ thus 0-0, 0-1 and 0-2 emission bands are observed [53,54]. A consequence of this heat loss is that the energy of fluorescence emission is lower than that of absorption i.e. fluorescence is red-shifted this is known as the Stokes shift. The Stokes shift is incredibly useful as it allows for the seperation of fluorescence emission from the light used for excitation. The equal spacing between vibrational levels often results in mirror symmetry of the absorbance and emission spectrum as shown for perylene in cyclohexane **Figure 5** [55]. The energy transitions are denoted in a simplified Jablonski diagram. In this case S_0 and S_1 denote the electronic ground singlet and 1st electronic excited singlet state respectively.
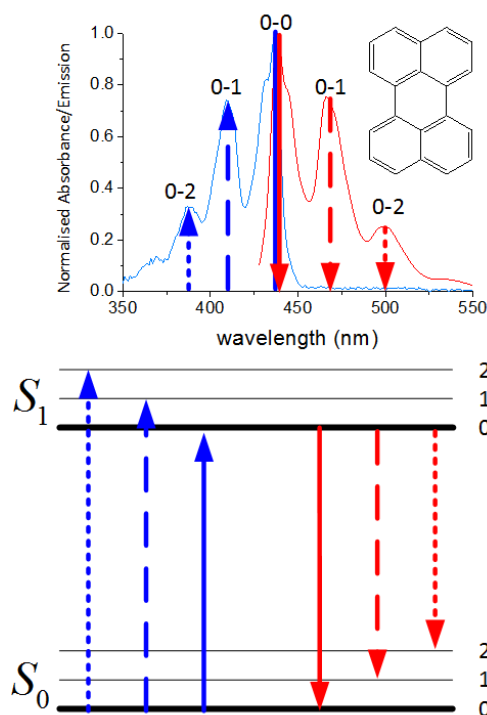
Figure 5: Normalised absorbance and fluorescence emission of perylene in cyclohexane with an absorbance peak of 0.1 (top) and Jablonski diagram (bottom).

Spectroscopy uses S_0 to denote the singlet ground electronic state, S_1 to denote the first singlet excitated state, S_2 to denote the second singlet excited state and S_N the Nth singlet excited state. Singlet electronic states have a spin quantum number S=0 and triplet electronic states have a spin quantum number S=1. The terms singlet and triplet can be derived by looking at the spins of an electron pair using quantum mechanics [56]. A simple explanation will be used here. In general it is the outer electron pair that is involved in an electronic transition. For a pair of electrons each electron can have either spin up ↑ or spin down ↓. This naturally leads to 4 different combinations ↑↑, ↑↓, ↓↑ or ↓↓. However as the electrons are indistinguishable instead of having either ↑↓ or ↓↑ a symmetric and antisymmetric combination of these states must be made. This results in three variations that have a symmetrical spin component ↑↑, ↓↓ and ↑↓+↓↑ and one variation that has a symmetical spin component ↑↓–↓↑. Using the time independent Schrödinger equation the total wavefunction can be split into spin and space parts. The Pauli exclusion principle states that the total wavefunction must be anti-symmetric, it therefore follows that ↑↑, ↓↓ and ↑↓+↓↑ have an antisymmetic spatial component and ↑↓–↓↑ has a symmetric spatial component. The singlet state ↑↓–↓↑ has symmetric space eigenfunctions so as the two electrons approach each other the wavefunction is enhanced c.f. m=0, 2 wavefunctions in

Figure 4. The three states ↑↑, ↓↓ and ↑↓+↓↑ have antisymmetric space eigenfunctions so as the two electrons approach each they repel one another c.f. m=1 wavefunction in **Figure 4**. As a consequence the single ↑↓–↓↑ (S=0, m_z=0) or singlet electronic state is lower in energy than the three ↑↑ (S=1, m_z=1), ↓↓ (S=1, m_z=–1) and ↑↓+↓↑ (S=1, m_z=0) states otherwise known as the triplet state. ↑↑, ↓↓ and ↑↓+↓↑ are equal in energy in the absense of an applied magnetic field. When a magnetic field is applied the spin projection on the z axis m_z is different for each of these states so the line from each of these can be seen seperately.

For spin-orbit coupling quantum selection rules must be satisfied for an electronic transition to be allowed. The first rule states that an allowed transition must involve the promotion of electrons without a change in their spin i.e. ΔS=0. The second rule states that if a molecule has a centre of symmetry, transitions within a given set of p or d orbitals are forbidden i.e. changes in the total orbital angular momentum L cannot be 0, $\Delta L \neq 0$. For each electronic state 0,1,2 indicates the vibrational energy of the excited state. Absorption (the blue upwards line) is a very fast process that has a characteristic time of $\approx 10^{-15}$ s. For most fluorophores internal conversion (where any additional electronic energy is dissipated as heat) is the most dominant process between the $S_N \rightarrow S_1$ electronic levels where N>0,1 because of the close spacing of these electronic levels. Internal conversion is a non-radiative transition between two electronic states of the same multiplicity and has a characteristic time of 10^{-14}-10^{-10} s. For molecules in solution internal conversion is subsequently followed by vibrational relaxation ($\sim 10^{-12}$-10^{-10} s) towards the lowest vibration state of the S_1 excited electronic state [57,58].

The process of solvent relaxation can be best demonstrated using a polar fluorophore or polar solvent. **Figure 5** showed an absorption spectrum where the 0-0, 0-1 and 0-2 absorption transitions and 0-0, 0-1 and 0-2 emission transitions were clearly distnguished this was perylene (non-polar) in cyclohexane (non-polar). In polar solvents and polar solutions the situation is usually different and the spectra appear structureless **Figure 6**. For a polar fluorophore there are a continuum of configurations in which solvent molecules may arrange themselves around a polar fluorophore and each of these configurations has a slightly different energy. Usually what happens is that the absorption transition 0-0 overlaps with 0-1 and 0-1 overlaps with 0-2 so a broadband absorbance spectrum is shown. A similar argument can be made for the emission spectrum.
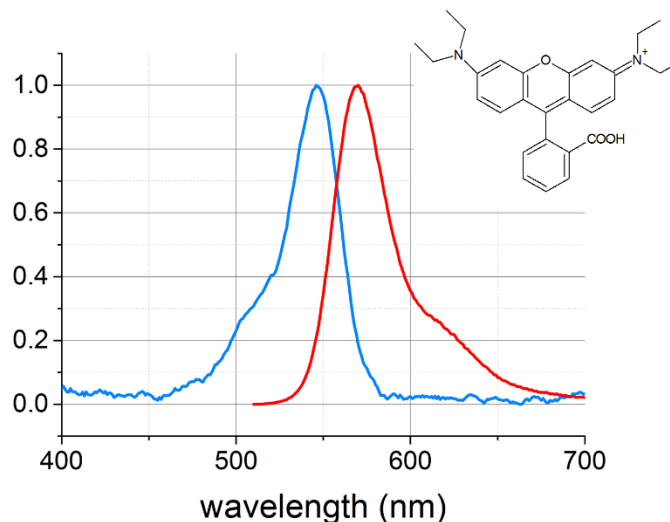
Figure 6: Normalised absorbance and fluorescence emission of Rhodamine B in methanol with an absorbance peak of 0.1. The spectra appear broad and featureless with respect to perylene **Figure 5**.

The Franck-Condon principle may be diagrammatically shown **Figure 7** using solvent relaxation of a polar molecule and a polar solvent. The solvent molecules will arrange themselves into an energetically favourable conformation which minimises any repulsion of solvent to the fluorophore's (molecule which exhibits fluorescence) dipole. When the fluorophore absorbs a photon, its excited state dipole may face a different direction to the ground state dipole. As absorption is a very rapid process $\approx 10^{-15}$ s this results in an unfavourable arrangement of the excited state known as the S_1^{FC} state. Solvent molecules will then act to re-orientate themselves around the fluorophore's excited state so that the excited state reaches an energetically favourable configuration S_1^{REL}. Recalling that the dimensions of solvent molecules such as water are much smaller than the fluorophore itself. The fluorophore will remain in this excited state $\approx 10^{-10}$-10^{-7} s until it spontaneously emits a photon and returns to the ground state. The solvent molecules in this ground state S_0^{FC} will once again be arranged in an unfavourable configuration. The solvent molecules will once again act to re-orientate themselves around the fluorophore's ground state so that the ground state reaches an energetically favourable configuration S_0. The net result is that the solvent relaxation broadens the vibrational bands to the extent that separate vibrational bands may be indistinguishable. There is also an increased red-shift than that for a non-polar molecule in a non-polar solvent.
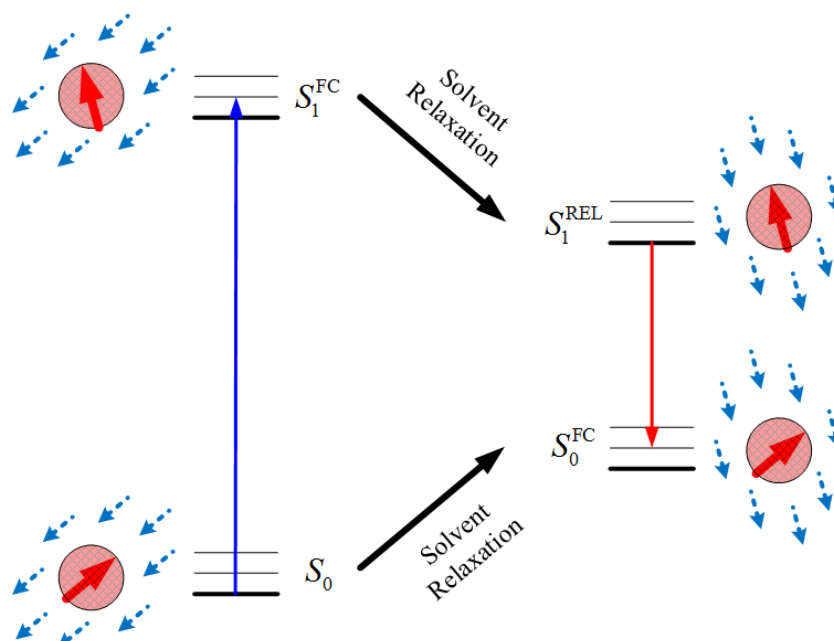
Figure 7: Illustration of the Franck-Condon principle of a polar molecule in a polar solvent.[4] The wavelength red shift between absorption and emission increases with respect to solvent polarity, the magnitude of the fluorophores dipole and the greater the difference between the absorption and emission dipole.

Although the case was made for a polar fluorophore and polar solvent. This phenomenon occurs to a lesser extent in systems with non-polar fluorophores and non-polar solvents. The lines in **Figure 5** are not infinitely narrow and their thickness is temperature dependent. The difference in energy between S_0 and S_1^{FC} or S_1^{Rel} and S_0^{FC} and thus the Stokes shift is therefore dependent on the chemical environment. Fluorescence emission therefore occurs from the lowest vibrational state of S_1. The emission of a photon itself is a spontaneous process but the fluorophore can remain in an excited state for some time $\sim 10^{-10}$-10^{-7} s before emission occurs. To simplify the photophysics the ideal simplest case **Figure 8** will first be considered and then be built up later accordingly. At $t=0$ there will be an initial population of excited molecules $[M^*](0)$ which will fall as a function of time according to the rate equation:

$$\frac{d[M^*]}{dt} = -k_M[M^*] \qquad (8)$$

---

[4] The Franck Condon principle makes the assumption that vibrational levels are preferred which correspond to a minimum change in the nuclear co-ordinates. This assumption may be used because the proton or neutron mass is ~1870 times larger than that of an electron and absorption is a very fast process.
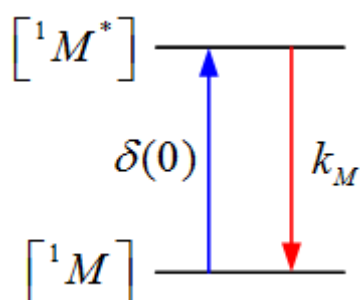
Figure 8: In the ideal simplest case a fluorophore is excited from ground state to an excited state via a δ-pulse at time $t=0$ and can only return back to ground via radiative emission characterised by the decay constant k_M.

Where k_M (s^{-1}) is the rate of decay. Providing that k_M isn't itself time-dependant i.e. that k_M is a rate constant, the solution to the above differential equation is an exponential decay:

$$\left[M^*\right](t) = \left[M^*\right](0)\exp(-k_M t) \tag{9}$$

The molecular decay constant can be inverted and instead expressed as a decay time where:

$$\tau_0 = \frac{1}{k_M} \tag{10}$$

In addition, as the fluorescence intensity is proportional to the number of molecules eqn. (9) can be re-expressed as:

$$I(t) = I_0 \exp\left(-\frac{t}{\tau_0}\right) \tag{11}$$

The molecular lifetime τ_0 is typically of the order of 1-100 ns. However, it's worth emphasising the statistical nature of this value, as very few molecules will emit photons at exactly τ_0 and there will be many molecules which exhibit individual decay times shorter and longer than τ_0 respectively. The molecular lifetime of the molecule τ_0 can be determined experimentally by measuring the time the fluorescence intensity takes to reach e^{-1} of its original value I_0 at $t=0$ [59]. Changes in the immediate microenvironment of the fluorophore such as solvent, viscosity, temperature, pH etc. will influence the steady-state spectra and the decay time. It is this sensitivity that is commonly taken advantage of when using fluorescence measurements to probe a system. The way each fluorophore interacts with its chemical environment is dependent on the chemical structure of the fluorophore and as a consequence a large number of commercial dyes are available for customised studies [60,61]. A more detailed Jablonski diagram **Figure 9** can now be used to depict additional processes involved in fluorescence spectroscopy [54,62].
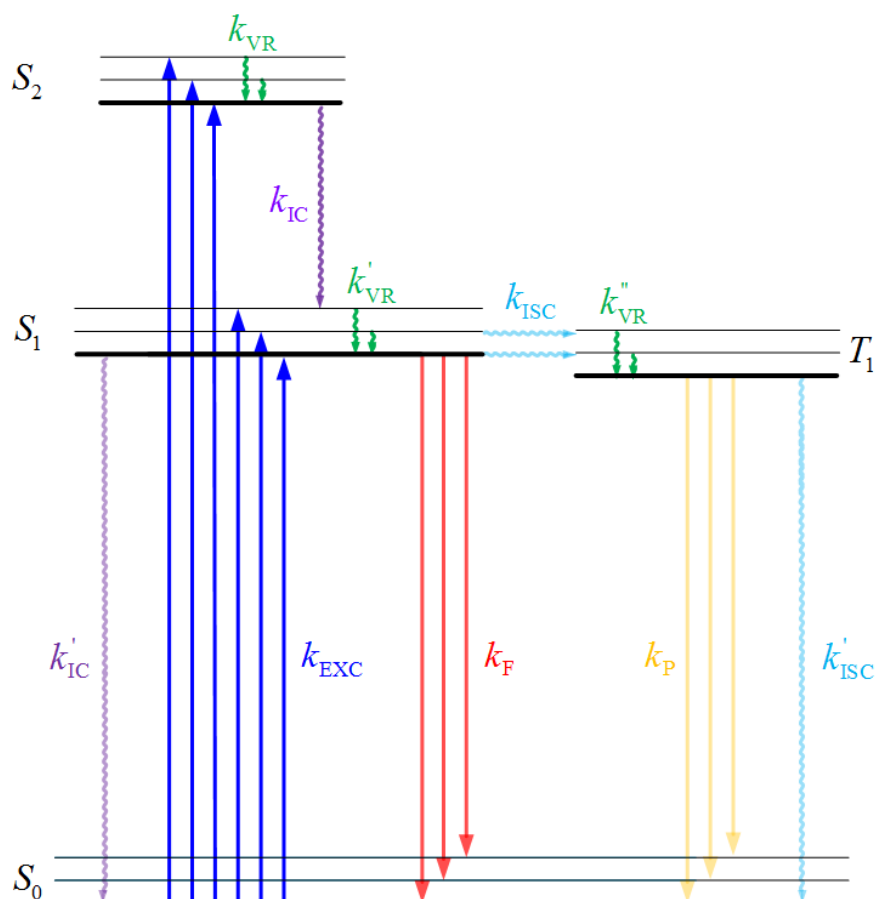
Figure 9: A simple Jablonski diagram denoting the singlet electronic states S_0 (the fundamental ground electronic state), S_1, S_2, … and the triplet states T_1, T_2, … For each electronic state there are associated vibrational levels. Straight lines denote radiative transitions and squiggly lines denote non-radiative transitions.

First of all absorption occurs with a rate $k_{EXC} \sim 10^{15}$ s^{-1}. Excitation may lead to a transistion to a S_2 singlet state or higher if this happens vibration relaxation and internal conversion (non-radiative transition with conservation of spin) will rapidly dissipate any additional energy bringing the system to the S_1 singlet state $k_{VR} + k_{IC} \sim 10^{10}$-$10^{14}$ s^{-1}. Vibrational relaxation will then occur from higher vibrational levels to the lowest vibrational level of S_1 $k'_{VR} \sim 10^6$-10^7 s^{-1}. At the lowest vibration level of S_1 three phenomena can happen, fluorescence with red-shifted Stokes emission with $k_F \sim 10^7$-10^9 s^{-1}, internal conversion (non-radiative transition with. conservation of spin) with $k_{IC} \sim 10^6$-10^7 s^{-1}. Internal conversion and solvent relaxation of higher energy states to S_1 is substantially faster than S_1 to S_0 due to the higher energy gap. Another non-radiative transition may occur, that is intersystem crossing to the triplet state T_1 although this transition is forbidden from the spectroscopic rule $\Delta S \neq 0$ forbidding spectroscopic transitions between singlet and triplet states, there is no prohibition if the transfer between the excited states occurs for instance kinetically via radiationless transitions induced by collisions. Such transfer is known as

13

intersystem crossing and can only occur close to the crossover point of the two potential curves [55,63] as shown in **Figure 10**.
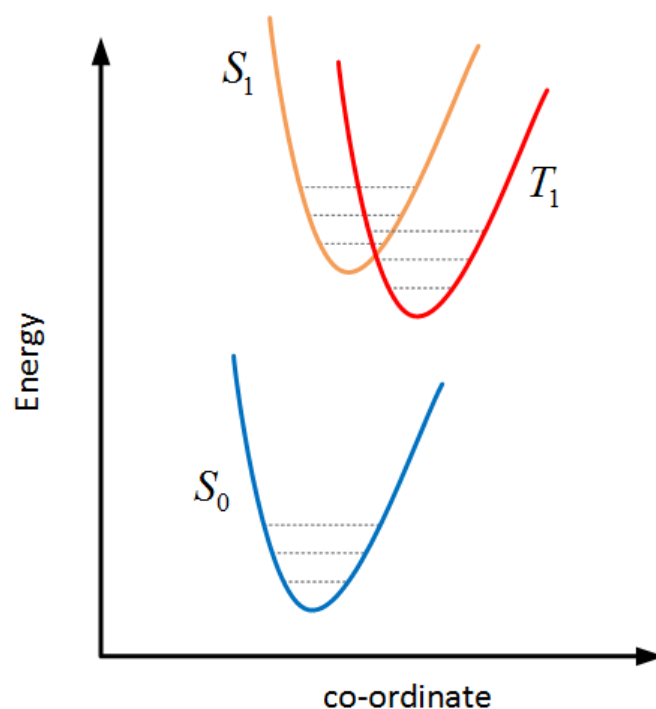
Figure 10: Potential curve of the ground singlet state S_0 (blue), 1st singlet excited state S_1 (orange) and 1st triplet state T_1 (red). Intersystem crossing can occur at the overlap of S_1 and T_1.

These transitions become weakly allowed and are able to compete with the rate of fluorescence $k_{ISC} \sim 10^5\text{-}10^8 \text{ s}^{-1}$. Transfer between the excited states may be enhanced kinetically via radiationless transitions induced by collisions. Phosphorescence emission can occur from this T_1 triplet state to the S_0 singlet ground state, again this weakly allowed so phosphorescence has a smaller rate than fluorescence $k_P \sim 10^{-2}\text{-}10^6 \text{ s}^{-1}$. Phosphorescence processes usually have a greater redshift than fluorescence processes. Its also possible to get non-radiative intersystem crossing $k'_{ISC} \sim 10^5\text{-}10^8 \text{ s}^{-1}$ to the ground single state S_0. The non-radiative interactions in the Jablonski diagram can influence the fluorescence decay. **Figure 8** may be built up to accommodate more complicated situations, which are commonly found within experimental systems. For instance, the addition of a non-radiative decay rate k_{IM} and the effect of collisional quenching $k_{QM}([Q])$.
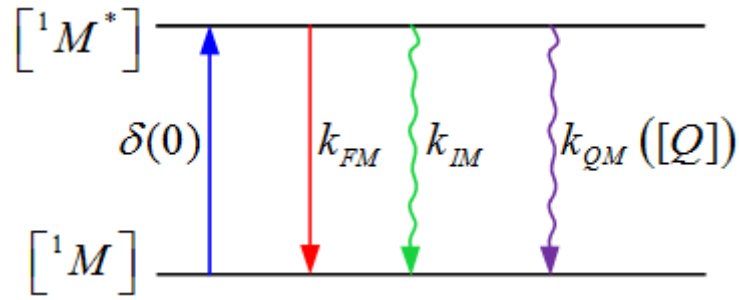
Figure 11: A fluorophore is excited from ground state to an excited state via a δ-pulse at time $t=0$ can return back to ground via radiative emission characterised by the decay constant k_{FM} or via a non-radiative mechanism with a decay rate k_{IM} or to collisional quenching $k_{QM}([Q])$ which is a function of the concentration $[Q]$ of quencher species.

Providing that none of these rate constants have a time-dependence the solution is the same form as eqn. (11):

$$I(t) = I_0 \exp\left(-\frac{t}{\tau_{FM} + \tau_{IM} + \tau_{QM}([Q])}\right) \qquad (12)$$

Grouping together all non-radiative processes $k_{NR} = k_{IM} + k_{QM}[Q]$ and $k_M = k_{FM} + k_{NR}$ then the relation of the rates gives the quantum yield Φ i.e. the ratio of the emitted photon rate to the photon absorption rate [64]. Quantum yield is quite a difficult quantity to accurately determine because it requires detecting fluorescence photons in all directions with an integration sphere.

$$\Phi = \frac{k_{FM}}{k_{FM} + k_{NR}} = \frac{k_{FM}}{k_M} = \frac{\tau_{FM} + \tau_{NR}}{\tau_{FM}} = \frac{\tau_M}{\tau_{FM}} \qquad (13)$$

One thing that's important to mention here is that the molecular rate constant k_M or its inverse the molecular lifetime τ_0 is usually the only fluorescence quantity measured directly. The other rate constants are usually inferred by looking at changes in the measured fluorescence lifetime τ and relating to variations in experimental conditions such quencher concentration. The simplest model for quenching of fluorescence for a mono-exponential decay is the Stern-Volmer relation [65,66]:

$$\frac{F_0}{F} = \frac{\Phi_0}{\Phi} = \frac{\tau_0}{\tau} = 1 + k_Q \tau_0 [Q] \qquad (14)$$

Where, F_0, Φ_0 and τ_0 are the fluorescence intensity, quantum yield and lifetime in the absence of quencher and F, Φ and τ are the fluorescence intensity, quantum yield and lifetime in the presence of quencher. One of the most common and efficient quenchers is

15

molecular oxygen which has a triplet ground state, is paramagnetic and is an electron acceptor [67]. To accurately determine the radiative fluorescent decay time of a fluorophore in a solvent τ_0, molecular oxygen must be removed by nitrogen purging for example [40,64,68].

There are other radiative processes which are of significance to fluorescence spectroscopy these are the scattering processes **Figure 12**. Rayleigh scattering is a form of elastic scattering and occurs on a similar time-scale to absorption $\sim 10^{-15}$ s. Raman scattering is inelastic and also occurs on $\sim 10^{-15}$ s time-scale, a molecule can be identified via its Raman spectrum [69–72]. Raman is however very weak compared to Rayleigh and other emissive processes like fluorescence.
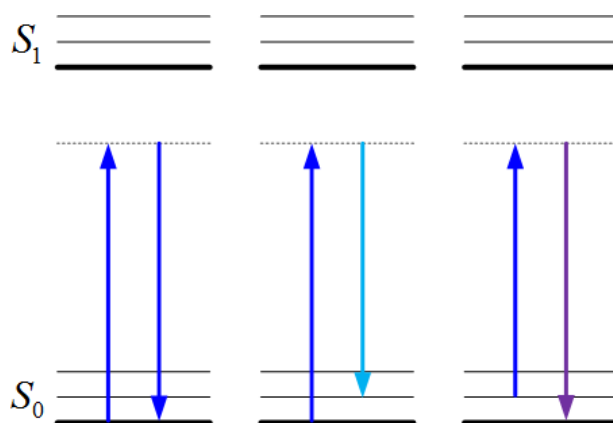
Figure 12: Depiction of Rayleigh, Stokes Raman and Anti-Stokes Raman scattering. In Rayleigh scattering a photon interacts with the molecule and the molecule reaches a virtual state. It is then bounced off the molecule without any change in wavelength. In Stokes Raman scattering the photon transfers some energy to a vibrational state of the molecule. As a consequence, the photon which scatters is lower in energy and is slightly red shifted. This interaction is quantised and the Raman shift can be used as a molecular finger print [73]. In Anti-Stokes Raman if the molecule is already at a higher vibration state due to thermal energy it may interact with a photon and transfer additional energy to the photon. Raman signals are extremely weak, usually $\sim 10^7$ photons are Rayleigh scattered for a single photon that is Raman scattered. Anti-Stokes Raman is even less frequent than Stokes Raman due to the low thermal probability due to the fact that over 99 % of the molecules are in the zero-point vibrational level of energy as discussed earlier. Raman is usually negligible compared to fluorescence as the Raman scattering cross-section is 10 orders of magnitude less than the fluorescence cross-section.

A fluorophore is an object that absorbs energy of a specific wavelength and then re-emits energy at a different, but equally specific wavelength. The wavelength and quantity of emitted energy of the fluorophore depend on both the chemical structure of the fluorophore and its immediate chemical environment. The most well-known and brightest fluorophores

are organic dyes which absorb and emit in the near ultraviolet and visible region i.e. the wavelength range between 300 and 700 nm. Such fluorophores possess conjugated aromatic groups which have π electrons available. These electrons can easily be promoted with near ultraviolet and visible light. As a rule of thumb organic dyes with smaller structures are more likely to emit in the UV and larger structure fluorophores will typically emit further into the red. Fluorophores that are rigid will have higher quantum yields as the bending of a fluorophore can leads can favour non-radiative pathways for de-excitation [74]. Conversely solvent molecules such as water in comparison would require a much higher energy for unfavourable bond breakage in order to promote an electron and as a consequence appear colourless as they do not absorb or emit in the visible region [75].

Examining the electrical part of $\vec{M}_{ji}$ in **Equation (3)** and returning to the simple schematic **Figure 3** it is easy to visualise the role polarization plays in regarding the probability of a transition. If the wave of incident light **Figure 3** had not been polarized alongside the dipole moment of the ground state, the electron wouldn't have resonated with the incident light and hence no absorption would have taken place to the excited state.
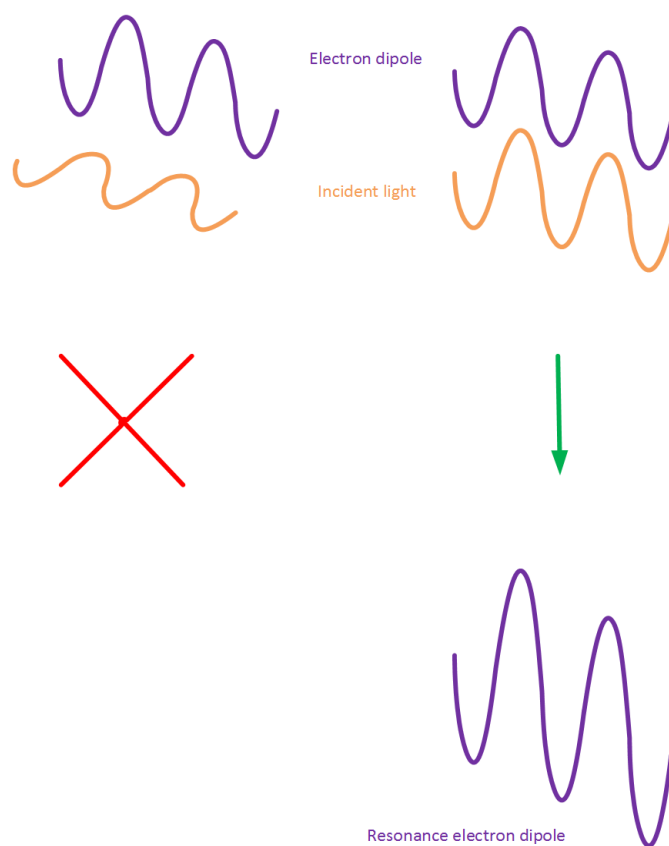

Figure 13: Simple schematic depicting the importance of polarized light with respect to an electronic transition. If the light is polarized in another orientation the electron will not

resonate with the light and a transition is unlikely to occur. If the light is polarized with the electron, the electron will resonate resulting in a transition.

In other words, there is a $\cos^2(\theta_A)$ dependence on the probability of a transition where θ_A is the angle between the fluorophore's transition moment and the electric field vector of the incident light **Figure 14**. This principle known as photoselection has an important implication for fluorescence measurements when a polarized light source is used.
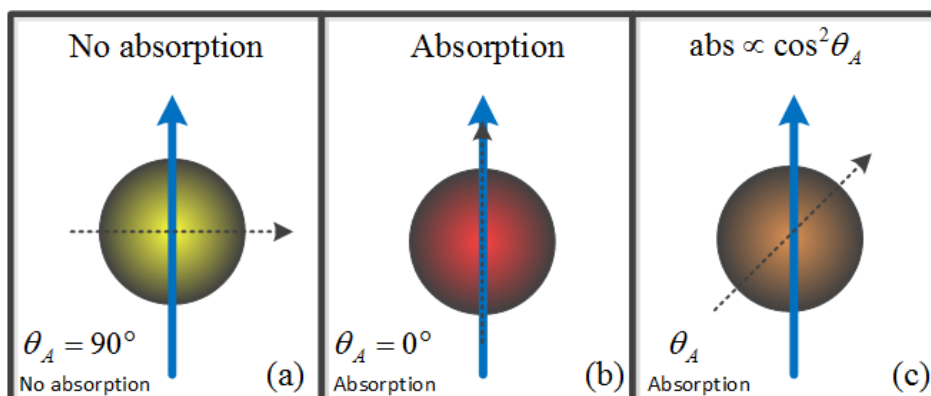
Figure 14: Illustration of photoselection. (a) a fluorophore's transition moment is perpendicular to the electric field vector and is not excited (yellow), (b) a fluorophore's transition moment is parallel to the electric field vector and is excited (red) and (c) a fluorophore has a random orientation and has a $\cos^2(\theta_A)$ probability of absorbing a photon.

Figure 15 illustrates the effect of a single pulse from a polarized light source on an assortment of randomly orientated unexcited yellow dye molecules suspended in solution. The subset with parallel absorption dipoles to the incident light get preferentially excited leading to an initial anisotropy of excited molecules at time zero. Assuming parallel absorption and emission dipoles which many molecules have this leads to an initial emission anisotropy depicted in red. This emission anisotropy may be lost due to thermal collisions with solute molecules which are depicted in purple. The summation of solute molecules colliding with dye molecules will result in a random "walk" of the dye molecules known as Brownian motion. This Brownian motion reduces the population of dye molecules which retain the initial polarization. Eventually enough dye molecules are introduced into other orientations so the emission becomes unpolarized. With Brownian motion objects will move faster if solute molecules are supplied with more thermal energy and move slower if the viscosity of the solvent is decreased. Larger objects will move more slowly than smaller objects. The rotational correlation time is an inverse measure of Brownian motion defined as the time it takes for a molecule to rotate 1 radian and is related to the hydrodynamic volume by the Stokes-Einstein equation:

18

$$\phi = \frac{\eta V}{k_B T} \qquad (15)$$

where k_B is Boltzmann's constant, T is the temperature in K, η is the viscosity in Pa and V is the hydrodynamic volume in m^3. The importance of polarization in fluorescence measurements will be discussed in a greater detail in **2.2.7 Steady State Fluorescence Anisotropy**.
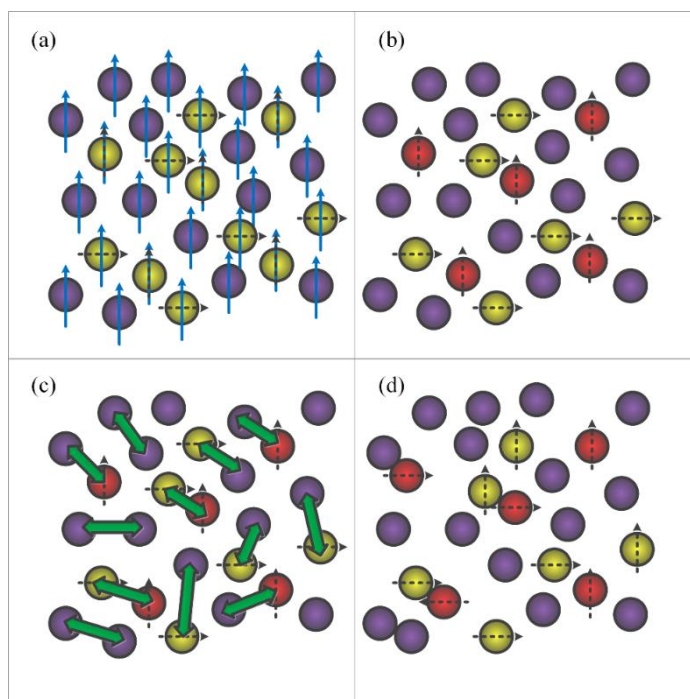
Figure 15: (a) The purple molecules illustrate the solute molecules and the yellow molecules illustrate fluorophores. In real life solute molecules are typically much smaller than fluorophores and for in the regime of fluorescence measurements there will be a much higher proportion of solute molecules to fluorophores than illustrated. The dashed arrows indicate the absorption dipole of the fluorophores. An electric field from a polarized laser source illustrated as a blue line. (b) Photoselection of the fluorophores occurs, that is the preference for absorption dipoles parallel to the electric field of the excitation source. Excited fluorophores are illustrated in red. (c) As solutions are dynamic, that is millions of collisions are occurring between solute molecules and fluorophores every second the fluorophore will randomly move and randomly rotate. Any change in direction of the transition moment during the lifetime of the excited state will cause this anisotropy to decrease. i.e. will induce a partial or total depolarisation of the fluorescence. (d) If the fluorescence decay time is long enough these collisions will return the system back an isotropic state with complete depolarized fluorescence.

It should be noted that the fluorophore is rarely measured in vacuum but usually dissolved in a solvent therefore solvent effects will come into play introducing solvent specific non-radiative and collisional mechanisms. The fluorescence lifetime of a fluorophore may differ substantially between solvents particularly in a polar solvent such

19

as water and a non-polar solvent such as ethanol [76]. It should be appreciated that the fluorescence lifetime is an extremely sensitive measurement, slight changes on solvent purity, in dissolved oxygen and in temperature may alter the fluorescence lifetime. All of these parameters should be held constant when comparing fluorescence lifetime data from instrument to instrument or from lab to lab. The degree of sensitivity of each fluorophore to environmental changes can be a blessing or curse depending on the application of the fluorescence measurement. The sensitivity of a fluorophores fluorescence lifetime to environmental changes is naturally dependent on its chemical structure and hence there are an array of fluorophores available to customise a study [40,77,78]. It should be mentioned that in most applications particularly the vast application area of the life sciences, removing molecular oxygen is impractical as doing so takes time and would also destroy the sample, therefore the quenching effect of oxygen is typically ignored alongside the effect of any non-radiative mechanisms arising from the solvent. In many measurements e.g. food quality measurements it is sufficient to only measure the change in τ under standard conditions, these changes can then be compared to well characterised control data to determine the quality of the food. Up until this point only a single fluorescence lifetime has been considered, it should be noted however that not all fluorophores have a single radiative mechanism and therefore may exhibit multiple decay times. Moreover, since the fluorescence decay is extremely sensitive to its immediate chemical environment, a fluorophore with a mono-exponential decay may exhibit multiple decay times when present in two extremely different chemical environments that are simultaneously measured for example a mixture of water and oil or within a protein where the fluorophore experiences a variance in exposure to water and/or rigidity. A vast number of fluorophores are commercially available and globally under investigation [79]. Commercial fluorophores are in general tailored to exhibit desired photophysical traits for specific applications and likely to possess chemical linkers when necessary [80]. Dyes are designed which exhibit decay times sensitive to pH [81], ions [82], temperature [83], and rotors sensitive rigidity/viscosity [84–87] as well as an array of specific analytes. It should be stressed that selecting the correct physical model and fluorophore [88] are of paramount importance for the success of any fluorescence application.

2. Experimental Details

This section gives an introduction to fluorescence instrumentation alongside some useful calibration checks. It should be stressed that fluorescence is a multi-parameter phenomenon that can be described by a number of factors such as intensity, polarisation, excitation wavelength and emission wavelength, position in x, y and z, time-scale and quantum yield. This section discusses some of the basic fluorescence measurements and builds up the more advanced techniques which are usually combinations of basic measurements i.e. multi-parameter measurements.

2.1 Absorbance – Spectrophotometer

When dealing with a fluorescence measurement the acquisition of an absorbance spectrum via a spectrophotometer as shown is usually one of the first measurements undertaken. Strictly speaking absorbance is not a fluorescence measurement but it should be thought of as complementary to a fluorescence measurement.
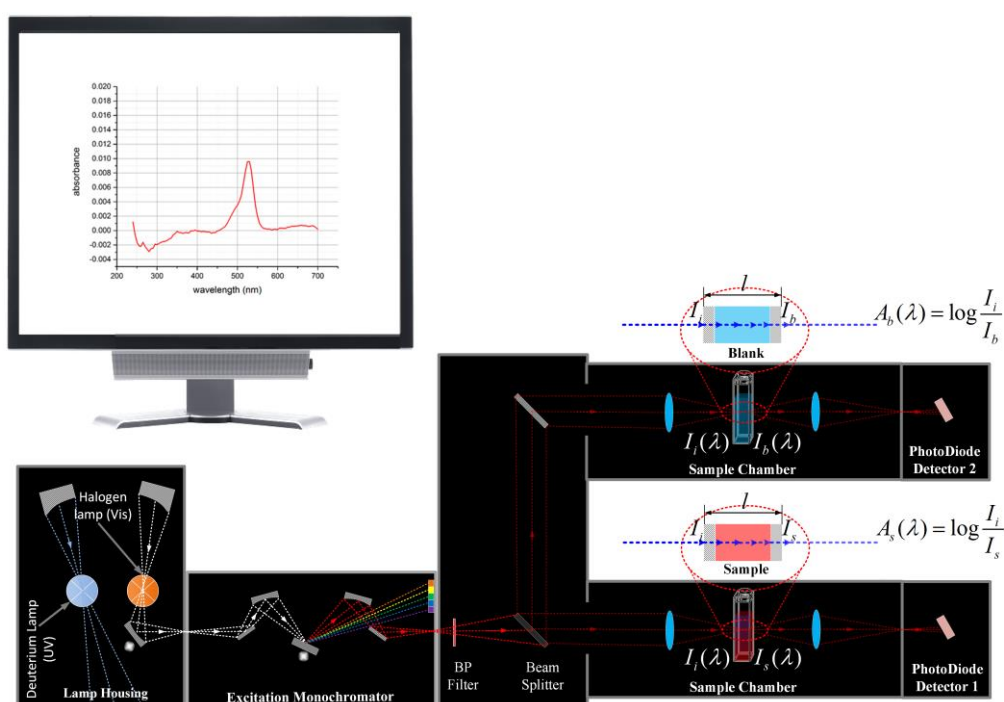
Figure 16: Experimentally the spectrophotometer consists of one or multiple steady state light sources; typically, a 25 W deuterium lamp for UV excitation 190-330 nm and a 20 W halogen lamp for Visible/NIR excitation 330-1100 nm. The light emitted passes through an excitation monochromator[5] and through the sample to the detector.[6] The intensity of the

---

[5] Usually a set of bandpass filters are present on a filter wheel in order to prevent second order effects.
[6] In this case a circular-cage type photomultiplier tube is illustrated.

light passing through the sample is recorded and this is compared with a baseline measurement to obtain the samples absorbance or transmittance [50,89].

Figure 16 shows double compartment spectrophotometer; light from the excitation monochromator is split by a beam splitter to the sample and baseline compartments. Two detectors are used to measure the sample and blank simultaneously. The simultaneous measurement reduces the change of error due to lamp fluctuation. In other cases a set of choppers can be used [90]. The principle of the spectrometer instrument is shown in **Figure 16**. The absorbance $A(\lambda)$ is defined as:

$$A(\lambda) = \log \frac{I_0(\lambda)}{I(\lambda)} = -\log T(\lambda) \tag{16}$$

where $I_0(\lambda)$ is the incident intensity, $I(\lambda)$ is the departing intensity and $T(\lambda)$ is the transmission. Experimentally a baseline measurement is taken to compensate for the absorbance/transmission of the solvent and the cuvette.

$$A(\lambda) = A_s(\lambda) - A_b(\lambda) = \log \frac{I_s(\lambda)}{I_i(\lambda)} - \log \frac{I_b(\lambda)}{I_i(\lambda)} = \log \frac{I_s(\lambda)}{I_b(\lambda)} \tag{17}$$

where $I_i(\lambda)$ is the incident intensity on the cuvette, $I_s(\lambda)$ is the intensity after passing through the sample and $I_b(\lambda)$ is the intensity after passing through the baseline see schematic **Figure 16**. The Beer-Lambert law is a mathematical means of expressing how much light is absorbed by matter (liquid solution, solid or gas). The law states that the amount of light emerging from a sample is diminished by three physical phenomena; the amount of absorbing material or concentration c, the optical path length l which is the distance the light must travel through the sample and the extinction coefficient of the sample ε, which is a measure of the probability that a photon of a certain wavelength will be absorbed by the sample.

$$A(\lambda) \approx \varepsilon(\lambda)lc \tag{18}$$

where l is the length of the cuvette (in cm), c is the concentration (in mol L^{-1}) and $\varepsilon(\lambda)$ is the molar absorption coefficient (in L mol^{-1} cm^{-1}). The absorbance spectrum highlights the prime area(s) for excitation. It should be noted that the extinction coefficient and hence absorption are strongly wavelength dependant and so should be quoted with respect to wavelength[7]. Fluorescence measurements are generally taken at low concentrations of

---

[7] It should be noted that the extinction coefficient of common fluorophores lies generally within the range of 10^4-10^5 L mol^{-1} cm^{-1} and is usually quoted by dye manufacturers for a specific solvent. Interaction of the

fluorophore typically within the nM to µM regime which satisfy $A \leq 0.1$ and hence the linear relationship with concentration in accordance to the Beer-Lambert law[8]. At higher concentrations non-linearity effects will come into play due to the inner filter effect and
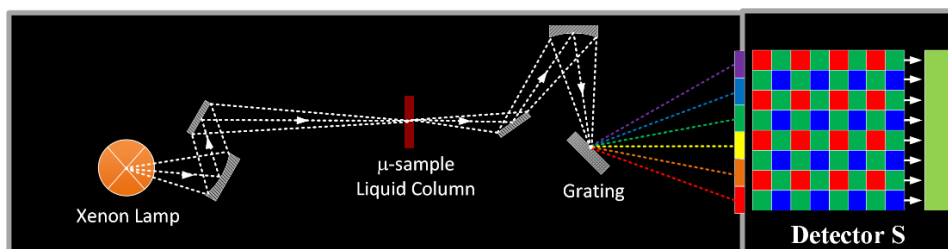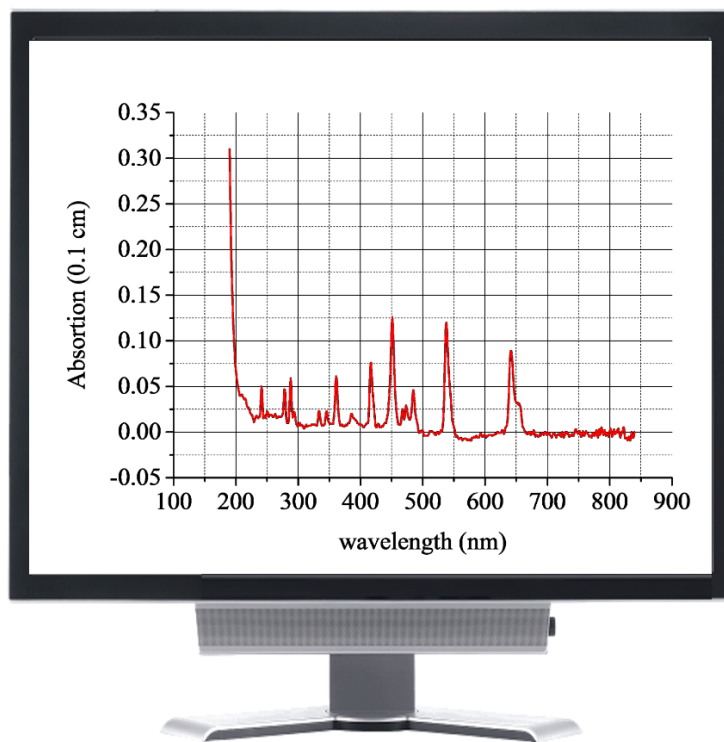
Figure 17: The Thermo Scientific NanoDrop 2000c is a short pathlength spectrophotometer. The sample is a 1-2 µl drop which forms a liquid column between two ends of the optical fibre held together by surface tension giving a path length of 0.05-0.10 mm. For excitation a white light source is used and directly focused onto the sample's liquid column. Light from the sample is dispersed onto a grating which is collected by a multi-channel Charged Coupled Device (CCD) detector. The working wavelength regime of the NanoDrop 2000c is 190-840 nm with a spectral resolution of 1.8 nm. The integration time is usually fixed to 5 s. The CCD and PMT will be discussed in more detail in subsequent sections.

---

fluorophore with other molecules (e.g. a different solvent) can change the extinction coefficient and hence lead to changes in peak intensity and a shift in peak wavelength of the absorption spectra [61].

[8] For the Beer-Lambert law to be valid it is assumed the sample is homogeneous, which is an acceptable assumption for cuvettes containing liquid solution as mentioned in this discussion, but one should note that it will break down for non-linear systems where a more difficult model will be required.

also from aggregate formation; some fluorophores will dimerise for example [64]. Higher concentrations can be measured by using shorter path length cuvettes. One innovative solution however is the Thermo Scientific NanoDrop 2000c [91] **Figure 17**. In this instrument the sample volume is a 1-2 μl drop. A liquid column is created between two ends of the optical fibre held together by surface tension and gives a path length of 0.05-0.10 mm. A white light source is used directly to excite the sample. After the beam passes through the sample a grating is used to separate the individual wavelengths of light onto a CCD multi-channel detector. Typically, a 5 s integration time is used.

Multiple spectrophotometers were commonly employed throughout the work in this thesis. A Perkin Elmer Lambda 2, a Perkin Elmer Lambda 25 which both had UVWinLab version 6.0 instrument acquisition software, a Thermo Scientific NanoDrop 2000c which had NanoDrop 2000c instrument acquisition software and a Shimadzu UV-1800 Spectrophotometer using the inbuilt front panel. Spekwin32 analysis software was used to process spectra [92]. The Horiba Scientific Aqualog/Dual FL was also used which is able to simultaneously measure absorbance and emission spectra and will be discussed later.

2.1.1 Spectrophotometer Calibration
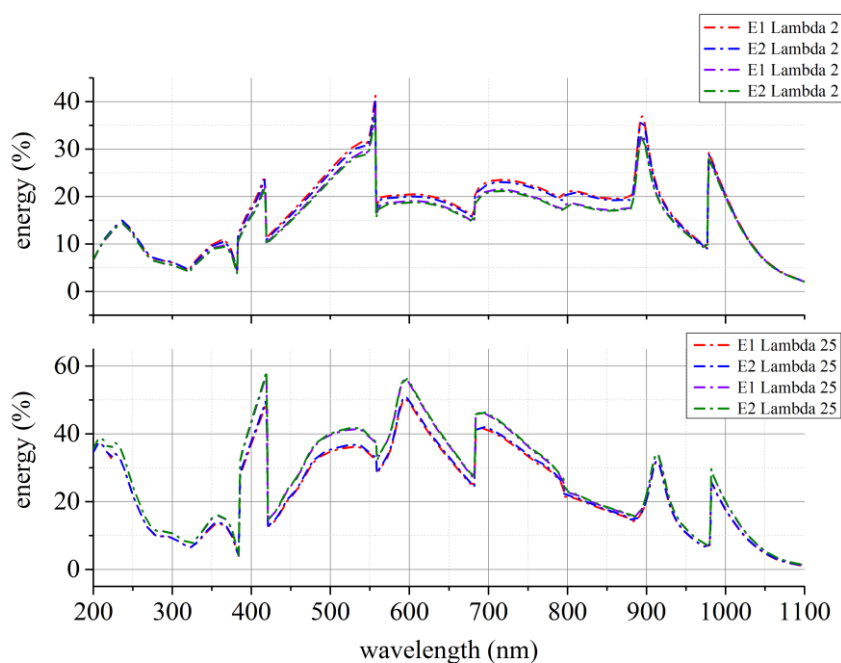

Figure 18: The energy spectra[9] E1 and E2 measured by the two photodiodes 1 and 2 respectively of a Perkin Elmer Lambda 2 and Lambda 25 **Figure 16**. These are measured without a sample or blank 5 minutes after powering up and 30 minutes after powering up.

---

[9] The sharp lines present in the energy spectra are due to the change-over of bandpass filters during measurement.

The spectra are observed to be stable with time and there is little bias for one compartment over the other. The scan was run from 200-1100 nm in 1 nm increments with an integration time of 0.125 s. The energy scan is typically computed as a percentage where 100 % corresponds to the upper limit of the detectors linear regime. Before measurement the shutter is closed and the level of dark counts are measured for 10 times the integration time. The average dark counts otherwise known as the dark offset is subtracted from the energy scans. The minimum energy for the deuterium lamp is observed at 323 nm and for the halogen lamp is 382 nm. If these values are not above 2 % the lamps should be replaced.

In order to measure absorbance spectra, the energy output of the lamp with respect to wavelength[10] needs to be sufficient and stable over the time period of measurement. It is worthwhile periodically running an energy scan as shown in **Figure 18** of the sample E1 and the reference E2 compartments to ensure that they are both stable and that there is no major bias for one compartment over the other c.f. **Figure 16**. If the E1 and E2 energy scans are significantly different then it is worthwhile trying to align the heights of the sample chambers. Before an absorbance or transmission spectra is measured, one has to perform a blank beam measurement; the blank beam measurement essentially measures both E1 and E2 in the background[11] but doesn't display the data to the user. This background measurement takes into account any slight bias between the energy of the compartments and removes it from the final absorbance or transmission spectra. Although E1 and E2 are typically measured without cuvettes and solvent, it is more insightful to measure the energy scan using matched cuvettes and solvent to that used for the sample. If micro-cuvettes are being used which partially mask off and hence constrict the size of the beam, these should be placed in the sample compartment before doing the blank energy scan. Results will suffer a high degree of inaccuracy otherwise.

Holmium oxide has been used as a wavelength calibration standard for over 4 decades as it possesses a number of sharp lines within the visible region of the absorbance spectrum [93]. Wavelength calibration of the spectrophotometers **Figure 19** was carried out by using an empty quartz cuvette as a reference and filled with a 5% weight per volume solution of holmium oxide in 1.4 N perchloric acid[12]. For spectrophotometers with a longer

---

[10] As absorbance is measured as a ratio the deviations in measured energy output of the lamp are negated and do not distort the spectra.

[11] For microcuvettes, it's recommended to insert the empty micro-cuvettes into the sample compartments when carrying out the blank beam measurement. This allows one to measure the energy going through the micro-cuvette which will be significantly different from the energy going through the empty compartments.

[12] In the NanoDrop the baseline was empty and 10 µl of 5% weight per volume solution of holmium oxide in 1.4 N perchloric acid was measured.

working wavelength range it is possible to do a more in depth calibration using a mixture of holmium oxide, samarium oxide, dydprosium oxide and erbium oxide [94–96].
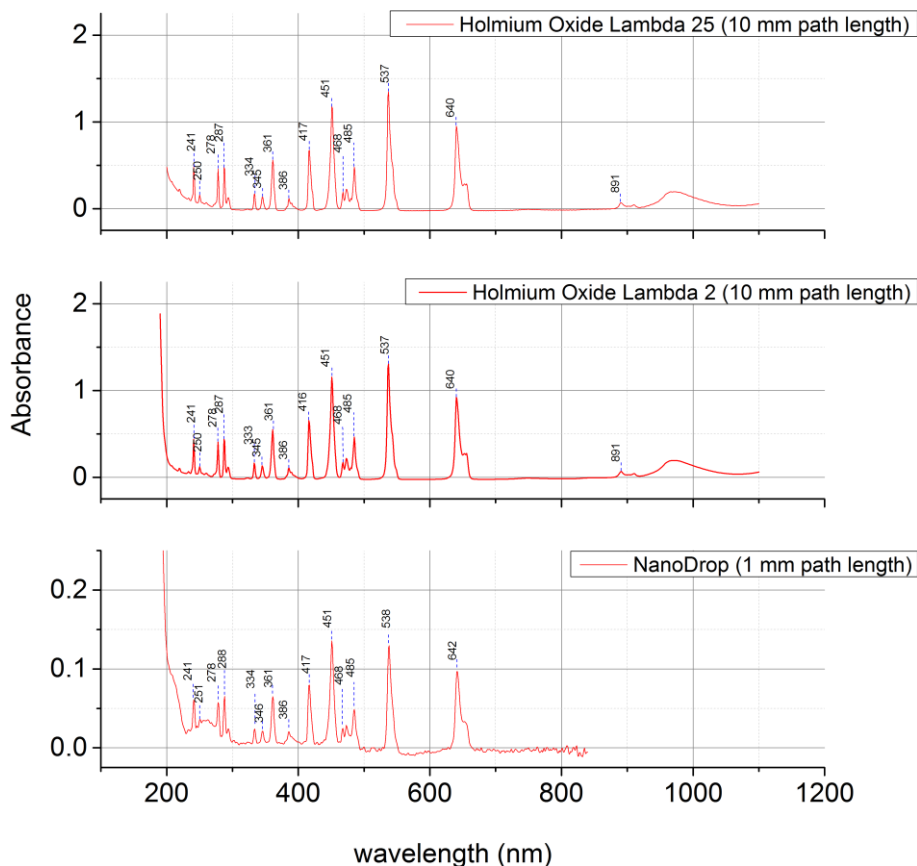
Figure 19: Absorbance spectra of a 5% weight per volume solution of holmium oxide in 1.4 N perchloric acid (BDH Chemicals) measured using a Perkin Elmer Lambda 25, Perkin Elmer Lambda 2 and NanoDrop averaged over 3 measurements. The accepted wavelengths are 241.1±0.1, 249.7±0.1, 278.7±0.1, 287.1±0.1, 333.4±0.1, 345.5±0.1, 361.5±0.1, 385.4±0.2, 416.3±0.2, 450.8±0.2, 452.3±0.2, 467.6±0.2, 485.8±0.2, 536.4±0.2, 641.1±0.2, 891±1, 1159±1 and 1190±1 n m respectively [97,98]. The working range of the Lambda 2 and 25 is between 190-1100 nm meaning the last 2 peaks could not be measured on the Lambda 2 and 25. The monochromators were stepped in 1 nm increments with a 0.125 s integration time. The NanoDrop 2000c was ran over its working range 190-840 nm using a 5 s integration time. This meant the last 3 peaks could not be measured on the NanoDrop. Since the Lambda 2 and Lambda 25 were stepped in 1 nm increments and the NanoDrop 2000c has a 1.8 nm spectra resolution the 2 peaks at 450.8 nm and 452.3 nm are indistinguishable and so only one peak at 451 nm was measured. The results for all instruments are in good agreement to the accepted values however since the NanoDrop is designed for higher absorbance samples it yields slightly noisier data than the Lambda 2 and 25.

A number of standards may be made up to predetermined concentrations with spectroscopic grade solvent to assess the linearity of the spectrophotometer, the preferred choice for a spectrophotometer characterisation is usually potassium dichromate in 0.001 M perchloric acid [99,100]. Strictly speaking fluorescent standards are less preferred for a spectrophotometer characterisation however as this work is more focused on fluorescence spectroscopy Rhodamine 6G which has an extinction coefficient of 10.5×10^{-4} mol^{-1} L cm^{-1} in ethanol at 530 nm according to supplier data [77]. Rhodamine 6G [101] solutions of 10 known concentrations were made up which had absorbance values made up between ~0.01-0.10 **Figure 20**. The extinction coefficient was measured to be $\varepsilon = (10.66 \pm 0.04) \times 10^4$ mol^{-1} L cm^{-1} with $R^2 = 0.9999$ in a Perkin Lambda 25 spectrophotometer and $\varepsilon = (10.63 \pm 0.04) \times 10^4$ mol^{-1} L cm^{-1} with $R^2 = 0.9998$ in a Perkin Elmer Lambda 2 spectrophotometer. Results are in good agreement to literature values. The same samples will later be used to test the linearity in a fluorimeter.
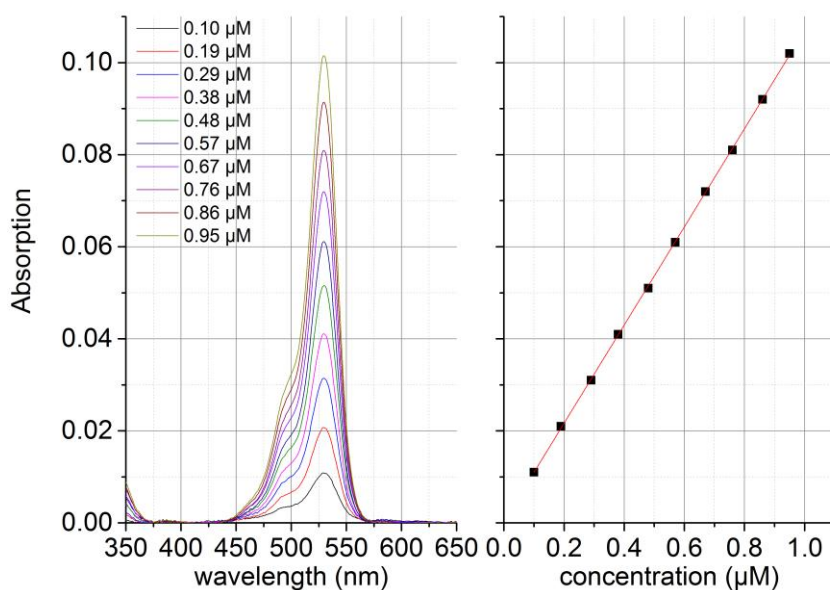
Figure 20: The absorbance spectra of Rhodamine 6G in ethanol measured using a Lambda 25 at low concentrations. The scan was run from 350-650 nm in 1 nm steps with a 0.125 s integration time was used. Data was baseline corrected and the peak absorbance was measured to be at 530 nm and observed to be linear with respect to concentration. A linear fit gave an absorption coefficient of $\varepsilon = (10.66 \pm 0.04) \times 10^4$ Mol^{-1} L cm^{-1} with $R^2 = 0.9999$. The Lambda 2 gave similar data with an absorption coefficient of $\varepsilon = (10.63 \pm 0.04) \times 10^4$ Mol^{-1} L cm^{-1} with $R^2 = 0.9998$.

2.1.2 Transmission of Optical Components and Filters

It is insightful to check the transmission spectra of any optical components used for experiments such as longpass **Figure 21**, bandpass and neutral density **Figure 23**, **Figure 24** filters as well as cuvettes **Figure 22** [102] and polarizers. Transmission spectra are usually supplied with such components making verification of the spectra a good test for the spectrophotometer. It is also important to get a good understanding of the optical components utilised as well as their working range. Absorbance and fluorescence data measured outside a component's working range is often meaningless. As the transmission spectra of such components should be constant they may also be used to quickly diagnose any defects in the spectrophotometer. In addition to the optical components mentioned above it shouldn't be forgotten that solvents likewise have an optical effect and an associated working transmission range [102,103]. The transmission spectra is also a useful check for the alignment of the system particularly the alignment of a beam when using specialised micro-cuvettes for low volumes [104]. The spectrophotometer is a useful instrument to check the transmission properties of optical components and the absorbance spectrum can be used to determine an analyte and give a measure of an analytes concentration as shown in **Figure 20**.

Figure 21: The transmission spectra of the longpass filters inventory measured using a Perkin Elmer Lambda 25 spectrophotometer ran from 200-1100 nm in 1 nm increments. A 0.125 s integration time was used. Longpass filters are usually characterised by the wavelength where they attenuate the wavelength by 50 %.

Figure 22: The transmission spectra of cuvettes inventory measured using a Perkin Elmer Lambda 25 spectrophotometer ran from 200-1100 nm in 1 nm increments. A 0.125 s integration time was used. The transmission spectra of a PMMA UV grade, which is stated to have a usable range of 280-900 nm, of a glass cuvette which is stated to have a usable range of 334-2500 nm and of a quartz cuvette which is stated to have a usable range of 170-2700 nm measured using a Perkin Elmer Lambda 2.
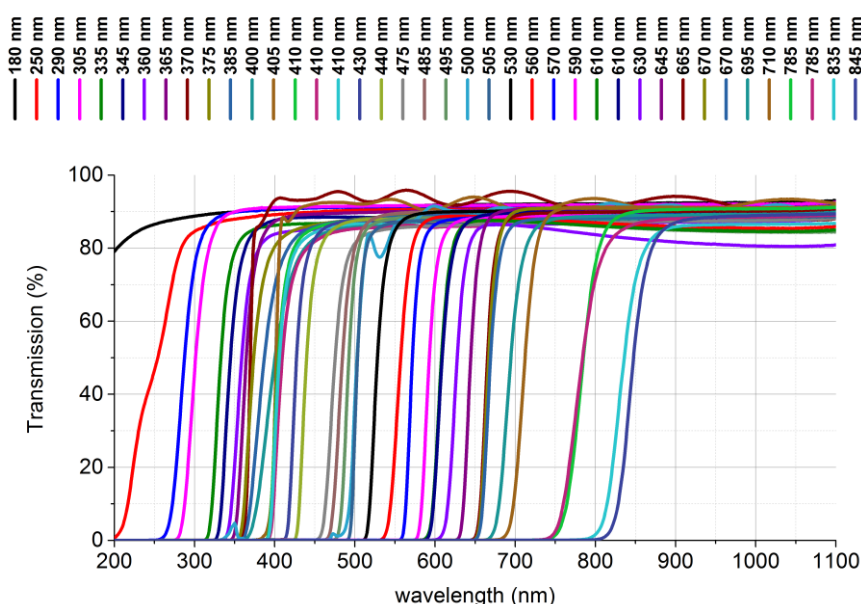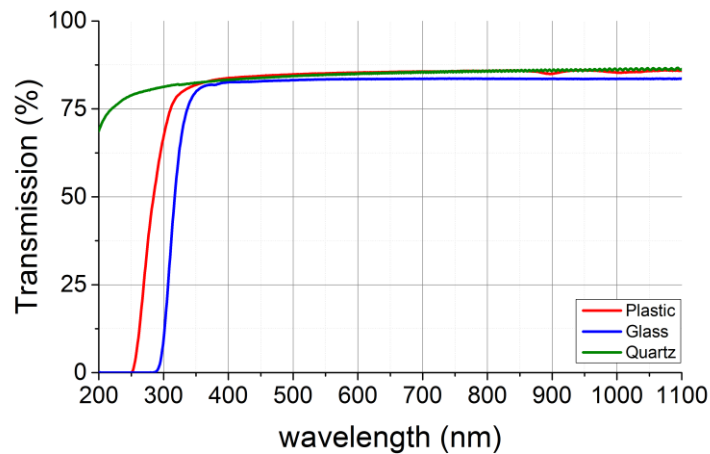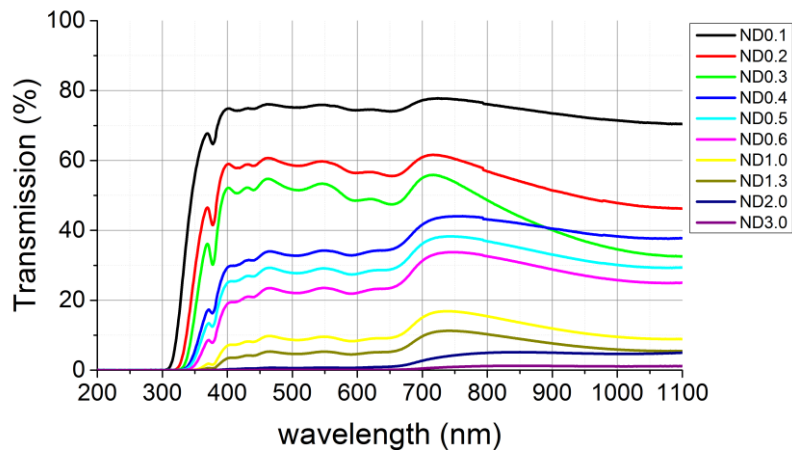

Figure 23: The transmission spectra of Schott Neutral Density filters measured using a Perkin Elmer Lambda 2 spectrophotometer ran from 200-1100 nm in 1 nm increments. A 0.125 s integration time was used. The spectra match those provided by the supplier and demonstrate that these components are unsuitable for measuring in the UV region and work optimally between 400-650 nm region.
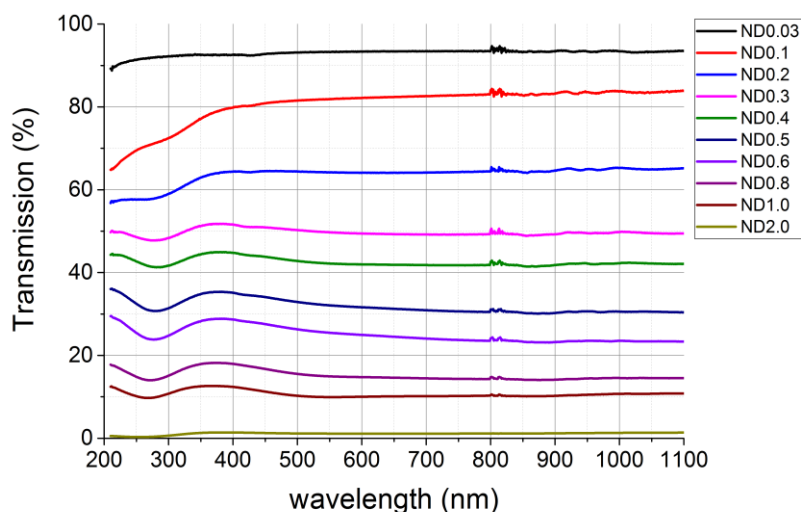
Figure 24: The transmission spectra of UV Metallic Neutral Density filters provided by the supplier which demonstrates that these components are suitable for measuring in the UV region right through to the NIR regime.

2.1.3 Limitations

Absorbance spectroscopy however has two limitations the first is of sensitivity. The analyte measured Rhodamine 6G is a dye with an extinction coefficient $\varepsilon = (10.66 \pm 0.04) \times 10^4$ mol^{-1} L cm^{-1}. Many analytes that one would wish to investigate in particular biological molecules such as proteins will have an extinction coefficient significantly lower. Moreover, proteins are considerably larger that dye molecules like Rhodamine 6G and hence have a large cross-section which enhances Rayleigh scattering. **Figure 25** illustrates the problem of Rayleigh scattering with absorbance spectra. LUDOX SM-AS is a silica nanoparticle with $R = 3.5$ nm and is commonly used in fluorescence measurements to make a scattering solution. The increase in measured "absorbance" as the concentration of scattering solution increases is due to scattered light and not from actually absorbance of LUDOX SM-AS. Scattered light has a λ^{-4} dependence [105] and hence distorts the UV regime the most. It should be noted that the relationship between the quantity of scattering specie in this case LUDOX SM-AS and the magnitude of the absorbance is clearly non-linear. Biological molecules such as proteins typically have an absorbance spectrum in the UV but may also highly scatter making it difficult to separate out their actual absorbance spectra. In general, for the same material the larger the size of the nanoparticle, the more intense the scattering. This phenomenon is taken advantage when using light scattering techniques such as Nanoparticle Tracking Analysis (NTA) on nanoparticles >50 nm [106,107]. Finally, absorbance has the limitation of sensitivity, in the Perkin Elmer Lambda

2 and Perkin Elmer 25 used it is hard to accurately measure below A~0.01 for a 1 cm path length due to the difficulty in accurately distinguishing small differences in two relatively large signals. Sensitivity can be helped slightly by use of longer path length cuvettes.
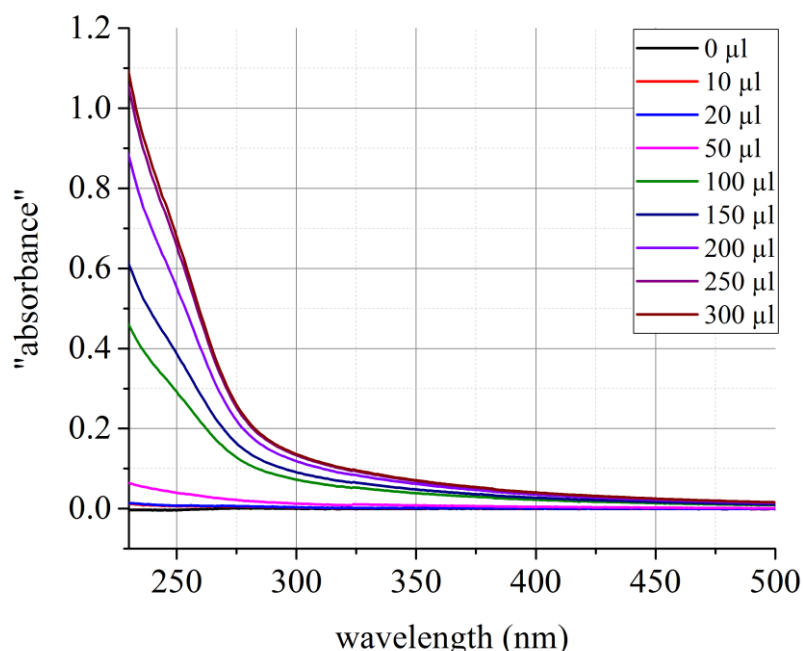
Figure 25: "Absorbance" of LUDOX SM-AS solutions in distilled water measured in a Perkin Elmer Lambda 25 spectrophotometer ran from 230-500 nm in 1 nm increments. A 0.125 s integration time was used. In each case the volume of LUDOX SM-AS stated in the legend was added to 3 ml of distilled water.

This is illustrated in **Figure 25** with the 0 µl control i.e. distilled water where an absorbance of –0.006 is measured at 240 nm. In the case of a biological molecule such as a protein there is problem of a lower extinction coefficient e.g. 43824 mol^{-1} L cm^{-1} [108] and a practical limitation of measuring absorbance values below 0.01. For a 1 cm cuvette using **Equation (18)** it will be hard to accurately measure the µM range and the nM range certainly is out of reach. On the other hand, high absorbance values are difficult to measure accurately because of non-linear effects such as scattering. Fluorescence techniques on the other hand are boasted of being capable of measuring concentration values of up to one million times smaller than absorption techniques [109] with up to pM sensitivity being reported [110].

2.2 Emission – Spectrofluorimeter
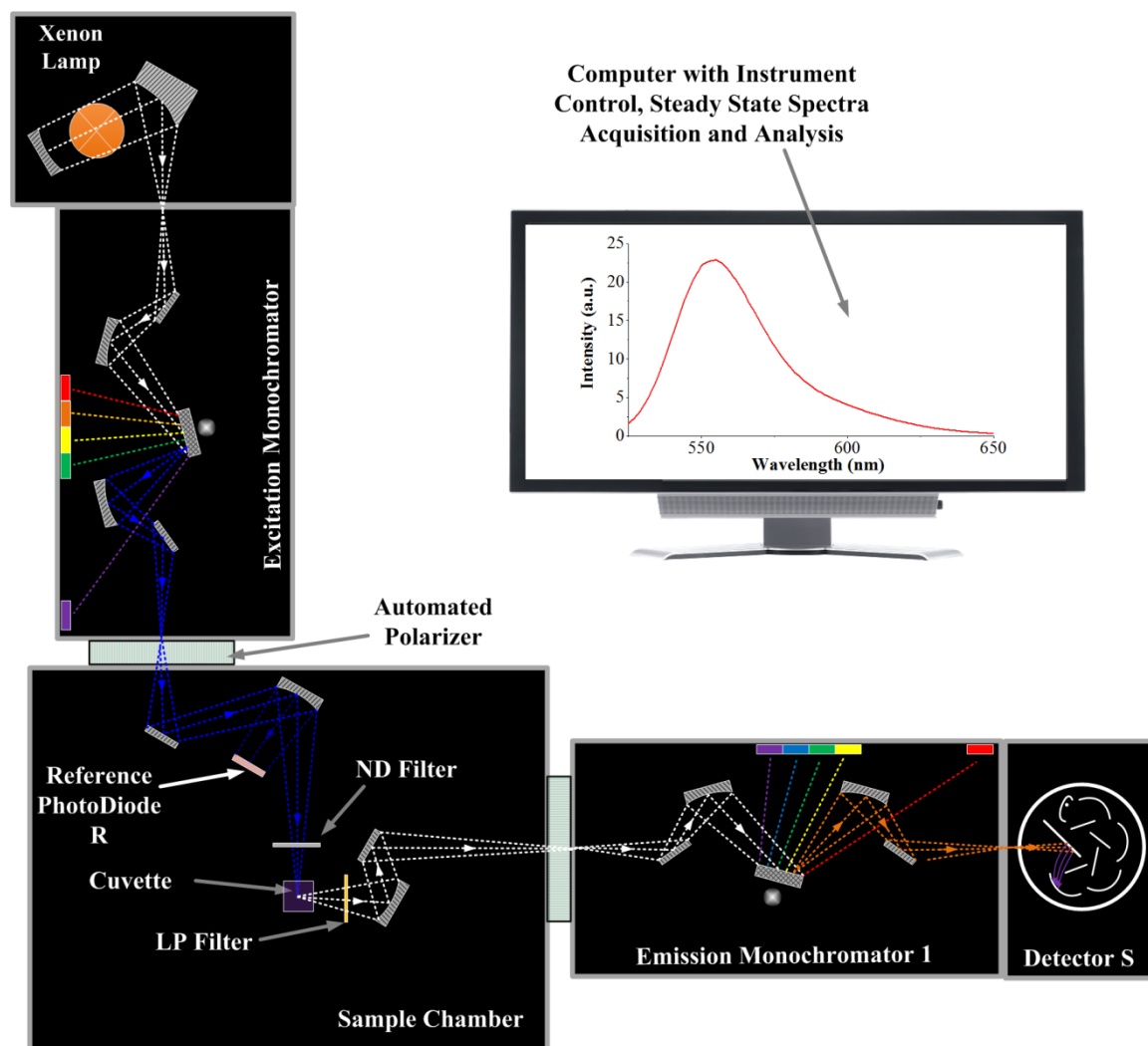
Figure 26: The excitation optics of the spectrofluorimeter are similar to that of a spectrophotometer consisting of a xenon arc lamp, excitation monochromator and sample compartment. The detection optics differ in the fact that they are situated at right angles from the excitation arm[13] and there is an additional monochromator to select emission wavelength[14]. If polarization effects are present, excitation and emission polarizers may also be present. The monochromators are drawn in Czerny-Turner geometry.

Fluorescence techniques can use extremely low amounts of fluorophore (µM-nM concentrations) which is important to minimised perturbation of the system under investigation particularly in the application area of the life sciences. The steady state fluorescence properties of a sample may be investigated by usage of a spectrofluorimeter.

---

[13] Fluorescence occurs in all directions and is much weaker than the excitation signal. The right angle conformation is used to reduce the proportion of excited light to fluorescence emission. In addition, the xenon arc lamp is typically much more powerful than the deuterium and halogen lamps used in a spectrophotometer.
[14] The detection wavelength is typically different to the excitation wavelength unlike in the spectrophotometer.

As fluorescence spectroscopy involves looking at an emission signal with a low background level that is Stokes shifted in wavelength from the excitation source, fluorescence can be as much as 1000 times more sensitive than absorption spectroscopy which in contrast involves looking at comparing two relatively large signals which will be very similar at low absorbance values. The excitation optics are similar to the optics of a spectrophotometer[15] however in general a more intense excitation source is used because the fluorescence signal is typically orders of magnitude less than the excitation light. The excitation source is a 450 W Xenon lamp for the modular Fluorolog 3 and a 150 W Xenon lamp for the benchtop Fluoromax. Two single grating monochromators are drawn in **Figure 26** which is the standard configuration for the Fluoromax 4 and the basic configuration for the Fluorolog 3 (Fluorolog 3-11). Blazed gratings are manufactured to produce maximum efficiency at certain wavelengths. Typically, a grating blazed for a lower wavelength is used for the excitation to maximise the relatively low output of the Xenon lamp than the emission which is typically measured at higher wavelengths. For example, a grating with 1200 lines/mm blazed at 330 nm may be used for excitation and a grating with 1200 lines/mm blazed at 500 nm may be used for emission as shown in **Figure 27**. For optimal results [111]:

$$\frac{2}{3}\lambda_{\text{Blaze}} < \lambda_{\text{Range}} < 2\lambda_{\text{Blaze}} \qquad (19)$$

Therefore, the 1200/330 grating gives a good excitation range between ~200-600 nm and the 1200/500 grating gives a good emission range between ~250-1000 nm. The Fluorolog 3 may be customised to a Fluorolog 3-22[16] which has double grating monochromators and offers superior stray light rejection. As steady fluorescence emission is a quantitative measurement as opposed to a ratio like absorbance, it is dependent on the intensity of the excitation source. In order to measure the output of the lamp and hence correct for any drift in output, a small fraction of the excitation light ~8 % is directed onto a reference

---

[15] The spectrofluorimeter can be used as a spectrophotometer if a detector such as a photodiode is placed perpendicularly after the sample.
[16] The Fluorolog 3 is usually denoted by its monochromator configuration XYZ. X=1,2 and stands for the excitation monochromator. The photodiode on the excitation side is denoted R1 (reference). Y=1,2 and stands for the emission monochromator on the right side. The detector on the right side is denoted as S1 (signal). Additional detectors can be configured on the right side and if present are denoted as S2 and S3. Z=1,2 and stands for the emission monochromator on the left side if configured. The detectors on the left side are denoted as T1, T2, T3 (for T format). Finally, any detectors on the front side such as an absorbance photodiode accessory are denoted A for auxiliary.
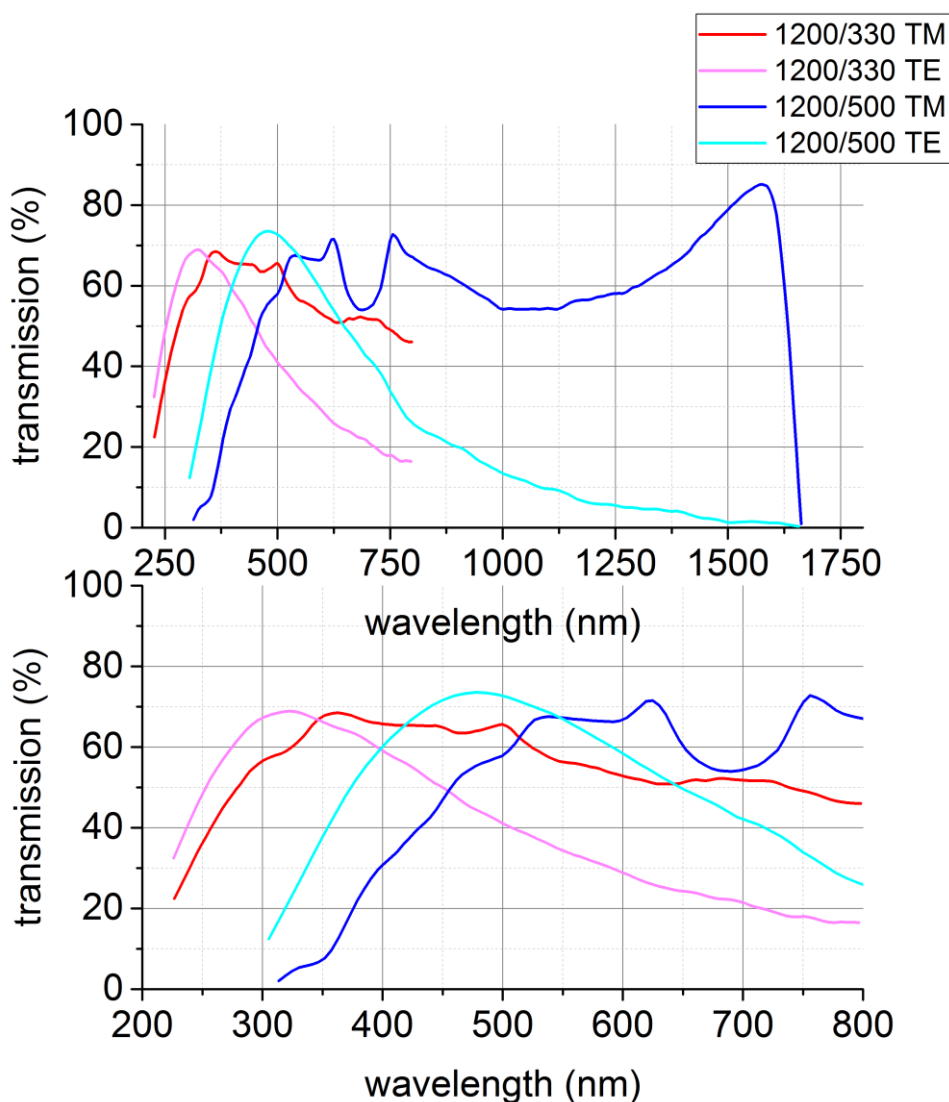
Figure 27: The transmission spectra of the 1200/330 and 1200/500 gratings used for excitation in the Fluoromax 4 and Fluorolog 3 steady state fluorimeters for transverse electric (horizontally polarized) and transverse magnetic (vertically polarized).

photodiode, signal R (μA) and the rest of the excitation light is sent to the sample as shown in **Figure 26**. The basic configuration of the Fluorolog 3 and Fluoromax 4 employ a Hamamatsu R928 photomultiplier PMT as a detector. The emission monochromator may be replaced with a spectrograph and the PMT may be replaced with a Charged Coupled Device (CCD) for example in the modular Nanolog or the benchtop Dual FL or Aqualog (specialised benchtop fluorimeter for water quality). The Dual FL/Aqualog possesses an integrated absorbance photodiode and can simultaneously measure emission and absorbance spectra. This functionality can be added to a Fluorolog/Nanolog with an

34
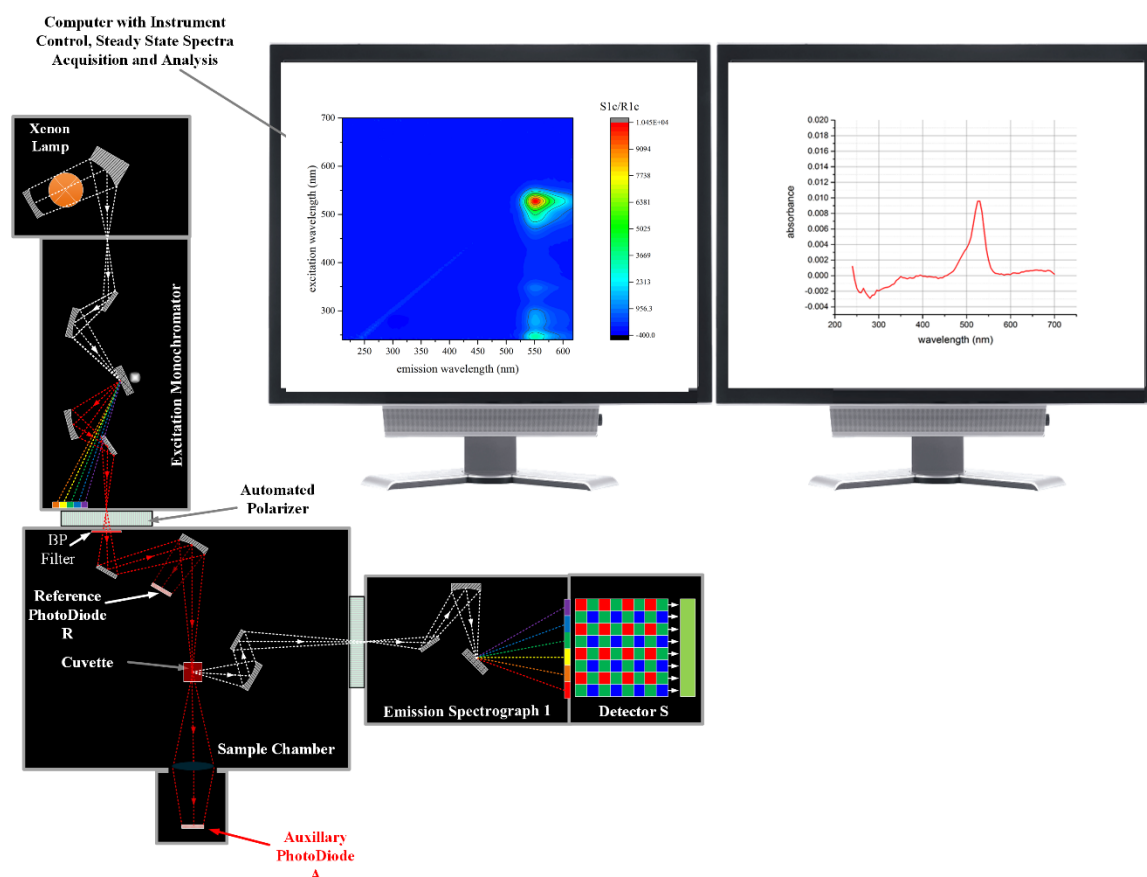
Figure 28: A steady state fluorimeter may be configured with a spectrograph and a CCD opposed to an emission monochromator and a photomultiplier tube. The CCD and spectrograph have the advantage that all wavelengths are measured simultaneously allowing for rapid acquisition of emission spectrum which is particularly useful for excitation emission matrices (EEMs) discussed in detail later on. If a photodiode is placed on the auxiliary port the system can simultaneously measure the absorbance of the sample and the fluorescence which allows for the correction of inner-filtering discussed in detail later on.

absorbance accessory which attaches to the front of the instrument, parallel to the excitation monochromator. Emission spectra are the most common spectra measured in a fluorimeter and are typically obtained by parking the excitation monochromator to a wavelength regime where the sample has high absorbance, for example the absorbance peak[17] and scanning the fluorescence intensity as a function of emission wavelength. To block out excitation light and fluorescence measured at second order wavelengths a longpass LP filter may be placed before the emission monochromator. The work in this thesis was done in conjunction to 2 HORIBA Scientific application labs Glasgow IBH and New Jersey ISA as well as the Photophysics Research Group at Strathclyde and as a consequence a vast

---

[17] For samples with a short Stokes shift a lower excitation wavelength than the absorption peak may be utilised in order to see more of the emission spectra.

range of HORIBA Scientific steady state fluorescence instruments were used in this thesis. These include legacy instruments such as the Fluoromax 2 and Skinskan running with Datamax acquisition software installed in a Virtual Machine. The Virtual Machine was assigned control to the RS232 communication port and a virtual floppy boot drive was made to initialise the Skinskan. Data was read and analysis carried out using SpekWin32 [92]. The current line-up and top of the range of instruments such as the Fluorolog 3-22, Nanolog 3-22iHR320, Fluoromax 4 and Aqualog ran the latest version of FluorEssence (OriginPro 8.6 analysis software with bundled macros for data acquisition).

2.2.1 Monochromator Calibration and Signal to Noise

There are 3 calibration checks typically performed on a spectrofluorimeter, the xenon lamp scan, the water Raman scan and the kinetic water Raman scan [112]. The xenon lamp scan is used to verify that the excitation monochromator is in working order. The xenon lamp has a characteristic peak at 467 nm which is used for as a reference wavelength to align the excitation monochromator [113]. The tolerance is usually set to 467.0±0.5 nm. An extended xenon scan may be ran up to 1150 nm to observe an additional characteristic peak at 991 nm. The tolerance for this peak is at 991±1 nm [114,115]. The intensity across the photodiode will differ with respect to time as the xenon lamp ages however the lamp spectra should appear stable with well-defined peaks as shown in **Figure 29**. When the lamp is initially turned on the lamp spectrum will be unstable as it takes time, for the xenon lamp to reach local thermal equilibrium. In general, a 15 minute warm-up time is required, if the lamp spectrum is still unstable after this time the lamp will need replacing. A typical lamp has a useable lifetime of 1000-2000 hours. When the lamp is running it generates heat and as a consequence must be cooled with a fan. The benchtop systems with the 150 W xenon lamp utilise the same switch for the lamp and the fan. Modular systems such as the Fluorolog 3 and Nanolog utilise a high power 450 W xenon lamp which need to be efficiently cooled with a dedicated fan. Turning on the fan is a perquisite for turning on the lamp, however it is recommended to keep the fan running 5-10 minutes after powering off the lamp to efficiently cool it otherwise the lamp will begin to fail before its expected lifetime. Turning off and on the lamp is equivalent to 1-hour usage so it is recommended to leave the lamp running if the system is idle between measurements up to a couple of hours apart. The resolution is typically better in the visible than in the NIR.
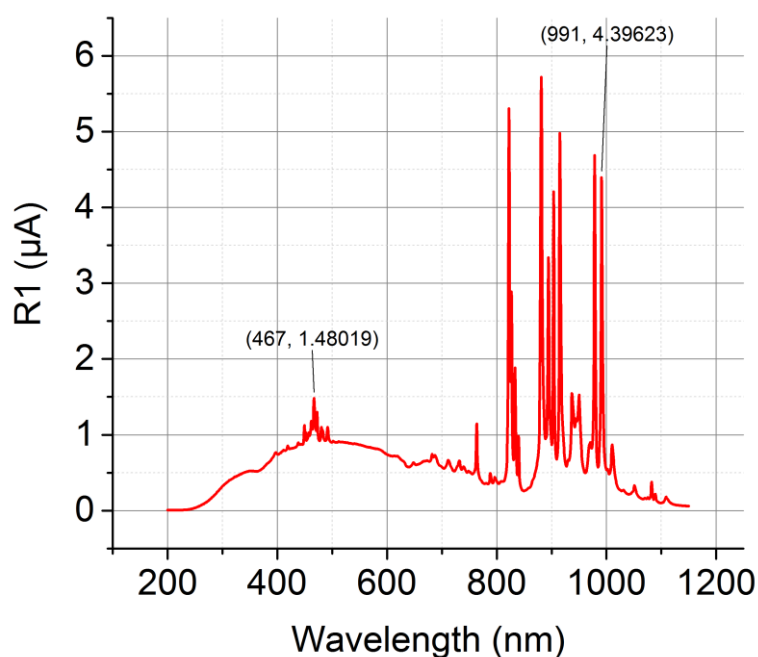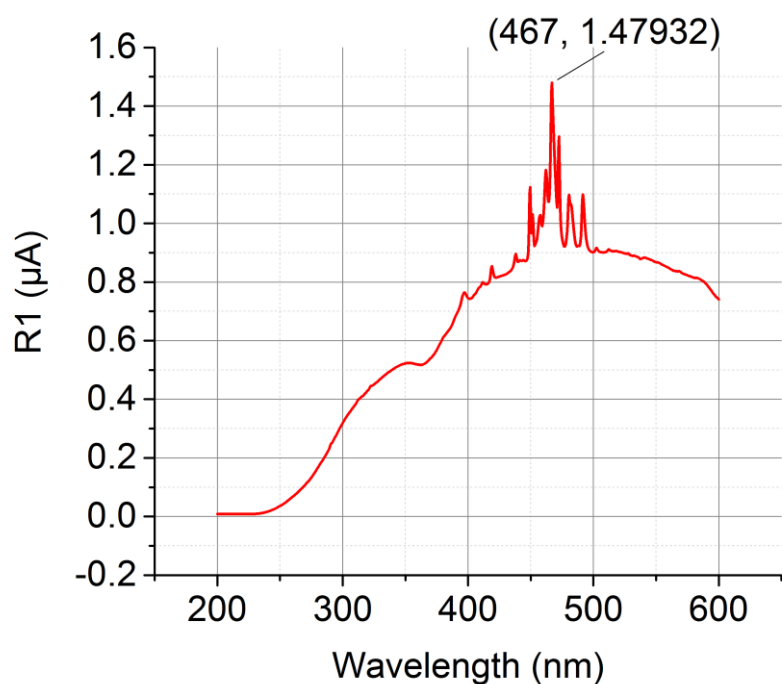
Figure 29: The excitation profile of the xenon lamp scan measured using the reference photodiode R1 on the Fluoromax 4 between the standard wavelength range 200 and 600 nm (top) or the extended wavelength range 200 and 1150 nm (bottom). In both cases an integration time of 0.1 s and a wavelength increment of 0.5 nm. The excitation monochromator (1200/330 grating) bandpass was set to 1 nm. For the lamp scan the emission channel and detector are not utilised and are left at 650 nm and 1 nm bandpass as default.

In order to calibrate the emission monochromator a series of narrow atomic emission lines of distinct wavelengths can be used for instance a Hg lamp [116]. However for a tuneable

wavelength fluorimeter, calibrating the position of each monochromator at one position is often sufficient to achieve the wavelength accuracy required throughout the useful spectral range of the instrument [115]. In order to validate the system performance a sample is desired that has a relatively weak signal, isn't prone to photobleaching and can easily be prepared. The Raman peak of distilled water is commonly used for this purpose [117]. The Raman shift of water is 3340 cm^{-1} (which can be expressed as 2941.2 nm) [118,119]. The Raman peak position of distilled water can thus be calculated from:

$$\lambda_{em} = \left(\frac{1}{\lambda_{ex}} - 3340 \text{ cm}^{-1} \right)^{-1} \tag{20}$$

An excitation wavelength of 350 nm therefore yields a water Raman line at 397 nm.

Figure 30: Emission scan of Starna Raman certified Raman Standard 3-Q-10/WATER measured using a Fluoromax 4. The excitation monochromator (1200/330 grating) was set to an excitation wavelength of 350 nm and a bandpass of 5 nm. The emission monochromator (1200/500 grating) was scanned from 365-450 nm with a 5 nm bandpass at 0.5 nm increments for an integration time of 1 s. A R928 PMT detector was used.

This water Raman peak serves dual purposes to align the emission monochromator and as an indicator for instrument system performance. The tolerance for this peak is 397.0±0.5 nm. Two additional points are highlighted on **Figure 30**. The value at 365 nm gives an indication of the level of stray light [120]. Stray light is unwanted light that is light that lies out with the selected wavelength and bandwidth [121,122]. The Fluoromax 4 has a single

grating monochromator however higher end systems such as the Fluorolog 3-2yz utilise a double grating monochromator which significantly lowers the value of the stray light from the source [115,123]. The value at 450 nm is used as an indicator of the system noise and further examined using a kinetic scan. It should be noted that any fluorescence impurities in water will lead to a fluorescence signal measured at 450 nm and this fluorescence contamination will be taken as additional noise therefore as a consequence the computed signal to noise ratio can be significantly lower than expected. Stray light will also increase the level of noise at 450 nm but is more pronounced at 365 nm. End users measuring signal to noise ratios with a lower purity of water often obtain significantly lower results than the manufacturers values which use an expensive water Raman certified standard. It is insightful for an end user to compare the SNR obtained from a certified standard to their laboratory water and to assess whether their laboratory water purification system is acceptable.

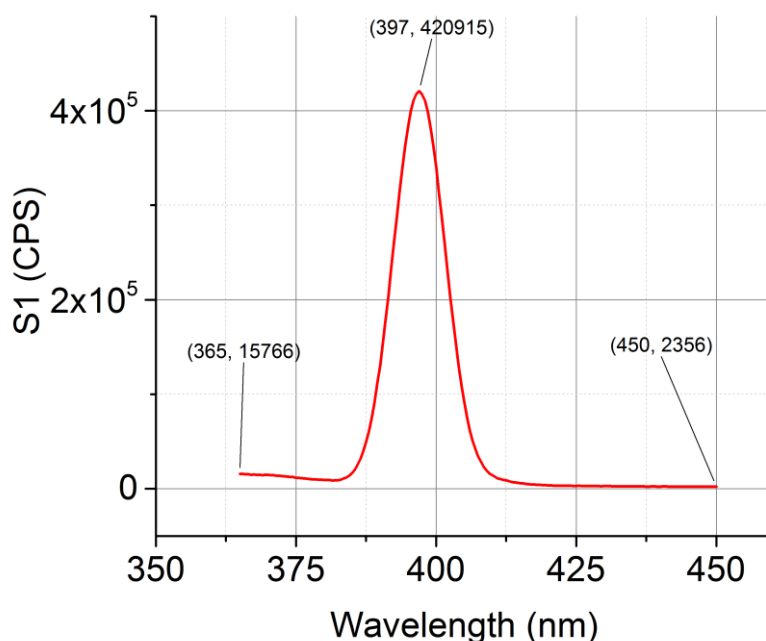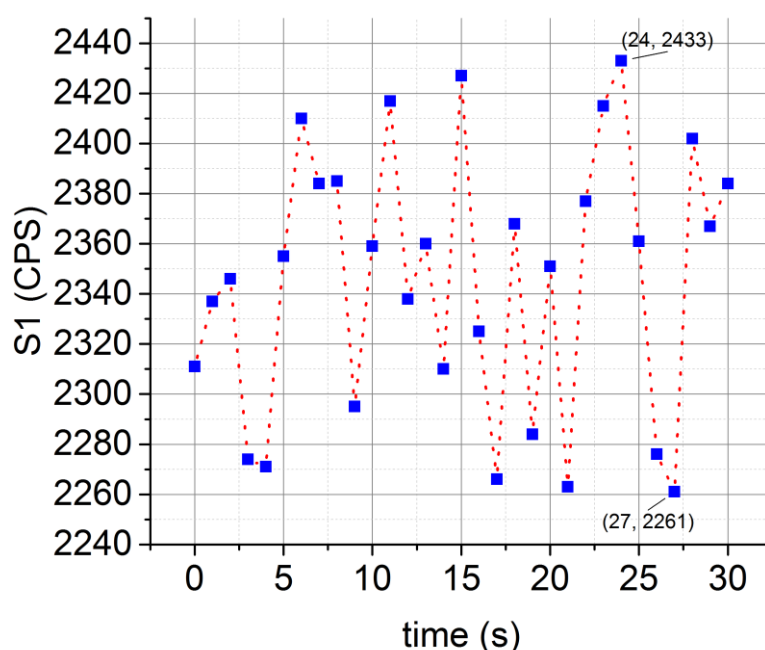**Figure 31**: The associated kinetic scan of the noise of the Starna Raman certified Raman Standard 3-Q-10/WATER measured using a Fluoromax 4. The excitation monochromator (1200/330 grating) was set to an excitation wavelength of 350 nm and a bandpass of 5 nm. The emission monochromator (1200/500 grating) was set to 450 nm with a 5 nm bandpass. The integration time was set to 1 s for a total accumulation time of 30 s. A R928 PMT detector was used.

Two commonly signal to noise ratios (SNR) are commonly employed the SNR_{FSD} and SNF_{RMS}. The signal to noise first standard deviation can be calculated from the maxima of the emission peak (A) and the noise level either side of the peak (B).

$$SNR_{FSD} = \frac{(A-B)}{\sqrt{B}} \qquad (21)$$

The SNR_{FSD} will likely decrease with time as the lamp burns out and the lamp should be replaced if it falls below 1000.

$$SNR_{RMS} = \frac{(A-B)}{RMS_B} \qquad (22)$$

The RMS_B is usually estimated as

$$RMS_B \approx \frac{\text{Peak to Peak Noise}_B}{5} \qquad (23)$$

where

$$\text{Peak to Peak Noise}_B = \frac{\sum_{i=1}^{j} \left| S1_B(i) - S1_B(i+1) \right|}{(j-1)} \qquad (24)$$

For the Fluoromax 4 the $SNR_{FSD}=8643$ and $SNR_{RMS}=35017$.

2.2.2 Corrected Excitation and Emission Spectra

Steady state fluorescence measurements yield intensity signals that contain both analyte specific and instrumental distortions and there is hence a demand to remove the former from the later to compare data across instruments, laboratories and over time [124]. **Figure 32** illustrates the stark contrast of a quartz tungsten filament when measured with 2 different monochromators and 3 different detectors[18]. The use of corrected fluorescence data [125] naturally depends on the application. If one is merely looking at differences in fluorescence intensity in an individual instrument to interrogate changes in their sample i.e. for a comparative difference one may not need to apply instrumental corrections. However, if one wants to perform peak fitting, in order to prescribe the components of their measured fluorescence spectrum, correcting the fluorescence data is very important. It should also be noted that there are also some limitations in the application of correction factors particularly

---

[18] The emission ratios of the 3 detectors differs for the 2 emission arms likely due to slight variances in alignment. For this reason, correction factors should be remeasured every time a serious change has been made to the emission optics of the system.

in the case for extremely weak signals. The first correction to the measured spectrum is the dark offset. The dark offset is usually measured before measurement of the sample; to measure the dark offset the shutter to the xenon lamp is closed and the dark counts at the detector are recorded. The integration time of the dark offset for $t_{int}<1$ s and $t_{DO}=10$ s for $t_{int} \geq 1$ s. The number of dark counts corresponding to the integration time t_{int} is then calculated and subtracted from the measured steady state spectrum. It should be noted that the dark offset only accounts for the dark counts measured by the detector and does not account for any background fluorescence from the solvent or cuvette. An additional blank subtract can carried out by using the solvent in a matching cuvette (necessary for simultaneous fluorescence and absorbance measurements).
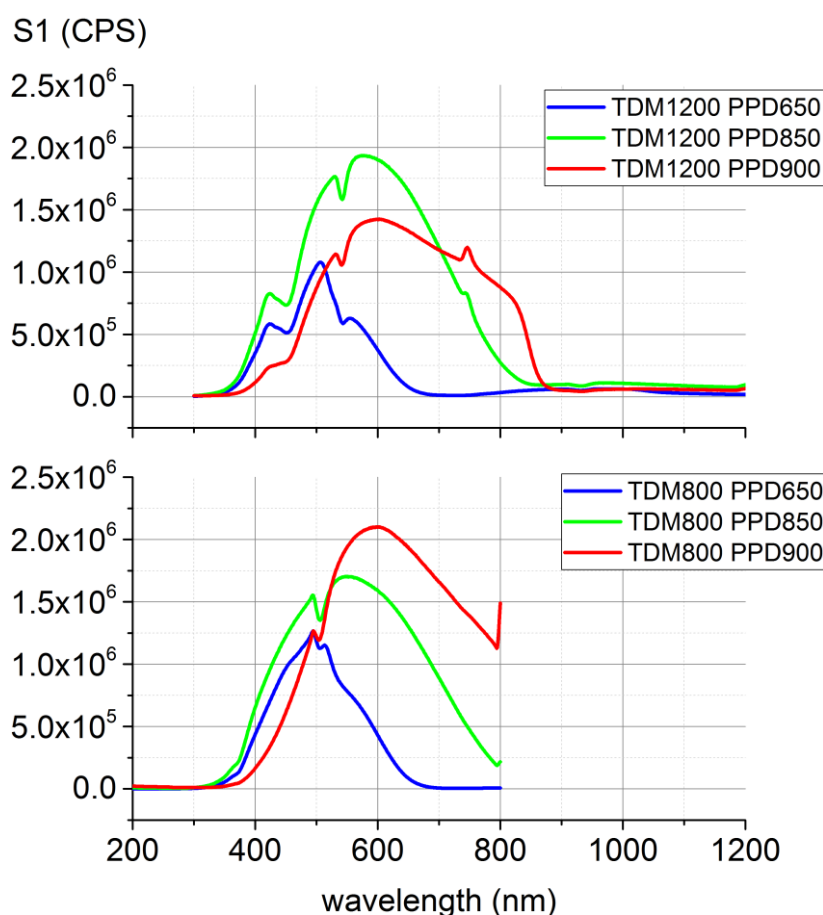
Figure 32: The steady state spectra of an Osram 64640 HLX mounted in a DeltaDiode case ran at 1.58 A and 6.9 V affixed to the excitation port (no excitation monochromator) of a T-format DeltaFlex. On the T side TDM800 (1200/350 grating), bandpass 12 nm and on the S side TDM1200, bandpass 16 nm with DeltaHub. A Teflon block was placed in a front face cuvette holder. To ensure the counts were ~1-2×10⁶ CPS a UV ND 1.0 and 2 UV ND 0.3 were placed on the emission arm with the TDM800 (1200/350 grating) and a UV ND 1.0 and UV ND 0.3 were placed on the second emission arm with the TDM1200. Three detectors a PPD650, PPD850 and PPD900 were swapped between both emission arms. A

focus scan at 500 nm was ran before measurement. The steady-state emission of the Osram 64640 HLX was ran in 1 nm steps over the working range of the monochromators.

As in the case of the spectrophotometer[19] the lamp energy as well as detector response are not perfect. For the spectrophotometer this didn't matter much as the spectra obtained was a ratio and hence any differences in energy output or detector efficiency were divided out. Fluorescence emission on the other hand is not a ratio and is highly distorted by the wavelength dependency of the system optics. A correction factor curve for each signal must be measured and applied to any raw data to give the true spectral shape. Wavelength correction factors are measured before each HORIBA Scientific spectrofluorimeter leaves production and their function is to compensate for the non-linear wavelength response of the system [118]. In general wavelength correction factors are measured separately for the excitation and emission paths.
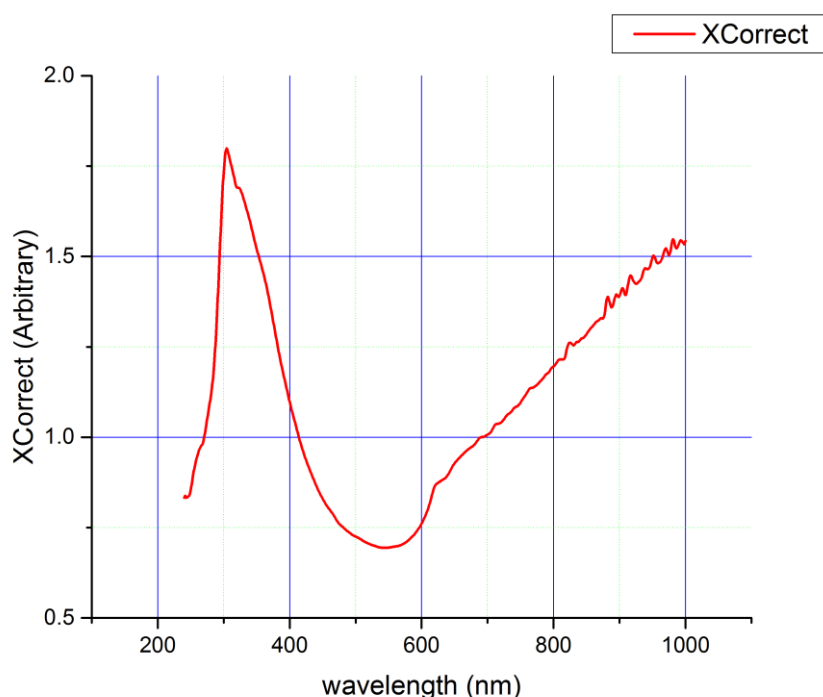
Figure 33: The excitation wavelength correction factor commonly referred to as XCorrect. The XCorrect is measured during instrument manufacture by measuring the lamp and excitation optics profile with the reference detector and simultaneously measuring it with a corrected photodiode. Typically for a xenon lamp this is measured with the excitation monochromator (1200/330 grating) scanning from 240-1050 nm with a 3 nm bandpass, 1 nm increment and 1 s integration time. The dark offset for both detectors is applied. The XCorrect is created by dividing the signal from the corrected photodiode by that measured

---

[19] Non-linear measured energy output was demonstrated in **Figure 18** with respect to the spectrophotometer but in a spectrofluorimeter there is the influence of both excitation and emission optics.

from the reference detector and normalising this plot to 1 at 414 nm. This XCorrect was measured in a Fluoromax 4 but it should be noted that the XCorrect is unique for each instrument.

The excitation spectra correction factor can be obtained by use of a quantum counter; that is "a system which has a high constant fluorescence quantum yield over a broad spectral range" [126–130]. In practice however, use of a calibrated photodiode is preferred. The calibrated photodiode is placed in the auxiliary of the spectrofluorimeter and the signals $A1_{DO}$ and $R1_{DO}$ are measured simultaneously. The excitation wavelength correction factor otherwise known as XCorrect is calculated by dividing $A1_{DO}$ by $R1_{DO}$ and normalising to 414 nm. The wavelength range of the XCorrect is typically 240-1050 nm. The xenon lamp profile will differ in shape depending on whether a single or double grating monochromator is used and on the individual grating of the excitation monochromator and these differences must be accounted for. The emission wavelength correction factor also is highly influenced by the quantum efficiency of the detector [105] for example those shown in **Figure 34**[20]. The emission wavelength correction factor is typically measured in one of two ways, using a calibration lamp or a series of standard reference materials (SRMs) **Figure 35**. The calibration lamp such as the Gooch and Housego OL220c is a tungsten filament in quartz and possesses a wide spectral output [111,131]. Its spectrum is measured in a metrology lab and provided with the OL220c. To measure a MCorrect it is mounted at a set height and the a scattering block is placed in the sample compartment [115,132,133]. For the scattering block sintered polytetrafluoroethylene (PTFE) commonly known by the trademark Teflon is preferred. High purity Teflon necessary for calibration in the UV is branded Spectralon [134]. Spectralon is a highly reflective material with a fairly uniform reflectance >0.94 for the range 250-2500 nm [135,136]. To calibrate with the calibration lamp, the spectrofluorimeters excitation xenon lamp is turned off and the sample mount is replaced with the spectralon scattering block. Room lights are turned off and the lamp is mounted above the scattering block at a fixed height and the emission monochromator is moved to 540 nm with 0 nm slit size. The lamp is turned on and the current is adjusted to 6.500 A and left 10 minutes to stabilise. The emission bandpass is slowly increased until the measured signal at 540 nm is about half that of the linear range of the detector $\sim 1 \times 10^6$ CPS for a R928.

---

[20] Note detector quantum efficiency is often plotted in log scale. Log scale is commonly employed when a comparison between a large number and a small number is made in the same plot. The small number becomes more pronounced on a log scale while the large number becomes less pronounced.
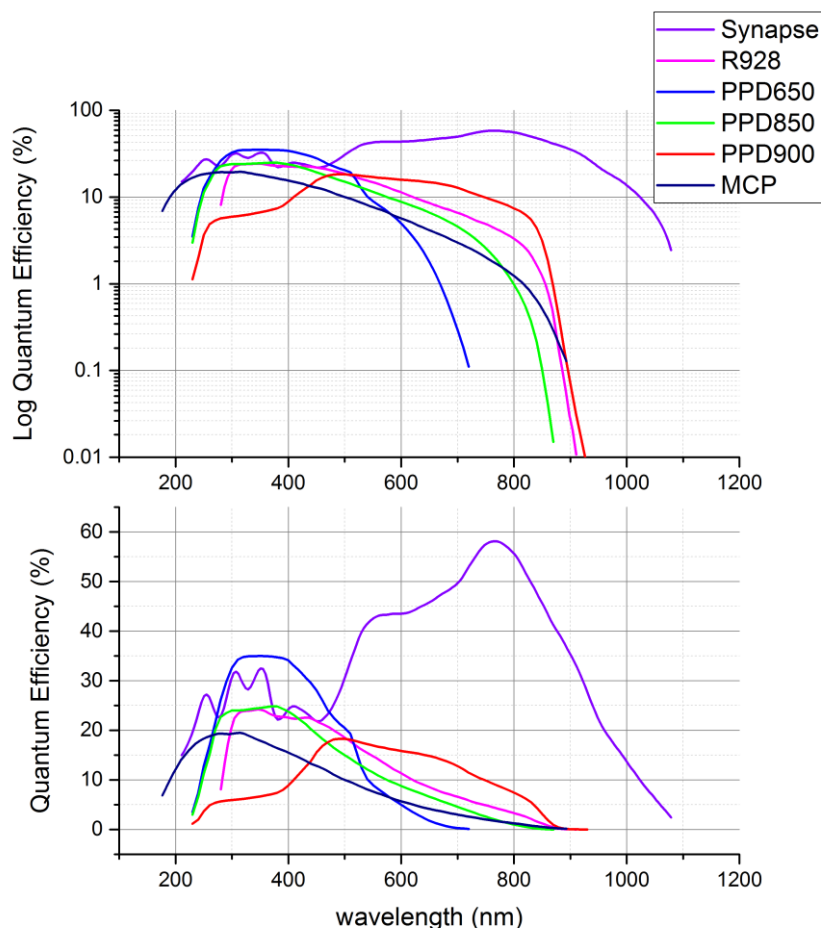
Figure 34: Quantum efficiency of the R928 photomultiplier tube, a commonly employed detection source in the basic configuration of the Fluorolog 3 and Fluoromax 4 taken from [137]. The quantum efficiency of the latest range of HORIBA Scientific PPD detectors, the HORIBA Scientific Synapse 1024×256 Open-Electrode CCD detector and MCP detector. The earlier versions the TBX650 and TBX850c will have slightly lower quantum efficiency curves that their PPD replacements. Quantum efficiency curves are plotted in both log scale and in linear scale.

The spectra of $S1_{DO}^{OL220C\ ON}$ is measured over the working wavelength range of the OL220c and the detector. For example, in the cases of the R928 the lowest wavelength that can be calibrated is about 290 nm as the output of the lamp is too poor to accurately calibrate below 290 nm and the upper wavelength is about 850 nm as the quantum efficiency is <1 % above 850 nm. The time interval is typically t_{int}=1 s and a wavelength increment of 5 nm to match the spectrum of OL220C has 5 nm increments. The calibration lamp is turned off for 10 minutes and $S1_{DO}^{OL220C\ OFF}$ is then measured using the same settings; this is subtracted to compensate for photons measured from the room because there is an opening at the top of the spectrofluorimeter when the calibration lamp is used. The emission wavelength correction factor otherwise known as MCorrect is then calculated by:

44

$$MCorrect = \frac{NIST^{OL220C}}{S1_{DO}^{OL220C\ ON} - S1_{DO}^{OL220C\ OFF}} \tag{25}$$

In general, only a relative wavelength calibration is performed so the MCorrect used is normalised to its minimum value[21]. The area of the spectralon block will not fully resemble the optical path of a cuvette and thus it cannot be used to perform an absolute ratiometric calibration. If a wavelength increment of less than 5 nm is used during measurement the MCorrect is typically interpolated. For ease of use and stability SRMs are typically ion-doped glasses made in the shape of a standard 4 ml cuvette however since no SRM covers the entire wavelength range used for measurement multiple have to be used in conjunction and a calibration curve has to be summed up from individual SRMs e.g. 2940-2944 [138–142]. SRMs usually have the advantage that are usually certified for every 1 nm opposed to 5 nm so less interpolation of the correction factor is required for measurements at low bandpasses. For the series of SRMs because a different excitation wavelength is used for each SRM the correction of the excitation optics has to also be compensated for:

$$MCorrect = \sum_{x=0}^{4} \frac{NIST^{SRM294x}}{\dfrac{S1_{DO}^{SRM294x}}{R1_{DO}^{SRM294x} \times XCorrect}} \tag{26}$$
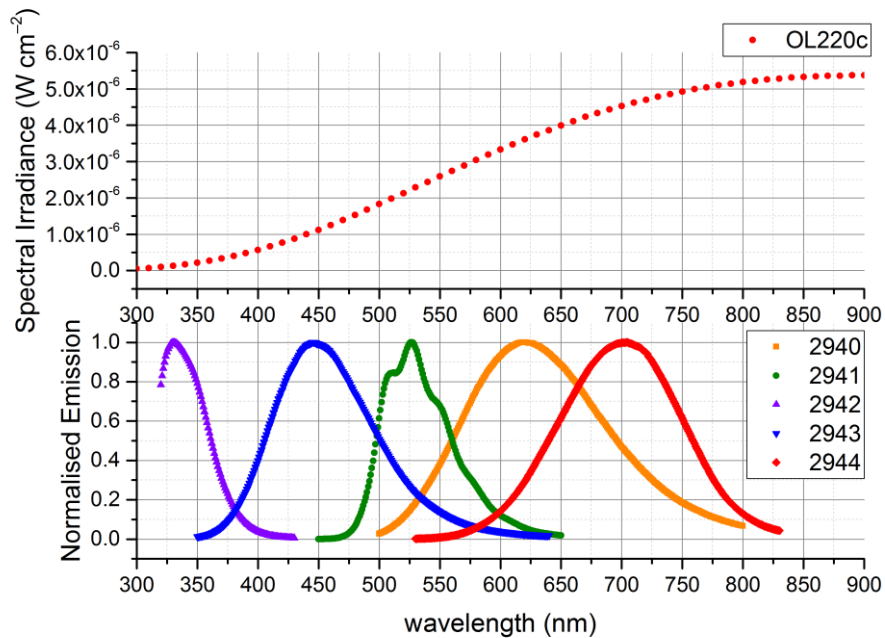
Figure 35: Typical SRM data scaled to the visible region for the OL220c and SRMs 2940-4. Data taken from the manufacturers websites respectively [143,144]. Because OL220c has a smooth irradiance curve data can be interpolated.

---

[21] Strictly speaking it would be preferred if MCorrect and XCorrect were instead normalised to their maximum value. The number of counts is usually substantially artificially inflated by the correction factors when normalised by their minimum value. The greatest error in correction factors is however at their extreme.
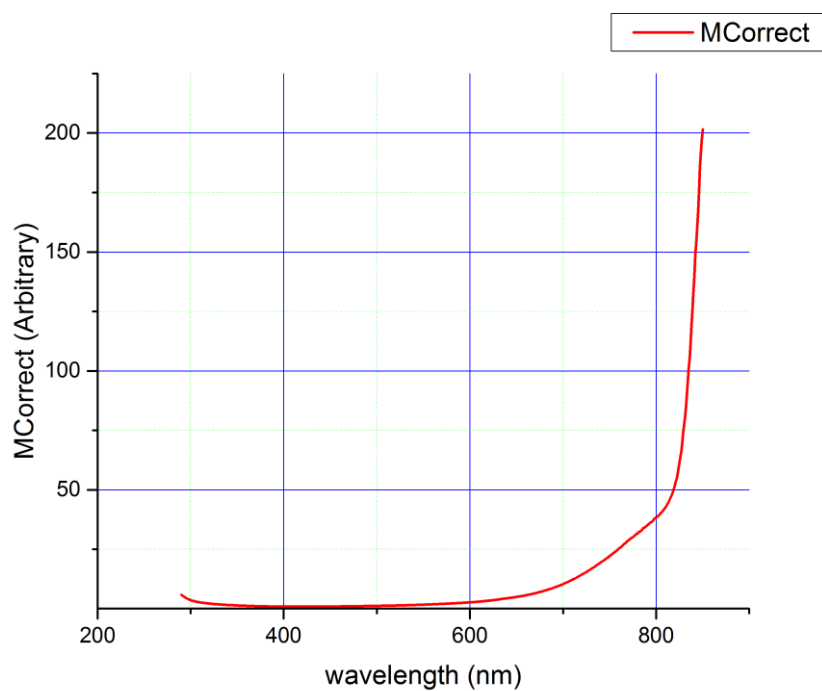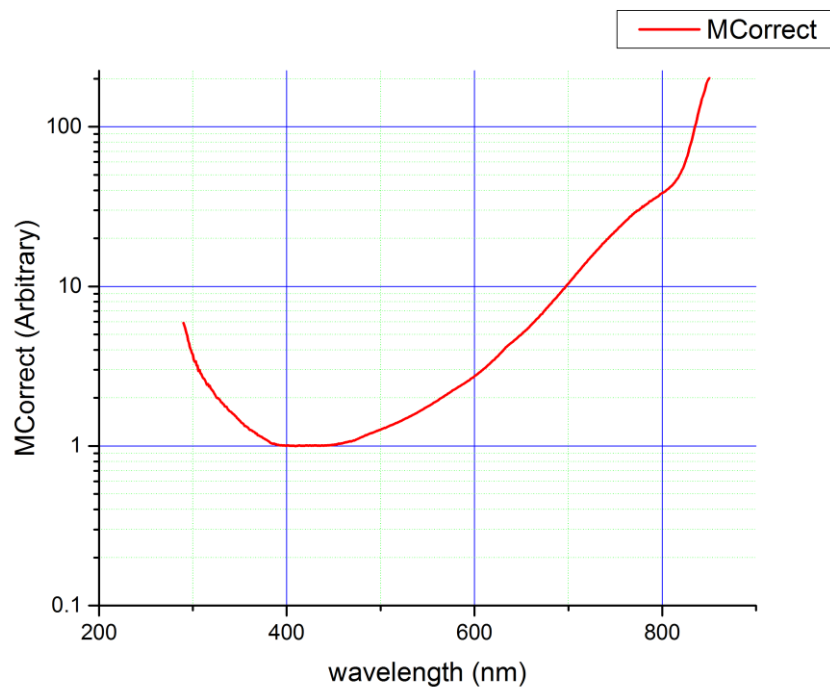
Figure 36: The emission wavelength correction factor MCorrect plotted in linear and log scale measured on a Fluoromax 4 with a R928 PMT detector using a 220C calibration lamp. In this case the emission monochromator (1200/500 grating) was set to a 0.1 nm bandpass and scanned from 290-850 nm in 1 nm increments. Like the MCorrect, the XCorrect is unique to the instrument.

Table 1: Excitation wavelength and working emission wavelength range of NIST SRMs

SRM		λ_{ex} (nm)	Cal Range λ_{em} (nm)
2940	Mn-ion-doped glass	412	500-800
2941	Uranyl-ion-doped glass	427	450-650
2942	Ce-ion-doped glass	310	320-430
2943	Cu-ion-doped glass	330	350-640
2944	Bi-ion-doped glass	515	530-830
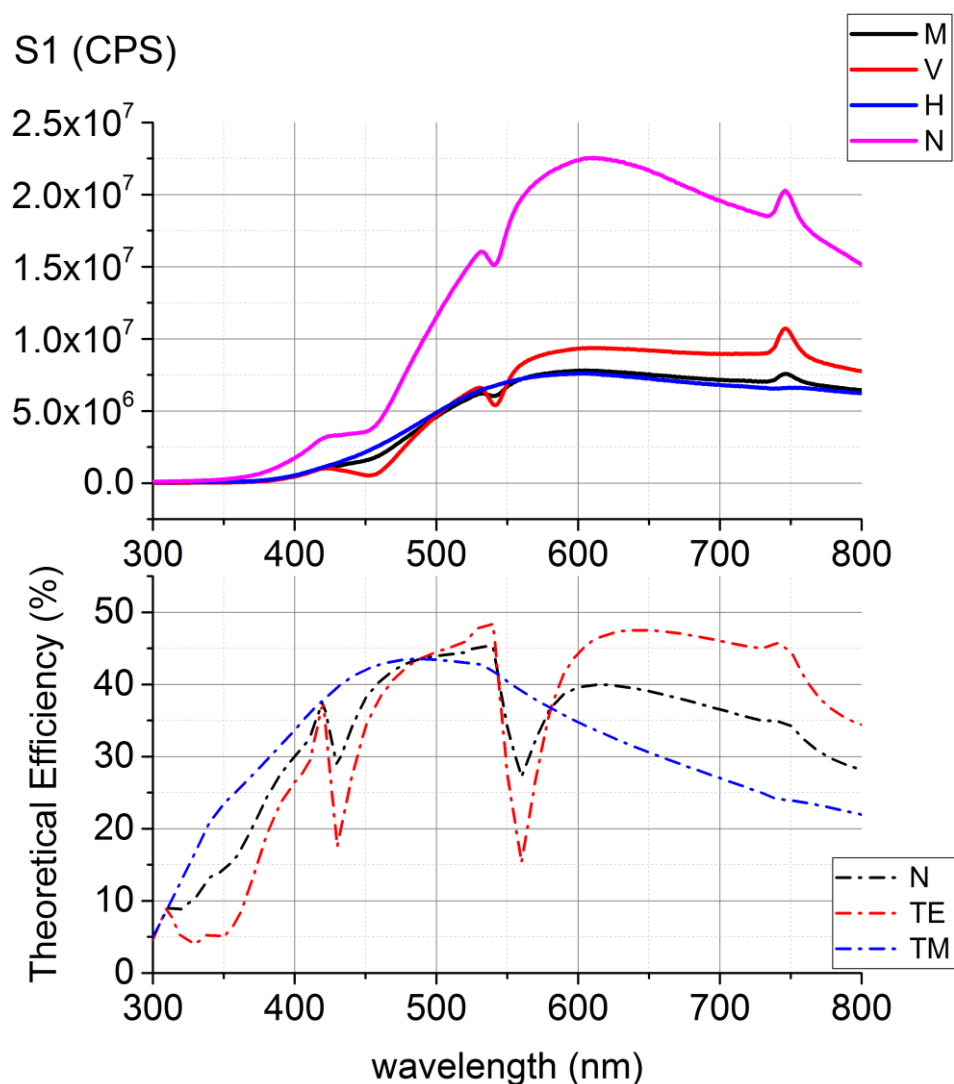
Figure 37: The steady state spectra of an Osram 64640 HLX mounted in a DeltaDiode case ran at 1.58 A and 6.9 V affixed to the excitation port (no excitation monochromator) of a DeltaFlex. The emission monochromator TDM1200 with a bandpass of 12 nm was scanned from 200-800 nm in 1 nm increments. A PPD850 detector was used with DeltaHub timing electronics. A Teflon block was placed in a front face cuvette holder. A UV Linear Grid

Polarizer and PPD850 in the emission optics at different emission polarizer configurations. The defect at 510 nm is due to the Wood's anomaly and is vertically polarization biased. If one suspects a Wood's anomaly and has no wavelength correction factors they can run the measurement with the emission polarizer horizontally orientated. The count rate was optimised for the vertical polarization using a UV ND 1.0 and UV ND 0.3 on the excitation arm for no polarizer and a UV ND 1.0 for all other polarizer orientations. This retained a detector linear response ($<2\times10^{6}$ CPS), data is divided by the transmission spectrum of the UV ND filters **Figure 24** to compensate for their use. The sudden dips in intensity are due to Wood's anomaly's which come from the grating. The manufacturer's theoretical grating efficiency is plotted below the measured data and the measured dips align with the Wood's anomaly's.

The presence of the Wood's anomaly can create a significant kink in the MCorrect file [145,146] as shown at approximately 550 nm in **Figure 37**. Uncorrected spectra within this wavelength range are unfortunately frequently published with incorrect conclusions such as the fitting of multiple peaks brought about by instrumental distortion. The relative quality of the correction factor can be assessed by the measurement of the lamp three times and dividing the SD by the mean alongside the SNR_{FSD} with respect to the emission wavelength by using *A* as the on value and *B* as the off value c.f. **Equation (21)**. The output of V is weakest at 290 nm the minimal output of the lamp.
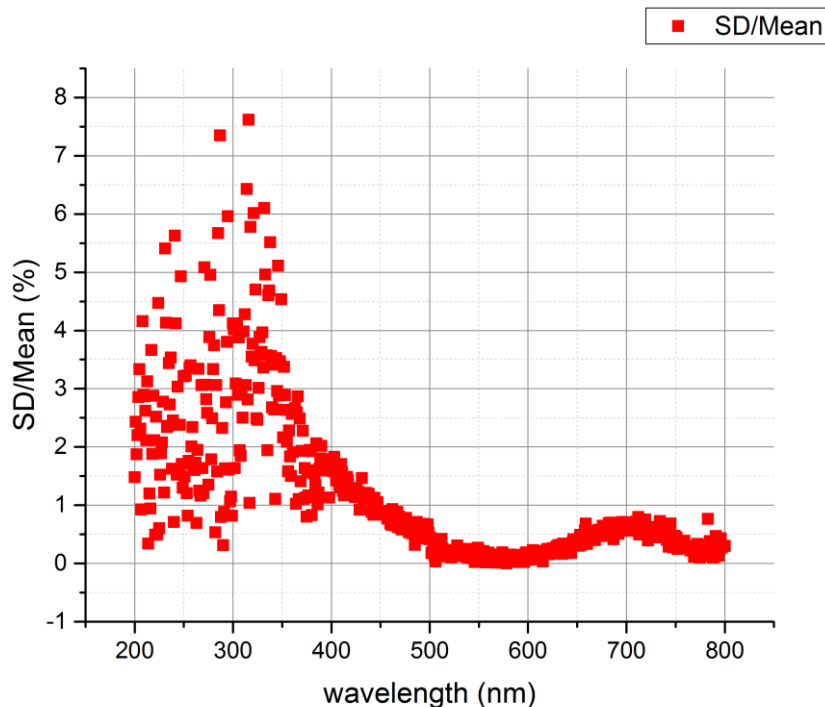
**Figure 38**: The SD/mean of V (lowest output in the UV) normalised at its peak 578 nm (**Figure 37**) measured 3 times. The Osram 64640 HLX mounted in a DeltaDiode case ran at 1.58 A and 6.9 V affixed to the excitation port (no excitation monochromator) of a

48

DeltaFlex was deliberately tilted at slight angles (to over-emulate user error). $\text{SNR}_{\text{FSD}}(290$ nm)=200 and $\text{SNR}_{\text{FSD}}(578$ nm)=263000.

Care should be taken care when using the MCorrect particularly when second order effects come into play[22] for this reason it is always worthwhile plotting both the corrected and uncorrected signals. Strictly speaking the measurement with the calibration lamp used to make MCorrect itself will be somewhat influenced by second order wavelength effects but fortunately the output of the filament is weak in the UV and maximal in the NIR minimising this effect. When using the XCorrect and MCorrect the dark offset should be applied otherwise the dark counts measured by the detector will be incorrectly artificially amplified by the correction factor which can be a problem particularly near the edge of the detectors range, for example in the R928 at 800-850 nm where MCorrect is massive. The corrected signals R1c and S1c are computed by:

$$R1c = \left(R1 - R1_{\text{Dark}}\right) \times XCorrect = R1_{\text{DO}} \times XCorrect \qquad (27)$$

$$S1c = \left(S1 - S1_{\text{Dark}}\right) \times MCorrect = S1_{\text{DO}} \times MCorrect \qquad (28)$$

Figure 39: An extended water Raman emission scan of Starna Raman certified Raman Standard 3-Q-10/WATER measured using a Fluoromax 4. The excitation monochromator (1200/330 grating) was set at 350 nm with a bandpass of 5 nm. The emission monochromator (1200/500 grating) was scanned from 290-850 nm with a 5 nm bandpass at 0.5 nm increments for an integration time of 1 s. The first peak at 350 nm is the 1st order

---

[22] The monochromator will allow light to pass at wavelengths $n\lambda$ where n is an integer therefore when only a monochromators and detector are employed light at 400 nm will be re-measured at 800 nm. The efficiency will be lower at second order wavelength and be dependent on the grating. Second order effects can be removed by using SP, LP and BP filters in conjunction with the monochromator.

Rayleigh and a low level of stray light can be observed after this peak. This is followed by the 1st order water Raman peak at 397 nm. These are re-measured when the emission monochromator is at second order wavelengths of 700 nm and 794 nm respectively. These plots are scaled to look at the noise at the baseline in more detail. In the top graph there is a dark offset of 329.4 counts. In the middle plot the MCorrect is seen to multiply S1 and this incorrectly amplifies second order effects. When the dark offset is disabled, the dark counts will also be incorrectly multiplied.

The importance of applying both the dark offset and wavelength correction factors is illustrated in **Figure 39**. Solvent properties such as Raman lines and instrumental stray light will likewise in the same manner be multiplied out by the wavelength correction factor. When measuring samples to minimise these additional effects, a blank subtract of the solvent in a matching cuvette may also be carried out. The water Raman line at 397 nm with a 350 nm excitation may be examined in more detail using both an excitation and emission scan with correction factors and normalisation by the lamp. If one decides to omit use of the XCorrect and division by the lamp for the emission spectrum, comparison of 2 emission spectra at different wavelengths will be invalid. Likewise, if one decides to omit use of MCorrect for an excitation spectrum, comparison of 2 or more excitation spectrum at different wavelengths may be invalid. If one wants to compare an excitation to an emission spectrum division by the reference and application of both XCorrect and MCorrect must be applied as demonstrated in **Figure 40**, **Figure 41** and **Figure 42**. Although the data may be corrected by subtracting dark counts, dividing by the reference of the lamp and multiplying by wavelength correction factors one major issue is the CPS and CPS/µA units are in a manner of speaking arbitrary because the instrumental correction factors are relative and not ratiometric. This means a sample measured will yield a different intensity value (CPS/µA) when measured on two different instruments even if they are the same model which can lead to difficulties when comparing data from lab to lab. To compensate for this in some fields standards of dilute quinine sulphate are used and the expression of fluorescence is given in quinine sulphate units. The water Raman peak may also be used so data can be expressed in water Raman units [118,147]. These units are particularly popular within the field of water quality measurements however most research groups tend to stick to their single instrument when carrying out a fluorescence study and hence measure in CPS or CPS/µA [148,149]. Correction factors are also influenced by 2nd order effects which will be illustrated in some more detail later.

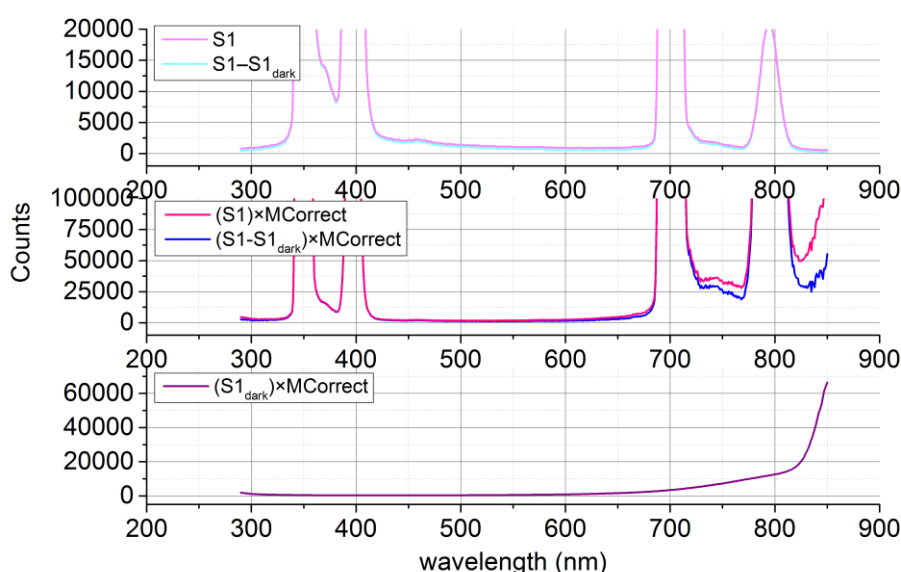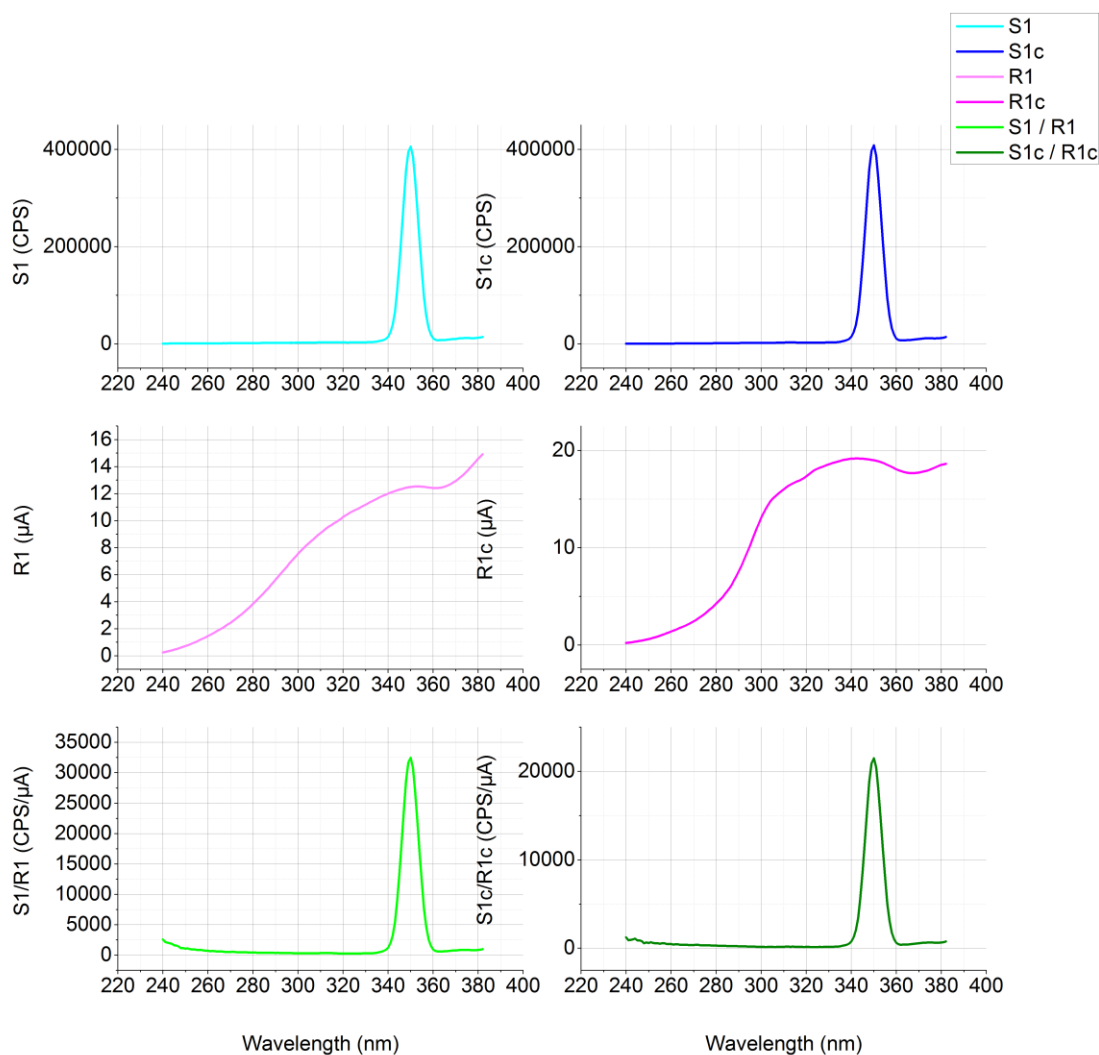**Figure 40**: A water Raman excitation scan of Starna Raman certified Raman Standard 3-Q-10/WATER measured using a Fluoromax 4. The emission monochromator (1200/500 grating) was set to 397 nm with a bandpass of 5 nm. The excitation monochromator (1200/330 grating) was scanned from 240-380 nm with a 5 nm bandpass at 0.5 nm increments using an integration time of 1 s. 6 sets of signals were recorded; S1 and R1 which are the raw signals – its useful recording these signals to check that the measurement is within the working linear range of the detectors, in addition the corrected versions to see the wavelength corrected shape of S1c and R1c respectively. For an excitation spectrum the MCorrect multiplies the spectra by a constant value and in some cases it is not necessary. For an excitation spectrum it is necessary to divide S1/R1 in order to compensate for differing lamp intensity at each excitation wavelength. The wavelength corrected S1c/R1c is the true spectrum which is the spectrum which should be used if peak fitting is to be carried out. The excitation spectrum of the water Raman peak at the emission wavelength of 397 nm gives an excitation wavelength maximum at 350 nm as expected.
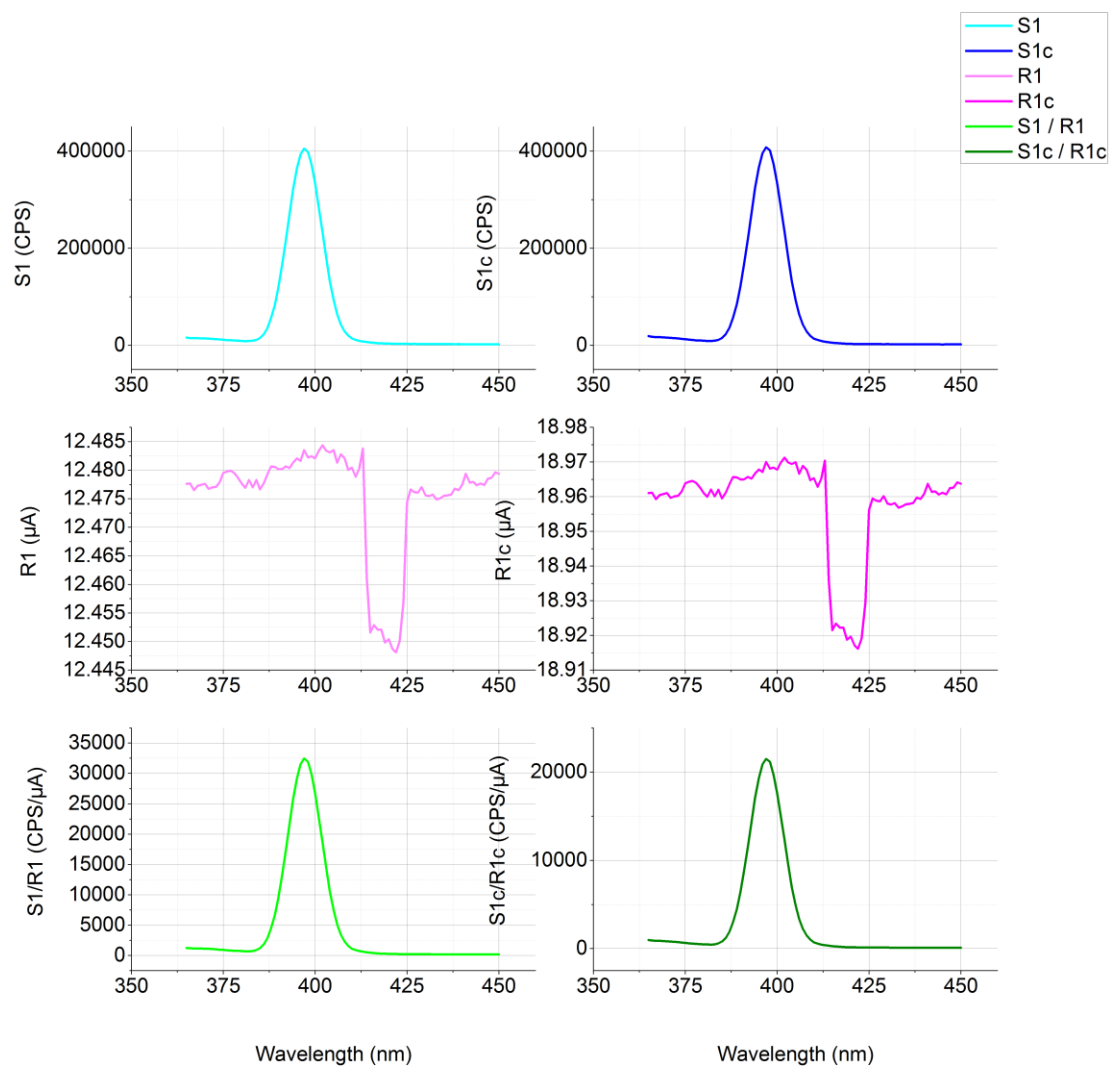
Figure 41: Emission scan of Starna Raman certified Raman Standard 3-Q-10/WATER measured using a Fluoromax 4. The excitation monochromator (1200/330 grating) was set to 350 nm with a bandpass of 5 nm. The emission monochromator (1200/500 grating) was scanned from 365-450 nm with a 5 nm bandpass at 0.5 nm increments for an integration time of 1 s. 6 sets of signals were again recorded. For the emission spectrum in some cases one may get away without dividing by the lamp or using the XCorrect which multiples the lamp signal by a constant value. It is however recommended to divide by the lamp to account for any drift in the lamp between long periods of measurement.
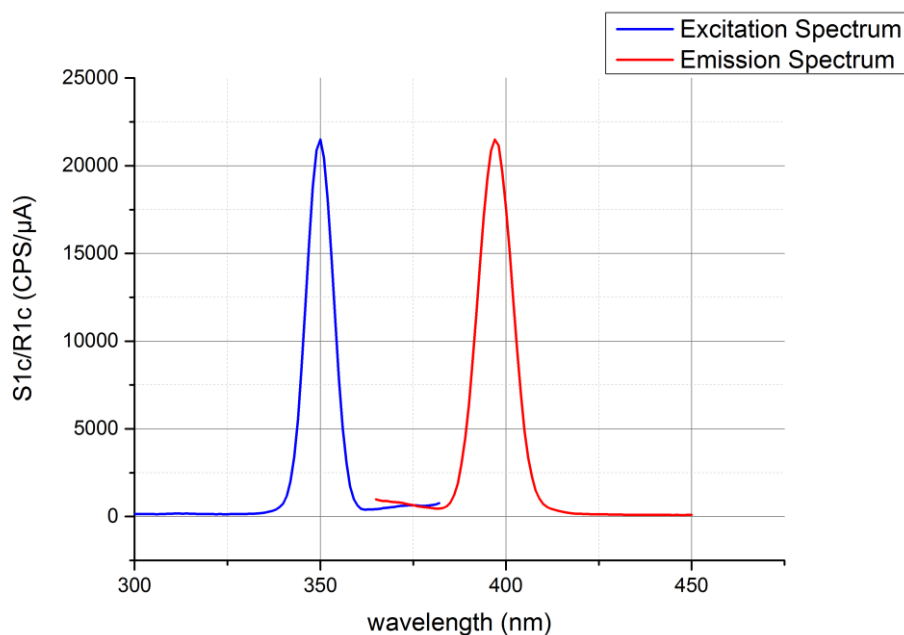
Figure 42: The corrected water Raman excitation (S1c/R1c) and emission (S1c/R1c) spectra of the water Raman peak excited at 350 nm with 397 nm emission. The excitation peak was fitted to a Gaussian with base=230±20 CPS/µA, centre=350 nm, FWHM=8.32±0.06 nm and area 188000±1000 nm CPS/µA with a R^2=0.997. The emission peak was fitted to a Gaussian with base=220±30 CPS/µA, centre=397 nm, FWHM=10.64±0.07 nm and area=240000±2000 nm CPS/µA with a R^2=0.998.

2.2.3 Monochromator Bandpass

When the bandpass of a monochromator is opened up, the throughput of the monochromator increases. This will increase the signal to noise ratio for weak samples however if the bandpass is set too high it is possible that spectral wavelength resolution will be lost. This is illustrated in **Figure 43**, which shows an ideal measurement, uninfluenced by the detector or sample strength. In practice, the selection of bandpasses used for a measurement will be dependent on both the detector and sample. A weak Raman signal such as that from cyclohexane can be used to demonstrate the trade-off between throughput and bandpass **Figure 44**. When the bandpasses are too low the signal of even the strongest Raman peak at 628 nm cannot be observed. As the bandpass is opened up the signal of the main peak at 628 nm can be distinguished from the noise and 4 smaller individual peaks can be seen between 550-580 nm. As the bandpasses are opened wider these 4 peaks merge and appear to be a single structure.
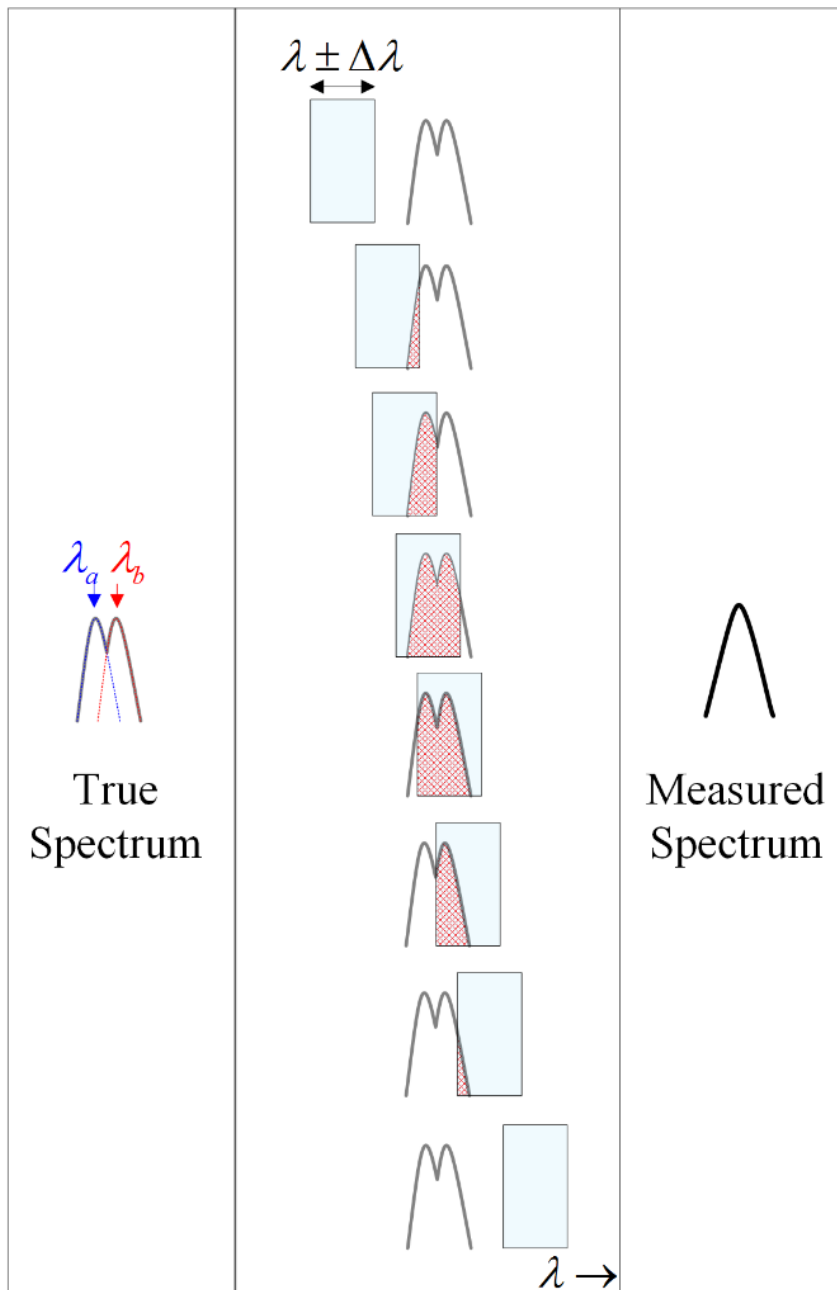
Figure 43: If the bandpass of an instrument is set too high spectral resolution may be substantially lost. Two distinct peaks are shown on the left and these are measured with a wide bandpass as shown in the middle. The recorded intensity reading per wavelength increment is illustrated by the red cross-section. The computed spectrum from this data is displayed to the right and illustrates that the measured spectrum has merged two spectral peaks into a singular one i.e. lost spectral resolution [28].
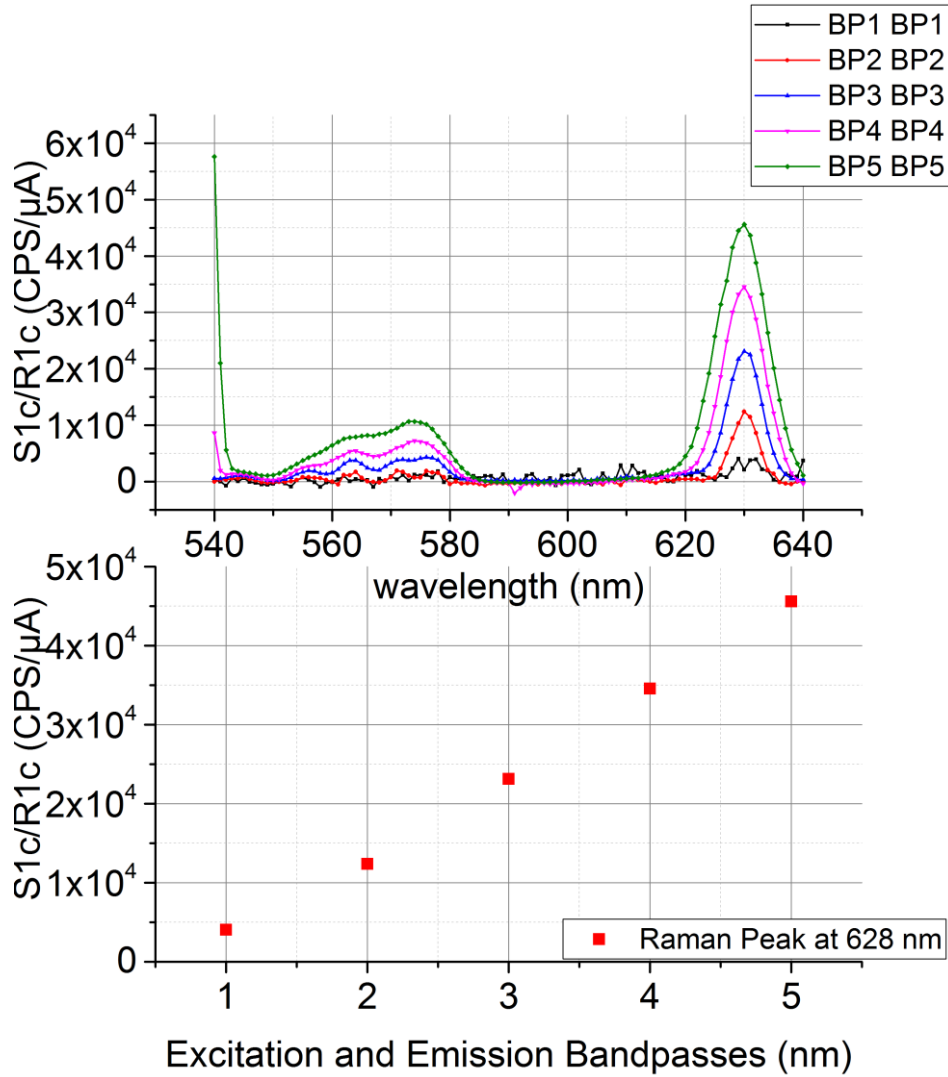
Figure 44: Raman spectrum of cyclohexane measured in a Fluorolog 3-22 with a R928 PMT. The excitation monochromator (1200/330 double grating) was set to 532 nm and the emission monochromator (1200/500 double grating) was scanned from 540-640 nm in 1 nm increments using an integration time of 30 s. The bandpass of the monochromators were doubled. The well-defined Raman peaks at 550-580 nm measured with excitation and emission bandpasses of 2 nm and 2 nm respectively are poorly resolved when the bandpasses are opened up to 5 nm and 5 nm respectively.

Since fluorescence is red-shifted in comparison to excitation and one does not want to measure Rayleigh scattering in general the following conditions are setup for running emission and excitation spectra respectively:

$$\lambda_{em}^{Start} \geq \lambda_{ex} + BP_{em} + BP_{ex} \qquad (29)$$

$$\lambda_{ex}^{End} \leq \lambda_{em} - BP_{em} - BP_{ex} \qquad (30)$$

In order to remove second order Rayleigh, for an emission spectrum a LP filter with $\lambda_{cut} > \lambda_{ex} + 10$ nm is placed on the emission arm and for an excitation spectrum a LP filter

with $\lambda_{cut}<\lambda_{em}-10$ nm. In the case of **Figure 44** when both excitation and emission bandpasses are set to 5 nm **Equation (29)** is not satisfied and the edge of the Rayleigh line can be observed. The raw data S1 and R1 **Figure 45** can be examined in more detail. Any fluctuations in the lamps output R1 are clearly mimicked in S1 this is seen specifically at the 628 nm Raman peak where the lamp fluctuates for the measurement at 5 nm bandpasses. Comparing the ratio of the heights of the peaks at 628 nm for the raw S1 data **Figure 45** with the S1c/R1c data **Figure 44** one can see that division by R compensates for the increase in output when the excitation monochromator is opened up. However, no such compensation is made for opening the emission monochromator bandpass. S1c/R1c is therefore influence by the emission bandpass as mentioned wavelength correction factors are carried out at a single bandpass and are relative (not absolute).
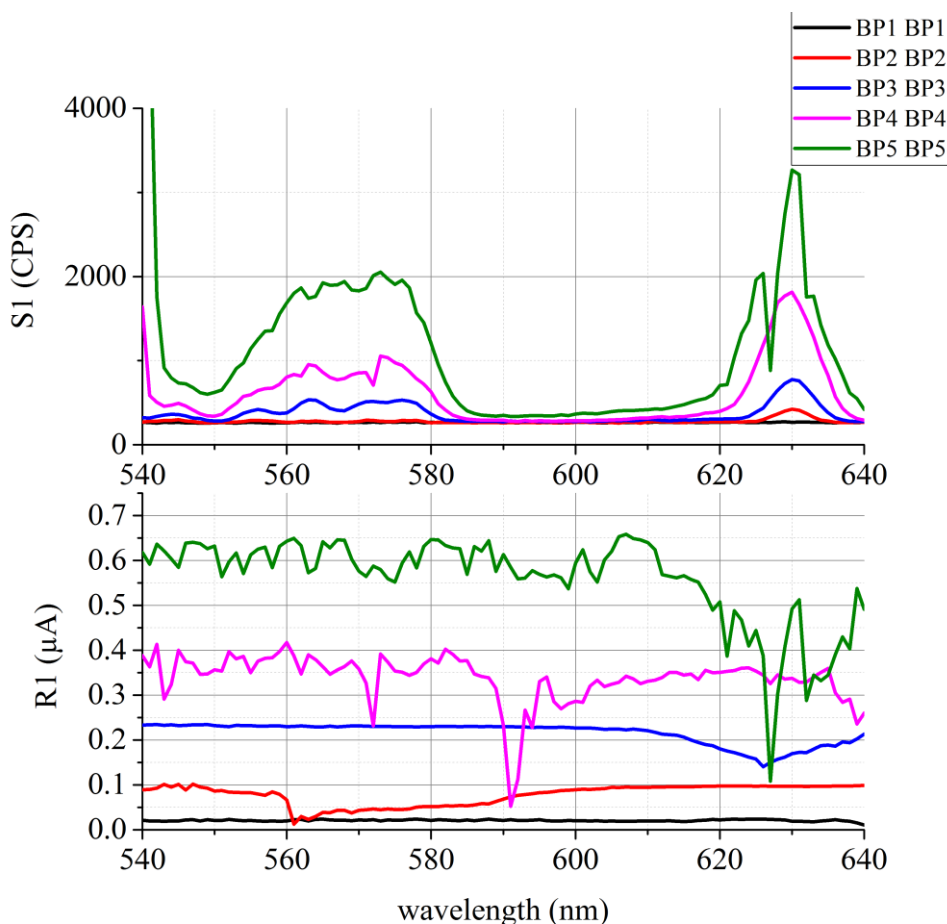
Figure 45: Its insightful to look at the uncorrected data from **Figure 44**. The number of counts in S1 is actually much lower than the number of counts reported in S1c/R1c data. However, because a 30 s integration time was used the total number of counts measured is 30 times that plotted. Fluctuations in the lamp output R1 are clearly reflected in the S1, particularly at the 628 nm peak when the bandpasses were set to 5 nm.

When a weak sample is used with a low bandpass another consideration is the integration time. In **Figure 44** when the bandpasses were set to 2 nm and the integration time was set to 30 s a decent Raman spectrum could be measured. If this integration time is lowered to 0.1 s the Raman spectrum is completely lost in the noise **Figure 46**.
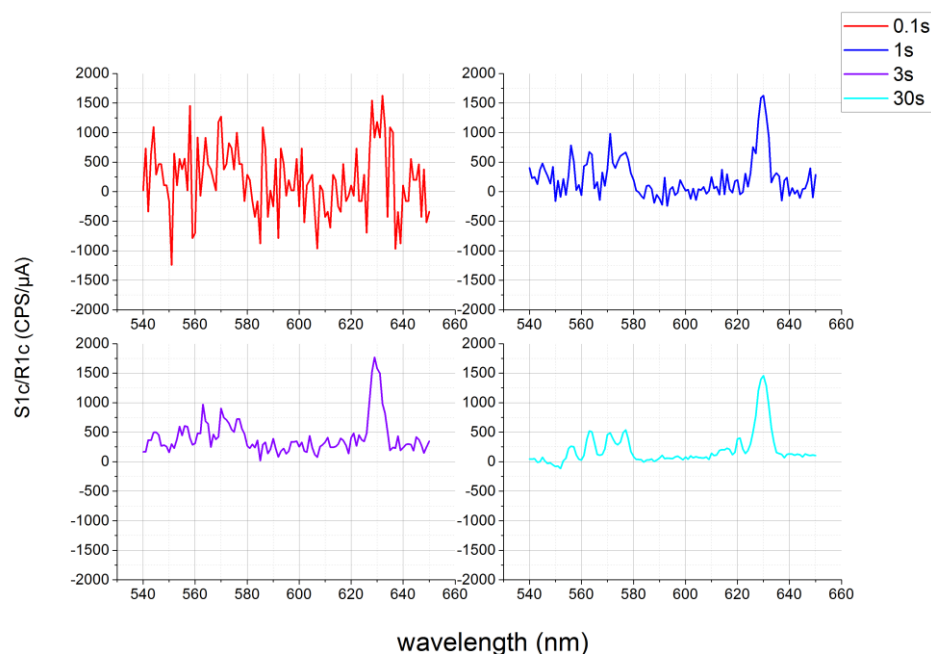
Figure 46: Raman spectra of cyclohexane measured at 0.1 s, 1 s, 3 s and 30 s integration time using a Fluorolog 3-22. The excitation monochromator (1200/330 double grating) was set to 531 nm and a 2 nm bandpass. The emission monochromator (1200/500 double grating) was scanned from 540 nm to 640 nm in 1 nm increments. The peaks are similar to that reported in literature [150].

Figure 47 looks at the effect of altering the bandpasses on a strong fluorescence sample with fixed integration time. As the bandpasses are opened from 0.5 nm to 5 nm one can observe the following trends. At low bandpasses the fluorescence intensity is too low and the measured spectra are seen to be unacceptably noisy. As the bandpasses are opened wider more counts are allowed through to the detector and acceptable spectra are measured. In practice the best spectrum is obtained when the number of counts at the peak are 50-100 % of the linear range of the detector. As the bandpass is increased further the detector stops behaving linearly and the spectra become artificially broadened. If the bandpass is opened even further the detector begins to switch off leaving a series of dips and the apparent measurement of multiple peaks. When taking measurements, the bandpass is usually altered with respect to the intensity of the sample; weak fluorescent samples may require the slits to be opened up in order to obtain enough counts to measure a fluorescence spectrum. In

these cases, clearly one has to make an appropriate trade-off between throughput and spectral resolution. In the example above for simplicity both monochromators had matching bandpasses however in order to obtain a high resolution emission spectrum for a weak sample the excitation bandpass may opened wide and the emission bandpass may be narrowed. In a similar argument for an excitation spectrum the emission bandpass may be widened and the excitation bandpass may be narrowed.
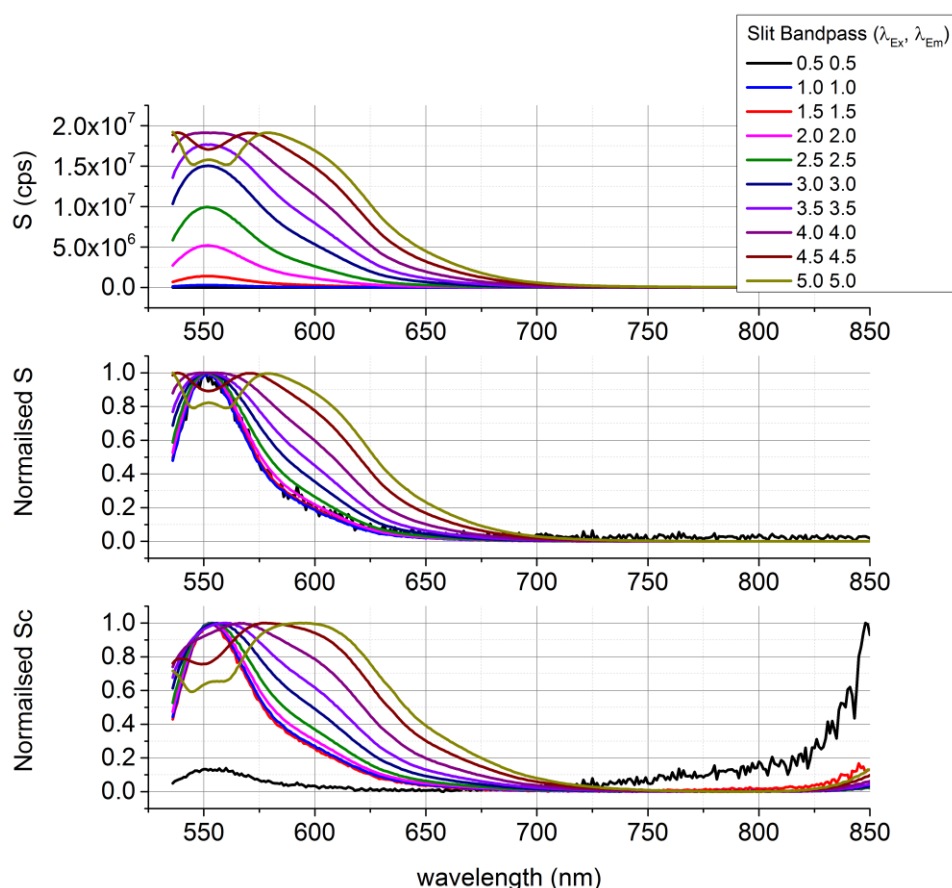
Figure 47: The emission spectra of Rhodamine 6G in ethanol with an absorbance maximum of ~0.1 measured under different excitation and emission slit widths in a Fluoromax 2 with a R928 PMT. The emission monochromator (1200/330 grating) was set to 475 nm and measurements were carried out with an integration time of 0.1 s. The emission monochromator was scanned from 540-850 nm in 1 nm increments. The top plot is the raw S signal in CPS. At low slit widths for example the black curve the signal to noise ratio is poor and this can be seen in more detail when the data is normalised and in particular when the correction factor is applied. As the slit widths of the monochromators increase, the signal to noise ratio is observed to increase however as the linear range of the detector is surpassed, the signal is observed to square off towards the peak. At even higher wavelengths, the detector begins to switch off and one or more dips are observed instead of the emission peak maxima. The linear range of the detector for the R928 PMT is stated to be 2×10^6 CPS [115].

2.2.4 Detector Type

A brief example of the importance of signal to noise with regards to steady-state fluorescence measurements is given in **Figure 46**. The signal to noise ratio SNR is naturally dependent on all the components of a fluorimeter however the main component governing the SNR is the detector; the choice of detector naturally depends on the ultimate application and budget however it's worth discussion how the PMT **Figure 48** and CCD **Figure 49** work and their sources of noise [151]. For sensitive spectroscopy applications, the signal to noise ratio is an important parameter as it gives a measure of how weak a signal can be distinguished from background noise. There are a number of different types of noise which influence the data quality of the recorded signal. The first source of noise is the shot noise and this is the random statistical variations of the incident light. The shot noise is proportional to the square root of the signal:

$$\text{Shot Noise} = \sqrt{\text{Signal}} \qquad (31)$$

Next there is the Dark signal; this type of noise will occur for detectors which utilise components like a cathode such as the photomultiplier tube illustrated in **Figure 48**. In addition to the electrons that occur as the result of an interaction of the photocathode with the incident photon. Thermal fluctuations may also result in the release of an electron from the dynodes resulting in a voltage at the anode. Although a discriminator will be used to discriminate voltages above a certain threshold, there will still be some dark counts which exceed this threshold and are measured. This type of noise is called the Johnson noise or dark signal as these are thermally dependant, a cooled detector will exhibit less dark noise.

$$\text{Dark Signal} \propto T \qquad (32)$$

The dark signal will also have a statistical noise associated with it known as the dark noise:

$$\text{Dark Noise} = \sqrt{\text{Dark Signal}} \qquad (33)$$

One additional noise source to consider is the electronic readout noise. Although this is present in all electronic devices, it is particularly pronounced in a detector such as a CCD which has multiple readouts of each individual row and column. In general, a PMT is noise limited by the dark counts and a CCD is noise limited by the readout noise. For steady-state measurements the PMTs detector saturation is governed by how fast the PMT can collect in counts per second, CPS, while the CCDs saturation limit on the other hand is limited by the number of levels it possesses. A 16 bit CCD will have a maximum of 65,000 levels and also depending on the setting the number of electrons it has available. A CCD usually is

setup with a number of settings which have differences in the number of electrons per count. The high light setting has the more electrons per count, the high sensitivity setting has the least electrons per count and the best dynamic range setting is between these two settings.
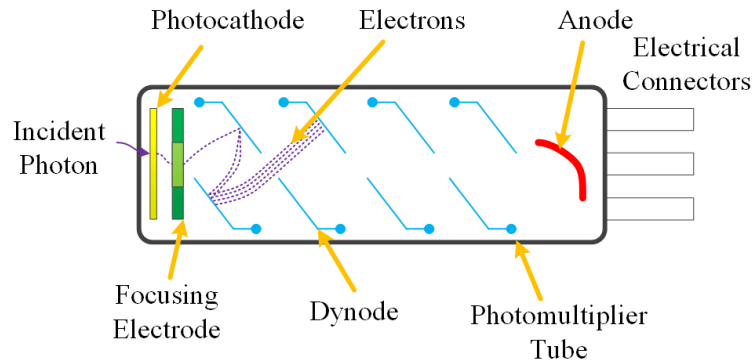
Figure 48: Principle of a photomultiplier tube, an incident photon impinges on a photocathode and releases an electron, this electron interacts with a dynode chain which increases releases multiple electrons and the voltage of the anode is recorded. [137]
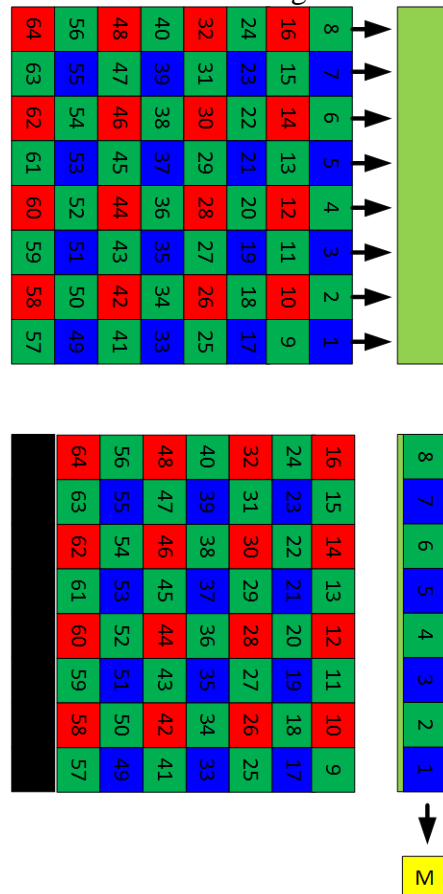
Figure 49: Illustration of CCD readout, there is a parallel register shift of 1 row and then a serial register of 1 column. The charge of each pixel in the first column is read out in sequence until the entire row is read. Then there is another parallel register shift and the process continues until all the rows are read out i.e. the charge of each CCD pixel is read out sequentially (1-64 in the diagram). There is a source of each noise for each readout operation and these can summate.

60

Figure 50: Top the emission scan of Starna Raman certified Raman Standard 3-Q-10/WATER measured using a Nanolog at an excitation wavelength of 350 nm and the excitation monochromators (1200/330 double grating) bandpass was set to 5 nm. The emission monochromator (1200/500 grating) was scanned from 365-450 nm with a 5 nm bandpass at 0.5 nm increments for an integration time of 1–18 s using a double grating excitation monochromator and a single grating monochromator on the emission with a R928 PMT. Bottom the calculated SNR_{FSD} with respect to integration time.
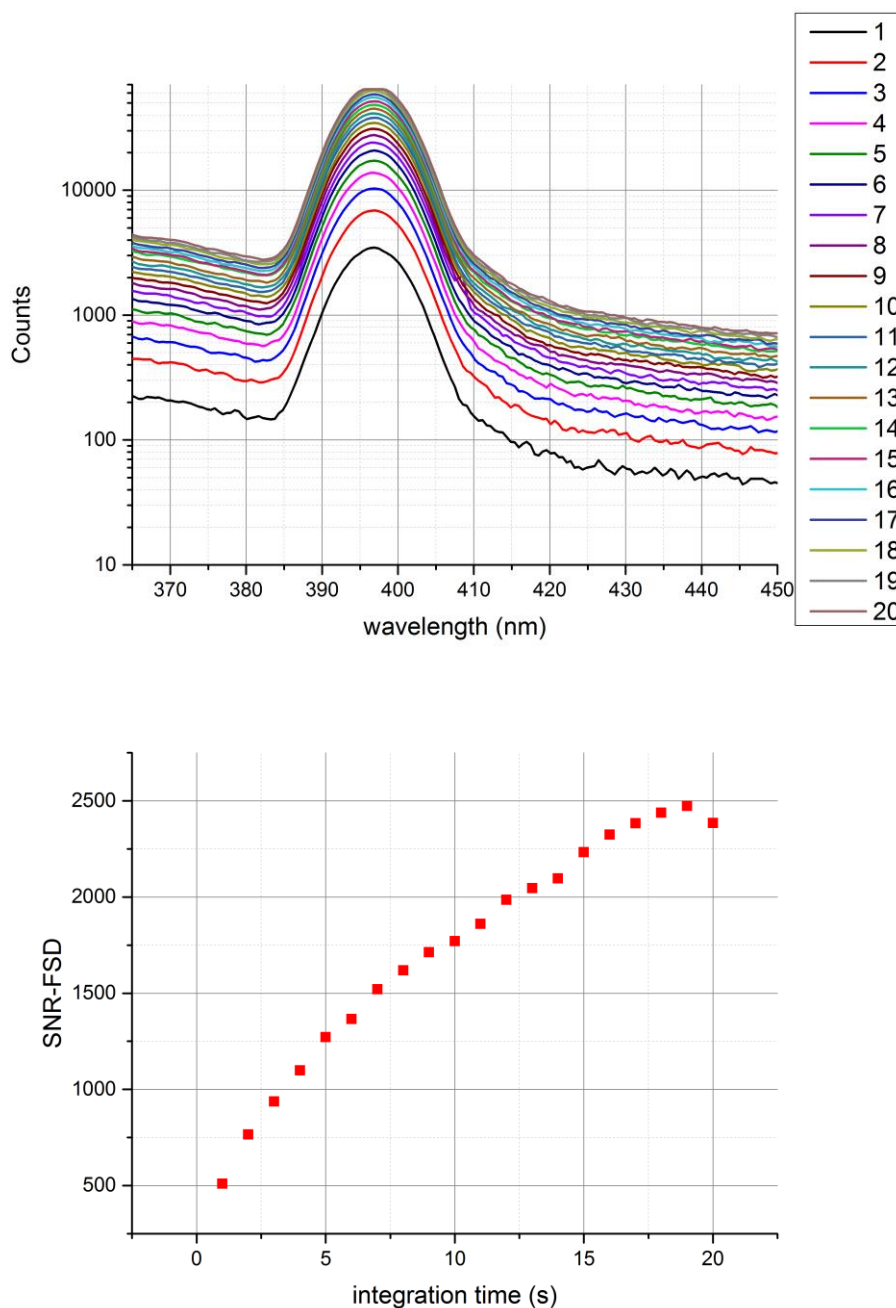
Figure 51: Top the emission scan of Starna Raman certified Raman Standard 3-Q-10/WATER measured using a Nanolog at an excitation wavelength of 350 nm and the excitation monochromators (1200/330 double grating) bandpass was set to 5 nm. The iHR320 emission spectrograph (300/500 grating) bandpass was set to 5 nm[23]. The Synapse 1024×256 open-electrode CCD detector was set to run using the Best Dynamic Range setting (2.570 electrons per count) with the electron read out speed at 20 kHz. The integration time was increased from 1-20 s. For the CCD to function there is a ~1000 counts background noise, it is assumed this is constant and it is subtracted from each curve. The SNR$_{FSD}$ measured with respect to integration time (bottom).

---

[23] The emission range of the spectrograph is not user selected like in the case of a scanning monochromator. Instead it is dictated by the working wavelength regime of the grating across the spectrograph. Data is recorded across the entire spectrograph at the highest wavelength resolution. The end user can crop the recorded data to suit their regime of interest.

A comparison of **Figure 50** and **Figure 51** shows that the SNR increases for the PMT as the integration time increases t is consistently higher than the CCD moreover the CCD shows detector saturation at an 18 s integration time. It should be noted however that the CCD measures the entire spectrum in the specified integration time whereas the PMT only measures one wavelength in the specified integration time, the spectrograph/CCD combination has the advantage that it can measure a vast range of emission wavelengths simultaneously [152]. The CCD has the analogy of being like a bucket; it can be filled, emptied and refilled allowing one to measure more counts than with a single acquisition however there may be spills every time the bucket is emptied, in the case of the CCD this manifests itself as readout noise.

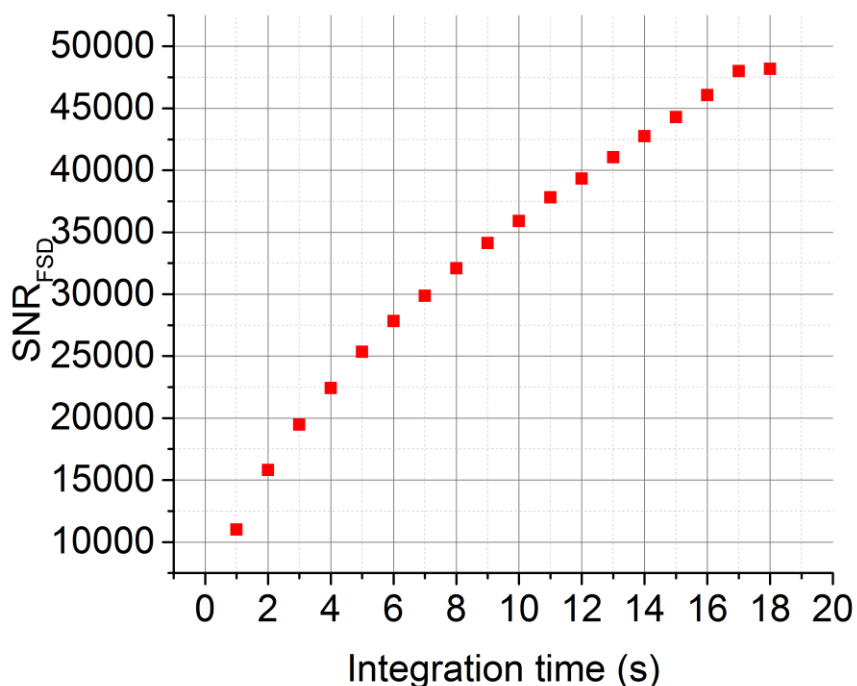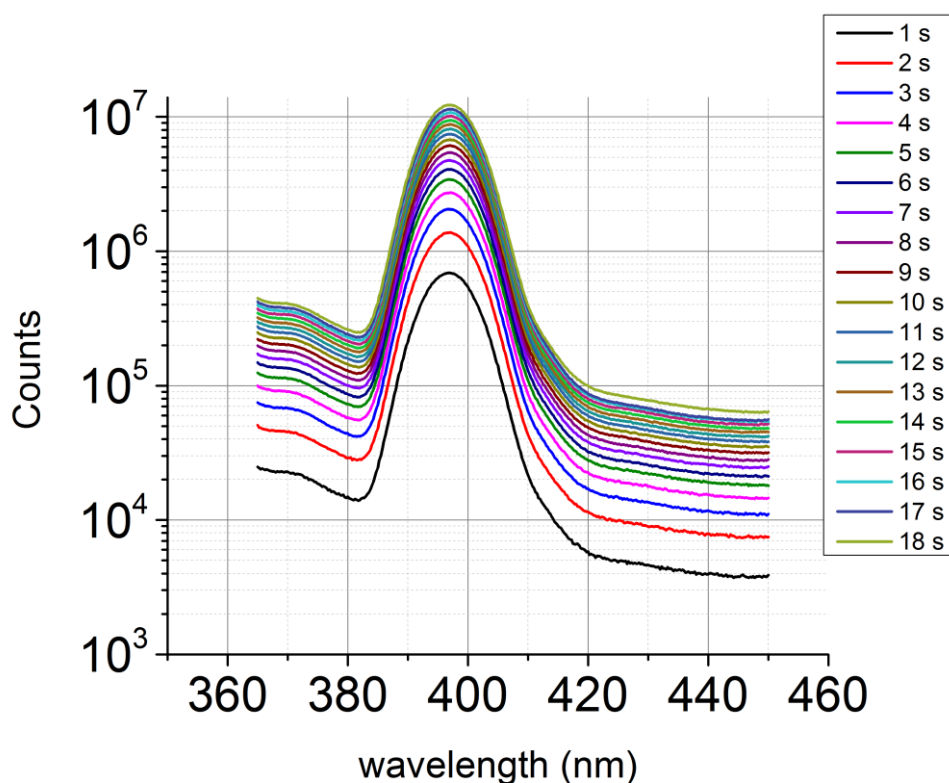**Figure 52**: The emission scan of Starna Raman certified Raman Standard 3-Q-10/WATER measured using a Nanolog at an excitation wavelength of 350 nm and the excitation monochromators (1200/330 double grating) bandpass was set to 5 nm. The iHR320 emission spectrograph (300/500 grating) bandpass was set to 5 nm. The Synapse 1024×256 open-electrode CCD detector was set to run using the Best Dynamic Range setting (2.570 electrons per count) with the electron read out speed at 20 kHz. For the water Raman peak to be near the limit of the detector, it took about 18 s. The data shows this 18 s increment split between 1 single measurements and 18 1 s measurements. The artificial offset of 1000 counts was removed for each acquisition.
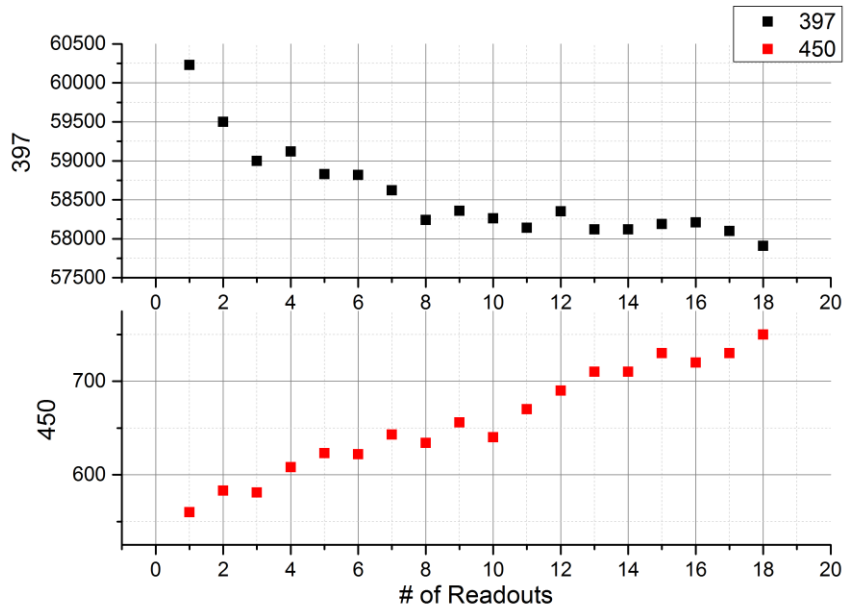
Figure 53: Looking at the two positions 397 nm, the water Raman peak and 450 nm a position representative of noise. One can see that the signal at the peak is falling while the noise simultaneously increases.
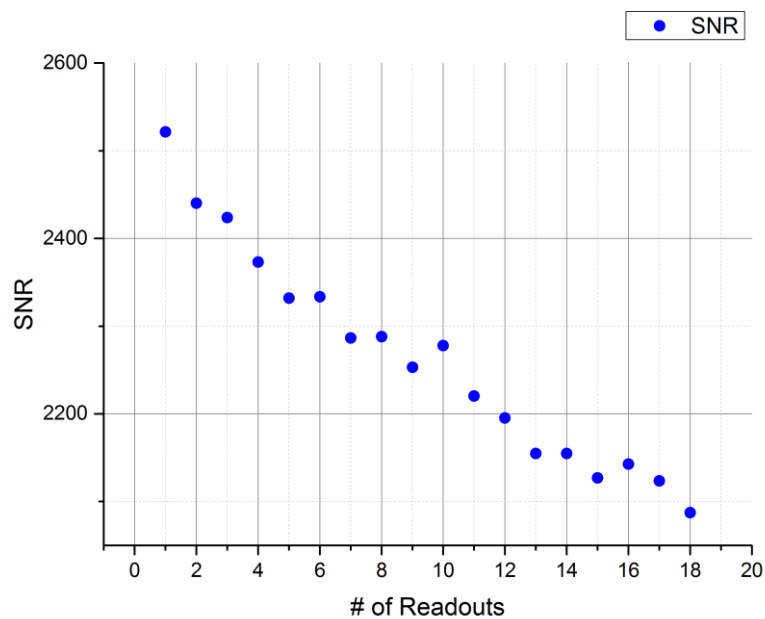
Figure 54: The SNR ratio measured as the number of readouts is increased. This data fits to a linear line with an intercept of 2480±10, a slope of –23±1 and a R^2=0.954.

The effect of multiple accumulations vs a single accumulation for the same total integration time of 18 s is shown in **Figure 52**. The plot uses a log scale so the difference in noise can also clearly be depicted. As the number of accumulations increases, stronger signals such as the Rayleigh lines can be measured alongside the weaker water Raman signal increasing the dynamic range of the measurement as the number of levels that the total measurement

has access to is $n \times 65000$. The trade-off however is that the noise increases substantially with the number of readouts. The magnitude of the water Raman line falls with respect to the overall number of accumulations however the noise is clearly increased as the number of accumulations increases, naturally this decreases the signal to noise ratio. For the CCD there is hence a trade-off between dynamic range and signal to noise.
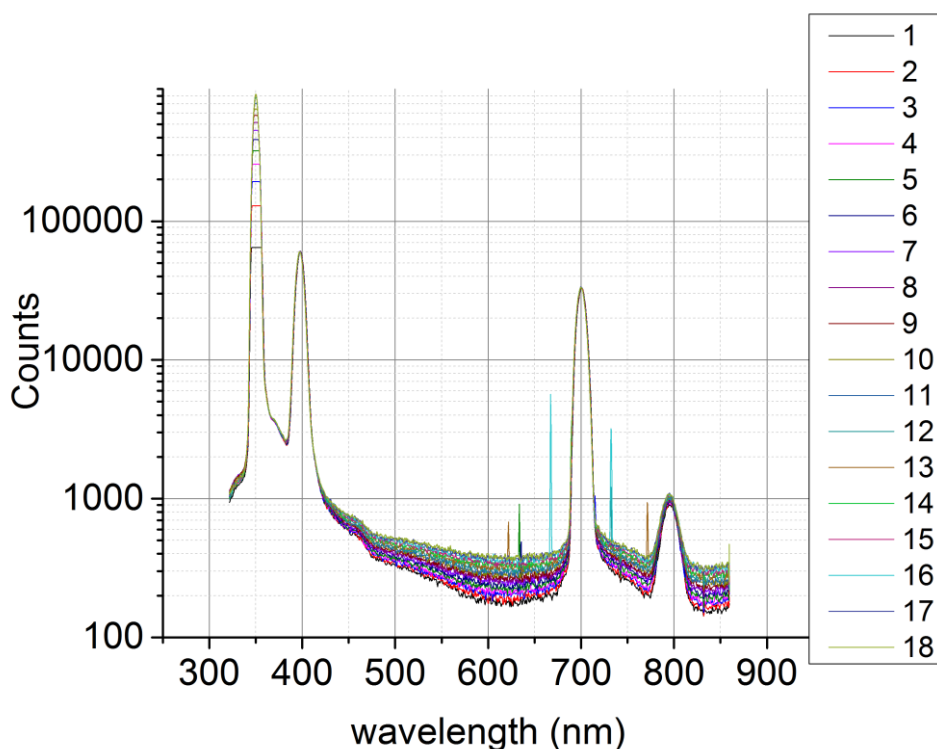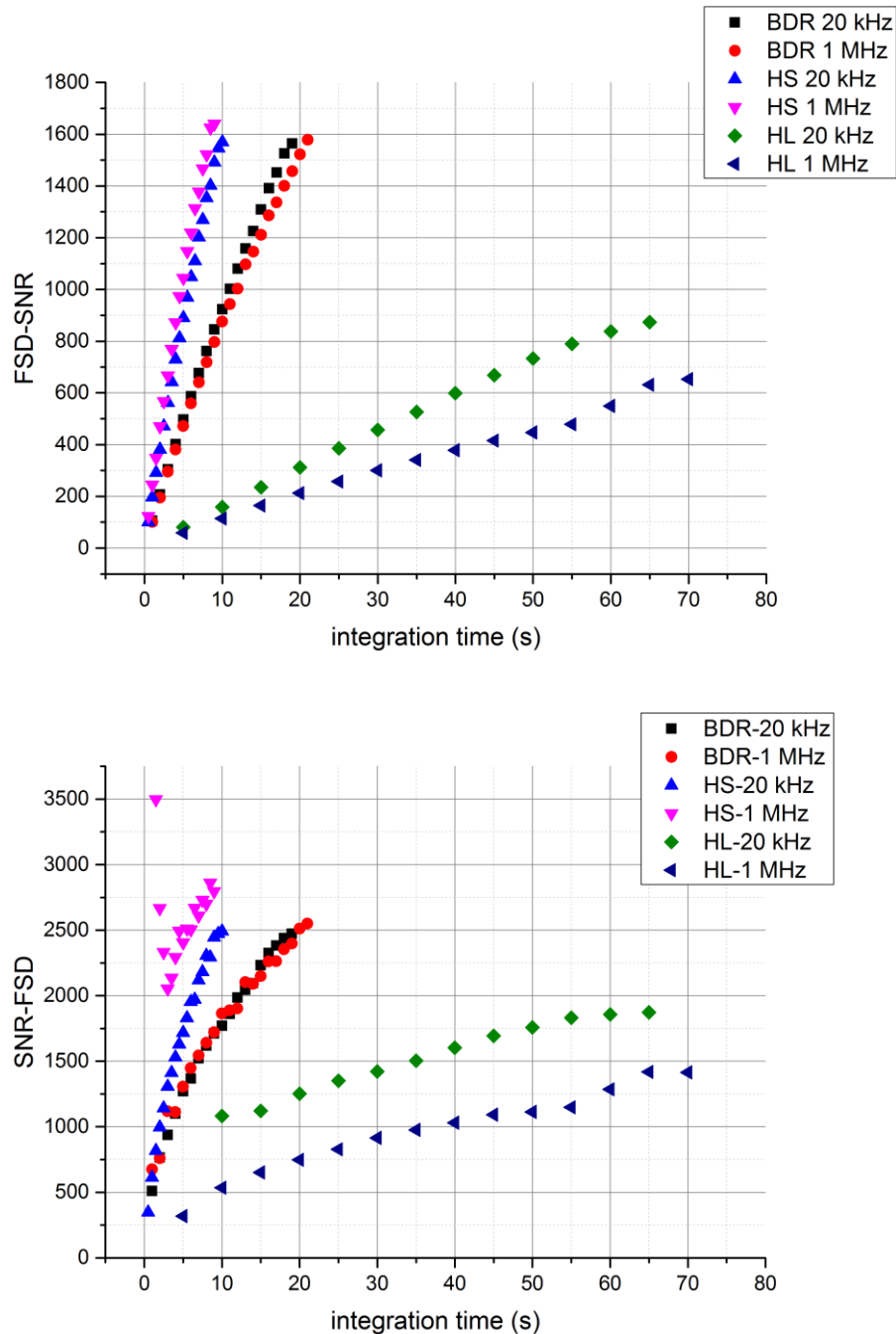

Figure 55: The emission scan of Starna Raman certified Raman Standard 3-Q-10/WATER measured using a Nanolog at an excitation wavelength of 350 nm and the excitation monochromators (1200/330 double grating) bandpass was set to 5 nm. The iHR320 emission spectrograph (300/500 grating) bandpass was set to 5 nm. The Synapse 1024×256

Open-Electrode CCD was operated in the following modes, Best Dynamic Range (2.570 electrons per count), High Sensitivity (1.283 electrons per count) and High Light (18.162 electrons per count) with electron speeds at 20 KHz and 1 MHz respectively. The subtraction of the artificial 1000 counts offset for HS and HL led to some negative data points at 450 nm for HS and HL which is why some data points are missing at the start. For BDR and HL an increased readout speed of 1 MHz results in a slightly poorer SNR, for HS the 1 MHz readout speed results in a slightly better SNR but there are more difficulties in subtracting the 1000 count artificial background at low integration times. The recorded signals for BDR and HS max out at 65,000 counts with a SNR-FSD of about 2500 due to the 16 bit limit of the CCD. For HL the signal saturates at ~32,000 counts, this limitation is brought about due to the limitation of number electrons available in the system opposed to the levels of the CCD. The SNR-FSD for HS at 1 MHz is artificially higher due to the incorrect offset. In this case the HS data looks more realistic and there are no negative values. The reported SNR is smaller than the data compensated for the 1000 counts.
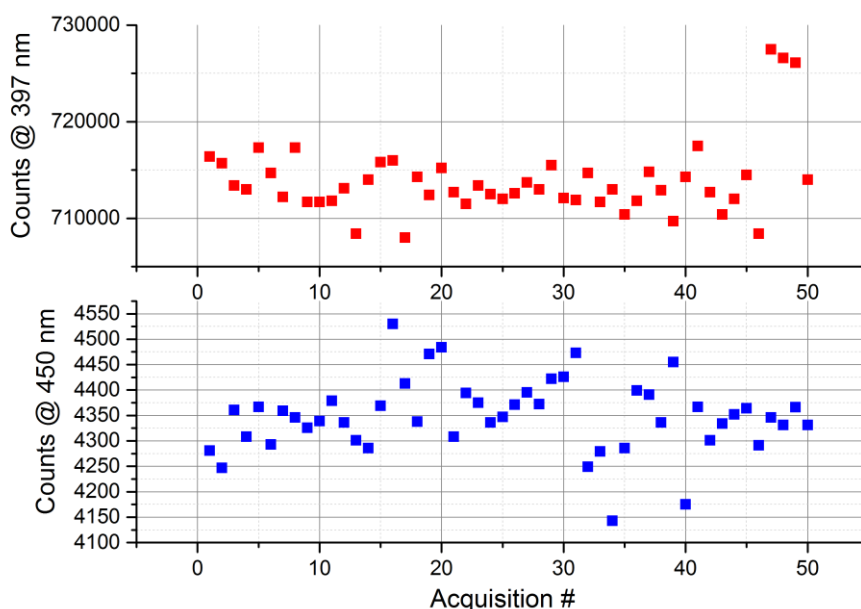
Figure 56: The measured number of counts at 397 nm and 450 nm using the R928 PMT T1 for a series of 50 water Raman emission acquisitions using the same conditions as in **Figure 50** with a 1 s integration time. Descriptive statistics give the number of counts at 397 nm to be 713,000±2,000 and 450 nm to be 4350±70. The SNR-FSD is calculated to be 10800±100. The 3 outliers were removed from the calculation as they were likely due to a lamp fluctuation.

The number of electrons and electron repetition rate can be varied for the CCD however the maximum SNR-FSD for the water Raman is a maximum at 1600 without compensation for the baseline or 2500 when compensation is applied due to the fact the CCD can only measure 65000 counts in a single accumulation. In order to compare a PMT and CCD side by side a Nanolog was used with a double grating excitation monochromator and a single channel emission monochromator on the T side and an iHR320 spectrograph with a

Synapse CCD on the S side. For a fair comparison similar gratings were used on both sides. The CCD was setup for a single acquisition such that the signal to noise was maximised (18 s acquisition) and the photomultiplier tube was setup for a 1 s integration time. The signal of the Synapse S2 was measured after the PMT T1 in a batch with an outer loop of 50. This measurement sequence reduces the bias of lamp drift over one measurement with respect to the other.
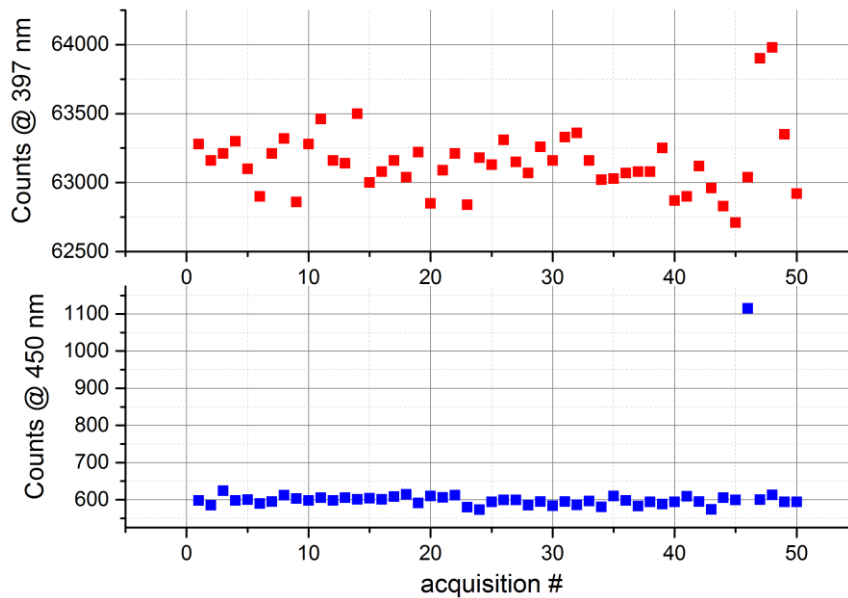
Figure 57: The measured number of counts at 397 nm and 450 nm using the Synapse 1024×256 Open Electrode CCD S2 for a series of 50 water Raman emission acquisitions using the same conditions as in **Figure 51** with an 18 s integration time. Descriptive statistics give the number of counts at 397 nm to be 63,100±200 and at 450 nm to be 600±10. The SNR-FSD is calculated to be 2560±30. The 2 outliers were removed from the calculation as they were likely due to a lamp fluctuation.

Table 2: Comparison of the CCD and PMT data and their computed signal to noise ratios.

	iHR-320 (300/500) Synapse	Single grating (1200/500) R928
Counts at 397	63100±200	713000±2,000
Signal/SD at 397 nm	315.5	356.5
Counts at 450 nm	600±10	4350±70
Signal/SD at 450 nm	60.0	62.1
SNR-FSD	2560±30	10800±100

An analysis of data **Table 2** shows that under the conditions used, that the PMT gives better signal to noise ratios both at the 397 nm, the water Raman peak and also in the consistency in the signal at 450 nm. The SNR-FSD is higher for the PMT when compared to the CCD. The total number of counts for the CCD at the peak is less than that for the CCD making the comparison slightly more bias towards the PMT. Moreover, the CCD had a single integration time of 18 s whereas the PMT on the other hand had an integration time of 1 s for every 0.5 nm between 365-450 nm=170 s. For a fair comparison conditions can be set so the CCD is run with multiple accumulations for the same total time as the PMT however the main advantage of the CCD i.e. speed of accumulation is lost. Ignoring the 3 outliers however and taking the summation of the remaining 47 points for the CCD data. The total number of counts at 397 nm for the CCD is 2966670 and 450 nm of 28062. The number of counts at the peak and the overall integration time is above that given to the PMT and the computed FSD-SNR in this case is 8120 which is still below that of the PMT. Biasing the CCD ~5 times the total integration time of the PMT gives a better comparison as in this time the PMT may scan ~400 nm vs 85 nm which is more practical for measurement of a broad fluorescence spectrum opposed to a narrow Raman line. In conclusion the PMT gives a better overall SNR than the CCD probably due to the read noise but a CCD has the merits in that it can capture full emission spectra without scanning. It should be noted however that this experiment can't be classified as the ultimate comparison as there are a number of experimental alterations which could be made to help either side. For the PMT, a double grating emission monochromator could be used to increase the SNR and the PMT could also be cooled. There are similar improvements which could increase the CCD performance. The CCD is faster when fast spectral accumulation is important however the PMT on the other hand is faster for acquisition of a single point which is certainly important for time-resolved fluorescence measurements which will be discussed in detail later where the CCD is not fast enough. This water Raman experiment was setup to give a basic comparison between the CCD and PMT naturally for more advanced experiments such as the EEM the CCD has more of an advantage.

2.2.5 The Excitation-Emission Matrix (EEM)

The emission and excitation spectra may be combined by scanning through both monochromators or a scanning through an excitation monochromator with an emission spectrograph to form a 3D emission-excitation matrix (EEM). Clearly the two dimensional wavelength axes of steady-state fluorescence allow a greater degree of selectivity than the

single wavelength axis of an absorbance measurement and the use of an addition axis in fluorescence measurements allows for the separation of differing fluorophores. The excitation and emission spectrum may be combined to form an excitation emission matrix **Figure 58**. For samples involving complex mixtures, it is useful to run a 3D matrix of excitation, emission and fluorescence intensity from now on denoted EEM. For an EEM the raw and corrected signals should be collected as with the 2D spectra. In order to run an EEM properly both excitation and emission wavelength corrections must be applied alongside the dark offset. S1c/R1c must be measured compensating for the difference in lamp output at different excitation wavelengths.
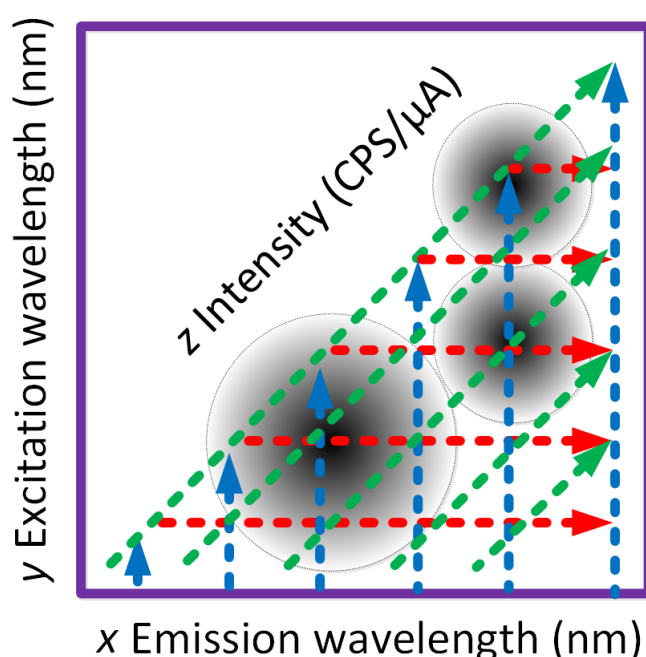
Figure 58: An illustration of an emission, excitation matrix or EEM. The EEM contains all the 2D information of an arbitrary emission scan (horizontal red lines), excitation scan (vertical blue lines) or the synchronous scan (45°green line) [153–156][24].

The water Raman peak at excitation 350 nm, 397 nm is used to assess a fluorimeters performance. At this regime most PMT detectors respond optimally and there is less stray light. The water Raman EEM **Figure 59** can give a more vigorous overview of the fluorimeters performance over its entire usable range [147]. There are two sources of scatter for an EEM as shown in **Figure 59**. The main source is the strong 1st order Rayleigh scattering where the scattering of excitation light occurs at a matching emission wavelength

---

[24] All EEMs in this work will be plotted using the *x*-axis for emission, the *y*-axis for excitation and the *z*-axis for intensity. In literature the *x* and *y* axes are commonly swapped.

to the excitation source. The second source of scattering is 1st order Raman scattering. Rayleigh is much more intense than Raman as demonstrated in the EEM. Log scale is used to emphasise the weak Raman ridge with respect to the strong Rayleigh ridge. In the EEM however the Rayleigh lines are underrepresented as the detector will respond non-linearly at the high counts of the Rayleigh lines c.f. **Figure 47**. Besides scattering, the EEM of a water sample will highlight fluorescence impurities, light leaks and also will give an indication of the presence of some stray light which is seen in regime of UV excitation just off the Rayleigh line. Close observation of the Rayleigh scattering shows that the fluorescence intensity falls quickly with respect to the excitation wavelength, as a λ^{-4} dependence [105].
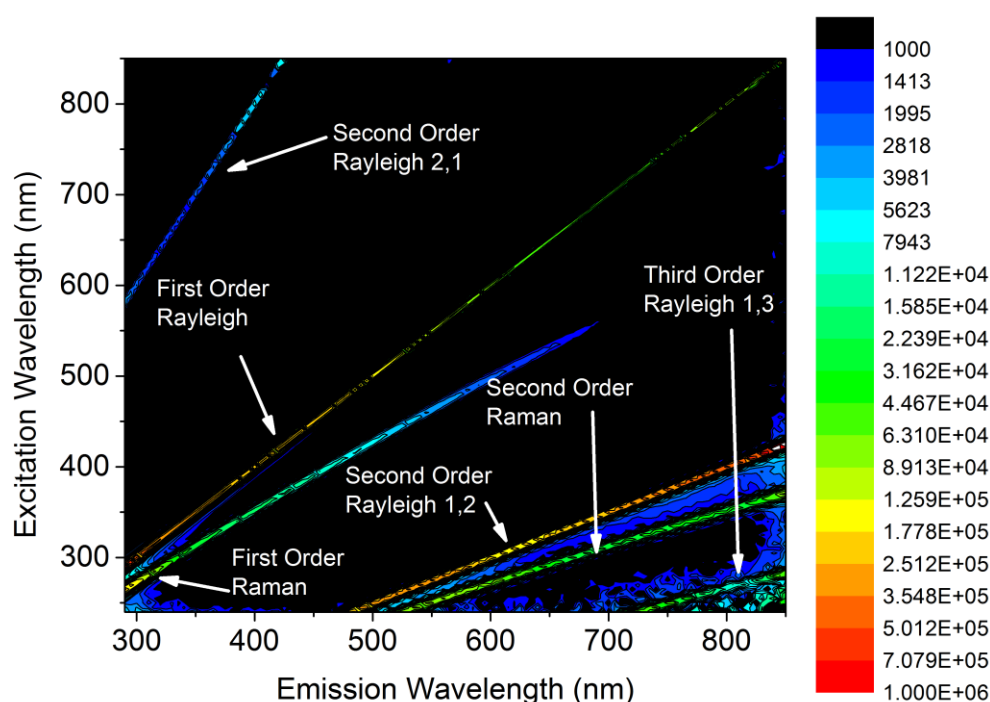
Figure 59: The corrected S1c/R1c (z in CPS/μA) Excitation Emission Matrix EEM of the Raman reference standard Starna 3-Q-10/Water measured using a HORIBA Scientific Fluoromax 4. The excitation monochromator (1200/330 grating) was set to a 5 nm bandpass and scanned from 240-850 nm in 5 nm increments. For each excitation wavelength the emission monochromator (1200/500 grating) was set to a 5 nm bandpass and scanned from 240-850 nm in 5 nm increments. A R928 PMT was used. Each point had a 1 s integration time. A log scale was used in order to display both the water Raman and Rayleigh lines.

Although 2nd order was mentioned briefly earlier on it is more insightful to see the effects in the EEM. The grating of the monochromator will obey the grating equation:

$$d\sin(\theta_m) = m\lambda = k \qquad (34)$$

where $m=0,1,2,\ldots$ and k is a constant. Therefore at 0 order, the grating acts as a mirror allowing light of all wavelengths through. The wavelength selection of a grating is controlled by the grating angle θ_m, and as a consequence of the grating equation when θ_m is altered to suit a wavelength of 800 nm it will also allow light to pass through that has a wavelength of 400 nm and 200 nm. 2nd order also gets incorrectly amplified by the wavelength correction factors which can lead to a significant distortion and thus care must be taken in particular at the edge of the detectors working range. The quantum efficiency
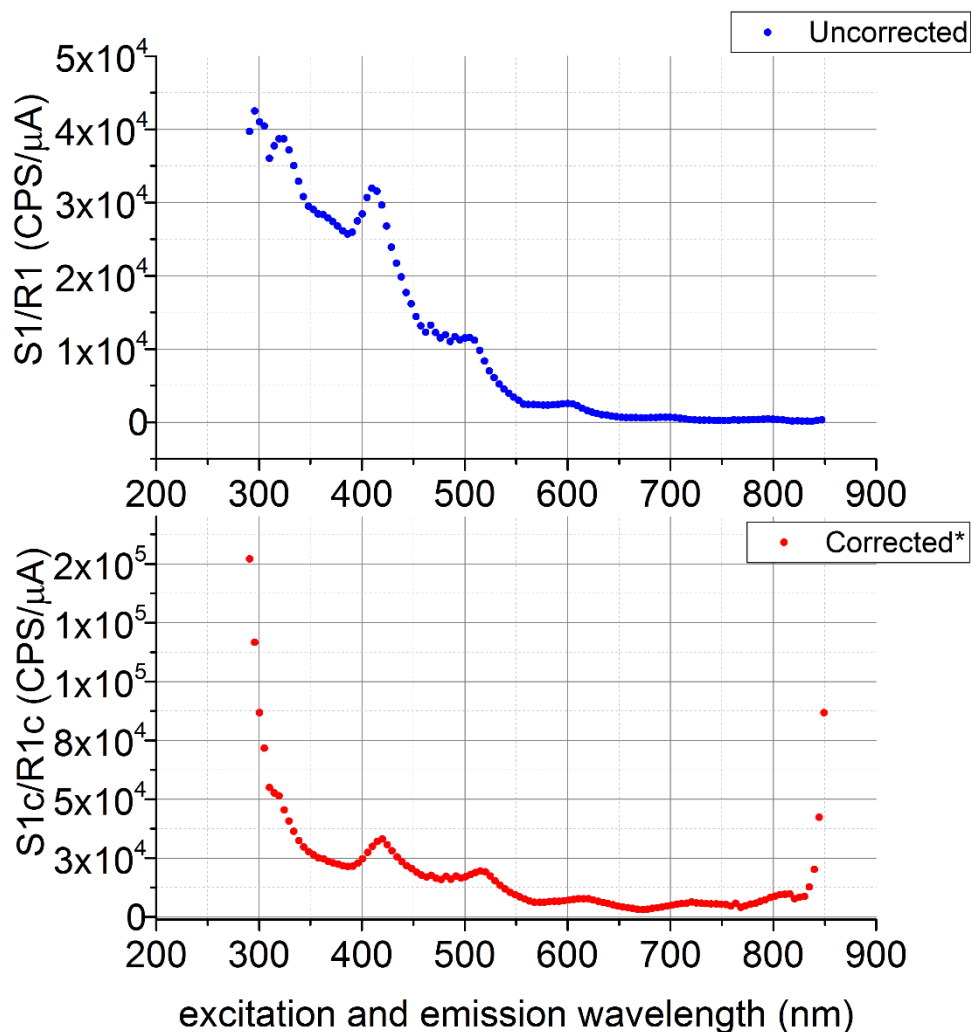
Figure 60: The 1st order Rayleigh line as expected occurs has a maximum when the excitation and emission wavelengths match thus highlighting the fact that the monochromators are calibrated with respect to each other over the entire range of measurement. The corrected data shows that Rayleigh scattering falls rapidly with respect to wavelength. *The data saturated the detector and this is likely responsible for the additional peaks in the spectrum.

of the R928 PMT is low ~2 % at 800 nm and high ~25 % at 400 nm. A 2nd order photon of 400 nm passing through the detector at 800 nm will therefore be incorrectly amplified by MCorrect >12.5 times ignoring additional differences in other optics such as the grating efficiency which are likely to increase the magnitude of MCorrect at this wavelength. The Rayleigh second order lines 2,1 and 1,2 are not equal in magnitude to each other and the 1st order Rayleigh line because the efficiency of the gratings at second order differs with respect to wavelength and **Equation (19)** is not satisfied in some cases. 2nd order Raman lines are also observed however due to the fact that the water Raman signal is weak and also the fact that the efficiency of the gratings is lower at 2,1 this line is barely above 1000 counts which was the lower limit of the plot. The Raman line 2,1 is barely indistinguishable from the noise however 1,2 can be seen clearly. All fluorescence measurements will exhibit 2nd order effects. In order to remove second order effects, wavelength cut-off filters can be used in conjunction with the monochromators. Some fluorimeters have a set of these on a filter wheel which move in sync with the monochromator but most only have manual filter holders. The additional optics may slightly lower the SNR and also increase the cost of the instrument. Use of additional optics should strictly require remeasurement of correction factors however spectrum measured using filters may be approximately corrected by dividing the measured spectrum through by the product of transmission spectra of the filters.

Table 3: Example of grating dispersion and order. Grey italic values are absorbed by air taken from [157].

Order	Wavelength (nm)					Dispersion at central wavelength (nm/mm)
1st	200	400	600	800	1000	10
2nd	*100*	200	300	400	500	5
3rd	*66.6*	*133.3*	200	266.6	333.3	3.3
4th	*50*	*100*	*150*	200	250	2.5
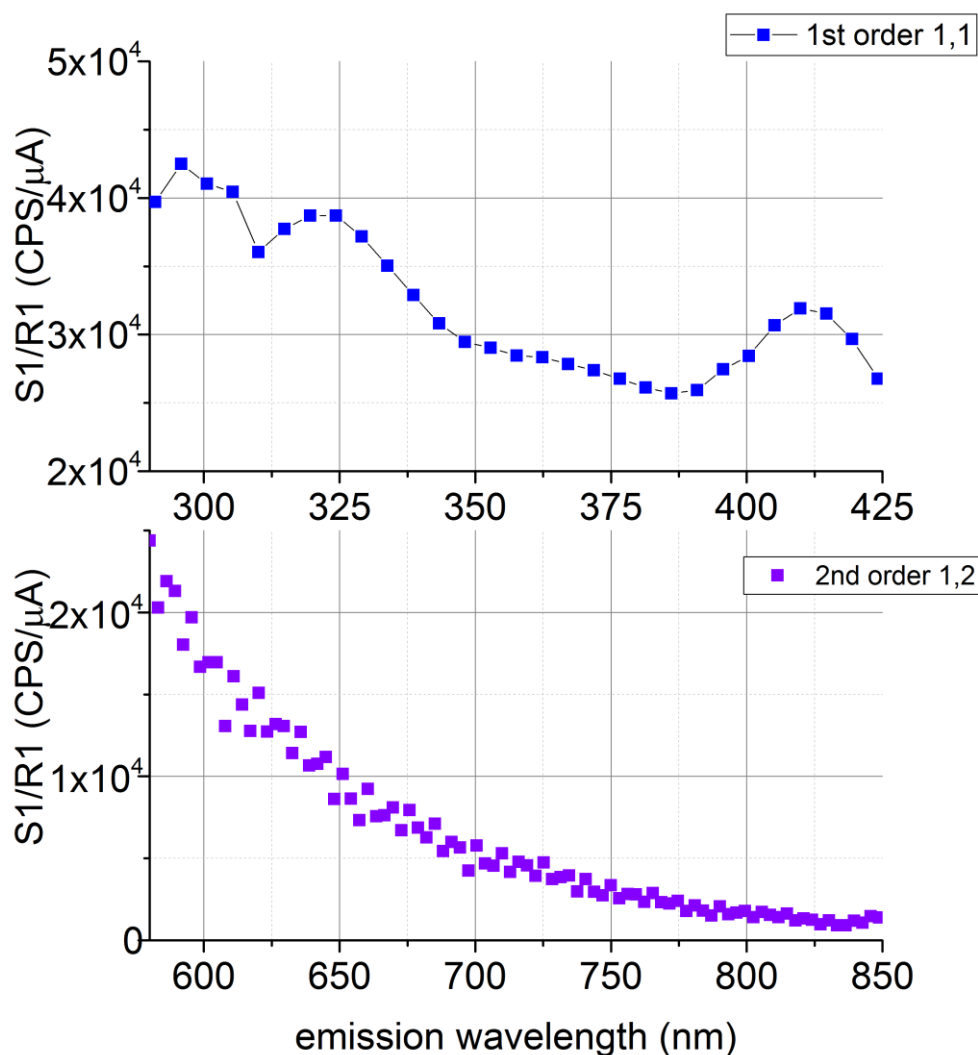
Figure 61: 1st order Rayleigh plotted with respect to excitation and emission wavelength plotted alongside 2nd order Rayleigh at the same excitation wavelength but second order emission wavelength. As the intensity of the 2nd Rayleigh is lower it didn't saturate the detector and therefore doesn't exhibit the peaks shown in the 1st order Rayleigh plot.

Although the Rayleigh lines were shown in **Figure 59** they are typically the strongest signal in the EEM and usually saturate the detector and overwhelm any fluorescence or Raman signal of interest. Because the position of Rayleigh lines and bandpasses of both monochromators are known there is an option to block them while measuring or later masking this section of the EEM. In the vast majority of cases these regions are simply blanked however data can also be interpolated to remove any discontinuity in the matrix [158]. The water EEM may be Rayleigh masked and plotted as a contour profile **Figure 62**.
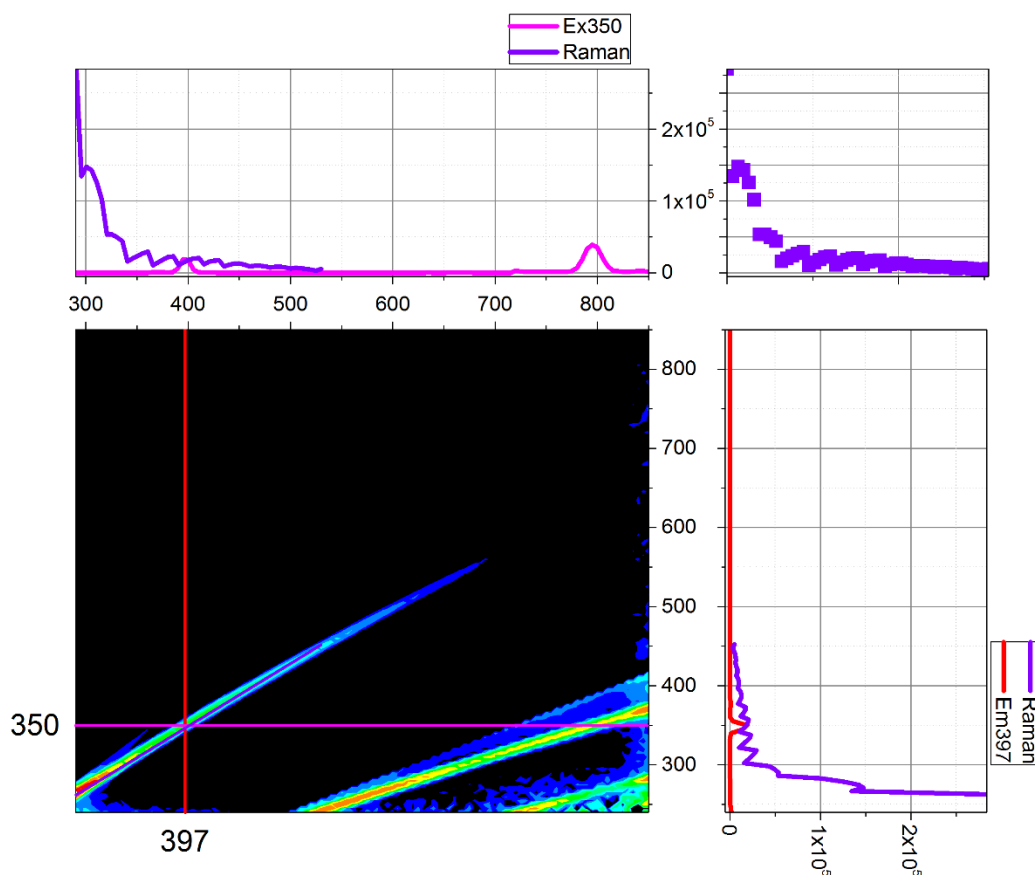
Figure 62: Rayleigh masked **Figure 59** plotted as a contour profile. The water Raman excitation at 397 nm emission and emission spectrum at 350 nm excitation are shown respectively as profiles along *y* and *x*. The water Raman ridge may be followed using a diagonal line.

This measurement was carried out using a Fluoromax 4 however if greater sensitivity is required a Fluorolog with a double grating monochromator particularly on the excitation arm should be selected to minimise stray light. Naturally the amount of scatter can be enhanced by replacing the sample with a colloidal silica solution such as LUDOX or will differ in measurements with larger objects such as proteins which scatter light more than distilled water. Plastic disposable fluorescence cuvettes or even low quality glass cuvettes may exhibit fluorescence [102]. An EEM of a water blank can also be used to determine how effective cleaning practices were on any high quality Quartz cuvettes [159]. It is recommended to run an EEM as well as a transmission spectrum for any new optical component used for fluorescence measurements. Provided that the fluorescence intensity of the cuvette is weak it may be ignored or compensated for using a blank subtract. Solvent Raman scattering and weak third order Rayleigh can also be removed using a blank subtract.

The Aqualog is a specialised steady-state fluorimeter specifically designed for rapid acquisition of EEMs for water quality measurements. It has an emission spectrograph and an inbuilt absorbance photodiode meaning it can simultaneously measure the absorbance spectrum as well as the EEM. Hardware wise the Dual FL is the twin of the Aqualog but its acquisition software is less tailored to the field of water quality. The main advantage in being able to measure the absorbance and EEM simultaneously is that it allows one to account for EEM distortion via inner-filtering **Figure 63**. There are two types of inner-filtering, primary inner-filtering and secondary inner-filtering. Primary inner-filtering is when the excitation light interacts with analyte molecules (e.g. absorption, scattering) before reaching the centre of the cuvette, this distorts the excitation spectrum while leaving the spectral shape of the emission spectrum relatively intact. Secondary inner-filtering is when emission light from the centre of the cuvette likewise interacts with analyte before it leaves the cuvette, this distorts the emission spectrum spectral shape. The measured signal is attenuated in both cases [160,161]. Inner-filtering is typically taken to be negligible when the peak absorbance <0.05 (1 cm path length). In practice however peak absorbance readings <0.1 are usually not corrected for [162].
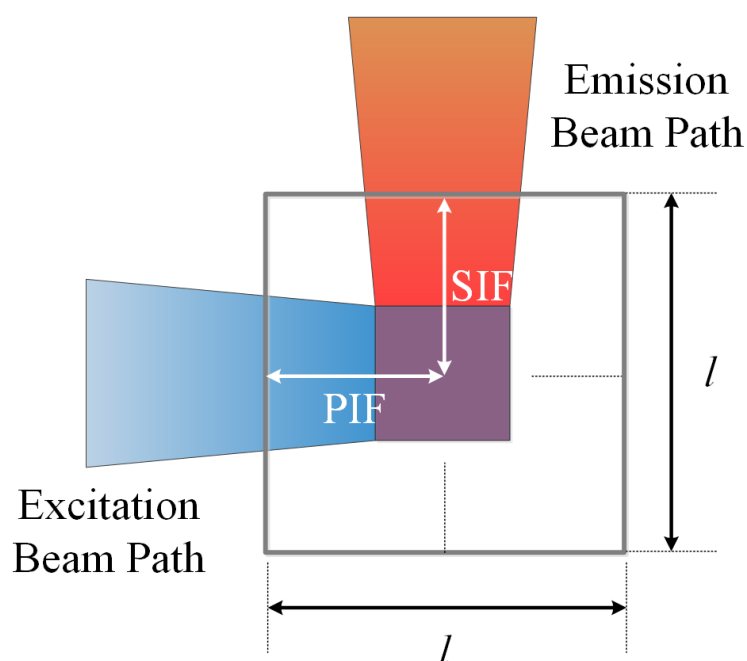
Figure 63: A plan view of the optical beam path through a 1 cm cuvette [112]. The primary filter effects occur when most of the excitation light is absorbed by the sample via fluorescing or non-fluorescing species before it reaches the cross-section with the emission beam. The secondary inner filters occur when the fluorescence emission is absorbed by the sample before it leaves the cuvette and hence doesn't reach the detector. The inner-filter effects therefore lower the fluorescence emission detected and red-shift it.

By re-arranging **Equation (16)** and assuming the primary inner-filter and secondary inner-filter effects to occur each at a distance of $l/2$, the transmission spectrum may be used to correct the EEM from inner- filtering.

$$I_{\text{Correct}} = I_{\text{Inner-Filtering}} \times 10^{\frac{A(\lambda_{\text{ex}})+A(\lambda_{\text{em}})}{2}} = I_{\text{Inner-Filtering}} \times \frac{2}{T(\lambda_{\text{ex}})+T(\lambda_{\text{em}})} \quad (35)$$

This correction has been demonstrated to work with an absorbance ~1 [163]. Because of the break-down of the Beer-Lambert law at higher concentrations and the difficulty to measure high absorbance readings (low transmission values) with sufficient accuracy, one should be sceptical applying this correction at higher absorbance readings. There are a number of more sophisticated ways of correcting the EEM [164] such as using the water Raman peak [165]. **Figure 64** and **Figure 65** show the absorbance and EEM of a Rhodamine 6G sample in methanol made to have an absorbance peak of ~0.1. The EEM has already been corrected using the absorbance/transmission spectrum. The EEM is plotted in 3D where one can clearly see the EEM is a series of emission spectrum at varying excitation wavelength and it is also plotted as a contour profile in this case demonstrating an emission spectrum at 525 nm excitation and an excitation spectrum at 545 nm emission.
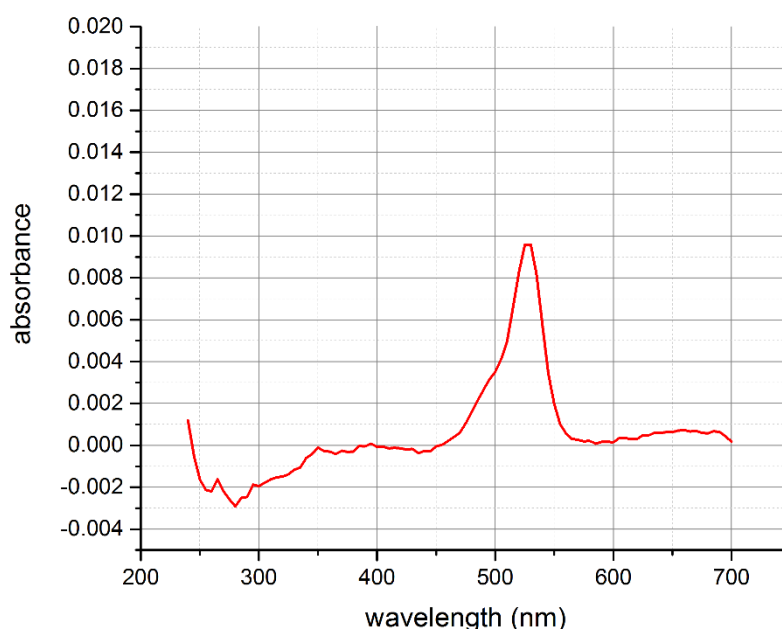
Figure 64: The absorbance spectrum of Rhodamine 6G in methanol measured using a HORIBA Scientific Dual FL 650. The excitation monochromator (1200/300 grating) was set to a 3 nm bandpass scanned from 240-700 nm in 5 nm increments. A methanol sample in a matching quartz cuvette was used as a blank. This absorbance spectrum was recorded simultaneously to the EEM **Figure 65**.

Figure 65: The EEM of Rhodamine 6G in methanol measured using a HORIBA Scientific Dual FL 650. The excitation monochromator (1200/300 grating) was set to a 3 nm bandpass scanned from 240-700 nm in 5 nm increments. For each excitation wavelength the emission spectrograph (285/250 grating) was set to a 3 nm bandpass and the emission spectrum was recorded. An integration time of 0.015 s was used for each emission spectrum recorded. A methanol sample in a matching quartz cuvette was used as a blank.

Figure 66 and **Figure 67** show the absorbance and EEM of a Rubrene sample in methanol made to have an absorbance peak of ~0.01 at 520 nm. The EEM has already been corrected using the absorbance/transmission spectrum. The EEM is plotted in 3D where one can clearly see the EEM is a series of emission spectrum at varying excitation wavelength and it is also plotted as a contour profile in this case demonstrating an emission spectrum at 525 nm excitation and an excitation spectrum at 545 nm emission. Additional absorption in the regime 350-400 nm and 240-270 nm is prescribed to an impurity. On the EEM the fluorescence emission of the impurity showing at 350-450 nm emission and 350-400 nm, 240-270 nm excitation is clearly separated out from that of Rubrene showing emission at 520-650 nm and 260-320 nm, 400-550 nm excitation.
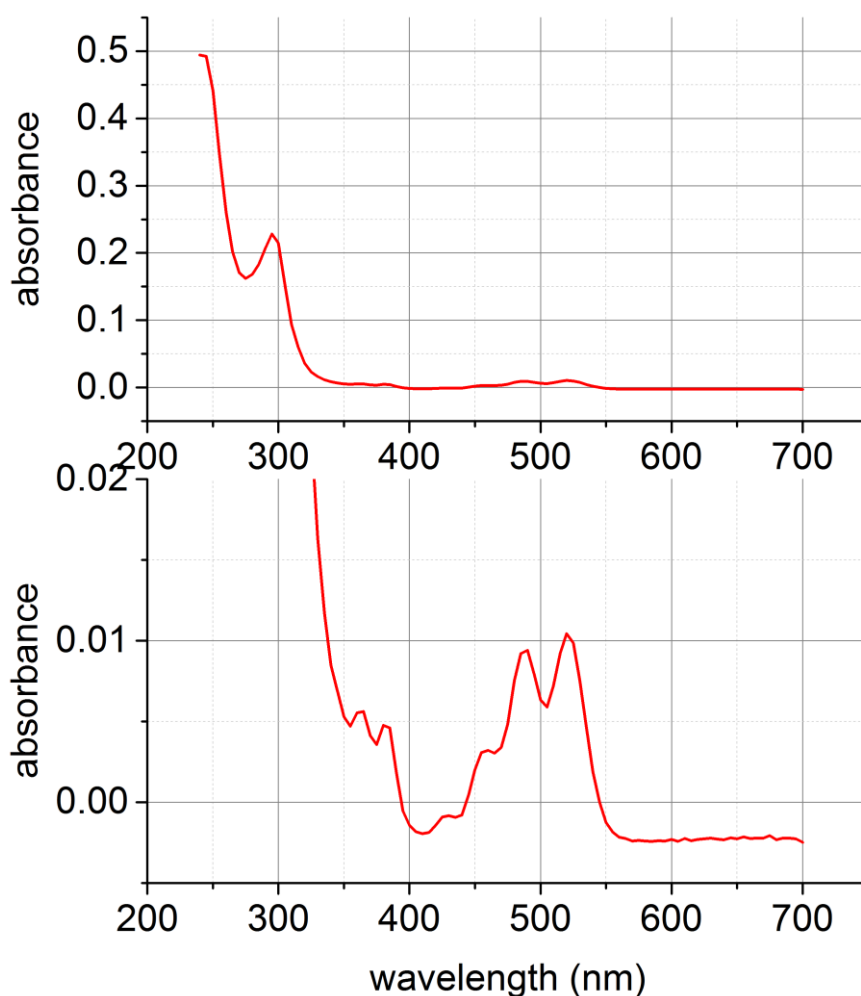
Figure 66: The absorbance spectrum of Rubrene in methanol measured using a HORIBA Scientific Dual FL 650. The excitation monochromator (1200/300 grating) was set to a 3 nm bandpass scanned from 240-700 nm in 5 nm increments. A methanol sample in a

matching quartz cuvette was used as a blank. This absorbance spectrum was recorded simultaneously to the EEM **Figure 67**.
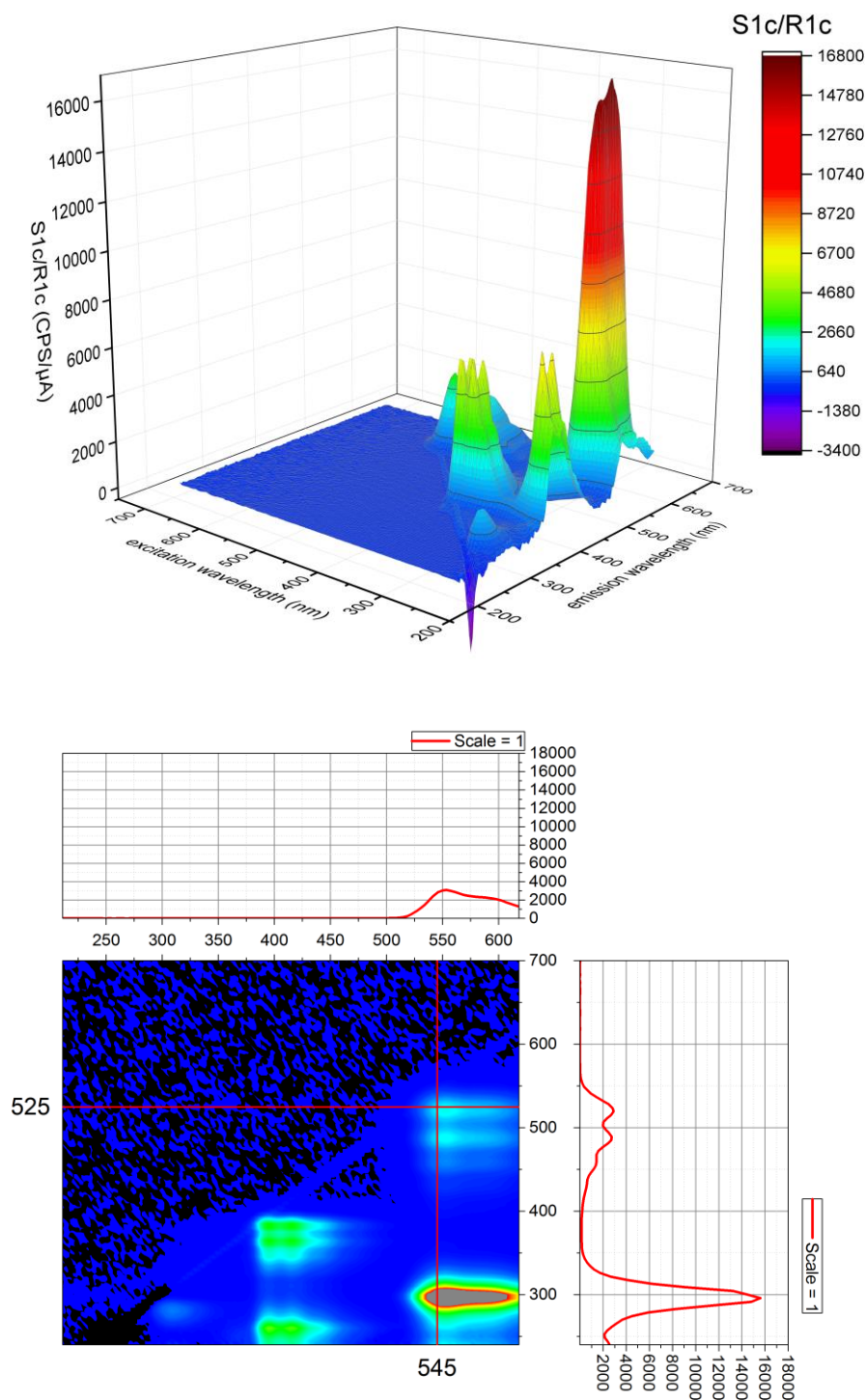
Figure 67: The EEM of Rubrene in methanol measured using a HORIBA Scientific Dual FL 650. The excitation monochromator (1200/300 grating) was set to a 3 nm bandpass scanned from 240-700 nm in 5 nm increments. For each excitation wavelength the emission spectrograph (285/250 grating) was set to a 3 nm bandpass and the emission spectrum was recorded. An integration time of 0.015 s was used for each emission spectrum recorded. A methanol sample in a matching quartz cuvette was used as a blank.

One of the biggest difficulties in determining fluorescence components from an unknown mixture occurs when the spectra overlay on both axes. This can be illustrated from a 0.5:0.5 mixture of the two solutions of **Figure 64** and **Figure 66**. At first glance the absorbance at 400-600 nm **Figure 68** may appear to look like a spectrum from a single fluorophore. Likewise, the emission at 520-650 nm, 500-550 nm excitation in the EEM **Figure 69** heavily overlaps again appearing at first glance to be emission from a single fluorophore. This sample will be further investigated later using time-resolved fluorescence.
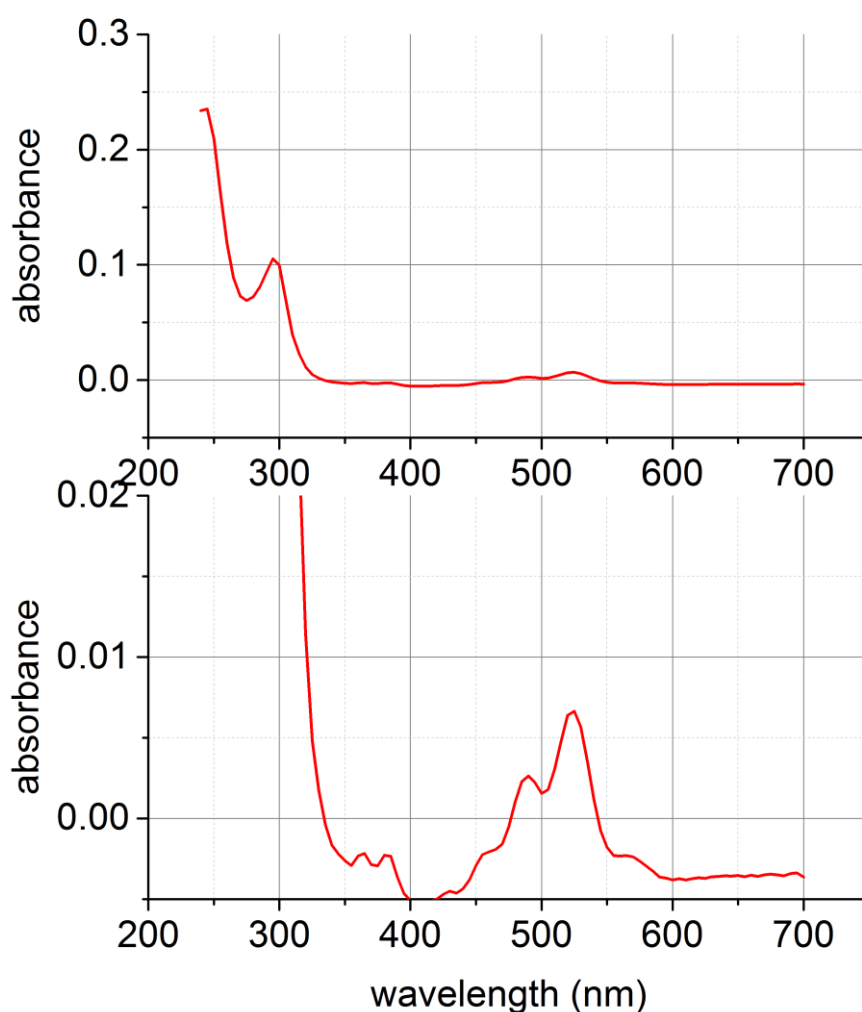
Figure 68: The absorbance spectrum of 0.5 **Figure 64**:0.5 **Figure 66** mixture measured using a HORIBA Scientific Dual FL 650. The excitation monochromator (1200/300 grating) was set to a 3 nm bandpass scanned from 240-700 nm in 5 nm increments. A methanol sample in a matching quartz cuvette was used as a blank. This absorbance spectrum was recorded simultaneously to the EEM **Figure 69**.
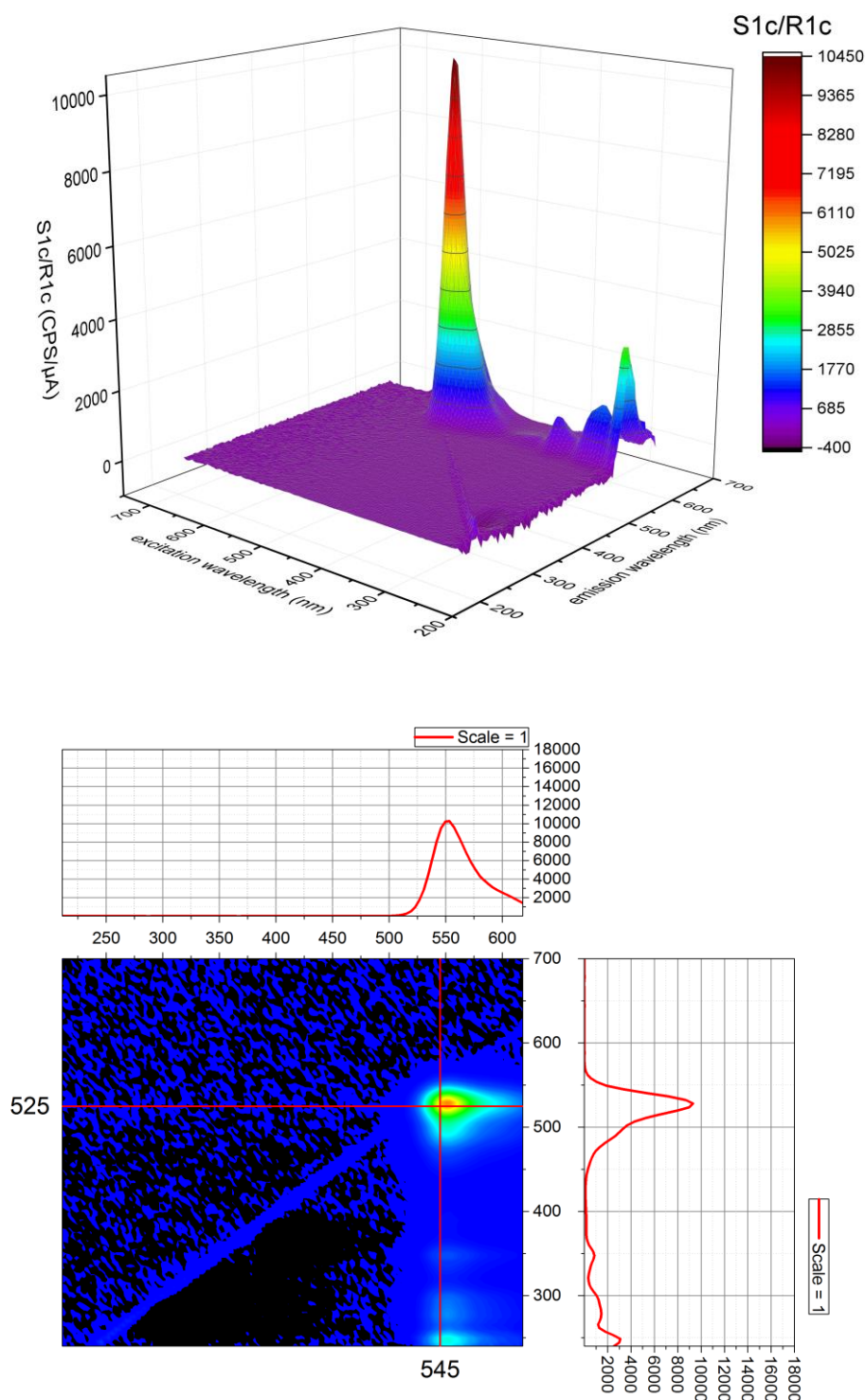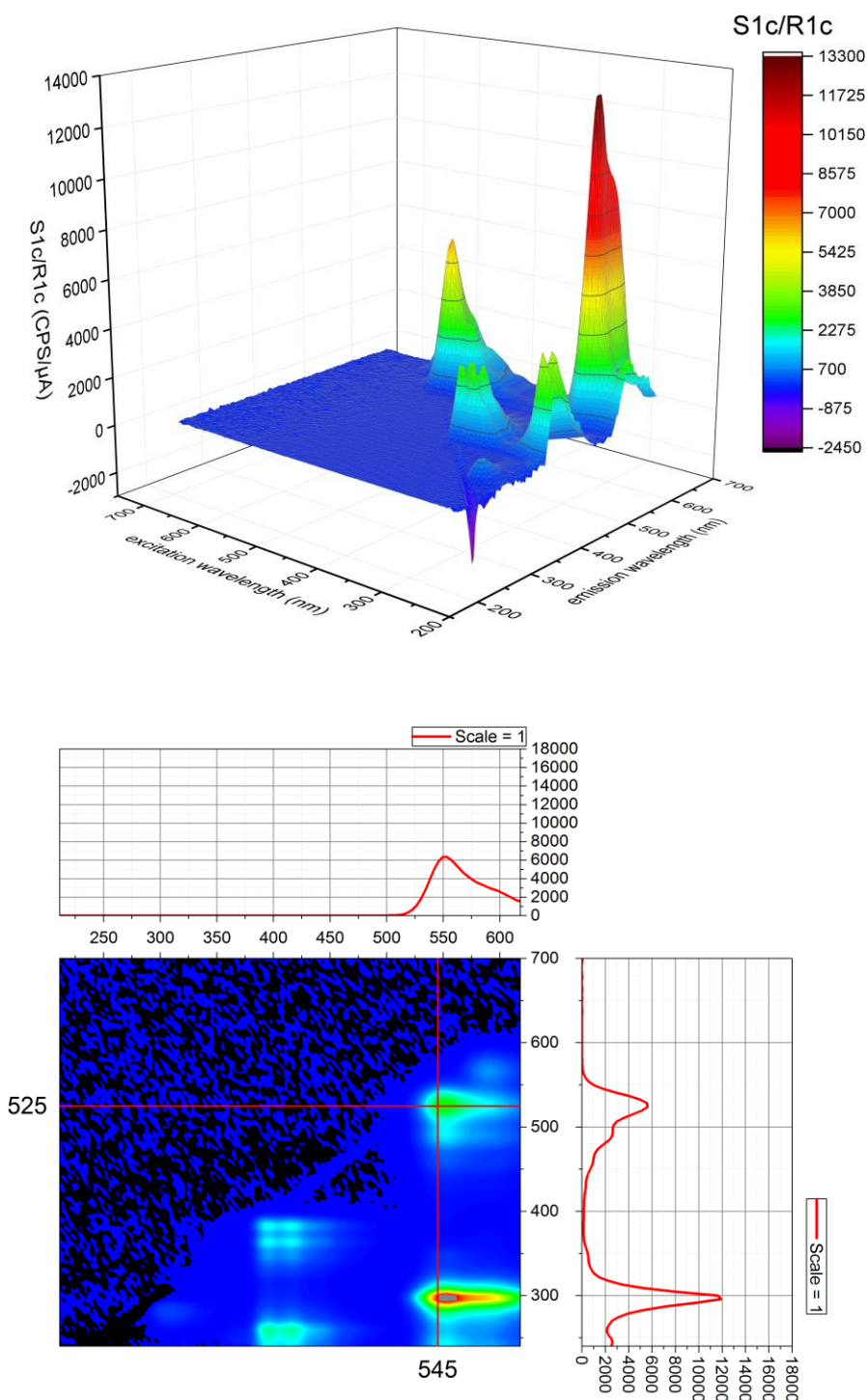
Figure 69: The EEM of 0.5 **Figure 65**:0.5 **Figure 67** mixture measured using a HORIBA Scientific Dual FL 650. The excitation monochromator (1200/300 grating) was set to a 3 nm bandpass scanned from 240-700 nm in 5 nm increments. For each excitation wavelength the emission spectrograph (285/250 grating) was set to a 3 nm bandpass and the emission spectrum was recorded. An integration time of 0.015 s was used for each emission spectrum recorded. A methanol sample in a matching quartz cuvette was used as a blank.

Chemo-metric analysis tools such as Parallel Factor Analysis (PARAFAC) are under development to make analysis of EEMs of unknown composition routine [149,166,167]. The biggest application area of PARAFAC with EEMs has been in water-quality research as there is a need to measure and quantify impurities, remove them and re-measure the treated water to determine if it is safe for human consumption [168,169].

2.2.6 Highly Concentrated Samples – The Front Face Measurement

For highly concentrated samples, measurement under standard conditions will result in a distorted spectrum due to inner-filtering effects as discussed above [170]. While inner-filtering can be combatted by correcting fluorescence spectrum via the transmission spectrum this correction is limited due to the difficulty in accurately being able to measure the absorbance and hence transmission of samples with high optical densities.
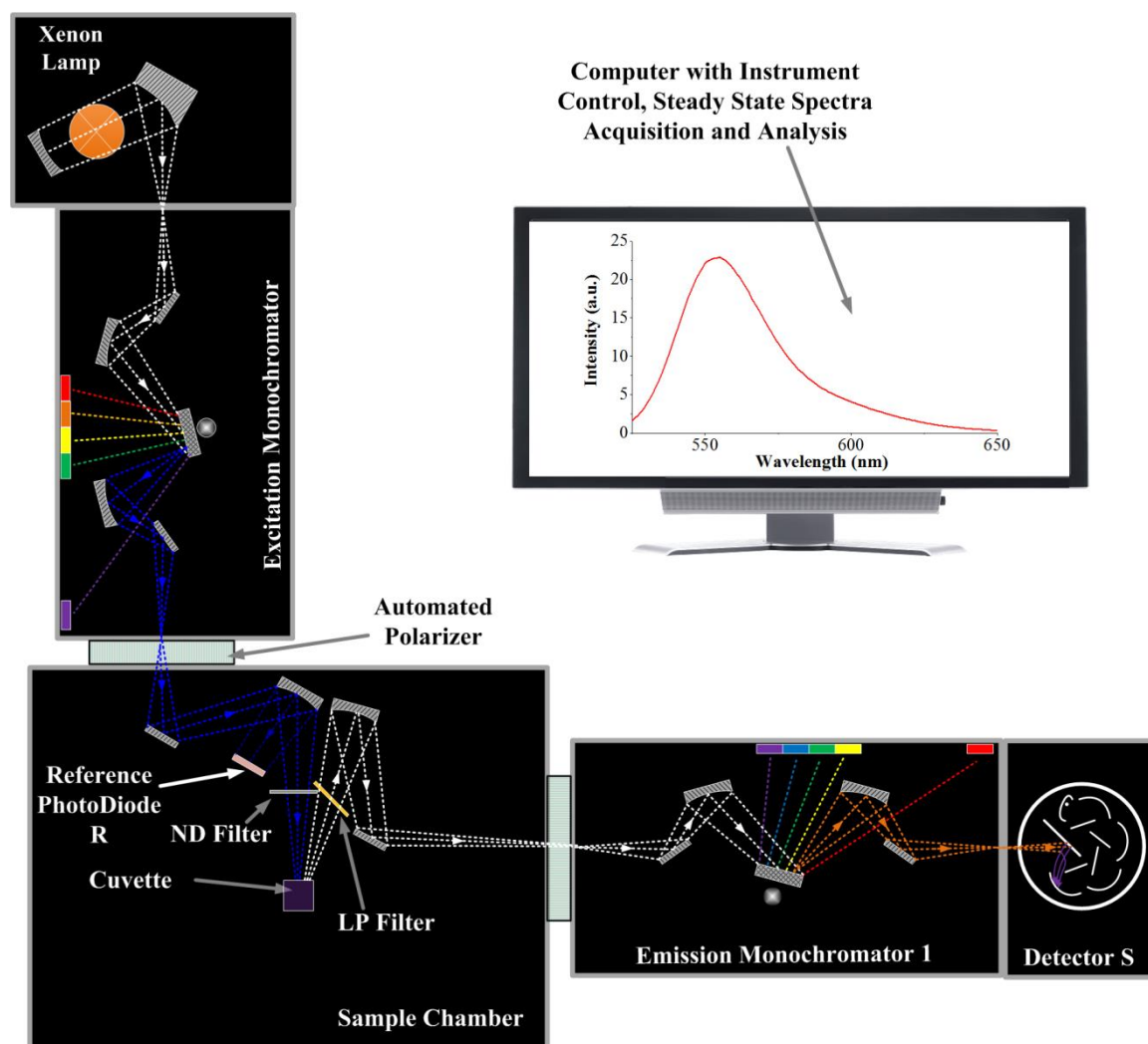
Figure 70: Illustration of a spectrofluorimeter operated in front face configuration. A mirror is used to focus the measured fluorescence beam towards the front face of the cuvette.

One way to combat inner-filtering is to dilute the sample or alternatively reduce the optical path e.g. by using a cuvette with <1 cm path length. However, there will be some cases where one will require a combination of high concentration, sample stirring and temperature control in order to drive a specific reaction. It is therefore appropriate to perform a front face measurement to overcome inner filtering effects **Figure 70**. **Figure 71** clearly shows the effect of primary inner-filtering in a concentrated sample of Bovine Serum Albumin (25 mg/ml) gently stirred at 37°C. The ratio of the 1st and 2nd peaks with respect to the 3rd peak fall significantly when measured using right angle geometry in comparison to front face because excitation light of lower wavelengths suffers the primary inner-filtering effect, that is a large proportion of the UV excitation light is used to excite the sample before reaching the centre of the cuvette and hence results in a reduced emission. Because the front face measurement looks at the fluorescence from the edge of the cuvette, the spectra isn't distorted in the same manner. As expected a wider bandpass is also required to get a signal at right angle geometry with respect to front face geometry.
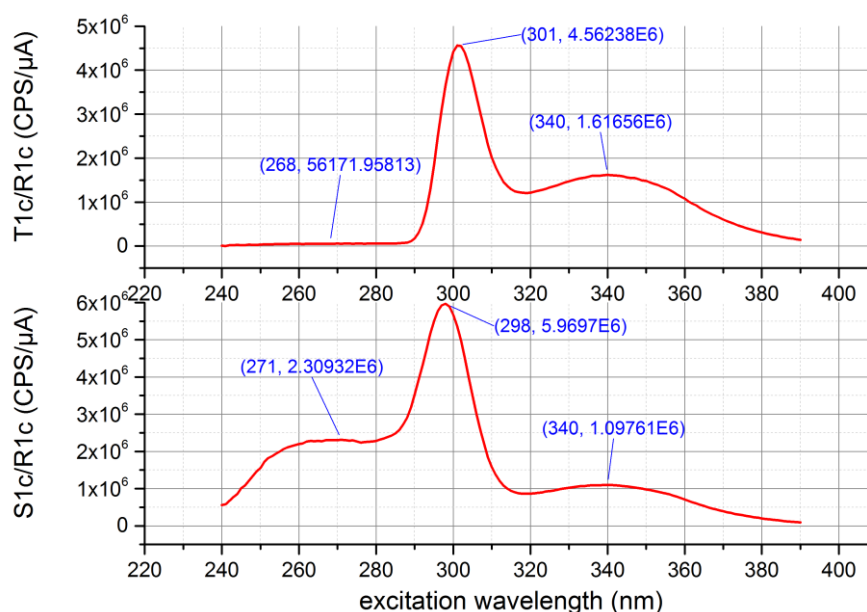
Figure 71: Excitation spectra of 25 mg/ml of BSA measured in a Fluorolog 3-222. The emission monochromator (1200/500 double grating) on the S side was set to 405 nm and the front face mirror was rotated so emission was recorded on front face. The emission monochromator (1200/500 double grating) on the T side was set to 405 nm without front face optics. The excitation monochromator (1200/330 double grating) was set to a 5 nm bandpass and scanned between 240-390 nm in 1 nm increments. An integration time of 1 s was used. Dual R928 PMTs were used as detectors. To ensure both PMTs were operating in the linear regime the emission monochromators were set to a 1 nm bandpass for the S side and 2.8 nm for the T side respectively. The ratios of the 1st and 2nd peak with comparison to the 3rd peak are both shorter in RA geometry than FF geometry 5.45 P2 298:

P3 340 FF 0.48 P1 271: P3 340 FF in comparison to 2.88 P2 301:P3 340 RA 0.38 P1 268:P3 340 RA.

2.2.7 Steady State Fluorescence Anisotropy

Polarization effects on the fluorescence emission may also be studied by using polarizers on both the excitation and emission arm. The fluorescence emission can be measured by using polarizers of different orientations three orientations are commonly employed; vertical (V), horizontal (H) and magic angle (M=54.7º) [171]. The reason for this particular magic angle can be obtained by comparison of the theoretical values[25] of the intensity to the measured values. If a vertical polarizer is placed at the excitation arm the sample is excited along the direction of *z*-axis thus:

$$I_{\parallel}' = I_z' \qquad (36)$$

And symmetry dictates that:

$$I_{\perp}' = I_x' = I_y' \qquad (37)$$

Thus the total intensity [172]:

$$I' = I_x' + I_y' + I_z' = I_{\parallel}' + 2I_{\perp}' \qquad (38)$$

The experimentally values[26] of I will be lower than the theoretical value I' due to detection efficiency which is typically less than 10 % [173]. Behind a polarizer:

$$I_{\parallel} = \cos^2(\theta) I \qquad (39)$$

$$I_{\perp} = \sin^2(\theta) I \qquad (40)$$

At the magic angle 54.7º:

$$I_{\parallel} = 0.333 I \qquad (41)$$

$$I_{\perp} = 0.666 I \qquad (42)$$

Strictly speaking one should always measure with polarizers in the configuration VM. For steady state fluorimeters it is normally assumed that the light source is unpolarised. A NIST paper reports however that the intensity of the excitation beam in a Fluorolog 3-22 $I_H:I_V$ was stated to be ~1 at 300 nm (unpolarised), ~2 at 400 nm, ~4 at 550 nm and ~10 at 750 nm (horizontally polarised) respectively [115]. Clearly there will be a polarization bias in steady state measurements. In general practice however polarizers are not used in the bulk of steady state measurements because they significantly lower the fluorescence intensity

---

[25] The theoretical values are indicated with primed notation.
[26] The experimental values are indicated without primed notation.

particularly in the UV. Moreover, wavelength correction factors are typically not measured with polarizers because the calibration lamp has a weak output in the UV. Thus at this angle the measured intensity is proportional to the theoretical intensity [174]. **Figure 72** shows the transmission and extinction ratio for UV Wiregrid and UV Wiregrid polarizers.
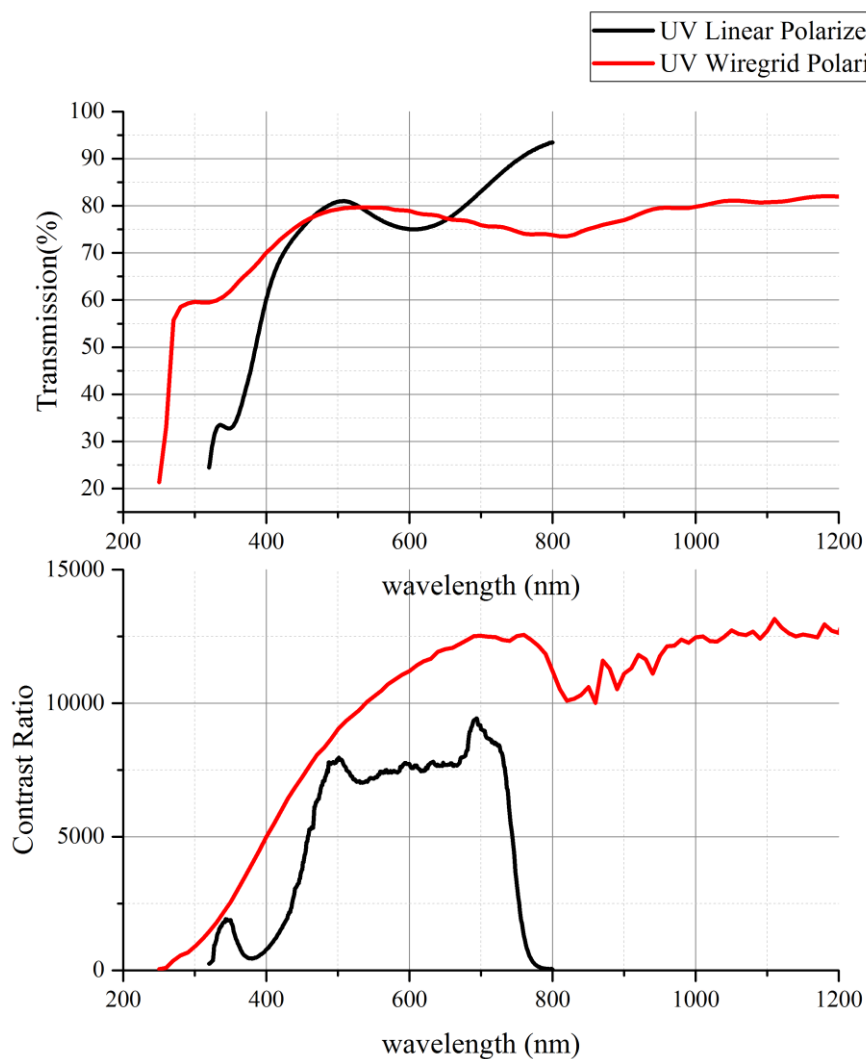
Figure 72: Transmission spectrum and extinction ratio I_V/I_H of UV Linear polarizers and UV Wiregrid polarizers taken from typical supplier data.

When considering polarizers clearly there are three optical considerations to take into account, the transmission spectrum, the extinction ratio that is the ratio of transmission through a pair of crossed polarizers to a pair of identically aligned polarizers and of course the damage threshold. For fluorescence anisotropy measurements an extinction ratio of at least 500 is required [175]. The UV Wiregrid polarizers have increased UV range but as a trade-off to damage threshold and are harder to manufacturer so have a higher associated

cost. If steady-state measurements are measured with polarizer conditions at VM then a new XCorrect and MCorrect must be created which takes into account for the transmission of the additional optical components. Although not strictly true typical fluorescence measurements taken in a steady state fluorimeter are assumed to involve an unpolarised light source so are measured without polarizers, the trade-off between the loss in fluorescence intensity and hence the sensitivity are usually not worthwhile for the additional correction to be carried out.

The principle of anisotropy involves photoselection and Brownian motion. **Figure 14** illustrated the principle of photoselection leading to an initial anisotropy bias and **Figure 15** depicted the deterioration of this initial anisotropy due to random collisions with solute molecules. The most important steady-state fluorescence measurement involving polarization is the steady-state fluorescence anisotropy. Steady-state fluorescence anisotropy is obtained by measuring the samples fluorescence intensity with polarizer orientations at VV, VH, HV and HH respectively **Figure 73** with the notation of the first polarizer being on the excitation arm and the second polarizer on the emission arm.
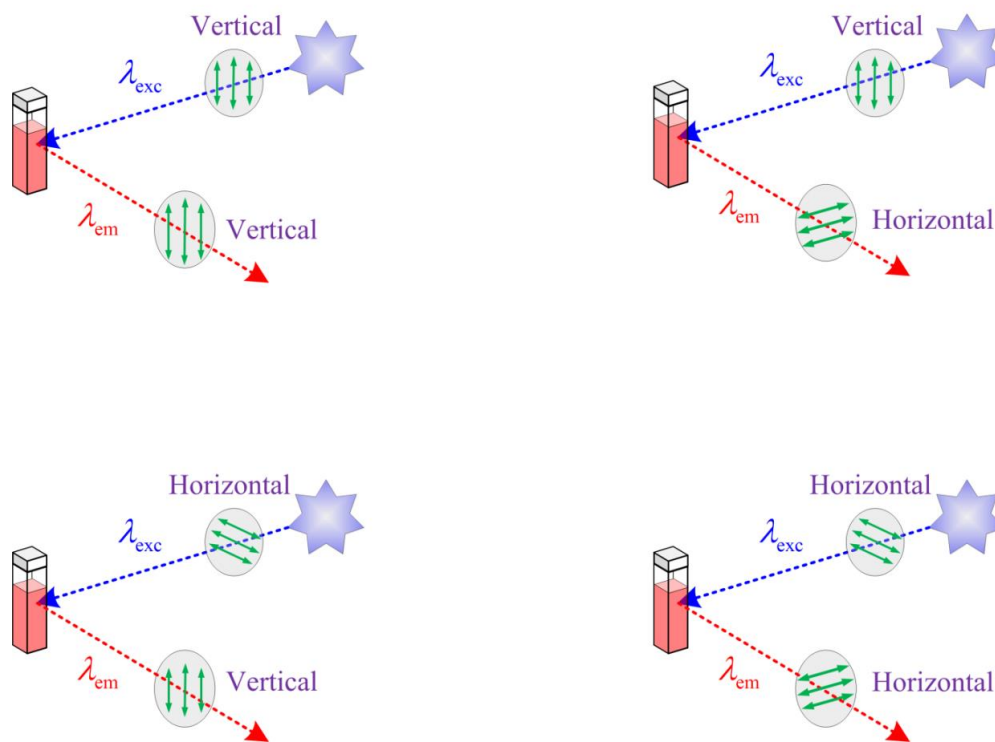
Figure 73: Top line, polarizer configurations used for anisotropy, anisotropy is typically measured to a difference of at least 10000 counts. Bottom line, polarizer configurations for the grating factor typically 500-1000 counts for these decays suffice.

The four spectra I_{VV}, I_{VH}, I_{HV} and I_{HV} allow one to compute the steady state anisotropy with respect to wavelength:

$$r(\lambda_{ex}, \lambda_{em}) = \frac{GI_{VV}(\lambda_{ex}, \lambda_{em}) - (\lambda_{ex}, \lambda_{em})I_{VH}(\lambda_{ex}, \lambda_{em})}{GI_{VV}(\lambda_{ex}, \lambda_{em}) + 2(\lambda_{ex}, \lambda_{em})I_{VH}(\lambda_{ex}, \lambda_{em})} \tag{43}$$

Anisotropy is a measure of polarization but differs in the fact that it is normalised by the total fluorescence emission. The grating factor G is defined as:

$$G(\lambda_{ex}, \lambda_{em}) = \frac{I_{HH}(\lambda_{ex}, \lambda_{em})}{I_{HV}(\lambda_{ex}, \lambda_{em})} \tag{44}$$

The anisotropy function should only be examined in regions where the fluorescence signal is strong otherwise the SNR may not be sufficient making the results meaningless. As the anisotropy is an intensity ratio, the S1 signal only needs to be recorded as wavelength dependencies will be cancelled out however a larger integration time of 5 s or more is recommended. Steady state anisotropy measurements should be carried out with a dark offset as detector dark counts may otherwise bias the anisotropy measurement. As fluorescence anisotropy is a ratio, like absorbance measurements any wavelength dependence on the intensity gets divided out. For best practice when recording anisotropy data the four signals $I_{VV}(\lambda_{ex}, \lambda_{em})$, $I_{VH}(\lambda_{ex}, \lambda_{em})$, $I_{HV}(\lambda_{ex}, \lambda_{em})$ and $I_{HH}(\lambda_{ex}, \lambda_{em})$ should be computed to ensure that all four signals are sufficiently larger than the background noise of the detector but retain within the detectors linear range. r_0 is defined as the anisotropy observed in the absence of depolarization processes such as rotational diffusion or energy transfer. It is dependent on the angle between the absorption and emission dipoles:

$$r_0 = \frac{2}{5}\left(\frac{3\cos^2\beta - 1}{2}\right) \tag{45}$$

If the excitation and emission dipoles are parallel, then $\beta = 0°$ and consequently $r_0 = 0.4$. If the excitation and emission dipoles are perpendicular, then $\beta = 90°$ and $r_0 = -0.2$. These are the upper and lower limits for single photon excitation respectively [171]. The definition of the grating factor was taken following the convention used in Horiba Scientific Decay Analysis Software DAS 6.8.14, it should be noted that in literature and in some other software packages the definition of the grating factor is inverted and as a consequence the anisotropy may be expressed accordingly:

$$G'(\lambda_{ex},\lambda_{em}) = \frac{1}{G(\lambda_{ex},\lambda_{em})} = \frac{I_{HV}(\lambda_{ex},\lambda_{em})}{I_{HH}(\lambda_{ex},\lambda_{em})} \qquad (46)$$

$$r(\lambda_{ex},\lambda_{em}) = \frac{(\lambda_{ex},\lambda_{em})I_{VV}(\lambda_{ex},\lambda_{em}) - G'I_{VH}(\lambda_{ex},\lambda_{em})}{(\lambda_{ex},\lambda_{em})I_{VV}(\lambda_{ex},\lambda_{em}) + 2G'I_{VH}(\lambda_{ex},\lambda_{em})} \qquad (47)$$

The reason G is preferred opposed to G' is to prevent the grating factor from exceeding unity in most cases. If a grating factor greater than unity is utilised, then the measured data is inflated and as a consequence the data quality may be perceived to be higher than it actually is. Before using fluorescence anisotropy on a sample, the properties of the fluorophore itself should be characterised. This characterisation can be done using a highly viscous solvent such as glycerol at room temperature **Figure 74**. Under such viscous conditions Brownian motion is severely hindered and the steady-state anisotropy measured should be close to the initial anisotropy r_0. In general, the excitation anisotropy spectrum looks at different transitions and will elucidate if the dipoles are perpendicular or parallel for each transition. The emission anisotropy spectrum on the other hand usually only examines one transition and is hence usually less interesting. These measurements can however be combined into an anisotropy EEM measurement as shown in **Figure 74** for example. Anisotropy EEMs are currently not measured as standard due to the time it takes scanning two monochromators and toggling two polarizers. However CCD technology makes them more feasible to measure and newer data analysis methods are in development [176,177]. The relation of the steady-state anisotropy to viscosity is illustrated in **Figure 75**. A fluorophore bound to nanoparticle objects increasing in size in a non-viscous solution such as water will have a similar trend and this is one of the main application areas examined in this thesis. The steady-state fluorescence anisotropy gives an "average value" of $\bar{r}$ for each wavelength pair, this average value cannot be easily related back to the rotational correlation time in **Equation (15)** and this averaging may lower the dynamic range of a steady-state anisotropy measurement. The later section on **2.3.9 Time-Resolved Fluorescence Anisotropy Decay Measurements** builds upon the steady-state date and relates to the initial anisotropy at time 0, r_0 and the rotational correlation time ϕ.
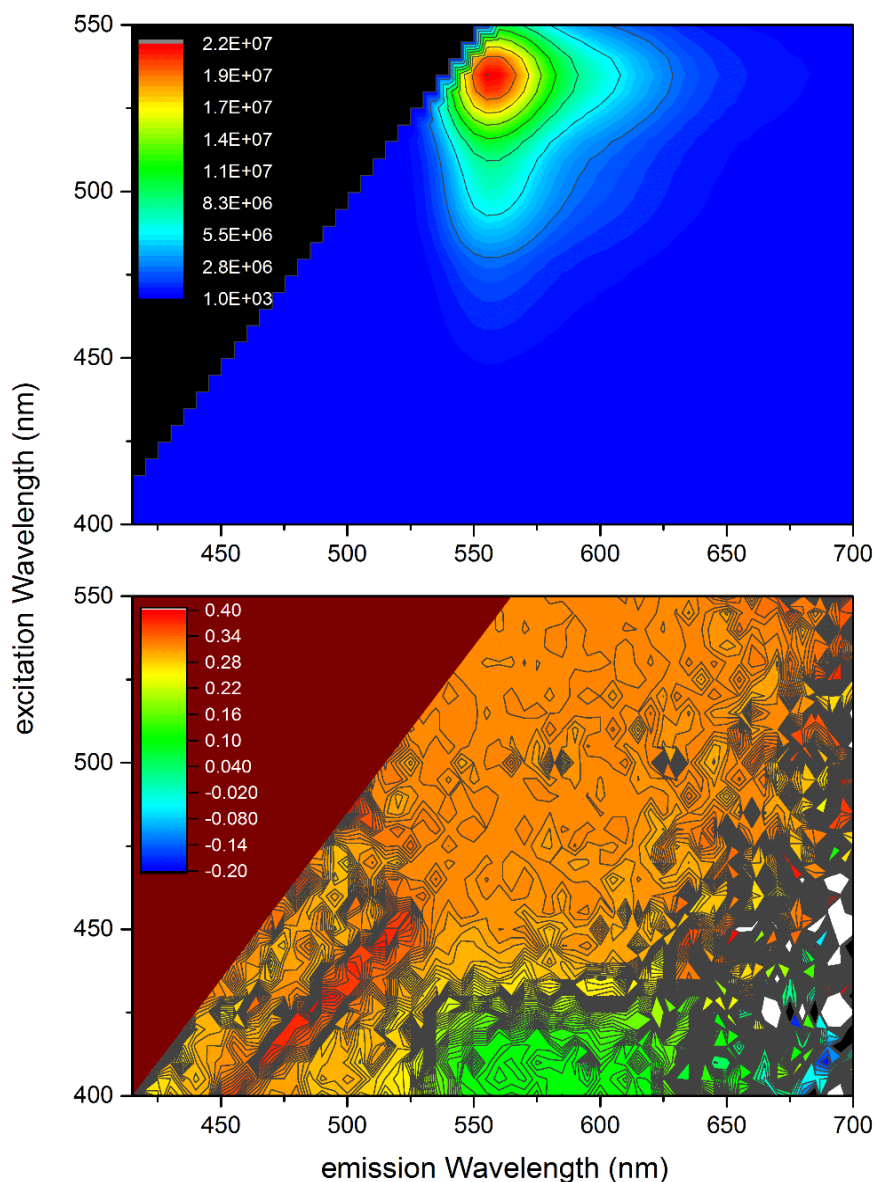
Figure 74: The EEM and anisotropy EEM of Rhodamine 6G in glycerol measured in a Fluorolog 3-22 with R928 PMT. For the EEM the excitation monochromator (1200/330 double grating) was scanned between 400-550 nm in 5 nm increments. For each excitation wavelength the emission monochromator (1200/500 double grating) was scanned between 420-700 nm in 5 nm increments. An integration time of 0.2 s was used for each point. z is in CPS/µA. The anisotropy EEM was recorded in a similar manner. Instead of a single measurement at each excitation, emission wavelength pair 4 measurements were carried out with 4 different polarizer orientations VV, VH, HV and HH respectively. For the anisotropy EEM as the polarizers reduce the light intensity the bandpasses were opened up to 5 nm in both monochromators and an increased integration time of 5 s was used. z is dimensionless. In both EEMs a LP395 was placed on the excitation arm and a LP410 was

placed on the emission arm to prevent 2nd order effects. The ridge to the left of the EEM where $\bar{r}$ appears to be >0.4 is due to glycerol Raman scattering. The anisotropy is close to 0.32 in all regimes of interest (where the Rhodamine 6G fluorescence is strong) meaning the excitation and emission dipoles are close to parallel and any wavelength pair where the fluorescence of Rhodamine 6G is strong is a good place for anisotropy measurements.
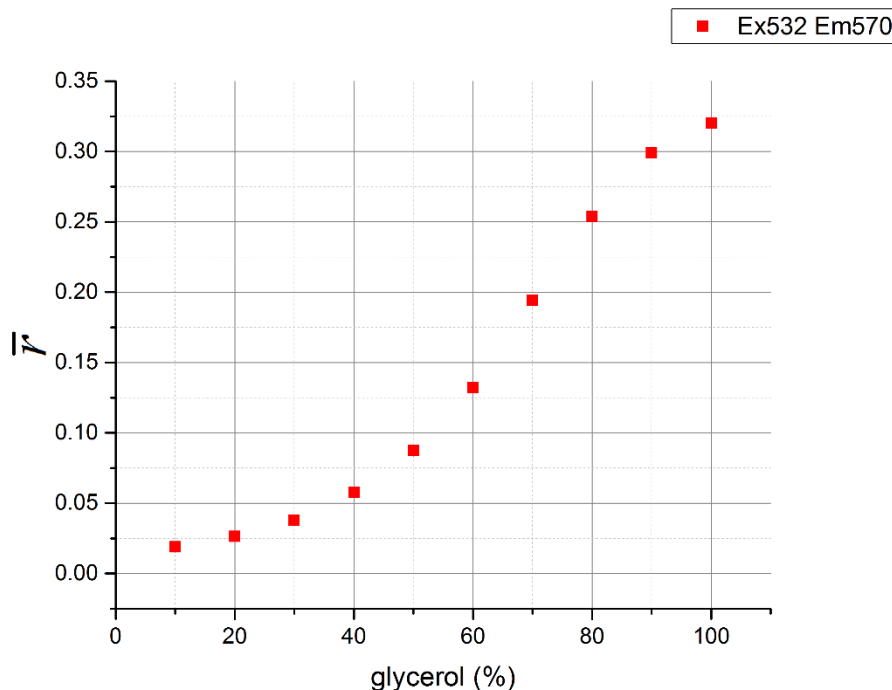
Figure 75: The steady-state fluorescence anisotropy of Rhodamine 6G with respect to increasing percentage of glycerol solution measured in a Fluorolog 3-22 with a R928 PMT. The excitation monochromator (1200/330 double grating) was set to 532 nm with a 5 nm bandpass. The emission monochromator (1200/500 double grating) was set to 570 nm with a 5 nm bandpass. For each excitation, emission wavelength pair 4 measurements were carried out with 4 different polarizer orientations VV, VH, HV and HH respectively. A 2 s integration time was used for each polarization with a maximum of 25 trials (set to get a standard deviation of 5 %). As the viscosity increases, the Brownian motion of Rhodamine 6G slows down and a higher anisotropy is reported.

2.3 Time Resolved Emission – Spectrofluorometer

Unlike the fluorescence intensity which is usually expressed in arbitrary units, the fluorescence lifetime is an absolute number derived from a histogram. The fluorescence lifetime isn't distorted to the same extent as raw intensity measurements are with inner-filtering effects or by photobleaching [178]. The fluorescence lifetime of a fluorophore can be tailored to be extremely sensitive or robust to changes in its local environment which may be due to the presence of a specific analyte for example. In many texts the fluorescence lifetime is quoted as *independent* of the fluorophore's concentration. This assumption is only valid providing the appropriate concentration regime for fluorescence measurements is adhered to[27].
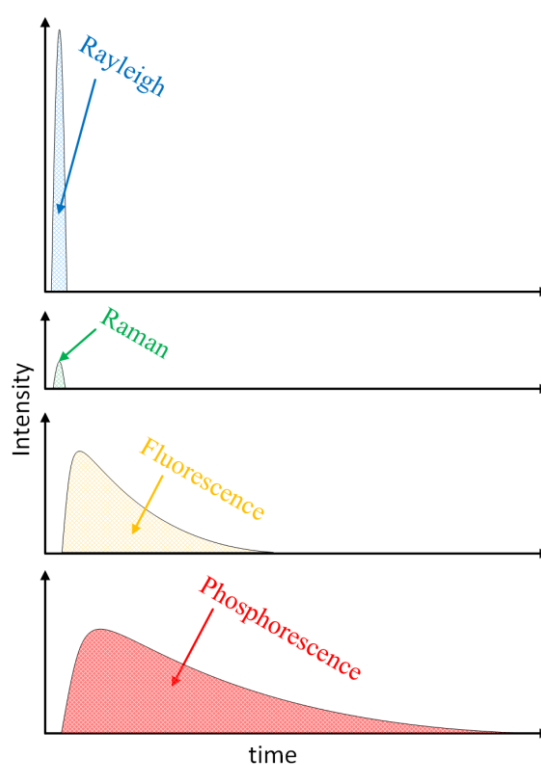
Figure 76: Illustration of the time-scale of Rayleigh scattering at the wavelength of the excitation source. At longer wavelengths there may be weak Raman (Stokes) scattering and the processes that are of the most interest, fluorescence and phosphorescence. These processes may be distinguished via measurement of their time scale.

---

[27] Lifetime is often quoted as being independent of intensity. Care should be taken with this statement as it's only true within the small concentration regimes typically used for fluorescence measurements. Too much fluorophore will change the environment and hence the fluorescence lifetime. If the fluorophore is part of a large structure for instance a decrease in lifetime may occur due to increased collisions and an assortment of energy transfer mechanisms between fluorophores.

In sensing applications the fluorescence intensity and the fluorescence lifetime may both be used in conjunction to infer the concentration of an analyte however the fluorescence intensity may decrease over time due to photobleaching and hence erroneously reporting a lower analyte concentration whereas the fluorescence lifetime on the other hand as an absolute number will remain consistent [17]. The change in the fluorescence lifetime can therefore act as a far more accurate sensor. In the introduction the time scale of both scattering phenomena and photoluminescence was discussed, these processes have differing time scales; Rayleigh (elastic scattering) ~fs, Raman (inelastic scattering) ~fs-ps, fluorescence ~ns and phosphorescence ~µs-s. The fact that these processes have a different time-scales is of great importance to time-resolved measurements and is routinely taken advantage of. It is possible to separate out these processes by using time as an additional axis as demonstrated later. The optics of instrumentation for time-resolved fluorescence is unsurprisingly similar to that of steady-state fluorescence counterpart; the main difference is the excitation source is pulsed in a time interval which is ideally much shorter than the fluorescence decay time of interest and the system needs to incorporate timing electronics sufficiently fast enough to detect the decay. Monochromators which have less surfaces are usually preferred for optimal time-resolution so a dedicated system is preferred opposed to a hybrid. As the light sources used for fluorescence lifetime measurements are already monochromatic an excitation monochromator is not usually required. Timing electronics are added to count the difference between the start (light source) and stop (detector) pulses. In the HORIBA Scientific DeltaPro and TemPro there are no emission or excitation monochromators and the separation of the fluorescence emission from the excitation is solely controlled by the right angle orientation and use of a series of longpass or bandpass filters as shown in **Figure 21**. Such a configuration is extremely useful for weak signals providing the sample doesn't scatter too much. The steady-state fluorimeters such as the HORIBA Scientific Fluorolog or Fluoromax can be upgraded with the pulsed light source and timing electronics to become a HORIBA Scientific Deltatime hybrid systems. Mainstream light sources employed for time resolved fluorescence are discrete lasers and diodes.
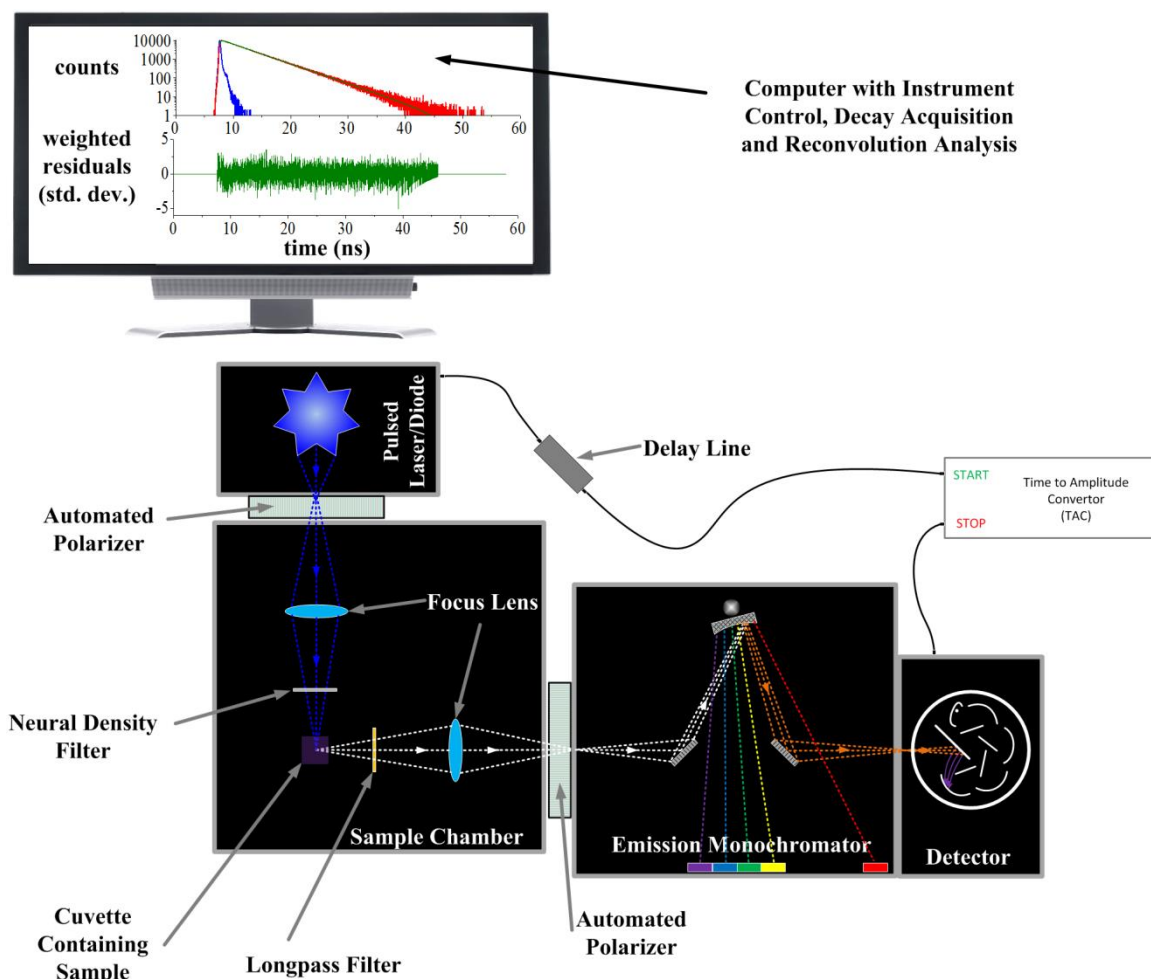
Figure 77: The optics of a time-resolved spectrofluorometer are very similar to steady-state counterpart the spectrofluorimeter. In this case the monochromators are drawn in Seya-Namioka geometry which is typical for the HORIBA Scientific DeltaFlex, FluoroCube and Ultima systems. The light source[28] is usually a laser diode or diode of discrete wavelength such as the HORIBA Scientific DeltaDiode and NanoLEDs or the SpectraLEDs for phosphorescence measurements. The detector is usually a TBX650/TBX850c for FluoroCube systems, a PPD-650/TBX850c for DeltaFlex systems or a Precision Photomultiplier MCP for Ultima systems.

In such a configuration there is no XCorrect correction factor and no ability to measure an excitation spectrum. Laser diodes and diodes are much more stable in output than the xenon arc lamp so there is usually no need to divide by a reference when using them for a kinetic measurement.

---

[28] The light sources will be denoted DD, NL and SL for a DeltaDiode, NanoLED and SpectraLED respectively. Next the wavelength will be denoted as xxx and then L or D will be added to denote a laser or a diode. For example, a DeltaDiode laser with a peak wavelength at 503 nm will be called DD503L.
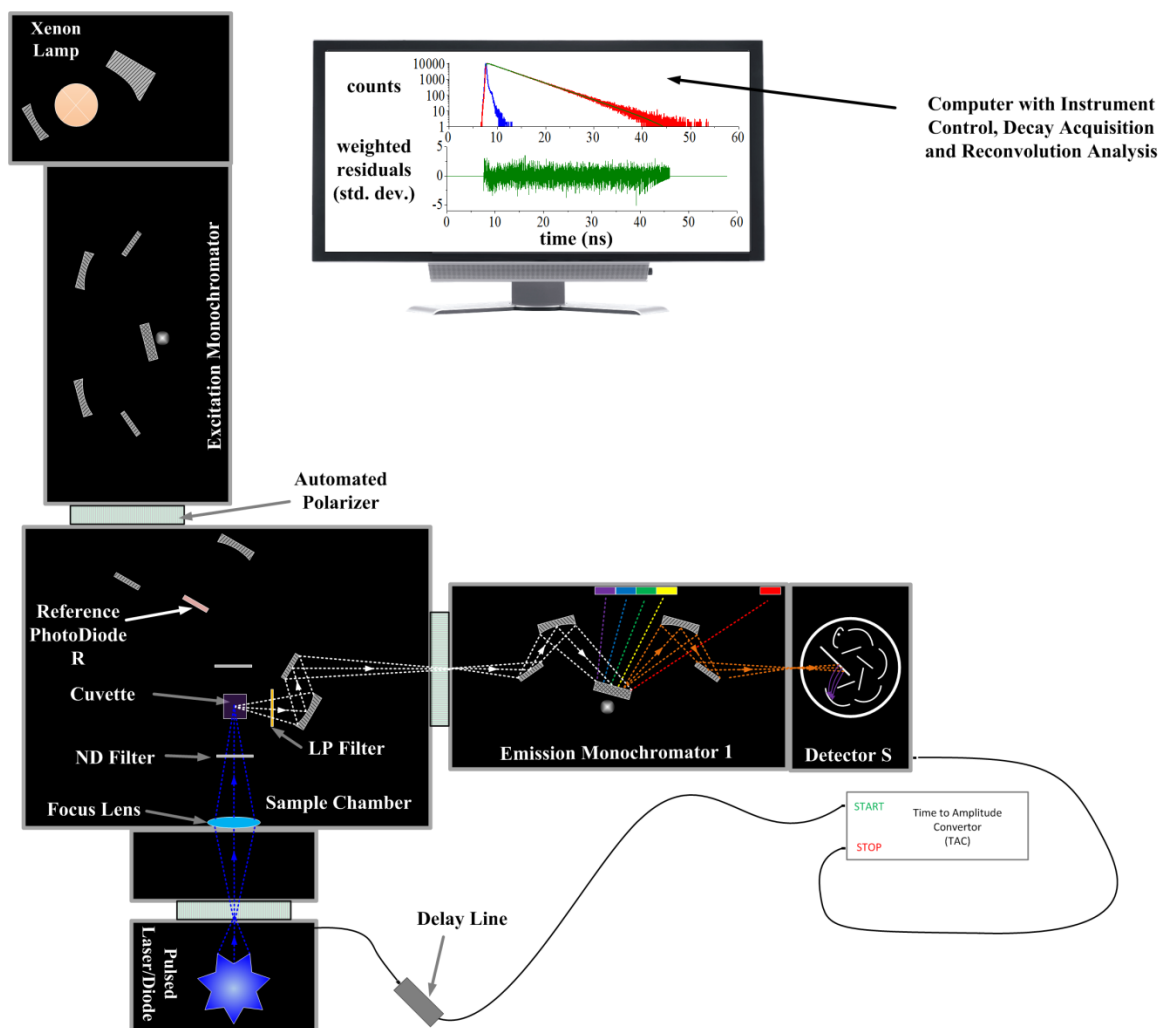
Figure 78: Addition of timing electronics DeltaHub and TB02 and a pulsed light source DeltaDiode/NanoLED/SpectraLED to a HORIBA Scientific Fluorolog 3-22 to form the HORIBA Scientific Deltatime system[29]. The xenon lamp is switched off during operation of the pulsed light source.

In a few extremely high end systems a super-continuum laser is used as a light source, for example in the Fluorolog Extreme where the xenon arc lamp is replaced by a NKT super-continuum laser and timing electronics are added between the light source and the detector. Also in the DeltaFlex Extreme where the excitation monochromator and NKT laser is used as an excitation source. Although the NKT super-continuum laser may appear to be the best light source regarding dynamic wavelength range, it should be noted it misses a substantial proportion in lower end of the visible range and UV range which are used for an assortment

---

[29] Note for fluorescence lifetime measurements a double grating monochromator is not as efficient as a Time Domain Monochromator. The number of surfaces the emission beam has to interact with on a double grating monochromator is increased making the wavelength time-spread larger thus it is harder to resolve smaller decay times. Deltatime systems typically invoke a single grating monochromator in a T format e.g. Fluorolog 3-211 (not shown) to reduce the number of surfaces. This configuration has a lower time resolution than a dedicated time-resolved system such as a DeltaFlex and certainly an Ultima.

94

of fluorescence measurements. Moreover, it has limitations in the number of repetition rates and this hence limits its overall usability in the number of time ranges where it can be employed. Its output per wavelength may be significantly lower than the DeltaDiode lasers. As the work in this thesis was carried out in conjunction with HORIBA Scientific multiple development spectrofluorometers of varying configurations were employed. Previous generations of hardware include the HORIBA Scientific FluoroCube and HORIBA Scientific TemPro systems with HORIBA Scientific Hub A and inbuilt NanoLED controller. The timing electronics incorporated the FastComTech MCA-3 and National Instruments NI-6602 PCI cards. For TCSPC the best time-resolution per channel is ~7 ps ch^{-1} or 0.7 ps ch^{-1} with a time expander and the electronic deadtime is ~1 μs. NanoLED light sources can be pulsed from 10 kHz to 1 MHz. For MCS the maximum time-resolution per channel is 500 ns ch^{-1}. To accommodate the timing electronics a custom computer was built and the latest release of DataStation was installed. State of the art HORIBA Scientific DeltaFlex and DeltaPro systems were used with DeltaHub and DeltaDiode electronics. The best time-resolution for TCSPC is slightly higher at ~13 ps ch^{-1} however the instrument deadtime is 10 ns, a factor of 100 less than previous instrumentation moreover DeltaDiode light sources can be pulsed from 10 kHz-100 MHz. The low deadtime of the DeltaHub in combination to the higher repetition rates of the DeltaDiodes significantly speeds up data acquisition on smaller time ranges making these high-throughput systems [179] and hence widen the application area which is important for applications such as enzyme kinetics. For MCS the maximum resolution is ~85 ns ch^{-1}. For DeltaHub electronics no special cards are required so a standard computer was used with the latest release of DataStation. The DeltaFlex and FluoroCube may or may not have an excitation monochromator; the reason for omitting the excitation monochromator on these systems is that typically excitation sources such as laser diodes or diodes are used which have a defined wavelength and hence all an excitation monochromator will do is attenuate the signal. Although a super-continuum laser with an excitation monochromator would apparently make a more versatile system, it is not as cost-effective as multiple laser diode sources and the output may be significantly lower at some wavelengths with no output in the UV range. The DeltaPro and TemPro systems are systems without any monochromators and typically one or more long pass filters are used to select the emission wavelength, although these systems aren't as versatile as the DeltaFlex and TemPro systems they can have the advantage when measuring samples with weak fluorescence emission.

2.3.1 Measuring a Long Lived Phosphorescent Fluorescence Decay with Simple Electronics

A long lived phosphorescence decay such as the emission from lanthanides [180] of the order of 0.1 ms may be recorded in a multitude of different ways, some more efficient than others. A sparked light source such as a xenon flash lamp may be used as a relatively cheap excitation source covering a vast range of wavelengths. A PMT is typically used as a detector; CCDs are in general not fast enough for phosphorescence decays. The phosphorescent decay may be obtained by using simple electronics. **Figure 79** and **Figure 81** demonstrate measuring a fluorescence decay using the decay by delay and decay by window methods accordingly. In the decay by delay protocol an initial delay is set after the lamp pulse and a measurement window with a fixed integration time is utilised. The xenon lamp is flashed and the number of photons within the measurement window is recorded. The measurement window is then moved by a specified delay increment, the xenon lamp is again pulsed and the number of photons measured is again recorded. This continues until the desired range is scanned. Normally the lamp is told to flash 1-999 times per delay interval. Just like steady-state measurements one has to ensure that the detector is working in its linear range. The maximum number of counts per measurement:

$$\text{No of Counts}_{\text{Max}} = \frac{\text{Linear Range of PMT}}{t_{\text{Window}}} \times \text{No of Flashes} \qquad (48)$$

where the linear range of the detector is taken from the specification sheet in CPS. The window integration t_{Window} time is taken in s and the no of flashes is dimensionless. If the number of counts > No of Counts$_{\text{Max}}$ the earlier windows which should have the most counts i.e. the start of the decay will experience photon pile-up **Figure 80**. Later windows where the long lived fluorescence/phosphorescence has significantly decayed won't have as many counts and hence won't experience pile-up. As pile-up essentially reduces the collection efficiency of the detector at shorter channels, the decay will be biased to longer decay times. For this type of measurement, the minimum feasible window integration time is about 5 µs. The initial delay is usually set to greater than 50 µs to ensure that there is no distortion on the measured long lived fluorescence/phosphorescence decay caused by the lamp profile, direct exponential fits of the decays can be used after the initial 50 µs. This method is good for crude measurements of long phosphorescence decay times. Measuring a fluorescence decay using this type of measurement and pushing for superior time resolution and hence better statistics is possible, but the cost comes at the data-acquisition 12 hours to acquire. The measurement of the decay by window shares the same limitations.
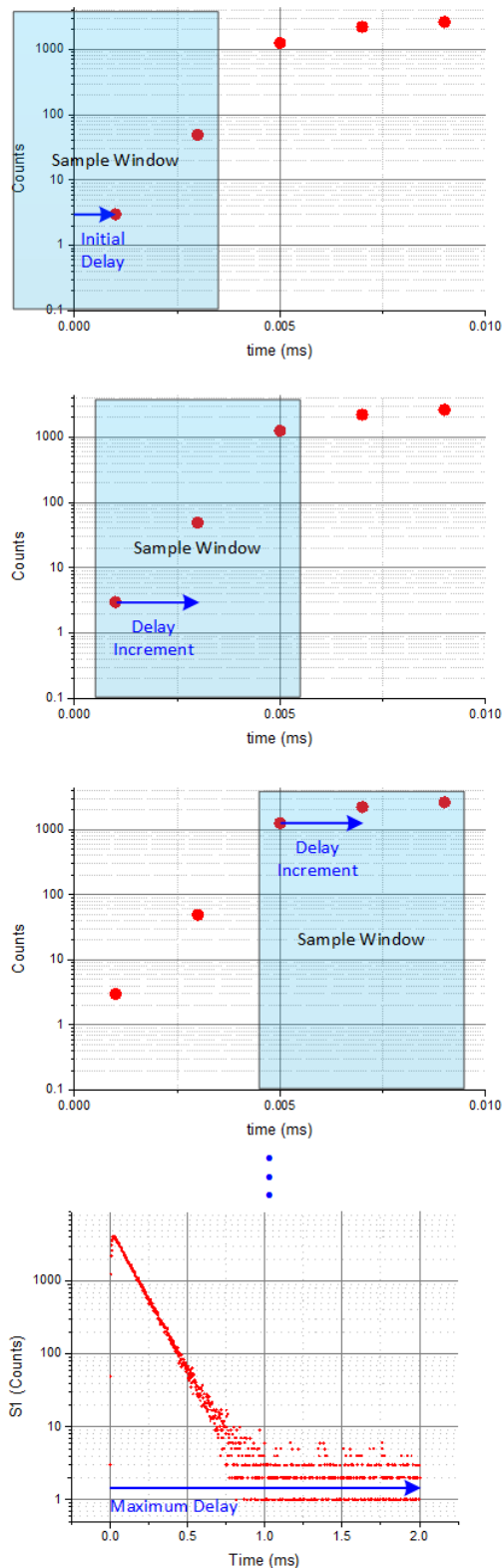
Figure 79: In the decay by delay, the time per flash and number of flashes per point are prescribed. An initial delay is set and a fixed sample window is specified. The delay is then increased by the specified increment and the number of counts within the measurement window is recorded. This continues until the maximum delay prescribed is reached.
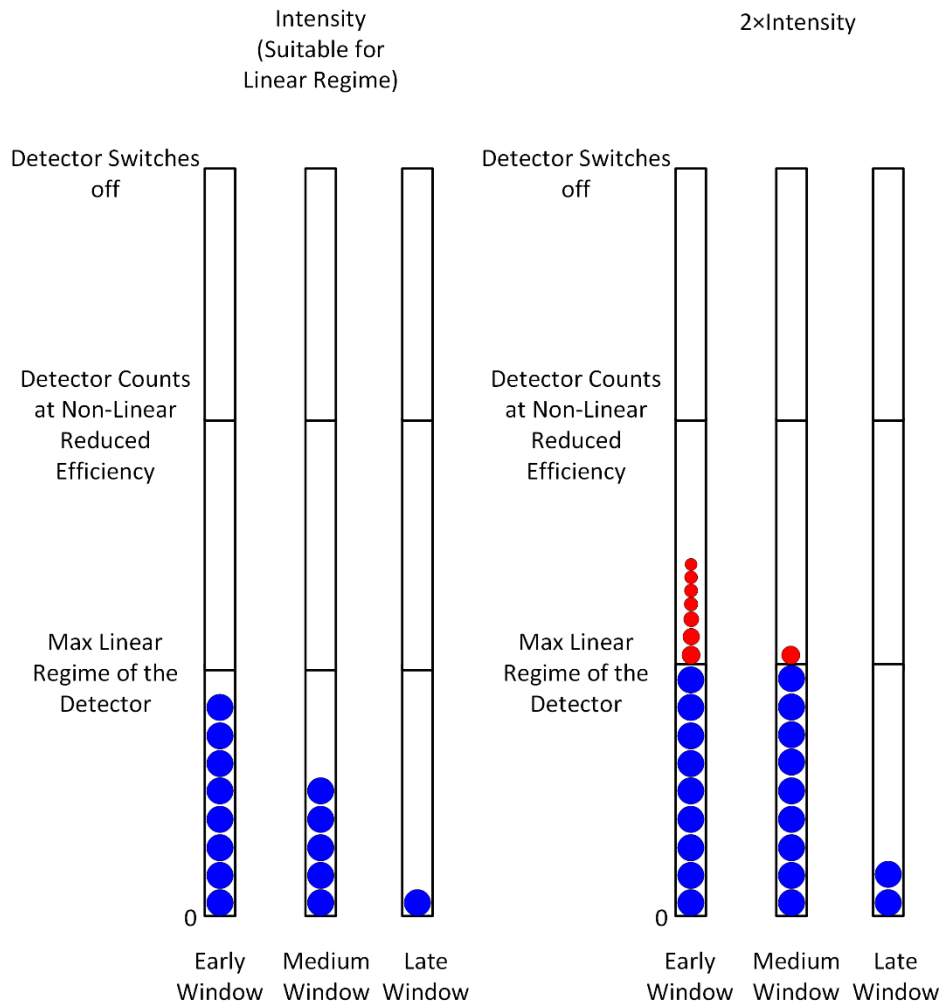
Figure 80: Schematic to illustrate pile-up in the Delay by window method. Under the correct measurement conditions (left) each window will have a photon count rate within the linear regime of the detector. **Figure 47** depicts the non-linear response of the detector at higher count rates and the switching off of the detector at extreme count rates. When out with the linear regime (right) early windows will have a count rate which exceeds the linear regime of the and as a consequence the counting efficiency will drop significantly. Medium windows will experience slight pile-up conditions and experience a diminished counting efficiency although to a lesser extent. Later windows will not experience pile-up and have standard counting efficiency. Comparing the ratios of heights Early:Medium:Late on the left versus the right the net effect is to bias the decay to longer decay times
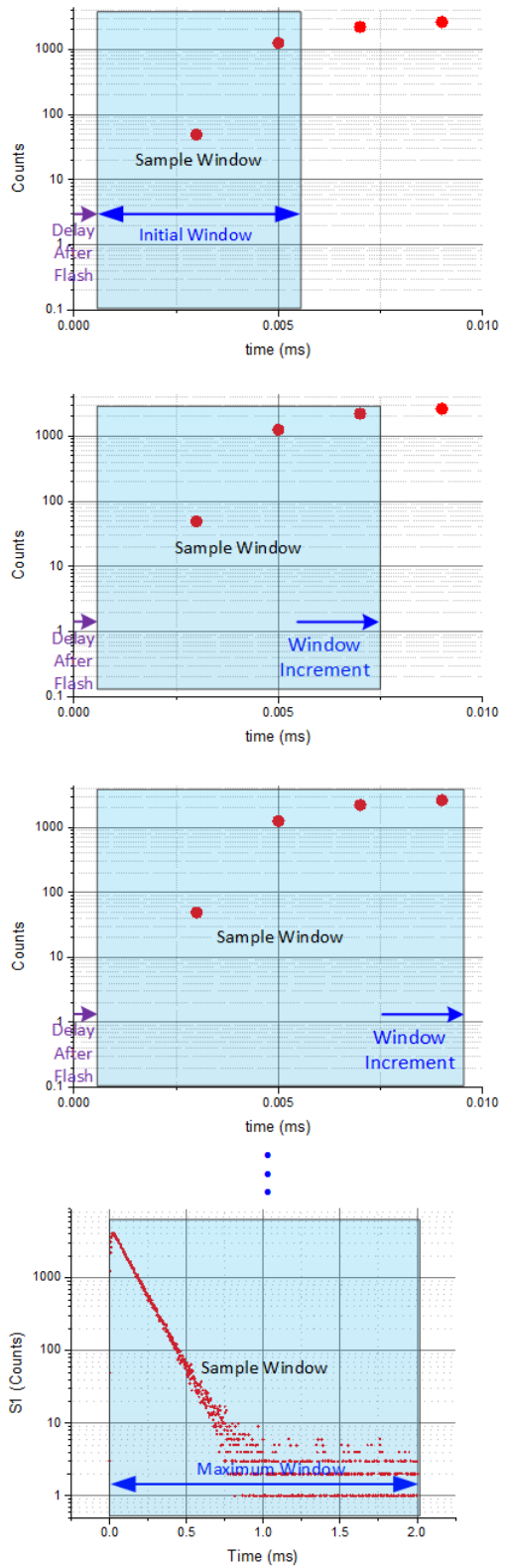
Figure 81: In the decay by window, the time per flash and number of flashes per point are prescribed. An initial delay is set and fixed; the minimum sample window is then specified with a windows increment. The windows increment is then increased by the specified increment and the number of counts within the measurement window is recorded. This continues until the maximum delay prescribed is reached.

Figure 82: Phosphorescence decay of aqueous europium chloride made to an absorbance of 0.1 measured in a Fluorolog 3-22 with R928 PMT. A xenon flash lamp was used as an excitation source. The excitation monochromator (1200/330 grating) was set to 392 nm with a bandpass of 5 nm and the emission monochromator (1200/500 grating) was set to 590 nm with a bandpass of 2 nm. The phosphorescence decay of the $^5D_0 \rightarrow ^7F_1$ transition is $\approx 110\,\mu s$ [181]. This was setup using the internal electronics in the decay by delay operation. The time per flash was set to 41 ms (the maximum repetition rate for the Xenon Flash lamp is 25 kHz) and a flash count of 100. Top the initial delay was setup at 50 µs with a sample Window of 20 µs and a decay increment of 20 µs was used until the maximum delay of 2 ms was reached. This gave a mono-exponential decay time of 111±3 µs with a χ^2=1.340 and took approximately 10 minutes to acquire. Bottom the system was pushed to its limits with a flash count of 999. The initial delay was setup at 1 µs with a sample Window of 5 µs (the smallest Window size with a large enough number of counts over the background noise). In order to look at the decay in more detail an increment of 2 µs was used until the maximum delay of 2 ms was reached. This gave a mono-exponential decay time of 111.2±0.9 µs with a χ^2=1.064. This measurement took 12 hours acquisition time!

2.3.2 Multi-Channel Scaling (MCS)

A multi-channel scaler can be considered as a series of single photon counters, with one counter for each data-channel in the decay trace. The timing electronics of the DeltaHub can use MCS with a time-resolution of ~85 ns ch^{-1} while the MCA-3/NI6602 cards in the Hub A have a maximum resolution of 500 ns ch^{-1}. MCS is a more direct measurement of the fluorescence decay. The timing electronics of a MCS are far superior to that of the xenon flash lamp natively. Apart from the advantage of time resolution the main advantage is that the entire long lived fluorescence/phosphorescence decay is captured by the electronics in a single sweep of the multi-channel scaler. In comparison to the decay by window method, a multi-channel scaler can be thought as up to four thousand windows side by side known as channels **Figure 83**.

Figure 83: Concept of MCS with respect to the decay by delay method. 4000 windows (channels) are placed side by side and the entire decay is obtained in a sweep. A series of sweeps are measured until the desired peak preset or time preset is reached.

In a MCS measurement, a peak preset or time preset is usually set in order to achieve the desired number of counts. The advantage of MCS compared to the decay to delay window is illustrated when comparing **Figure 84** to **Figure 82**, which is the same sample, measured

in the same instrument with and without DeltaHub electronics. The measurement with the DeltaHub electronics uses MCS, has a higher time resolution, and takes 15 minutes, the measurement without the DeltaHub electronics has a worse time-resolution and takes 12 hours to measure. The DeltaHub in the case of this sample therefore leads to a 100-fold increase in throughput while achieving superior time-resolution. Pile-up conditions will affect the channels with the most counts in exactly the same manner as the decay by delay measurement type. In order to avoid pile-up for a MCS measurement the number of photons recorded is typically attenuated with neutral density filters to be less than 2 % of the start rate where necessary.
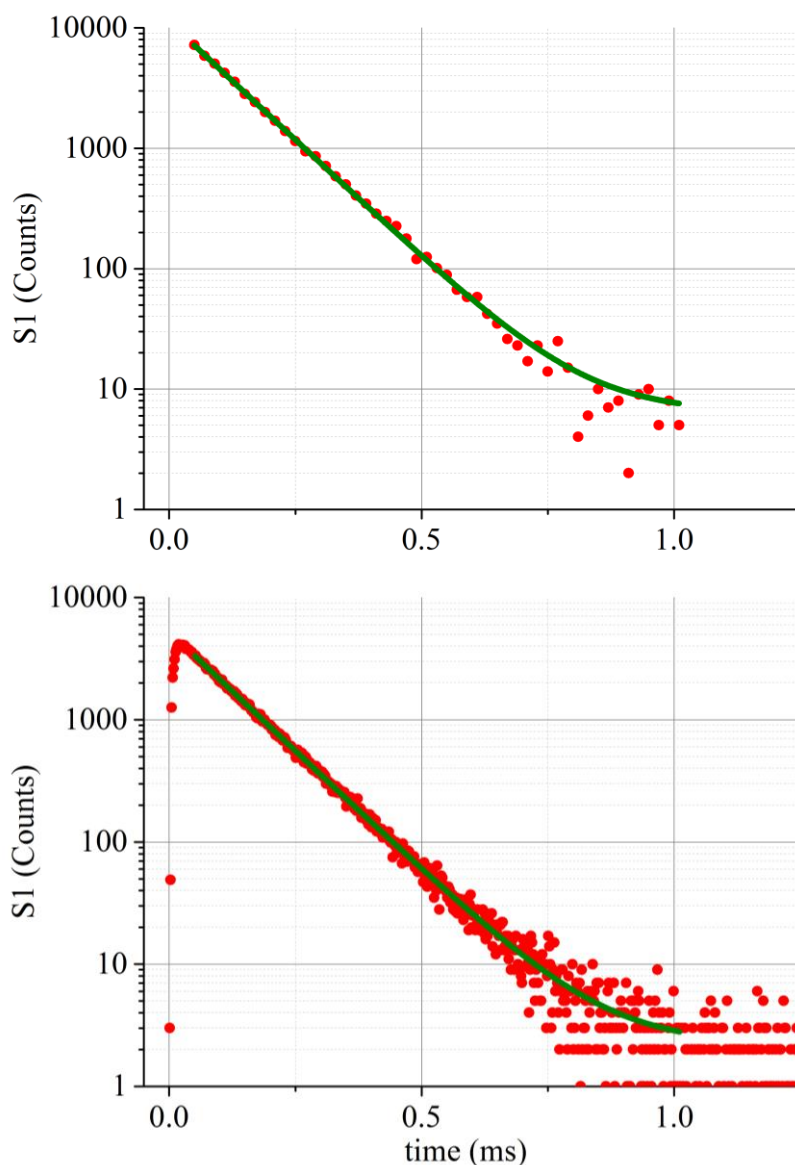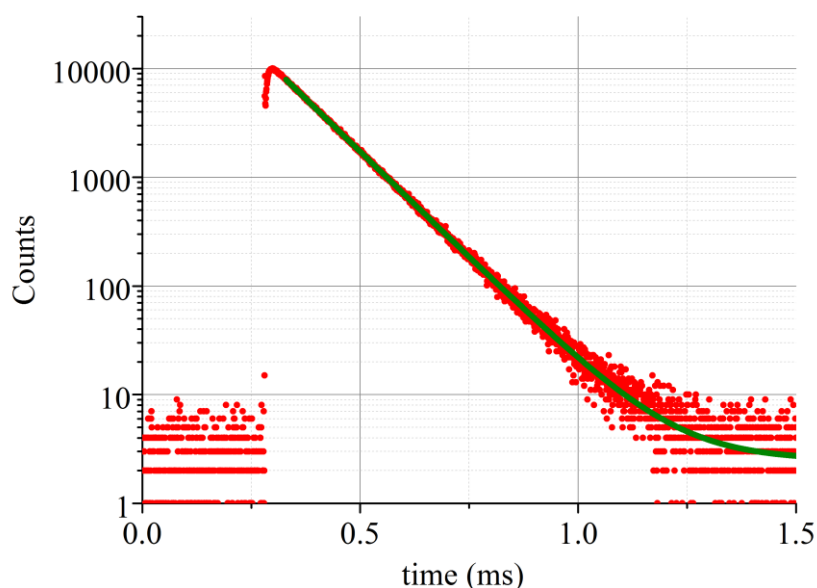

Figure 84: Phosphorescence decay of aqueous europium chloride made to an absorbance of 0.1 measured in the same Fluorolog 3-22 with a R928 PMT. The optics were setup identical to **Figure 83** however a DeltaHub was used to measure the phosphorescence using multi-channel scaling with a time range of 2.7 ms and peak preset of 10,000 counts. This gave a time calibration of ~667 ns ch^{-1} and measured to a peak preset of 10,000 counts in 15 minutes. This gave a mono-exponential decay time of 111.7±0.3 µs with a χ^2=1.041.

HORIBA Scientific SpectraLEDs typically have a broad ~30 ns pulse. Although they are of discrete wavelengths, SpectraLEDs are better excitation sources for phosphorescence measurements and do not possess an afterglow which may be present in some Xenon Lamps [182]. When using SpectraLEDs for a MCS measurement there is the ability to

select an optional delay[30] and duration of continuous excitation; the continuous excitation allows the sample to reach a steady-state which may not be achieved in the time of a xenon lamp flash[31]. After continuous excitation the light source is switched off and the fluorescence decay is recorded. The form of a MCS recorded with a SpectraLED is characteristic of **Figure 85**; initially it takes some time to excite the sample so there is a lag at the start until the sample has reached steady conditions i.e. the plot is flat. After continuous excitation the SpectraLED is turned off and the long lived fluorescence/phosphorescence decay is recorded.
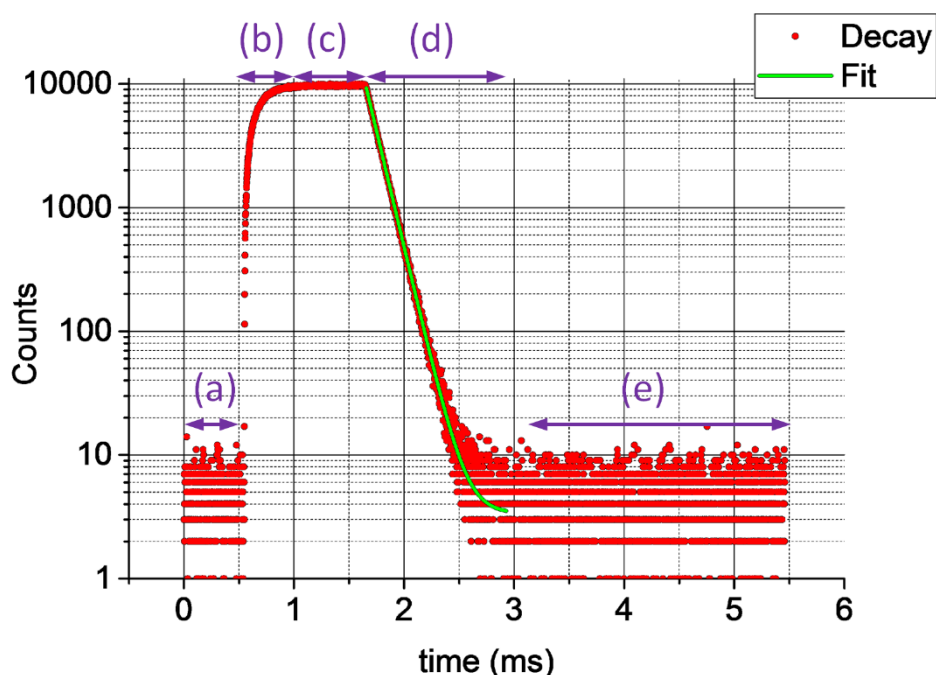
Figure 85: MCS phosphorescence decay of aqueous europium chloride made to an absorbance of 0.1 measured in a DeltaFlex hybrid using a SL373D as an excitation source. The emission monochromator TDM800 (1200/350 grating) was set to 590 nm with a bandpass of 2 nm. A TBX850c was used for detection. A DeltaHub was used to measure the phosphorescence using multi-channel scaling using a time range of 5.4 ms and a peak preset of 10,000 counts. This gave a time calibration of ~ 1333 ns ch[-1] and measured to a peak preset of 10,000 counts in 30 minutes. A delay of 10 % the time range was selected (a) then the SpectraLED was turned on. The emission from the sample takes some time (b) to reach steady state (c). In this case the SpectraLED was turned on for 25 % of the time range (b+c). The phosphorescence decay is observed after the SpectraLED is turned off (d). The end of the decay (e) should be flat and of equal height to the start of the decay (a). This gave a mono-exponential decay time of 116±5 µs with a χ^2=1.249.

---

[30] As a guide the optional delay is usually selected to be about 10 % of the time range and used as a check to ensure the noise level at the start and end of the time range is flat i.e. that there is no longer lived component present.

[31] The sample does not need to reach this steady state condition but this condition ensures the maximum number of photons per sweep and hence minimises the acquisition time.

DeltaDiode lasers can also be used as a source for MCS. Like the SpectraLED an initial delay can be set. Then the DeltaDiode can be pulsed at 80-100 MHz[32] for a period of time. Finally, they can then be switched off to measure the decay. When measuring a phosphorescence decays care needs to be taken in order to avoid re-excitation of the sample before the decay completes, failure to do so will result in a non-linear background before the decay and after the decay.
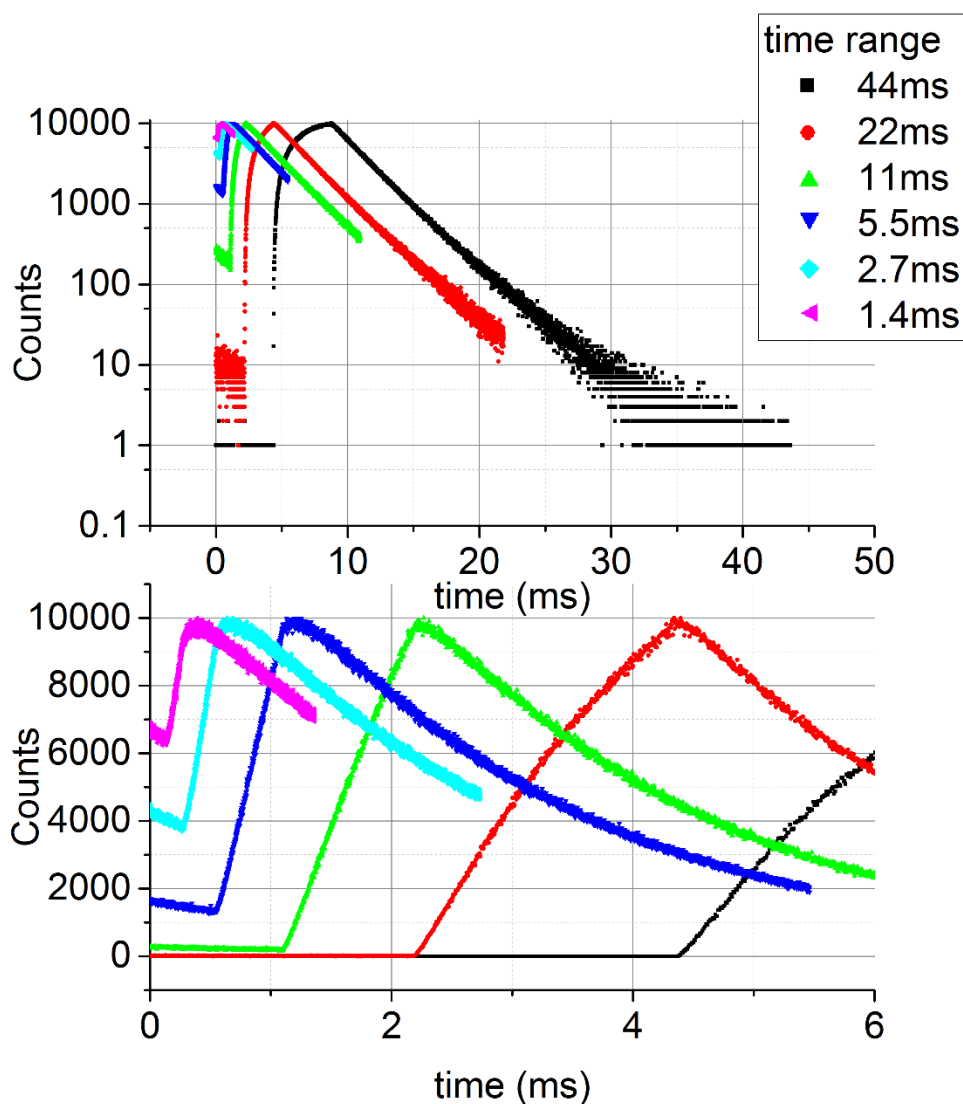
Figure 86: A MCS measurement of Tb in glass (IBH test sample) using a DeltaFlex with a SL373 excitation source and with an emission monochromator TDM800 (1200/450 grating) at 545 nm with a 12 nm bandpass. The DeltaHub timing electronics were used with a PPD850 detector. A peak preset of 10000 counts was selected. The SL373D is ran with a 10 % delay and 10 % duration for each time range. When the time range of 44 ms is used a complete phosphorescence decay is observed, the background noise before the decay is flat this regime is shown in the bottom graph in more detail. As the time range of

---

[32] At the large time-ranges MCS operates this can be considered as continuous excitation.

measurement is increased the background before the decay is observed to increase and the background is no longer flat. This is because the phosphorescence decay has not fell to zero from the previous sweep before the next sweep is initiated. To an untrained eye this may be mistaken as high dark counts.

2.3.3 Time Correlated Single Photon Counting Principle

Current timing electronics are not fast enough to directly measure the complete fluorescence decay in the ns time-range because of the significant deadtime of timing electronics which can often be many orders of magnitude larger than the lifetime of a fluorescence decay for older electronics. **Figure 87** illustrates the bias to shorter decay times because photons arriving at the detector during the electronic deadtime are not detected. Time Correlated Single Photon Counting (TCSPC) is an indirect measurement of the fluorescence decay. With TCSPC the hit rate that is the ratio of Stop/Start pulses is usually constrained to 2 %. For low deadtime electronics this limitation can be relaxed to 8-10 %. In practice this is carried out use of neutral density filters for strong samples c.f. **Figure 23** and **Figure 24**. The timing electronics which can be thought of as a sophisticated stop watch **Figure 88** with three buttons. The constraint of the hit rate means that for the majority of measurements the timing electronics will Start and no photon will be detected, the end of the time range will be reached and then the system will Reset. After a Reset one must wait for the system deadtime to pass before beginning the procedure over and over
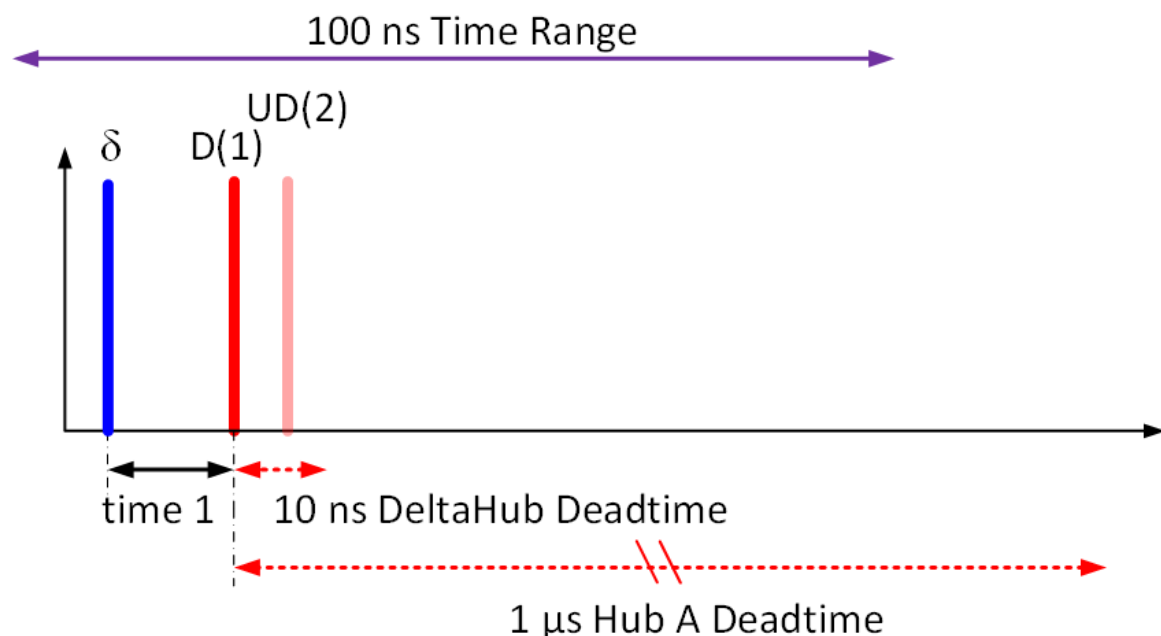
Figure 87: The sample is excited by a δ-pulse and a photon D(1) is detected. After this photon is detected the timing electronics are reset. During this reset time otherwise known as deadtime no detections are possible. A second photon arriving at this time is thus

undetected UD(2). If this procedure continues the measured decay is extremely biased to shorter decay times.
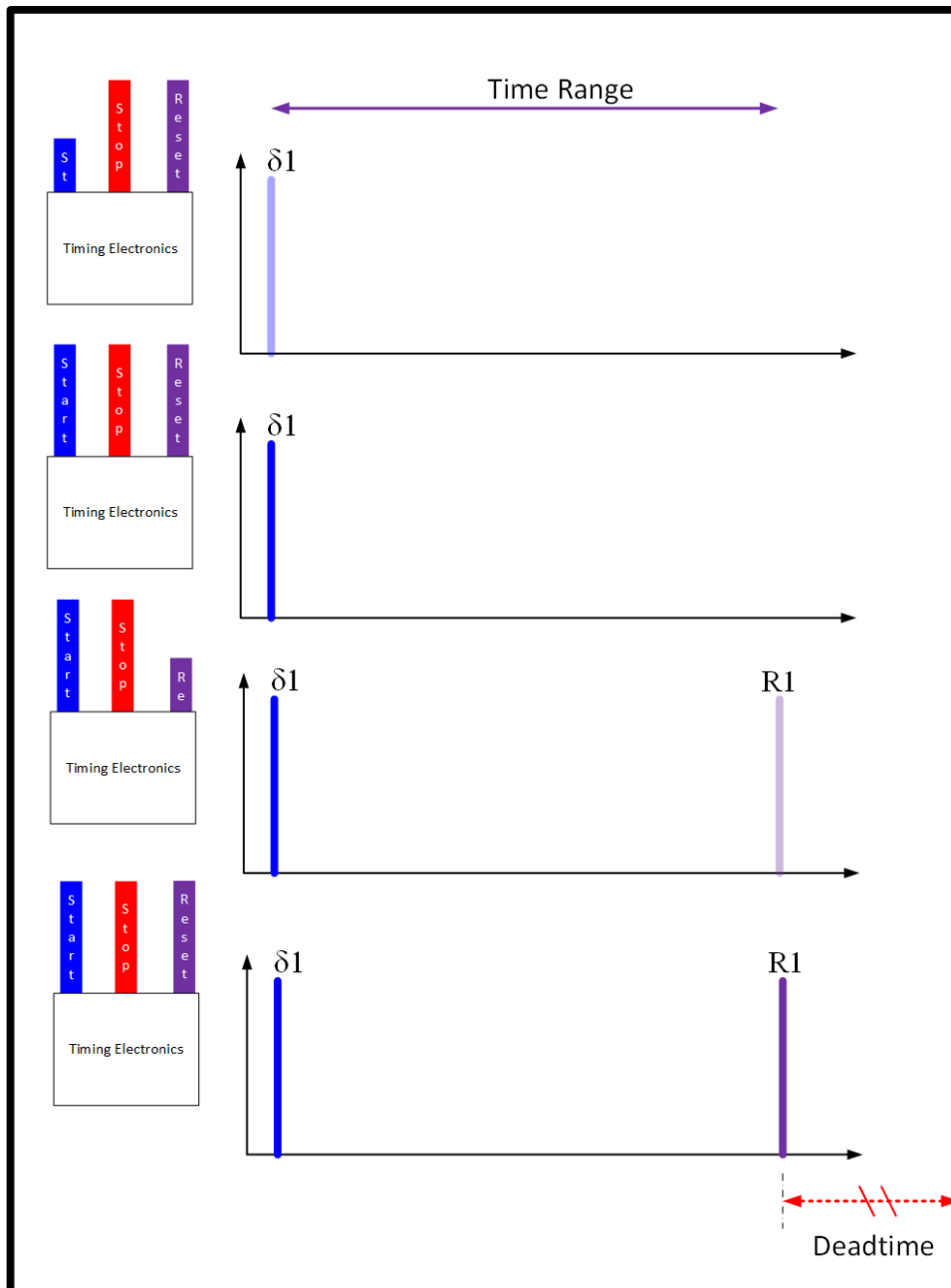
Figure 88: The timing electronics can be thought of as like a stop watch with three buttons. Start, Stop and Restart. In single photon counting mode, the stop/start ratio is constrained to prevent detection and timing of a single photon and the failure to detect a second photon during the system's deadtime. This constraint means that in the bulk of cases the system will start timing (1st frame), the time of the Start will be recorded (2nd frame) and no photon will be detected. The systems electronics will then reset (3rd frame) and then the system will have to wait on the deadtime until it can begin the entire process again (4th frame) [183,184].
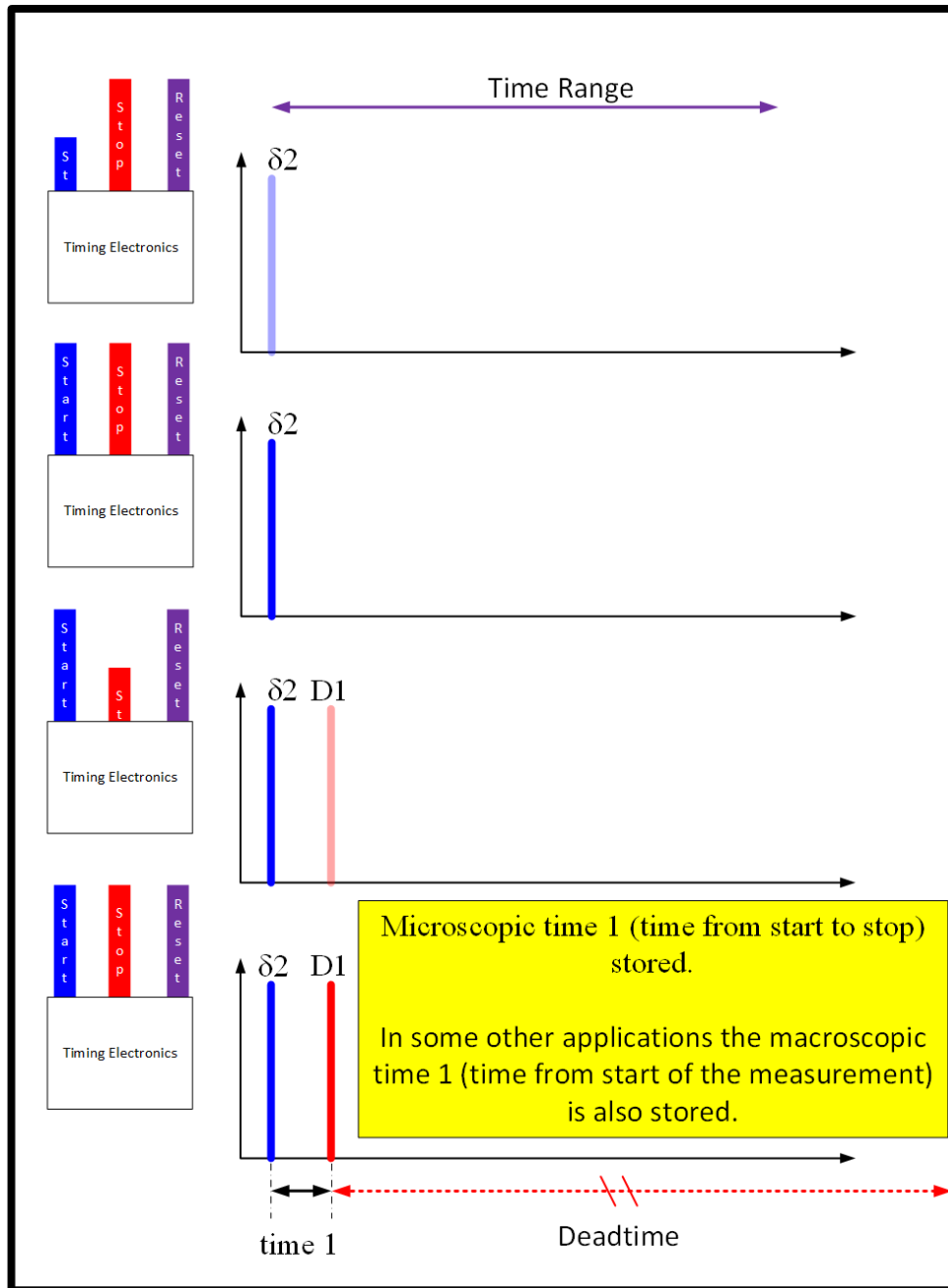
Figure 89: The timing electronics can be thought of as like a stop watch with three buttons. Start, Stop and Restart. In single photon counting mode, the stop/start ratio is constrained to prevent detection and timing of a single photon and the failure to detect a second photon during the system's deadtime. This constraint means that only in some cases the system will start timing (1st frame), the time of the Start will be recorded (2nd frame) and a photon will be detected (3rd frame). The microscopic time (time between the start and stop) and in some cases the macroscopic time (time from the start of the reaction) will be stored. The systems electronics will then reset (4th frame) and then the system will have to wait on the deadtime until it can begin the timing process again [183,184].

again. In a small fraction of the timing cycles a photon will be detected leading to a Stop. The microscopic time that is the time between the start and stop is stored and in some cases the macroscopic time, that is the time from the start of the measurement is stored. After a Stop the timing electronics Reset and again one has to wait on deadtime before it can begin timing again. Like MCS the time range consists of a number of channels and each channel is assigned a finite time width. A histogram is built up to a designated peak preset typically 10,000 counts or a designated integration time preset.

2.3.4 Instrumental Response

Any fluorometer will have its own instrumental response; the instrumental response is brought about by the fact that the excitation pulse is not a δ-pulse and may also be broadened from imperfections in both the electronic [185] and optical [173] components. The main limitation is the non-linear detector response which is brought about as a result of the transit time spread of the photomultiplier [186–188]. This instrumental response must be measured in order to extract meaningful data for short time ranges. Rayleigh scattering is of the order of ($\sim 10^{-15}$ s) and thus with the respect to the response of a time-resolved fluorometer can be thought of as instantaneous. By measuring Rayleigh scattering one can hence get a measure of the instruments response. The instrumental response of the system or prompt is typically measured using a dilute colloidal solution usually LUDOX SM-AS which will be examined in more detail later. When measuring the prompt the emission monochromator is set to the excitation wavelength and both polarizers are set to the vertical orientation (if present). These conditions are optimised to measure Rayleigh scattering[33]
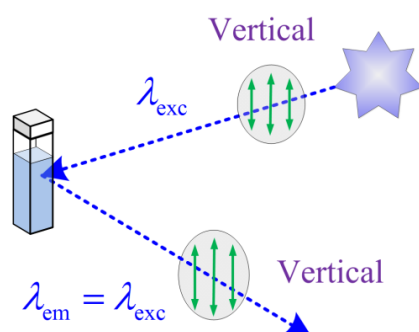
Figure 90: Typical polarizer and monochromator conditions for the scatter or prompt measurement. If an unpolarised Diode is used as an excitation source, polarizers aren't required.

---

[33] VV polarizer configurations are used for the Prompt as Rayleigh scattering is fast and hence the most prominent in the VV orientation.

108

and to minimise the effects of fluorescence. The instrumental response from a Xenon lamp may be quite broad due to the profile of the Xenon flash lamp. In this case a FWHM ~0.5 µs was recorded using MCS, this is negligible compared to the 116 µs decay time measured in **Figure 82** and **Figure 84** which was satisfactorily tail fitted. Clearly however this type of light source is not suitable for ns decay times.
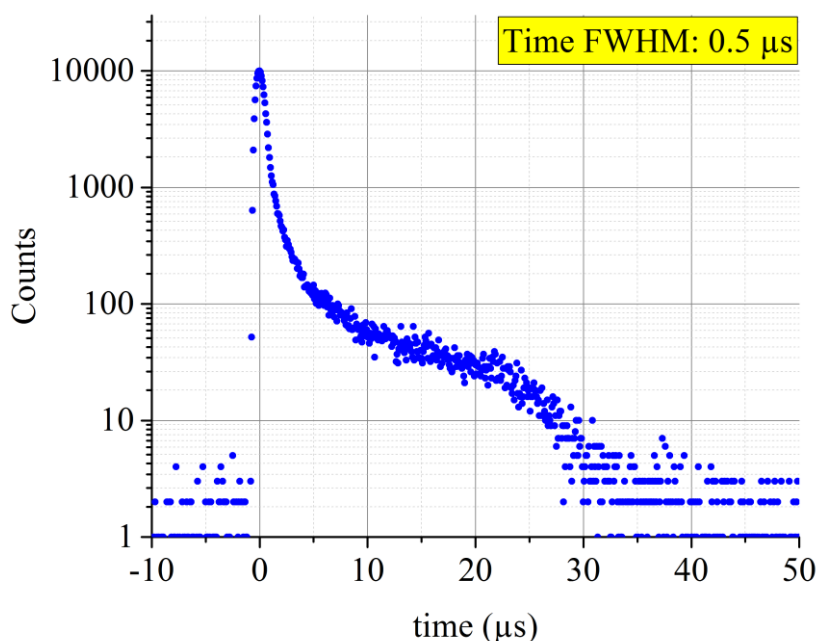
Figure 91: The time-profile of the xenon flash lamp measured on a Fluorolog 3-22 with DeltaHub and R928 PMT. The excitation monochromator (1200/330 double grating) was set to 392 nm with a 3 nm bandpass. The emission monochromator was set to 392 nm with a 3 nm bandpass. A dilute LUDOX SM-AS solution was used as a scattering solution. The maximum time resolution for MCS was utilised ~85 ns ch^{-1}.

The DeltaDiode, diode sources typically have a FWHM~750-1000 ps for example DD280D and DD295D. Such pulses have quite a smooth appearance when measured with modern electronics see **Figure 92**. DeltaDiode sources also have a monochromatic output; the second peak observed is due to second order effects of the monochromator which allow some excitation light to reach the detector. It should be noted that this can be prevented in fluorescence measurements by the addition of a long pass filter of appropriate wavelength. Laser sources on the other hand can have a much smaller instrumental response which can fall into the ps or even fs regime. However the transit time spread of the photomultiplier for example in the TBX650/PPD-650 and TBX850c/PPD-850c picosecond detection modules are ~180-250 ps [137]. The prompt of DD405L has a FWHM of ~200 ps with the TBX850c. The appearance of the prompt shows a second peak which is an artefact due to

the non-linear transit spread time of the detector. This afterpulse is caused by the elastic scattering of electrons off the first dynode c.f. **Figure 48** [189,190]. In order to overcome this problem and to accurately to measure decay curves at small time ranges re-convolution analysis must be applied which will be discussed later. It should be noted that extremely old TBX picosecond detection modules may also exhibit later after-pulses. All these after-pulses will also be taken into account when re-convolution analysis is used.

If the system is not very aligned or additional optics are used additional peaks may appear in the instrumental response due to reflections **Figure 94**. When a light source is swapped with another source of differing wavelength or the cuvette holder is swapped the system should be checked for alignment and the focusing optics should be optimised using a Focus Scan. The effect of the broadening of Rayleigh scattering from the DD405L (Rep Rate=20 MHz) by detector response and electronics may be seen by plotting both a prompt measured with a Hub A/MCP system alongside a prompt measured with a DeltaFlex/PPD850 **Figure 96**. Care must be taken when using the MCP as it has a lower dynamic range than other PMTs (50000 CPS opposed to 2000000 CPS) and if the number of counts is too high the pulse will broaden. The timing electronics of the Hub A and MCP must be given some time to stabilise after powering on otherwise the pulse will likewise broaden. Optical alignment and reflections are more significant when trying to get a fast pulse on a MCP system. Measurement of the DD405L on the MCP systems shows that the instrumental response is limited by the laser profile. The laser profile is significantly faster than the Diode or Xenon flash lamp but it takes some time for the electronics to switch off the laser which is measurable on a MCP system.
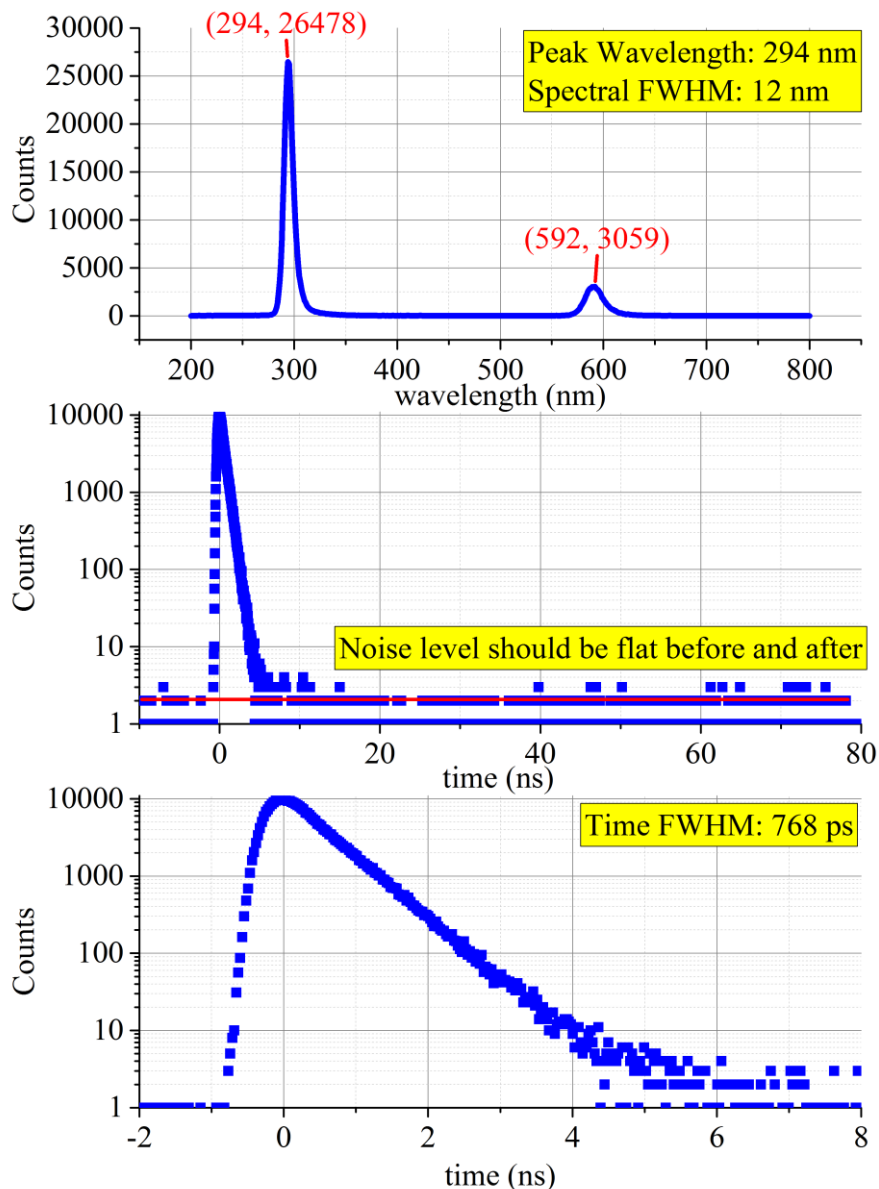
Figure 92: Steady-state and instrumental response of DD295D (Rep Rate=20 MHz) measured on a DeltaFlex with a TDM800 (1200/350 grating) with a PPD850. For steady-state the emission bandpass is constrained to 2 nm and the monochromator is scanned at 1 nm increments over its entire working range the emission peak is found to be λ_{peak}=294 nm with FWHM of 12 nm. For the time-profile the emission bandpass is opened to 12 nm and the time profile is measured to have a FWHM=768 ps at the peak wavelength. DeltaHub electronics are set to a time range of 100 ns (4000 channels). The monochromator when set to 592 nm allows second order emission of the excitation light; it should be stressed that this light is not the DeltaDiode lasing at 592 nm but the monochromator allowing light of 295 nm to reach the detector. The peak may be identified as second order because it resembles the 1st order peak but is lower in amplitude and is stretched out twice as wide. The 2nd order peak can be removed using a long pass filter alongside the monochromator. This was measured in a DeltaFlex[34] with DeltaHub electronics and a PPD-850c. No additional ND filters were used and polarizers were removed. Diodes have a broad FWHM

---

[34] In order to do this measurement on a FluoroCube with both an excitation and emission monochromator, the excitation monochromator may be set to 0 nm wavelength where it acts as a mirror.

and are unpolarised in output. A dilute LUDOX SM-AS solution was used as a scattering solution.
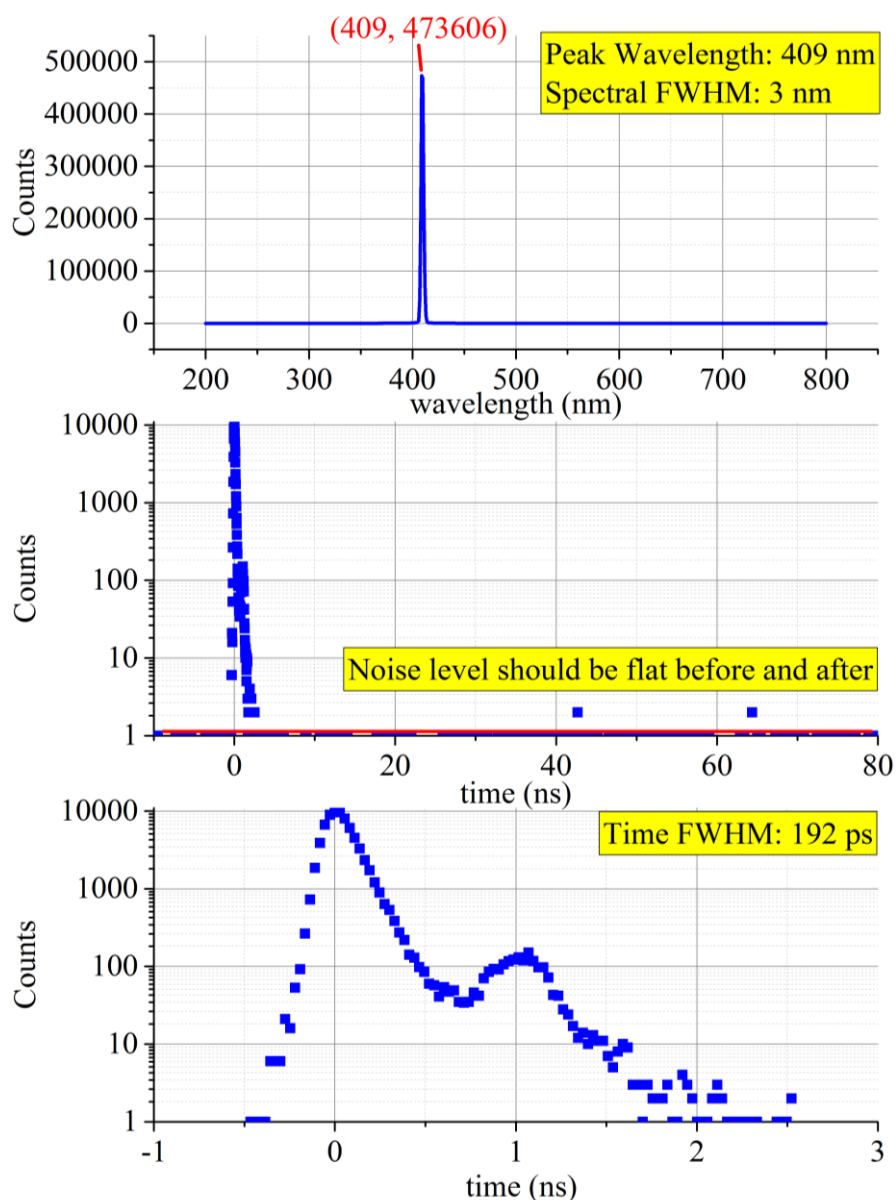
Figure 93: Steady-state and instrumental response of DD405L (Rep Rate=20 MHz) measured on a DeltaFlex with a TDM800 (1200/350 grating) with a PPD850. For steady-state the emission bandpass is constrained to 2 nm and the monochromator is scanned at 1 nm increments over its entire working range the emission peak is found to be λ_{peak}=409 nm with FWHM of 3 nm. For the time-profile the emission bandpass is opened to 12 nm and the time profile is measured to have a FWHM=192 ps at the peak wavelength. DeltaHub electronics are set to a time range of 100 ns (4000 channels). As a laser is used polarizers were both at vertical orientation. The emission bandpass was set to 2 nm and to ensure that the counts were below 2×10^6 CPS at the peak emission UV ND 2.0 and UV ND 1.0 were added to the excitation arm. It should be noted that the FWHM in this case is limited by the detector and not by the laser. A dilute LUDOX SM-AS solution was used as a scattering solution.
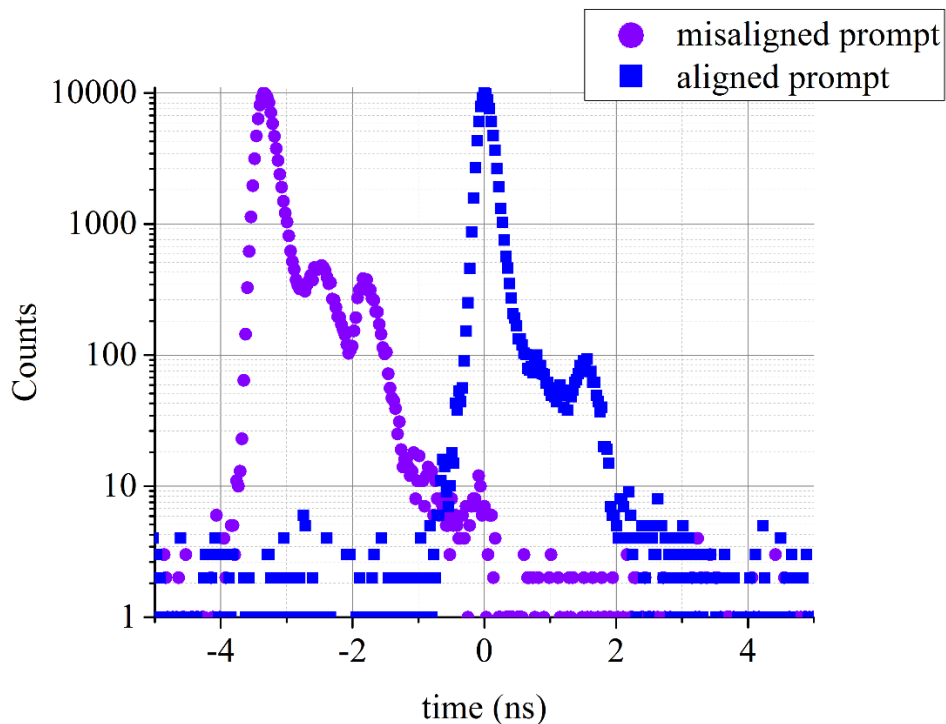
Figure 94: The focusing of optics is naturally important for the laser FWHM. The dashed line illustrates a badly aligned system. The solid blue line is the system focused scanned and the time delay changed slightly for clarity. (a) is the laser pulse of DeltaDiode on a 100 ns TAC range (4000 channels), (b) is an additional peak arising due to a reflection and (c) is the non-linear detector response.
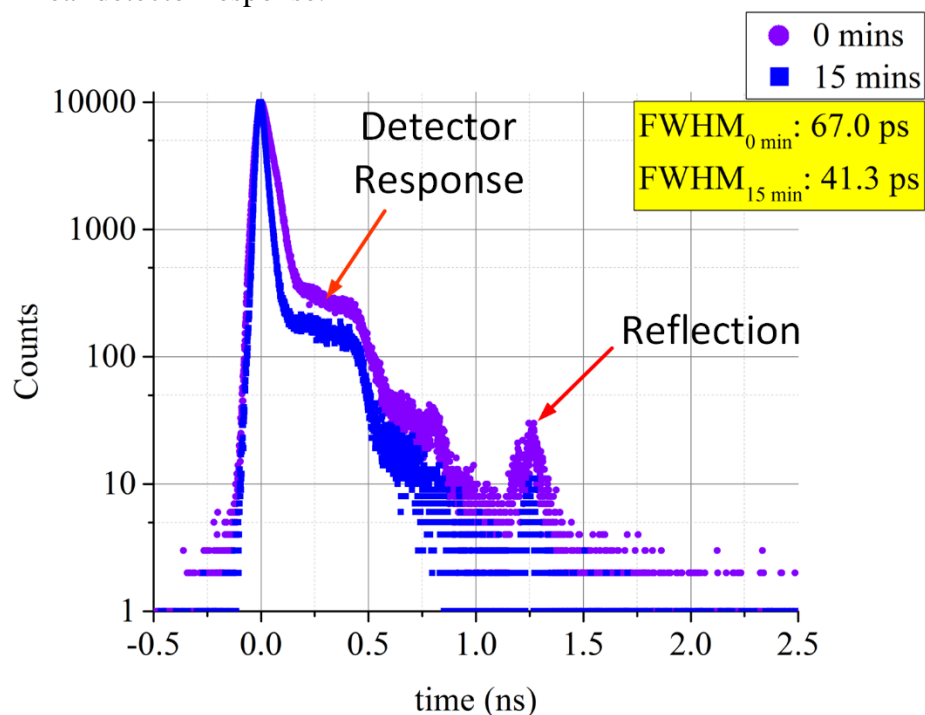
Figure 95: In order to illustrate the effect of detector response in more detail. The same DD405L (Rep Rate=20 MHz) was measured using a HORIBA Scientific Ultima using the diode sync for optimum stability. This system has the Hub A electronics with the time expander enabled (0.701 ps ch^{-1}) and a Precision Photomultiplier MCP [191] as a detector. In order to prevent the MPT from exceeding 50000 CPS 1 UV ND 2.0 and 1 UV ND 1.0

were used on each arm optic conditions were otherwise identical to **Figure 93**. Detector response is illustrated by measuring a prompt as soon as the detector is powered up and 15 minutes after it is stabilised. The FWHM was measured to be 67.0 ps and 41.3 ps respectively.
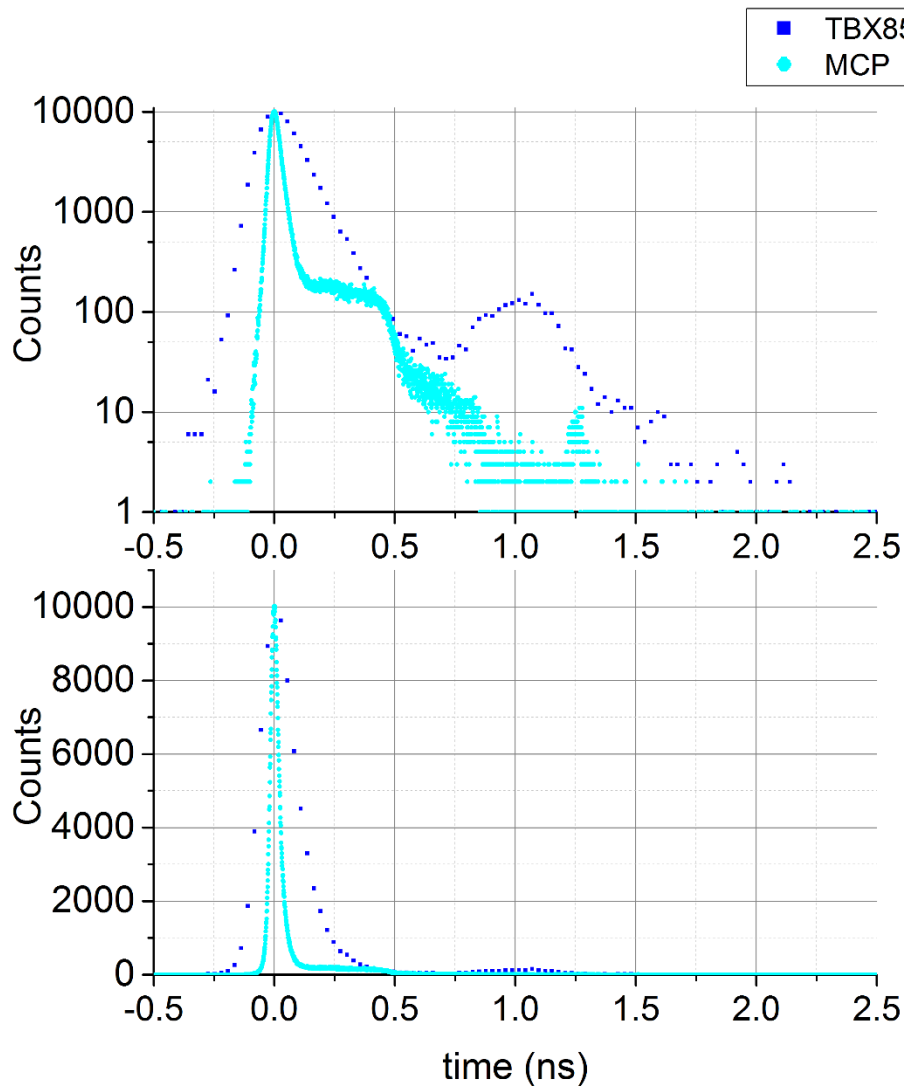
Figure 96: Artificial broadening of DD405L by the PPD850 can be seen by setting the peak of the prompt to 0 ns and plotting the prompts (**Figure 94** and **Figure 95**) overlaid in time opposed to channels. It is insightful to see this in both log and linear scale. Now that the data is plotted with respect to time, the reflection can be discussed in more detail. Recall that the speed of light is 3×10^8 m s^{-1} and in 40 ps, light travels 1.2 cm. This 1.2 cm is comparable with the size of the square sample compartment ~25 cm×25 cm. The reflection in the case of **Figure 96** is measured ~1.25 ns after the main peak. This means light has travelled ~37.5 cm. In actual fact the reflected light has gone off in a diagonal bounced off the corner of the sample compartment and arrived at the detector 1.25 ns later. The overlay of both prompts shows the reflection measured at 1.25 ns in the case of the MCP would have been drowned out by the broadened detector response of the PPD850.

2.3.5 Delay lines, Repetition Rate and TAC Range

A time range must be selected to suit the sample under investigation. Typically, the time range selected is 10-20 times the fluorescence lifetime of the sample. Samples usually have one decay time or multiple decay times of similar orders of magnitude so it's usually an easy selection. The repetition rate is automatically selected when the NanoLED, DeltaDiode Laser or DeltaDiode Diode is coupled to the DeltaHub, Hub A or Hub B. NanoLEDs all have a maximum repetition rate of 1 MHz, DeltaDiode Diodes has a maximum repetition rate of 20 MHz and most DeltaDiode Lasers have a maximum repetition rate of 100 MHz. At factory the spectral and time FWHM of each source is measured using a system with a MCP c.f. **Figure 92**-**Figure 95** and the power is measured using a power meter. Characterisation is carried out at various repetition rates to ensure the source passes or exceeds specifications. In order to obtain a complete fluorescence decay within a given time range the repetition rate of the light source has to be adjusted so that the following conditions are satisfied:

$$\text{Max Rep Rate} < \frac{1}{\text{Time Range}} \qquad (49)$$

This is automatically selected in most cases however in some non-routine measurements a manual selection may be required. Samples which possess multiple species may include a very short decay time as well as a very long decay time. Adjustment of the time range to measure the long lived time component may give insufficient time-resolution to accurately measure the short lived component (there are a finite number of channels and these get stretched wider as the time range increased). In such complicated samples a short time range may be selected alongside a lower repetition rate in order to prevent sample re-excitation before the decay reaches noise[35] c.f. **Figure 86**. The delay between the start and stop may have to be adjusted so the fluorescence decay is measured by an appropriate are of the TAC **Figure 97**. If forward mode is employed once the appropriate delay is set for the 100 ns time range, in general it doesn't need to be altered if the time range is increased although there may need to be a slight adjustment for shorter time ranges.

---

[35] In such complicated measurements the repetition rate should be lowered on the smaller time range to match the repetition rate that would be used in the larger time range in order to prevent re-excitation of the sample during measurement. The DeltaDiode can be disconnected from the DeltaHub to be manually controlled for such advanced measurements.

For the older MCA3/NI6602 systems however reverse mode is commonly employed in order to reduce measurement deadtime. When acquiring data at the short time ranges t_{TAC}=50-200 ns the deadtime of the timing electronics Hub A $t_{Dead}^{Hub\,A}$=1 µs becomes significant. For ease of calculation taking the 50 ns time range and 1 % hit rate as an example **Figure 98**. In forward mode one Starts the TAC with every excitation pulse. With a hit rate of 1 % only one of these excitation pulses leads to a detected photon thus in the vast majority of cases one measures for 50 ns and then Stops the TAC. With each Stop one has to wait 1 µs for the electronics to reset. The time to record a single photon is thus $100 \times$ 50 ns + 100×1 µs ≈ 0.150 ms. In reverse mode one only Starts timing when a photon is detected and as the timing from the excitation pulse leading to this photon detection is not recorded, the time from this photon to the next excitation pulse is instead computed. The recorded data may then later be flipped so it appears like forward mode data using acquisition/analysis software. The time to record a single photon is thus reduced to $100 \times$ 50 ns + 1×1 µs ≈ 6 µs.
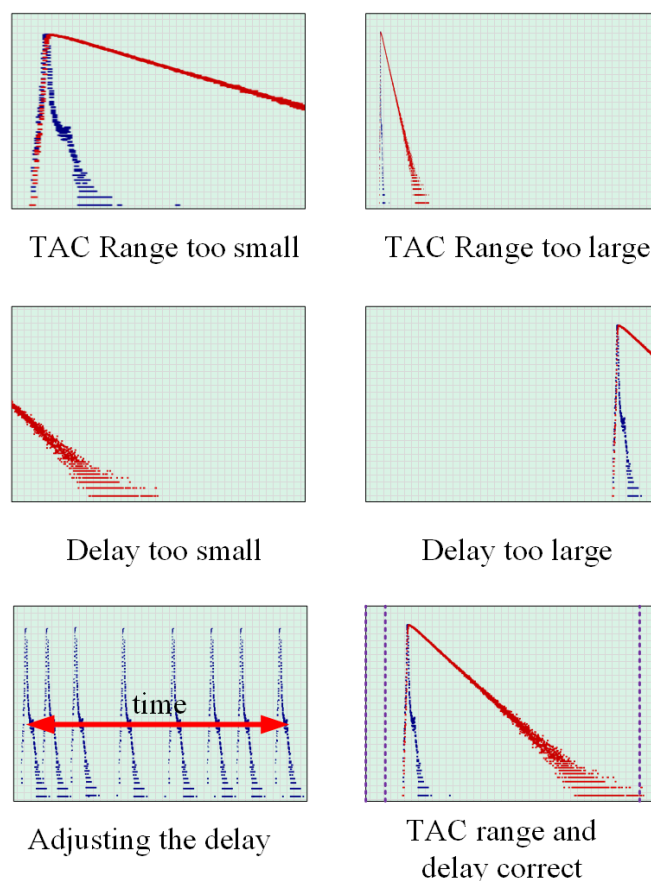
Figure 97: Illustration of TAC Range and Delay adjustment for a mono-exponential sample. The TAC range is in generally selected to be 10-20 times that of the fluorescence lifetime. The top left illustration depicts a correct delay but incorrect TAC range, missing much of the decay curve. Because the repetition rate is also too high, before the prompt

116

part of a previous decay can be observed. The top right depicts again a correct decay but too large a TAC range, therefore less channels are used and the time resolution of the measurement is lowered. The middle left and right diagrams depicts a correct TAC range but too small and too large a decay respectively, missing much of the lifetime curve. The bottom left diagram depicts movement of the prompt with respect to the delay. Note time calibration of the TAC can be achieved by measuring the peak of the prompt with respect to the decay. The bottom right image depicts use of the correct delay and TAC range. Note the noise before the peak of the prompt is at the same level as the noise at the end of the decay meaning the complete decay has been measured and no re-excitation has occurred. In addition to the repetition rate the delay lines have to be adjusted so the fluorescence decay is observed within the measurement window.

If the deadtime of the timing electronics is significantly larger than that of the time range being measured, reverse mode is commonly employed. In reverse mode the start and stop inputs are reversed so that the systems timing electronics measure the time between a detected photon and the next start pulse. The advantage of reverse mode is the timing electronics only "start" to measure for every photon detected opposed to every excitation pulse and hence there is no need to wait for the deadtime of excitation pulses, which do not lead to a detection. Taking a 1 % hit rate for example, data acquisition can be significantly speed up due to only having t_{Dead} opposed to $100t_{\text{Dead}}$ for every 100 excitation pulses. The fluorescence histogram is reversed compared to that traditionally measured in forward mode and additional delay lines may be required. The data can however easily be reversed in software and delay lines don't affect the parameters obtained from the decay curve.
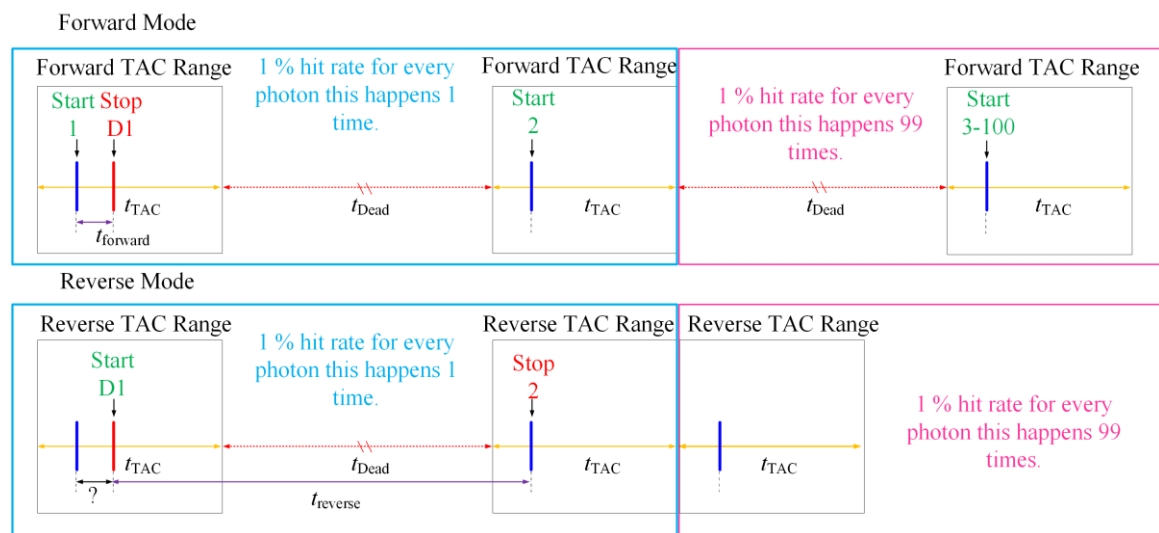
Figure 98: An illustration of forward mode operation vs. reverse mode operation where the time between the start and the stop t_{forward} is the times recorded in order to obtain a decay histogram in forward mode. The time range t_{TAC} and the system deadtime t_{Dead} are constant during measurement. It therefore follows that the time between the reverse start and stop $t_{\text{reverse}} = t_{\text{Dead}} + t_{\text{TAC}} - t_{\text{forward}}$. Due to the 1 % hit rate, the processes in the magenta

boxes occur 99 times for every photon detected whilst the processes of interest in the cyan box occur 1 time.
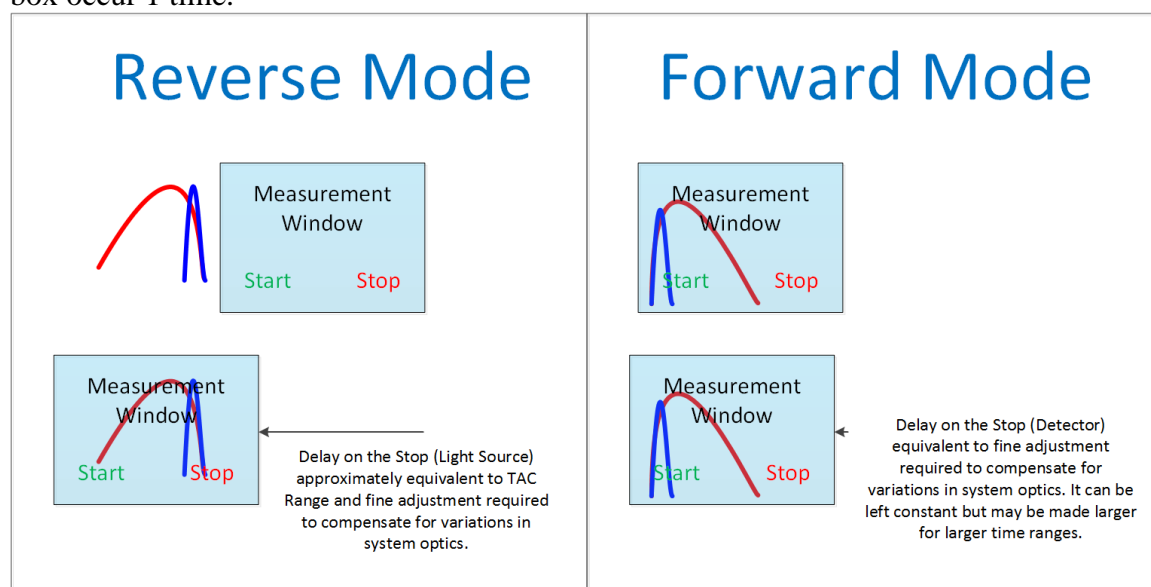
Figure 99: An illustration of how the delay on the stop moves the measurement window for reverse mode (data not reversed) and forward mode. A delay on the start will push the measurement window in the opposite direction. In both cases a delay is required to account for fine adjustments in system optics. In reverse mode the prompt should be present in the measurement window just before the Stop of the TAC. In forward mode the prompt should be present just after the start of the TAC. Data acquisition on screen is typically reversed when running in reverse mode so the decay curve looks like it is ran using forward mode.

Reverse mode requires a delay on the Stop input approximately equal to that of the time range see **Figure 99**. For longer time ranges reverse mode is not applied due to the large delay required to move the prompt the full length of the time-range. The maximum delay that can be applied on the Start/Stop inputs of the Hub A is ~320 ns, if any more delay is added, the impedance is too high and the signal is lost however the advantage of reverse mode becomes less relevant as the system reaches a similar order of magnitude to the time range. The higher repetition rate of DeltaDiodes and low deadtime of the DeltaHub $t_{\mathrm{Dead}}^{\mathrm{DeltaHub}}$ =10 ns greatly increases throughput when short time ranges are employed. As the deadtime is shorter or equal to the TAC range in all cases for the DeltaHub reverse mode is never used with the DeltaHub. The maximum repetition rate of the light source is inversely proportional to the time range used TCSPC becomes very inefficient at higher time ranges. For example, a 100 ns TAC range can utilise a fast repetition rate of 10 MHz but in practice is usually lowered to 8 MHz in case the time range is slightly larger than 100 ns and hence rapid acquisition of fluorescence decays can be achieved. Conversely the 13 μs TAC range can utilise a maximum repetition rate of 75 kHz, which in practice is usually constricted to 50 kHz in case the actual time range is slightly longer than 13 μs.

118

Data acquisition time can be substantially longer due to the use of the low repetition rate. Fortunately, the need for TCSPC diminishes at such time ranges because the timing-electronics become sufficiently fast enough to measure longer decays using more direct measurements such as Multi-Channel Scaling (MCS). The most time-consuming measurement is a measurement of a short decay and a long decay mixture where one wants to accurately resolve the short decay component and consequently has to use high time resolution but simultaneously lower the repetition rate of the laser to prevent re-excitation.

2.3.6 Time Calibration

The time calibration per channel can drift over long periods of time especially in older systems which are capacitor based. In general, this drift is only significant for smaller time ranges, in particular, the 50-200 ns ranges and hence these time ranges should be periodically calibrated. A spectrofluorometers time calibration per channel can be measured using the prompt of a laser source with respect to variable delay lines or use of a TAC calibrator. For a quick calibration mono-exponential, lifetime standards can be prepared and used however care should be taken when comparing decay times from mono-exponential standards to that of reference data as the decay times of reference data may be reported for N_2 purged samples. This may hence lead to an incorrect calibration due to the large discrepancy between the decay times for samples measured without N_2 purging and for those with N_2 purging as demonstrated later in **Figure 138**. If a NanoLED is being used it should be given at least 30 minutes to stabilise before using it for a time calibration, as it needs to stabilise its temperature, DeltaDiodes on the other hand are temperature stabilised and can be hot-swapped. To make a calibration plot the channel of the peak of the prompt can be plotted with respect to the delay time as demonstrated in **Figure 100** for the 50 ns range in a FluoroCube with a MCA-3/NI-6602 cards. Each time range used should be separately calibrated. Newer systems such as the DeltaHub have newer electronics which do not require user recalibration. The calibration can of course be checked with external delay lines. Using delay lines yielded a time calibration of 25.5 ps ch^{-1} which is in good agreement to the 26.0 ps ch^{-1} reported by the DeltaHub. The full width at half maximum FWHM measured in a DeltaHub however varies substantially more per channel and gives a higher fluctuation than that of the Hub A. This comes at the cost of the higher throughput. It should be noted that in most systems there is a finite number of channels therefore as the time range is increased, the time calibration per channel must also increase. Difficulty comes in measuring samples which exhibit both short decay times and long decay times

simultaneously; in order to measure the long decay time, the repetition rate has to be lowered and the time range has to be increased, lowering the time calibration per channel this clearly comes at the expense of the time resolution of the short decay time however the long component can be measured and tail fitted in order to accurately determine its decay time. The time range may then be lowered however the repetition rate should be constrained in order to prevent re-excitation of the sample before the long-component has finished decaying. This allows for a fit of the short component by fixing the value of the long decay time to the value that was previously measured.
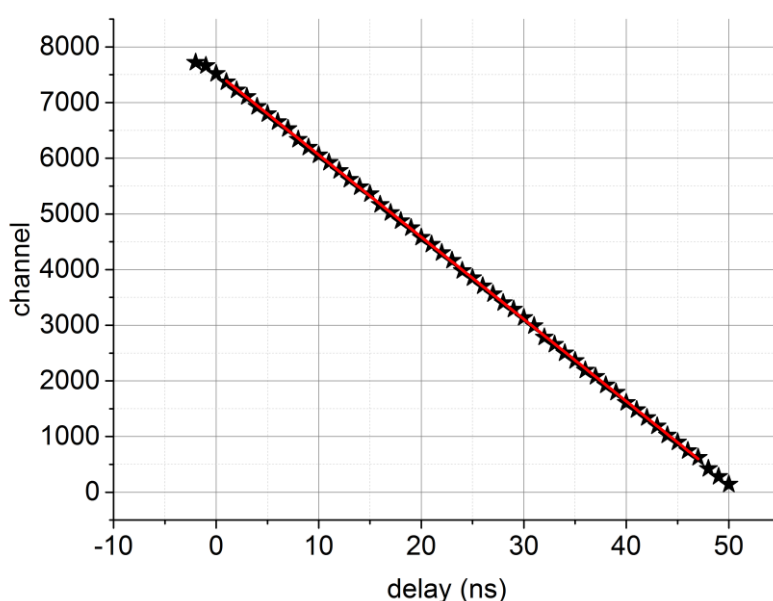
Figure 100: Time calibration check using an Ortec Model 425A Nanosecond Delay Box with variable delay from 0-63 ns on a 50 ns TAC range. The FluoroCube was equipped with a NL474L excitation source. The excitation monochromator TDM800 (1200/350 grating) was set to 474 nm with a 32 nm bandpass and the excitation polarizer was fixed to V. The emission monochromator TDM800 (1200/350 grating) was set to 474 nm with an 8 nm bandpass and the emission polarizer was fixed to V. Hub A timing electronics were operated in reverse mode with a TBX850. The time calibration was experimentally determined using a dilute scatter solution of LUDOX SM30 in a Quartz cuvette. A prompt was measured to a peak preset of 1000 counts and its peak channel plotted alongside its full width at half maximum. The variable delay on the Ortec delay box was altered and the procedure repeated until prompts across the entire time-range were recorded. The time calibration was found to be $T_{Cal}=67.74$ ps ch^{-1} with a $R^2=1.000$[36].

---

[36] Note the edges of the TAC were omitted when measuring the time calibration as these regions of the TAC are non-linear and not used for measurement.
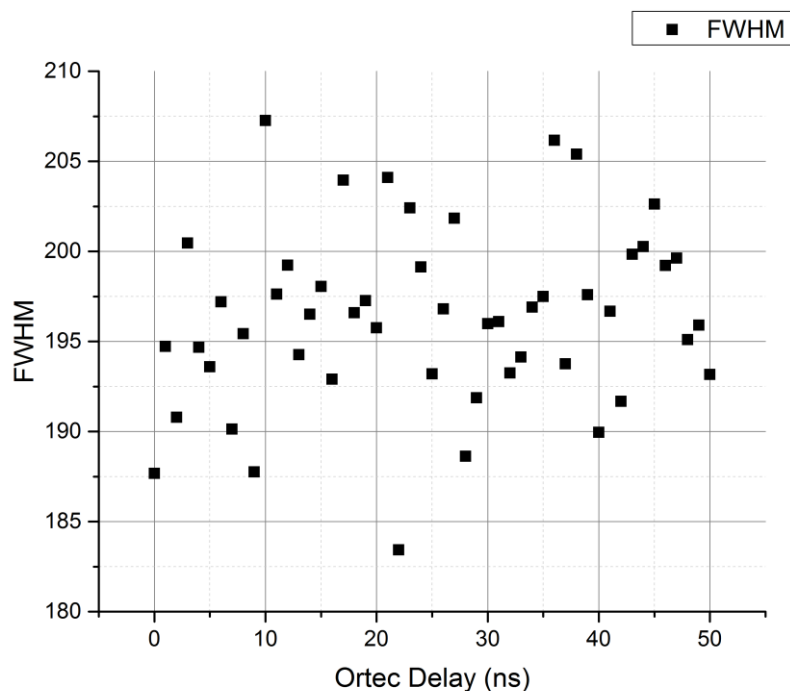
Figure 101: The full width at half maximum of the prompt measured as a function of delay of the Ortec Model 425A Nanosecond Delay Box. The FWHM is 200±20 ps and gives an indication of the lowest time-scale which can be measured with this instrument. Reconvolution analysis can accommodate decay times which are smaller than one tenth of the prompt however the lower limit is quoted as ~50 ps due to the slight time drift in the FWHM.

2.3.7 Data Fitting - Fluorescence Decay Curves

The data obtained via a fluorescence lifetime measurement is convoluted with the instrumental response which is typically more significant for smaller time scales than those of larger time scales. Thus one cannot directly obtain the desired decay parameters directly from the data.

$$P(t) \otimes T(t) = F(t) \tag{50}$$

A prompt $P(t)$ is measured using a scattering solution with the emission monochromator set to the same wavelength of the excitation source. Re-convolution analysis is then applied. Re-convolution analysis relies on the correct theoretical model $T(t)$ to be selected to fit the data. Typically, $T(t)$ is series of exponentials with associated decay times and pre-exponential factors. The first guess is usually the simplest case; a mono-exponential then the complexity is gradually built up [192]. The HORIBA Scientific DAS 6.8.14 software allows up to 5 exponentials to be fitted. In this work only the sum of exponential decays

are used however a number of additional theoretical models are available for complicated [193].

$$T_1(t) = \frac{1}{\tau} \exp\left(-\frac{t}{\tau}\right) \tag{51}$$

$$T_2(t) = b_1 \exp\left(-\frac{t}{\tau_1}\right) + b_2 \exp\left(-\frac{t}{\tau_2}\right) \tag{52}$$

$$T_x(t) = b_1 \exp\left(-\frac{t}{\tau_1}\right) + \ldots + b_x \exp\left(-\frac{t}{\tau_x}\right) \tag{53}$$
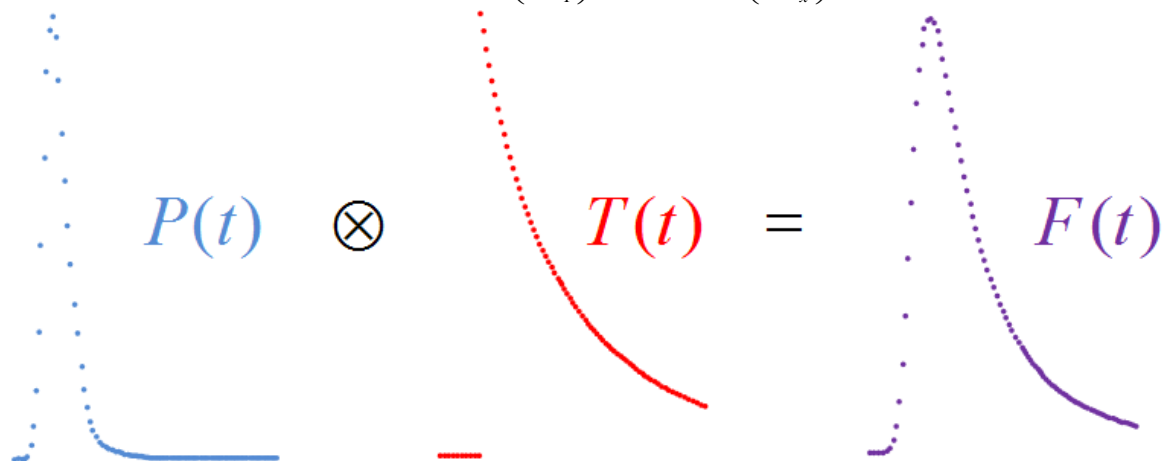
$$P(t) \quad \otimes \quad T(t) \quad = \quad F(t)$$

Figure 102: Principle of reconvolution analysis. $P(t)$ is convoluted with $T(t)$ and compared with $F(t)$ using Non Linear Least Squares.

The goodness of fit criterion χ^2 and Poissonian statistics are then used to compare $F(t)$ to $P(t) \otimes i(t)$:

$$\chi^2 = \sum_{\text{Data pts}} \left\{ \frac{F(t) - P(t) \otimes T(t)}{[F(t)]^{1/2}} \right\}^2 \tag{54}$$

For a good model the residuals have to be random and the χ^2 value has to be close to 1.0 preferably $0.9 \leq \chi^2 \leq 1.25$.[37] For non-random residuals the bias of the residuals allows one to see if they need to fit an extra exponential component or not and whether this component is positive or negative. If the system is poorly configured e.g. has tangled cables, there may be a damped sinusoidal wave present which is typical of radio frequency interference and one must check the cabling. Radio Frequency Interference (RFI) can be seen easier by using the auto-correlation of the residuals. RFI in the vast majority of cases does not affect the

---

[37] It should be noted that typically the decays are taken to 10000 counts. For decays with a higher amount of counts fitting can prove more difficult due to systematic errors such as radio frequency interference χ^2 and may be >1 it is more important for the residuals to be random in these cases.

fitted decay times but only the quality of fit. When fitting there are several parameters which are useful $\tau_1,\ldots,\tau_i$ are the decay times of the sample, typically quoted in ns with a standard error of 3 standard deviations i.e. has a confidence interval of ~99 %. The raw pre-exponential factors $b_1,\ldots,b_j$ are often presented as normalised values $\alpha_1,\ldots,\alpha_j$ such that:

$$\alpha_i = \frac{b_i}{\sum_{j=1}^{n}|b_j|} \tag{55}$$

and

$$\sum_{j=1}^{j}|\alpha_j| = 1 \tag{56}$$

The pre-exponential factors may also be expressed as relative amplitudes:

$$f_i = \frac{b_i\tau_i}{\sum_{j=1}^{n}|\alpha_j|\tau_j} \times 100 \tag{57}$$

and

$$\sum_{i=1}^{n}|f_i| = 100 \tag{58}$$

The choice of $b_1,\ldots,b_j$, $\alpha_1,\ldots,\alpha_j$, $f_1,\ldots,f_j$, or $b_1\tau_1,\ldots,b_j\tau_j$ usually depends on the dataset used. For most standard decay curves the $\alpha_1,\ldots,\alpha_j$ are used as these are independent from the pre-selected peak count and can be compared and give the proportion of each fluorescing specie. On the other-hand $f_1,\ldots,f_j$ take into account the contribution of each species to the entire fluorescent decay and can be used to show contrast which can be useful for the likes of microscopy images and also relate to the steady-state data discussed in more detail; later[38]. There is also one additional parameter typically included in reconvolution analysis known as the shift parameter. The shift parameter is used to compensate for the wavelength dependence of the transit spread time of the photomultiplier [191,194,195] and is typically measured in nanoseconds or channels[39]. The shift is usually less than five channels depending on the time-resolution per channel. In general, one will only fit positive exponentials and hence obtain positive decay times however in some instances negative

---

[38] It should be noted that $f_1,\ldots,f_j$ and $b_1\tau_1,\ldots,b_j\tau_j$ are weighted by the decay times and hence are more highly influenced by the error of the decay times.

[39] The measurement for the scatter solution used to measure the instrumental response is typically carried out at the excitation light of the light source and not the wavelength the sample is measured.

exponential components exist, these result from the presence of excited state reactions. Most typical experiments don't have this but it is possible to observe excited state reactions if measuring the fluorescence emission at a wavelength where the absorption is quite high and it should be noted that excited state reactions are more prominent in solvents that have a high viscosity [196].

One of the first tests of reconvolution analysis and the optics of a time-resolved fluorometer is a monoexponential lifetime standard [197]. One of the most frequently used standards is POPOP in methanol made to have an absorbance of 0.1. When excited with a DD378L the emission at 425 nm has a relatively fast mono-exponential decay time of 1.3 ns [194] **Figure 103**. When fitting to a monoexponential the residuals should be random and the $\chi^2 \approx$ 1-1.25. As the log of an exponential is linear, the mono-exponential standard on log scale should look like a straight line. If there is any instrumental deviation particularly near the peak of the prompt, it can clearly be observed. These distortions can indicate a misaligned system which may result in a significant reflection in the prompt also. The lack of an emission polarizer, an emission polarizer at the wrong angle or a damaged polarizer will make the decay bi-exponential giving non-random residuals when fitted to a single decay (discussed in more detail in the next section). The residuals as mentioned should be flat, a damping sinusoidal waveform better picked up in the autocorrelation of the residuals implies the system has radio-frequency interference usually resulting from tangled cables. It is insightful to compare a multiple-exponential decay fitted to a mono-exponential, bi-exponential and three exponential decay model. BSA is a protein that is known to have a 3 tryptophan rotamer model [198,199]. **Figure 104** shows the decay at 272 nm excitation and 340 nm emission fitted to a mono-exponential decay, bi-exponential decay and three exponential decay. The mono-exponential model does not fit the data very well, with the fit missing most of the data at the tail of the decay. The residuals are not randomly distributed and the χ^2 is high. The curve down and up at (a) indicates another longer lived decay time and at (b) indicates a shorter lived decay time. The bi-exponential fit shows a minor curve and down at the start of the decay indicating the need for a shorter lived component, the χ^2 borders on acceptability. The fit to three exponentials gives random residuals indicative of a good fit and matches the expected three rotamer model. When fitting fluorescence decays a priori knowledge often helps to determine whether a bi-exponential or three exponential model is more suitable. Decays taken to a higher number

124

of counts or a larger dataset will reveal relatively weak third components. This example will be examined in more detail later.
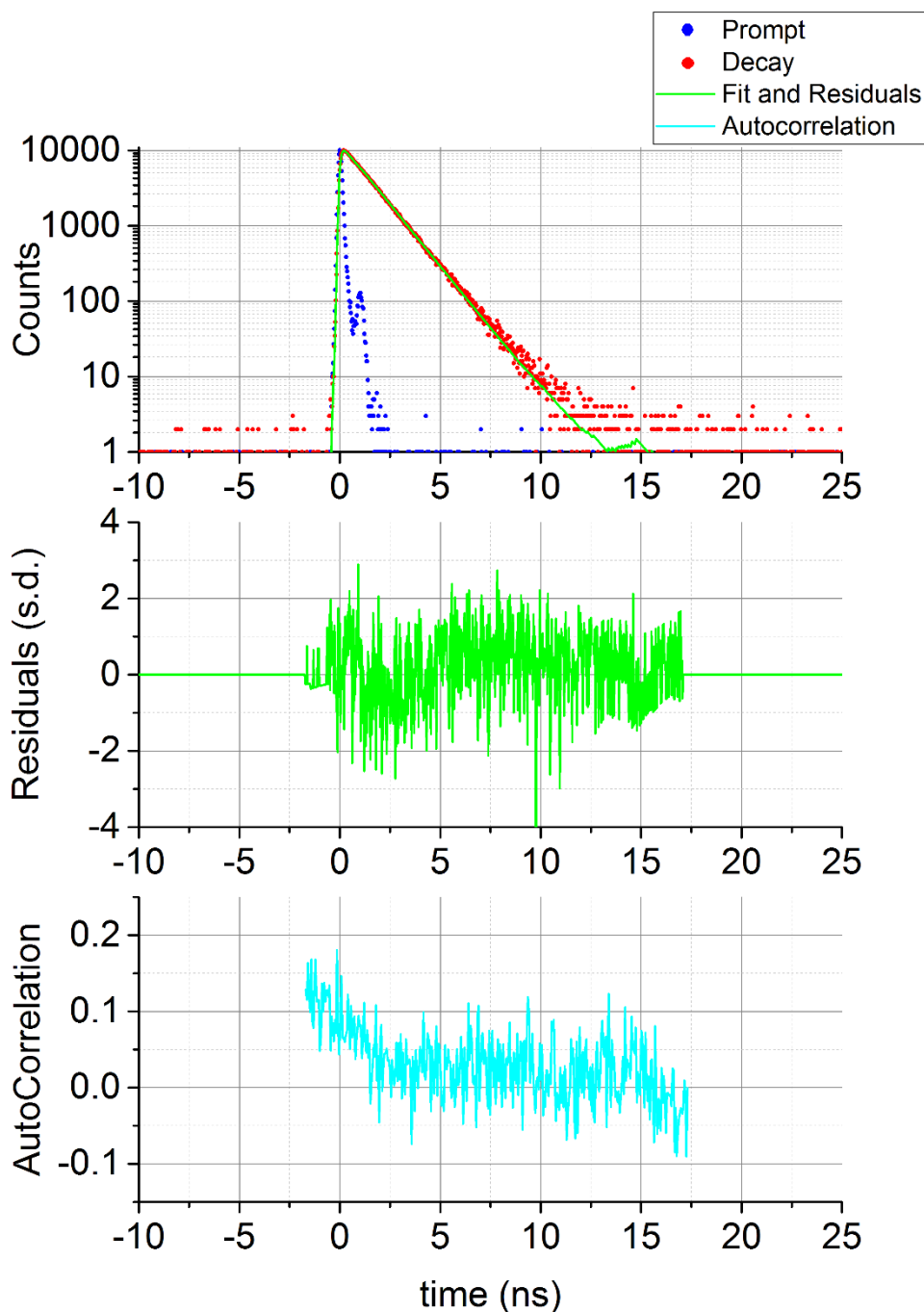
Figure 103: The fluorescence decay of POPOP measured using a DeltaFlex with a DD378L excitation source and a TDM800 (1200/450 grating) emission monochromator with a PPD850. DeltaHub electronics were used with the 100 ns TAC range (4000 channels). The DeltaDiode was set to an 8 MHz repetition rate (automatically adjusted to suit the time range). For the decay polarizers were set to VM and the emission monochromator set to 425 nm. For the prompt polarizers were set to VV and the emission monochromator set to 378 nm to match the excitation source. A peak preset of 10000 counts was used. The lifetime was found to be $\tau_1 = 1.313 \pm 0.006$ ns, $\chi^2 = 1.180$. Results are in good agreement to literature.
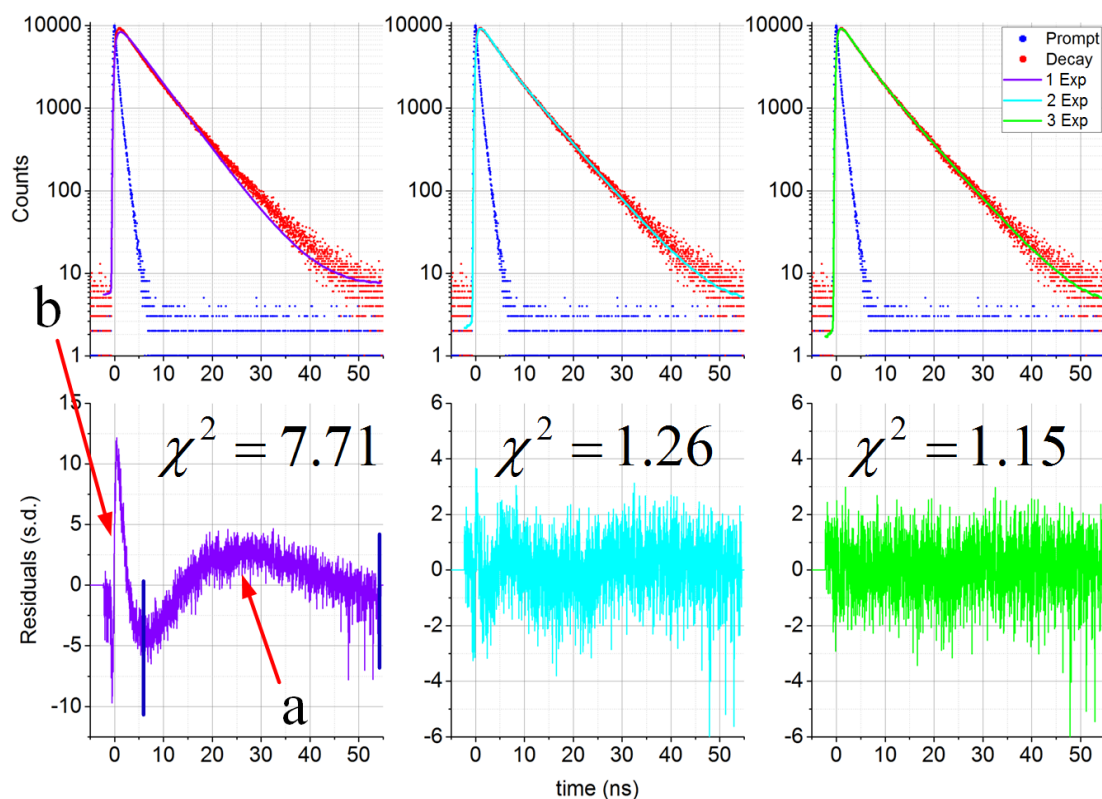
Figure 104: The residuals from a 3 exponential sample 1 μM BSA in PBS fitted to one, two and three exponentials respectively. The sample was measured in a Horiba Scientific DeltaFlex with a DD272D excitation source. The TDM800 emission monochromator (1200/350 grating) with a bandpass set to 16 nm and PPD850 detector. The prompt was measured with an emission wavelength of 272 nm to match the DeltaDiode. The decay was measured at 340 nm. Since an unpolarized UV diode source was used, no polarizers were required to measure the fluorescence decay. DeltaHub timing electronics were used with a 60 ns time range. Focusing on the bad fit of 1 exponential the residuals curve down and then up and back down (a) this is an evident indicator that a significant additional longer lived exponential component is required. (b) The start of the residuals is large and rapidly curve down and up, a smaller exponential component is required. Although inapplicable to this sample; for a highly scattering sample and a strong laser it is common to see such a short lived component as it is an artefact introduced by scattered light[40]. The mono-exponential fit results were $\tau_1 = 4.594 \pm 0.04$ ns, $\chi^2 = 7.706$, the bi-exponential fit results were $\tau_1 = 2.2 \pm 0.1$ ns ($\alpha_1 = 0.40$), $\tau_2 = 6.31 \pm 0.03$ ns ($\alpha_2 = 0.60$), $\chi^2 = 1.262$ and for the three exponential fit $\tau_1 = 0.64 \pm 0.02$ ns ($\alpha_1 = 0.34$), $\tau_2 = 3.0 \pm 0.3$ ns ($\alpha_2 = 0.17$), $\tau_3 = 6.52 \pm 0.05$ ns ($\alpha_2 = 0.49$), $\chi^2 = 1.146$.

2.3.8 Fluorescence Decay Measurements – The Magic Angle

Polarization effects are more important for time-resolved fluorescence than steady state fluorescence. A number of the pulsed laser sources used for TCSPC measurements are

---

[40] In such samples a better fit by accommodating for this by adding an extra exponential component with an initial guess of 0.5 channels. For longer lived samples tail fitting may also be employed.

lasers and so are vertically polarized[41]. In order to measure decay curves which aren't prone to polarisation effects magic angle conditions are often employed; the pulsed light source is placed behind a vertically orientated excitation polarizer while the emission polarizer is at the magic angle conditions which for a square geometry is 54.7º. Polarization effects are usually only significant at short time ranges.
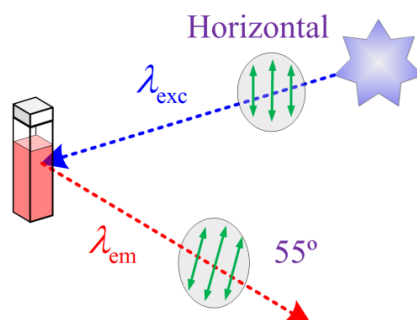
Figure 105: Correct polarizer and wavelength conditions for the fluorescent decay measurement.
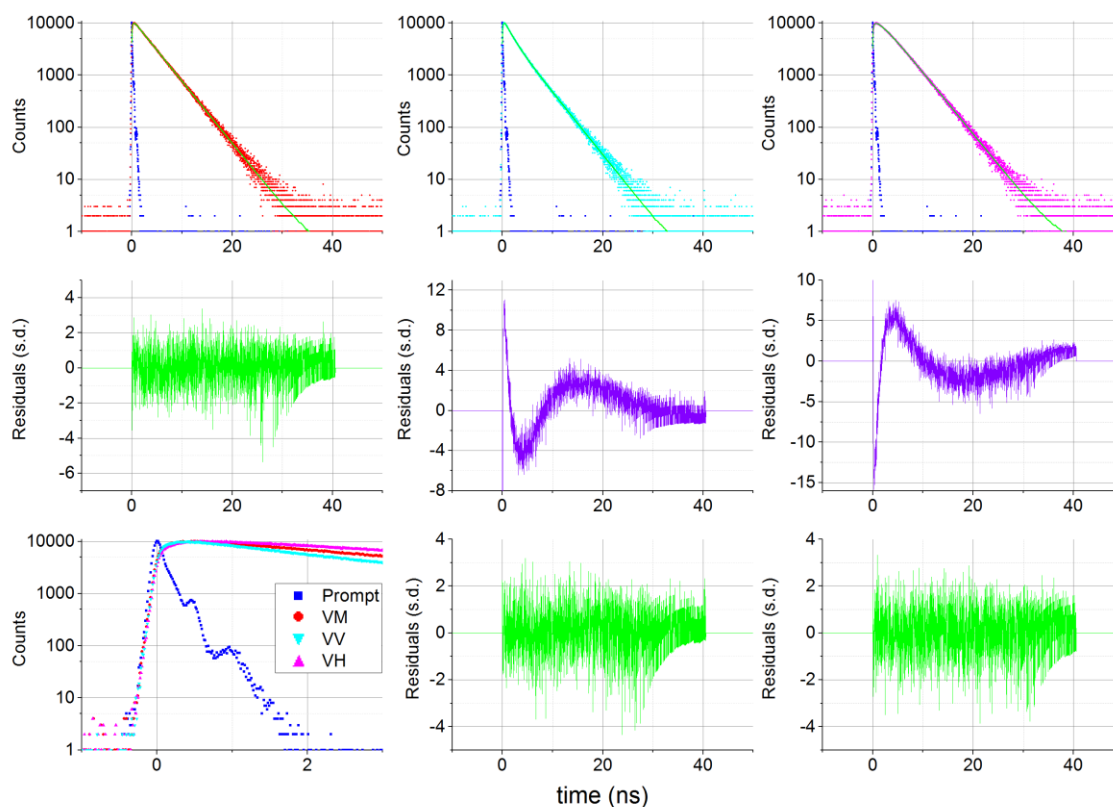
Figure 106: The time-resolved emission anisotropy decay of Rhodamine 6G measured at different polarizations VM, VV and VH. These were measured using a FluoroCube with a

---

[41] A number of light sources, particularly those in the UV region are unpolarized diodes and so the use of polarizers at magic angle conditions is unnecessary for these sources. Moreover, polarizers have poor transmittance in the UV region so shouldn't be used in such configurations. Often for laser sources measurements may be carried out without the excitation polarizer as the output from the sources are already sufficiently polarized.

DD532L excitation source and the excitation polarizer was fixed to V. The emission monochromator TDM800 (1200/350 grating) was set to 570 nm and a 6 nm bandpass. A TBX850 was used for detection with Hub A electronics operating in reverse mode using a TAC range of 100 ns (8000 channels). Each curve was measured with a peak preset of 10000 counts. The prompt was measured with the polarizer at V and the emission monochromator at 532 nm for a peak preset of 10000 counts. The VM data fitted to a single exponential with random residuals (τ_1=3.646±0.007 ns χ^2=1.056). The VV data required two exponentials for random residuals (τ_1=3.62±0.02 ns, α_1=0.58, τ_2=1.47±0.05 ns, α_2=0.42, χ^2=0.956) as the residuals to a single exponential fit revealed that a second decay time was needed with a positive pre-exponential factor, this second decay time is prescribed to the loss of excited state species via depolarization. The VH data likewise required two exponentials to fit (τ_1=3.685±0.009 ns, α_1=0.73, τ_2=1.49±0.05 ns α_2=–0.27 χ^2=0.979) as the residuals to a single exponential fit revealed that a second decay time was needed with a negative pre-exponential factor which is prescribed to the introduction in excited state species due to depolarization i.e. Brownian motion acts to depolarise fluorescing fluorophores from a vertically polarized orientation to a horizontally polarized orientation. The differences in the early part of the decay can be seen more clearly from the early plot of VM, VV and VH (bottom left) after the initial depolarization the 3 decays measured are approximately parallel showing that what is measured later is predominantly unpolarised fluorescence decays.

When other polarizer orientations are used the decay obtained may appear to be slightly more complex. It is insightful to have a look at the effect of polarizers on the fluorescence decay as this will give an understanding of the importance of polarizers and the merits of time-resolved fluorescence anisotropy. Measurements with polarizers at the vertical excitation and magic angle emission will not exhibit any polarization effects. Measurements at a vertical excitation and emission will exhibit an addition decay time corresponding to a loss of fluorescence due to rotation. In a similar argument, measurements taken at a vertical excitation and horizontal emission will correspondingly exhibit a rise time due to the introduction of more excited dyes that rotated from the vertical orientation. Rhodamine 6G in 60 % glycerol solution made to an absorbance of 0.01 is used as an example. Like steady-state measurements low absorbance values typically A<0.1 but ideally A~0.01-0.05 are preferred for fluorescence decay measurements; at higher absorbance values a deviation from a mono-exponential decay may be observed when measured at VM due to sample self-absorption, such a deviation is usually initially reflected in a slightly higher χ^2. The sample geometry may also influence the measured decay time particularly for highly concentrated samples [200,201].

2.3.9 Time-Resolved Fluorescence Anisotropy Decay Measurements

The theory of steady-state fluorescence anisotropy is identical to that of time resolved fluorescence anisotropy. The difference is the steady-state data derives an average value

and not an anisotropy decay. Clearly instead of four steady-state intensity measurements at VV, VH, HV and HH fluorescence decays are recorded instead. The wavelength dependency measured from the steady-state data clearly remains however this is usually dropped especially in the main application area of particle sizing. For time-resolved fluorescence anisotropy an excitation and emission wavelength pair are selected from the steady-state data which yield the maximum $\bar{r}$ and as illustrated earlier the fluorophores characteristics may be determined by measurement of free-dye in a viscous solvent such as glycerol. I_{HV} and I_{HH} are usually measured to a peak preset of >1000 counts and then I_{VV} and I_{VH} are then measured to a difference preset >10,000 counts. The Rhodamine 6G in 60 % glycerol sample may continue to be used for demonstration.
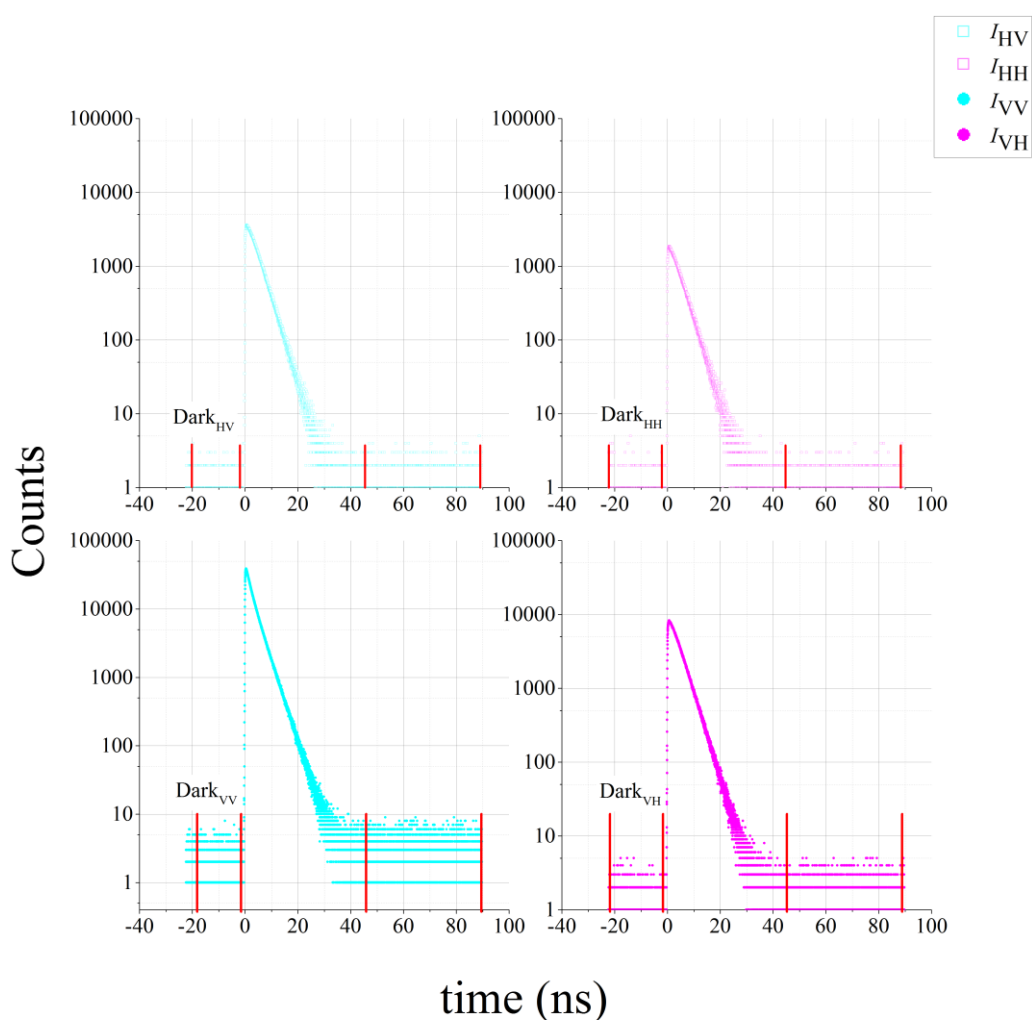
Figure 107: The 4 decay curves measured in a TRFA measurement. I_{HH} and I_{HV} are measured to calculate the *G*-factor and should have >1000 counts in the peak for an accurate G-factor determination. I_{VV} and I_{VH} are measured until they have a peak difference of >10,000 counts once *G* is determined which gives sufficient counts to construct an anisotropy decay curve. The first step in calculating the anisotropy decay curve is in the measurement of the background signal in each of the 4 decays which is the average number

of dark counts in the red regions indicated before the fluorescence decays. The background after the fluorescence decays should be equal to the background before the fluorescence decay in all cases. The VV and VH decays were measured using a FluoroCube with a DD532L excitation source and fixing the excitation polarizer to V. The emission monochromator TDM800 (1200/350 grating) was set to 570 nm and a 6 nm bandpass. The emission polarizer was toggled from V to H every 60 s until a peak preset of 25000 counts (~10000 counts once G has been applied). The decay curves HV and HH were measured by fixing the excitation polarizer to H and toggling the emission polarizer between V and H every 60 s until both curves had a peak count of at least 1000. A TBX850 was used for detection with Hub A electronics operating in reverse mode using a 100 ns time range (8000 channels).
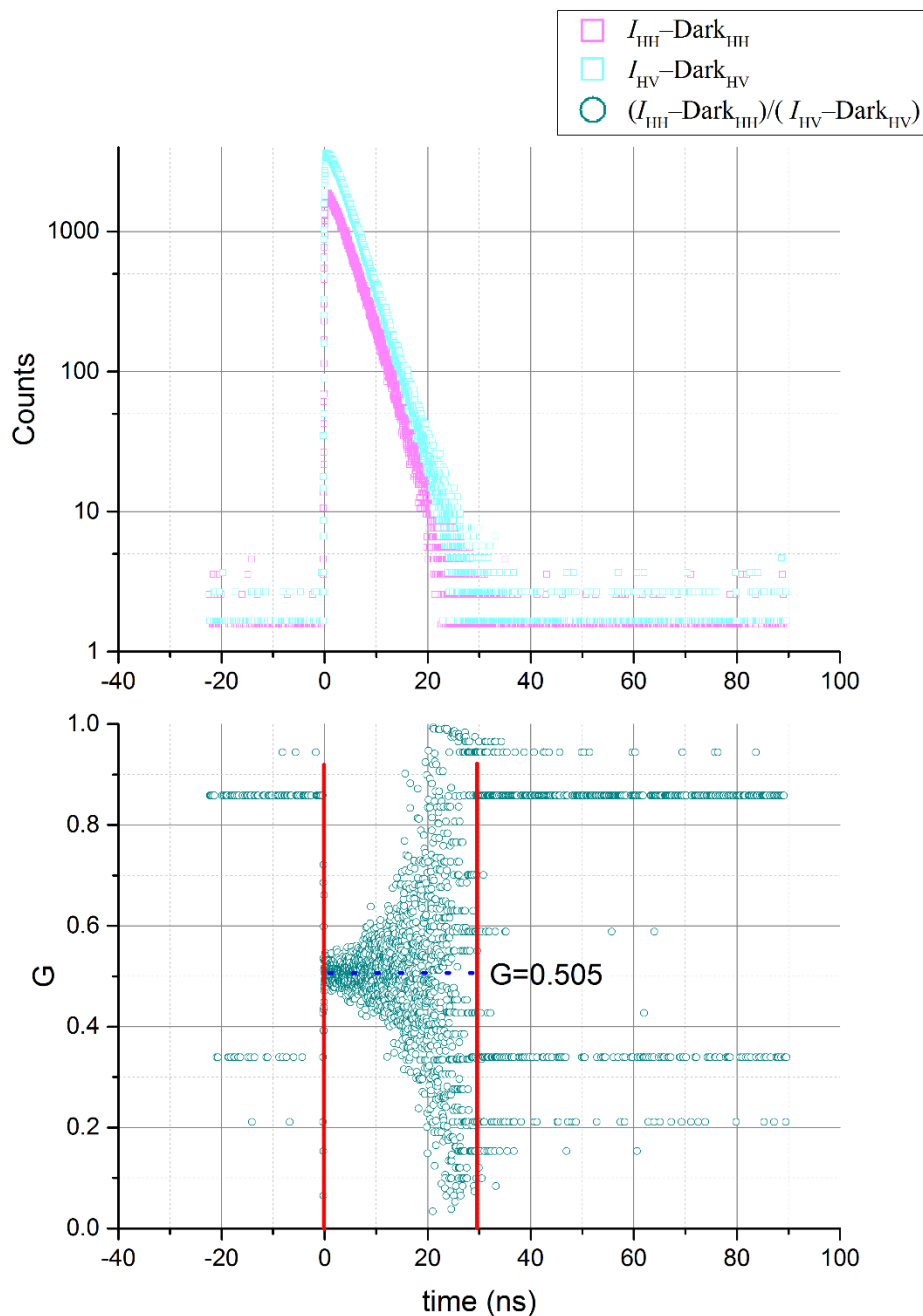
Figure 108: The *G*-factor is determined by division of I_{HH} by I_{HV}. Generally, the value is averaged over the entire time range where I_{HH} and I_{HV} have sufficient counts above the background noise.

The grating factor G has the same definition as the grating factor in the steady-state:

$$G = \frac{I_{HH}}{I_{HV}} = \frac{\sum_t I_{HH}(t)}{\sum_t I_{HV}(t)} \qquad (59)$$

Although the grating factor is typically measured as two individual decay curves they are averaged and in the end the G-factor is just a number corresponding to the instrumental bias for one orientation over the other **Figure 108**. $G \approx 1$ for a filter based system and for a system with an emission monochromator $G \sim 0.5$ it is of course wavelength and grating dependant. Often to save time the G-factor is measured once for a dataset that utilises the same excitation source, polarizers and emission wavelength, it is however recommended to be remeasured it if anything has been changed in the system particularly if the emission polarizer has been removed and replaced. When using a laser excitation source the laser is usually orientated 15-90° for a G-factor measurement otherwise there is a very weak signal because the horizontal polarizer blocks most of the output of the laser and as a consequence measurement of the G-factor may be very time-consuming. As G in the end is only a number the peak counts of these decay curves is sufficient at ~1000 counts are used. Because the G-factor is dependant only on the emission optics, rotation of the excitation source does not influence it. On the other hand while measuring the decay curves VV and VH if a laser source is used for excitation it is orientated in the vertical orientation to maximise output.[42] While holding the excitation polarizer at a vertical position the emission polarizer is toggled between vertical and horizontal for a specified dwell time until a specified peak difference is obtained usually for sufficient data quality the peak difference should be 10000 counts or superior once the G-factor has been taken into account as shown in **Figure 109**. The dwell time per cycle is usually set to 60 s or less to prevent bias of one orientation over the other. Laser Diodes and TCSPC electronics are stable for measurements of much longer duration but the sample itself may not be as stable for instance if significant photobleaching occurs during measurement and the cycle time is long then there will still be a bias of VV over VH. For the DeltaHub a single cycle should not have greater than 65000 counts in the peak channel as the data stored is 16 bit. Multiple cycles may take the peak channel above 65000 counts however. The actual dwell time may

---

[42] Change of laser orientation does not alter the measured G-factor as G is a correction to the emission optics only.

vary slightly for the set dwell time for each orientation due to a compensation in deadtime for each count rate.
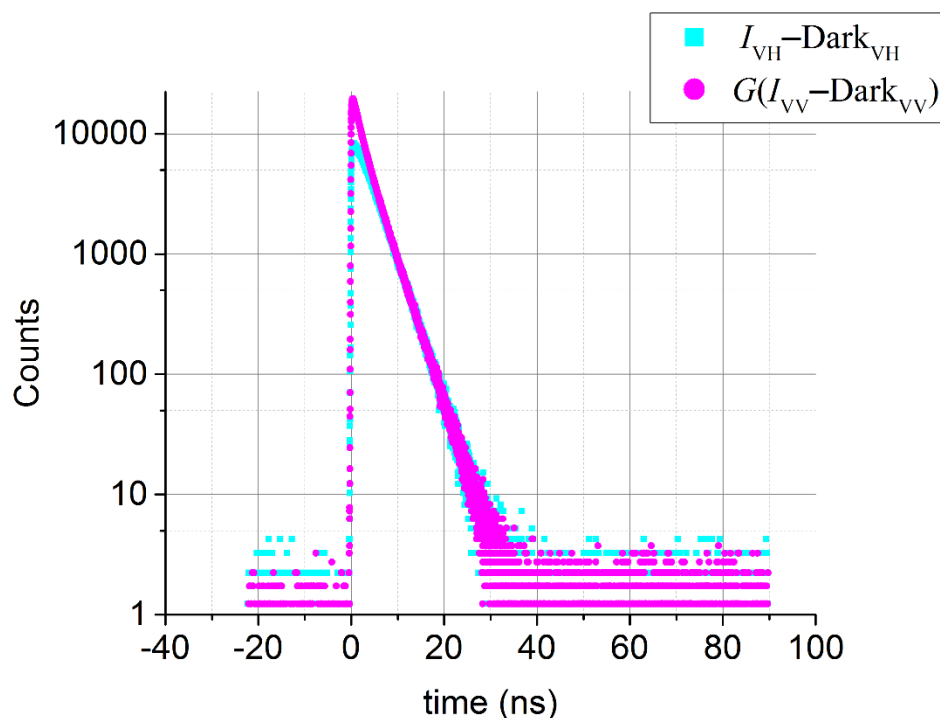
Figure 109: The plot of I_{VV} and I_{VH} compensated for both dark counts and noise. Immediately one can see that the difference between the two decay curves is only at the start and the curves are identical towards the end.
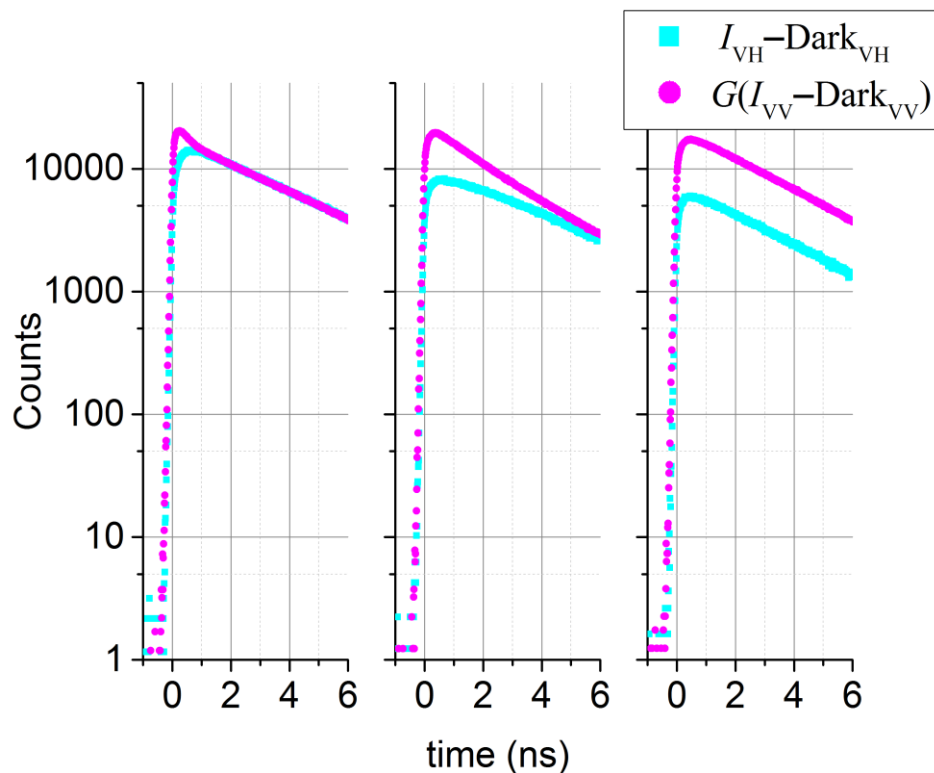
Figure 110: The plot of I_{VV} and I_{VH} compensated for both dark counts and noise for Rhodamine 6G in 10 %, 60 % and 100 % glycerol respectively zoomed to view the start of the decay curves. For the 10 % glycerol solution one can see the sharp fall in I_{VV} and the

initial rise in I_{VH} and these curves quickly become identical as the fluorescence is depolarised. For the 60 % and 100 % solution the depolarisation is more pronounced respectively.

These two decay curves alongside the computed grating factor allow one to construct the sum, difference and anisotropy decay curves [202]:

$$r(t) = \frac{GI_{VV}(t) - I_{VH}(t)}{GI_{VV}(t) + 2I_{VH}(t)} = \frac{D(t)}{S(t)} \tag{60}$$

Taking the simplest case of a spherical particle:

$$r(t) = r_0 \exp\left(-\frac{t}{\phi}\right) \tag{61}$$

where r_0 the initial anisotropy and ϕ the rotational correlation defined in earlier sections. In steady state measurements the average $\bar{r}$ is measured opposed to $r(t)$ and because data is averaged ϕ hence can't directly be determined. The time-resolved data on the other hand allows for determination of ϕ. Again assuming that the particle is spherical the hydrodynamic radius may be calculated by rearranging the Stokes-Einstein **Equation (15)**:

$$R = \sqrt[3]{\frac{3V}{4\pi}} = \sqrt[3]{\frac{3k_B T \phi}{4\pi\eta}} \tag{62}$$

For successful fluorescence anisotropy applications, steady-state and time-resolved anisotropy data should be complementary deployed. The steady-state fluorescence anisotropy EEM gives the target wavelengths for excitation and emission. The time-resolved anisotropy decay gives the initial anisotropy and rotational correlation time.

For anisotropy fitting typically sum-difference fitting is carried out, this is essentially reconvolution analysis twice. Sum fitting is identical to the decay fit mentioned above as the sum is equivalent to the decay at the magic angle, as can be seen by comparing the denominator of **Equation (60)** to that of **Equation (38)**. In practice however it is slightly harder to fit the sum than it is to fit the decay due to the larger number of counts in the sum[43]. Once the fitting of the sum is complete reconvolution analysis is once again carried out:

---

[43] Typically the decay is measured to 10000 counts at the peak but for an anisotropy measurement it is typically ran to a difference of 10000 counts at the peak. There can be ~50000 at the peak of the sum for a

$$S(t) \otimes r(t) = D(t) \tag{63}$$

The most complex model for the anisotropy $r(t)$ in HORIBA Scientific DAS 6.8.14 is which assumes all species are spherical:

$$r(t) = b_1' \exp\left(-\frac{t}{\phi_1}\right) + b_2' \exp\left(-\frac{t}{\phi_2}\right) + r_\infty \tag{64}$$

Where b_1' and b_2' are fractional contributions of the rotational correlation times ϕ_1 and ϕ_2 associated with species 1 and 2 respectively. The rotational correlation times are defined as the time it takes the respective species to rotate one radian. r_∞ is the residual anisotropy, the residual anisotropy is an additional term available for systems which have a proportion of fixed dyes. Anisotropy measurements of dye molecules affixed on a glass slide will have a residual anisotropy because their motion is fixed and they cannot rotate freely. $r_0 = b_1' + b_2'$ is the initial anisotropy. In the same manner as **Equations (55)-(58)** normalised pre-exponential factors $a_1', ..., a_j'$ and relative amplitudes $f_1', ..., f_j'$ may also be used to describe the difference/anisotropy decay. In this work only the simplest models were used for time-resolved fluorescence anisotropy fitting. There are an assortment of more complicated models [203] especially when anisotropy is used for macromolecules and membranes [49,204].

Figure 111: The sum and difference data constructed from the 60 % glycerol data in **Figure 109**. The sum fitted to a mono-exponential decay time with $\tau_1 = 3.666 \pm 0.005$ ns, $\chi^2 =$

---

sample that has a pronounced difference but this can be a lot larger for a sample that has a less pronounced difference curve.

1.249 which is in good agreement with the decay measured at VM in **Figure 106** as expected. The χ^2 for the sum data is usually slightly higher than the decay at VM due to the larger number of counts. The difference data gives a mono-exponential decay with a rotational correlation time $\phi_1 = 2.67 \pm 0.03$, $\chi^2 = 1.074$ and a $r_0 = 0.371 \pm 0.001$ when the assumption is made of a zero residual anisotropy ($r_\infty=0$). Alternatively, if the residual anisotropy is free the rotation correlation time $\phi_1 = 2.74 \pm 0.03$, $\chi^2 = 1.055$, $r_0 = 0.374 \pm 0.002$ and $r_\infty = -0.004 \pm 0.001$. The rotational correlation time is consistent in both cases.
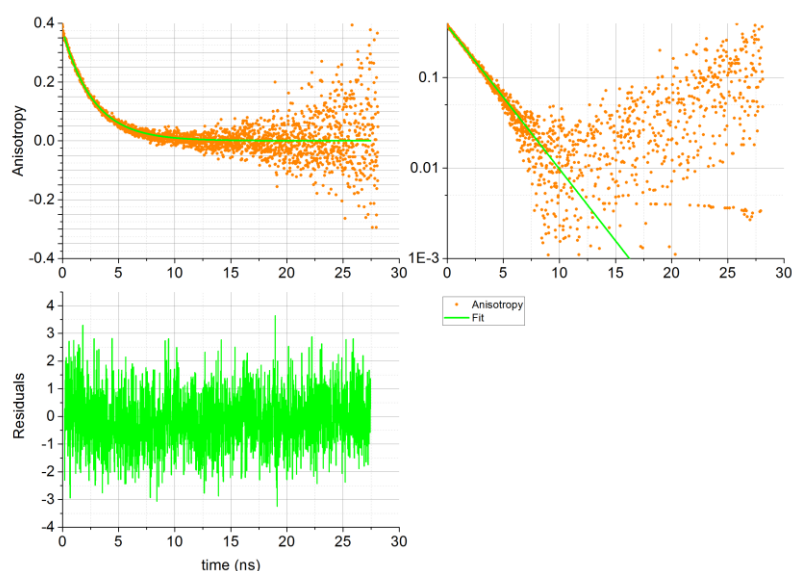
Figure 112: The anisotropy decay is usually shown in a linear scale as shown to the left however like the other decay curves it can be plotted in a logarithmic scale as shown in the right. Typically, the measurable anisotropy is to ~10^{-3}-10^{-4} so there is no point plotting data below this level. If the anisotropy decay time is significantly larger than the FWHM of the prompt, it can be fitted directly opposed to using reconvolution analysis. The direct fit to the anisotropy data gives a mono-exponential decay with a rotational correlation time $\phi_1=2.74\pm0.01$, $\chi^2=1.089$ and a $r_0=0.353\pm0.002$ when the assumption is made of a zero residual anisotropy ($r_\infty=0$). Alternatively, if the residual anisotropy is free the rotation correlation time $\phi_1=2.79\pm0.06$, $\chi^2=1.055$ and the $r_0=0.354\pm0.003$ and $r_\infty=-0.005\pm0.001$. The rotational correlation time is again more or less consistent in both cases. Note the fit to the anisotropy curve directly gives a lower R_0 as the decay is fitted after the prompt and the rotational decay times reported are slightly larger with the increase being ~ the FWHM of the prompt. In most cases when the residual anisotropy is floating there will be a small r_∞~$\pm1\times10^{-3}$ mainly due to the accuracy in polarizer alignment.

Figure 111 shows the sum and difference data for the Rhodamine 6G in 60 % glycerol sample. In this sample the rotational correlation time is of the same order of magnitude as the fluorescence decay time of the fluorophore which leads to optimal data quality. Both of the decays fit to a mono-exponential and the rotational correlation time is consistent when

a fixed residual or free residual anisotropy is used. The anisotropy decay time is also long enough to allow direct fitting to the anisotropy decay curve **Figure 112**. In the case of
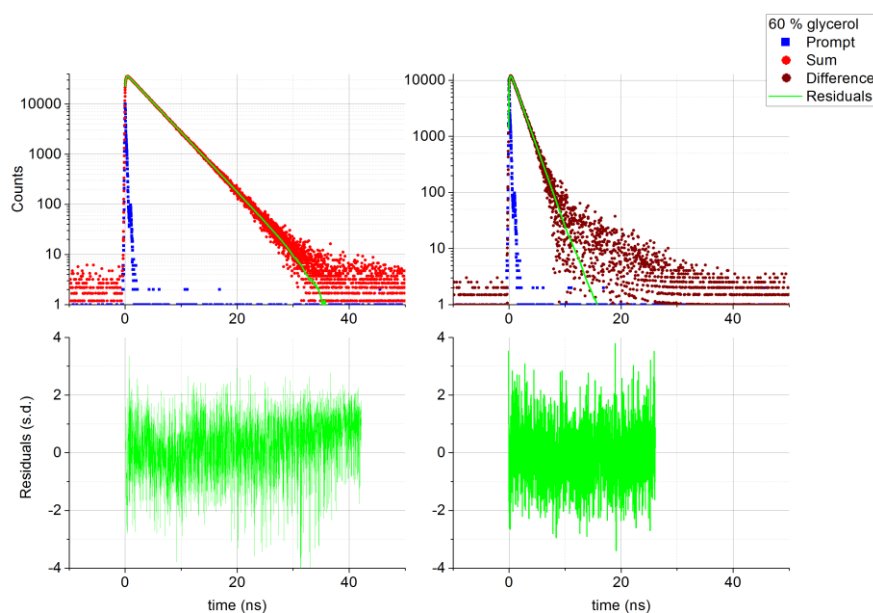

Figure 113: The sum and difference data constructed from the 10 % glycerol data **Figure 110**. The sum fitted to a mono-exponential decay time with $\tau_1 = 3.914 \pm 0.005$ ns, $\chi^2 = 1.249$. The difference data gives a mono-exponential decay with a rotational correlation time $\phi_1 = 0.295 \pm 0.007, \chi^2 = 0.947$ and a $r_0 = 0.370 \pm 0.003$ when the assumption is made of a zero residual anisotropy ($r_\infty=0$). Alternatively, if the residual anisotropy is free the rotation correlation time $\phi_1 = 0.295 \pm 0.007, \chi^2 = 0.943$, $r_0 = 0.374 \pm 0.003$ and $r_\infty = -0.006 \pm 0.008$. The rotational correlation time is again consistent in both cases.

Rhodamine 6G in the 10 % glycerol sample **Figure 113** the difference has a much smaller rotational correlation time than the sum, this data can still be fit with sum-difference analysis but there is a greater difficulty when directly fitting the anisotropy decay curve, this is because the instrumental response is more significant for smaller decay times. For some longer lived fluorophores as a consequence of a finite number of channels; the time-resolution of the difference may need to be sacrificed in order to measure the sum to a complete decay. On the other extreme the Rhodamine 6G in the 100 % glycerol sample **Figure 114** the difference has a much larger rotational correlation time than the sum, as a consequence the fluorescence lifetime is not sufficient enough to measure the entire fluorescence anisotropy decay to completion. This data is more difficult to fit using sum-difference analysis as shown from the appearance of the residuals but can be fitted directly as the decay is substantially larger than the prompt. The rotational correlation times in both cases show a significant different rotational correlation time with a free and fixed residual

136

anisotropy as a large proportion of the incomplete fluorescence anisotropy decay is prescribed to residual anisotropy.
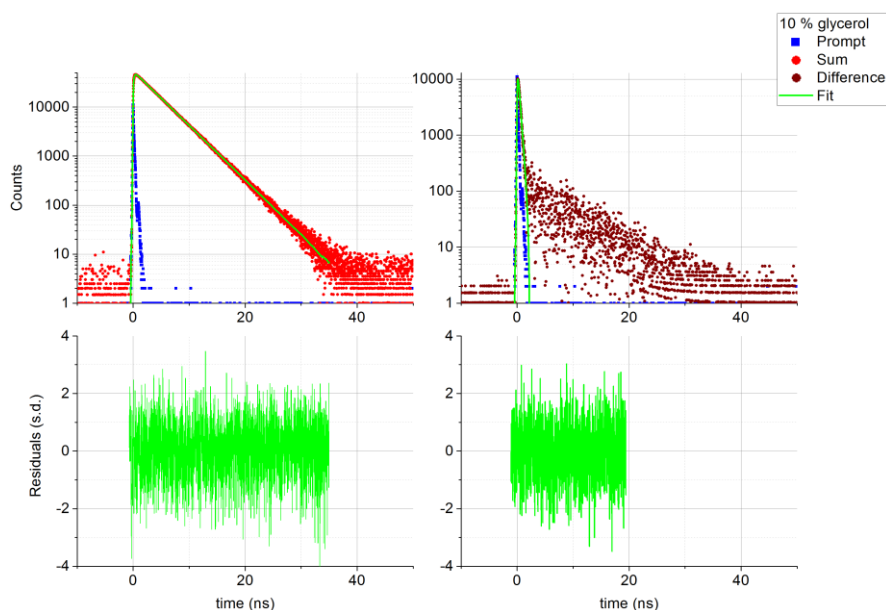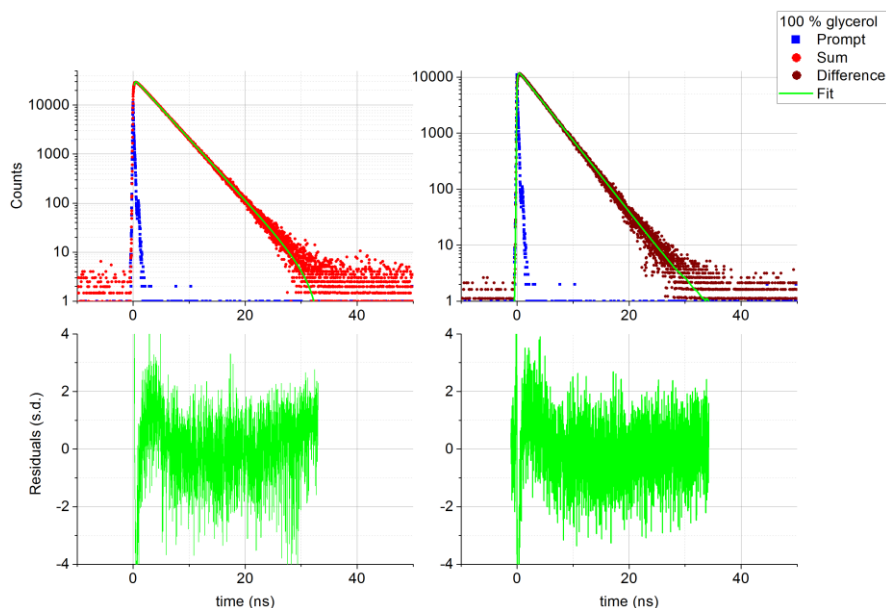

Figure 114: The sum and difference data constructed from the 100 % glycerol data **Figure 110**. The sum fitted to a mono-exponential decay time with $\tau_1 = 3.478 \pm 0.006$ ns, $\chi^2 = 1.628$. The difference data gives a mono-exponential decay with a rotational correlation time $\phi_1 = 180 \pm 20, \chi^2 = 1.63$ and a $r_0 = 0.392 \pm 0.001$ when the assumption is made of a zero residual anisotropy ($r_\infty = 0$). Alternatively, if the residual anisotropy is free the rotation correlation time $\phi_1 = 20 \pm 10, \chi^2 = 1.057, r_0 = 0.39 \pm 0.08$ and $r_\infty = 0.087 \pm 0.006$. The rotational correlation time is not consistent because much of the decay is prescribed to residual anisotropy when that parameter is left floating.
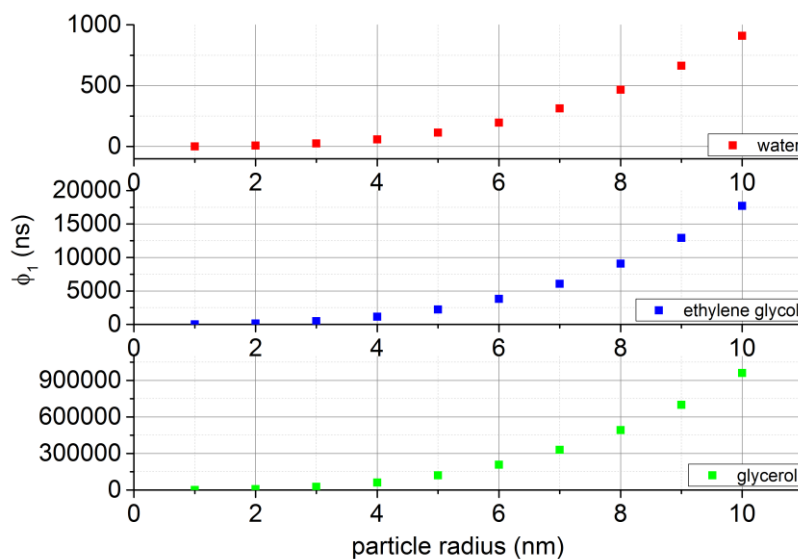
Figure 115 The rotational correlation times of nanoparticles with radii in the range 1-10 nm range calculated from **Equation (62)** for three solvents water, ethylene glycol and glycerol at 298 K[205–207].

Time-Resolved Fluorescence anisotropy is an important measurement technique as it has the applicability of measuring nanoparticles in low viscous solvents such as water within the 1-10 nm regime. These particles are too small for light-scattering techniques and current measurement techniques within this regime are currently time-consuming and expensive such as atomic force microscopy moreover fluorescence anisotropy has the advantage that it can be performed in solution and does not require drying out the sample [106]. **Figure 115** illustrates the relationship of ϕ_r to nanoparticle size at room temperature from **Equation (62)**. It can be observed that the rotational correlation time at room temperature for 1-10 nm spherical nanoparticles is 1 ns-1 µs for a low viscosity solvent (water), 15 ns-18 µs for a medium viscosity solvent (ethylene glycol) and 1 µs-1 ms for a very viscous solvents (glycerol). In most applications solvents with a similar viscosity to water are used. For successful nanometrology measurements one should select a photostable dye with a high quantum yield and with parallel excitation and emission dipoles, $r_0 \approx 0.4$ [64]. In practice $r_0 < 0.4$ as there will be an internal angle between the excitation and emission dipoles of the fluorophore [208]. The dye must also have a sufficiently long enough decay time in order to measure the rotational correlation time. For time-resolved fluorescence anisotropy particle sizing measurements a rigid fluorophore is preferred with a robust decay time and additional processes such as energy migration and excited state photophysics should be avoided as they complicate the anisotropy decay curve [209]. The fluorophore requirements and measurement principle is depicted in **Figure 116** for an ideal fluorophore with a mono-exponential lifetime. **Figure 117** shows a model real sample, Rhodamine 6G in varying solutions of glycerol, in this dataset the viscosity is altered instead of the size of Rhodamine 6G. The increase in viscosity increases the rotational correlation time and is better visualised on a log scale.

$$R_{np} = \sqrt[3]{\frac{3k_B T \phi}{4\pi\eta}}$$
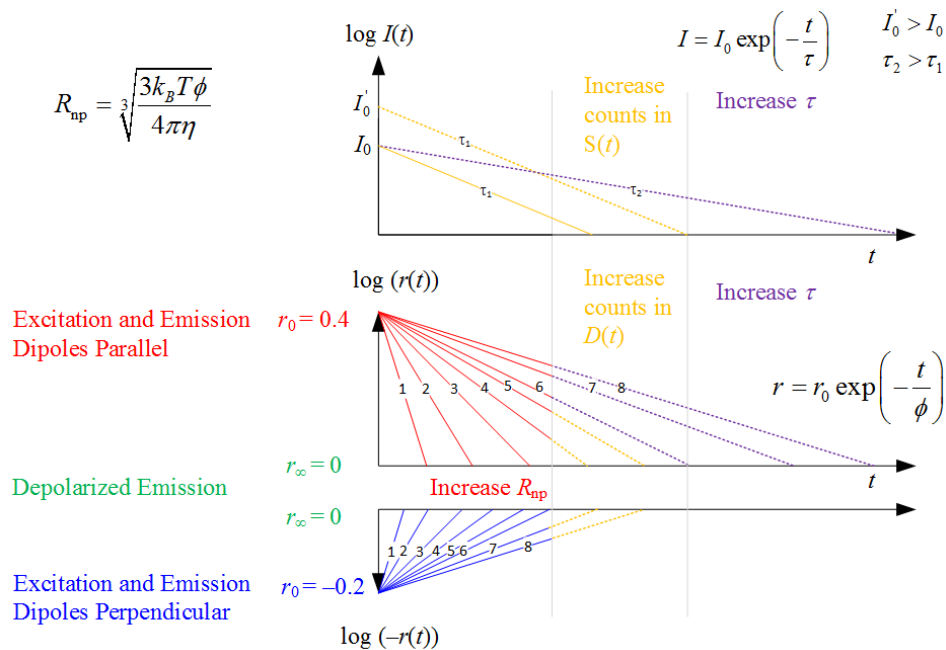
Figure 116: Principle of time-resolved fluorescence anisotropy with respect to particle sizing. The particle size increases from 1 to 8. The red anisotropy decay curves are for a fluorophore with parallel excitation and emission dipoles i.e. $r_0 = 0.4$ and the blue anisotropy decay curves are for a fluorophore with perpendicular excitation and emission dipoles i.e. $r_0 = -0.2$. In real life most fluorophores have a r_0 between the two extremes $+0.4$ and -0.2 for single photon excitation. Looking at the ideal red anisotropy decay curves (with no noise), small rotational correlation times can be measured to isotropy for particle sizes 1-3 i.e. a complete fluorescence anisotropy decay can be measured using a fluorophore with a lifetime τ_1. As the rotational correlation time ϕ increases above τ_1 as in the case of particle size 4-5 to measure the complete anisotropy decay curve more counts are taken which increases the measurement acquisition time and in practice will highlight instrumental distortion such as radio frequency interference and drift. For particle sizes 7-8 the complete anisotropy decay curve cannot be measured using a fluorophore with τ_1 and a suitable fluorophore with a larger decay time τ_2 must be used if available. In practice however a fluorophore with a suitable τ_2 may not be available because most fluorophores have a lifetime <4 ns [77,78]. In such cases the assumption that the residual anisotropy $r_\infty=0$ i.e. that the system becomes isotropic is used. This assumption helps with data analysis and this can be used to determine a rotational correlation time $\phi>25\ \tau$[44]. The particle size 1-8 is depicted to be the same in both the red and blue anisotropy decay curves. For an $r_0 = -0.2$ there is less data per decay making the determination of the rotational correlation time more difficult (particularly for the smaller rotational correlation times). In most cases a fluorophore and excitation conditions for an $r_0 \sim 0.4$ is therefore desired.

---

[44] Care must be taken using this assumption as gelled samples will have a residual anisotropy because the fluorophore/particle is fixed.
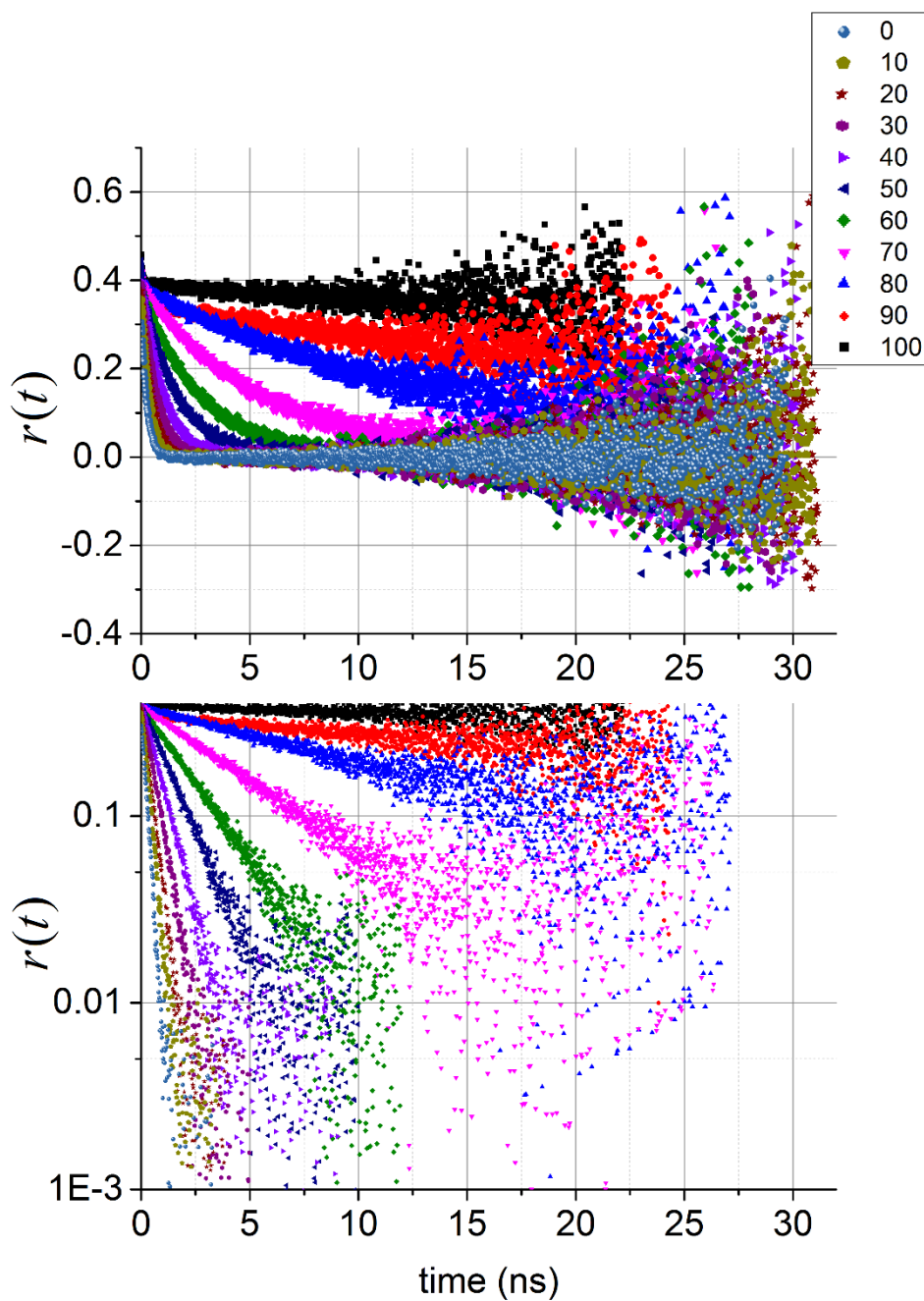
Figure 117: The increase in glycerol concentration increases the viscosity of the solution and hence increases the rotational correlation time. This gives an illustration of **Figure 116** using real data. For low viscosity solutions it can be seen that the anisotropy falls to 0 but for the higher viscosity solutions the fluorescence lifetime of Rhodamine 6G becomes insufficient to capture the entire anisotropy decay. Data fitting must be helped by fitting the residual anisotropy to 0.
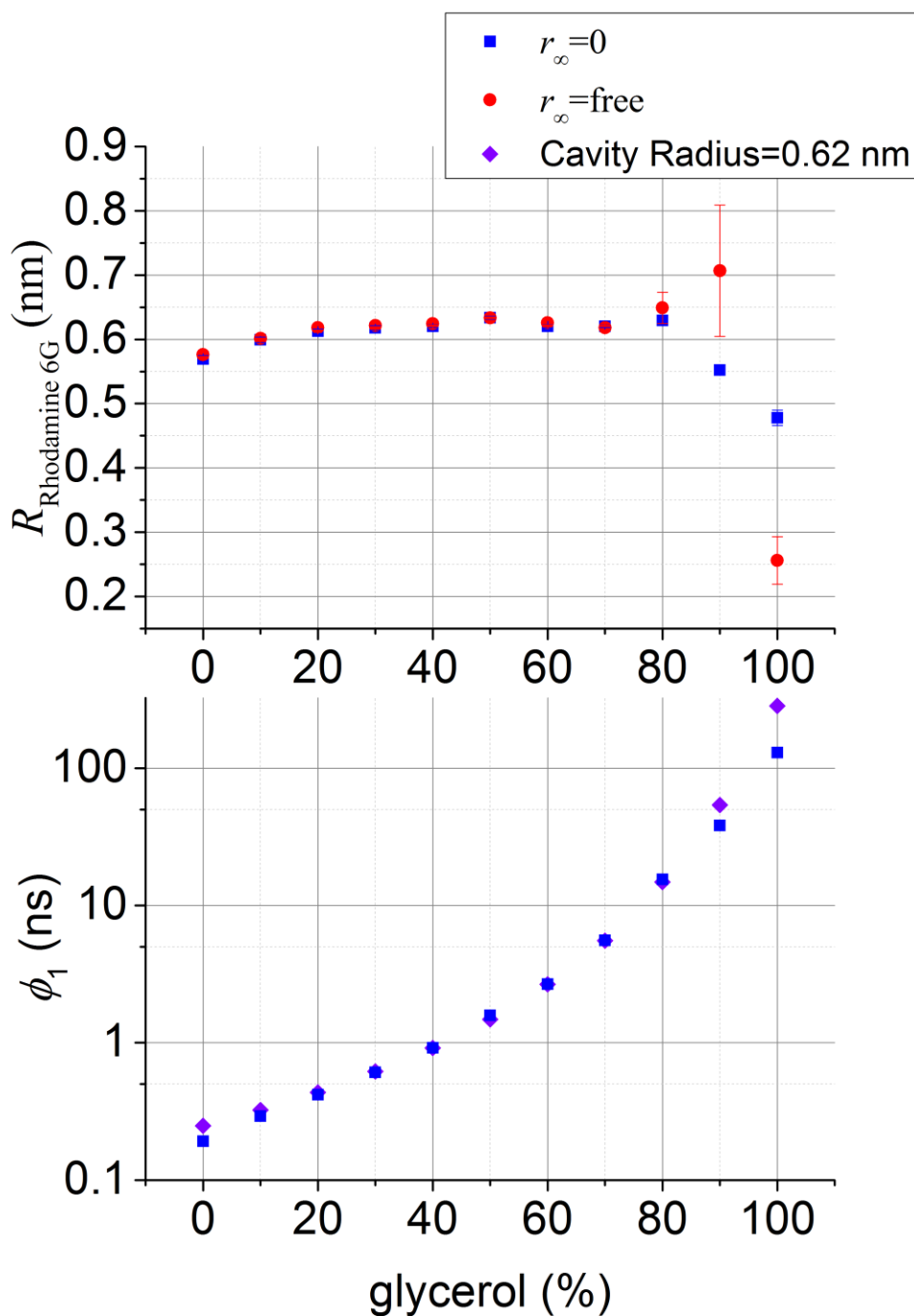
Figure 118: The hydrodynamic radius of Rhodamine 6G reported from each anisotropy decay. The radius reported is more or less constant (within error) for glycerol solutions 0-80 % regardless if the residual anisotropy is fixed or free. At 90-100 % leaving the residual anisotropy floating throws out the particle because there is not enough data in these decay curves to accurately determine the residual anisotropy. The cavity radius is expected to be 0.62 nm and the dataset is in strong agreement with this size. The 90-100 % data when the residual anisotropy is fixed to 0 gives a slightly smaller rotational correlation time and hence particle size that expected. This can be due to the inaccuracy of fitting due to only having data near the start of the anisotropy decay and the signal to noise being far too weak at the tail. It is also possible some anisotropy is lost due to self-absorption. Data is plotted

in log scale which is suitable given the differences in rotational correlation time and due to the cubic dependence of **Equation (62)**.
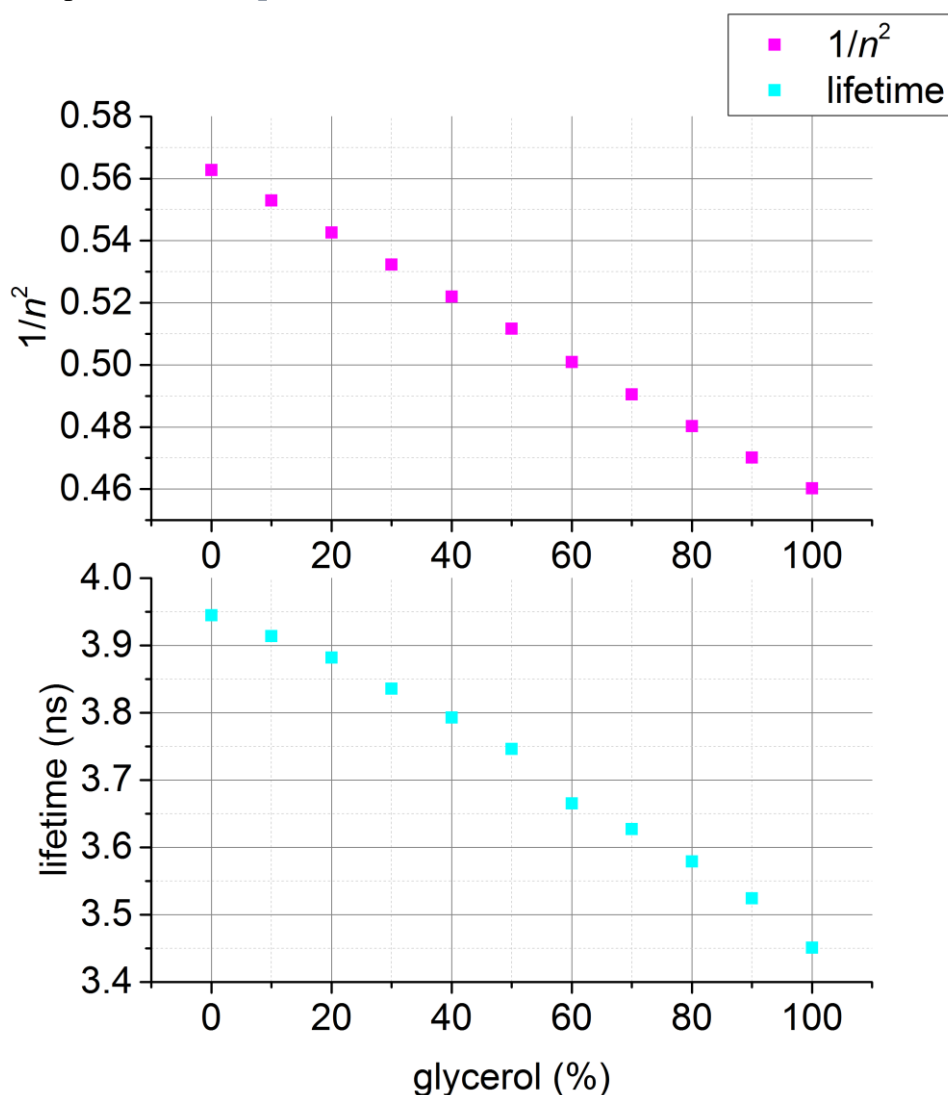
Figure 119: The lifetime data from the anisotropy sum of Rhodamine 6G decreases with respect to the increase in glycerol concentration. This increase is predicted by Strickler and Berg due to the inverse relationship $\tau \propto n^{-2}$, this relationship [210] is plotted alongside the lifetime data. All fluorescence sums were fitted to a mono-exponential. The high viscosity solutions however fitted better to two exponentials with the sum data fitted better to two exponentials for 100 % glycerol with a negative component of ~0.44±0.06 ns (–0.13 α_2). Self-absorption is more likely to occur at high viscosity solutions [211] which would explain the negative amplitude.
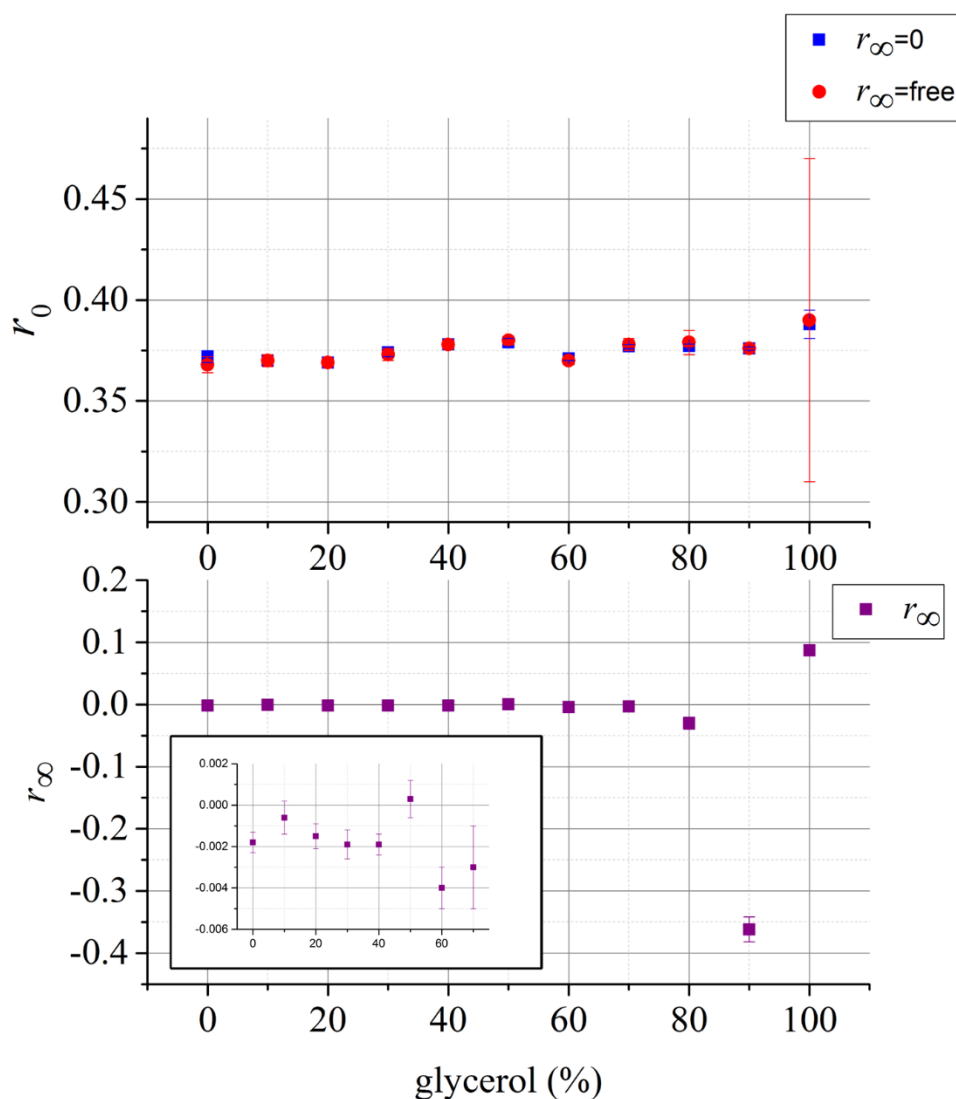
Figure 120: The particle size of Rhodamine 6G is seen to be agree well when the residual anisotropy is fixed to 0 and when it is floating. At high viscosity solutions, the rotational correlation time is too large to accurately be tracked and the data fitting gives generates a value for the residual anisotropy significantly different from 0 which is nonsense and throws out the fit significantly. The initial anisotropy is constant with respect to viscosity within the error of measurement.

Sum-difference fitting of all the anisotropy decays in **Figure 117** shows a consistent radius **Figure 118** of Rhodamine 6G from 0% to 80% glycerol solutions. At 90-100 % sum-difference analysis using the assumption the residual anisotropy is free gives a significant deviation from data where the assumption that the residual anisotropy is fixed is employed. It is insightful to look at the rest of the values from the anisotropy data. First the fluorescence lifetime data from the sum **Figure 119** where a mono-exponential model is fitted in each case. The lifetime is clearly seen to decrease with respect to viscosity, the reason for this is due to the inverse relation between the refractive index squared reported

by Strickler and Berg [212]. While it appears the lifetime of Rhodamine 6G can be used to measure the viscosity of glycerol, it should be noted that other fluorophores are specifically designed to measure changes in viscosity such as molecular rotors. Molecular rotors as the name suggests have a rotor structure that can spin, at low viscosities the structure can spin freely and at high viscosities the structure is rigid. In general the more rigid the fluorophore, the higher the quantum yield and the fluorescence intensity and decay time [213]. The initial anisotropy $r_0 \sim 0.37$ appears to be independent of glycerol concentration. This independence coupled to the clear $1/n^2$ relationship indicate that solvent relaxation is negligible. The lower limit of a fluorescence anisotropy decay is usually dictated by the time resolution of the system because the time range and time calibration per channel is usually adjusted to suit the overall lifetime of the fluorophore so the sum can accurately be fitted. Moreover, anisotropy decays of free fluorophores in low viscosity solutions will be difficult to fit because the sum data requires a large number of counts as a perquisite to obtain a set peak difference. This increases acquisition time and makes the sum data more prone to instrumental effects. The difference curve which will be short lived (likely to have a poor time-resolution per channel). Hence a direct fit to the anisotropy curve is of limited use and fitting will require application of reconvolution analysis twice. The upper size limit of time-resolved anisotropy on the other hand is ultimately dictated by the fluorescence lifetime of the fluorophore. If the rotational correlation time is much longer than the lifetime fluorophore, then the signal to noise ratio becomes too poor and one cannot measure a fluorescence anisotropy decay to completion. There are some additional tricks like taking the difference peak-preset to a larger number of counts in order to get a better signal to noise ratio at the tail however, this involves substantially larger acquisition times and is hence more prone to instrumental drift. Naturally, longer acquisition times cannot be used for an unstable sample. A longer lived fluorophore such as ADOTA which will be discussed in more detail later can be used to measure larger nanoparticles using fluorescence anisotropy with a higher accuracy [214]. In general, the time range used to measure an anisotropy decay is ≥ 20 τ. Rhodamine 6G has a lifetime of ~4 ns and a time range of 100 ns (DeltaHub ~27 ps ch^{-1}, DeltaDiode rep rate ≤ 8 MHz) and ADOTA has a lifetime of ~20 ns and a time range of 400 ns (DeltaHub ~108 ps ch^{-1}, rep rate ≤ 4 MHz) can be used for measurement. Taking a longer lived decay time of ~1 µs means a time range of >26 µs (DeltaHub ~3510 ps ch^{-1}, rep rate ≤ 25 kHz) is required which will take a substantial acquisition time and simultaneously lowers the time-resolution. The fluorophores lifetime,

measurement range (time calibration per channel) and repetition rate must all be carefully selected to accommodate the nanoparticle size range being measured. Other probes with larger decay times (~ms) can be used to look at even larger nanoparticles using MCS phosphorescence anisotropy [215] however in most cases the quantum yield of such complexes is usually much lower than that of short lived organic fluorophores and the initial anisotropy r_0 may be significantly smaller than 0.4 [216]. The closer r_0 is to 0.4 the better as it gives the most data for an anisotropy decay curve.

Anisotropy has some drawbacks because of the limitation that only 2 different species can adequately be tracked and only dilute solutions can be examined. $r(t)$ can rarely be measured with sufficient precision to determine more than one rotational time [217] even in model systems, such as free fluorophore in a viscous solvent fluorophores which are clearly not spherical objects and possess a differing x, y and z dimension. For this reason, the spherical model is usually selected with time-resolved fluorescence anisotropy data and the particle of the size of the object under investigation is estimated. Time-resolved fluorescence anisotropy data cannot be used to determine detailed structural details of the object under investigation, for instance the dye shape of Rhodamine 6G cannot be reconstructed by using time-resolved fluorescence anisotropy data. Moreover on the nanoscale it should be noted that solvent molecules will interact with fluorophores in a differing degree in processes known as solvent slip or stick [218,219]. Highly viscous molecules such as glycerol for example may form a solvent shell that sticks to the fluorophore and rotates with it [220] on the other hand dye in lower viscosity solvents such as methanol will rotate very rapidly allowing the system to obtain zero anisotropy very rapidly. It is also possible for water molecules to co-ordinate with fluorophores using hydrogen binding influencing the particle size. For the application of particle sizing decays of polydisperse systems cannot be easily fitted, moreover for systems that are labelled with fluorescence dye; free dye itself may become a decay component [209].

2.3.10 Time-Resolved Emission Spectra (TRES) and Decay Associated Spectra (DAS)

In general, a dedicated steady-state system such as a Fluorolog/Fluoromax/Dual FL will be used to measure steady-state spectra. Time-resolved systems such as the DeltaFlex and FluoroCube are usually not routinely used to measure steady-state spectra however can measure emission spectra in the same manner as the steady-state systems such as the Fluorolog using a NanoLED, DeltaDiode or super-continuum laser as an excitation source opposed to a Xenon lamp as shown in **Figure 121**. Time-resolved systems can also be used
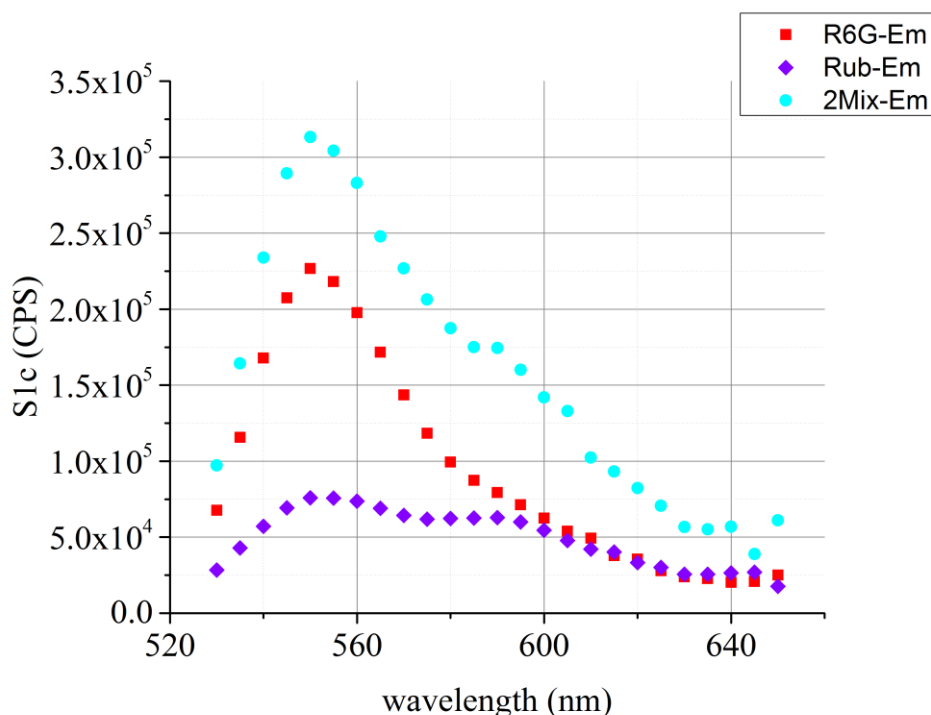
Figure 121: Emission steady-state spectra measured in a FluoroCube Extreme. The excitation monochromator TDM800 (1200/350 grating) was set to a bandpass of 8 nm at 525 nm and the emission monochromator TDM800 (1200/350 grating) was set to a bandpass of 8 nm and scanned from 530-650 nm in 5 nm increments. Polarizers were at VM and Hub A timing electronics were used in reverse mode with a TBX650. An integration time of 1 s per point was selected. The spectra measured are Rhodamine 6G, Rubrene and a mixture of both solutions 1:1 in methanol solvent. This data is equivalent to the S1c signal measured in a Fluorolog or Fluoromax.
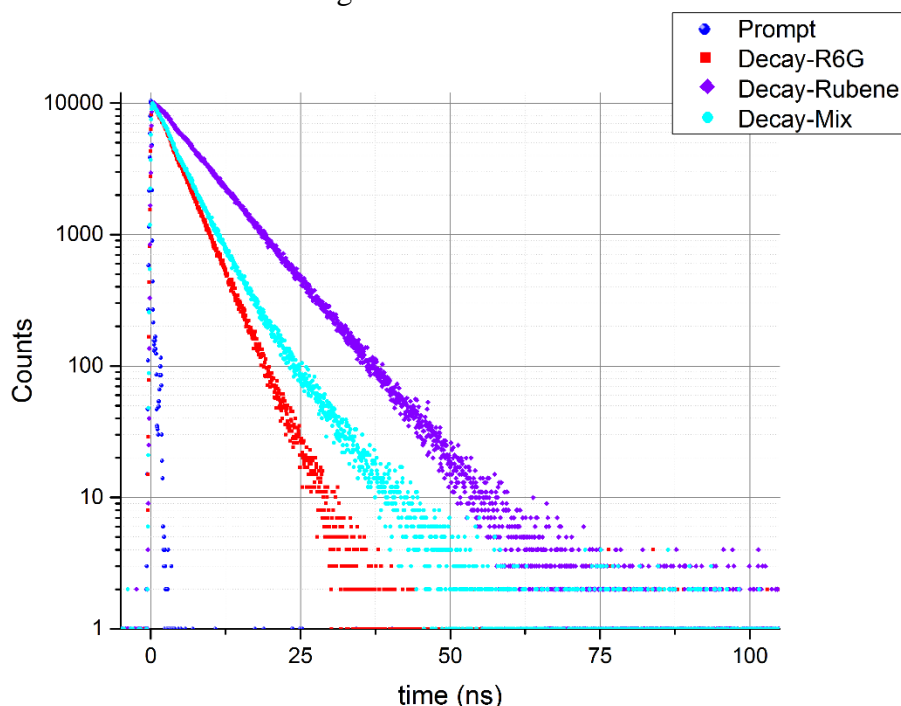
Figure 122: The decay of Rhodamine 6G, Rubrene and a mixture of both in methanol solvent measured in a FluoroCube Extreme with a 525 nm excitation wavelength and a 545

146

nm emission wavelength. These gave a decay time of 4.01±0.01 ns with a χ^2=1.036 for Rhodamine 6G on its own 7.81±0.02 ns with a χ^2=1.152 for rubrene on its own. For the mixture a bi-exponential was fitted with decay times τ_1=3.93±0.09 ns, α_1=0.82 and τ_2=7.4±0.2 ns, α_2=0.18, χ^2=1.049. Hub A timing electronics were used operated in reversion mode with a time range of 200 ns (8000 channels).

to measure the fluorescence decay as shown in **Figure 122**. Rhodamine 6G **Figure 65** and Rubrene **Figure 67** were already shown to have a significant overlap in their EEMs making them relatively hard to distinguish as a mixture **Figure 69**. The decay times of Rhodamine 6G 4.01 ns and Rubrene 7.4 ns are significantly distinct (differing by approximately a factor of 2) so the decay time may be used as a parameter to distinguish the fluorescence contribution from these two species. The information within **Figure 121** and **Figure 122** can be obtained in one measurement as depicted in **Figure 123**. Instead of measuring only the fluorescence intensity with respect to emission wavelength, a time-resolved system may be used to measure the fluorescence decay with respect to wavelength **Figure 124**. This dataset is known as a time-resolved emission spectrum and like an EEM may be plotted out as a waterfall plot **Figure 125**. Before carrying out a TRES it is useful to measure the steady state emission spectra of the sample to locate the peak emission wavelength **Figure 121**. The time for acquisition of the decay curve is important and is used to determine a suitable acquisition time for each decay curve in the TRES. It is therefore appropriate to measure the fluorescence decay at the peak emission wavelength to a peak preset of 10000 counts as normal **Figure 122** in order to determine an appropriate integration time to use for the TRES. Since a TRES consists of multiple decays which will be globally analysed together the peak count of the decay curve measured at the emission maxima does not need to be as high as 10,000 counts like what's recommended for a single decay but can be relaxed to ~2,000 counts at the peak decay. In general, the acquisition time to measure a decay is usually substantially longer than the integration time one would use to measure steady-state intensity because of the restriction of the hit rate to <2 % to prevent pile-up effects. To reduce the total acquisition time a larger wavelength increment between curves is commonly used, typically 5 nm. Before measuring the TRES a prompt is run to 10,000 counts as normal and the TRES is ran with the specified parameters; wavelength range, wavelength increment and acquisition time. It is insightful to plot out the fluorescence decays in log as they are typically measured and also in linear as spectrum are typically visualised. Once the emission wavelength correction factor has been applied, the data may also be plotted out as a contour profile and time-sliced **Figure 126**. Each time slice gives
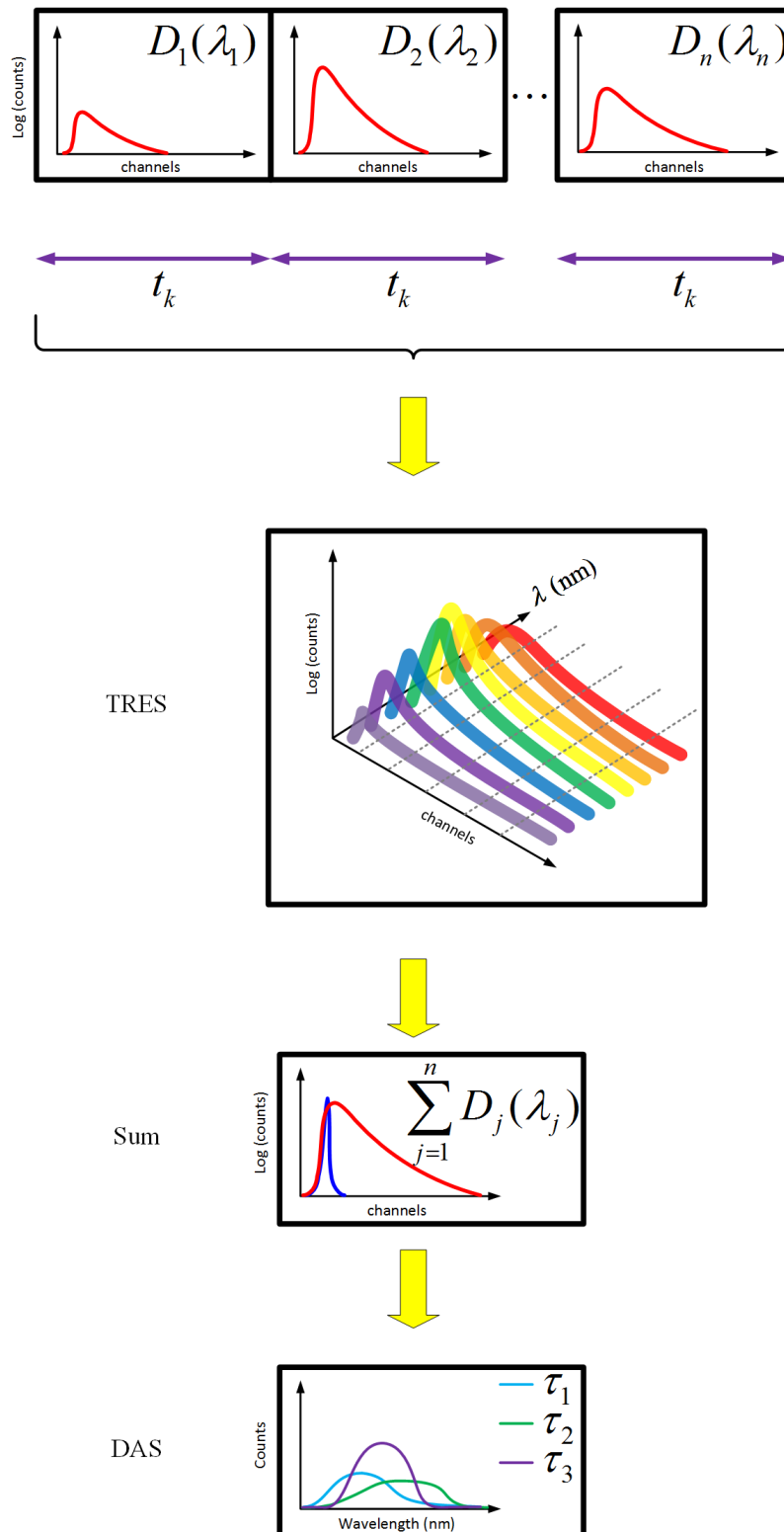
Figure 123: Principle of Decay Associated Spectra. A series of decay curves are measured with respect to emission wavelength with an acquisition time t_k per curve. The decay curves may be summed and fitted as normal. The pre-exponential factors $b_1(\lambda),\ldots,b_2(\lambda)$ for each decay may then be plotted as a function of wavelength to give the DAS. Alternatively, the TRES may be sliced with respect to the time axes. Each time slice will create a different spectrum which can be compared. τ_1, the shortest decay time may be observed in more detail at earlier time slices. In this illustration as the time-scale of τ_1 is shorter its decay will

die out faster than τ_2 and τ_3 which may be analysed at later time slices where they are more prominent.
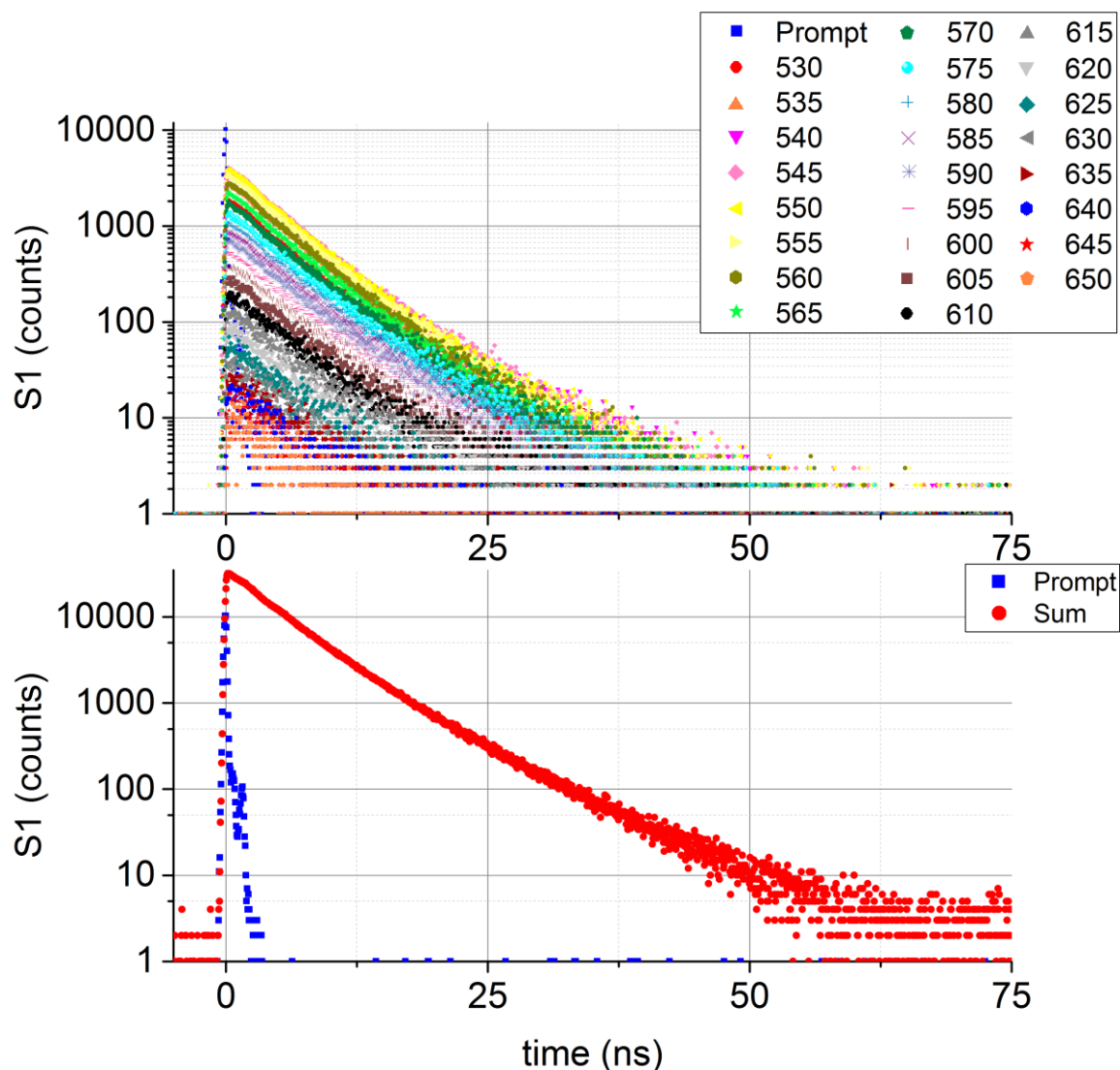
Figure 124: Raw decay data (top) used to construct a Time Resolved Emission Spectrum (TRES). The excitation monochromator TDM800 (1200/350 grating) was set to a bandpass of 8 nm at 525 nm and the emission monochromator TDM800 (1200/350 grating) was set to a bandpass of 8 nm and scanned from 530-650 nm in 5 nm increments. Polarizers were at VM and Hub A timing electronics were used in reverse mode using a 200 ns time range (8000 channels) with a TBX650. An integration time of 15 s per decay was selected. The spectra measured are Rhodamine 6G, Rubrene and a mixture of both solutions 1:1 in methanol solvent. Each decay curve may have sufficiently less than 10000 counts but the summation of data (bottom) which can likewise be globally analysed is far greater than 10000 counts.
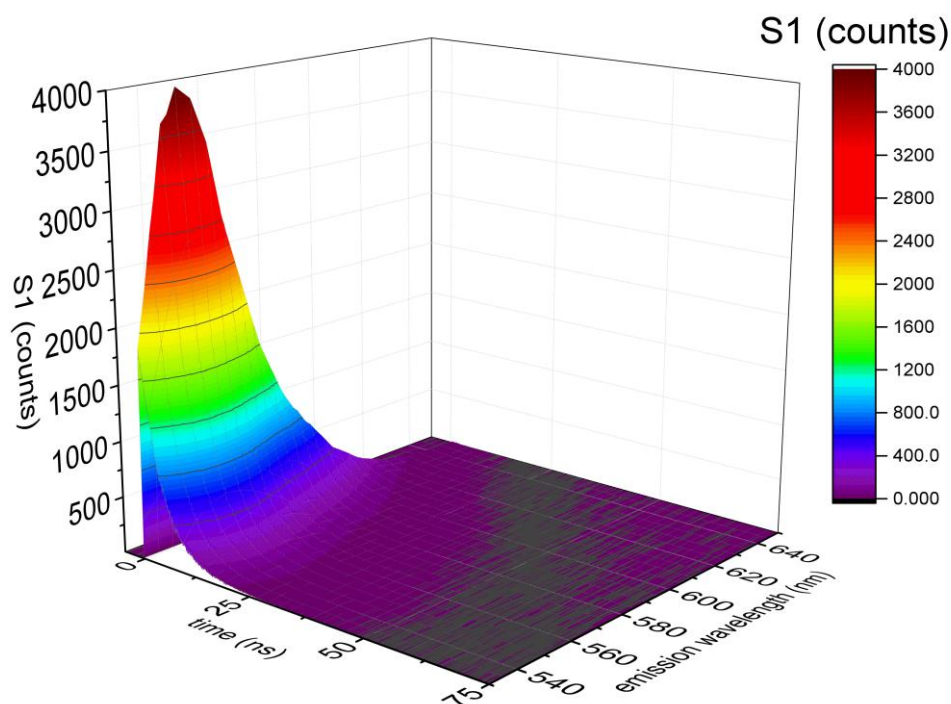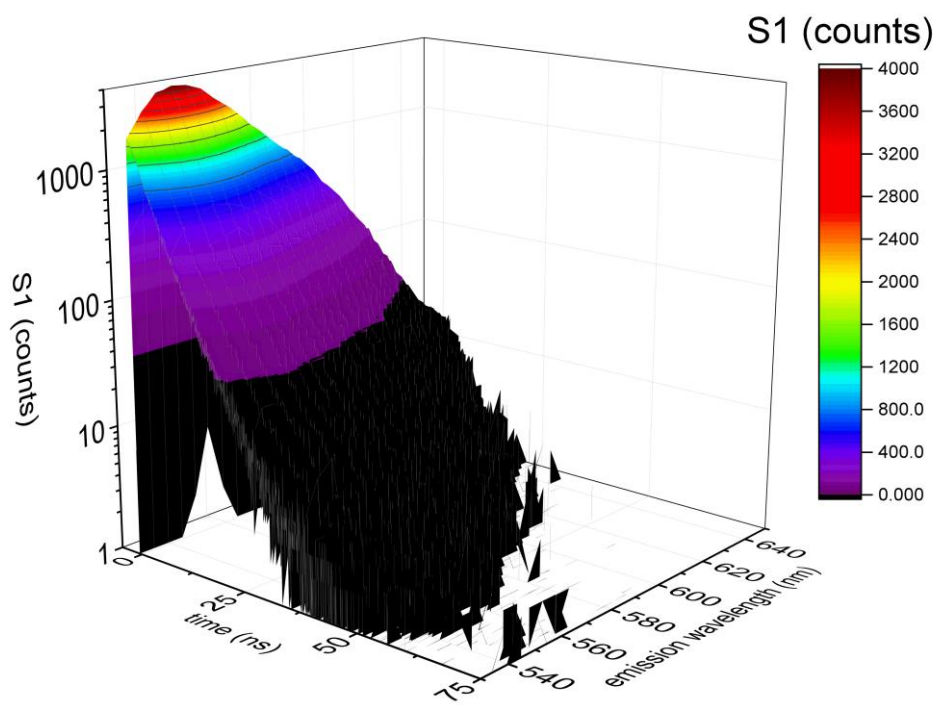
Figure 125: The raw decay data **Figure 124** may be plotted out in 3D in a similar manner to the EEM. Fluorescence decays are typically plotted in a log (top) whereas spectrum are typically plotted in linear (bottom). Each time slice gives an uncorrected emission spectrum which will be examined in more detail once the MCorrect is applied and a contour profile is used.

150
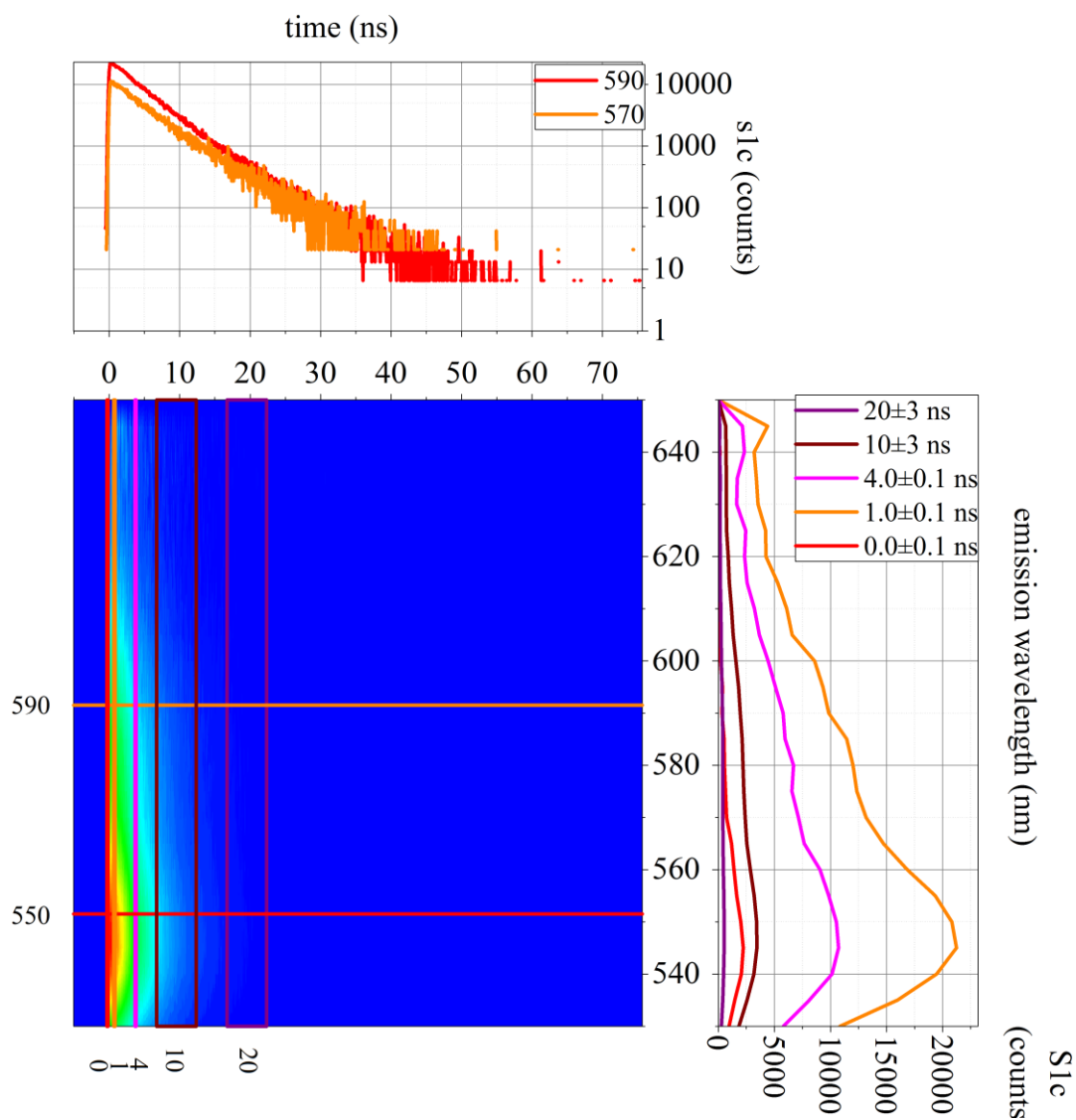
Figure 126: The emission corrected decay data **Figure 124** may be plotted out as a contour profile in a similar manner to the EEM. Fluorescence decays are typically plotted in a log (top) whereas spectrum are typically plotted in linear (right)[45]. Each time slice gives an uncorrected emission spectrum (right).

an emission spectrum at that moment in time. Earlier time slices however have a much higher number of counts than later time slices and it is hence therefore usually appropriate to normalise the spectrum **Figure 127**. The early time slices are dominated by shorter-lived processes. Usually this is dominated by the short-lived fluorescence however for very weakly fluorescing samples if the time-resolved emission spectrum is measured with short time ranges (50-200 ns) Raman may also be picked-up **Figure 76**. At later time slices the

---

[45] The convention used throughout this work form time-resolved emission spectra is to have time as the *x*-axis and emission spectrum as the *y*-axis.

short-lived processes have decayed and the longer decay processes are more dominant. For **Figure 127** the early time-slices resemble the emission spectrum of Rhodamine 6G and the later time-slices resemble the emission spectrum of Rubrene. Later spectrum are much more noisy due to the lower number of counts per slice. Reconvolution analysis can also be applied to obtain a decay associated spectrum. Data may be analysed by summing all the individual decay curves **Figure 124** to obtain global decay times.
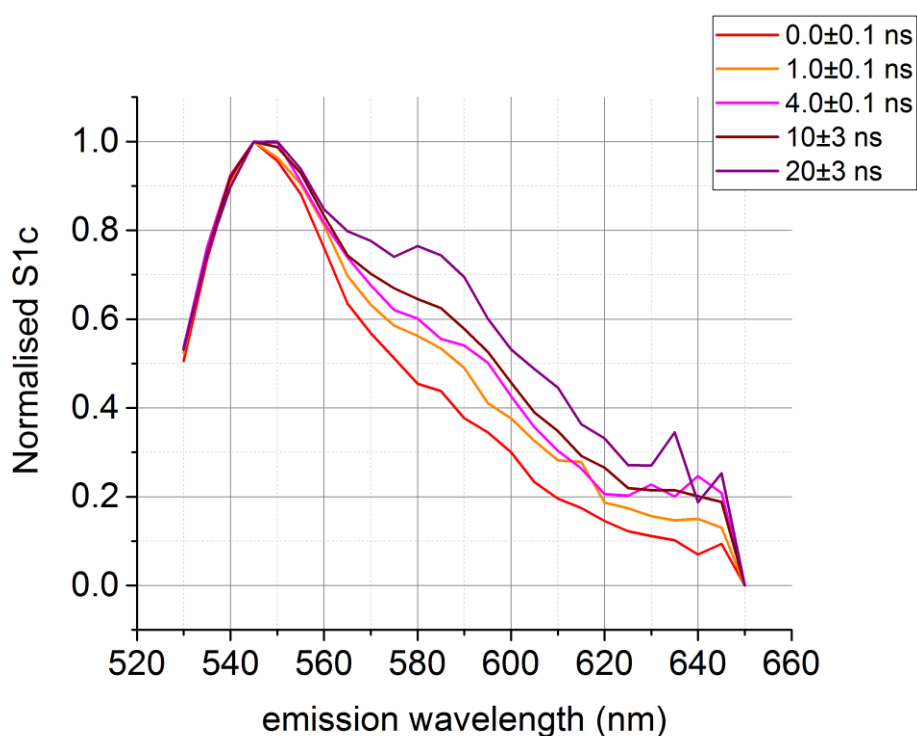
Figure 127: Normalised time slices from **Figure 126**. In earlier time slices the contribution of Rhodamine 6G is dominant and hence the spectrum resembles Rhodamine 6G **Figure 121**. At later time slices the relative contribution to the fluorescence decay is dominated by the longer lived Rubrene as fluorescence emission from Rhodamine 6G has already decayed.
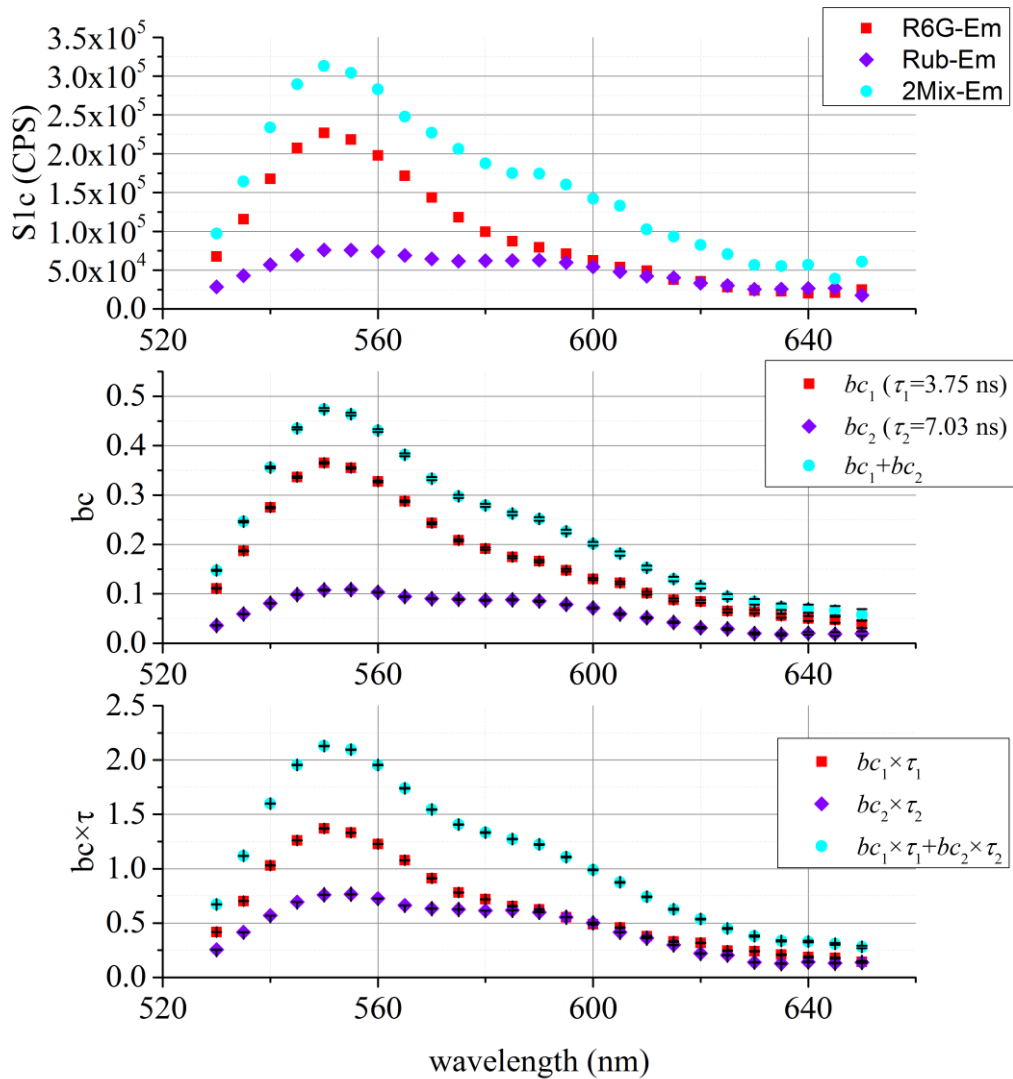
Figure 128: An example of the steady state spectra of Rhodamine 6G, Rubrene and a mixture of both plotted (top) alongside the DAS (middle) and DAS^W (bottom) of the mixture plotted side by side. The DAS shows that it is possible to resolve the spectra of each individual component using its decay time, in this case a global decay time of 3.75 ns and 7.03 ns was selected by fitting from the summation of all measured decays. Scatter was removed by fixing the first decay time to half a channel (not plotted).

The entire data set is then fitted using these decay times as a basis and the pre-exponential factors[46] $b_1(\lambda),\ldots,b_j(\lambda)$ are obtained with respect to wavelength which gives the uncorrected Decay Associated Spectra (DAS). Multiplication by MCorrect[47] gives the corrected DAS **Figure 128**. The DAS weighted by the decay times i.e. spectra of $b_1\tau_1(\lambda),\ldots,b_j\tau_j(\lambda)$ should theoretically be identical in form to the steady state emission spectra:

$$\text{Steady State Spectra} = \sum_{j=1}^{n} b_j \tau_j(\lambda) \qquad (65)$$

DAS^W will be used to denote DAS weighted by the decay times from unweighted DAS. Although the DAS^W in **Figure 128** strongly resembles the steady-state spectrum in practice it's difficult to get a DAS^W to exactly resemble the ratio of amplitudes of all the individual components of the steady state spectra due to larger overall errors in decay times particularly when a Global Analysis is used. The decay time and spectral shape of each component in the DAS is important and it can be in particular useful for identifying whether a small component is an artefact such as Raman scatter. During reconvolution analysis of TRES data, Raman scattering is typically fixed to half a channel as it is significantly smaller than the time-resolution of the system. The DAS can also conversely be used to remove weak fluorescence background from a Raman spectrum [221].

In some cases, it may also be possible to construct a DAS using decay times from a single decay curve. **Figure 129** illustrates the construction of a DAS and DAS^W using the global decay times of **Figure 122**. As these decay times are relatively close to the global decay times **Figure 128** and **Figure 129** strongly resemble one another. The Rhodamine 6G and Rubrene samples can be readily made analysed separately and mixed together to form a more complicated sample. The properties of the mixture can be prescribed to the two individual components separated by their decay time and their individual DAS^W can be obtained and compared as a good match to their steady-state counterparts. This sample illustrates the concept behind the time-resolved emission spectrum and how it can be used to distinguish species which have a similar excitation and emission profile but differing decay time. The TRES measurement is of course routinely used to interrogate a sample

---

[46] Normalised pre-exponential factors $\alpha_1(\lambda),\ldots,\alpha_j(\lambda)$, relative amplitudes $f_1(\lambda),\ldots,f_j(\lambda)$, or using a peak pre-set instead of a time pre-set cannot be used to construct the DAS or TRES, the sum of the curves will be presented as a straight line if these values or conditions are used.

[47] Strictly speaking a plot of a TRES should have a dark offset applied. For the DAS on the otherhand each decay is fitted with A which is prescribed to its background noise and hence no additional dark offset is required for a DAS.

where less is known about the individual components. For such a sample the DAS and EEM measurements greatly complement one another. A recent review shows their joint deployment for investigating bioactive compounds in food [222]. A more complicated sample will now be revisited showing the merits of the DAS^W.
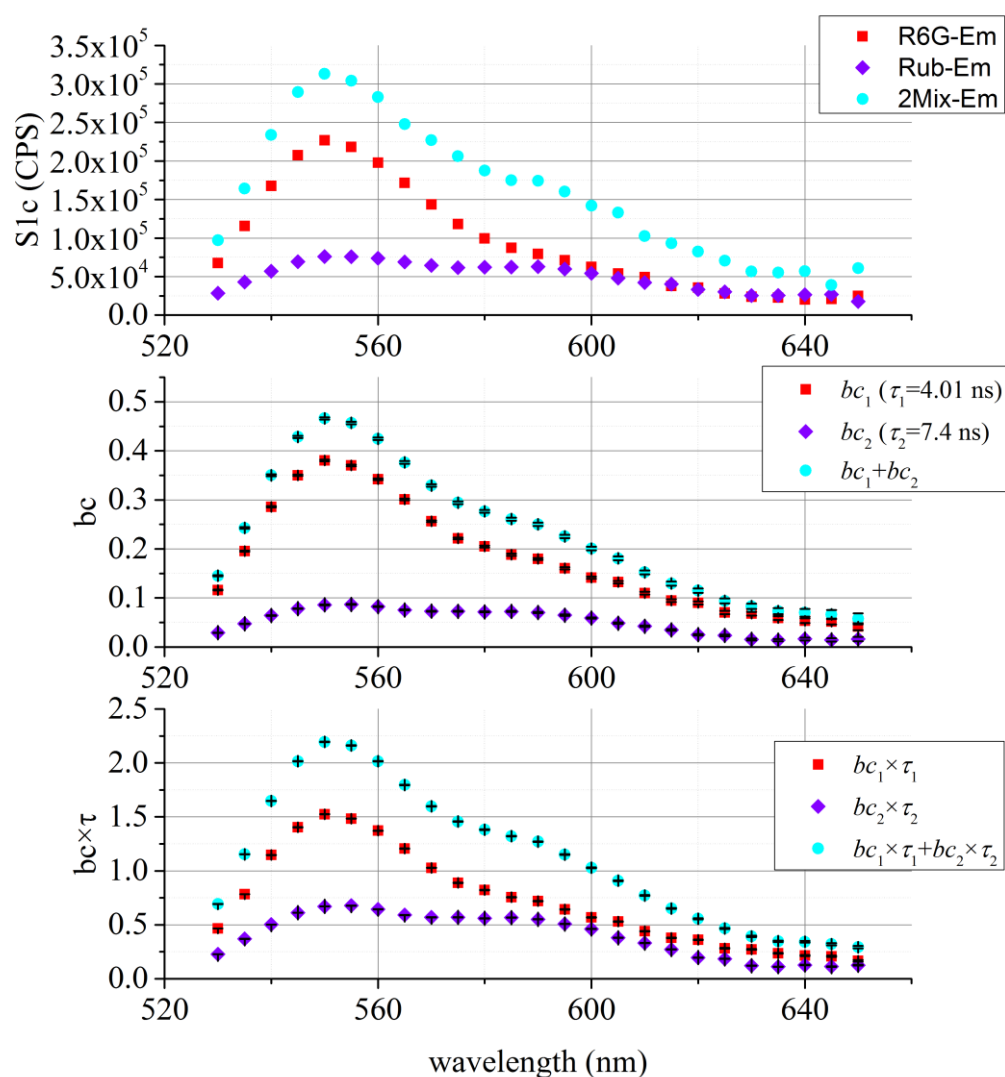
Figure 129: The decay times from the mixture **Figure 122** 4.01 ns and 7.4 ns were used to fit the TRES data. Scatter was removed by fixing the first decay time to half a channel (not plotted). The steady state spectra of Rhodamine 6G, Rubrene and a mixture of both plotted (top) alongside the DAS (middle) and DAS^W (bottom) of the mixture are again plotted side by side.

A model example was shown to demonstrate the principle of a TRES measurement. The 3 trytophan rotamer model **Figure 104** fitted well to a three exponential model. Some more information may be determined by looking at a control BSA sample 1 µM BSA in PBS and a chemically denatured sample 1 µM BSA in PBS with 4 g l^{-1} urea [223]. Urea denatures BSA via direct hydrogen bonding interactions with the BSA through its NH functional groups which results in protein unfolding [224]. Upon chemically denaturing with urea the sample's absorbance appears to increase while the fluorescence emission is seen to plummet **Figure 130**. Urea itself absorbs from 200-250 nm, the increase in absorbance seen is primarily due to scatter c.f. **Figure 25** and the actual absorbance of BSA changes little [224]. The fluorescence decay at 340 nm was already measured and analysed to fit to a 3 exponential $\tau_1 = 0.64 \pm 0.02$ ns ($\alpha_1 = 0.34$), $\tau_2 = 3.0 \pm 0.3$ ns ($\alpha_2 = 0.17$) and $\tau_3 = 6.52 \pm 0.05$ ns ($\alpha_2 = 0.49$). The two smaller decay times, τ_1 and τ_2 are observed in free tryptophan in distilled water [225] and are observed in proteins with 1 or 2 tryptophan residues, the larger decay time τ_3 results in interaction with the protein amino acids [226].
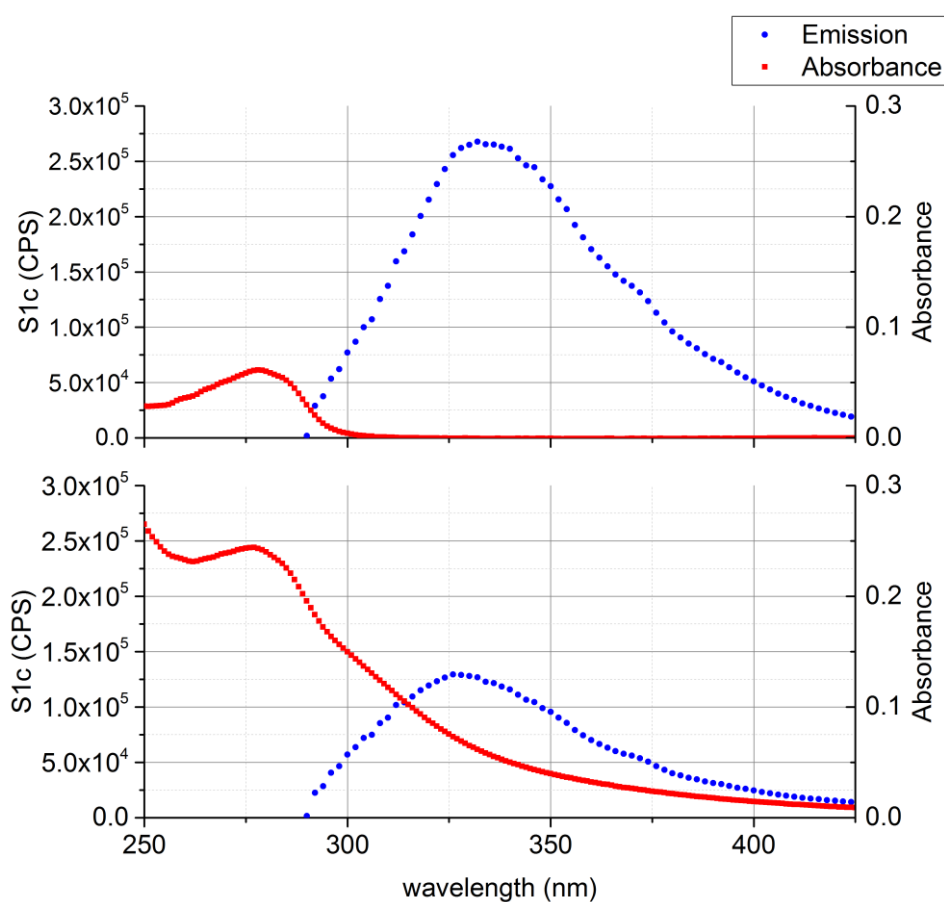
Figure 130: Corrected steady state spectra of control (top) and denatured Sample (bottom). The emission spectrum was measured in a Horiba Scientific DeltaFlex with a DD270D excitation source, TDM800 monochromator (1200/350 grating) with a bandpass set to 16

nm and PPD850 detector using a step of 2 nm from 290-425 nm with an integration time of 10 s. A Shimadzu UV-1800 was used to measure the absorption spectra using an integration time of 0.1 s every 1 nm from 250-425 nm.
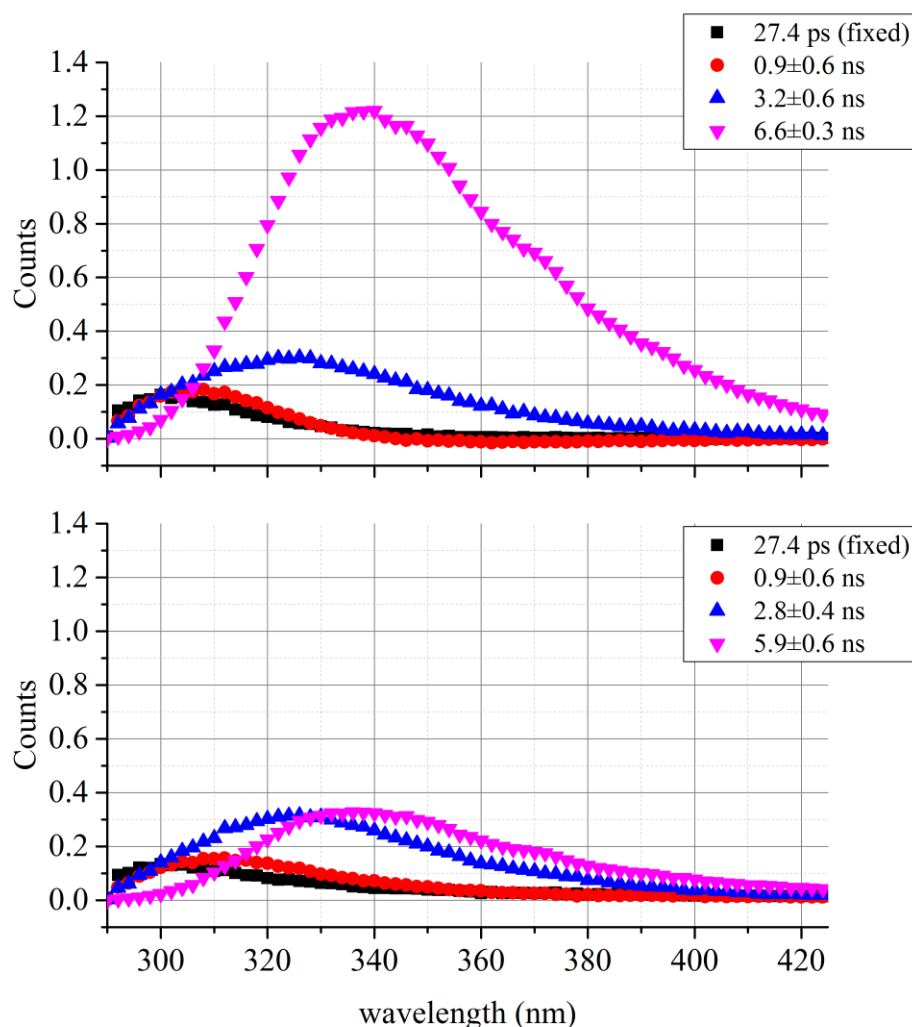
Figure 131: DAS^W of control (top) and denatured Sample (bottom). The TRES was measured in a Horiba Scientific DeltaFlex with a DD270D excitation source, TDM800 monochromator (1200/250 grating) with a bandpass set to 16 nm and PPD850 detector. A decay from 290-425 nm was measured every 2 nm using an integration time of 10 s per decay. A 4 exponential model was selected for the data, three of the exponentials are prescribed to the 3 tryptophan rotors as measured in **Figure 104** and the fourth component is fitted to half a channel and is prescribed to water Raman scattering (c.f. **Figure 59**). It is evident that the main decrease in fluorescence is due to the ~6 ns component. The rest of the components have a similar magnitude in the control and denatured sample. This component is due to a tryptophan embedded in the BSA, as the BSA opens up it gets exposed to solvent and its intensity decreases.

BSA has two tryptophan residues Try-214 which is deeply embedded in a hydrophobic cleft and Try-135 which is on the surface [224,227]. The larger decay time ~6 ns is prescribed to Try-214 and the smaller decay time ~3 ns is prescribed to Try-135. **Figure 131** shows a DAS^W of BSA and denatured BSA. This data is fitted to 4 exponentials.
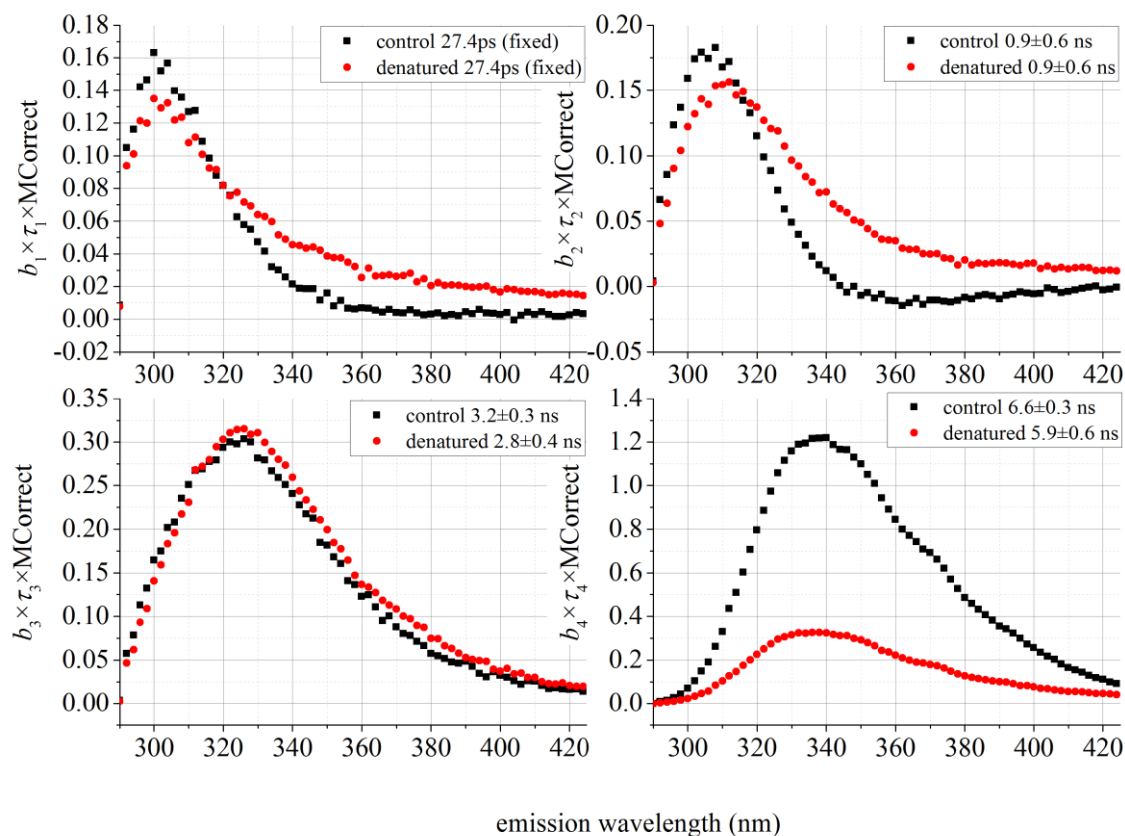
Figure 132: Each component of the DAS^W of the control and denatured BSA **Figure 131** plotted out separately.

The first exponential is half a channel and is prescribed to Raman scattering. The other three global decay times are prescribed to the BSA. Plotting out each component individually **Figure 132** allows for a direct comparison. The intensity of the water Raman peak τ_1 is seen to fall slightly but have a higher background elsewhere. This could possibly be a result of short lived scattered light as seen in the absorbance spectrum c.f. **Figure 130** and **Figure 25**. The intensity and decay time τ_3 is the same in the sample and the control and is expected as Try-135 is on the surface and hence doesn't experience much change in its local environment as a result of BSA protein unfolding. τ_4 shows the most drastic change as the protein unfolds, this is because the local environment of Try-214 will change drastically as the protein unfolds. τ_2 also reinforces a change in intensity and wavelength shift as the protein unfolds. The emission wavelength maxima of tryptophan redshifts when

158

the residue in a protein is exposed to a polar solvent which reinforces the fact that Try-214 is being exposed to water as the protein unfolds. Since there are two tryptophan residues in BSA and tryptophan in solution has a bi-exponential decay, one might suspect a 4 exponential decay. τ_2 has a relatively large error and is likely to be a combination of the shorter decay times in both Try-135 and Try-214. The difference between the short components of these two residues is not large enough to resolve out each component separately which is one experimental limitation of Decay Associated Spectra.

2.3.12 Time Resolved Excitation Emission Matrix (TREEM) and Decay Associated Excitation Emission Matrix (DAEEM)

Since most time-resolved systems utilise series of NanoLEDs or DeltaDiodes which are discrete laser diodes it is not usually possible to run an excitation spectrum on these configurations for this reason DAS, DAS$^{\mathrm{W}}$ and TRES are commonly assumed to be emission spectra. The excitation source used for **Figure 121**-**Figure 129** was a NKT super-continuum laser so it is possible to change the position of the excitation monochromator, while holding the emission monochromator steady to make an excitation spectrum and Time-Resolved Excitation Spectrum **Figure 133**. Strictly speaking the laser profile will change with respect to excitation wavelength but use of a single prompt at the emission wavelength 545 nm sufficed to bring out a satisfactory DAS$^{\mathrm{W}}$ again using the decay times 4.01 ns and 7.4 ns from the decay of the mixture at the excitation wavelength of 525 nm and emission wavelength 545 nm **Figure 122**. As discussed previously with excitation spectra one has to account for the differing power of the excitation source with respect to wavelength as well as an XCorrect and MCorrect to account for the non-linear response of the optics and detectors. As the FluoroCube Extreme has no reference photodiode the sample compartment was removed so a HORIBA RAD-f Radiometer/Photometer could be seated in its place. This allowed a relative R to be recorded, a super-continuum laser is much more stable than the output of a Xenon lamp so this R can be assumed not to drift substantially in time. The HORIBA RAD-f Radiometer/Photometer had a known spectral response and this was used to create an XCorrect. The dark offset of the HORIBA RAD-f Radiometer/Photometer was assumed to be negligible. The MCorrect was measured before using the tungsten calibration lamp and the dark offset for emission as mentioned earlier is not required as dark counts are taken into account when using reconvolution analysis.
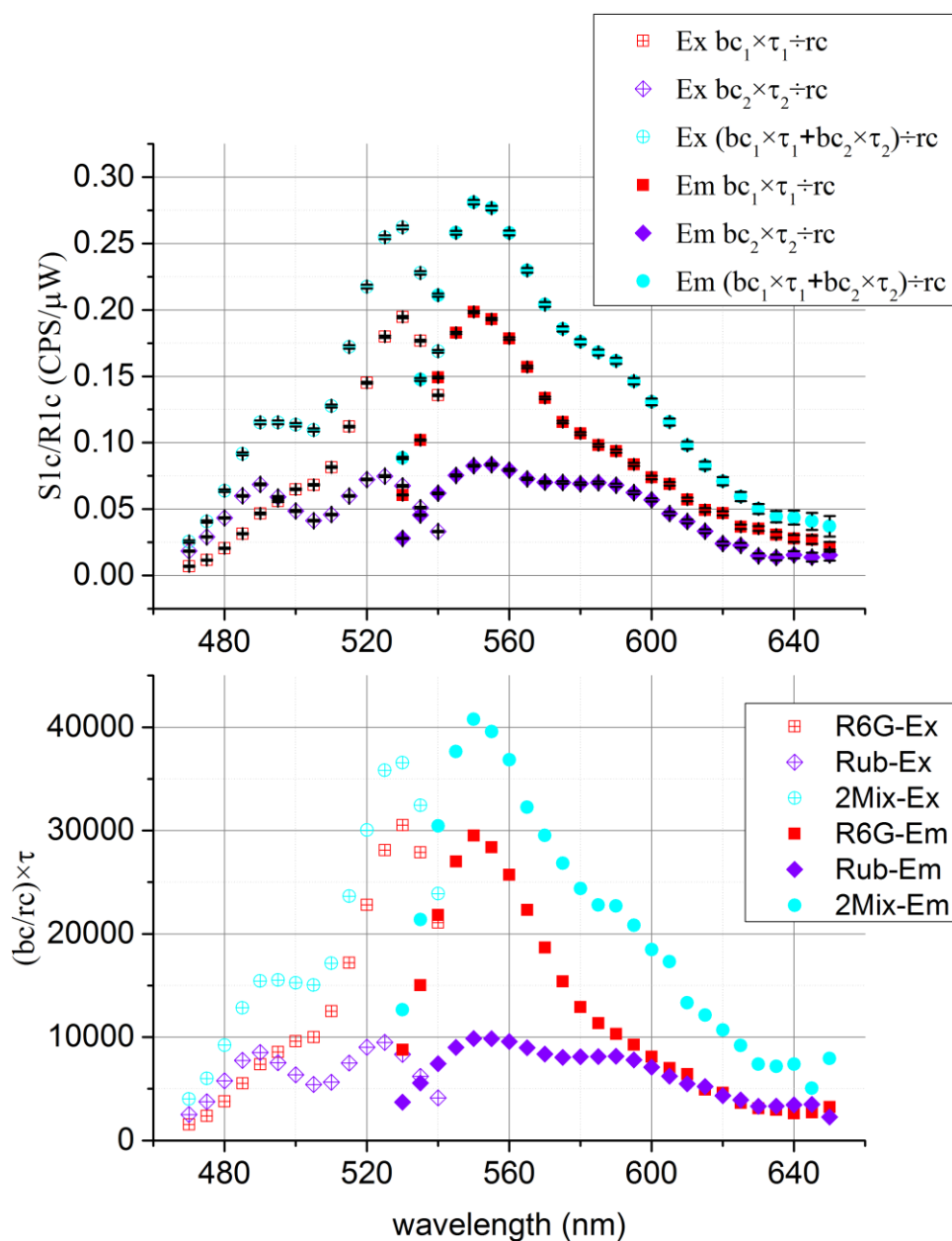
Figure 133: Excitation and emission steady-state spectra measured in a FluoroCube Extreme. For the excitation scan the emission monochromator TDM800 (1200/350 grating) was set to a bandpass of 8 nm at 545 nm and the excitation monochromator TDM800 (1200/350 grating) was set to a bandpass of 8 nm and scanned from 470-540 nm in 5 nm increments. For the emission scan the excitation monochromator TDM800 (1200/350 grating) was set to a bandpass of 8 nm at 525 nm and the emission monochromator TDM800 (1200/350 grating) was set to a bandpass of 8 nm and scanned from 530-650 nm in 5 nm increments. Polarizers were at VM and Hub A timing electronics were used in reverse mode with a TBX650. An integration time of 15 s per point was selected. The decay times were fixed to 4.01 ns and 7.4 ns taken from **Figure 122**. The spectra measured are Rhodamine 6G, rubrene and a mixture of both solutions 1:1 in methanol solvent. This data is equivalent to the S1c/R1c signal measured in a Fluorolog or Fluoromax.

As discussed earlier two of the most powerful spectroscopy techniques the Decay Associated Spectra (DAS) and Excitation Emission Matrix (EEM) are often employed together. Their union hence could result in a very powerful spectroscopic measurement. With a super-continuum excitation source one may now advance the measurement further and measure a series of Time Resolved Emission Spectra at incrementing excitation wavelengths. This creates a 4 dimensional Time-Resolved Excitation Emission Matrix (TREEM). Reconvolution analysis on the raw data can be used to plot out the pre-exponential factors with respect to excitation and emission wavelengths for each component to make an uncorrected Decay Associated Excitation Emission Matrix (DAEEM). Correction factors and weighting by decay times can finally make the corrected DAEEM^W. Under the same experimental parameters as **Figure 133** a series of TRES measurements (5 nm increments) were ran at varying excitation wavelengths (5 nm increments). To save time data was only recorded at wavelengths where the emission was greater or equal to the excitation wavelength. Each TRES was fitted to a 3exponential model with $\tau_1 = 28.3$ ps (fixed), $\tau_2 = 4.01$ ns (fixed) and $\tau_3 = 7.4$ ns (fixed). **Figure 134** shows data from the first uncorrected component of the DAEEM with $\tau_1 = 28.3$ ps (half a channel), this short lived component is most prominent at the Rayleigh line as expected. There is also a slightly negative artefact, perhaps due to a misfit between the decay and prompt i.e. fitting a negative pre-exponential to this short decay time instead of using the correct shift value. The other two components are of more interest, for a direct
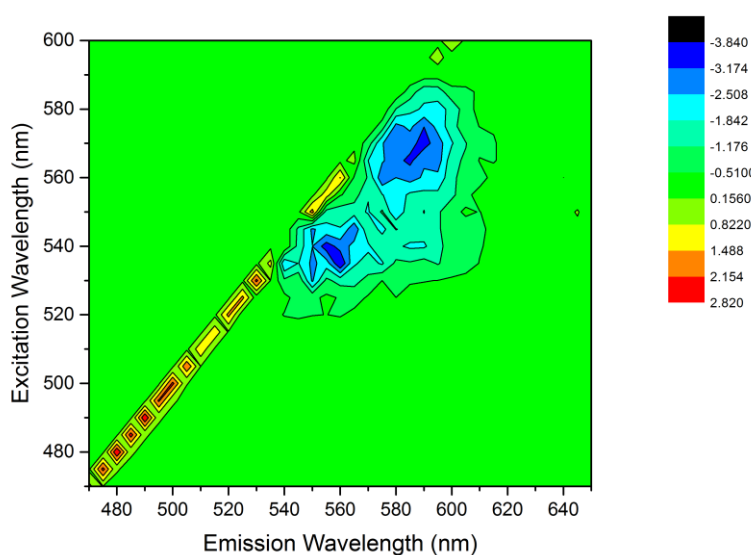
Figure 134: The uncorrected first component of the DAEEM. The first component fixed to half a channel (28.3 ps) was attributed to scatter. A plot of the first uncorrected pre-

exponential factor forms the first uncorrected component of the DAEEM. The Rayleigh lines as expected show the highest intensity of scatter. There is also a small negative artefact.
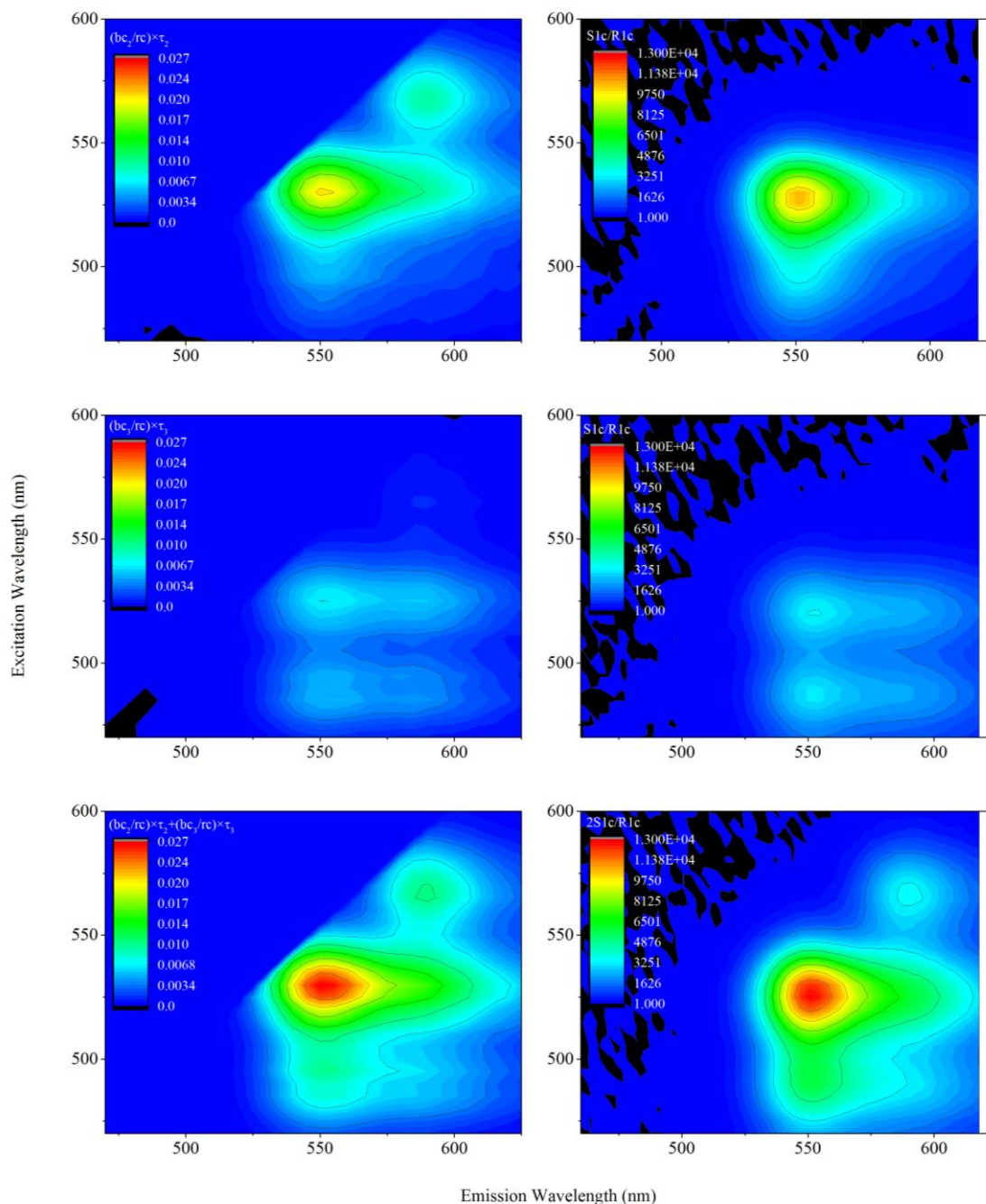
Figure 135: The DAEEM^W of the 4.01 ns component (top left), the 7.4 ns component (middle left) and the sum of both components (bottom left) compared to the EEMs measured on the Aqualog for Rhodamine 6G **Figure 65**, Rubrene **Figure 67** and the 1:1 mixture of both **Figure 69** multiplied by two.

comparison they are plotted side by side with their steady-state EEMs measured in an Aqualog **Figure 135**. In both datasets the colour map is set up for the mixture. The first 4.01 ns DAEEM^W greatly resembles the EEM of Rhodamine 6G and the 7.4 ns DAEEM^W greatly resembles the EEM of Rubrene. The DAEEM^W mixture resembles the 2× the EEM of a 0.5:0.5 mixture of Rhodamine 6G and Rubrene. In the mixture there is additional fluorescence emission at an excitation wavelength of 565 nm and emission wavelength of 590 nm. The cause of this additional emission is unknown; it is unlikely to be molecular interaction due to the low concentration of fluorophore used in these samples and other effects such as energy transfer should influence the decay times and overlay with the existing EEMs. Aggregation of fluorophores is also unlikely due to the stability of both samples and the low concentrations used in the mixture. The DAEEM^W of Rhodamine 6G shows the bulk of this additional component suggesting its decay time is on the similar order of Rhodamine 6G or perhaps is additional from Rhodamine 6G. The TREEM is an advanced fluorescence measurement yet to be widely adopted due to the high cost and limitations of the super-continuum laser and the relatively high acquisition time due to the use of two scanning monochromators and finally the associated difficulty of analysing a complicated dataset however they likely will have significant future potential as a spectroscopic technique. Once the cost of hardware goes down and data analysis is made easier for this type of measurement it may be a valuable extension to PARAFAC analysis.

2.3.13 Kinetic TCSPC

Kinetic TCSPC is the time evolution of the fluorescence decay [228]. It employs the heart of the TCSPC technique taking full advantage of the DeltaHubs timing electronics. The main difference between standard TCSPC and Kinetic TCSPC is that the dataset is binned into micro-acquisition t_k windows over a macro-acquisition time t_n as shown in **Figure 136**. Kinetic TCSPC on a DeltaFlex has several advantages to a steady state kinetic measurement on the Fluorolog as the fluorescence intensity is reported in addition to the fluorescence decay times and their appropriate amplitudes. One can therefore analyse the time-resolved data to further investigate a kinetic reaction by looking at reactants and products separately. A laser source or diode has a much steadier output than the xenon-arc lamp; therefore, there is no need to divide the kinetic data taken from a time-resolved system by a reference. The output of a DeltaDiode source is stronger than the xenon-arc lamp. Kinetic TCSPC data may be analysed as a batch file, fitting each decay curve individually to a series of
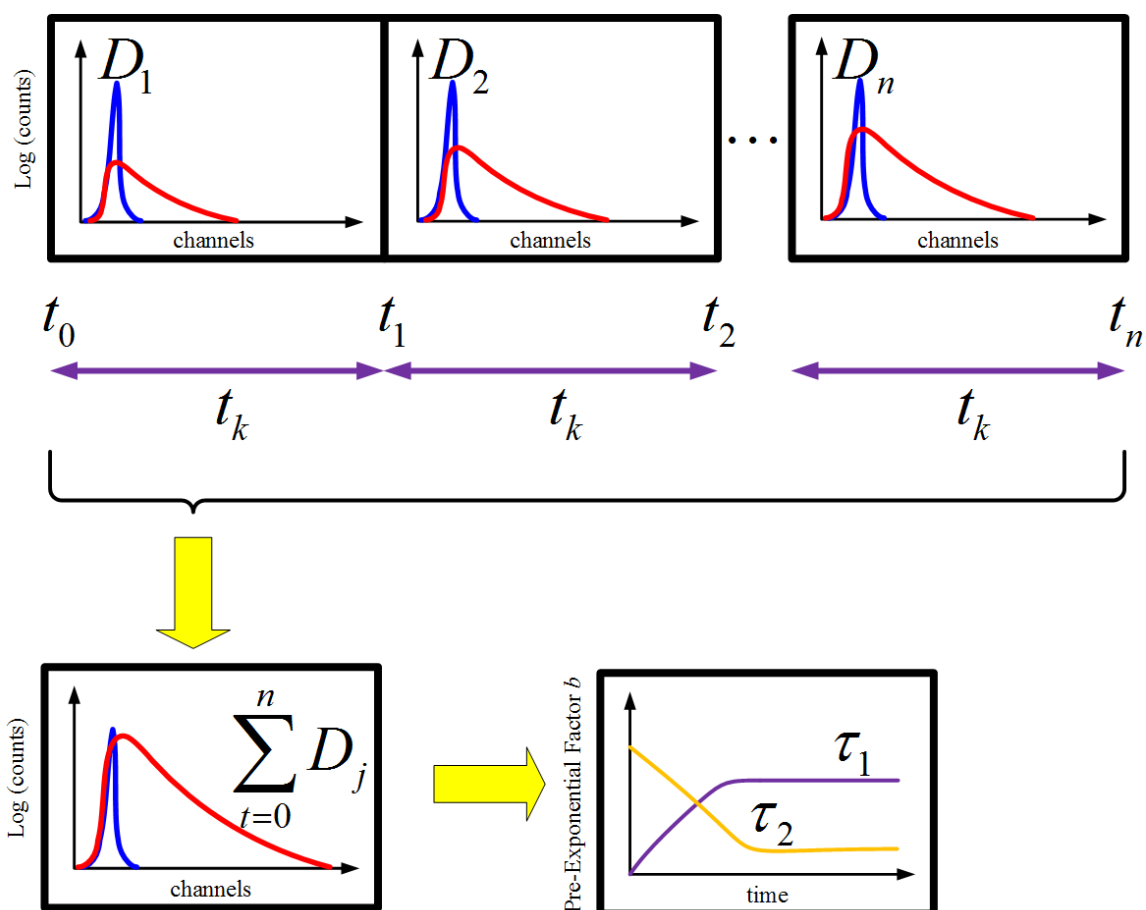
Figure 136: Illustration of Kinetic TCSPC. A fluorescence decay curve of a kinetic system which increases its fluorescence output with respect to time is collected during the macro-time interval t_n and binned into micro-time intervals t_k. The Kinetic TCSPC may all be binned into one decay curve which is what a normal TCSPC measurement would yield.

exponentials. The restriction for the batch file is usually 100 decay curves. To demonstrate kinetic TCSPC with a batch scan a simple system will be used. Fluorophores with a long decay time are usually heavily influenced by quenchers; one particularly common quencher is molecular oxygen. Rubrene in spectroscopic grade methanol will be used as an example **Figure 137**. The fluorescence lifetime of rubrene measured under standard conditions is 7.67 ns, when the system is nitrogen purges it is 9.74 ns. The dimensional Henry solubility H^{CC}=0.246 [229], multiplying this by the gas constant and temperature gives the Henry solubility defined by concentration H^{CP}=0.010 mol L^{-1} Atm^{-1}. Assuming 21 % of oxygen is in the air this gives the concentration of oxygen in methanol [Q] to be 0.002 mol L^{-1}. From **Equation (14)** k_Q=1.3×10^{10} mol l^{-1} s^{-1}.

164
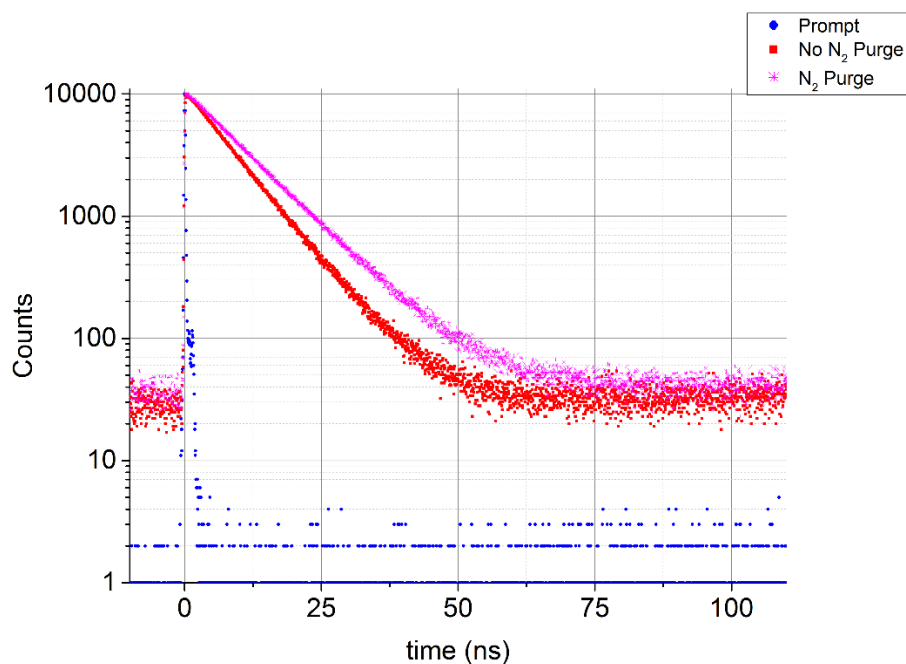
Figure 137: The fluorescence decay time of Rubrene in methanol measured in a DeltaFlex with a TBX850c detector. A DD482L was connected to the excitation port and the emission monochromator TDM800 (1200/350 grating) was set to 575 nm with a bandpass of 16 nm with excitation and emission polarizers at V and M respectively. Each decay curve was measured using a peak preset of 10000 counts with and without N_2 purging. The prompt was measured to 10000 counts with the emission monochromator set to the excitation wavelength 482 nm and the emission polarizer at V. The N_2 purge removes molecular oxygen and the decay time is observed to increase from $\tau_{Room}=7.67\pm0.02$ ns ($\chi^2=1.185$) to $\tau_{Purge}=9.74\pm0.03$ ns ($\chi^2=1.153$). The second decay time matches the accepted value [76]. The time for acquisition was 69 s and 65 s respectively. The DeltaHub wias set to a time range of 200 ns (4000 channels).

Since N_2 is being slowly added to the system and more importantly slowly displacing any dissolved molecular oxygen in the system, it's expected that the decay time changes continuously from 7.67 ns to 9.74 ns i.e. the measured decay time changes as a function of molecular oxygen concentration. This system can be also examined in more detail with a kinetic TCSPC **Figure 138**. For a successful kinetic TCSPC measurement two experimental time parameters are important, the integration time per decay measurement and the total acquisition time. The integration time should be large enough in order to allow each individual decay to have sufficient counts to fit but it should be constrained to prevent an individual decay from reaching 65,000 counts which is the upper limit for the DeltaHub (16 bit channels). In this case it took about 69 s to get 10,000 counts in the peak so a time increment of 15 s will have about ~2,000 counts in the peak and is appropriate. **Figure 138** shows the increase in fluorescence lifetime and fluorescence intensity with respect to time purged with N_2 gas. The lifetime and fluorescence increase due to a reduction in collisional

quenching as the oxygen is displaced from the system. The ratio of the ending to starting intensities equals the ratio of ending to starting intensities 492950 counts /382497 counts=9.74 ns/7.67 ns=1.282 as expected from **Equation (14)**, this means that the concentration of dye hasn't changed during the purging i.e. methanol solvent hasn't evaporated.
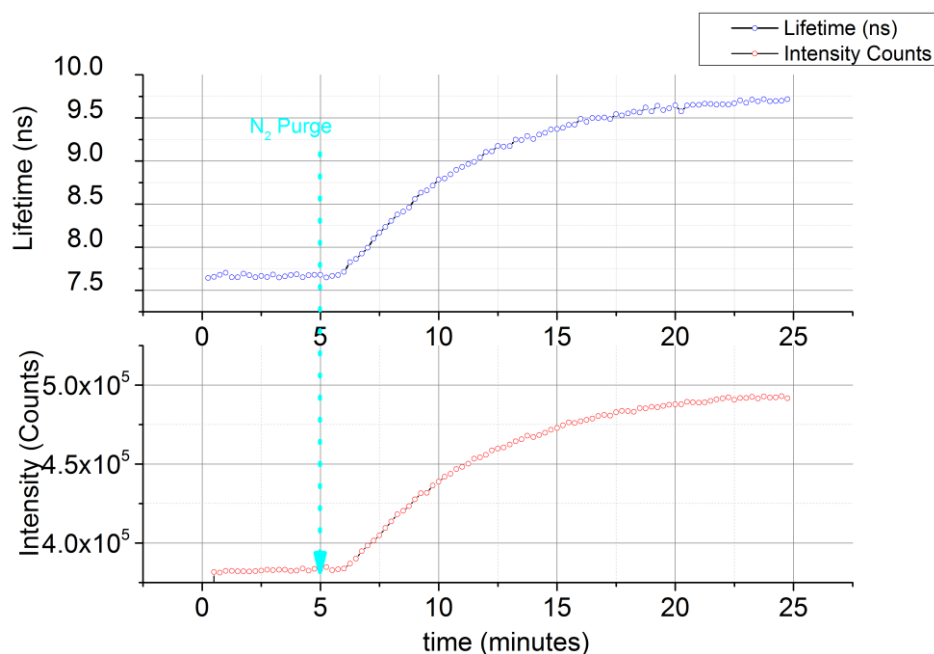
Figure 138: The kinetic TCSPC of rubrene in methanol measured in a DeltaFlex with a TBX850c detector during N_2 purging. A DD482L was connected to the excitation port and the emission monochromator TDM800 (1200/350 grating) was set to 575 nm with a bandpass of 16 nm with excitation and emission polarizers at V and M respectively. 100 sequential decay curves were measured for 15 s integration time. At the start of the measurement the prompt was measured to 10000 counts with the emission monochromator set to the excitation wavelength 482 nm and the emission polarizer at V. Both sets of data fit well to a Boltzmann distribution.

This dataset was a series of discrete fluorescence decay times and each curve had sufficient counts to determine its decay time. Often the number of photons counted isn't so high and there may be complications constraining conditions at the start of the reaction to ensure the stronger fluorescence emission at the end of the reaction doesn't exceed 65000 counts per decay or vice versa. In many cases a kinetic reaction may involve products and reactants with distinct fluorescence decay times. In such a case the data can be summated from all individual decay curves and this sum may be fitted to a series of exponentials to determine the decay times. Alternatively, a suitable representative decay curve may be selected and fitted. The global fit then uses these decay times to fit each decay curve and yields a readout of the normalised pre-exponential b amplitudes for each decay curve. These can be plotted

166

with respect to time and any changes in gradients of these can be prescribed to the kinetics of the reaction under investigation. Kinetic TCSPC will also give a readout on the average lifetime and the fluorescence intensity with respect to time.

2.4 Confocal Microscopy

This section gives an overview of the confocal microscopy and developments to surpass the conventional diffraction limit necessary for nanometrology.

2.4.1 Confocal Microscopy Techniques and the Diffraction Limit

Up until this point, cuvette based fluorescence measurements were mainly discussed, i.e. samples in solution that are homogeneous. Positional information of fluorescence can be measured by use of a microscope [230] for instance the standard confocal microscope for example the inverted microscope **Figure 139**. The standard confocal microscope typically uses an optical fibre [231] to allow light through from the excitation source; this can be a set of laser(s) or a xenon lamp with an excitation monochromator. In general, a dichroic mirror, pinhole and bandpass filter are used to separate out the excitation light from the fluorescence. The sample is usually on a slide or on a chamber and moved to position on a calibrated stage. It is possible to add other components to the system such as a monochromator or spectrograph on the emission; as well as excitation and emission polarizers depending on the specific application. If a laser is used as an excitation source and a PMT is used as a detector, timing electronics may be added to the system to perform fluorescence lifetime imaging microscopy [232]. Essentially all the measurements discussed in the previous section can be carried out in a microscope giving fluorescence data of a sample with respect to position. Calibration objects for instance a stage micrometre can readily be used to calibrate a conventional microscopy image [233]. The applications of confocal microscopy are very wide, especially in the life science field, where it is used on a daily routine. Much of the principles discussed above with steady-state and time-resolved measurements can equally be applied to microscopy with the additional dimensions in x, y and z. To change the position of the sample typically a translation stage is used. Light is focused onto the sample using an objective lens which can be placed above or below the sample, below the sample is usually preferred as it allows the use of chambers as well as microscope slides. If a PMT is used as a detector the stage must be moved in x, y with respect to the objective and PMT. The fluorescence intensity or decay curve can be acquired by using a fixed integration time per co-ordinate.
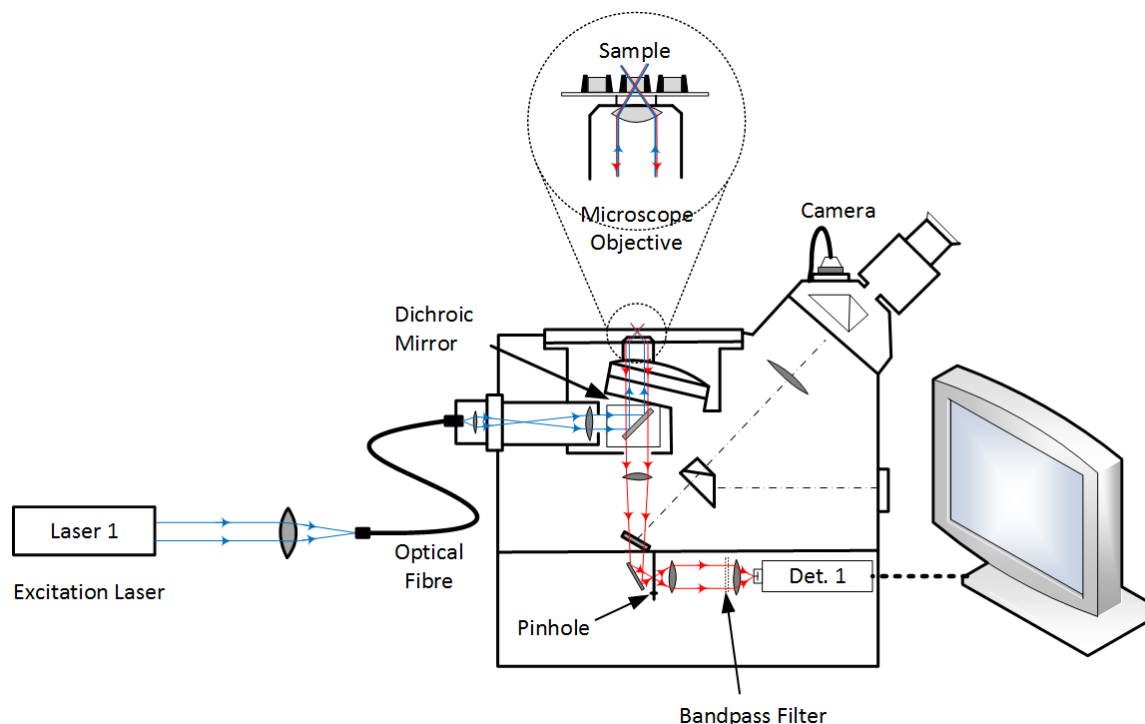
Figure 139: Illustration of an inverted confocal microscope, the sample is excited by a xenon lamp or laser which is fed through an optical fibre. The excitation light is then focused onto a dichroic mirror which directs the excitation light through the sample. Once the sample is excited, fluorescence photons are let through the dichroic mirror and focused through a pinhole. A bandpass filter is placed in front of the detector to reject any stray excitation light.

Theoretically all the measurements discussed in the earlier sections can be done on a microscope. The practicality of scanning in another 2-3 dimensions and complexity of data however prevents many of the advanced measurements from being carried out routinely. The measurement of a TREEM in x, y and z would for instance be a 7 dimensional dataset! For this reason, it is more common to use a set of discrete laser as excitation sources for confocal microscopy with a set of emission filters opposed to two monochromators and a xenon lamp. It is also more common to use an imaging CCD [234] opposed to a PMT because it has the advantage of being able to measure the intensity of each of its pixels simultaneously. Hardware wise in order to measure a confocal microscopy image, clearly the image from the sample has to be projected to the detector which is typically a CCD. The CCD has to have enough pixels and the optics have to give enough magnification to see the object being measured. Naturally in order to measure fluorescence in a pixel an object such as a fluorophore that exhibits fluorescence for the selected λ_{ex}, λ_{em} needs to be within close proximity to the pixel. The Nyquist sampling theorem must be satisfied which is:

$$d_f \approx \frac{d'}{2} \qquad (66)$$

where d_f is the minimum separation between fluorophores for the distance d' [235]. The Nyquist criterion is shown pictorially for a simple straight line **Figure 141**. In microscopy measurements particularly for weak fluorescing samples one has to make a trade-off in resolution and in sample spacing. Naturally if one opens up the pinhole of the confocal microscope the intensity will increase as more fluorescence emission is allowed to reach through to the detector however the resolution per point will decrease. Like the monochromator bandpass and wavelength spectral resolution; for microscopy measurements there is a trade-off between the pinhole and positional resolution. The fluorescence throughput and integration time must be carefully tailored in the same manner.
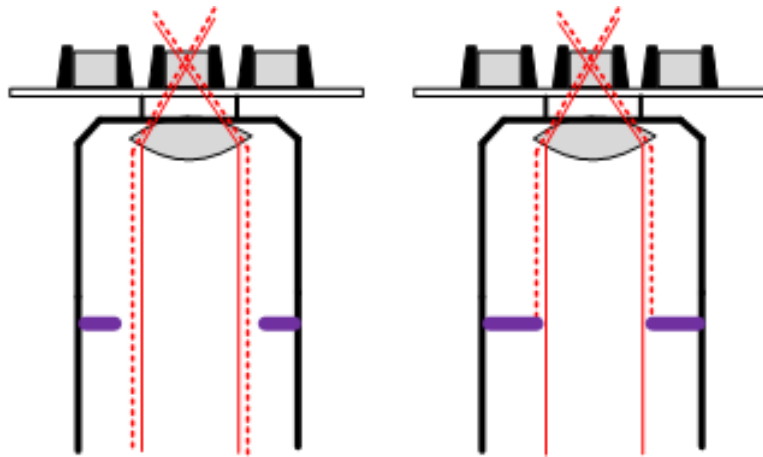
Figure 140: Simplified schematic of a sample exhibiting fluorescence from a plane in focus (solid line) and an out of focus plane (dotted line). When the pinhole (purple) is wide, fluorescence from both planes is allowed to pass through to the detector. When the pinhole (purple) is narrow, fluorescence from the plane in focus is allowed to pass through to the detector and out of focus fluorescence is blocked by the pinhole.

For a strong sample the pinhole **Figure 140** may be constrained to the size of the Airy diameter. The Airy diameter is the diameter of the first dark ring, generated by destructively interfering diffracted wavefronts for a single point emitter **Figure 142** [236]. The Airy diameter:

$$d_{Airy} = \frac{1.22\lambda}{2(n\sin\alpha)} = \frac{1.22\lambda}{2NA} \qquad (67)$$

where n is the refractive index of the medium between the object and the objective, and α is the half-angle of the collected rays from the object point. NA is the numerical aperture $NA = n\sin(\alpha)$. One can use a pinhole to confine the emission an Airy diameter of 1 or 0.5

which will give the maximal diffraction limited resolution. As two point sources approach the Airy diameter **Figure 142**, the constructively and destructively interfering wavefronts from each source become indistinguishable and one cannot resolve the two single point sources [237]. Taking for example green visible light (500 nm) and well-designed optics with NA≈1 then the diffraction limit is approximately 250 nm or 0.25 μm. From **Equation (66)**, closely spaced fluorophores are required to image a sample at higher resolution however from **Equation (67)** two separate fluorophores cannot be resolved at a separation of <0.25 μm. This restricts the resolution to ~0.25 micrometre hence the name microscope. It is possible to perform most of the steady state fluorescence and time-resolved fluorescence based measurements above the diffraction limit given the right hardware configuration and fluorophore.
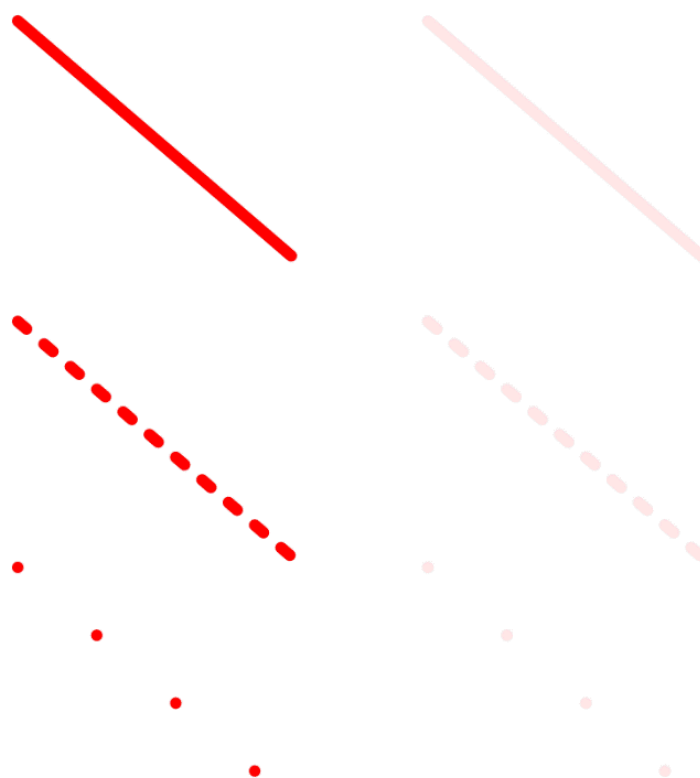
Figure 141: Schematic of the Nyquist sampling criterion. Top left, a line drawn solid, dashed and in dotted formats. The Nyquist sampling for the ink in each line is clearly different in the case of the solid line to the eye one can clearly state that it is a straight line, the dashed line on the other hand still has enough points and enough spacing to be called a straight line. The dotted line at the bottom only has 4 points these are widely spaced, there is not enough data to prescribe these 4 points as a line. To the right are the same lines drawn with lower transparency, these lines are much harder to visualise as the red line (signal) to white page (noise) is much lower.
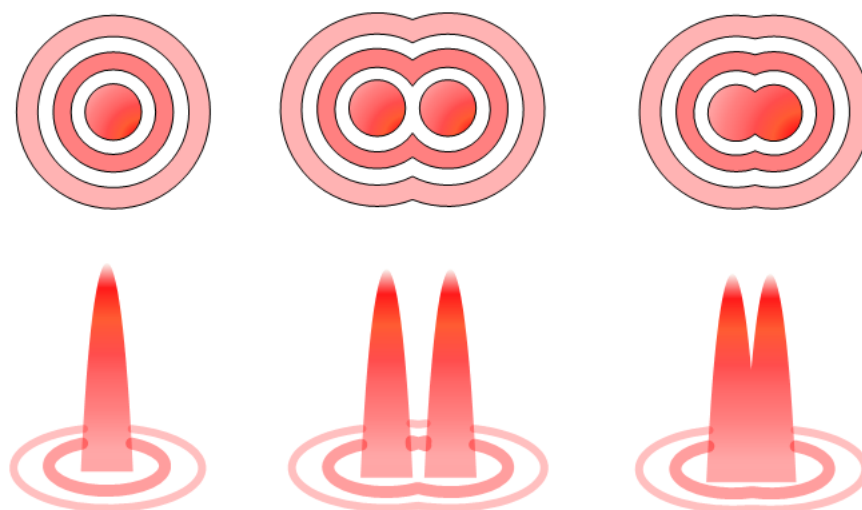
Figure 142: Airy disc in *x,y* and x,*z* for a single point emitter (left). There are a series of maxima and minima generated by constructively and destructively interfering wavefronts respectively. The Airy disc is defined as the diameter of the first dark ring, generated by destructively interfering diffracted wavefronts. The Airy disc in *x,y* and x,*z* for two single point emitter (middle), the two airy discs are far enough apart that they can be distinguished meaning the two single point emitters can be resolved. As these two sources are moved closer together (right), the two airy discs become indistinguishable and cannot be resolved.

Single molecule behaviour of bright fluorophores can be routinely measured in extremely dilute concentrations however in order to form a standard microscopy image, multiple points are required and for a resolution on the molecular level a vast number $>10^5$ fluorophores must be present per μm^2 [238]. Clearly the mandatory requirement of Nyquist labelling **Figure 141** conflicts with the diffraction **Figure 142** and is problematic when one wishes to acquire higher-resolution data using conventional methods. For this reason, most nanometrology measurements are indirect and deal with low concentration samples in solution inferring the particle size indirectly by use of Brownian motion. Nanoparticle Tracking Analysis is a light scattering technique which utilises Rayleigh scattering and Brownian motion to determine nanoparticles using their motion. In NTA the nanoparticles are individually tracked and their particle size is determined from the solvents viscosity, temperature and their overall motion. NTA can be used for nanoparticles that are >50 nm in size. As the size of the nanoparticle decreases the Rayleigh scattering of the nanoparticle becomes difficult to distinguish from the Rayleigh scattering from solvent molecules. To increase sensitivity fluorescence labels can instead be used. In Fluorescence Correlation Spectroscopy (FCS) one examines the steady-state fluorescence fluctuations within a ~ fL (10^{-15} L) volume brought about as systems labelled with fluorophores diffuse in and out

172

due to Brownian motion. One can look at the autocorrelation of these fluctuations to obtain the nanoparticles diffusion time which in turn can be used to determine the nanoparticles size [239–241]. This technique can be performed with multiple labels and colours such as in Fluorescence Cross Correlation Spectroscopy (FCCS) or combined with fluorescence lifetime measurements to filter out different species as in the case of Fluorescence Lifetime Correlation Spectroscopy (FLCS) [242]. Time-Resolved Fluorescence Anisotropy (TRFA) which was discussed in detail previously can also be used to determine nanoparticles size without use of a microscope using the rotational correlation time which embeds information regarding polarized fluorescence. Naturally techniques such as FCS can be combined with TRFA [243]. Unfortunately, all these techniques while they have their uses suffer from the limitation of low concentrations, the difficulty to distinguish more than a handful of species and the difficulty of determining shape of the object in question. As a consequence, limited information is available on the complex interplay of individual molecules on the single-molecule level. Expensive scientific instrumentation such as atomic force microscopes (AFM) have been available for some time but have the additional disadvantage of complicated sample preparation. This typically involves drying out the sample which can severely alter a biological sample particularly on the single-molecule level. Having reliable fluorescence positional information within the nanoscale could lead to a significant increase in the understanding of biological systems.

2.4.2 Confocal Nanoscopy Techniques

This diffraction limit is unfortunately 1-2 orders of magnitude then the typical molecular length scales in biological objects such as cells [244]. **Figure 143** depicts the size and scale of common biological objects alongside fluorescence measurement techniques. The techniques revolving around Brownian motion give limited information however a cell is arguably much, much more than merely the sum of its individual components. An array of endless questions pushes the need to be able to look at individual cellular components and their interplay but this in turn is blocked from view by the diffraction limit. Thus there is a demand to image at a higher resolution than the conventional diffraction limit i.e. to image in the nanoscale which traditional diffraction-limited confocal microscopy techniques cannot handle. Techniques which surpass the diffraction limit are collectively marketed as super-resolution microscopy techniques however by definition they may also be referred to as Nanoscopy [245]. The nanoscale is very important in the study of many cellular biological systems and having the ability to utilise fluorescence measurements for highly

packed complex samples within this scale would unlock a vast quantity of currently obscured information that is very difficult to measure and piece together using other measurement techniques. Super-resolution microscopy or nanoscopy should be thought of as the fluorescence measurement of highly packed single molecules and the removal of the interfering fluorescence signal from neighbouring single-molecules [246].
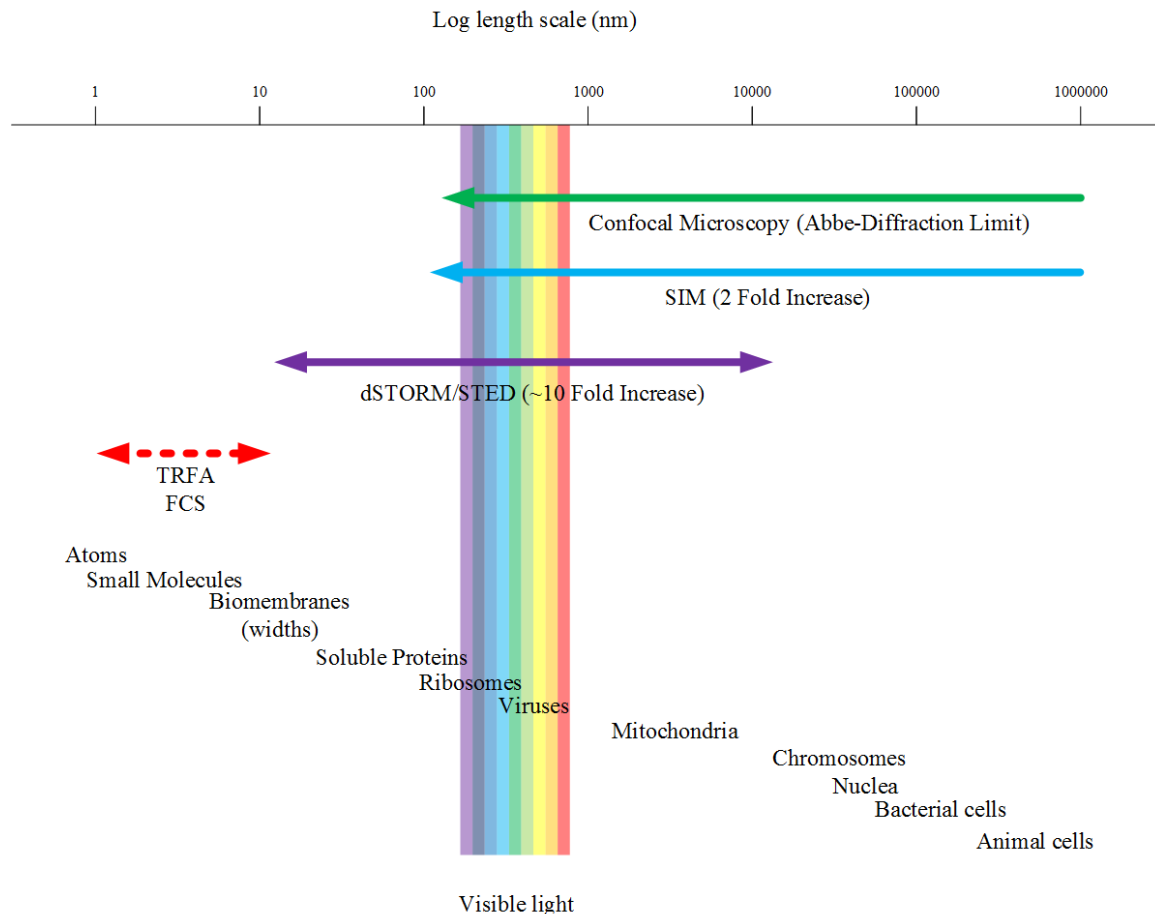
Figure 143: Illustration of the approximate size of biological structures on the nanoscale. Visible light is also shown. Microscopy techniques such as standard confocal microscopy, structured illumination microscopy, direct Stochastic Optical Reconstruction Microscopy and Stimulated Emission Depletion Microscopy are shown and nanosizing techniques which require dilute solutions such as fluorescence anisotropy and fluorescence correlation spectroscopy [247,248].

Super-resolution is typically tackled using 2 different directions; the first direction referred to as deterministic super-resolution involves changing the excitation or emission beam profiles from the traditional Gaussian shape to a smarter profile which has an inherently smaller diffraction limit or contains additional scrambled information which can be computationally extracted. The second direction is referred to as location microscopy which involves temporal-separation and subsequent reconstruction of fluorescence information. An example of deterministic super-resolution is Structured Illumination

Microscopy (SIM). For SIM the sample is illuminated with a pattern, typically the image of a grating [249] as shown in **Figure 144** [250]. The sample is imaged multiple times while the grid-pattern is rotated at various angles. In a linear SIM measurement, the grid is rotated about 0° to get I_1, 120° to get I_2 and 240° to get I_3 [251–253].
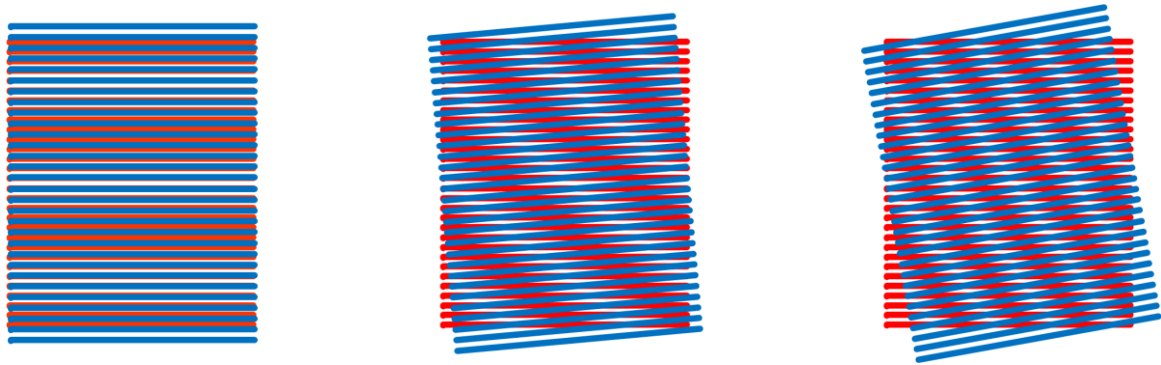
Figure 144: The top blue grid (known spacing) is used to image the bottom red grid (unknown spacing). The top grid has fringes of slightly wider spacing than the bottom grid and is tilted in this case at 0°, 5° and 10° for illustration. Regularly spaced Moire fringes can be observed which contain scrambled information about the unknown pattern of the underlying grid. As the angle between the grids is increased, the frequency of the Moire fringes increase. In a SIM higher frequency information can be unscrambled by taking an image at 0°, 120° and 240°. Decoding this higher frequency information allows for rejection of out-of-focus background and hence a sharper reconstructed image.

These three images are all spaced $2\pi/3$ apart. A super-resolution image 2× the resolution of the diffraction limit ~100 nm may be constructed by:

$$I_p = \left[(I_1 - I_2)^2 + (I_1 - I_3)^2 + (I_2 - I_3)^2 \right]^{1/2} \qquad (68)$$

This derivation is given in detail by Neil, M et al. [254]. The non-linear response of fluorescence emission at high laser-power causes additional harmonics. A harmonic of $n=3$ for instance will require images to be taken at a spacing of $2\pi/3n$ meaning 9 separate images are required opposed to 3. The need to acquire more images combined with the use of high laser power is a practical consideration that must be taken into account when trying to push this technique to its limits. Naturally the mandate to acquire more images makes reconstruction more computationally demanding [255]. This procedure is mathematically demanding. The next super-resolution technique is Stimulated Emission Depletion Microscopy (STED). The principle of stimulated emission is depicted in **Figure 45**. In Simulated Emission Depletion Microscopy (STED) [256] **Figure 146** the sample gets excited with a normal Gaussian blurred excitation beam. Fluorescence emission should likewise have a similar blurred Gaussian profile however the interaction with the STED

beam in a donut profile (also diffraction limited) removes a portion of the measured fluorescence by shifting it to a coherent higher wavelength that is hence blocked by the bandpass filter **Figure 145**. As the STED laser power is introduced the stimulated emission
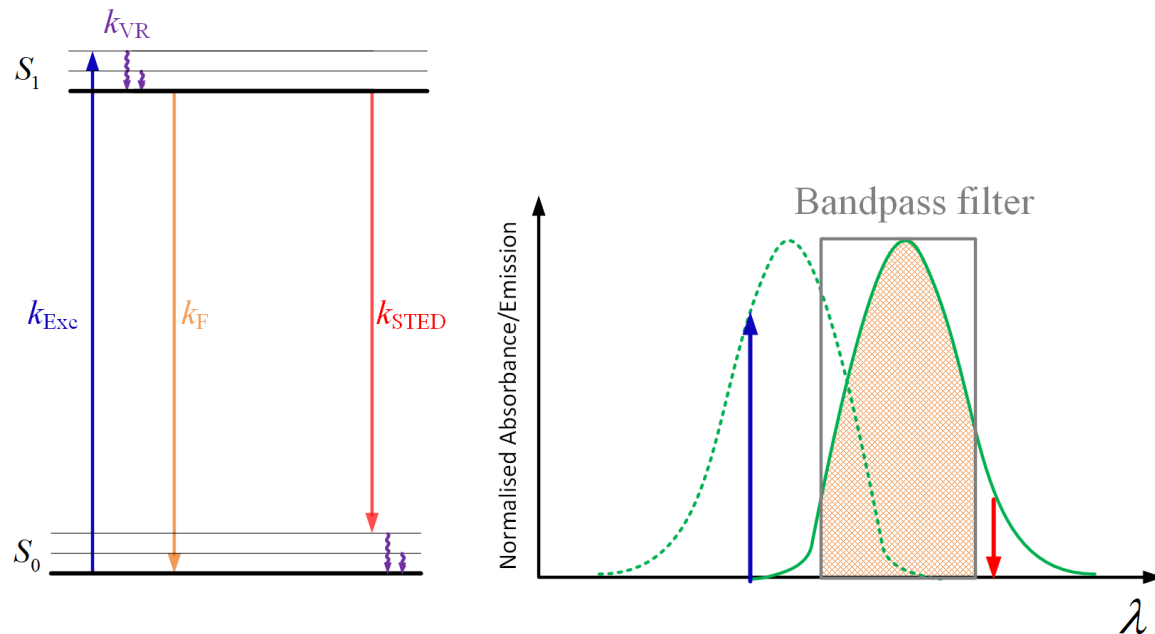
Figure 145: Jablonski diagram depicting absorption (blue) due to the promotion of an electron to the ground state to the excited state brought about by an excitation laser. Vibrational relaxation and standard fluorescence emission (orange) are also shown. The fluorescence can be stimulated to emit at a higher wavelength using stimulated emission (red). Stimulated coherent emission can be brought about using a second laser known as a STED laser. This STED laser is red-shifted with respect to the main emission peak of the fluorescence. Any remaining fluorescence emission can be measured separately from both the excitation laser and the STED laser using a bandpass filter.
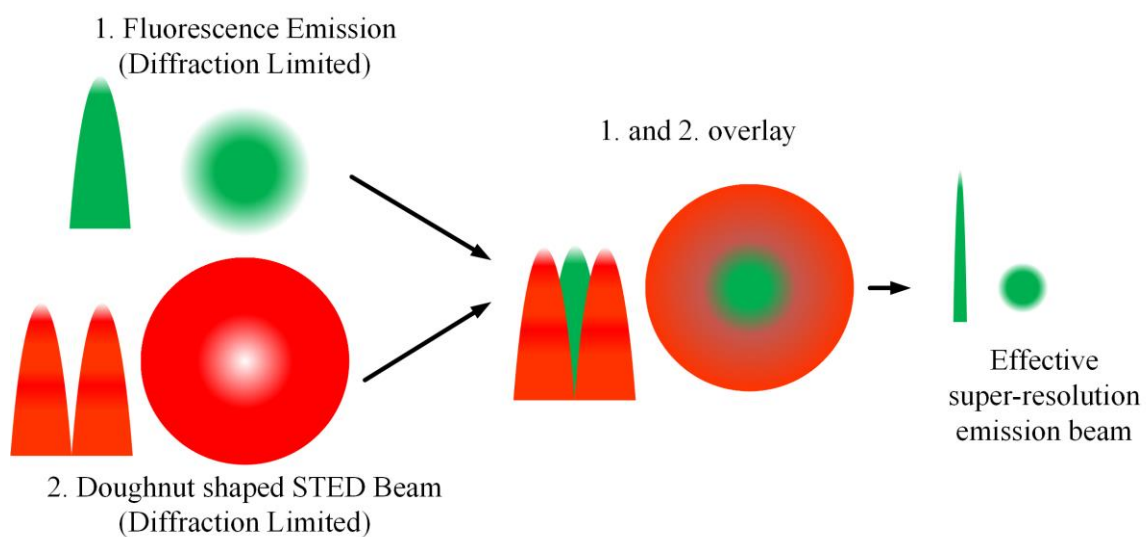
Figure 146: Principle of Simulated Emission Depletion Microscopy STED. The Gaussian diffraction limited excitation beam (1) is overlaid with the diffraction limited STED

doughnut shaped beam which removes fluorescence. This creates a smaller effective fluorescence emission beam which is beyond the resolution of the diffraction limit.

region expands and as a consequence the fluorescence signal can only be observed from a small region around the focal point which reduces the point spread function of the measured fluorescence emission [257] The principle is to create an "effective emission beam" with an extremely narrow profile. With such a narrow effective emission beam one can measure emission from a single fluorophore without interfering emission from its neighbouring fluorophores. This allows one to systematically measure the fluorescence emission of the fluorophores one by one in order to construct a super-resolution image. The main issues with STED are the fact that one has to utilise higher and higher laser powers in order to constrict the point spread function of the emission beam in order to enhance resolution. Naturally one has to then scan both beams across the sample (or alternatively move the sample with respect to the beams using an automated stage). In order to achieve super-resolution, the spacing between the pixels need to be adequate i.e. pixel spacing needs to become closer and closer for higher and higher resolution and as a consequence, the time to acquire an image may increase. Increased acquisition time at high laser power is undesirable. STED may also take advantage of photoswitchable (can be turned on and off) fluorophores which can be photoswitched by use of different wavelengths of light [258–263]. Other super-resolution techniques such as location microscopy also take advantage of photoswitchable fluorophores [264–266]. Location microscopy is in its essence a series of temporally and spatially resolved single-molecule fluorescence measurements and will be discussed in more detail below. The pioneering work in this field is extremely multi-disciplinary and was awarded the Nobel Prize in Chemistry in 2014 [267]. The work in this thesis will look at dSTORM in particular in the next section. Nanoscopy requires an even higher labelling ratio than normal microscopy techniques. Moreover the size of the fluorophore(s) and their affixed linkers will also become more important on the nanoscale as these may widen the structure being investigated.

2.4.3 Location Nanoscopy

The raw data for localisation microscopy is essentially a fast captured video. A series of frames are recorded at the highest resolution possible for as small a cycle time as possible. Localisation microscopy involves the use of stochastic fluorophores or "blinking fluorophores". The desired raw data is the measurement of single molecule blinks of

individual fluorophores without the influence of neighbouring fluorophores. i.e. time-resolve the single molecule blinks [268]. As such the success of location microscopy is intimately linked to single-molecule fluorescence studies [269]. Single molecule fluorescence behaviour has to be considered differently to ensemble fluorescence measurements mentioned above. Individual fluorophores will undergo blinking (on, off, on again), photobleaching (on, off forever) and will have a unique fluorescence lifetime. Single-molecule fluorescence is inherently much more sensitive. Although the fine details of diffraction limited object such as a single fluorophore are obscured by the diffraction limit, the measured fluorescence from a single molecule blink can be mathematically fitted to a Gaussian profile with the centre of the profile being indicative of the position of the fluorophore otherwise known as a localisation. A localisation can have nm precision [270].
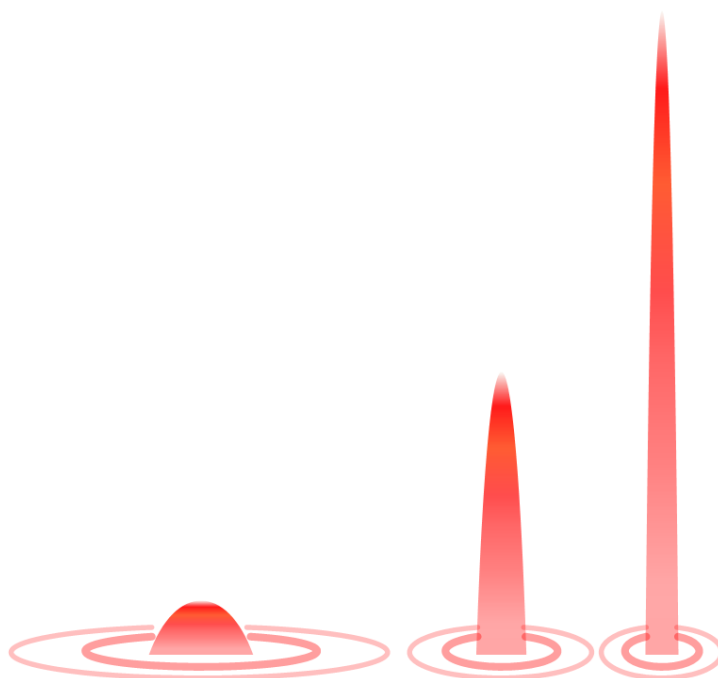
Figure 147: The concept of localisation of a single fluorophore. A single-molecule blink will give a diffraction limited blur. The central point of the fluorophore in the absence of any other fluorophores may be localised, that is fitted mathematically. A fluorophore which exhibits a Gaussian profile with a large number of counts and low background noise such as that shown on the right can be localised to a higher precision than a fluorophore with a low number of counts and higher background noise such as that shown on the left.

Theoretically a localisation of a single molecule could lead to infinite resolution. However, in practical terms the localisation precision Δx is dictated by a number of parameters. Naturally there are instrumental properties such as the side-length of the detector pixels a, the background noise level b which in the case of the CCD is influenced highly by the

readout noise of the CCD and of course the overall stability of the local environment including temperature; any changes in temperature will cause a drift in the system for super-resolution images. Finally, there is also the number of photons detected N. The random variance of is estimated by:

$$\left\langle \left(\Delta x^2\right)\right\rangle = \frac{s^2 + \frac{a^2}{12}}{N} + \frac{8\pi s^4 b^4}{a^2 N^2} \approx \sigma^2 \tag{69}$$

where the optical point spread function is approximately Gaussian and has a standard deviation s. **Equation (69)** may appear to be complex at first glance however assuming one has adequate pixels the main concepts may be shown pictorially in **Figure 47**. The positional errors for 2 dimensional circular symmetry, is assumed to be independently normally-distributed so that the probability density for a fluorophore with position x_0 to be localised at position x is $p(x)$:

$$p(x) = \frac{1}{2\pi\sigma^2} \exp\left(-\frac{|x - x_0|^2}{2\sigma^2}\right) \tag{70}$$

Assuming that each fluorophore is distinct a Dirac delta function can be used to represent M distinct fluorophores:

$$\rho_0(x) = \sum_{i=1}^{M} \delta\left(x - x_i\right) \tag{71}$$

The localisation microscope therefore identifies fluorophore positions obtained from the probability distribution:

$$\rho_m(x) = \frac{1}{M}\rho_0 \otimes p = \frac{1}{2M\pi\sigma^2}\sum_{i=1}^{M}\exp\left(-\frac{|x - x_i|^2}{2\sigma^2}\right) \tag{72}$$

The plot of localisations can be used to form a single image – a super-resolution image [271]. **Figure 148** illustrates mathematical localisation if two diffraction limited fluorophores with a simple 1D model. If they are measured simultaneously they cannot be resolved as one just measures a diffraction limited blur. If, however there is a means of measuring them temporally, that is to hypothetically measure fluorophore 1 without fluorophore 2 enabling the localisation of fluorophore 1 and then later measure fluorophore 2 without fluorophore 1 enabling its localisation then one can plot an image with both localisations. This reconstructed information will be super-resolution i.e. contain information beyond the diffraction limit. Naturally, having multiple points within the

179

diffraction limited area is also a mandatory requirement in order to construct a high quality "super-resolution" image. The labelling density is usually high so that multiple individual fluorophores lie within the diffraction-limited area. **Figure 149** illustrates the principle
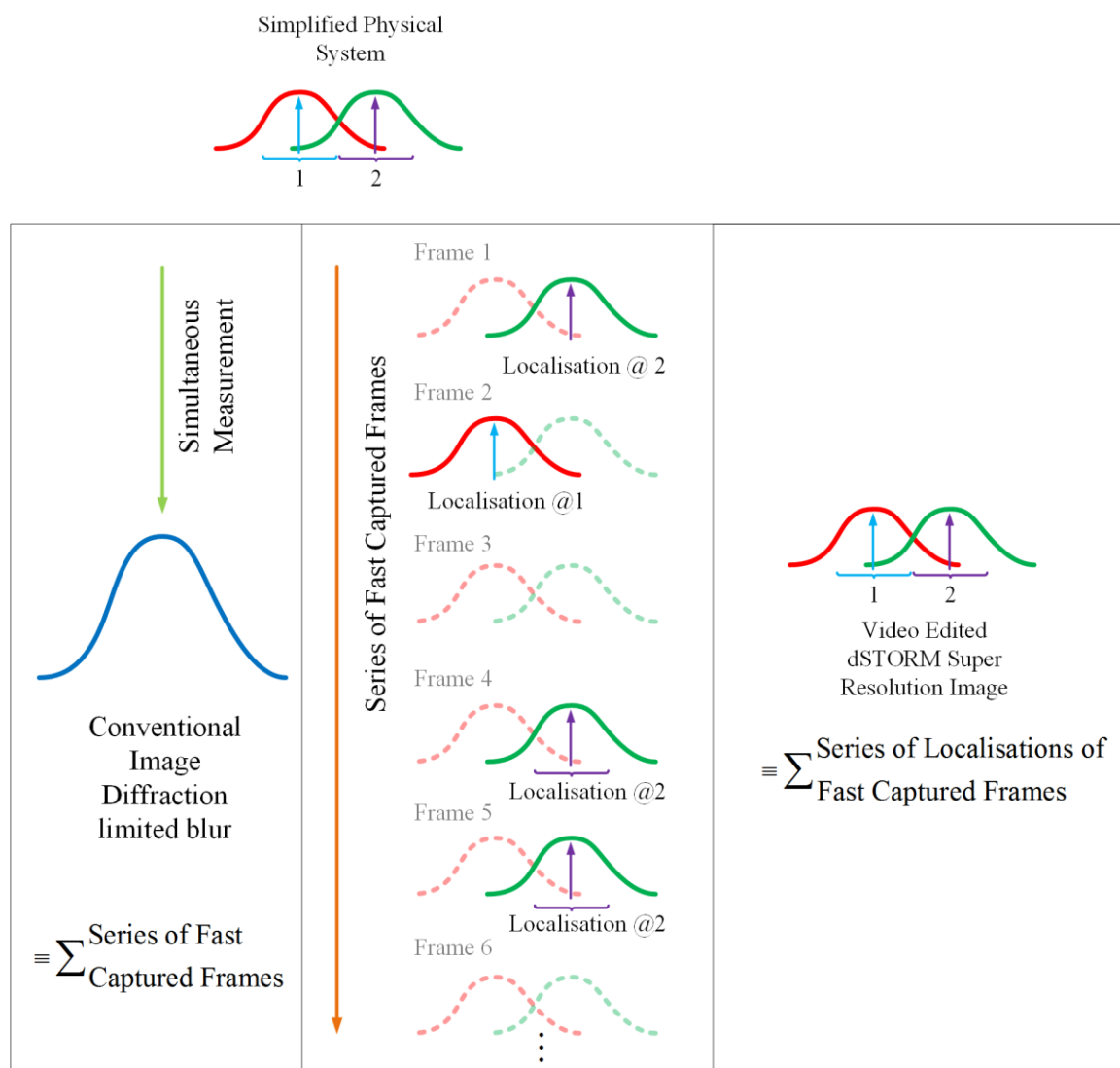
Figure 148: Simplified illustration of conventional fluorescence microscopy measurement (left) with a series of fast captured frames (right). In order to measure a series of fast captured frames conditions are setup so the two fluorophore are stochastically blinking; this stochastic blinking must be slow enough to match the capabilities of the fast imaging CCD, which must be setup with a suitable capture rate. The schematic in the middle indicated molecules are off with the faded, dashed line and on with the solid line. Moreover, conditions must be setup in a certain manner to enable measurement of 1 when 2 is off (e.g. frame 2) and 2 when 1 is off (e.g. frames 1, 4 and 5). In order to meet these conditions there will naturally be many frames when neither 1 nor 2 are switched on (e.g. frame 3) and only noise is measured. Good video editing will give the dSTORM super-resolution image, which should closer resemble the system being measured and bad video editing will give the same results as the diffraction limited blur. Naturally the more times each individual blink is measured, the more certain one may be of its localisation and hence resolution.

of location microscopy in 2D to form a super-resolution image. A super-resolution image is usually shown via a Gaussian visualisation plot of fluorescence intensity where each localisation is plotted as a small Gaussian blur [272,273].
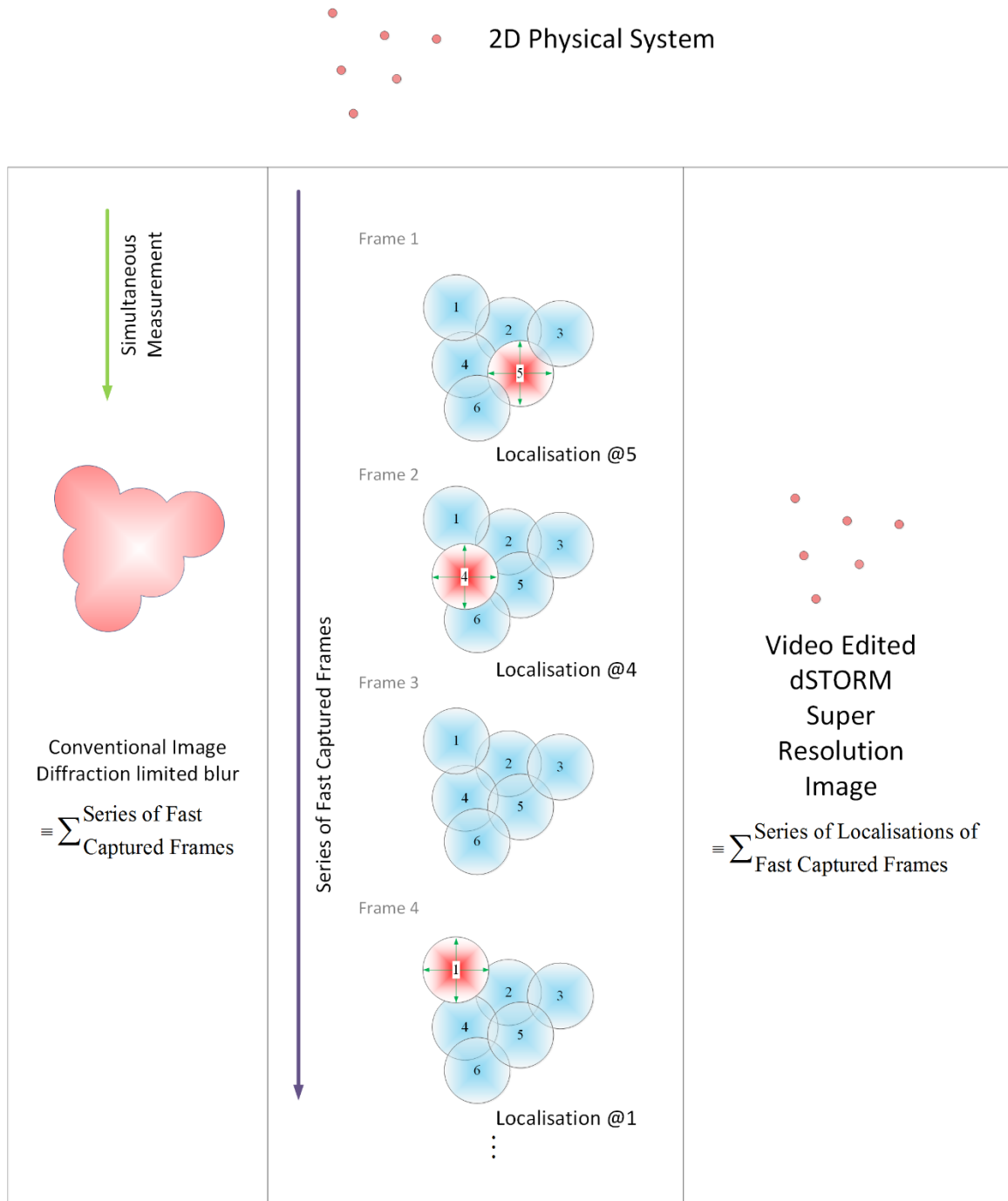
Figure 149: Principle of standard confocal microscopy and location microscopy in 2 dimensions. Fluorophores are used to label closely packed objects for example biological molecules within the diffraction limited volume. Each single molecule blink is localised in *x* and *y* and the summation of single molecule blinks is equivalent to the diffraction limited blur. The reconstructed super-resolution image of the localisations on the other hand overcomes the diffraction limit and find structure which was blurred out may be observed.

In laymen terms the super-resolution image is made by video editing the fast captured single molecule video data **Figure 150** by fitting each single molecule blink to the centre of a circle known as a localisation. All localisations are then mapped onto a single image and this image is "super-resolution". This mapped image otherwise known as a super-resolution image defeats the inherent limitation of the diffraction limit. Poor video editing, for example made by summing up all the individual images together, will simply restore the diffraction limited image that is normally measured. Treating each fluorophore
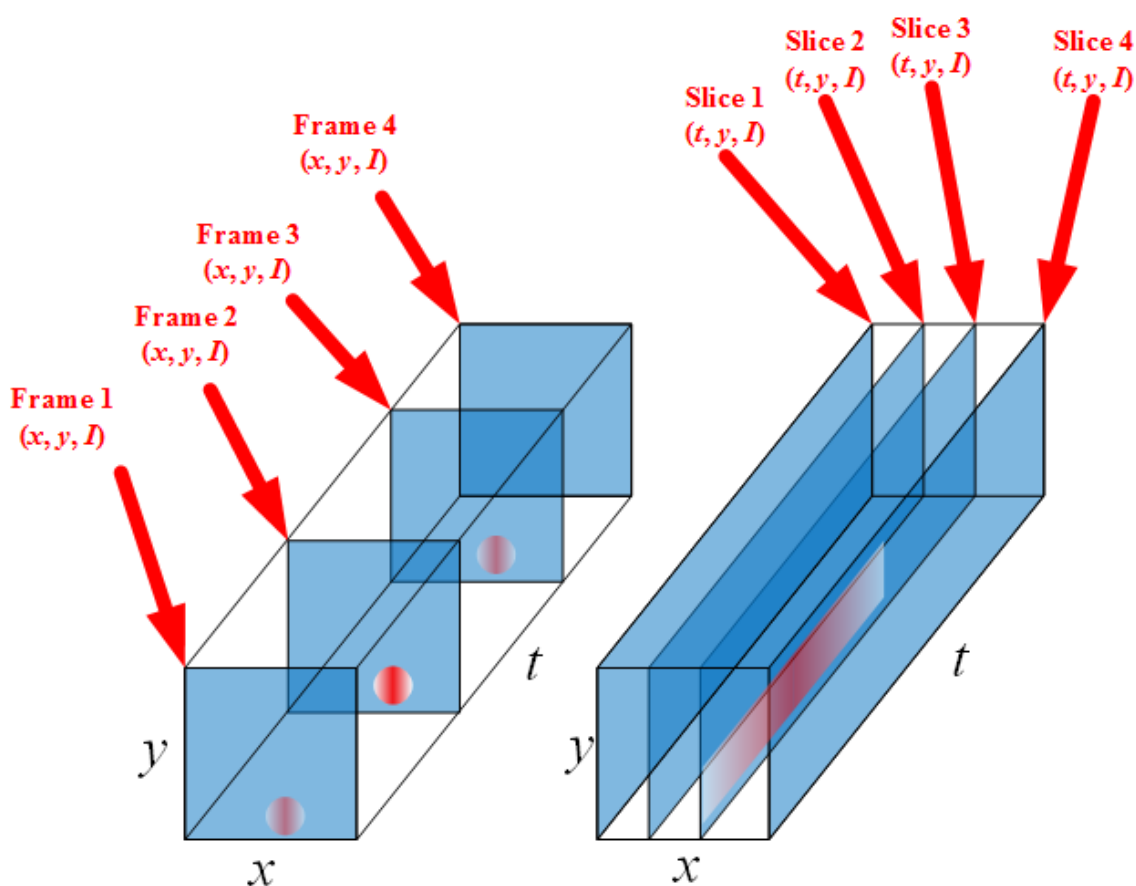
Figure 150: Raw data is usually measured as a series of images with respect to time. Each frame is measured with a set number of pixels in *x* and *y* and each pixel has intensity information *I*. The time *t* each frame is recorded. Normally the camera manufacturer specifies a pixel calibration e.g. for the Andor EMCCD iXon Ultra 897 camera this is 16 µm/pixel. For the measurement any magnification e.g. 100× objective has to be taken into account which would make the end pixel calibration 0.16 µm/pixel. Each frame is acquired for a certain exposure time however in addition to that exposure time there is a readout time or deadtime. Thus it is the cycle time that is important when looking at the duration of single molecule blinks. Ideally the cycle time should be as small as possible to give the best time resolution. However, as observed from the steady state data, the signal to noise ratio is dependent on the cycle time and will be poor for extremely small exposure times with faint single molecule data. Data can also be visualised as "slices" by taking orthogonal slices with each slice have the information *t*, *y* and *I* at a certain pixel in *x*.

separately in this manner gives a viable workaround to the diffraction limit where conventionally two or more fluorophores in close proximity would simultaneously be emitting photons which have indistinguishable point spread functions and limit resolution. Naturally the number of single-molecule blinks (they must be sparse enough to be temporarily resolved), brightness (needed to obtain a good SNR) and duration of single molecule blinks must be characterised for a fluorophore [274]. Since the frames which one uses to acquire an image **Figure 150** are very closely spaced, the raw data may be resliced in order to visualise the duration of single-molecule blinks. In order to visualise single-molecule blinks the duty cycle:

$$t_{\text{Duty}} = \frac{t_{\text{on}}}{t_{\text{on}} + t_{\text{off}}} \tag{73}$$

where t_{off} is the time a single molecule spends off and t_{on} is the time a single-molecule spends on must be relatively low otherwise one cannot temporally resolve the single molecule blinks and simply measures a diffraction limited blur [275]. The idea of a duty cycle is merely an extension of constricting the hit rate to 2 % in a TCSPC measurement in order to ensure single photon counting conditions. For location nanoscopy one wants to prevent two or more neighbouring fluorophores from emitting at the same time in order to avoid simultaneously imaging them. In TCSPC this limitation was due to the deadtime of the electronics. The deadtime of the electronics is also a serious hindrance to localisation microscopy and now will be discussed. In order to obtain an image a multi-channel detector such as a CCD is desired. Modern day CCDs have a capture rate of ~ms which is far from the ps readout time required in order to capture single molecule blinks that are required to be both temporally and spatially resolved from the likes of a short-lived ~ns fluorescence decay. As a consequence, only longer lived processes can be temporally resolved by the imaging CCD. One may hence conclude phosphorescence is the way forward for location microscopy unfortunately phosphorescence usually has a much lower quantum yield and extinction coefficient then fluorescence and single molecule phosphorescence blinks become much harder to distinguish from the relatively high readout noise of the CCD. The PMT with TCSPC on the other hand does have the capabilities to temporally measure single molecule fluorescence blinks, its main problem however is that is a single channel detector and so the sample's stage has to be scanned with respect to both the excitation source and the PMT. As a consequence this configuration is unsuitable for location microscopy but

can be used in conjunction with STED which constricts the point-spread function of the emission [276].
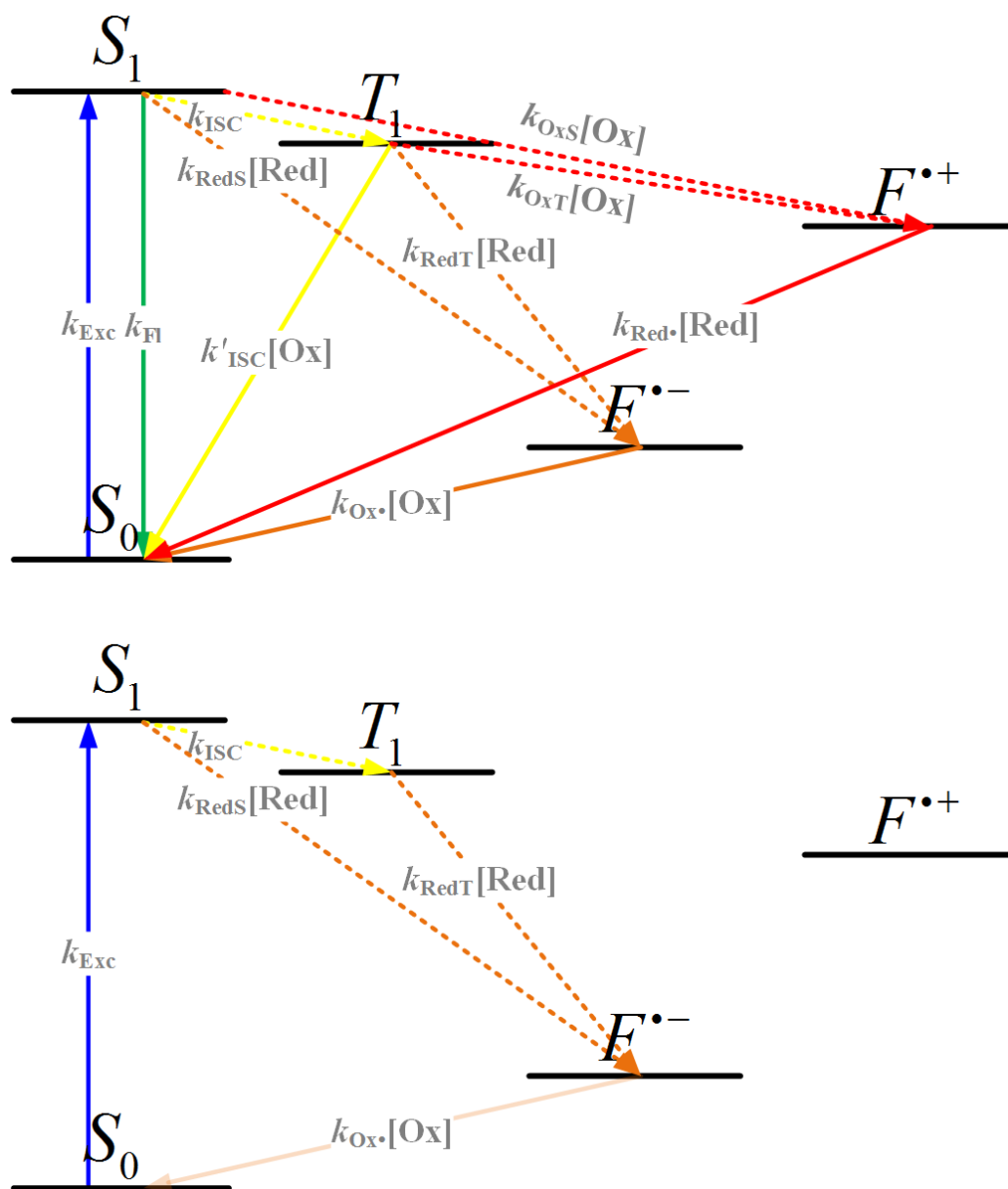
Figure 151: High excitation laser power can lead to the formation of an excited state dye radical $F^{\bullet+}$ or $F^{\bullet-}$. The prevalence and stability of the radical depends on the buffer conditions. In dSTORM measurements switching buffer is used which incorporates MEA or thiols to facilitate reduction while a catalase/glucose oxidase system facilitates oxygen removal. The switching buffer therefore facilitates and stabilises the production of $F^{\bullet-}$ while removing any $F^{\bullet+}$ and simultaneously reducing the rate of emission $k_{Ox\bullet}[Ox]$. This effectively creates a long lived dark state t_{off} and fluorescence emission t_{on} is a rare event. It should be noted that for success in super-resolution experiments three requirements should be met $t_{off} \gg t_{on}$ this condition is necessary for single molecule blinking to occur, $t_{on} \sim t_{CCD\text{-}CAP}$ (the capture rate of the CCD) allows for optimal acquisition of these single molecule blinks and finally $I_{on} \gg I_{off\bullet}+$CCD Readout Noise should be satisfied in order to get a sufficient signal to noise ratio.

One may hence conclude that the concept of location microscopy is entirely theoretical however physical chemical conditions allow for a t_{on} compatible with the capture rate of the CCD and a t_{off} long enough to ensure single molecule blinks. In dSTORM (direct Stochastic Optical Reconstruction Microscopy) this is achieved by use of high laser power to form a pair of dye radicals **Figure 151**. Like all radicals these are unstable however the stability of one radical and the destruction of the offer may be greatly enhanced by use of appropriate buffer. Highly reducing buffer for instance will stabilise the negative radical ion $F^{\bullet-}$ and annihilate the positive radical ion $F^{\bullet+}$. Maintaining the high laser power in these buffer conditions will ensure that each dye molecule becomes a negative radical ion $F^{\bullet-}$ which is non-emissive t_{off} and simultaneously ensure that the emission of a photon t_{on} is a rare event [277]. The dSTORM buffer used in this work favours reduction and consists of 3 stock solutions. The 50 µl of enzyme stock solution (A) and 400 µl of glucose stock solution (B) which act together as an oxygen scavenging system removing oxidation pathways during measurement. 50-100 µl of MEA stock solution (C) acts as a reduction agent stabilising the reduction pathways. These 3 solutions are topped up with biological buffer such as PBS (450-500 µl) within a sealed LabTek chamber. In more detail enzyme stock solution A is made up of 100 µl of 1 g ml^{-1} of catalase, 200 µl of 1 M TCEP, 25 ml of glycerol, 22.5 ml of water, 1.25 ml of 1 M KCl, 1 ml of 1 M Tris-HCL (pH 7.5) and 50 mg of glucose oxidase. Glucose stock solution (B) is made up of 5 g of glucose, 5 ml of glycerol and 45 ml of water. MEA-Stock solution (C) is made up of 1136 mg of MEA-HCl in 10 ml of water. These are all aliquoted and stored at –20 °C [278,279]. The additional pathways are best shown in an advanced Jablonski diagram incorporating dye radicals and both oxidation and reduction pathways as shown in **Figure 151** [280,281]. In the case of dSTORM buffer the $F^{\bullet-}$ radical is strongly stabilised and the process of emission facilitated by oxygen is a rare event.

The hardware of a current day super-resolution microscope for dSTORM is remarkably similar to that of a conventional inverted epi-fluorescence microscope [237,247,282] however the illumination source needs a higher power output than that required for conventional microscopy and on the detection side a fast capture device such as an imaging CCD camera is vital. Advances in the capture rate of imaging CCDs will allow for the measurement of more fluorophores which have blink cycles too fast for current CCDs to measure. Importantly they will also reduce the overall time of measurement. The large acquisition time of ~60-90 s to acquire a super-resolution image

using dSTORM typically involves fixing the sample and hence limits its applications in kinetic systems. The dSTORM measurements were made using an inverted Olympus LX71 microscope with a UAPON 100XOTIRF objective. Four lasers were used as excitation sources, a 640 nm Toptica Photonics IBEAM-SMART-640-S 150 mW, a 488 nm Coherent Sapphire 488-150 CW 150 mW, a 561 nm Coherent Sapphire 561-200 CW 200 mW and a 405 nm Mitsubishi ML320G2-11 150 mW (Laser Diode). An Andor EMCCD iXon Ultra 897 camera was used for data acquisition. This camera was air cooled at –80 °C. It has 512×512 pixels, with a pixel size of 16×16 µm and a 16 bit digitisation [283]. The resolution per pixel with the 100× objective is therefore 0.16×0.16 µm. Data acquisition was carried out using a LabView program written in house and single molecule localisation image processing was carried out using rainSTORM MATLAB GUI [273,284]. Slices were viewed using Image J. A Labtek chamber slide was used for the sample.
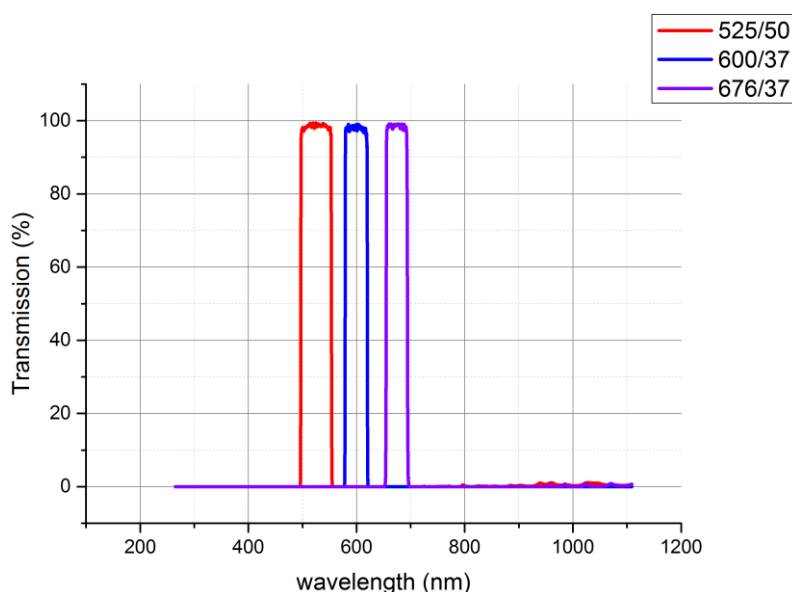
Figure 152: The following three bandpass filters were used to collect emission at 525nm, 600 nm and 676 nm respectively.

The success in location microscopy measurements is highly limited by the number of available fluorophores with desired traits. It should be noted that it is sample dependent parameters which currently govern the resolution as they influence N and b. Looking at **Equation (69)** in more detail it can be observed that the localisation precision has a $N^{-1/2}$ dependence when the system under investigation is shot noise limited. In other words, the localisation precision is limited by statistics i.e. N with the best fluorophores giving ~6000 photons per on cycle [285] on current hardware. It should be noted however that naturally

N will be artificially lower due to the deadtime of the CCD and the quantum efficiency of the CCD. There is also the case where the localisation precision is background noise limited. There can be three causes of this, the first is capture rate of the CCD which may be set too fast and hence yield too much background noise, the second is if only partial photoswitching to the dark-state occurs and there is out of focus fluorescence and the third is if the brightness (extinction efficient, quantum yield) of single molecule blinks from some fluorophores is too low [271]. Thus in order to use dSTORM it is necessary to find a fluorophore suitable for the capture rate of the camera which has a good signal to noise ratio and exhibits single molecule blinks which can be recorded in enough frames to get enough counts to minimise the localisation precision to the level desired for imaging. The testing of existing fluorescence dyes and suitable buffer conditions to accommodate single-molecule blinking characteristics with appropriate duty cycles and photostability is of paramount importance for future applications of dSTORM. One of the best overviews for current commercially available probes optimised for location microscopy is by Dempsey et al [286]. The work in this thesis looks at the use of stable ADOTA dyes for super-resolution and also of the Au_{25} nanoclusters. ADOTA and Au_{25} nanoclusters were selected because of their high quantum yield and because they were likely to be more resistant to photobleaching.

It should be noted that in all microscopy techniques, there is a four-fold trade-off between spatial resolution, photoxicity, temporal resolution and imaging depth and all four factors have naturally to be weighed up when considering a real microscopy application. Techniques such as non-linear SIM, STED and location microscopy have the best spatial resolution but the current requirement of high laser power in all four techniques means that any super-resolution data should be treated with a pinch of salt. A well-cooked biological specimen may be substantially different from a live and healthy biological specimen.

3. Nanometrology using TRFA

Fluorescence anisotropy allows for the measurement of the hydrodynamic radius for biomolecules and nanoparticles of dilute concentrations that have a fairly homogeneous distribution.
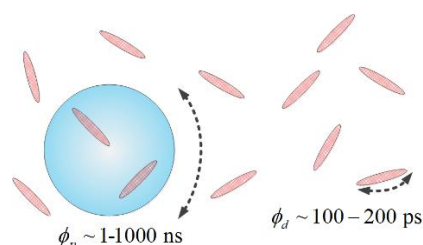
Figure 153: Illustration of fluorescence anisotropy used in the labelling of biomolecules such as trypsin and BSA. In a low viscosity solvent such as water, the rotation correlation time of free dye ϕ_d is of the order of 100-200 ps and for nanoparticles (ϕ_p) with a 1-10 nm radii the rotation correlation time is of the order of 1-1000 ns.

3.1 Protein

Trypsin and bovine serum aluminium (BSA) will be used as an example of labelling biomolecules. An anionic dye can be linked to BSA such as 1-anilino-8-naphthalene sulfonate [287] or a covalently bound amine linked dye such as dansyl chloride [288,289] or fluorescein isothiocyantate (FITC) [78,101,290] or as part of a cleverly designed immunoassay [291]. Free dye may then be separated from bound dye using a size exclusion column **Figure 154** or by use of dialysis for best results.
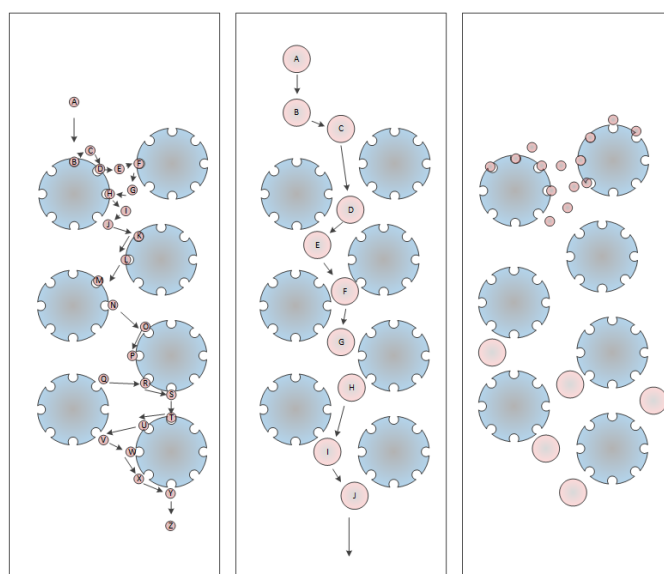
Figure 154: Desalting size-exclusion column. The desalting column consists of porous media. Small molecules such as unbound dye may spend some time diffusing in and out of

the pores (left). Larger molecules on the other hand are too large with respect to the pores and do not interact with them (middle). Thus small molecules can be separated from large molecules (right) [292].
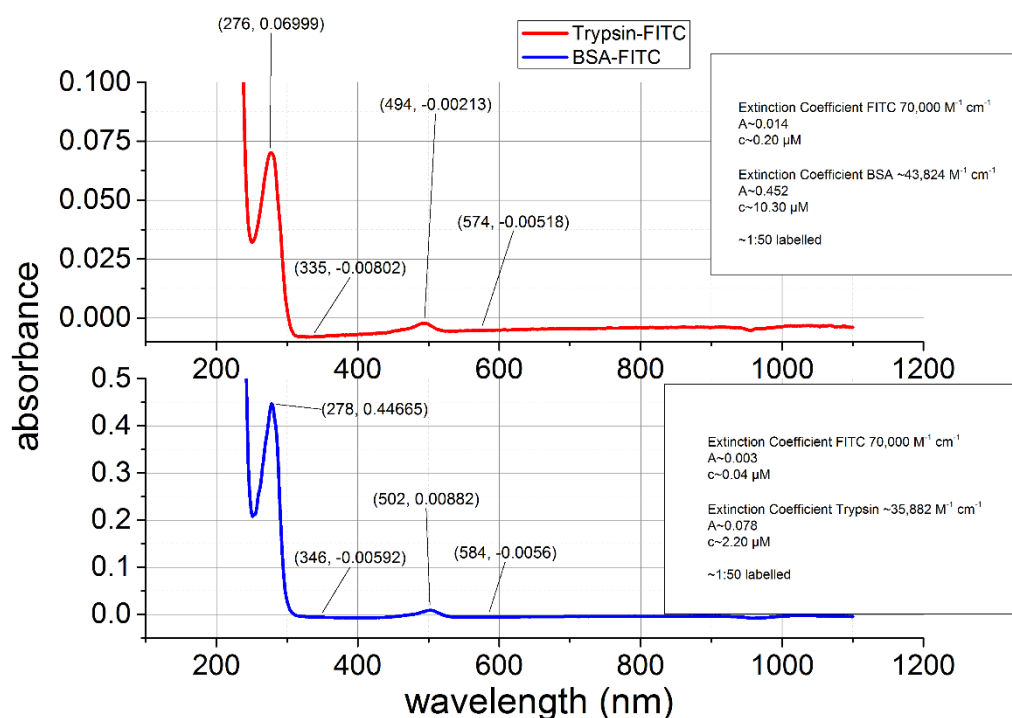
Figure 155: The absorbance spectra of BSA-FITC and Trypsin-FITC measured using a Lambda 25 at low concentrations. The scan was run from 200-1100 nm in 1 nm steps with a 0.125 s integration time. Comparison of the peak ~280 nm with the peak at ~495 nm indicates a final ~1:50 labelling ratio with the BSA sample being slightly more concentrated.
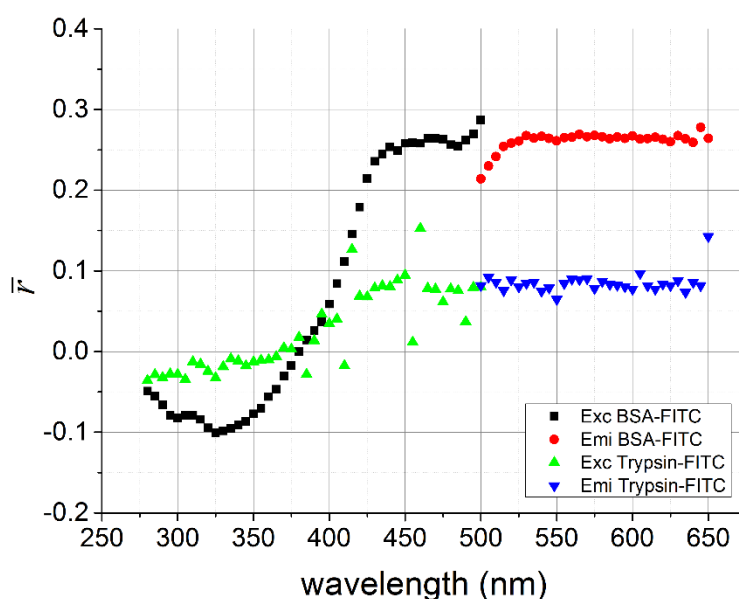
Figure 156: The steady state anisotropy of BSA-FITC and Trypsin-BSA measured using a Fluorolog 3-22. For the excitation anisotropy the emission monochromator (1200/500 double grating) was set to 530 nm and a bandpass of 5 nm. The excitation monochromator (1200/330 double grating) was set to a bandpass of 5 nm and stepped from 275-500 nm in

5 nm increments. For the emission anisotropy the excitation monochromator (1200/330 double grating) was set to 474 nm and a bandpass of 5 nm. The emission monochromator (1200/500 double grating) was scanned from 500-650 nm with a bandpass of 5 nm and stepped in 5 nm increments. The polarizers were toggled between VV, VH, HH and HV using an integration time of 5 s.

FITC was dissolved in DMF to make a stock solution of ~0.29 mMol l^{-1}. 0.76 mMol l^{-1} of protein was added to 0.1 M aqueous sodium carbonate buffer at pH 8.3 (4 ml) and reacted with 80 µl of the FITC stock solution to make up a final concentration of 7.6 µMol l^{-1} of FITC (1:100 labelling ratio). The solution was stirred for 24 hours and then run through a 5 kDa dextran desalting column. The sample was collected drop by drop and the fluorescence fractions were diluted in 0.1 M bicarbonate buffer. The absorbance spectra **Figure 156** can be used to determine the actual labelling ratio which was ~1:50 in the case of either protein. As BSA (66.5 kDa, R_{DLS}=3.5±0.3 nm from dynamic light scattering)[108] is a larger molecule than tryptophan (23.3 kDa, R=1.9±0.3 nm)[293] the molecule rotates less and the steady state anisotropy is higher. At lower excitation wavelengths the steady-state anisotropy of FITC in glycerol is negative (negative anisotropy will be discussed in more detail later) so the trend observed is expected. For time-resolved anisotropy applications an excitation, emission wavelength pair where $\bar{r}$ is high is preferred. NL474L can be used for excitation and emission can be collected using a LP530 filter. In terms of nanometrology, time-resolved anisotropy is more useful than steady state anisotropy as one may determine the rotational correlation time and particle size as previously discussed.
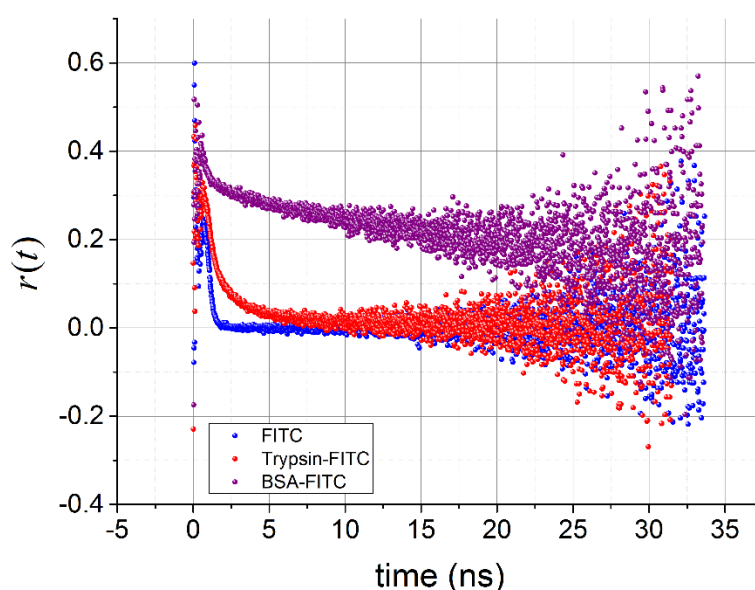
Figure 157: The time-resolved emission anisotropy decay of FITC, Trypsin-FITC and BSA-FITC. These were measured using a FluoroCube with a NL474L excitation source

connected to an excitation monochromator TDM800 (1200/350 grating) which was set to 474 nm with a 32 nm bandpass. The emission monochromator TDM800 (1200/350 grating) was set to 530 nm and an 8 nm bandpass. A TBX650 was used for detection with Hub A electronics operating in reverse mode with a time range of 100 ns (8000 channels). Polarizers were toggled between VV and VH every 30 s until a peak difference of 25000 counts (~10000 counts when G is taken into account). HH and HV were measured every 30 seconds until HH had >1000 counts in the peak. The prompt was measured at 474 nm to 10000 counts with polarizers at VV. The anisotropy decay of FITC is seen to rapidly fall to 0, the anisotropy decay of Trypsin-FITC decay falls significantly slower and the anisotropy decay of BSA-FITC falls even more slowly. Assumptions have to be made that the residual anisotropy r_∞=0 when fitting the anisotropy decays of Trypsin-FITC and in particular BSA-FITC as the lifetime of the dye is inefficient to follow the entire anisotropy decay to 0.

Table 4: Sum, difference data for Trypsin-FITC, BSA-FITC and free FITC.

Sum Data						
τ_1 (ns)	α_1	τ_2 (ns)	α_2	τ_3 (ns)	α_3	χ^2
0.18±0.05	0.19	1.68±0.09	0.17	3.89±0.007	0.64	1.168
0.12±0.04	0.3	1.69±0.08	0.16	4.3±0.008	0.54	1.186
		1.6±0.1	0.12	3.925±0.006	0.88	1.552

Difference Data								
r_0	r_∞	ϕ_1 (ns)	R_1 (nm)	α_1	ϕ_2 (ns)	R_2 (nm)	α_2	χ^2
0.282±0.003	0 (fixed)	0.5±0.05	0.78±0.03	0.7	4.3±0.2	1.61±0.02	0.3	1.143
0.341±0.002	0 (fixed)	1.4±0.4	1.1±0.1	0.1	41±2	3.43±0.05	0.9	0.985
0.38±0.004	0.0000± 0.0005	0.1±0.01	0.51±0.01	1				1.014

The rotation correlation times given for Trypsin and BSA match closely with those previously reported in literature and the rotational time of free FITC matches closely with the dimensions of the fluorophore. The other two radii reported for Trypsin and BSA are prescribed as dye wobbling. Protein aggregation should lead to an increase in the rotational correlation time ϕ and steady-state anisotropy $\bar{r}$ [294].

3.2 Silica Nanoparticles

There are 3 commercially available silica nanoparticle colloids LUDOX SM30 with Ø7 nm [295], LUDOX AM with Ø12 nm [296] and LUDOX AS40 with Ø22 nm [297]. As these particles are relatively stable when stored under the correction conditions and have known particle sizes these are ideal candidates for nanometrology measurements. Previous work by the group has demonstrated the use of fluorescence anisotropy for measurement of these nanoparticles [298,299]. In previous work the 6-Methoxy Quinolinium based dyes and Rhodamine 6G were positively charged and electrostatically bound to the silica

nanoparticles. Silica nanoparticles can also be synthesised using the Stöber protocol **Figure 158** in particular the modified Stöber synthesis documented by Green et. Al. [300]. Stöber synthesis essentially involves a hydrolysis reaction of an orthosilicate using ammonia as a catalyst in an alcohol solvent. The reactants are mixed thoroughly to ensure homogeneity. Under these conditions orthosilicate will hydrolyse to form silicic acid monomers leaving alcohol as a by-product. Under controlled conditions (concentration, temperature and through stirring) the silicic acid monomers will sporadically combine via a condensation reaction and eventually form stable spherical structures of a specified size. The size of the final product will depend on the concentration of the initial reactants.
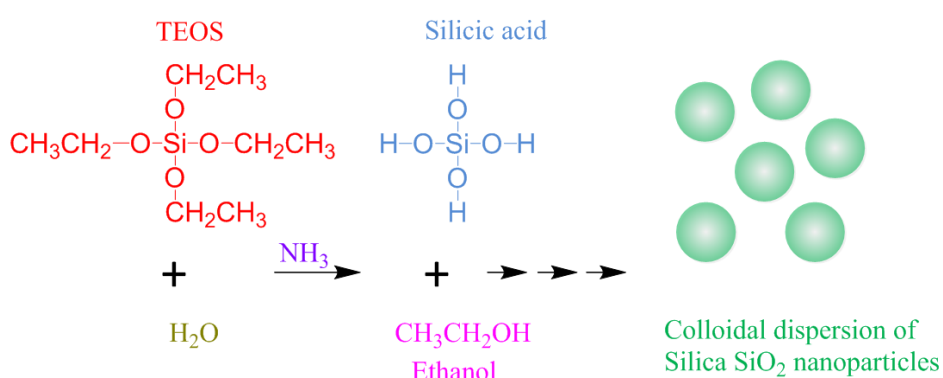
Figure 158: Diagrammatic schematic of the Stöber process used to form silica nanoparticles.

The formation of homogeneous monodispersed nanometre silica particles highly depends on the reaction conditions. TEOS is the source of the monomer and therefore the concentration of TEOS will determine the concentration of nuclei/primary particles present within the system. The aggregation of the primary particles results in the formation of more stable secondary particles. After the initial induction period, any primary particles or nuclei that form will dissolve and re-precipitate on the growing secondary particles through Ostwald ripening mechanism. This process will continue until all the primary particles are consumed or the system is stable. Too much TEOS will lead to a broad and multimodal distribution of particle sizes. Such a distribution is due to excessive generation of primary particles at super saturation state, while the consumption of the primary particles will occur at a much slower rate while the excess of primary particles will spontaneously aggregate to form stable secondary particles and result in multimodal distributions. The presence of ammonia will increase the hydrolysis rate of TEOS as well as condensation rate of hydrolysed monomers[301]. Stöber nanoparticles can be covalently labelled by using an

amino-silane linker **Figure 159** which has on one an end an amine reactive group that is reactive to a large number of commercially available amine reactive fluorophores such as FITC mentioned earlier and on the other end which is similar to the orthosilicate used to form silica nanoparticles and hence will react like an orthosilicate and latch the dye onto the silica nanoparticles. In addition, the silica nanoparticles will be negatively charged so a
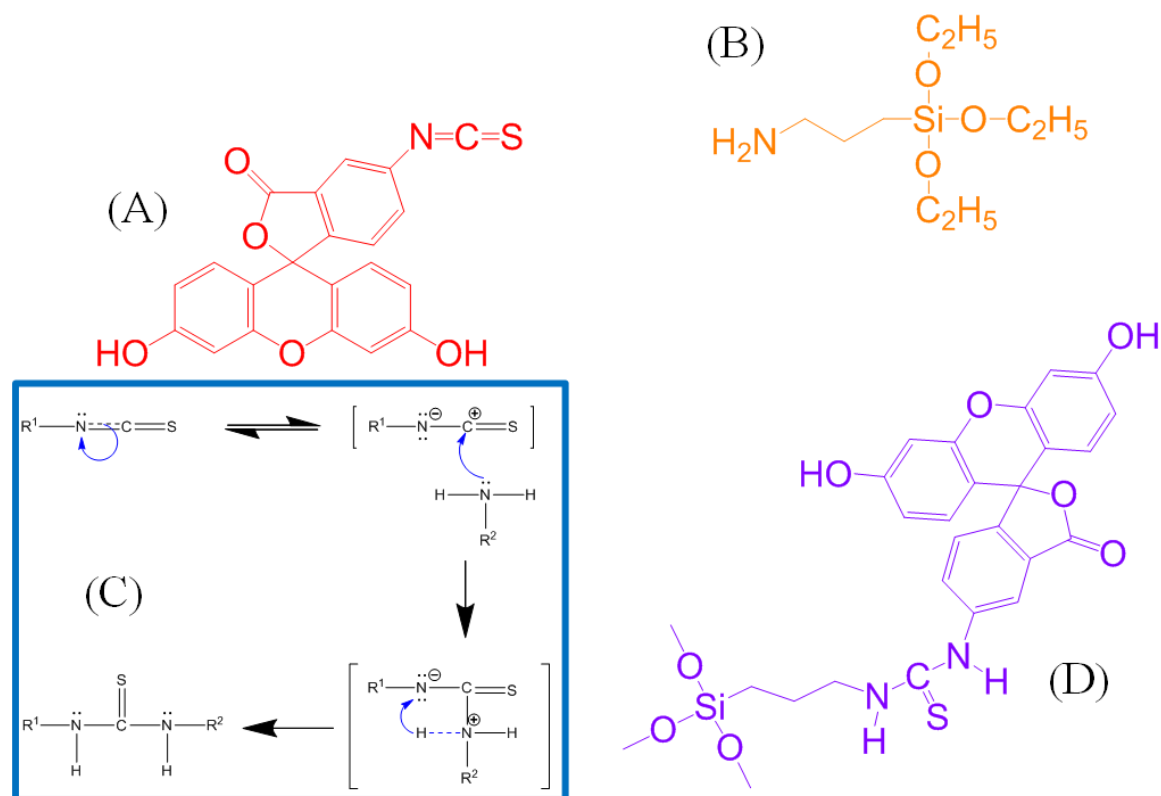
Figure 159: (a) FITC is bound to (b) 3-aminopropyltrimethoxysilane (APS) via the mechanism (c) to create FITC-APS. [302–304]

cationic fluorophore such as Rhodamine 6G can attach to them. The test sample prepared was the M4 sample in accordance to Green et al [300] where [NH$_3$]=0.05 M, [H$_2$O]=1.1 M and [TEOS]=0.5 M in methanol and the radius of gyration is R_g=4.2±0.2 nm. The viscosity of methanol at 298 K is 0.543 mPa s^{-1} [205] and this alongside the assumption of a spherical model can be used with the time-resolved fluorescence anisotropy decay to determine the particle size of the nanoparticle. **Figure 160** illustrates the slight increase of the rotational correlation time for free fluorescein, FITC and FITC-APS in comparison to the large change when FITC-APS is affixed to a nanoparticle. Kinetically changing systems, such as the growth of a sol-gel [305], are usually difficult to examine with fluorescence anisotropy due to the time required for their reaction. There is usually a compromise between data quality, the number of counts and time-resolution with respect to acquisition time in

previous work [306–310]. Advances in TCSPC such as the high repetition rate DeltaDiodes and faster timing electronics such as the DeltaHub can increase the versatility of time-resolved fluorescence anisotropy measurements.
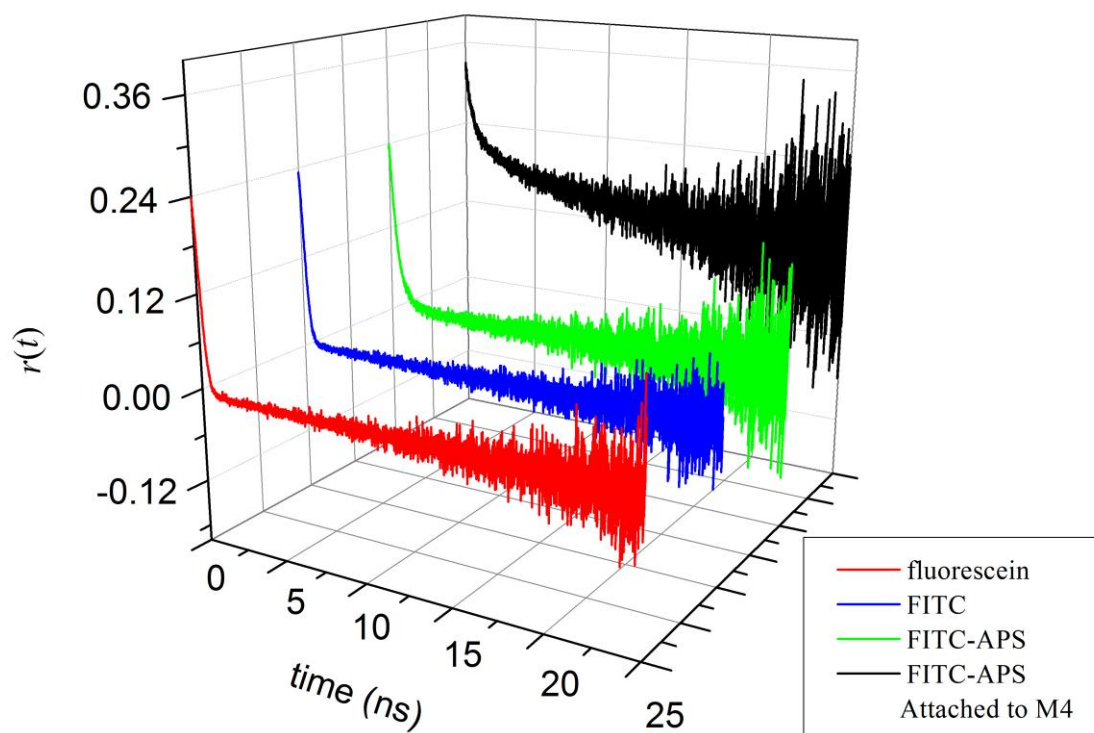
Figure 160: Illustration of anisotropy decay curves of free fluorescein, FITC and FITC-APS and FITC-APS-M4 in methanol. These were measured using a FluoroCube with a NL474L excitation source connected to an excitation monochromator TDM800 (1200/350 grating) which was set to 474 nm with a 32 nm bandpass. A LP530 filter (no emission monochromator) was selected to separate out the emission from the excitation. A TBX650 was used for detection with Hub A electronics operating in reverse mode with a time range of 100 ns (8000 channels). Polarizers were toggled between VV and VH every 30 s until a peak difference of 25000 counts (~10000 counts when G is taken into account). HH and HV were measured every 30 seconds until HH had >1000 counts in the peak. The prompt was measured without the LP530 filter to 10000 counts with polarizers at VV. Fluorescein and FITC with M4 in methanol showed little difference to the dye only in methanol because the dyes did not possess a relevant linker to bind to the silica. The rotational correlation times from a direct fit to the anisotropy curve were ϕ_1=0.74±0.06 ns (α_1=0.40), ϕ_2=39±2 ns (α_2=0.60) and χ^2=1.111 with r_0=0.286±0.003 and r_∞=0 (fixed). This gave a Stokes radii of 1.06±0.03 nm and 3.99±0.07 nm respectively. The second rotational time being in good agreement to that reported by Green [300].

Table 5: Chemical composition for the synthesis of measured Stöber nanoparticles.

Sample	[TEOS]		[NH$_3$]		[H$_2$O]	
PY1	0.50	mol l^{-1}	0.05	mol l^{-1}	10.00	mol l^{-1}
PY2	0.50	mol l^{-1}	0.05	mol l^{-1}	5.00	mol l^{-1}
PY3	0.50	mol l^{-1}	0.05	mol l^{-1}	2.50	mol l^{-1}
M4	0.50	mol l^{-1}	0.05	mol l^{-1}	1.10	mol l^{-1}
S1	0.17	mol l^{-1}	0.50	mol l^{-1}	3.00	mol l^{-1}
S2	0.50	mol l^{-1}	0.50	mol l^{-1}	1.00	mol l^{-1}
S3	0.17	mol l^{-1}	0.05	mol l^{-1}	0.34	mol l^{-1}

Table 6: Fitted parameters to the fluorescence anisotropy curve for the silica nanoparticles using FITC-APS as a fluorophore and measuring using the same experimental conditions as **Figure 160**. A fit using the reconvolution yielded similar results.

	r_0	ϕ_1 (ns)	r_1 (nm)	α_1	ϕ_2 (ns)	r_2 (nm)	α_2	χ^2
PY1	0.300±0.003	0.81±0.05	1.10±0.02	0.46	22.4±0.9	3.31±0.04	0.54	1.140
PY2	0.310±0.003	0.80±0.06	1.09±0.03	0.38	28±1	3.57±0.04	0.62	1.097
PY3	0.304±0.003	0.89±0.07	1.13±0.03	0.34	31±1	3.69±0.05	0.66	1.134
M4	0.286±0.003	0.74±0.06	1.06±0.03	0.40	39±2	4.0±0.1	0.60	1.111
S1	0.291±0.003	0.90±0.07	1.14±0.03	0.45	20.0±0.8	3.19±0.04	0.55	1.140
S2	0.276±0.003	0.79±0.05	1.09±0.02	0.48	20.9±0.8	3.24±0.04	0.52	1.146
S3	0.267±0.003	0.78±0.05	1.08±0.02	0.46	22.6±0.9	3.32±0.04	0.54	1.161
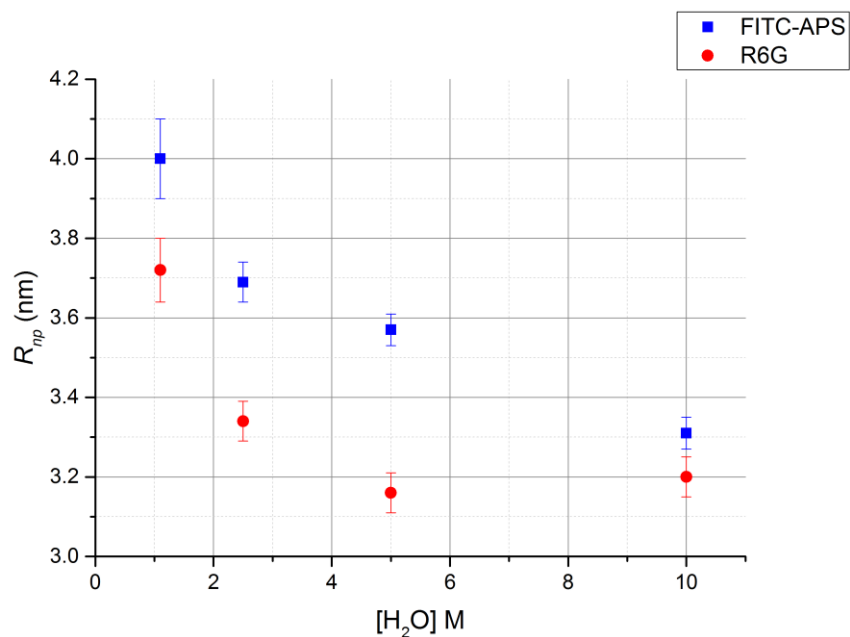
Figure 161: Water concentration with respect to particle size using for FITC-APS covalently bound and Rhodamine 6G electrostatically bound. A direct fit to the anisotropy decay and reconvolution yielded similar results for the FITC-APS covalently linked nanoparticles measured using the same conditions as **Figure 160**. For the electrostatically bound Rhodamine 6G the measurement conditions were the same with the exception to the light source, a NL490D was used and the excitation monochromator wavelength was hence set to 490 nm. Because the FWHM of the NL490D= 1.4 ns reconvolution analysis had to be used. A similar trend was reported in both cases with the size reported with the FITC-APS dye being slightly larger than that reported by Rhodamine 6G.
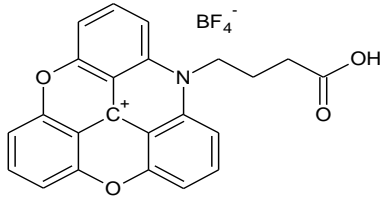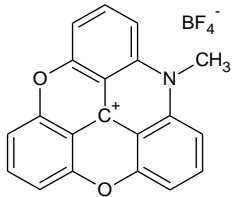
4. Spectroscopy of AzaDiOxaTriAngulenium (ADOTA) Fluorophores and their use for Nanometrology

ADOTA-Acid in particular which has a mono-exponential fluorescence decay time in water of 23.2 ns. The somewhat unique characteristics of ADOTA-Acid have already found widespread use in other fluorescence applications such as time-resolved fluorescence anisotropy [215] and FLCS [311]. This work examines the dyes use in TRFA applications in more detail.

Table 7: Chemical properties of AzaDiOxaTriAngulenium (ADOTA) in Acetonitrile [312,313].

ADOTA$^+$ in Acetonitrile		
λ_{ex}	541 nm	
λ_{em} λ_{em}	560 nm	
ε_{541}	9480 L mol^{-1} cm^{-1}	ADOTA-Acid
τ	23.2 ns	
Φ_{fl}	0.49	MeADOTA

Figure 162: The absorbance and emission spectra excited at 500 nm of ADOTA in methanol. The absorbance peak was ~0.05 suitable for fluorescence measurements and the

plot is normalised for comparison. Spectra were measured in a Perkin Elmer Lambda 2 and Fluorolog 3-22 respectively.

4.1 ADOTA as an Anisotropy Probe?

The steady-state EEM and anisotropy EEM in 100 % glycerol (**Figure 163**) gives a rough estimation of r_0 with respect to wavelength because at such a high viscosity the rotation should be extremely slow meaning there is only a weak depolarisation during measurement. The excitation spectrum is of more consequence as negative anisotropy occurs at lower excitation wavelengths and positive anisotropy occurs at higher excitation wavelengths. The anisotropy is more or less constant with respect to the emission wavelength. For anisotropy applications it is better to excite in the regime of high anisotropy as it increases the dynamic range that $r(t)$ or $\bar{r}$ can be measured however in both regimes positive and negative anisotropy can be examined using a 532 nm and 418 nm excitation wavelength respectively. The data demonstrates that excitation at 532 nm has a larger dynamic range as the magnitude of the initial anisotropy is larger giving it more scope to measure smaller rotational times. On first glance ADOTA (**Figure 164**) may seem to be a worse probe for 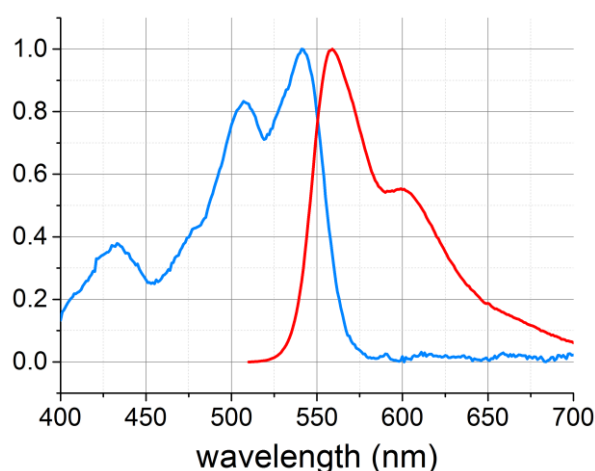fluorescence anisotropy measurements than Rhodamine 6G (**Figure 75**) as the steady-state $\bar{r}$ data is noisier at lower viscosities. One of the reasons is due to the fact that ADOTA is slightly smaller than Rhodamine 6G which should lower the rotational correlation time and hence report a lower anisotropy in this regime. Moreover, the main push is to increase the measurable rotational correlation time measurable with TRFA so larger nanoparticles can accurately be measured. The usefulness of ADOTA for TRFA opposed to traditional fluorophores is demonstrated in **Figure 165** as ADOTA has a longer decay time and the signal to noise is thus better at the tail of the anisotropy giving more data to fit and a more accurate determination of the rotational correlation time. The comparison of steady-state **Figure 164** with time-resolved fluorescence anisotropy data **Figure 166** and **Figure 167** for both the positive and negative anisotropy decays clearly highlights the fact that TRFA is more sensitive; the TRFA data can be used to distinguish between the 20-50 % glycerol solutions when SSFA data cannot. The lifetime data **Figure 168** together with the magnitude of the initial anisotropy **Figure 169** and **Figure 170** indicate solvent relaxation playing a more critical role at lower viscosities. This lowers the initial anisotropy r_0 with respect to viscosity [314]. $\bar{r}$ is lowered because both the rotational correlation time and r_0 decrease with respect to viscosity. The reason for this is likely due to the fact that ADOTA will be more rigid at a higher viscosity and hence the absorption and transition dipoles are

likely to be better separated. The long lived fluorescence of ADOTA allows a greater SNR at the tail of an anisotropy decay and hence increases the ability to measure larger nanoparticles. When using ADOTA as an anisotropy probe care had to be taken with its preparation and for best results A~0.01-0.05. With A~0.1 a small proportion of aggregates were measured, aggregation gives a blue-shifted emission with multiple decay times as elucidated in the DAS of a high concentration of ADOTA (A~0.5) in glycerol (**Figure 172**). Data from samples with low levels of aggregation required a second decay time to fit the sum data however one rotational correlation time remained sufficient to fit the difference data. Comparison of two samples in 60 % glycerol with and without aggregates gave a sum fit of τ_1=20.59±0.04 ns (α_1=0.88), τ_2=4.3±0.4 ns (α_2=0.12), χ^2=1.350 opposed to τ_1=20.47±0.02 ns with χ^2=1.069. The rotational correlation time reported for the sample with aggregates ϕ_1=1.65±0.03 ns, r_0=0.349±0.003, χ^2=1.043 was slightly larger than those without aggregates ϕ_1=1.28±0.03 ns, r_0=0.347±0.001, χ^2=1.142. It should be noted however that the single rotational time reported is that from an average ensemble of single dye molecules and aggregates; the aggregates are likely predominantly dimers which stack closely together and thus have a similar size to individual fluorophores. If a higher number of counts are used for the difference curve ~100,000 counts versus the normal 10,000 two rotational correlation times can be extracted, the sum fitted to τ_1=20.51±0.01 ns (α_1=0.88), τ_2=4.1±0.1 ns (α_2=0.12), χ^2=1.330 similar to before. The difference fitted to ϕ_1=1.45±0.01 ns, r_0=0.351±0.001, χ^2=1.338 for a one exponential model and $\phi_{ADOTA-Monomer}$=1.2±0.2 ns ($\alpha_{ADOTA-Monomer}$=0.77), $\phi_{ADOTA-Dimer}$=2.4±0.2 ns ($\alpha_{ADOTA-Dimer}$=0.23), r_0=0.351±0.001, χ^2=1.338 for a two exponential model. These times give $r_{ADOTA-Monomer}$=0.486±0.004 nm from the sample without dimers and $R_{ADOTA-Monomer}$=0.475±0.003 nm, $R_{ADOTA-Dimer}$=0.60±0.02 nm from the sample with dimers.
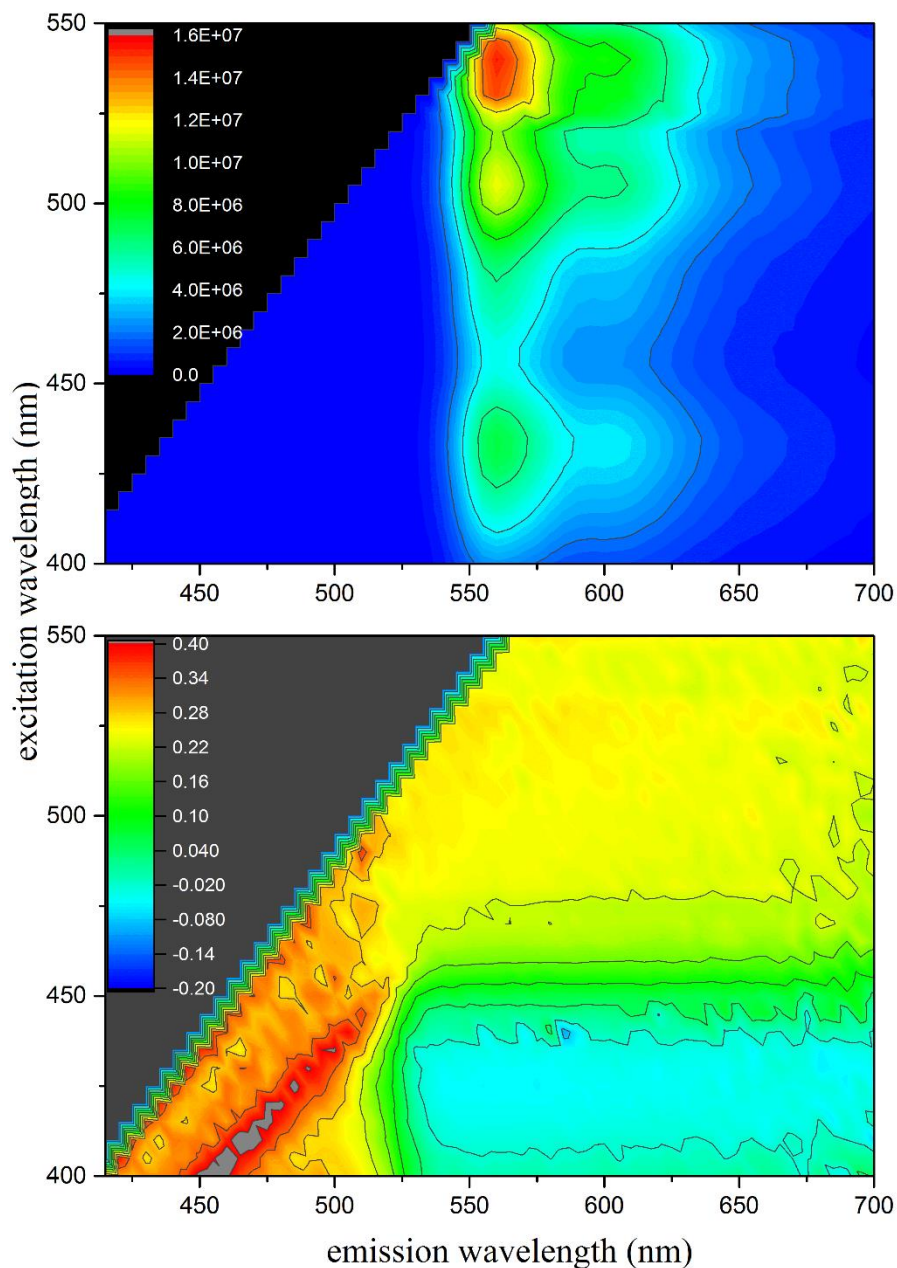
Figure 163: The EEM and Anisotropy EEM of ADOTA-Acid in glycerol measured in a Fluorolog 3-22. For the EEM an integration time of 0.2 s was used with a bandpass of 3 nm in both monochromators, 5 nm increments were used across both axes. For the Anisotropy EEM an integration time of 1 s was used for each polarizer orientation with a bandpass of 5 nm in both monochromators, 5 nm increments were used across both axes. In both cases a LP395 was placed on the excitation arm and a LP410 was placed on the emission arm to prevent 2nd order effects. The ridge to the left of the EEM where $\bar{r}$ appears to be >0.4 is again due to glycerol Raman scattering. The fact that the anisotropy within the first regime of interest i.e. at 475-550 nm excitation and 550-650 nm emission is positive indicating that the absorption and emission dipoles are close to parallel. The anisotropy at

the second regime of interest 400-450 nm excitation and 550-650 nm emission is negative indicating that the absorption and emission dipoles are close to perpendicular.
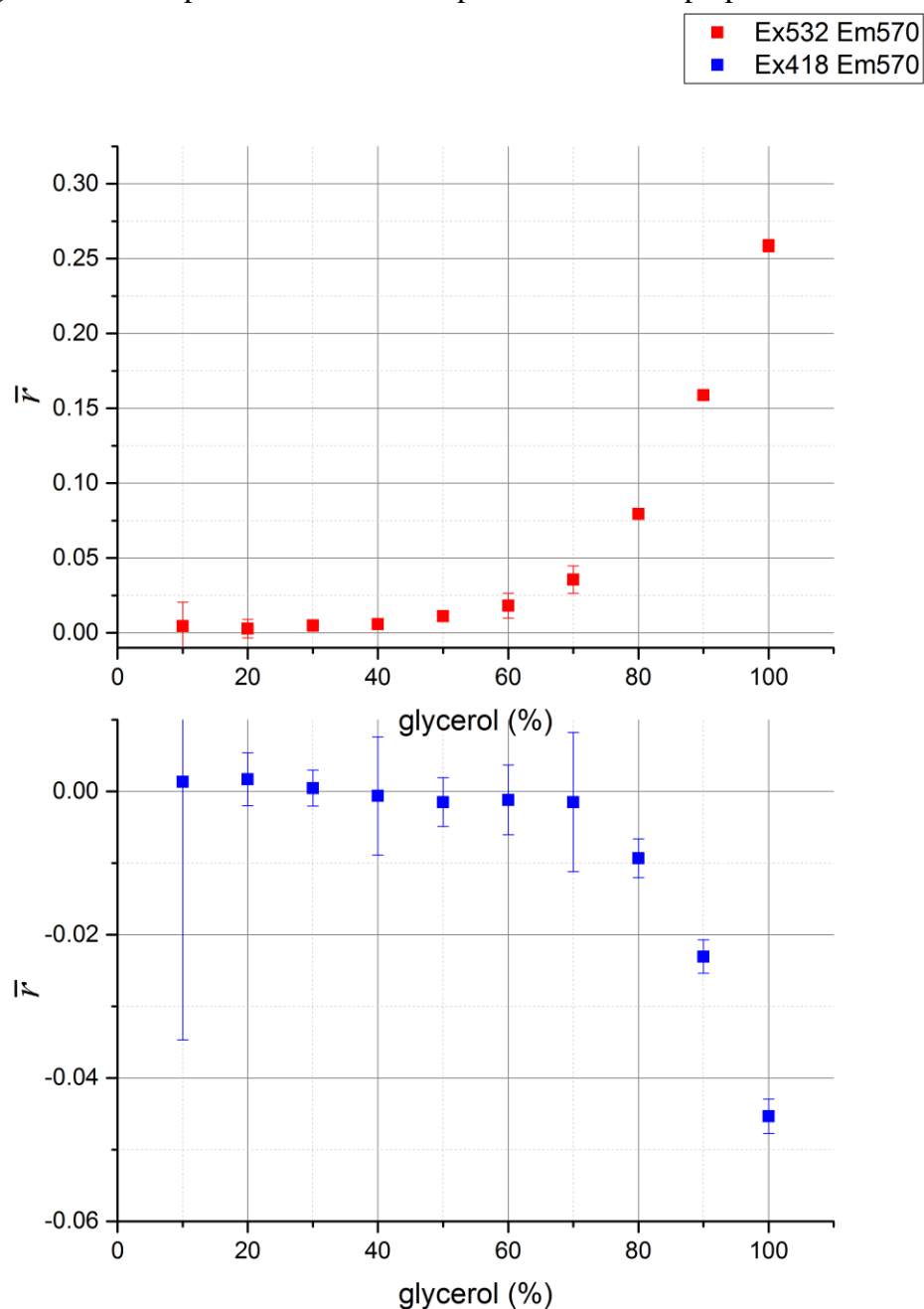
Figure 164: The steady-state fluorescence anisotropy of ADOTA with respect to increasing percentage of glycerol solution. As the viscosity increases, the Brownian motion of ADOTA slows down and a higher anisotropy is reported. This was measured in a Fluorolog 3-22 with an excitation wavelength of 418 nm and 532 nm and an emission wavelength of 570 nm in both cases. A bandpass of 5 nm was used for both monochromators and a 2 s integration time was used for each polarization with 25 trials.
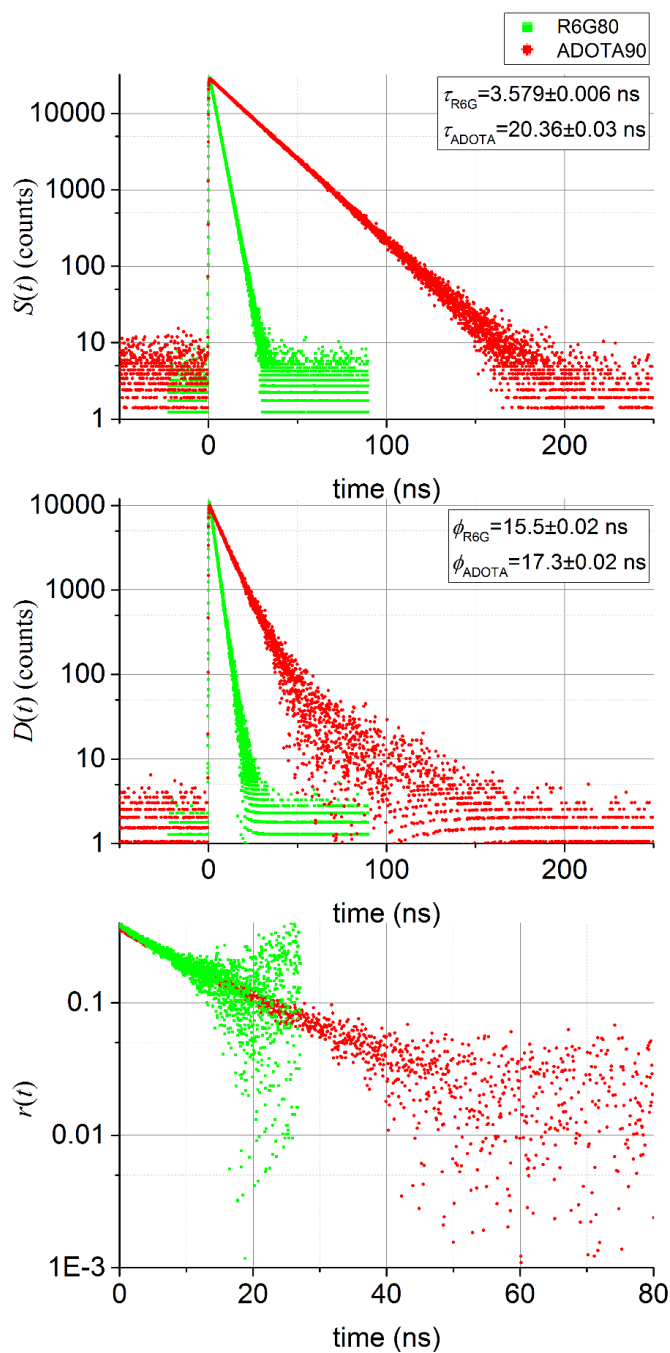
Figure 165: Comparison of TRFA data for Rhodamine 6G in 80 % glycerol and ADOTA in 90 % glycerol solution measured using the same measurement configuration as **Figure 107**. The sum data shows that ADOTA has a lifetime which is greater than 4 times that of Rhodamine 6G. Although the rotational correlation times are similar for both samples, as a consequence of ADOTA's longer lifetime the data in the difference curve is of a higher quality due there being a greater signal to noise in the tail. This can be illustrated when the anisotropy is plotted in log scale where ADOTA can be seen to fall closer to 0 anisotropy. In both cases the assumption has been made that the residual anisotropy is fixed to 0. Without this assumption the Rhodamine 6G fits to a high residual anisotropy leading to an inaccurate sizing of Rhodamine 6G. The fit to ADOTA in both cases leads to a similar sizing of ADOTA.
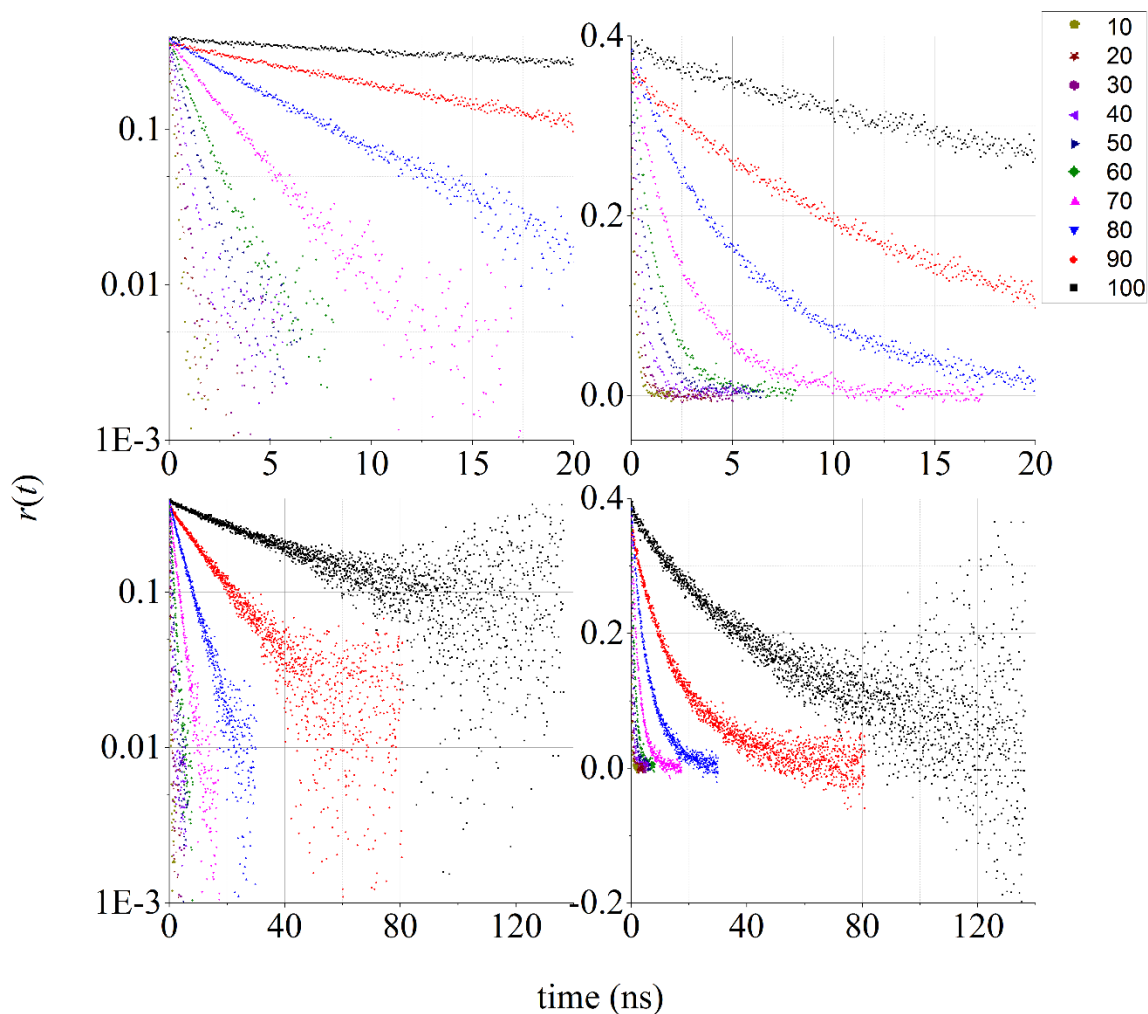
Figure 166: TRFA of Rhodamine ADOTA measured in solutions of glycerol excited with DD532L using the same measurement configuration as **Figure 107**. The increase in glycerol concentration increases the viscosity of the solution and hence increases the rotational correlation time. Data is plotted in log and linear scale and zoomed in to illustrate the smaller rotational correlation times in detail. More of the decays are seen to fall to 0 anisotropy than those measured with Rhodamine 6G as expected. The initial anisotropy however is seen to increase with respect to glycerol concentration and the decrease in this anisotropy likely contributes to the fact that the steady-state data couldn't accurately distinguish ADOTA in 10-40 % glycerol concentrations.
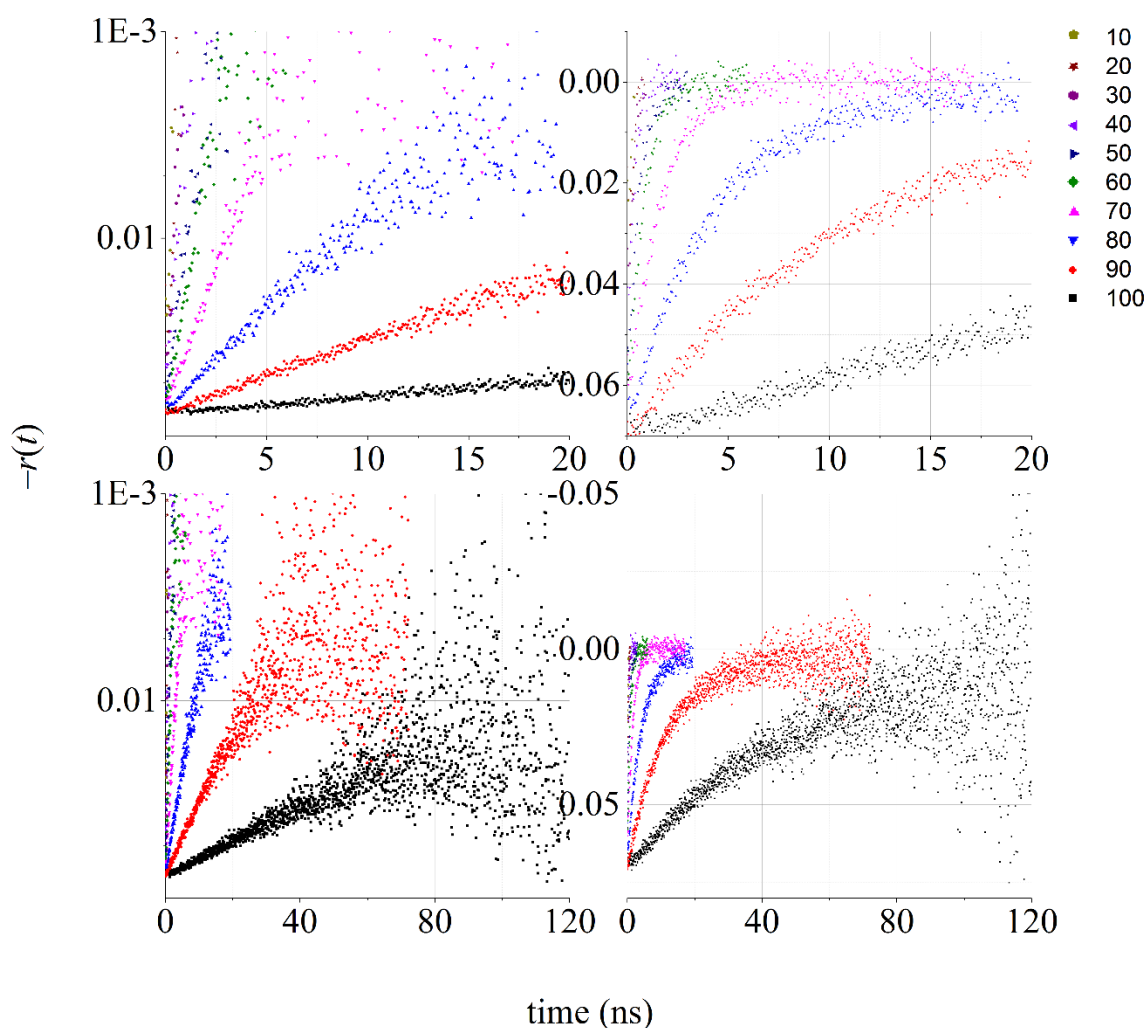
Figure 167: TRFA of Rhodamine ADOTA measured in solutions of glycerol excited with DD418L otherwise using the same measurement configuration as **Figure 107**. The increase in glycerol concentration increases the viscosity of the solution and hence increases the rotational correlation time. The negative of the data is plotted in log and linear scale and plotted upside to highlight the fact that it's negative. The magnitude of initial anisotropy is likewise seen to increase with respect to glycerol concentration and the decrease in this anisotropy contributes to the fact that the steady-state data couldn't accurately distinguish ADOTA in 10-70 % glycerol concentrations. Most of the data is clearly distinguished in the TRFA measurement however.
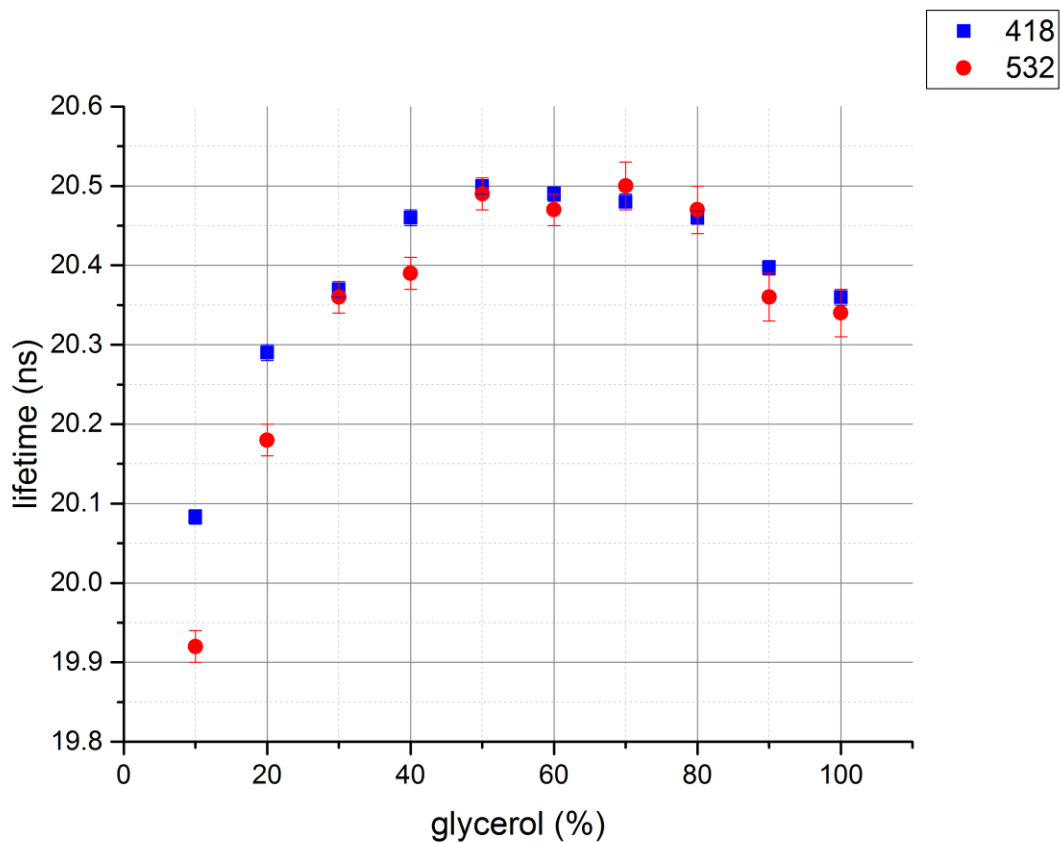
Figure 168: The lifetime data from the anisotropy sum of ADOTA. All fluorescence sums were fitted to a mono-exponential model. There is a clear deviation from the $\tau \propto n^{-2}$ as shown in **Figure 119** for Rhodamine 6G. As the viscosity decreases the lifetime of ADOTA decreases. This is likely due to solvent relaxation as depicted in **Figure 7**.
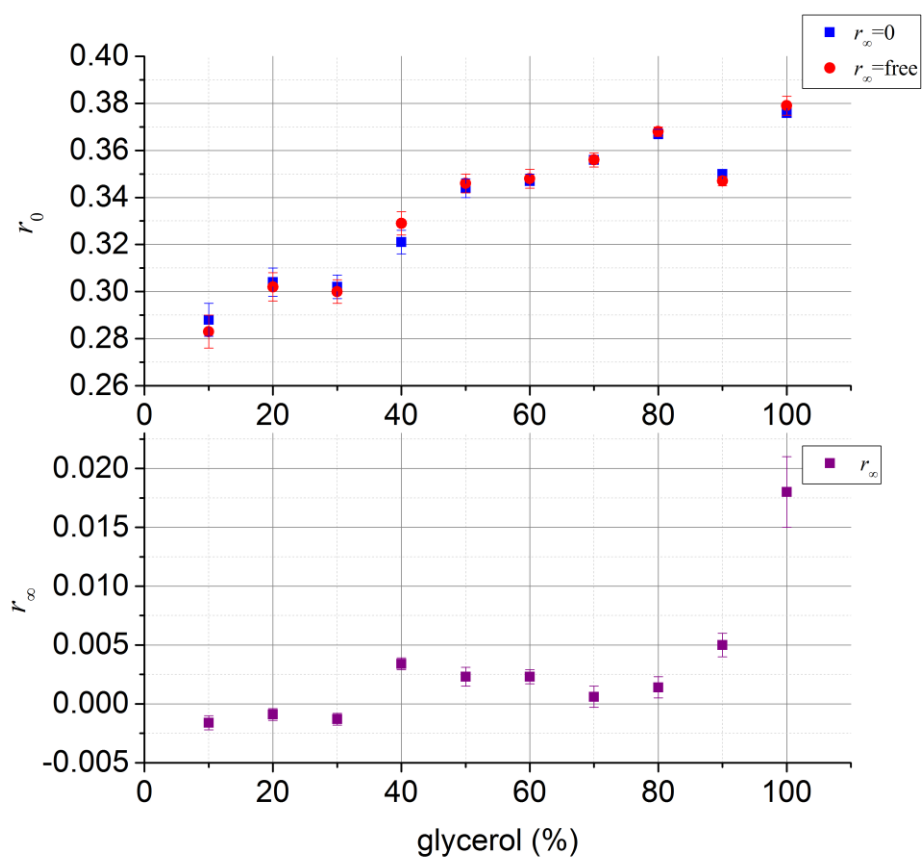
Figure 169: The initial anisotropy plotted with respect to glycerol concentration for DD532L excitation. The initial anisotropy increases with respect to viscosity again indicating solvent relaxation lowering the initial anisotropy. In all cases the fit to the difference with and without a residual anisotropy yields a similar rotational correlation time although the residual anisotropy begins to deviate significantly at 100 % when the rotational correlation time becomes larger than the lifetime of ADOTA.
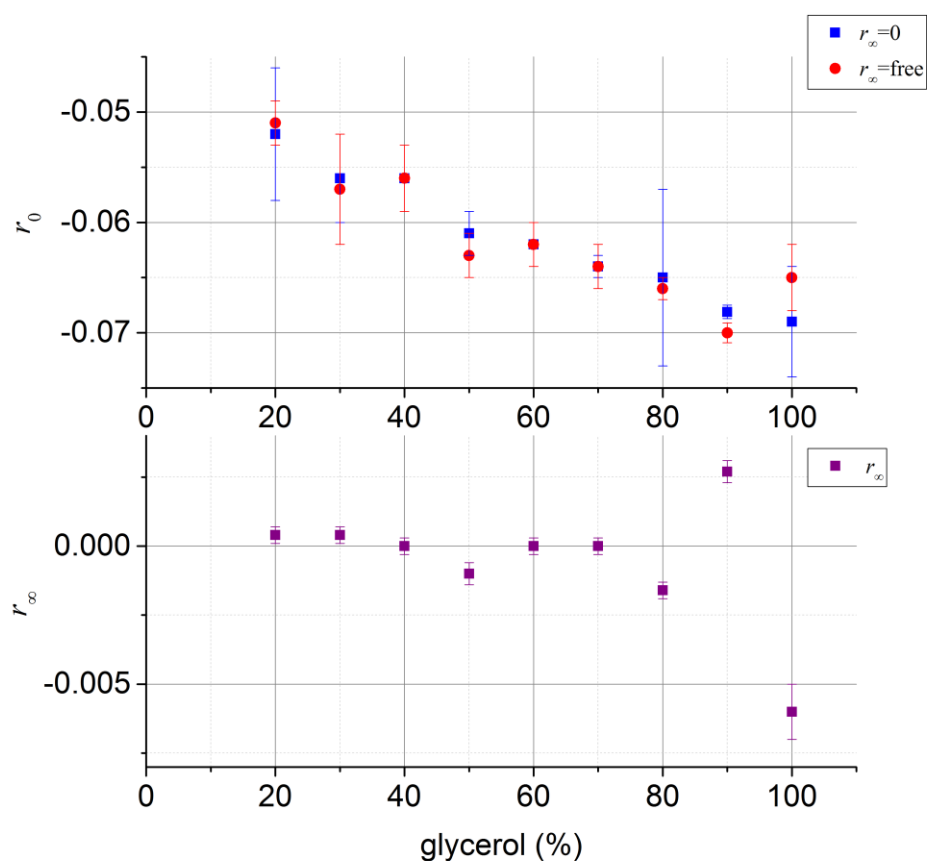
Figure 170: The initial anisotropy plotted with respect to glycerol concentration for DD418L excitation. The magnitude of the initial anisotropy increases with respect to viscosity again indicating solvent relaxation. In all cases the fit to the difference with and without a residual anisotropy yields a similar rotational correlation time although the residual anisotropy again begins to deviate at 100 % when the rotational correlation time becomes larger than the lifetime of ADOTA. The 10% glycerol concentration didn't have enough data at the time range used.
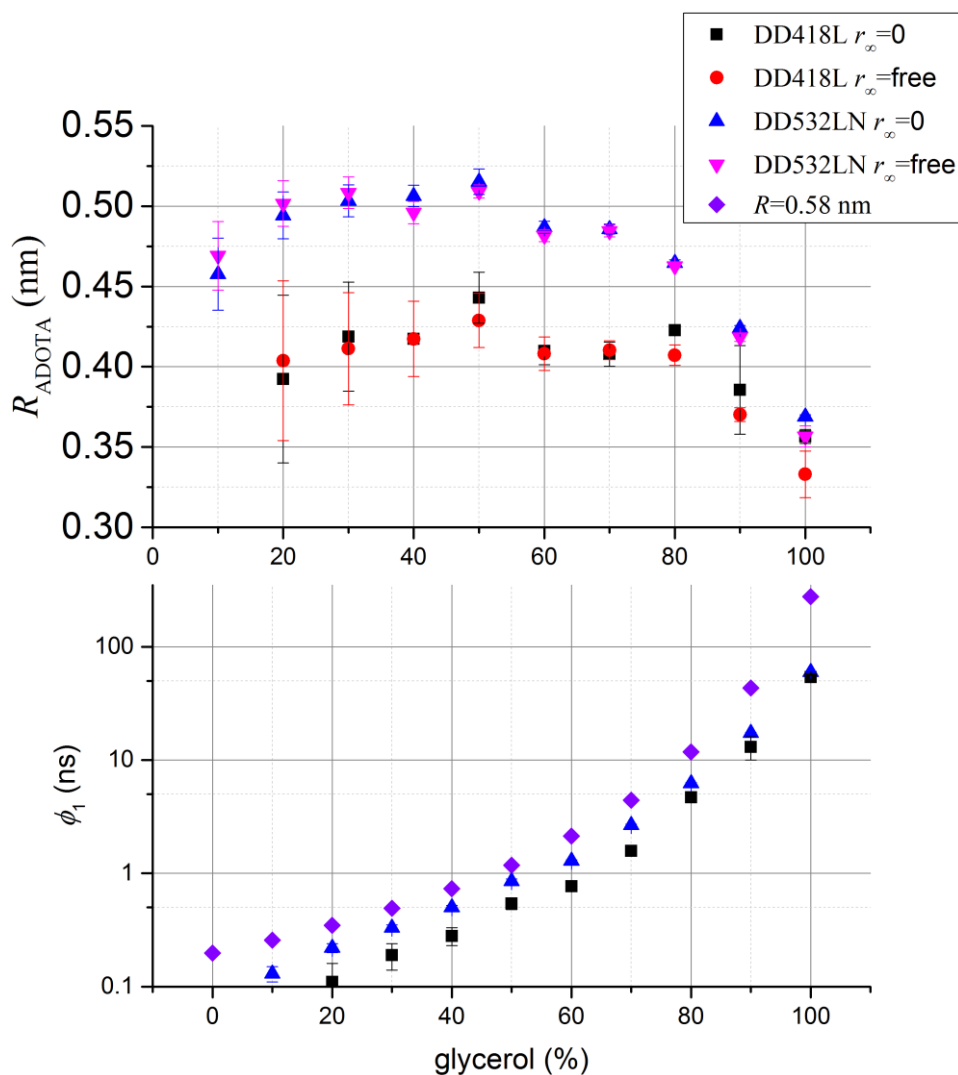
Figure 171: The hydrodynamic radius of ADOTA reported from each anisotropy decay. The radius reported is more or less constant (within error) for glycerol solutions 10-80 % but is measured to be slightly smaller at 90 and 100 %. The rotational correlation time data is smaller when excited with DD418L than with DD532L this is perhaps because ADOTA is smaller in the different transition state or alternatively because $r_0 \neq 0.4$ (DD532L) and $r_0 \neq 0.2$ (DD418L) meaning each decay may be a combination of both transitions. ADOTA has a radius cavity of 0.58 nm and the expected rotational correlation time is plotted alongside those measured. Data is plotted in log scale which is suitable given the differences in rotational correlation time and due to the cubic dependence of **Equation (62)**.
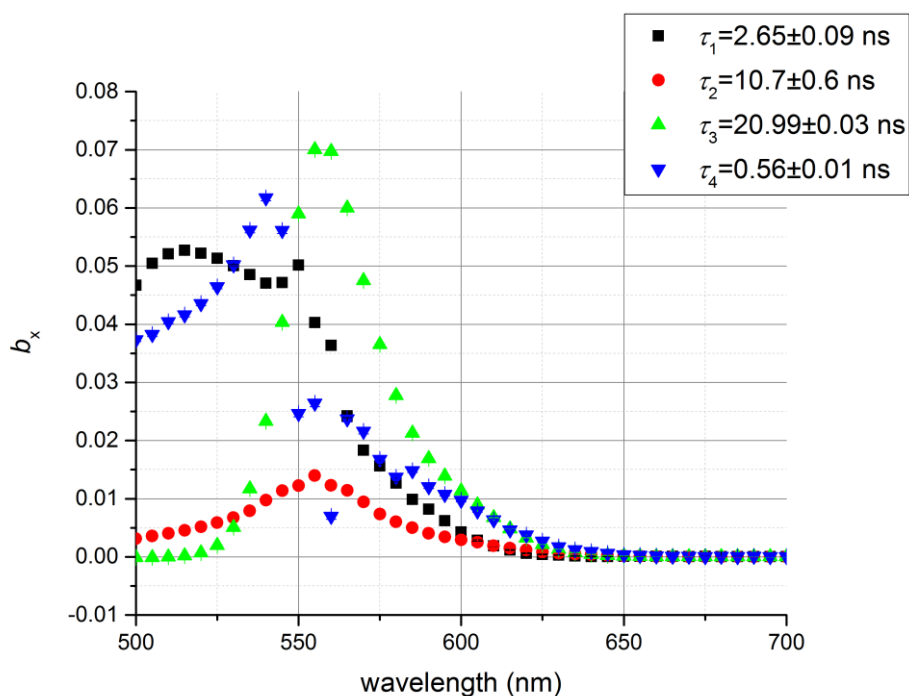
Figure 172: Uncorrected DAS of ADOTA-Acid with A~0.5 in 100 % glycerol measured using DD418L as an excitation source. The additional decay time at 10.7 ns and 2.65 ns are likely prescribed to ADOTA-Acid aggregates. From the DAS it can been seen that the presence of aggregates thus results in an additional shoulder in the steady-state data which is blue-shifted with respect to the fluorescence emission of non-aggregated ADOTA. The 4th component with a decay time of 0.56 ns is short lived, possibly also due to aggregates or to scattered light. Similar decay times are reported when ADOTA is used in thin films also likely to do with aggregation [315].

ADOTA shows some very favourable characteristics as a fluorescence anisotropy probe. It has a stable long-lived red emission which gives a superior signal to noise in particular at the anisotropy tail (**Figure 165**) essentially expanding the time axis which is the limitation of most TRFA metrology measurements. A drawback is that ADOTA has two different transitions, one with positive and the other with negative anisotropy (**Figure 163**) versus Rhodamine 6G (**Figure 74**) which has a single transition with a stable positive fluorescence anisotropy. The presence of the additional transition and solvent relaxation seems to give a viscosity dependence on the initial anisotropy (**Figure 169**). The more rigid the ADOTA the higher the residual anisotropy ranging from about r_0~0.38 (rigid glycerol) to r_0~0.28 (flexible water). For most TRFA metrology applications water will be used as a solvent and r_0~0.28 while this is still sufficient for TRFA measurements it is a slight disadvantage as it contracts the anisotropy axis when compared to a fluorophore such as Rhodamine 6G (**Figure 119**) that has a higher r_0~0.38. A comparison of reported particle size and expected particle size for Rhodamine 6G (**Figure 118**) shows good agreement with deviation being

slight at 90 and 100 % glycerol concentrations which could be due to the error in resolving the rotational correlation time or a solvent effect. ADOTA however is slightly undersized (**Figure 171**) when DD532LN is used as an excitation source and more so when DD418L is used as an excitation source. Although ADOTA has stable emission it is prone to aggregation (**Figure 172**). Low quantities of aggregate shouldn't change the rotational correlation time much when ADOTA is used for nanometrology measurements as the dimer attached to the nanoparticle will be much smaller than the nanoparticle of interest.

Variants of ADOTA based dyes was used as a probe to label BSA [316] as shown earlier with FITC (**Figure 157**). In the case of FITC-BSA the anisotropy was not measured to 0 because the rotational correlation time was ~10 times the size the lifetime of FITC. For the ADOTA data the rotational correlation time measured is ~1.5 times the size of the lifetime of the ADOTA dyes and it is thus possible to measure the decay to 0 anisotropy. The ADOTA data presented gives a slightly shorter rotational correlation time than that extracted with the FITC this slight difference is unsurprising giving the trend reported in **Figure 171**. Silica nanometrology was also carried out using variants of ADOTA based dyes [317].

4.2 ADOTA as a dSTORM Probe?

~1 mg/ml of ADOTA-Acid was prepared as a stock solution using DMF as a solvent. The dye was sonicated to ensure that it completely dissolved. 40 µl of this was mixed with 200 µl of 0.01 % 10,000 MW Dextran and left to incubate for 15 minutes in a LabTek Chamber. After incubation the solution was pipetted off and then the chamber was filled with dSTORM buffer and sealed with a cover slip. The emission of ADOTA in dSTORM buffer was found to be dependent on laser power as ADOTA-Acid formed a photostable dark dye radical (c.f. **Figure 151**) at high laser power as shown in **Figure 173**.
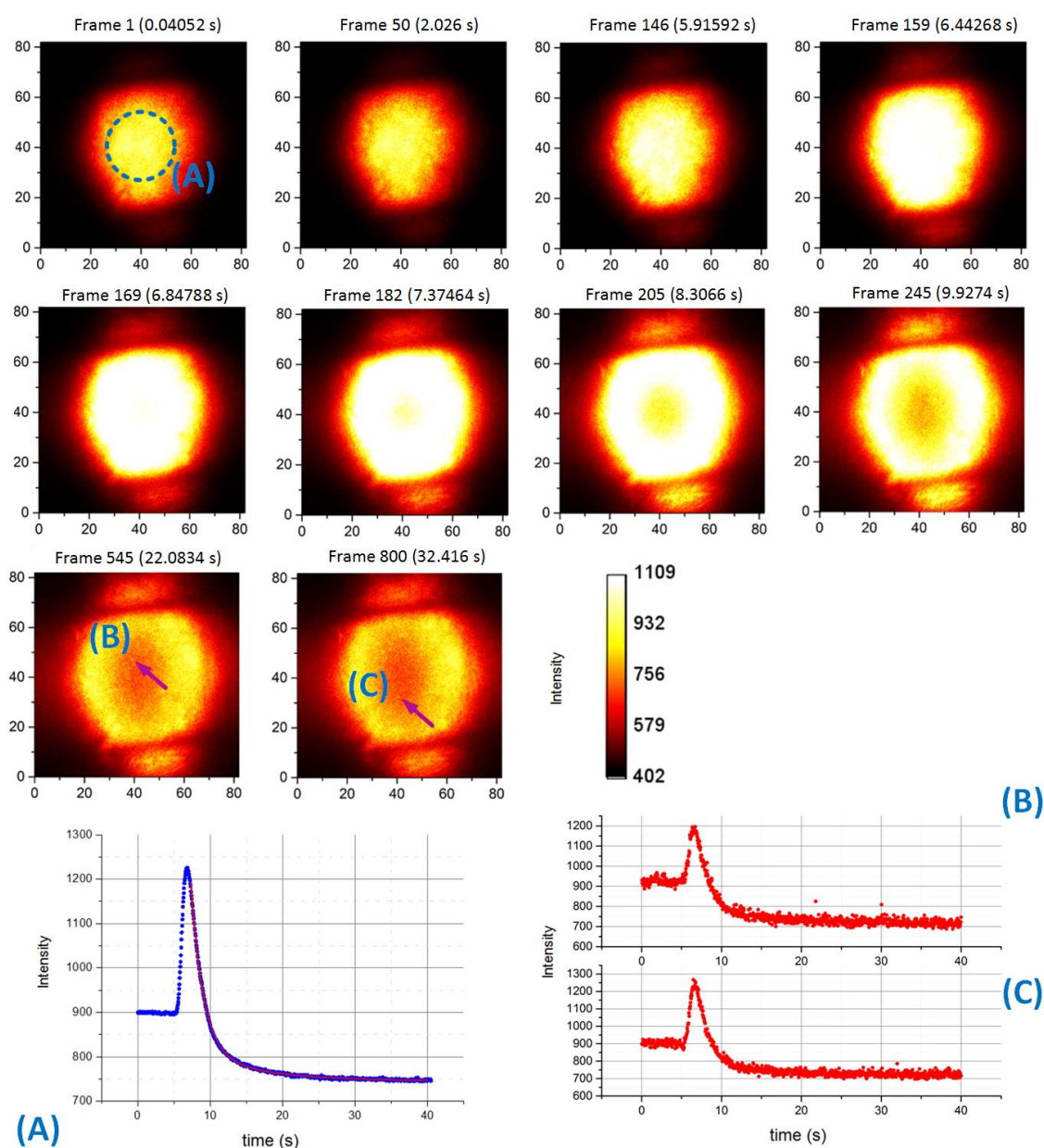

Figure 173: The continuous power of the 488 nm steady state laser was altered from 5 % to 90 % using a waveplate. A BP 525/50 nm was used at the emission. Each frame (512×512

pixel, 160 nm/pixel) had an acquisition time of 0.01 s but the overall cycle time was 0.04052 s due to the high readout time of the CCD. Data is plotted in µm and in real-time. Selected frames at time intervals as the laser power is ramped up. The fluorescence intensity from ADOTA-Acid is seen to resemble the Gaussian shape of the laser when the power is maintained at 5 % (Frames 1 and 50). As the laser power is increased to 90 % (Frames 146, 159 and 169) the fluorescence intensity is seen to increase firstly at the central spot and then towards the edges until a continuous fluorescence intensity is observed (Frame 169). The central spot then stops fluorescing as the high laser power leads to the formation of the stabilised ADOTA-Acid dye radical $F^{\bullet-}$ (Frame 182). The dark central spot of this donut increases in diameter (Frames 205, 245 and 545) while the edges of the donut which have less power than the central spot continue to fluoresce. Single molecule blinks (Frames 545 and 800) can be observed within the central donut. (A) is the average bulk intensity time profile over the central donut, (B) is the average intensity profile over the pixels where the single molecule blink as observed in Frame 545 and this blink is seen to repeat in Frame 740 and (C) is the average intensity profile over the pixels where the single molecule blink is observed in Frame 800.

The data in **Figure 173** may be resliced c.f. **Figure 150** in order to visualise the single molecule blinks in more detail. **Figure 174** shows reslicing by x with each slice corresponding to a pixel of 160 nm (512 slices). Looking at the slices in more detail particularly near the centre of y (~40 µm) and heading from the outside of x to the centre. Firstly, the dark counts can be seen to be ~400 counts likely predominated by the readout noise of the CCD. At the edge of the Gaussian laser beam (slices 6 and 106) weak fluorescence can be seen ~500 counts. Next the rims of the donut can be clearly seen (slices 56-106 and slices 406-456) and these have ~900 counts. Slices 206-306 show the photostable dark state achieved at high laser power which is approximately 700 counts. With the photostable dark state some single molecule blinks can be observed which have approximately 750-850 counts. Using these numbers with **Equation (21)** gives a SNR_{FSD}~2-6 which is extremely poor. The photoswitching is reversible, **Figure 175** shows the resliced data when the sample is illuminated with 90 % power and this is lowered back to 5 %. The fluorescence on the outside regimes is seen to decrease as the laser power is lowered as expected. In the middle the fluorescence returns as there is not enough power to form the stable ADOTA-Acid dye radical $F^{\bullet-}$. Naturally the laser power leads to the formation of the ADOTA-Acid dye radical $F^{\bullet-}$ and the increase of the laser power further may significantly reduce the dark counts closer to the level of the CCD dark counts which would give a minor improvement in the SNR. The maximum laser power in this instruments configuration was used moreover in the ideal case one is looking for a fluorophore which requires significantly less power to photoswitch in order to reduce photodamage for dSTORM applications. **Figure 176** shows the same central spot **Figure 173** measured when

the laser power is ramped up and down from 5 % to 50 %, 75 % and 90 % respectively. This data is fitted in **Table 8**. It can be observed that the overall fluorescence intensity of the central spot is higher at 50 % and 75 % because the formation of the ADOTA-Acid dye radical $F^{\bullet-}$ is less efficient. The single molecule blinking was similar for these laser powers but as the background level is higher the SNR_{FSD} is even worse. Normally for dSTORM measurements the full 512×512 pixels aren't used as only the central regime of the donut is of interest where photoswitching occurs. Using 128×128 pixels reduces the readout time (0.01912 s cycle time for a 0.1 s CCD capture rate) and the reduction in cycle time will allow for the measurement of single molecule blinks in more frames. When measured under these conditions the localisation precision obtained was ~75 nm (**Figure 177**). This resolution is superior to the diffraction limit but not higher than commercial fluorophores which can achieve a localisation precision <20 nm [286]. The main reason for the lower precision is that the brightness of each individual single-molecule blink is too low and hence the localisation precision is limited by the SNR. The low brightness is likely due to the extinction coefficient of ADOTA 9480 L mol^{-1} cm^{-1} being approximately a tenth of the value of high performing fluorophores [286]. For ADOTA reproducing the experimental results was difficult. At high concentration the sample tended to aggregate. The preparation of stock ADOTA-Acid using water instead of DMF in particular caused a high degree of aggregation. Aggregated ADOTA-Acid shows bright blinks and a large number of localisations. Because the aggregates are not single molecules the camera counts displayed a series of Gaussian peaks opposed to a single one **Figure 178**. The blink profile of an aggregate **Figure 179** shows an exponential decay opposed to a step function which would be observed for a single molecule blink. The profile of the aggregate also shows continuous emission and not on/off characteristics like a single molecule blink **Figure 180**. Use of meADOTA instead of ADOTA-Acid also resulted in aggregates presumably because of the lack of a functional group to interact with the dextran when labelling the slide. The aggregates are clearly observed in a diffraction limited context image **Figure 181**. ADOTA-Acid showed some desirable characteristics for dSTORM measurements and the above data nicely outlines the principle behind dSTORM showing how high laser power and a dSTORM buffer leads to a photostable dark state. ADOTA-Acids photostability is incredible and its switching behaviour is on the correct time scale required to quickly capture a series of blinks to form a super-resolution image.
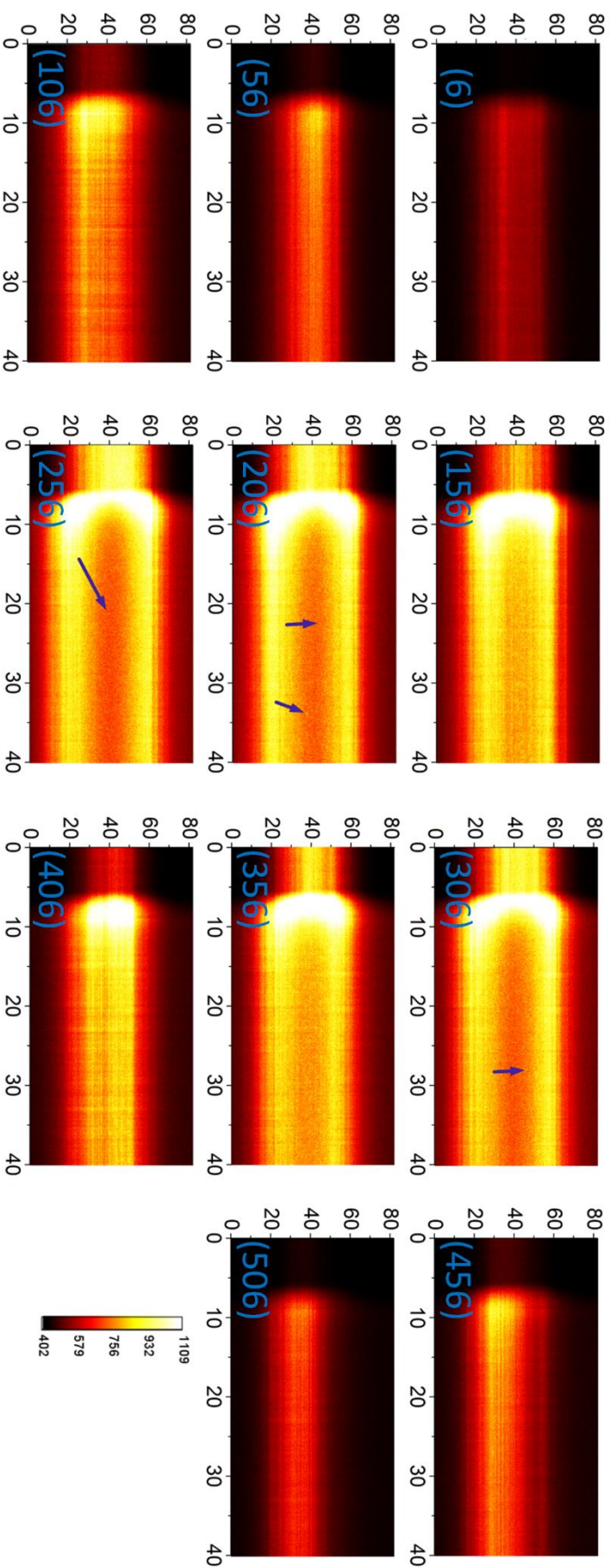
Figure 174: The data can also be resliced using Image J. That is cutting orthogonal slices through the image volume. The x and y axes displayed are t (s) and y (μm) respectively. The slices of x are 6, 56, 106, 156, 206, 256, 306, 356, 406, 456 and 506 pixels respectively (with 0.16 μ/pixel). Single molecule blinks are observed in frames 206, 256, 306 where the intensity of the laser is the highest. As mentioned these are difficult to see over the background noise.
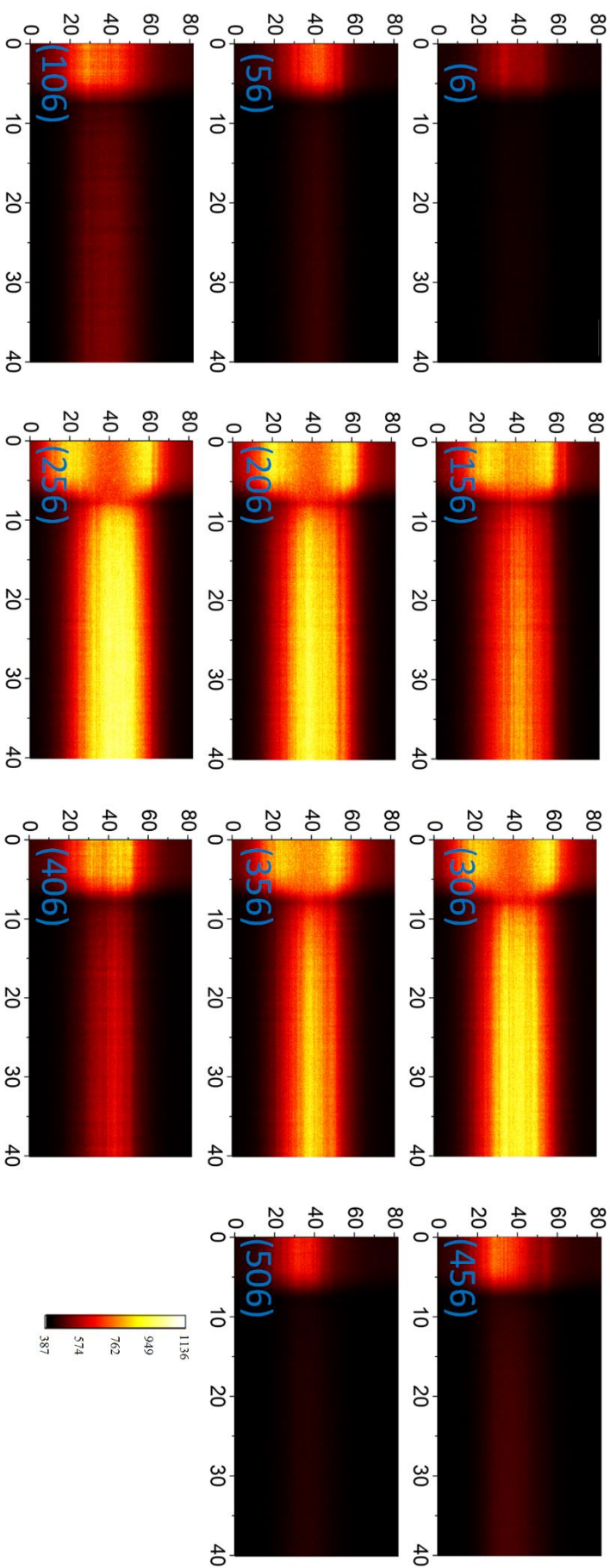
Figure 175: The same sample with the laser power set to 90 % and lowered back down to 5 %. The x and y axes displayed are t (s) and y (µm) respectively. Slices of x are 6, 56, 106, 156, 206, 256, 306, 356, 406, 456 and 506 pixels respectively (with 0.16 µ/pixel). Looking particularly at slices 205, 256 and 306 when the laser power is at 90 % the photoswitchable dark state is prominent with the presence of single molecule blinks. When the laser power is lowered back to 5 % the photoswitchable dark state fades and fluorescence from all the molecules is observed. The reaction is therefore reversible.

215
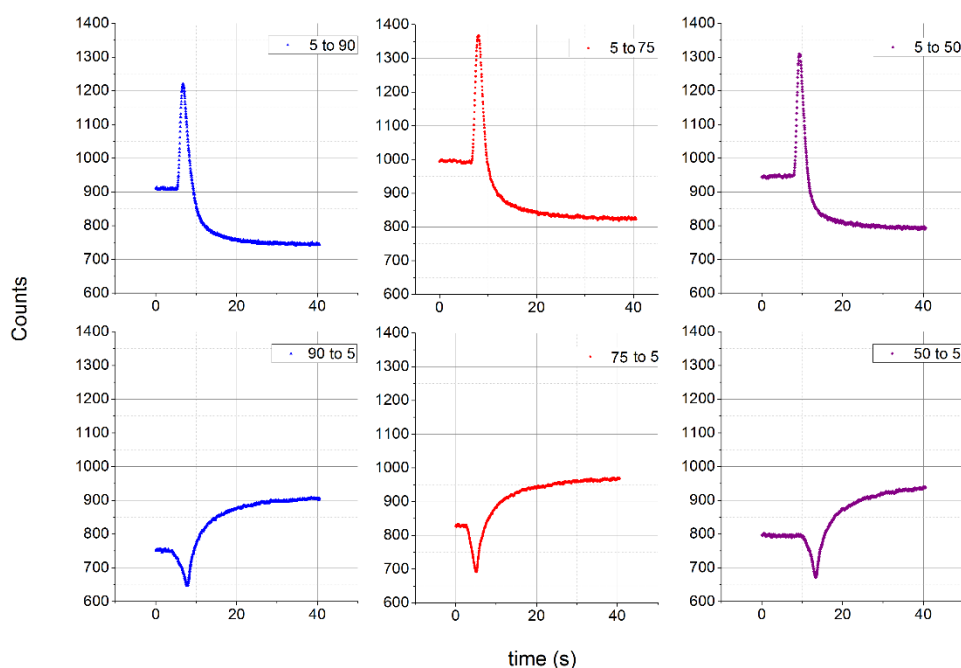
Figure 176: The effect of increasing and decreasing the laser from 5 to 90 % and back down to 5 %, 5 to 75 % and back to 5 % and 5 to 50 % and back down to 5 % respectively. A fresh field of view was selected for each power ramp.

Table 8: The fit of the exponential fall and rise when the laser power is raised and lowered. Two decay times were recorded. The first one is likely related to the time it takes for the waveplate to turn and the second is likely due to the loss of fluorescence via the formation of $F^{\bullet-}$ and vice-versa. The ramp up and down from 5 %→90 %→5 % shows a more or less completely reversible reaction with pre-exponential factors being similar and the rate and annihilation of $F^{\bullet-}$ being equivalent. In the cases of 5 %→75 %→5 % and 5 %→50 %→5 % the time for formation of $F^{\bullet-}$ takes longer than its annihilation. This dye is observed to be extremely photostable.

Power increase	b_1	τ_1 (s)	b_2	τ_2 (s)	R^2
5 to 90 %	14000±400	2.01±0.02	65±6	16±3	0.997
90 to 5 %	−11400±800	−1.78±0.04	−280±10	−9.3±0.2	0.998
5 to 75 %	430000±30000	1.20±0.04	220±20	8.7±0.5	0.995
75 to 5 %	−3000±100	−1.73±0.03	−212±5	−9.7±0.2	0.998
5 to 50 %	250000±20000	1.52±0.02	65±3	25±9	0.994
50 to 5 %	−240000±30000	−1.79±0.04	−490±20	−10.4±0.3	0.998
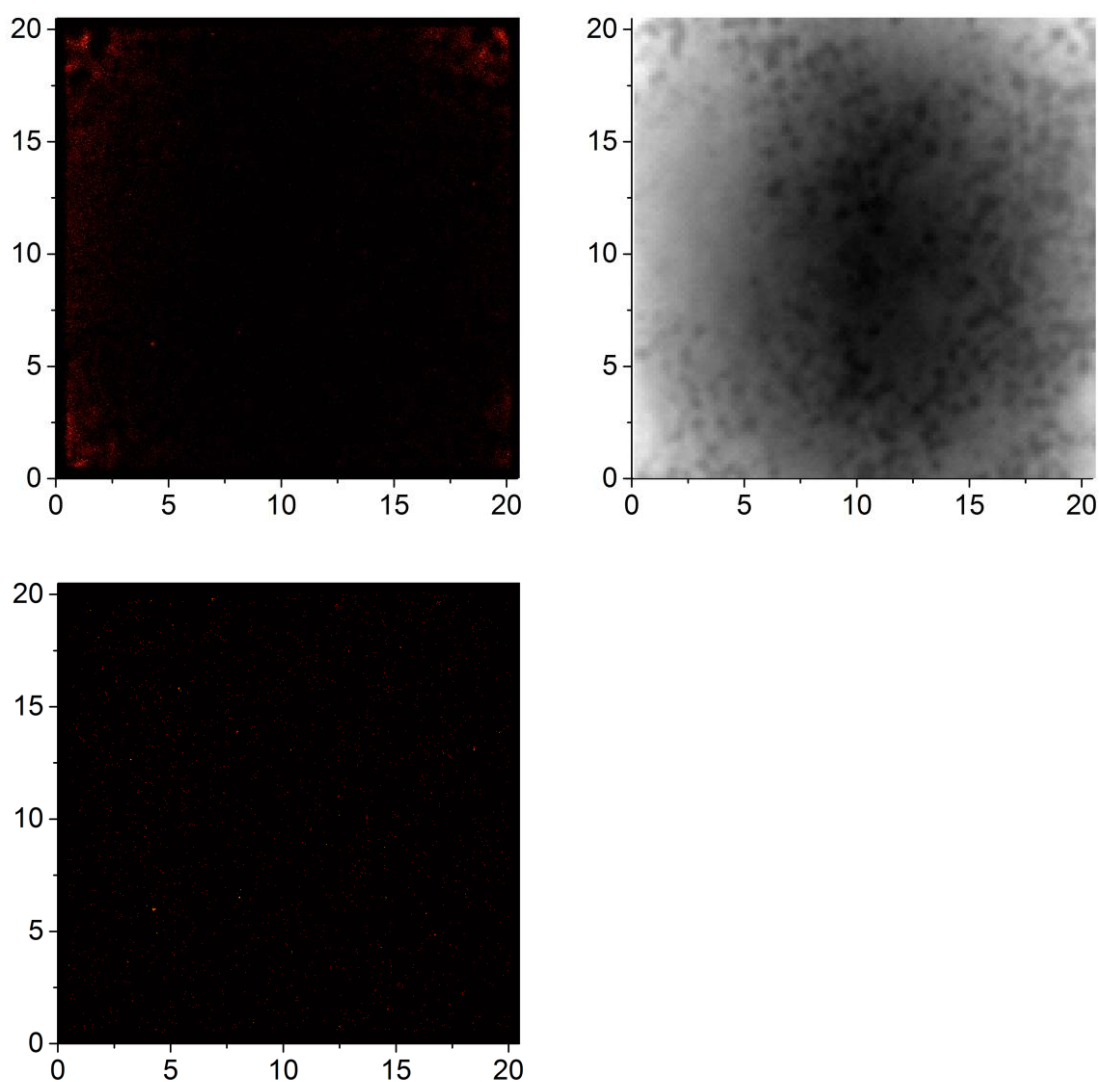
Figure 177: A look at the centre data measured using 10000 frames and an exposure time of 0.01 s (cycle time of 0.01912 s). The dataset was analysed by RainSTORM to get the plot of localisations (top left), diffraction limited sum (top right) and accepted localisations (bottom left) with a localisation precision of 77 nm in *x* and 73 nm in *y* respectively.
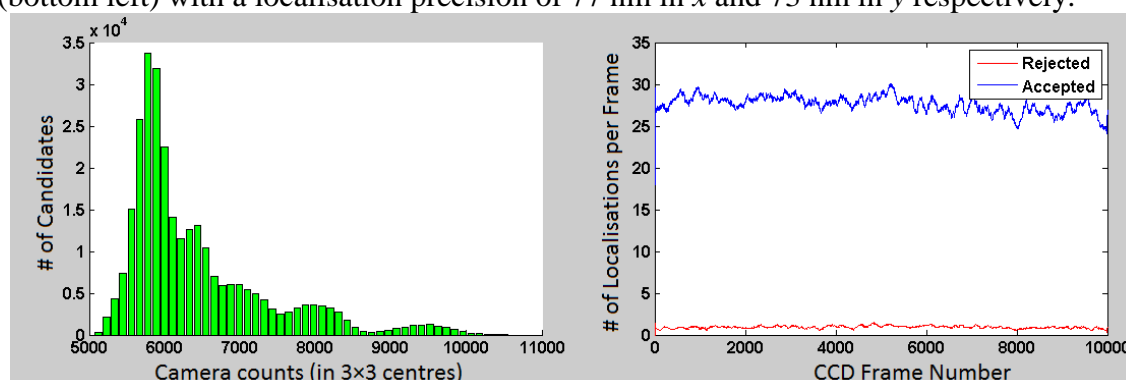
Figure 178: ADOTA carboxylic acid gave a high number of localisations per frame and the candidate brightness was high as desired however the candidate profile showed multiple distributions suggesting aggregation.
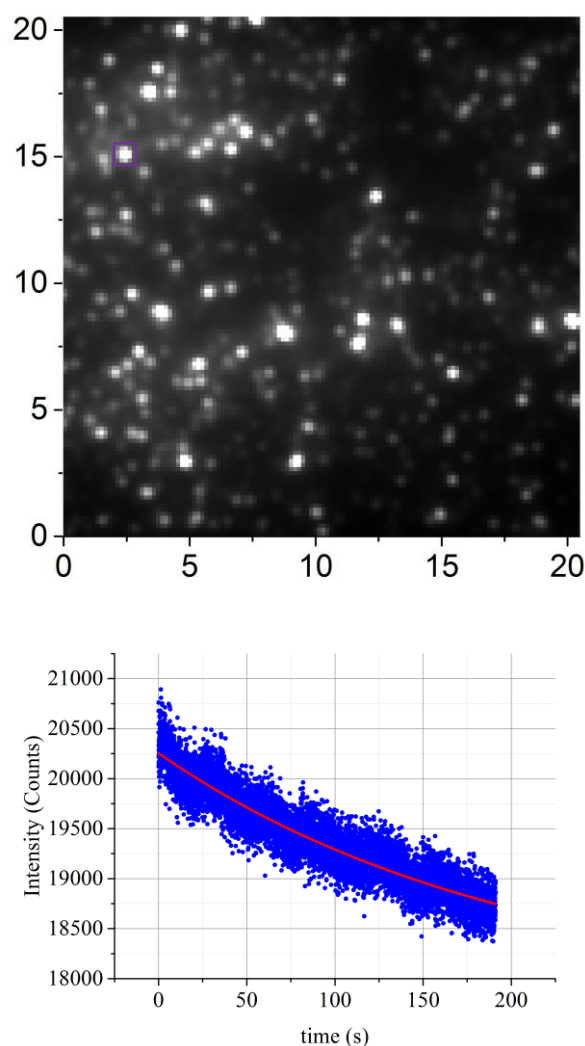
Figure 179: The sum image of the ADOTA-Acid measured with a CCD capture rate of 0.01912 s for 10000 frames. 128 pixels were used in both x and y at 160 nm/pixel. A bright blink was selected and examined in more detail. Its brightness was observed to decrease with respect to time and roughly fitted to an exponential decay of the form $y=A_1\exp(-x/t_1)+y_0$ where $y_0=17800\pm50$, $A_1=2450\pm40$, $t_1=200\pm6$ and $R^2=0.879$. This exponential decay confirms the formation of aggregates and is not characteristic of a single molecule blink.
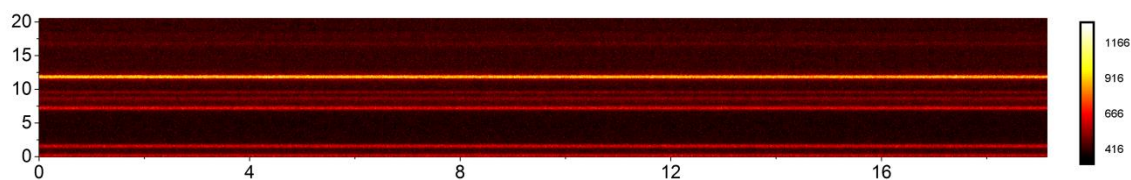
Figure 180: Image J reslice of the data from the top, pixel 77 (12.32 µm). The resliced data x scale bar being time in seconds and the y scale bar being the dimension in µm. The reslice shows continuous illumination of ADOTA-Acid. This is not desired for a dSTORM probe.
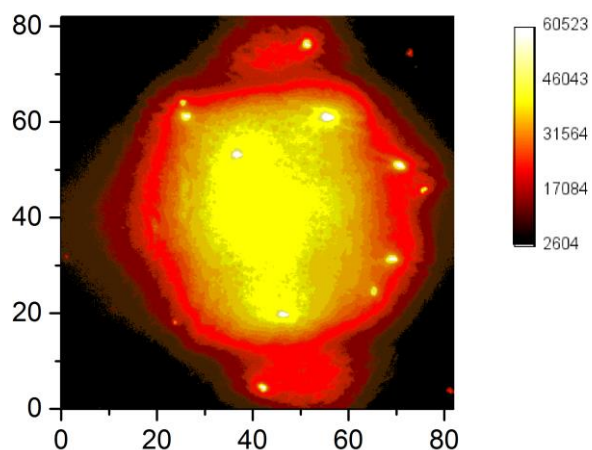
Figure 181: Context image of meADOTA shows the formation of very bright aggregates. The concentration of meADOTA was lowered significantly and showed a similar trend. This is likely due to the fact that the meADOTA did not have a functional group to react with the dextran and hence formed aggregates.

Although ADOTA shows favourable photoswitching characteristics and photostability. The two drawbacks limit its use as a probe for dSTORM. The first is the signal to noise as its single-molecule blinks are not bright enough to be clearly distinguished from the noise background and hence limiting the localisation precision. The second is its tendency to aggregate; aggregate molecules ironically overcome the signal to noise problem as they are extremely bright but paradoxically remove the single molecule blinking conditions necessary to circumvent the diffraction limit.

5. Spectroscopy of Gold Nanoclusters and their use for Nanometrology

Nanomaterials made from metal atoms is a growing research area, the understanding of their synthesis and tuning of their properties can lead to an array of next-generation nanomaterials including new types of fluorophores. It is widely accepted that the particles with diameters larger than 2.0 nm but less than 100 nm are called nanoparticles and particles with diameters smaller than 2 nm are called nanoclusters. Minuscule particles with core sizes smaller than 1 nm can be defined as sub-nanometre clusters [318]. Metal nanomaterials in the 1-100 nm range don't exhibit the typical behaviour of bulk metal materials which essentially have a continuum of electrons forming overlapping conduction and valence bands that are well described in most undergraduate solid-state physics textbooks [319]. They instead have a discrete number of electrons and therefore a number of discrete energy levels hence exhibiting photophysics more on par to that of a molecule. Nanoclusters are said to provide the missing link between the transitions of atomic to nanoparticle behaviour in metals [320]. They have an array of potential applications possessing high catalytic properties [321] and of consequence to this work strong photoluminescence [322–324]. Unfortunately the size-shape dependant behaviour of noble metals and the development of plasmon remain very poorly understood [320]. Similar to the production of silica nanoparticles a source of monomer is required. In general, this is gold salt $HAuCl_4$ and a reducing agent is required to liberate Au^0 from the salt. The final step is to stabilise the nanoclusters and functionalise them so they can be used as fluorescence probes. The stabilisation of nanoclusters i.e. the prevention of the further aggregation to bulk gold is the main difficulty of nanocluster synthesis. Recalling that in particular gold is regarded as the noblest metal making it extremely stable and relatively chemically inert [325]. The strong drive to form bulk gold and the nm regime hence make conventional synthesis methods extremely difficult. In practise many synthesis methods therefore use a template which helps both in the formation of the nanoclusters and once synthesised the template acts to protect them. Templates which contain sulphur are particularly effective as the Au-S bond is strong allowing stabilisation of the nanocluster [326] moreover in many cases the protection template itself can also act as a reducing agent [327]. Atomic gold nanoclusters tend to prefer to form clusters of magic sizes which are inherently more stable [328] unfortunately the size and constituent of the template can vary

these magic numbers [329,330]. These synthesis techniques are relatively easy to perform but difficult to purify and normally the template is significantly larger than the nanocluster. Spectroscopy of the nanoclusters is obviously important when considering nanoclusters as fluorophores however it is also useful in helping to characterise them and to optimise their synthesis. Stable clusters tend to adopt discrete electronic structures and exhibit unique nuclear/structure-dependant optical and electronic properties, magic numbers such as Au_{13} [331] or Au_{25} are particularly stable.

5.1 Au$_{25}$@BSA Protein Synthesised Gold Nanoclusters

One protocol to make these nanoclusters is by using a protein template [332] such as trypsin, BSA and HSA which all contain cysteine groups that facilitate Au-S bonds stabilising the nanocluster. Protein template gold nanoclusters boast high biocompatibility unlike quantum dots. As it is one of the most economic and readily available proteins BSA will be used as an example. Au_{25}@BSA nanoclusters were made according to the protocol mentioned by Xie et al [333,334]. A highly concentrated BSA solution is heated to 37°C (5 ml of 50 mg ml^{-1}) and stirred gently using a magnetic stirrer until it dissolved. 5 ml of 10 mM AuCl$_4$ was added to this mixture, maintaining the temperature to 37°C and using vigorous stirring. After 2 minutes, 1 ml of 1.0 M NaOH was added. For the synthesis of Au_{25}@BSA nanoclusters the protein concentration necessary to force the formation of the nanoclusters is very high making spectroscopy measurements more difficult.
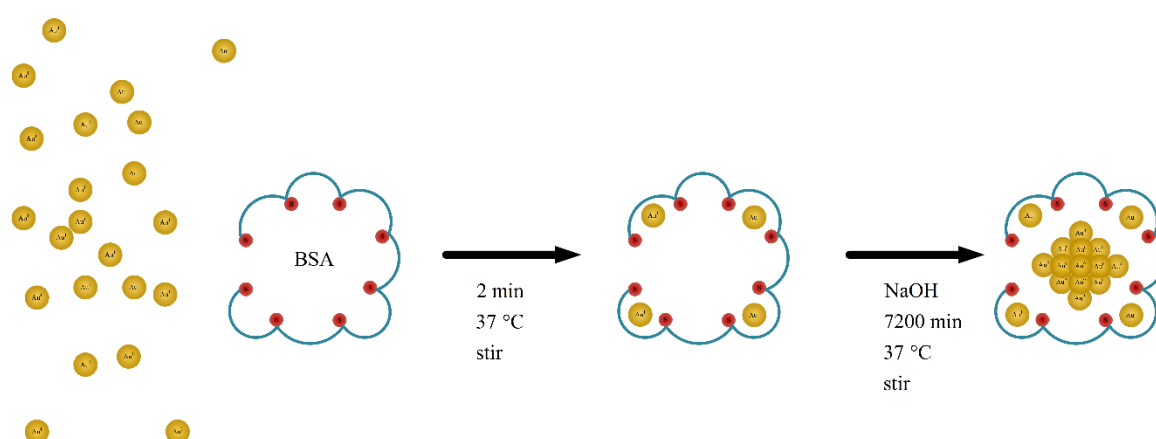
Figure 182: Principle of Au$_{25}$ nanocluster synthesis via the BSA protein template method as documented by Xie et al. [333]

From a spectroscopy point of view these nanoclusters are difficult to measure because they have a wide spectra meaning second order effects take effect and care has to be taken with

the correction factors. In addition, as they are synthesised using a BSA protein template at high concentrations meaning strong inner-filtering effects and dilution is not possible during synthesis as the high concentration is required to drive the kinetic reaction. The spectra reported here differ from previous publications [333–335] as wavelength correction factors are applied removing the double peak artefact from the Wood's anomaly. Moreover front-face configuration has been used to overcome inner-filtering effects which lead to incorrect conclusions [336].

In order to measure the absorbance spectrum with respect to time a NanoDrop 2000c was selected. This spectrophotometer has a 1 mm path length opposed to a standard 10 mm path length and is more ideally suited for the measurement of such high absorbance. The absorbance spectra were recorded every 5 minutes for 2 hours using a NanoDrop 2000c. Although a spectrophotometer which is designed to measure high absorbance samples via a shorter path length, scattering remains a significant problem with this dataset c.f. **Figure 25** the combination of high concentrations of BSA **Figure 130** and also gold results in high scatter. From **Figure 183** there is a change in the absorbance spectrum of Au_{25}@BSA nanoclusters compared to BSA but the actual spectra are highly distorted by scatter. There is a significant increase in the absorbance, both in the UV regime where BSA strongly absorbs, as well as the growth in absorbance at 300-500 nm where BSA has a smaller absorbance. To see the growth in absorbance in more detail, particularly at the tail, it is insightful to re-plot the absorbance on a log scale. The absorbance may also be plotted with respect to time for a single wavelength **Figure 184**. At 280 nm there is an increase in the absorbance from the beginning of the reaction. At 325 nm there is a dip in the absorbance for the first 5 minutes; as the BSA reacts with the 1.0 M NaOH, this drop is followed by a subsequence growth. At 420 nm there is a similar pattern however there is a fall in the absorbance for the first 20 minutes before a growth is observed. At 500 nm there is also a growth in the absorbance but this begins 30 minutes after the synthesis. It should be noted however that this data set is highly influenced by Rayleigh scatter. Raut et al. correct the absorption spectra for Rayleigh scattering and prescribe the absorption spectra to have 3 components [337].
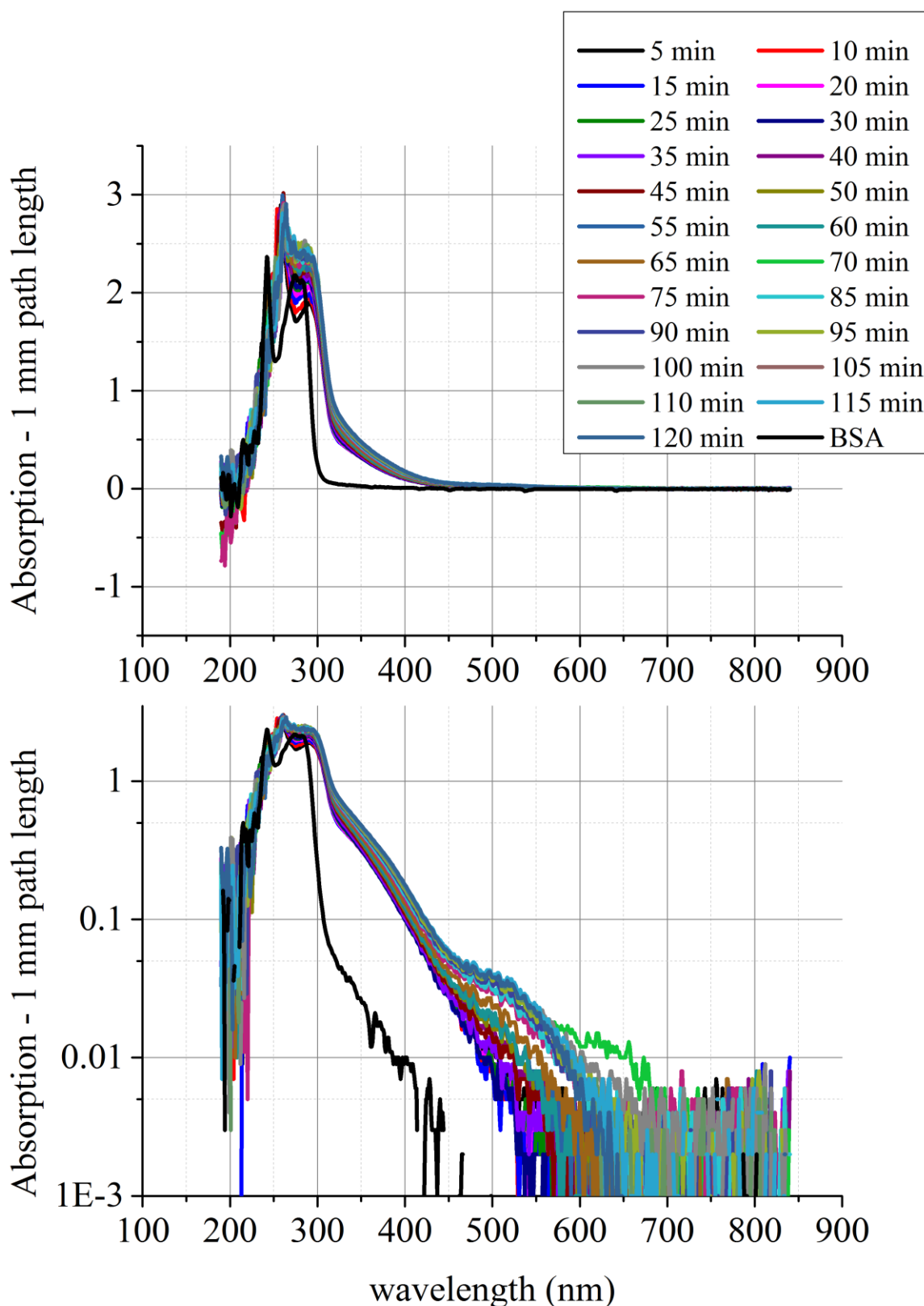
Figure 183: Absorption spectra of Au_{25}@BSA nanoclusters for the first 2 hours during formation, measured on a NanoDrop 2000c plotted in linear scale (top) and log scale (bottom). The concentration of this sample is near the upper limit for the NanoDrop 2000c as shown by distortion on the UV side of the spectra. The NanoDrop was ran from 190-840 nm with a wavelength increment of 1 nm.
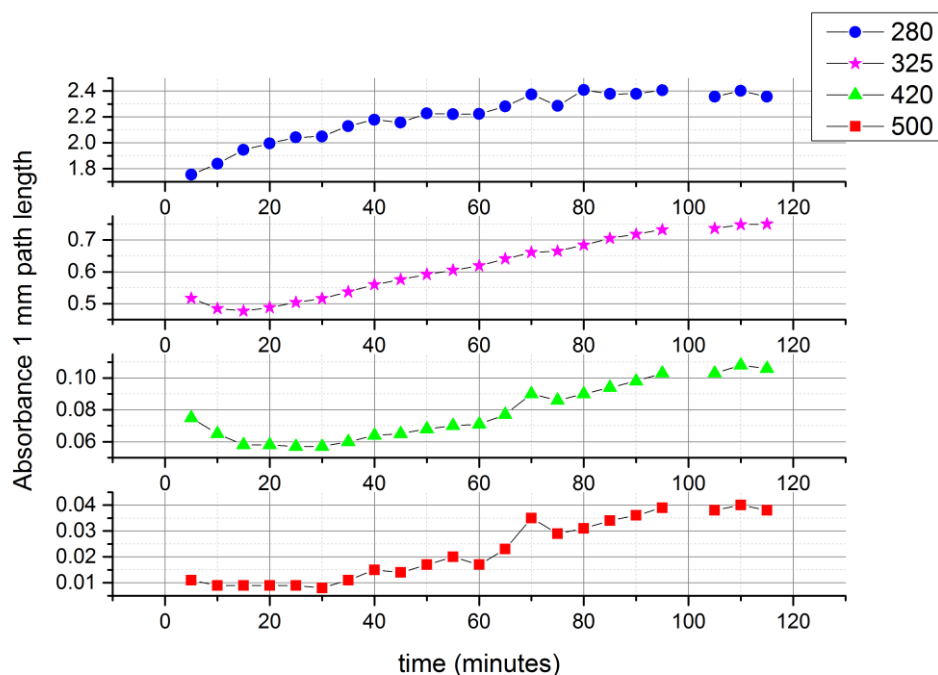
Figure 184: The absorbance of the Au$_{25}$@BSA with respect to time for a 1 mm path length measured using a NanoDrop 2000c. 4 wavelengths were selected; 280 nm, 325 nm, 420 nm and 500 nm.

Fluorescence is more sensitive and less influenced by scattering effects than absorbance. In order to analyse the sample in more detail, some clean-up was performed after its synthesis. The fluorescence profile of the nanoclusters is reported to be pH dependent [338] with ~pH 9 being reported to be the pH with the highest fluorescence intensity. In order to assess the inner-filtering effects the sample was dialysed into 0.1 M TRIZMA buffer using a 15 ml 10 K Slide-A-Lyzer G2 dialysis cassette. Dialysis will remove any small impurities such as free gold chloride salt and any fatty acid residues moreover, it ensured that dilution into buffer did not change any other parameter particularly pH except the optical density. The EEM of the Au$_{25}$@BSA nanoclusters is widespread and goes through several orders of magnitude so a linear scale does not do it justice, its more insightful to analyse it under a log scale. Dilution of the sample by 10 times shows a complete transformation in the measured EEM due to the inner filtering effect, the UV component of the excitation spectrum gets filtered out first as can be seen by comparing the 10 % and 20 % optical density samples. The components of the EEM at 300-400 nm excitation and 400-500 nm emission next gets highly distorted by the inner-filtering effects as the optical density increases. At high concentrations **Figure 185** the EEM is completely distorted with respect to the true EEM due to inner filtering effects shifting the spectra to higher wavelengths.
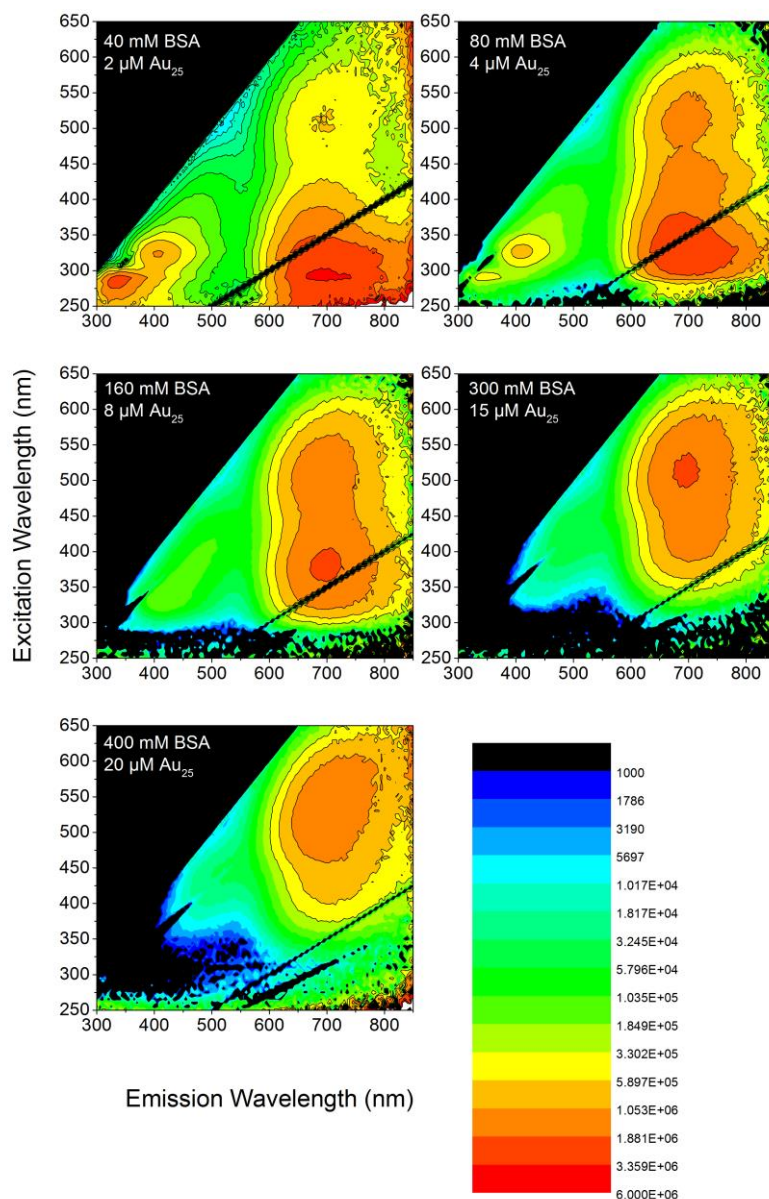
Figure 185: EEM of Au₂₅@BSA measured at right angle conditions as this Fluorolog 3-22 did not have the Front Face accessory. The excitation monochromator (double grating 1200/330) was set to a 5 nm bandpass and stepped from 250-650 nm in 5 nm increments. For each excitation wavelength the emission monochromator (double grating 1200/500) set to a 5 nm bandpass was scanned from 300-850 nm in 5 nm increments. The sample was diluted to 10 % (~40 mM BSA, 2 µM Au₂₅), 20 % (~80 mM BSA, 4 µM Au₂₅), 40 % (~160 mM BSA, 8 µM Au₂₅), 75 % (~300 mM BSA, 15 µM Au₂₅) and undiluted (~400 mM BSA, 20 µM Au₂₅). At concentrations up to 10 % dilution most of BSA's EEM is visible and the spectra appears relatively undistorted i.e. is similar to that obtained for concentrations at 1 % dilution. When the sample is more concentrated in the case where it's diluted to 20 % the emission of the BSA begins to get filtered out. This is more apparent when diluted to 40 % where there is no emission from lower wavelengths of excitation. At 75 % dilution the EEM maxima of the Au₂₅@BSA has completely shifted to higher wavelength. Finally,

the EEM of an undiluted sample is highly distorted to the extent that there is a high mismatch from the background subtraction (see the bottom and the right hand side of the spectra). The EEM measured in this case is completely different from the true EEM.

This sample is difficult to measure correctly, the EEM cannot accurately be corrected using the absorbance spectrum **Figure 184** due to the high distortion from scatter. One additional difficulty is the EEM is broad particularly in the red where the standard detector the R928 PMT begins to rapidly lose quantum efficiency c.f. **Figure 34** and hence has a huge associated wavelength correction factor. There is also the additional complication of secondary order effects c.f. **Table 3** as much of the intensity recorded at 280 nm excitation and 680 nm emission will be remeasured BSA 340 nm emission at second order. Longpass filters placed on the emission arm can be used to reduce second spectra distortions.
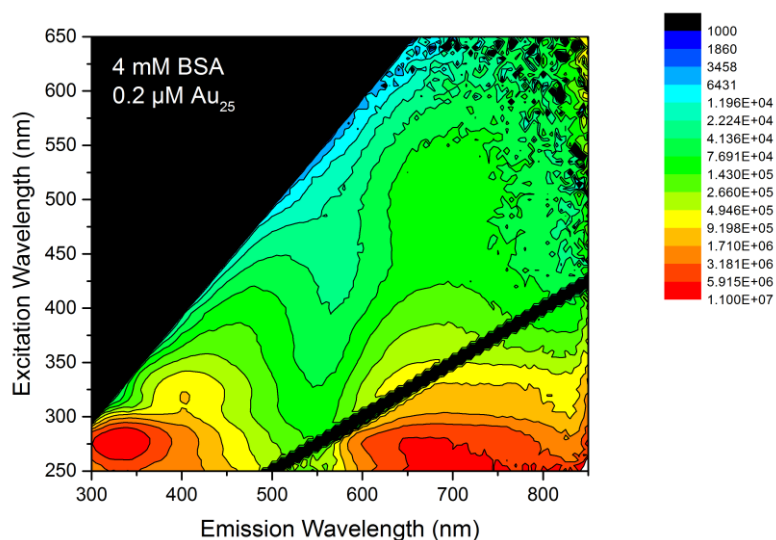
Figure 186: The EEM of 1 % Au$_{25}$@BSA nanoclusters in a 6Q quartz cuvette with 0.1 M TRIZMA buffer and subtracting a background EEM of a matching 6Q cuvette filled with 0.1 M TRIZMA buffer measured using the same experimental conditions as **Figure 185**.
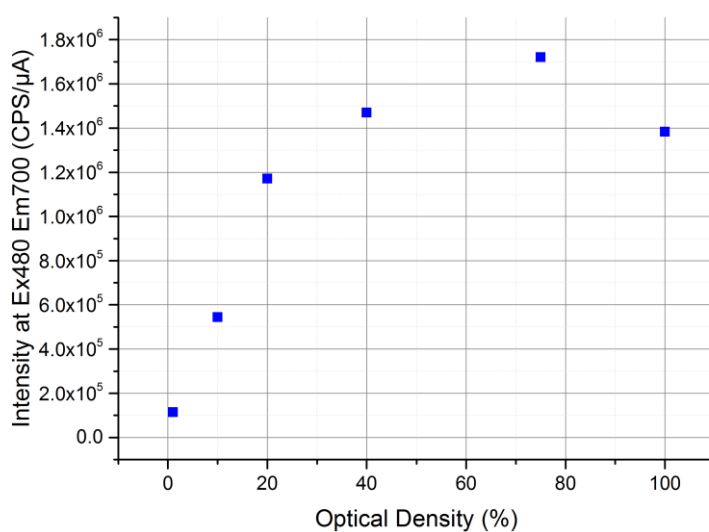
Figure 187: Effect on optical density on the fluorescence intensity of Au_{25}@BSA nanoclusters dialysed into TRIZMA buffer recorded at excitation wavelength of 480 nm and an emission wavelength of 700 nm. For this highly concentrated sample; the measured fluorescence intensity does not grow in proportion to the concentration this is due to severe inner-filtering. Even between 1 and 10 % optical density the intensity increases 5 fold opposed to 10 fold as expected. The growth dependence in fluorescence intensity gets progressively weaker as the concentration increases, until it reaches a point where the fluorescence intensity actually decreases due to increasing optical density.

To combat the effect of optical density on the fluorescence intensity (c.f. **Figure 185** and **Figure 187**) the cuvette was seated in a front face cuvette holder. The EEM was measured at full concentration after a completed reaction (**Figure 189**) and resembles the diluted EEM measured at right angle (**Figure 186**). This EEM can be compared with a BSA and NaOH control sample (**Figure 188**) also reacted under the same conditions. Unfortunately, as the EEM is extremely broad second order wavelength effects come into play which is more evident when examining the control sample. To prevent second order emission from the BSA overlapping with the red emission of the Au_{25}@BSA nanoclusters a LP505 filter on the emission arm. These EEMs were remeasured (**Figure 191** and **Figure 192**) in a state of the art Fluorolog 3-222 (Edison ISA application lab) which had a front face mirror and a cuvette stirrer and water bath. The EEMs of the completed samples revealed 3 hotspots in the BSA EEM which each exhibited second order. The nanocluster emission was seen to be strong in the red at excitation emission wavelengths of 420, 660 nm and 500, 680 nm respectively. It should be noted however that the kinetics of reaction in this instrument took slightly longer than normal which may be due to a small variance in reaction conditions in particular pH and temperature and the freshness of the chemicals used. Time on this

instrument was limited so the kinetic data could not be validated. The EEMs structure however resembles time-resolved data from decay associated spectra and thus has more supporting evidence (**Figure 193**). The proportion of emission with UV excitation in comparison to 400-500 nm excitation differs significantly in both EEMs and is assumed to be an optical effect (Front Face mirror vs Front Face cuvette holder).
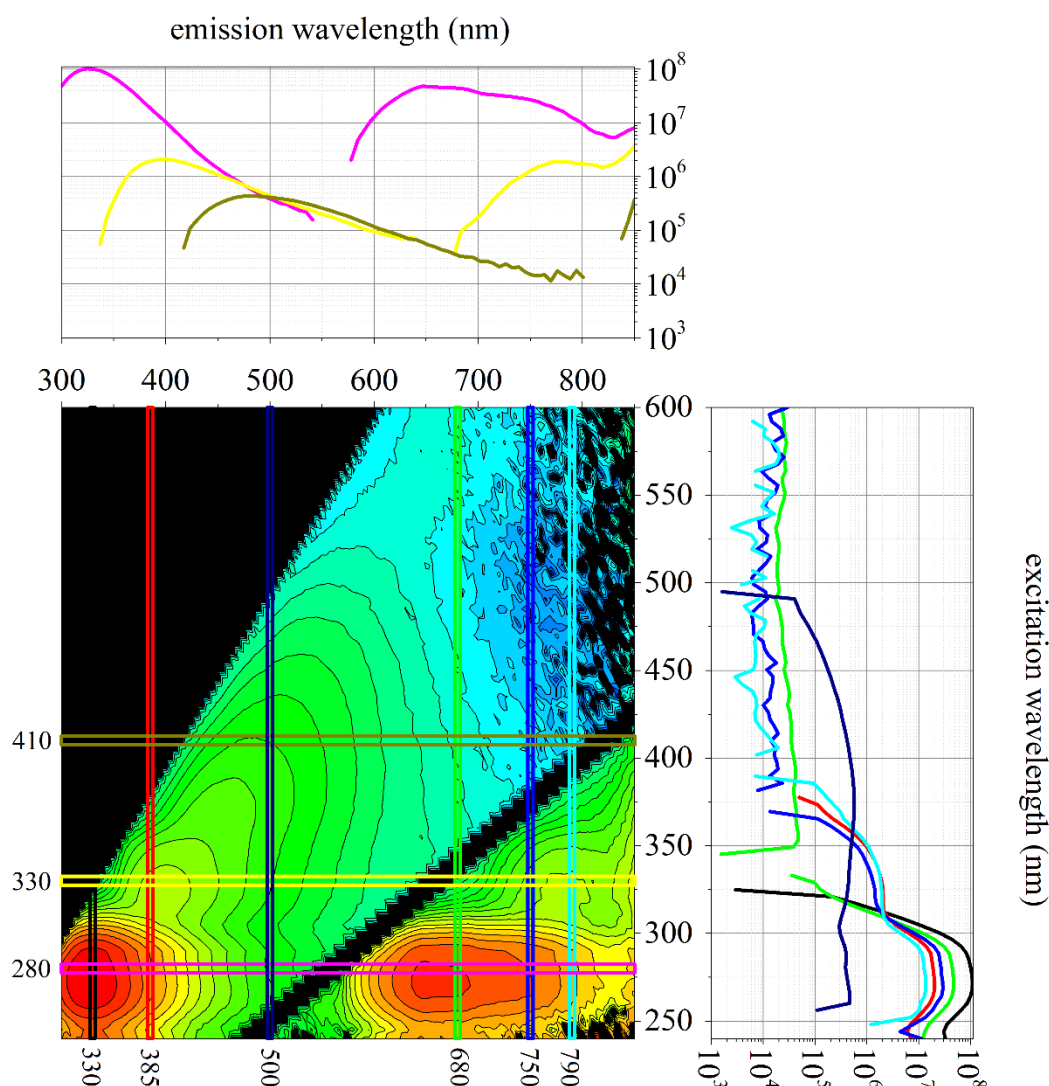
Figure 188: Corrected EEM of BSA and NaOH (Control) after 10 hours synthesis measured using a Fluorolog 3-22 using a FluoroCube front face cuvette holder plotted as a contour profile. The excitation monochromator (1200/330 grating) was set to a 4 nm bandpass and scanned from 240-850 nm in 5 nm increments. For each excitation wavelength the emission monochromator (1200/500 grating) was set to a 4 nm bandpass and scanned from 240-850 nm in 5 nm increments. A R928 PMT was used. Each point had a 0.2 s integration time. A log scale is used in order to emphasise weak emission.
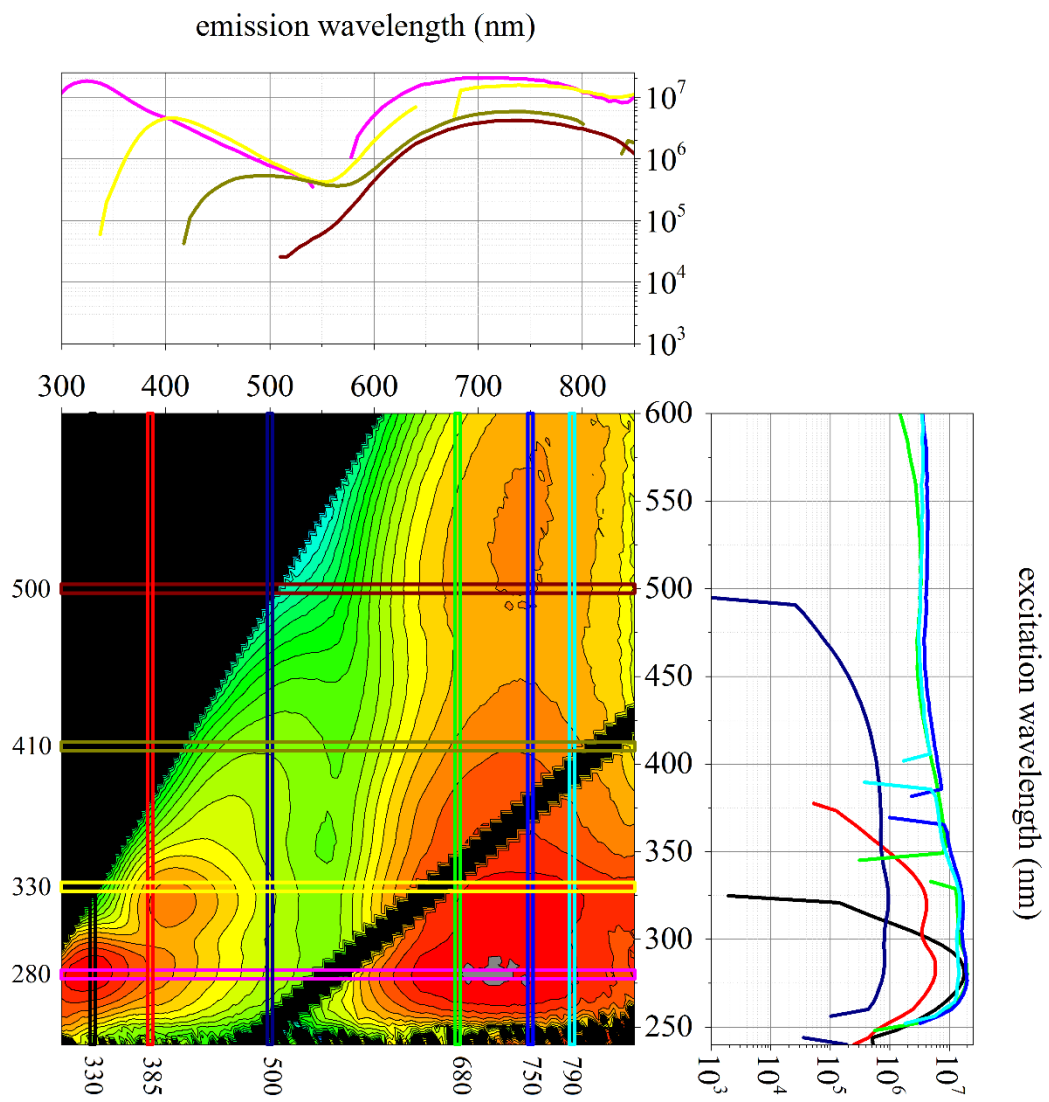
Figure 189: Corrected EEM Au25@BSA after 10 hours synthesis plotted as a contour profile and measured using the same experimental conditions as **Figure 188**.
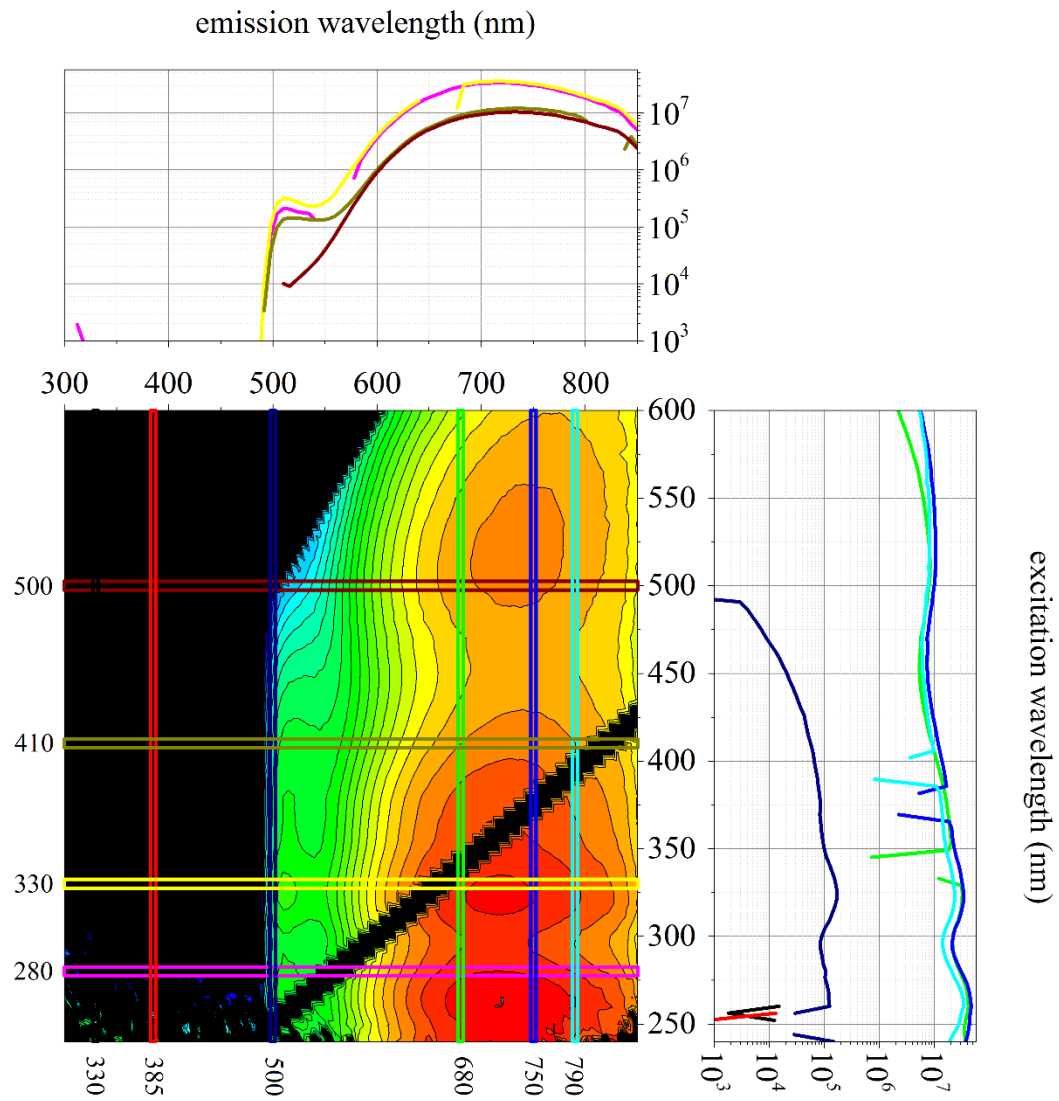
Figure 190: The EEM of **Figure 189** remeasured using a LP505 filter on the emission arm to filter out 2nd order emission from the BSA.
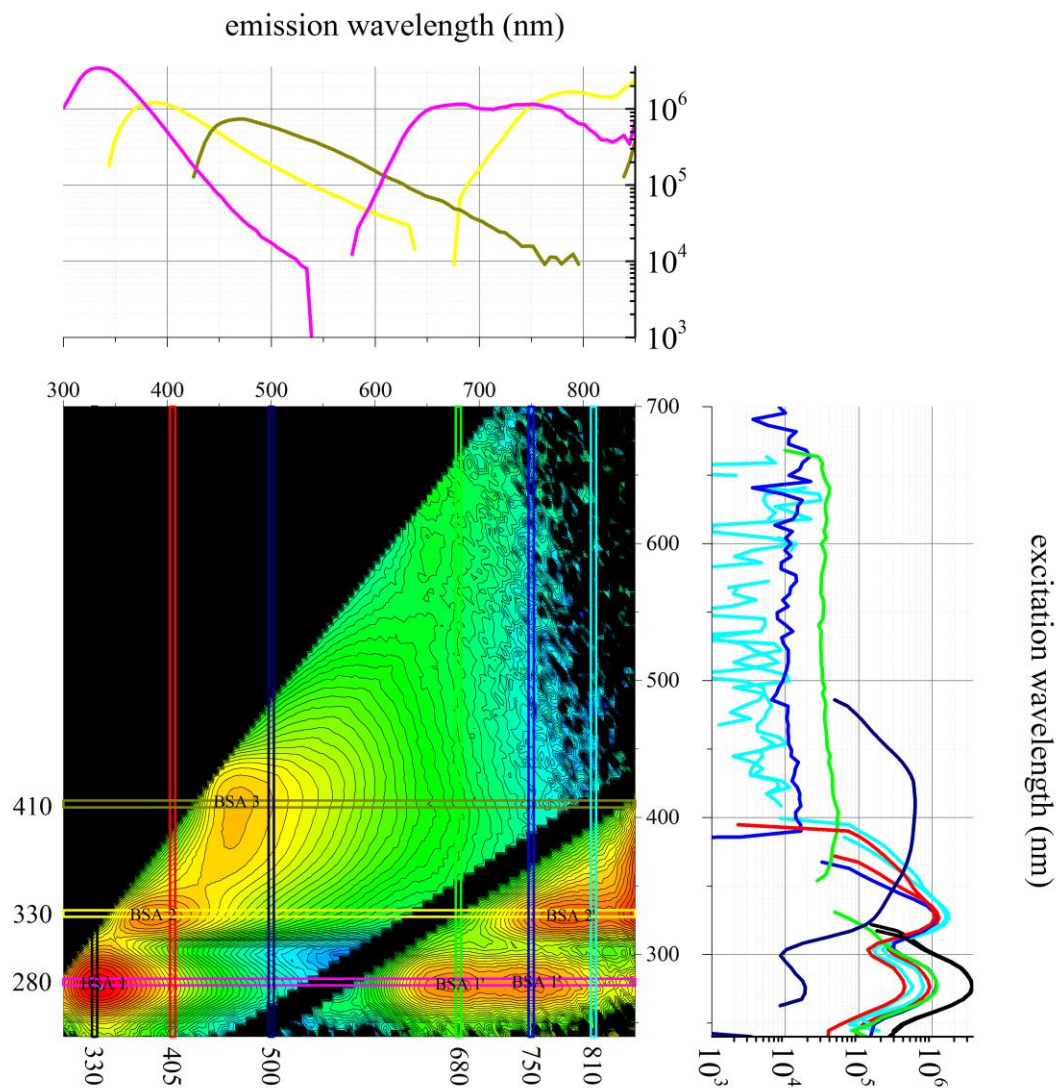
Figure 191: Contour profile of the EEM of BSA and NaOH control remeasured in a state of the art FluoroLog 3-222 (Edison application lab) using a front face mirror. The excitation monochromator (1200/330 grating) was set to a 5 nm bandpass and scanned from 240-850 nm in 5 nm increments. For each excitation wavelength the emission monochromator (1200/500 grating) was set to a 1.2 nm bandpass and scanned from 240-850 nm in 5 nm increments. A R928 PMT was used. Each point had a 0.1 s integration time. A log scale is used in order to emphasise weak emission. This EEM highlights 3 hot spots at (BSA1 Ex 280 nm Em 335 nm) likely due to tryptophan (BSA 2 Ex 330 nm Em 385 nm) and (BSA 3 Ex 410 nm, Em 465 nm). Second order emission of BSA 1 and BSA 2 were also recorded.
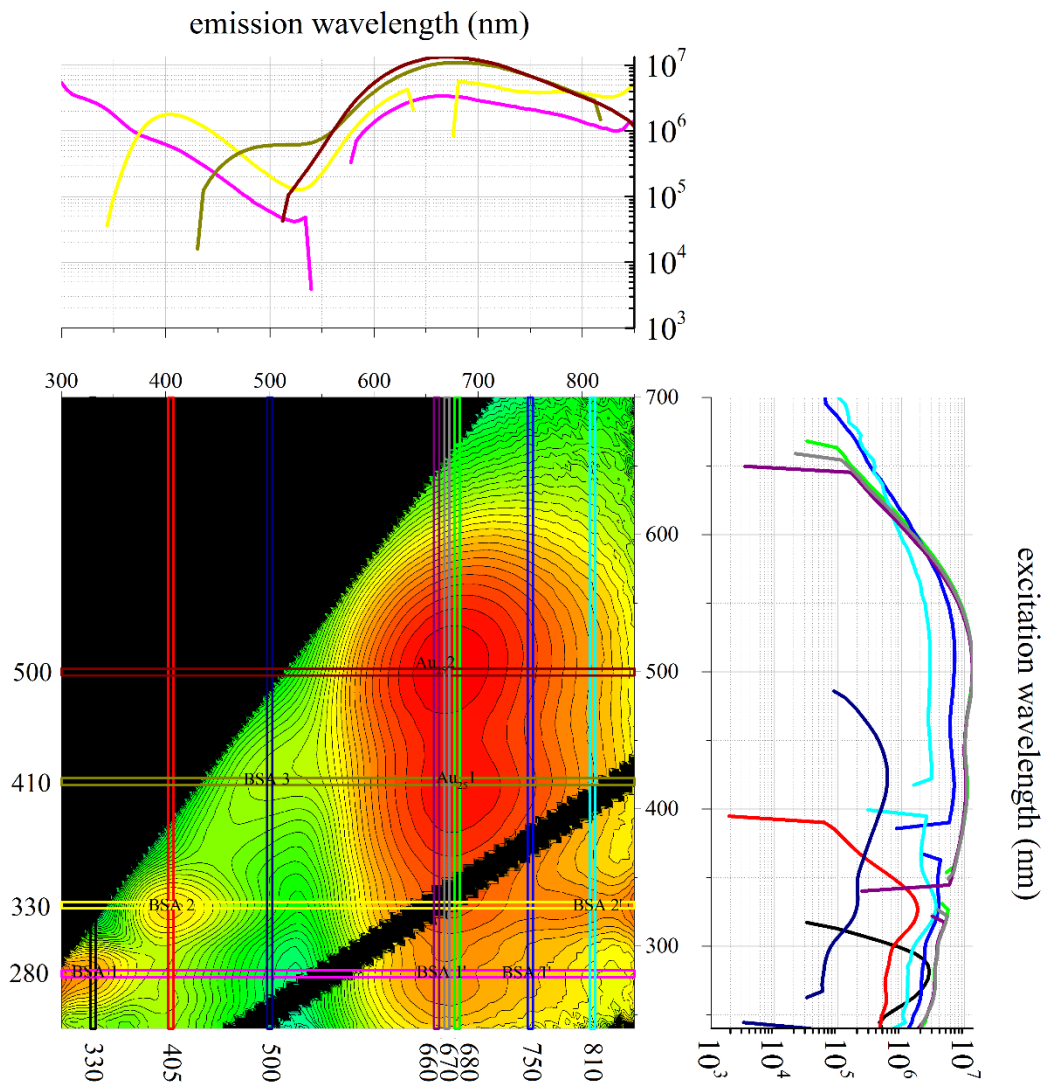
Figure 192: Contour profile of the EEM of Au$_{25}$@BSA measured under the same conditions as **Figure 191** which highlight the 3 hot spots with slightly shifted wavelengths (BSA1 Ex280 nm Em335 nm) likely due to tryptophan (BSA 2 Ex 330 nm Em405 nm) and (BSA 3 Ex420 nm, Em500 nm). Second order emission of BSA 1 and BSA 2 were also recorded. These shifts may be slightly pH dependant; the pH may not be exactly the same due to the presence of AuCl$_4$. Importantly there are 2 additional hotspots on the EEM at (Au$_{25}$1 Ex420, Em670) and (Au$_{25}$2 Ex500, Em670).
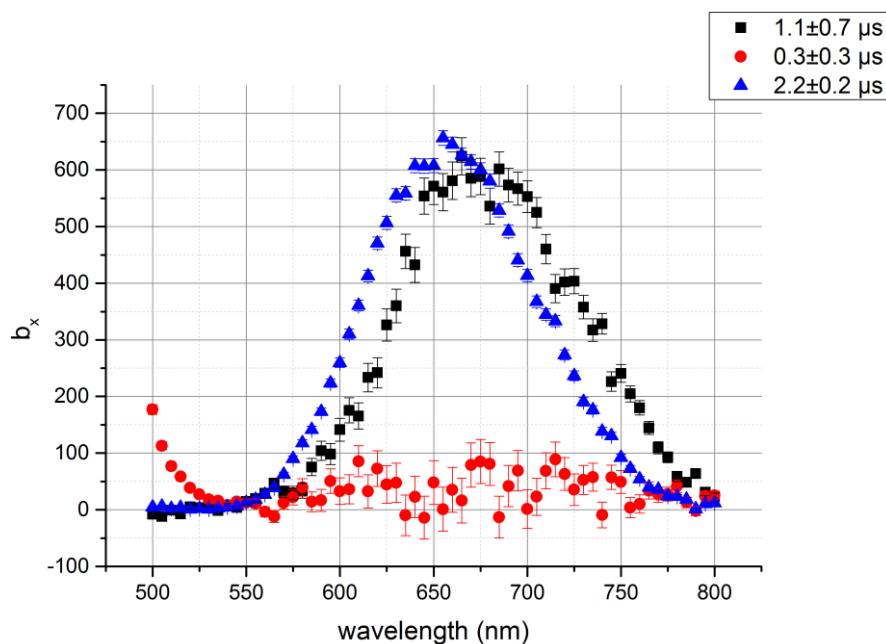
Figure 193: MCS DAS Au25@BSA using a SL471D with the FF cuvette holder. The SL471D was directly coupled to the sample compartment and the emission monochromator TDM800 (1200/350 grating) was scanned from 500-800 nm in 5 nm increments. A 200 s integration time was used for each decay. DeltaHub electronics were set to the 340 µs time range (4000 channels) with a TBX850c detector. A LP 530 nm filter was placed on the emission arm. A prompt was neglected due to the long time range. 2 main species and third component likely due scatter. This is the same sample as measured in **Figure 189** and **Figure 190**. Comparing with the higher sensitivity EEM of **Figure 192** the 2 µs component can be seen to correspond to $Au_{25}2$ and the 1 µs component corresponds to $Au_{25}1$. Errors in each decay time were too large to construct a meaningful DAS^W.

Kinetic measurements were carried out on the Fluorolog 3-22 with the FluoroCube front face cuvette holder however, since this holder didn't facilitate stirring and heating required for the reaction the samples were created using a hotplate stirrer and 3 ml was pipetted in a quartz cuvette for measurement and then returned to the bulk reaction every 5 minutes for 5 hours. A series of filters were used to prevent 2nd order. The sample shows a decreased emission at BSA1 and a slightly decreased emission at BSA3 however the emission at BSA3 is not sufficiently above the noise. In proteins tryptophan residues can be grouped into one of four types of residues, with respect to their spectroscopic properties. Residues that are fully solvent exposed $\lambda_{max} \approx 350$ nm, partially exposed on the surface of a protein $\lambda_{max} \approx 340$ nm, buried within a protein but interacting with a neighbouring polar group $\lambda_{max} \approx 315\text{-}330$ nm and completely buried in an apolar core $\lambda_{max} \approx 308$ nm [339]. The EEMs however give a maximum excitation emission pair of 272 nm, 328 nm for the control and 276 nm, 337 nm for the sample measured on the Fluorolog 3-22 and a maximum excitation emission pair of 280 nm, 335 nm for the control and 280 nm, 330 nm for the sample. It is

likely this difference is from variances in sample preparation as mentioned the time for a completed reaction was longer for the sample made in the Fluorolog 3-222 (Edison ISA). Thus trusting the data from the Fluorolog 3-22 it is likely that the control has the tryptophan buried within the protein but interacting with a neighbouring group and is partially exposed for the sample. The emission at BSA2 however is seen to rapidly increase in the sample with respect to the baseline. Most of this increase is seen in the first 25 minutes in advance of the formation of nanoclusters $Au_{25}1$ and $Au_{25}2$ which are seen to form after 25 minutes.

Figure 194: Kinetic scan at 280 nm excitation and 330 nm emission (BSA1) measured using a Fluorolog 3-22 with a FluoroCube FF cuvette holder. The excitation monochromator (1200/330 grating) was set to 280 nm with a 4 nm bandpass and the emission monochromator (1200/500 grating) was set to 330 nm with a 4 nm bandpass. A R928 PMT was used. Each point had a 1 s integration time. A BP335/45 filter was used to remove 2nd order effects. Since only a single wavelength was examined wavelength correction factors were ignored. BSA emission is significantly lower in the sample at the start. Slight growth in emission with respect to emission but data noisy.

Figure 195: Kinetic scan at 325 nm excitation and 405 nm emission (BSA2) measured using a Fluorolog 3-22 with a FluoroCube FF cuvette holder. The excitation monochromator (1200/330 grating) was set to 325 nm with a 4 nm bandpass and the emission monochromator (1200/500 grating) was set to 405 nm with a 4 nm bandpass. A R928 PMT was used. Each point had a 1 s integration time. A BP480/140 filter was used to remove 2nd order effects. Since only a single wavelength was examined wavelength correction factors were ignored. Growth in this component for the first 50 minutes and then levels off.
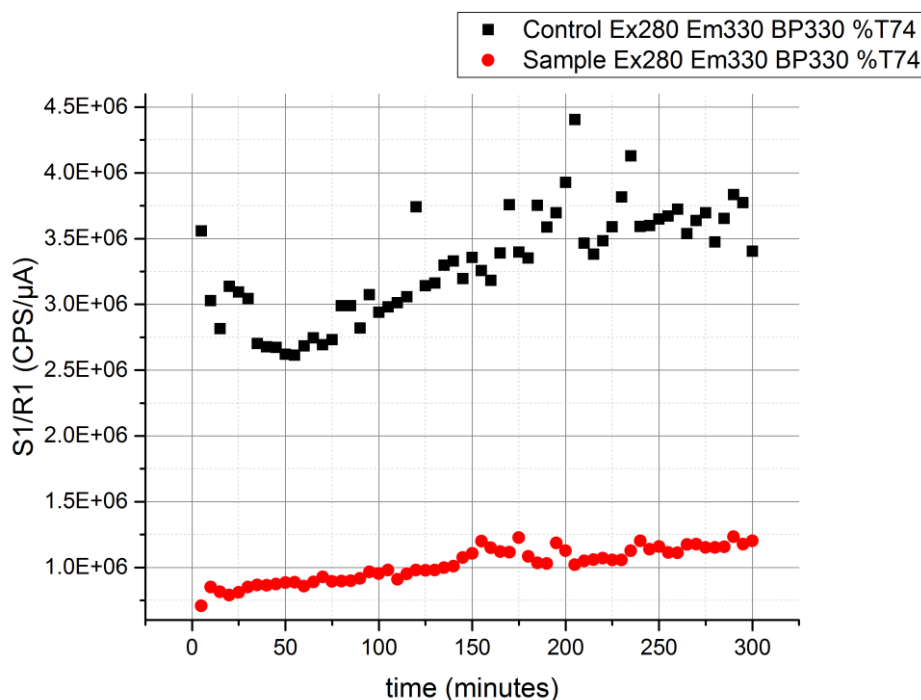

Figure 196: Kinetic scan at 410 nm excitation and 500 nm emission (BSA3) measured using a Fluorolog 3-22 with a FluoroCube FF cuvette holder. The excitation

monochromator (1200/330 grating) was set to 410 nm with a 4 nm bandpass and the emission monochromator (1200/500 grating) was set to 500 nm with a 4 nm bandpass. A R928 PMT was used. Each point had a 1 s integration time. A BP480/140 filter was used to remove 2nd order effects. Since only a single wavelength was examined wavelength correction factors were ignored. Emission is slightly weaker in Au_{25}@BSA nanoclusters but within error of measurement.

Figure 194, **Figure 195** and **Figure 196** look at the front face kinetic data of the hotspots at BSA1, BSA2 and BSA3 respectively in the BSA control and the BSA nanoclusters. For BSA1 the samples intensity is significantly lower than that of the control. Fluorescence decays were measured in a FluoroCube with a NL279D excitation source coupled to an excitation monochromator TDM800 (1200/350 grating) set to 279 nm with a 32 nm bandpass. The emission monochromator TDM800 (1200/350 grating) was set to 330 nm with an 8 nm bandpass and a LP330 filter was placed on the emission arm. Hub A electronics were operated in reverse mode using a 100 ns TAC range (8000 channels) and a TBX650c detector. For the prompt the emission monochromator TDM800 (1200/350 grating) was set to 279 nm with an 8 nm bandpass and the LP330 filter was removed from the emission arm. A 2 % LUDOX SM-AS solution was used as normal. Fits yielded a three exponential decay for the sample with τ_1=0.56±0.07 ns (α_1=0.70), τ_2=1.97±0.09 ns (α_2=0.27), τ_3=5.1±0.2 ns (α_3=0.04), χ^2=1.174 and for the control τ_1=0.23±0.02 ns (α_1=0.62), τ_2=1.99±0.09 ns (α_2=0.29), τ_3=5.2±0.5 ns (α_3=0.10), χ^2=1.169. These decay times are similar for BSA in PBS as shown in **Figure 131**. The lower proportion of $\alpha_{3:}\alpha_2$ in the sample with respect to the control suggests the protein is becoming slightly denatured c.f. **Figure 29** which looks at the influence of urea on BSA. For the hotspot BSA2 there is more emission from the sample than the control. Fluorescence decays were measured in a FluoroCube with a NL339D excitation source coupled to an excitation monochromator TDM800 (1200/350 grating) set to 339 nm with a 32 nm bandpass. The emission monochromator TDM800 (1200/350 grating) was set to 405 nm with an 8 nm bandpass and a BP480/140 filter was placed on the emission arm. Hub A electronics were operated in reverse mode using a 100 ns TAC range (8000 channels) and a TBX650c detector. For the prompt the emission monochromator TDM800 (1200/350 grating) was set to 339 nm with an 8 nm bandpass and the BP480/140 filter was removed from the emission arm. A 2 % LUDOX SM-AS solution was used as normal. Fits yielded a three exponential decay for the sample with τ_1=0.30±0.05 ns (α_1=0.52), τ_2=2.5±0.2 ns (α_2=0.30), τ_3=5.0±0.6 ns (α_3=0.18), χ^2=1.304 and for the control τ_1=0.26±0.02 ns (α_1=0.69), τ_2=3.1±0.2 ns

236

(α_2=0.23), τ_3=6.6±0.1 ns (α_3=0.08), χ^2=1.390. A four exponential fit for the sample gave τ_1=0.10±0.04 ns (α_1=0.64), τ_2=1.1±0.2 ns (α_2=0.13), τ_3=3.6±0.2 ns (α_3=0.21), τ_4=6.5±0.2 ns (α_4=0.03), χ^2=1.185 and for the control τ_1=0.10±0.02 ns (α_1=0.80), τ_2=1.1±0.2 ns (α_2=0.07), τ_3=4.2±0.2 ns (α_3=0.11), τ_4=9.0±0.3 ns (α_4=0.01), χ^2=1.239. The increase in intensity at BSA3 has been debated to be smaller nanoclusters in particular because the emission at BSA3 is reported in BSA, Pt@BSA, Au@BSA and Pt-Au@BSA nanoclusters in increasing intensity [340]. Fluorescence decays were measured in a FluoroCube with a N435L excitation source coupled to an excitation monochromator TDM800 (1200/350 grating) set to 435 nm with a 32 nm bandpass. The emission monochromator TDM800 (1200/350 grating) was set to 500 nm with an 8 nm bandpass and a BP470/100 filter was placed on the emission arm. Polarizers were used at VM for the decay. Hub A electronics were operated in reverse mode using a 100 ns TAC range (8000 channels) and a TBX650c detector. Fits yielded a three exponential decay for the sample with τ_1=0.23±0.01 ns (α_1=0.92), τ_2=2.4±0.1 ns (α_2=0.06), τ_3=7.8±0.2 ns (α_3=0.01), χ^2=1.371 and for the control τ_1=0.23±0.01 ns (α_1=0.80), τ_2=2.4±0.1 ns (α_2=0.16), τ_3=8.3±0.2 ns (α_3=0.04), χ^2=1.410. The decay times measured in these regimes are similar. The increase in intensity is due to the increased contribution of the longer lived normalised amplitudes α_3 and α_2.
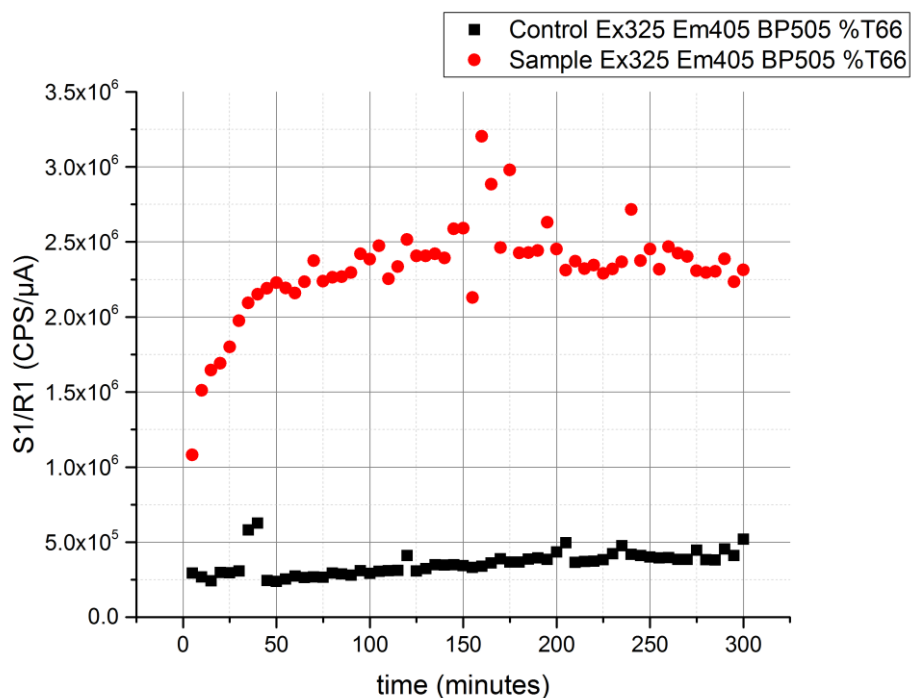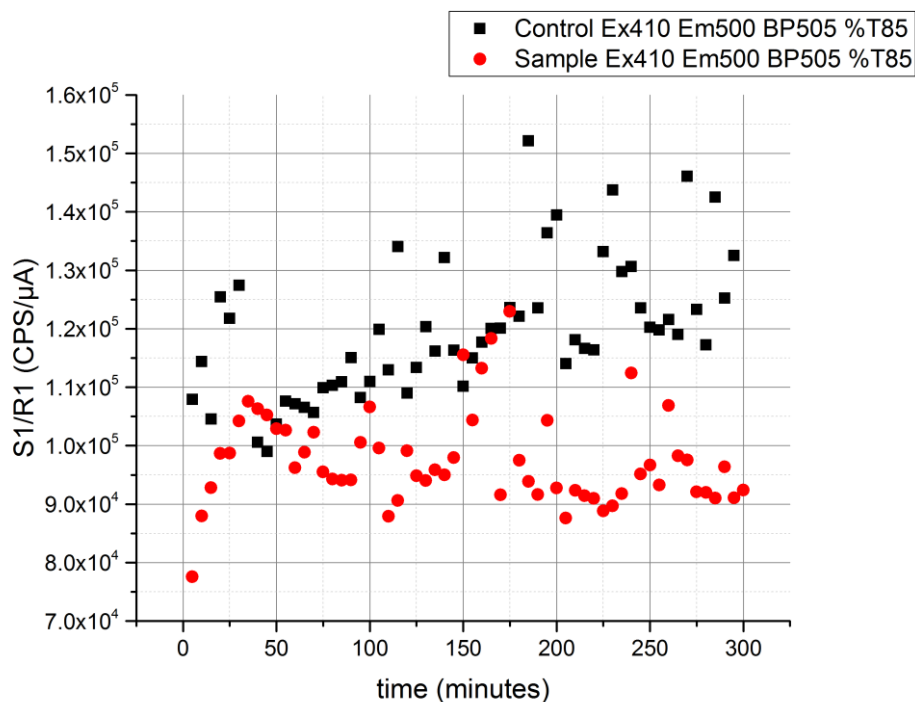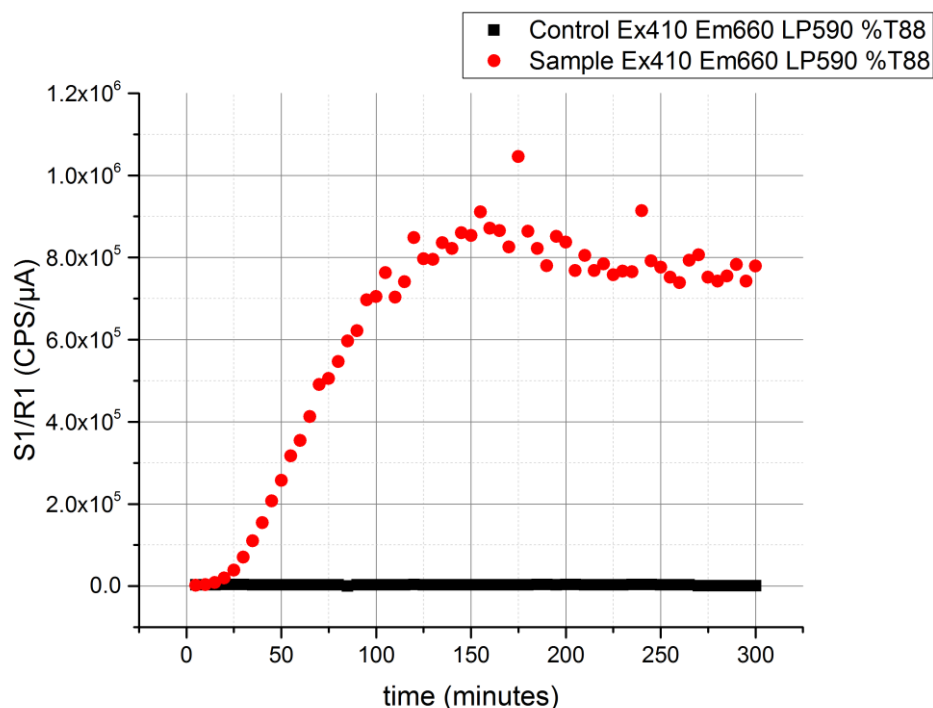

Figure 197: Kinetic scan at 410 nm excitation and 660 nm emission ($Au_{25}1$) measured using a Fluorolog 3-22 with a FluoroCube FF cuvette holder. The excitation monochromator (1200/330 grating) was set to 410 nm with a 4 nm bandpass and the

emission monochromator (1200/500 grating) was set to 500 nm with a 4 nm. A R928 PMT was used. Each point had a 1 s integration time. A LP590 filter was used to remove 2nd order effects. Since only a single wavelength was examined wavelength correction factors were ignored. Rapid growth is observed for 100 mins and then this levels off at 150 mins. There is then a small decline in intensity and it levels off again. BSA in NaOH has negligible emission here.
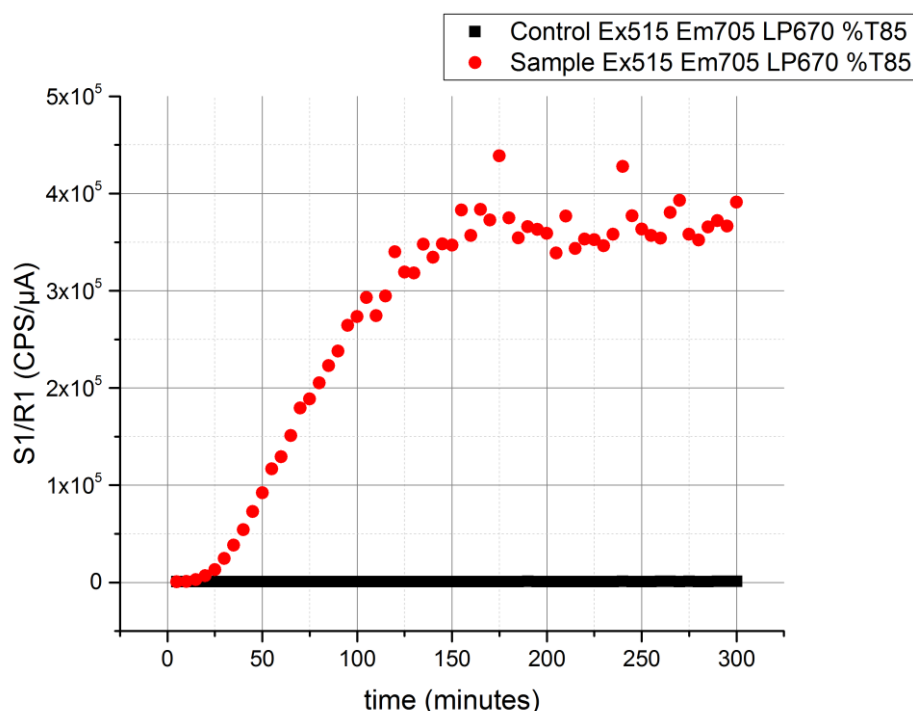
Figure 198: Kinetic scan at 515 nm excitation and 705 nm emission (Au$_{25}$2) measured using a Fluorolog 3-22 using a FluoroCube FF cuvette holder. The excitation monochromator (1200/330 grating) was set to 515 nm with a 4 nm bandpass and the emission monochromator (1200/500 grating) was set to 705 nm with a 4 nm bandpass. A R928 PMT was used. Each point had a 1 s integration time. A LP670 filter was used to remove 2nd order effects. Since only a single wavelength was examined wavelength correction factors were ignored. Rapid growth is observed for 100 mins this then levels off at 150 mins. Note the DeltaFlex intensity data shows a rapid increase for the first 100 mins and then falls presumably due to inner filtering.

Figure 197 and **Figure 198** show the rapid increase in emission from Au$_{25}$1 and Au$_{25}$2 that grows slowly for the first 25 minutes and then increases rapidly until 150 minutes where the emission begins to level out. In order to quickly resolve the longer lived components which are of more interest to this work without interference of the short components, MCS was carried out using a DeltaFlex **Figure 193**. Au$_{25}$1 and Au$_{25}$2 appear to correspond to the ~1 µs and ~2 µs component respectively. These components can be investigated in more details with a series of SpectraLEDs. When MCS is used all the short decay times attributed to the BSA get drowned out in the broad excitation pulse. Moreover, data acquisition is

significantly sped up as TCSPC is inefficient due to low repetition rates at such long time ranges. The lowest time range of 340 µs was selected with a time calibration of 83 ns ch^{-1} (DeltaHub). It should be noted that the decay measurement only uses approximately 500 channels opposed to the normal 4000 but it is sufficient enough to compute the decay times. For the 10 % sample dialysed in TRIZMA buffer, measurement with SL295D, SL377D and SL471D gave 3 global decay times; one close to 1 µs and another close to 2 µs which closely resemble τ_4 and τ_5 measured in the kinetic TCSPC data. The third component ~5 µs is very weak in the MCS DASE$_m$ and too long to be observed in TCSPC. The errors on the decay times were far too large to reliably construct a weighted DASE$_m$.
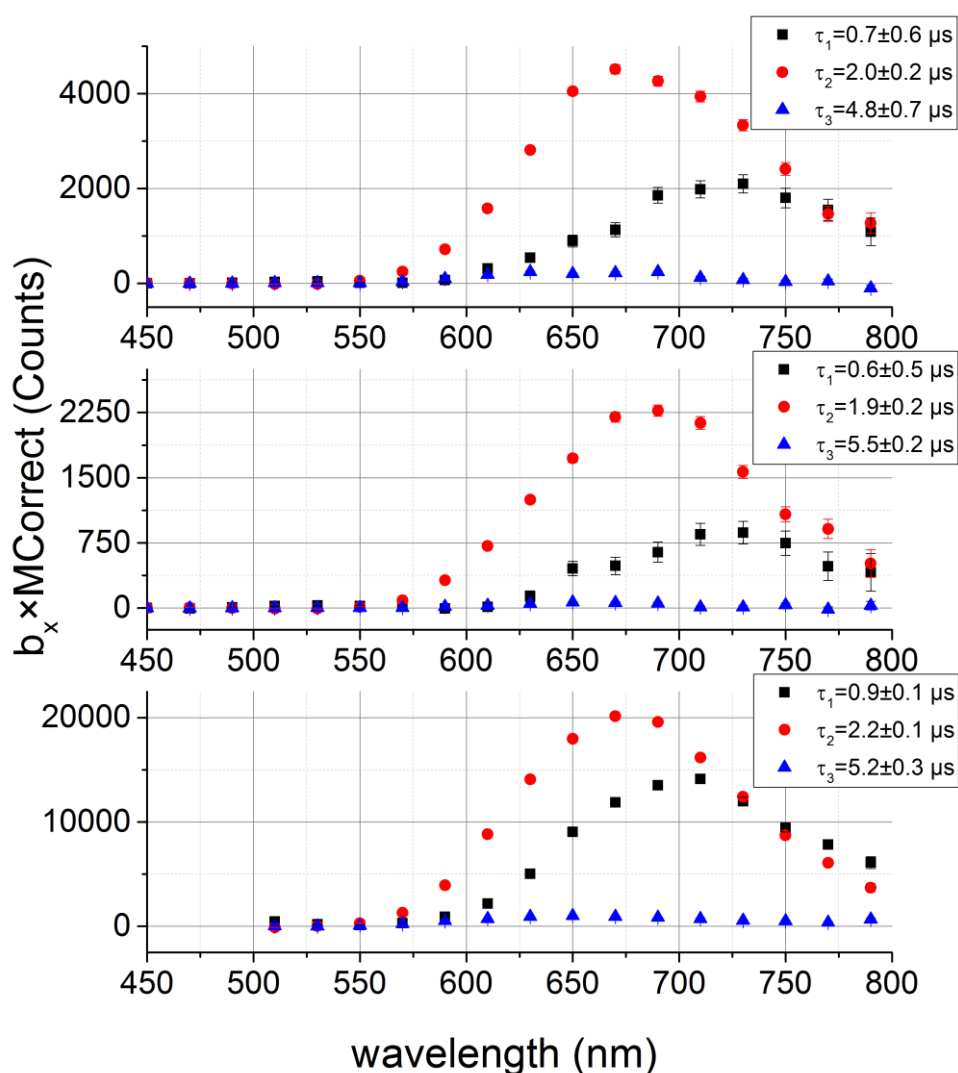
Figure 199: DAS$_{Em}$ for 10 % (~40 mM BSA, 2 µM Au$_{25}$) in TRIZMA buffer. MCS DAS were measured using a SL295D, SL377D and SL471D respectively. The SLxxxDs were

directly coupled to the sample compartment and the emission monochromator TDM800 (1200/350 grating) was scanned from 500-800 nm in 5 nm increments. A 1 hour integration time was used for each decay. DeltaHub electronics were set to the 340 µs time range (4000 channels) with a TBX850c detector. A LP 530 nm filter was placed on the emission arm. A prompt was neglected due to the long time range. 2 main species and third component likely due scatter. The DAS show two main decay times with the main component being close to 1 µs and the second component being near 2 µs in agreement with the 5 exponential fit from the kinetic TCSPC. In order to get random residuals a third component was required. This component is extremely weak in comparison to the main two components. Data was not weighted by the decay time as the errors in each decay time were too large.
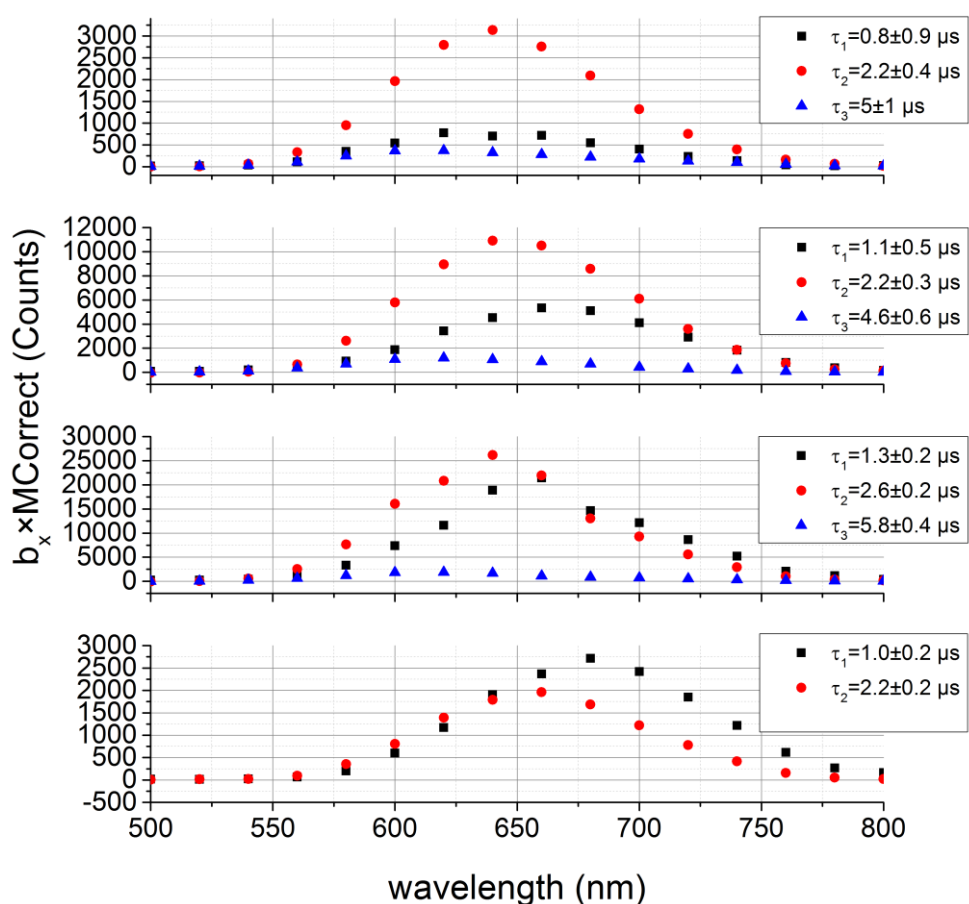
Figure 200: MCS-DAS$_{Em}$ with respect to pH measured with SL471 otherwise using the same experimental conditions as **Figure 199**. In all cases there are 2 predominant decay times of ~1 µs and 2 µs respectively. There is a third decay time needed for a goodness of fit for pH1, 7 and 9, addition of this component threw out the other decays for pH 12.

Following on from the work from Li et al. [335] as well as Cao et al. [338] decay associated spectra were examined at different pH values. pH1, pH7, pH9 and pH12. The structure of BSA has been well investigated [341,342] and forms 5 isomeric forms wih respect to pH. For pH stability, pH buffers were used for pH 1 a buffer of 0.1 M KCl was adjusted with HCl, for pH 7 0.1 M PBS buffer was adjusted with HCl, for pH9 0.1 M PBS buffer was

adjusted with NaOH and for pH12 a buffer of KCl was adjusted with NaOH. Four samples were made using a 30 ml sample volume using the protocol by Xie et. Al [333]. 3 ml of this sample was dialysed into each pH buffer using a 3 ml 10 K Slide-A-Lyzer G2 dialysis cassette. Dialysis was carried out into 2 l of buffer and was exchanged 3 times over a 2 day period.

Expanded 35 %	←---→ pH 2.7	Fast 45 %	←---→ pH 4.3	Normal 55 %	←---→ pH 8	Basic 48 %	←---→ pH 10	Aged 48 %
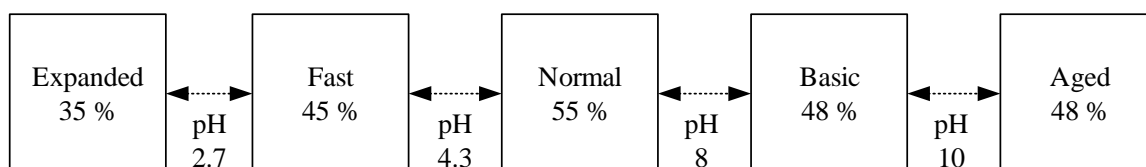
Figure 201: The 5 isomeric forms of BSA [341] with their % of helix and pH of transition. From the MCS-DAS$_{Em}$ with respect to pH (**Figure 200**) the formation of long lived luminescence with long decay times ~1 µs and ~2 µs decay time are favoured with the basic isomeric form of BSA. These are also present with the normal isomeric form at about half the intensity and seen with the expanded and aged isomeric forms at about ~1/10 of the intensity than in the basic isomeric form. The fluorescence intensity of Au$_{25}$@BSA nanoclusters have successfully been used as a sensor for copper ions by other research groups [343,344] as their intensity is pH dependant (**Figure 202**). A comparison of the ratio of the area under b_2 to b_1 may however be a more reliable indicator of the pH.
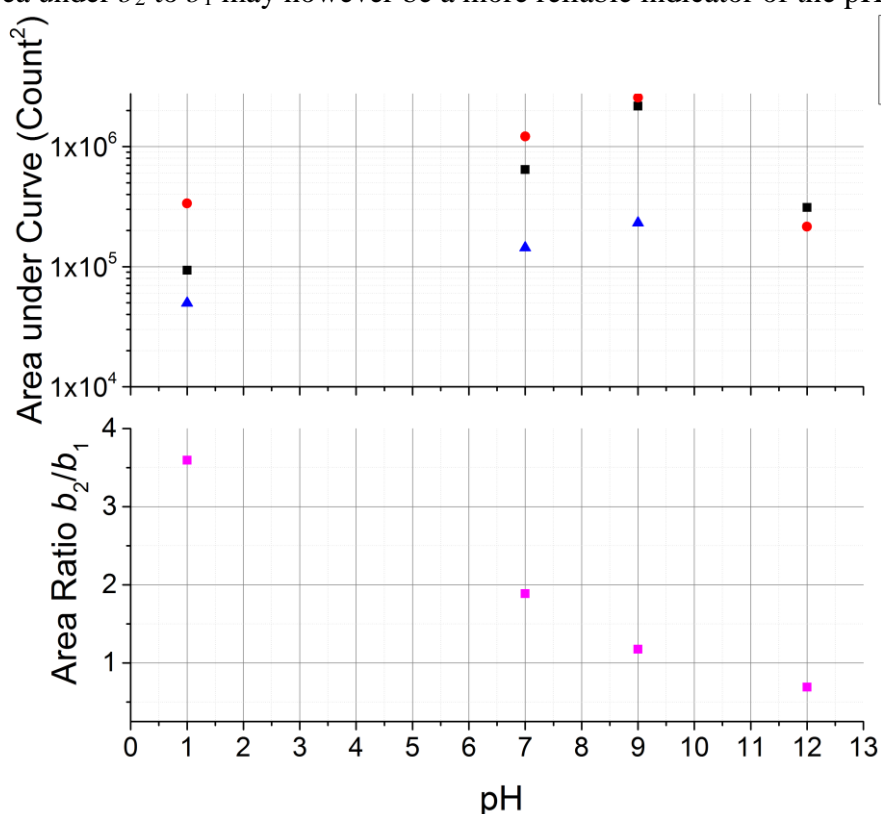
Figure 202: Integration of the area under the curve of b_1 and b_2 respectively. As mentioned pH 9 yields the brightest emission from the nanoclusters with significantly less emission at pH 1 and 12 (a log plot is used so they can be compared on the same scale).

The kinetic spectroscopy of these Au_{25}@BSA nanoclusters is difficult to measure due to the high concentrations necessary to force the formation of the Au_{25}@BSA nanoclusters. Moreover, the decay times for the nanoclusters are in the time-range where current MCS and TCSPC techniques overlap. At ~µs time range TCSPC becomes inefficient due to the low repetition rate of the laser and MCS lacks in time-resolution. Nevertheless, another sample of the same composition was measured in a state of the art DeltaFlex (HORIBA Scientific IBH Glasgow Applications Lab) and made using the peltier/stirrer accessory under the same conditions. A kinetic TCSPC measurement of a sample during synthesis was ran with DD482L as an excitation source. This was vertically mounted and coupled directly to the sample compartment without an excitation polarizer allowing through maximal light. The emission monochromator TDM800 (1200/350 grating) was set to 700 nm with a bandpass of 16 nm. The emission polarizer was set to the magic angle. DeltaHub timing electronics were used with a 13 µs with a PPD-850c detector. The kinetic TCSPC was set to acquire a fluorescence decay curve every minute. A prompt was neglected due to the use of a long time range.
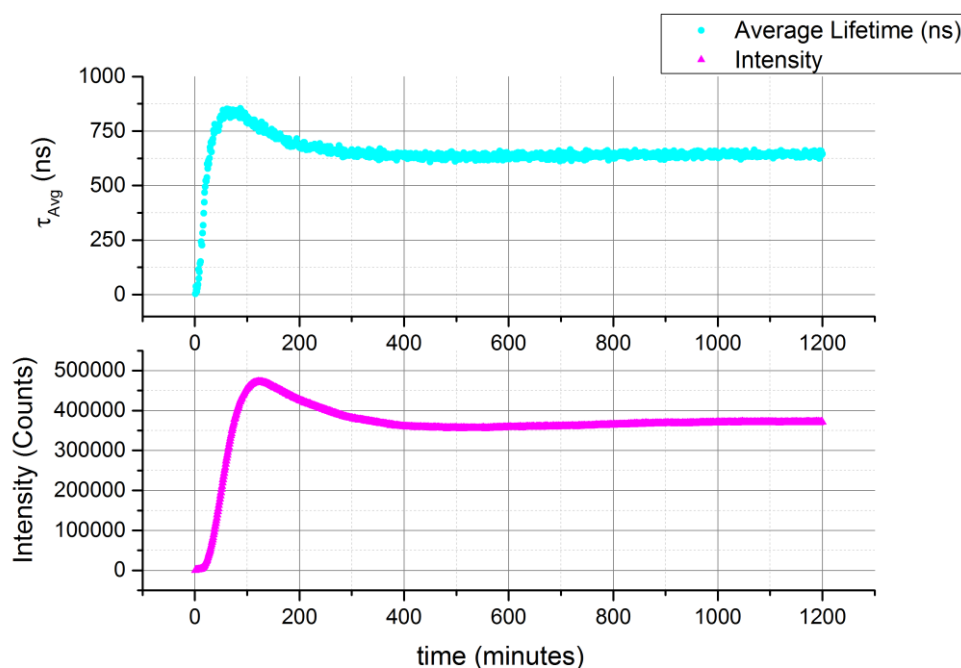
Figure 203: From the time resolved data, the average lifetime and the intensity with respect to time can be examined. Both show a rapid increase in intensity followed by the decrease in intensity until a plateau is reached. The maximum average lifetime value is observed at 70 minutes, while the maximum intensity on the other hand is observed at 130 minutes.

In this work the long-lived decay times were of more interest and hence a 13 µs TAC range was used at the expense of badly-resolved short decay times that were binned alongside the instrumental response at ~1-2 channels (t_{cal}=3.51166 ns ch^{-1}). This means that data can be tail fitted without taking a prompt into account. Even without the additional complications of reconvolution analysis the kinetic TCSPC for this sample was still difficult to analyse, looking at the raw intensity and average lifetime per curve **Figure 101** there is a clear relation between the average lifetime and intensity. Both are observed to rapidly increase, reach a maximum and then fall. The samples optical density will reduce the growth in the fluorescence intensity c.f. **Figure 187**. The average fluorescence lifetime on the other hand is a quantitative measurement and should thus be less influenced by the optical density moreover as the concentration of BSA is not changing with respect to time, there should be no drastic change in molecular collisions with respect to time. The discrepancies between the trend of average lifetime having a maxima at 70 minutes and fluorescence intensity having a later maxima at 130 minutes is likely due to a change in the relative abundance of a particular fluorescence species which can be examined in more detail. Intensity data will also be influenced by some extent by inner-filtering effects as observed in **Figure 187**. The data can be analysed with reconvolution analysis. Since this is a large dataset, the first type of analysis was tried by fitting a representative curve at 130 s **Figure 121** the peak of the
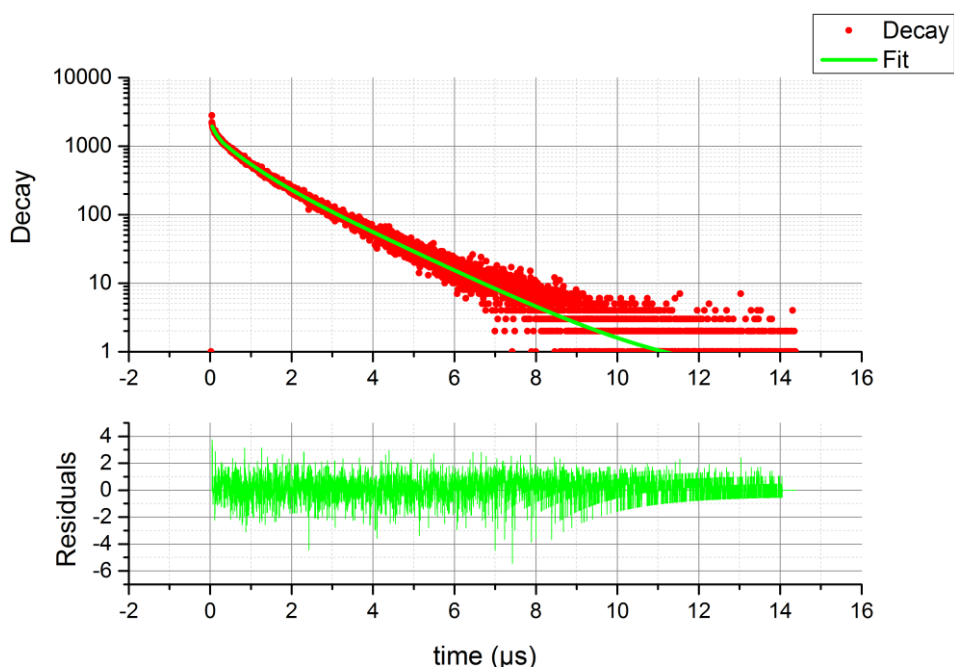
Figure 204: The fit of the decay curve measured at 130 minutes when the maximum intensity was observed to a 3 exponential model. The three decay times were τ_1=100±30 ns (α_1=0.28), τ_2=550±40 ns (α_2=0.48) and τ_3=1560±30 ns (α_3=0.25) and χ^2=0.921. The

data has a peak of about 2000 counts which is considerably smaller than the 10000 counts peak preset used for most fluorescence decay measurements.
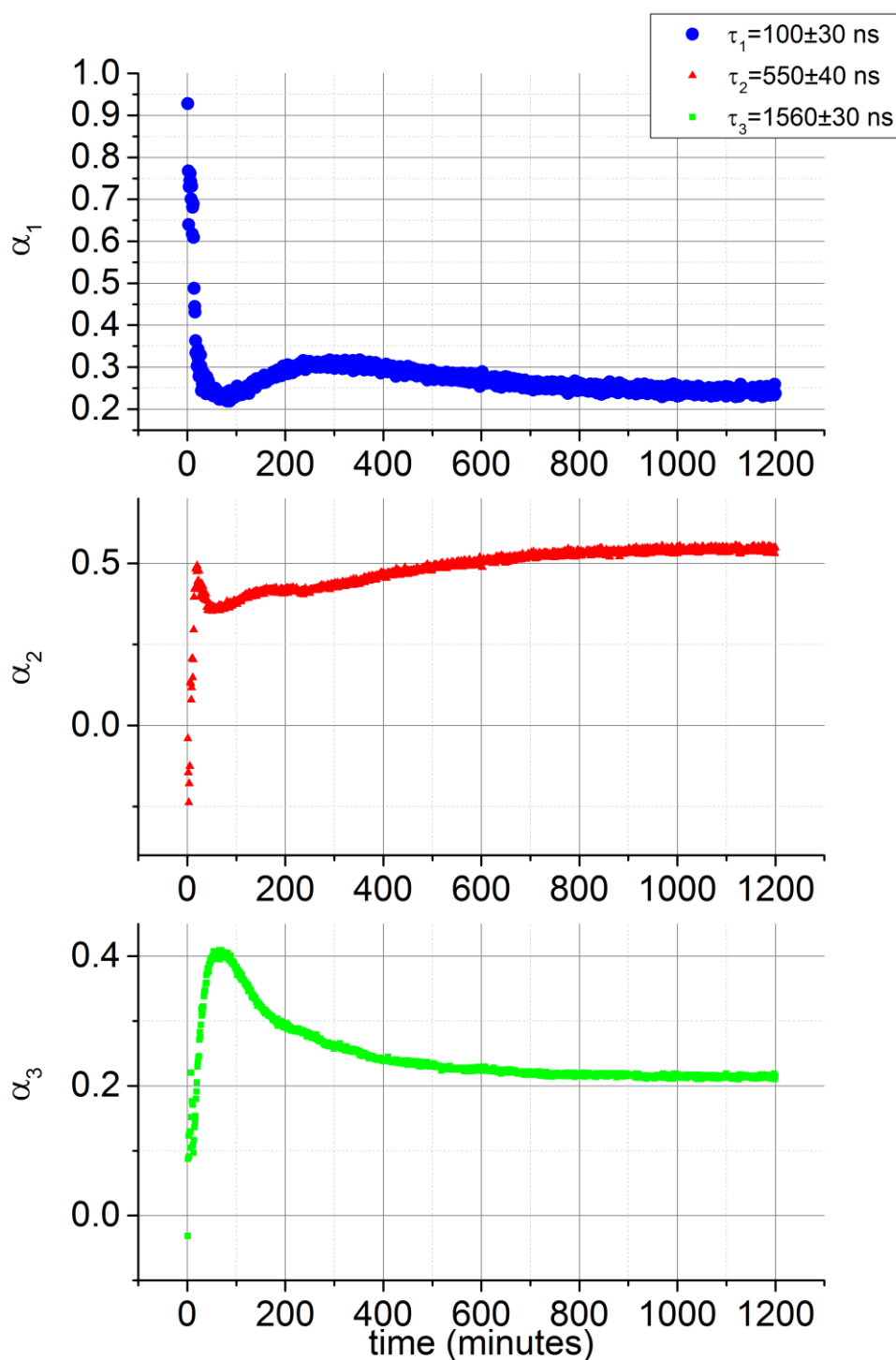
Figure 205: The plot of the normalised pre-exponential factors with respect to time. The first shortest lived component is observed to fall as the middle component is formed because the pre-exponential factors are normalised. After a small delay there is a growth in the longest lived component which reaches a maxima and then falls.

intensity data. It took a 3 exponential model to fit this decay curve. τ_1 and τ_2 are short values not well-resolved with MCS measurements. The normalised contributions show the development of the longer lived decay times as the reaction proceeds. The longest lived component seems to reach a maxima after 100 minutes and then decreases. Unfortunately, the error in τ_3 suggests it's a combination of the decay times from $Au_{25}1$ and $Au_{25}2$ c.f. **Figure 192** and **Figure 193**. Using a single decay curve as a representative decay and fitting to it may not be the best method for analysis of this dataset moreover, there is not enough data in each individual curve to fit a complex decay model so the χ^2 will be artificially reported as close to 1 or less than 1 even with an incorrect model **Figure 206**.
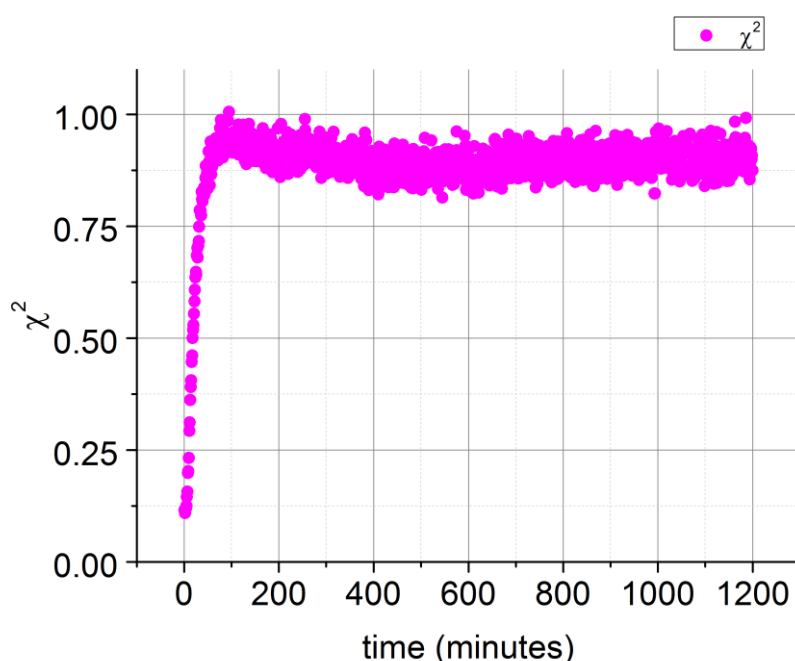
Figure 206: The χ^2 with respect to decay curve. For kinetic TCSPC, χ^2 begins to lose its meaning to an extent as the first curves usually don't have enough data and so appear to be over-fitted $\chi^2 \ll 1$. Even at the maximum intensity there is <2000 counts in the peak per decay curve and so this data may artificially give a $\chi^2 \sim 1$.

Data analysis can also be carried out by using data from all 1200 curves by summating them **Figure 207** which reconstructions the measurement that would have been taken under standard decay measurement conditions. Global decay times may be obtained from a fit of the sum. The decay times from the sum are then fitted to each individual decay curve to get a readout of the pre-exponential factors with respect to time. In the case of the summed data there are over 2,000,000 counts at the peak which is significantly larger than the 10,000 count peak preset normally used to acquire a decay curve. At such high counts it may be

difficult to get a χ^2 close to 1 and the shape of the residuals and the value of the decay times should be taken as a guide to a good fit. It took 5 exponentials to fit the sum, decay curve. In general caution should be applied when using such a complicated model however this is a very complicated system with both short and long loved species. The 5 exponential model was preferred as it aligns with the longer decay times **Figure 209** measured earlier by MCS.
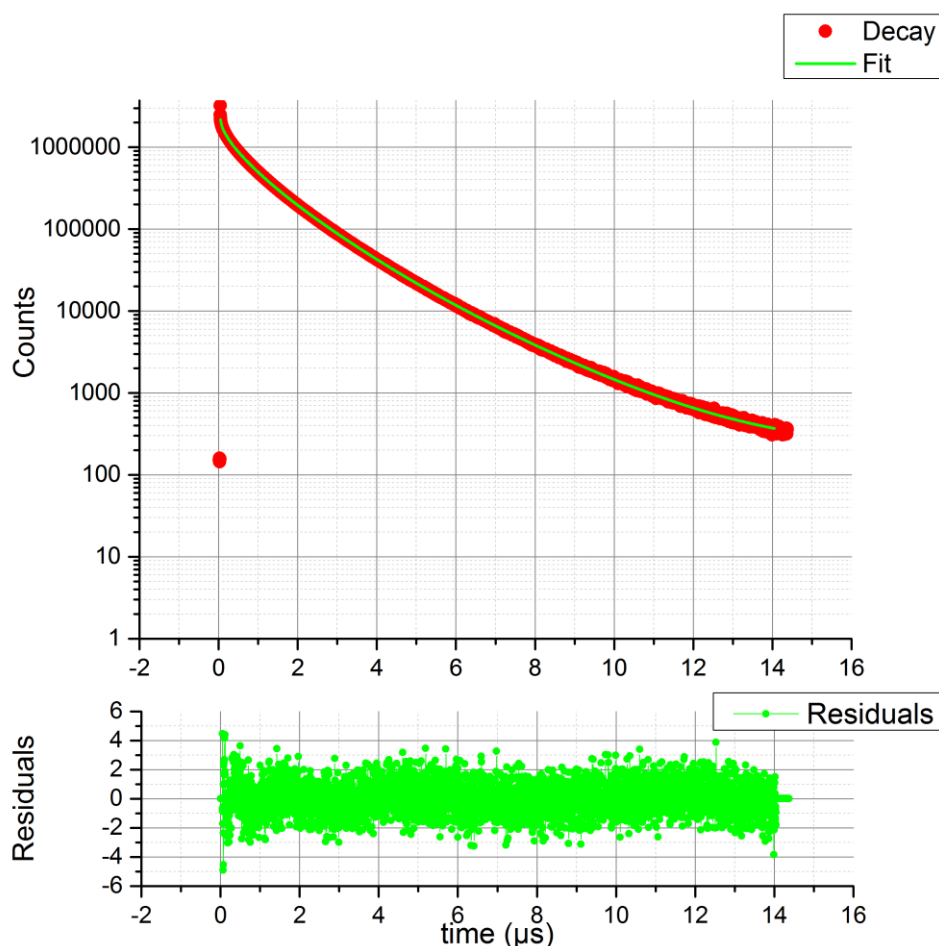
Figure 207: The summation of all data measured in the first 1200 minutes. A 5 exponential fit with decay times $\tau_1=19\pm1$ ns ($\alpha_1=0.10$), $\tau_2=117\pm3$ ns ($\alpha_2=0.19$), $\tau_3=441\pm6$ ns ($\alpha_3=0.25$), $\tau_4=1067\pm5$ ns ($\alpha_4=0.39$) and $\tau_5=2016\pm5$ ns ($\alpha_5=0.06$) was required to get random residuals and an acceptable $\chi^2=1.179$.

One of the difficulties about this sample is that it possesses a multitude of decay times from short ~ns components to larger ~µs components. In order to measure the long decay times, the time-resolution per channel increases and this results in an insufficient time-resolution to measure the short decay components. Moreover, the repetition rate of the laser has to be lowered to allow for a complete decay. Previous work by the research group looked at fluorescence anisotropy of this sample as short time ranges ~50-100 ns ranges and 1 MHz repetition rate more typical for fluorescence [335]. At these conditions the sample gets re-

excited before the decay completes and hence there is a wrap round of the previous decay before the start of the next prompt. The paper reports a markedly different size of Au$_{25}$@BSA nanoclusters to that reported of BSA by fluorescence anisotropy of BSA-FITC c.f. **Figure 157** and of other publications [289,345]. Anisotropy fitting under these conditions used primarily the short decay components as the long decay components was not well-defined. In any case the long component >1 µs is too long to adequately cover a small rotational time of ~30-40 ns with sufficient time-resolution. Although the time-range can be set to the 50-100 ns time range with a lower repetition rate (50 kHz) to allow a complete decay the acquisition time required to compute a large enough difference is too large for practical measurement. Moreover, any conclusions drawn from such a data set may highly be influenced by potential energy transfer mechanisms which may influence fluorescence anisotropy data e.g. between multiple gold nanoclusters that may exist protein template.
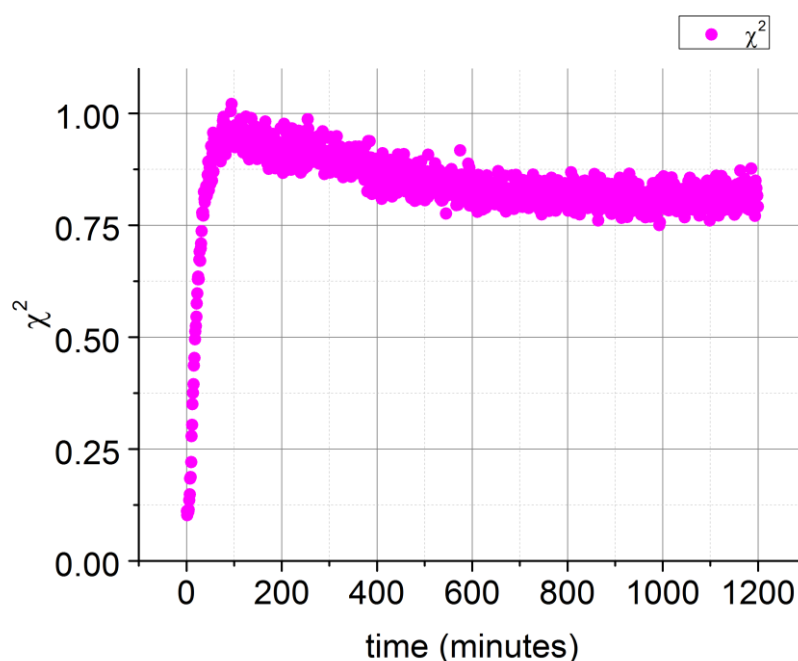
Figure 208: The χ^2 for each decay curve fitted for the 5 exponential model shows a similar trend to the 3 exponential model and has a similar dependence on the data quality of each individual decay curve. Although the data appears is over-fitted for each underlying decay curve and would be unacceptable for a single decay measurement. The 5 exponential model can be applied because the decay times are obtained from a larger global dataset.
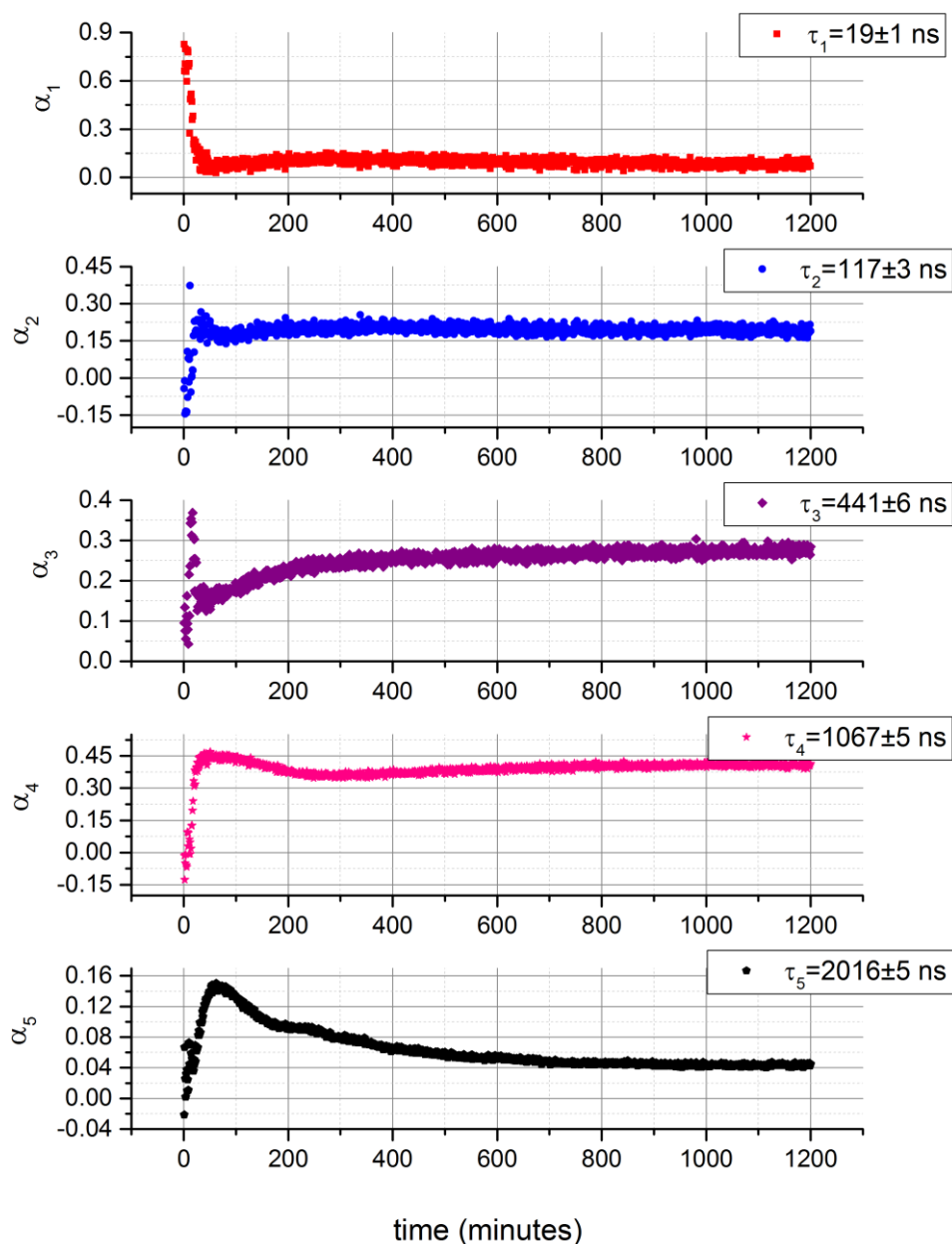
Figure 209: The normalised pre-exponential factors for the 5 decay times (**Figure 207**) plotted with respect to measurement time. α_1 is observed to be the dominant contribution in the fluorescence decay. τ_1=19±1 ns that is approximately 5 channels (t_{cal}=3.51166 ns ch^{-1}) and can be attributed as a mixture of scatter and short lived fluorescence and is too small to be accurately resolved on this time-range. Moreover, because such a large time range was used data was fitted without a prompt. This component is observed to fall as the other ones increase because the data is normalised. All components appear to be steady after 800 minutes.

Molecular dynamics were ran by a colleague Ben Russell his findings are reported briefly below [346]. The simulation showed that Au nanoclusters have a strong tendency to bind to hydrophobic pockets on BSAs surface, which traps them close to cysteine residues necessary for subsequent chemical interaction. Gold clusters were found to grow close to a number of cysteine sites within all three domains of BSA, although two major growth sites, which accommodate large clusters of size >12 atoms, were identified in domains IA and IIB.
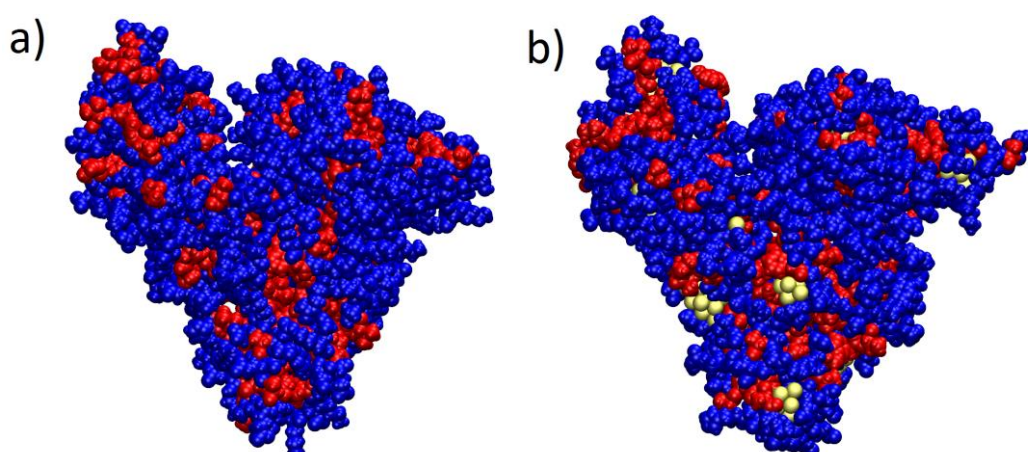
Figure 210: Hydrophobicity map of the BSA protein surface (a) before gold is introduced and (b) after gold has bonded to protein. Hydrophilic regions are represented by blue while hydrophobic regions are represented by red. Gold nanoclusters not fully buried under the surface (represented by yellow) can be seen binding to only hydrophobic regions. Figure taken with kind permission from Ben Russell [346].
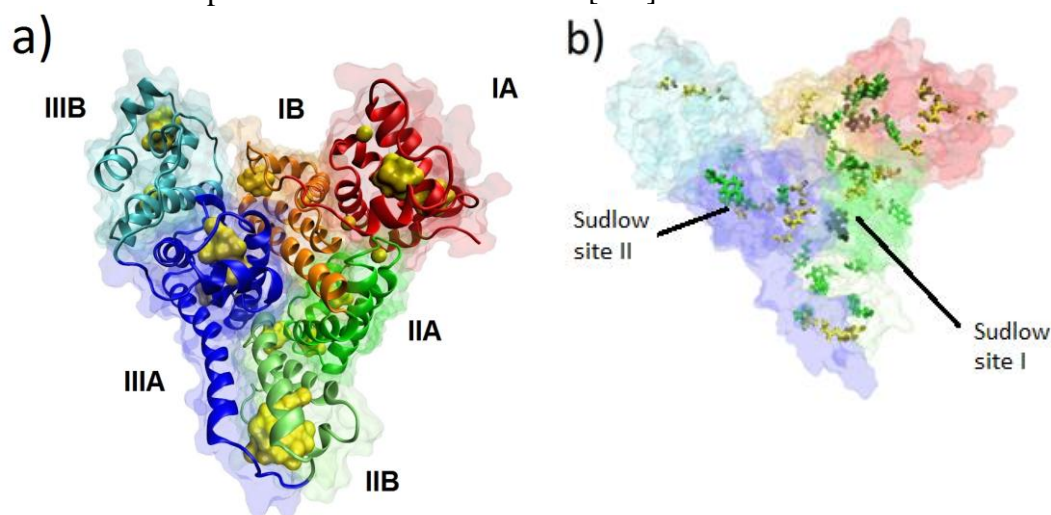
Figure 211: Molecular dynamic simulation of gold atoms nucleated within the protein after 600 ns of addition (a). Two large clusters can be seen in domains IA & IIB with smaller clusters dispersed throughout the protein. Gold clusters (yellow globules) can be seen to bond to sulphur atoms in cysteine residues. Cysteine residues can be seen in the same positions as the yellow globules in **Figure 210**a (represented by yellow chains). Tyrosine residues can be seen close to gold cluster location (represented by green chains).

Tryptophan molecules are shown in domain IB and IIA (shown by black chains). (b) Protein surface is shown as a ghost model in both cases, the colours indicate BSA subdomains: IA – red, IB – orange, IIA – green, IIB – light green, IIIA – blue, IIIB – cyan. The protein backbone is represented as a cartoon Figure taken with kind permission from Ben Russell [346].

The molecular dynamics indicate the formation of multiple smaller gold clusters as gold is introduced in random locations of the protein and the gold atoms and hence have the opportunity to interact with many different components of the protein surface, migrating to the nearest cysteine residues and forming covalent links. The presence of nearby tyrosine residues act to reduce gold salt resulting in the formation of clusters. The simulation showed two major nucleation sites in IA and IIB. IIB is close to the Sudlow binding site which is a hydrophobic pocket in subdomain IIA that binds an array of different molecules.

Although these nanoclusters are relatively easy to synthesise and give bright long loved stable emission the spectroscopy and the reason behind the formation of these new probes is still poorly understood. The kinetic spectroscopy of these nanoclusters can help elucidate the way they form however is relatively difficult to measure because of the high concentrations of protein necessary to drive their formation. These nanomaterials at current are being widely researched and it's hoped that they can be optimised as fluorescence probes.

5.2 Au$_{25}$@BSA Protein Synthesised Nanoclusters as a dSTORM Probe?

Au$_{25}$ nanoclusters have successfully been used as probes for imaging applications like FLIM which takes advantage of their long lifetime [347]. These probes were selected as candidates for dSTORM as it was hypothesised that their single molecule blinking could potentially be bright and that the gold would be resistant to photobleaching. Moreover because they are created with a reduced capping agent there may be no need to use specific dSTORM buffer.
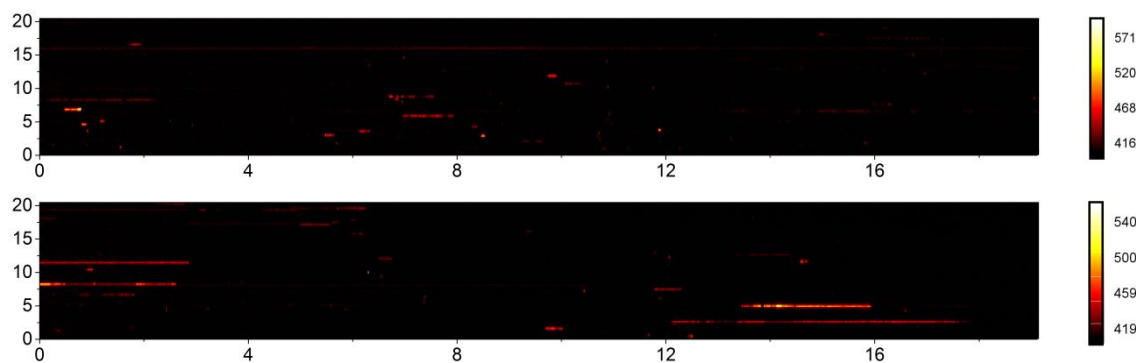
Figure 212: The maximum intensity of the *z*-project of Au_{25}@BSA nanoclusters measured with an excitation source of 561 nm at 50 % and 90 % power respectively and a BP600/37 nm at the emission. 1000 128×128 pixels were recorded at an exposure of 0.01 s (cycle time 0.01912 s). The *x* and *y* scales are in time (s) and length (μm).
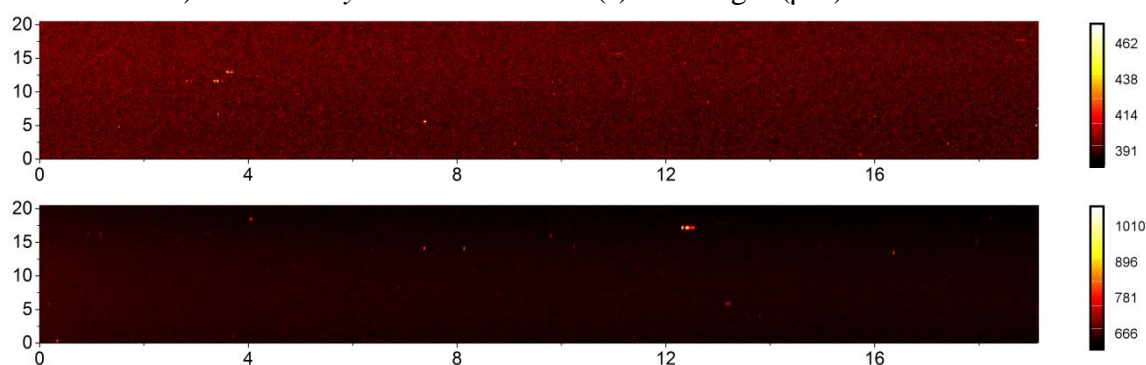
Figure 213: The maximum intensity of the *z*-project of Au_{25}@BSA nanoclusters dialysed into distilled water and TRIZMA buffer pH9 using membrane dialysis. Samples were measured with an excitation source of 561 nm at 90 % power and a BP600/37 nm at the emission. 1000 128×128 pixels were recorded at an exposure of 0.01 s (cycle time 0.01912 s). The *x* and *y* scales are in time (s) and length (μm).
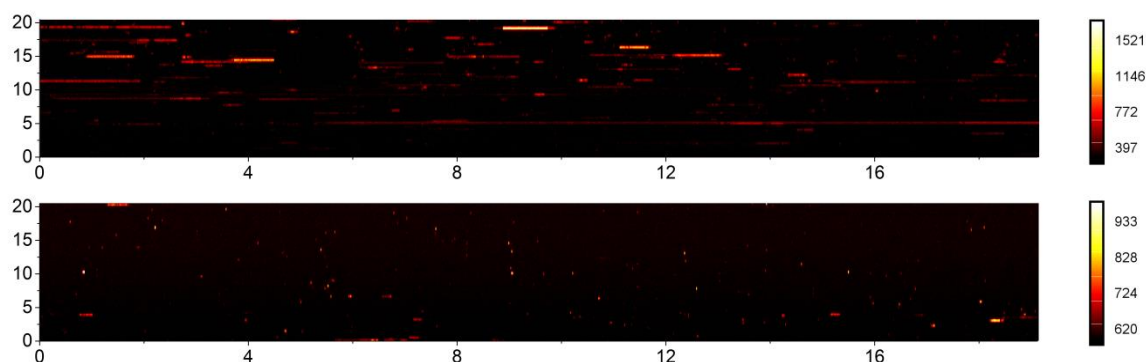
Figure 214: The maximum intensity of the *z*-project of Au_{25}@BSA nanoclusters dialysed into TRIZMA buffer pH9 using centrifugation dialysis. Samples were measured with an excitation source of 561 nm at 50 and 90 % power and a BP600/37 nm at the emission. 1000 128×128 pixels were recorded at an exposure of 0.01 s (cycle time 0.01912 s). The *x* and *y* scales are in time (s) and length (μm).

The single molecule blink profile of the Au_{25}@BSA nanoclusters was pretty complex when measured with a laser power of 50 % with a large number of relatively bright short lived blinks less than 0.05 s in addition to some dimmer long lived blinks that appeared for over 1 s, some dimmer long lived blinks even lasted for >19.12 s (>1000 frames of measurement). The increase in power to 90 % led to a higher proportion of these longer lived blinks with a slightly better signal to noise ratio. Because these Au_{25}@BSA nanoclusters are complex sample clean-up was attempted to see if the different blink species could be prescribed to impurities and hence removed. Dialysis of the sample was carried out using membrane dialysis into distilled water and 1.0 M pH 9 TRIZMA buffer. This led to a sparse set of short lived blinks ~0.05 s. The signal to noise ratio was observed to be significantly worse for the sample dialysed into distilled water than that kept in pH 9 TRIZMA buffer. Membrane dialysis however dilutes the sample which is a possible explanation for the lower number of blinks, centrifugation dialysis was then carried out into pH 9 TRIZMA buffer. This returned the longer lived blinks when excited with 50 % laser power and the brightness of these were significantly larger. A number of less bright shorter and longer lived blinks could also be observed. When the laser power was increased to 90 % the longer lived blinks disappeared and the signal to noise was slightly worse but still better than the untreated sample.
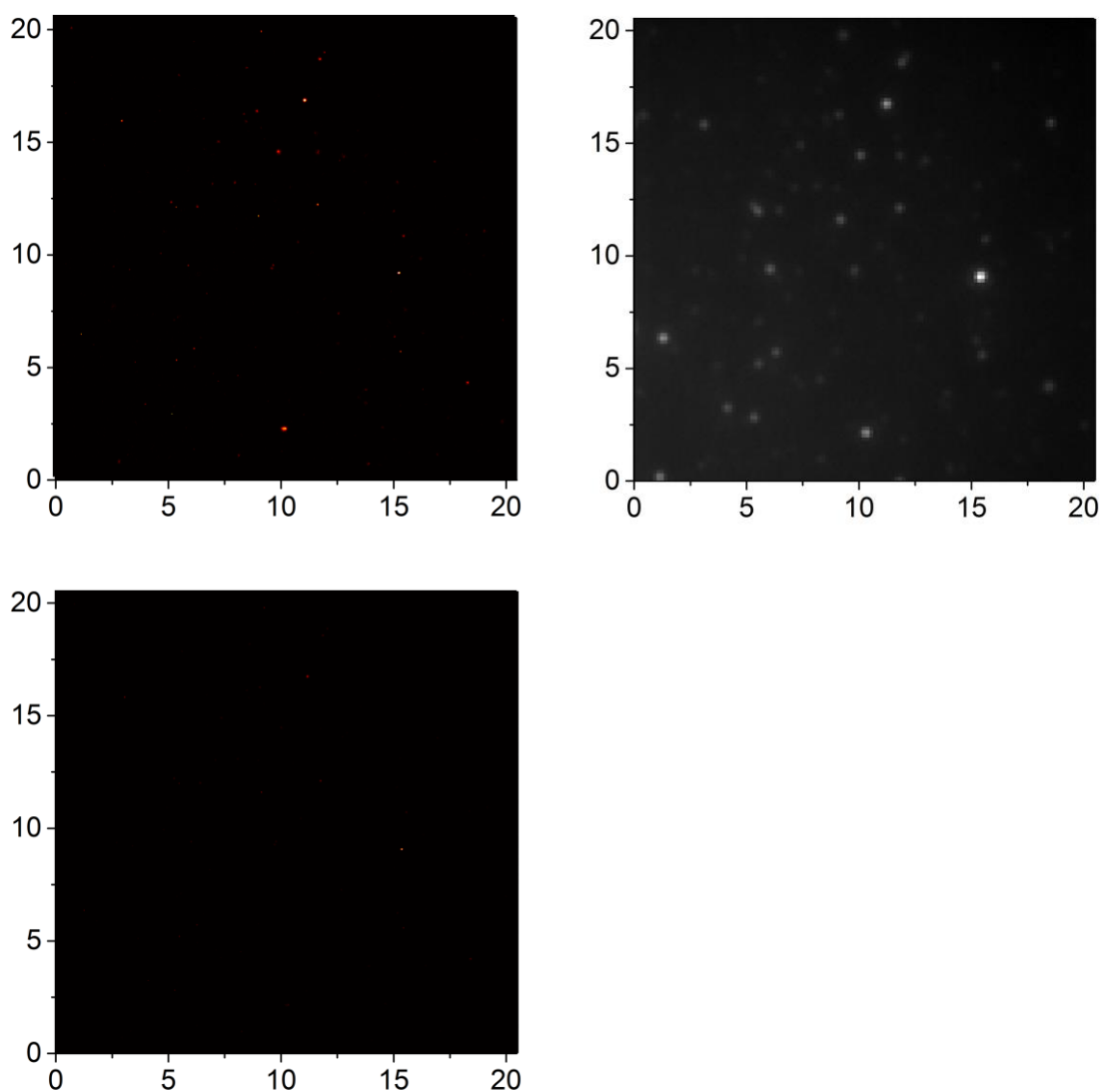
Figure 215: RainSTORM analysis of the 50 % power measurement (**Figure 214**). A localisation precision of 57 nm and 56 nm in *x* and *y* respectively was computed. Top left all localisations, top right the diffraction limited sum and bottom left the accepted localisations. The plot of accepted localisations only shows localisations smaller than the values of the Thompson precision. The standard deviations and Thompson localisation show no preference in *x* over *y* as expected.
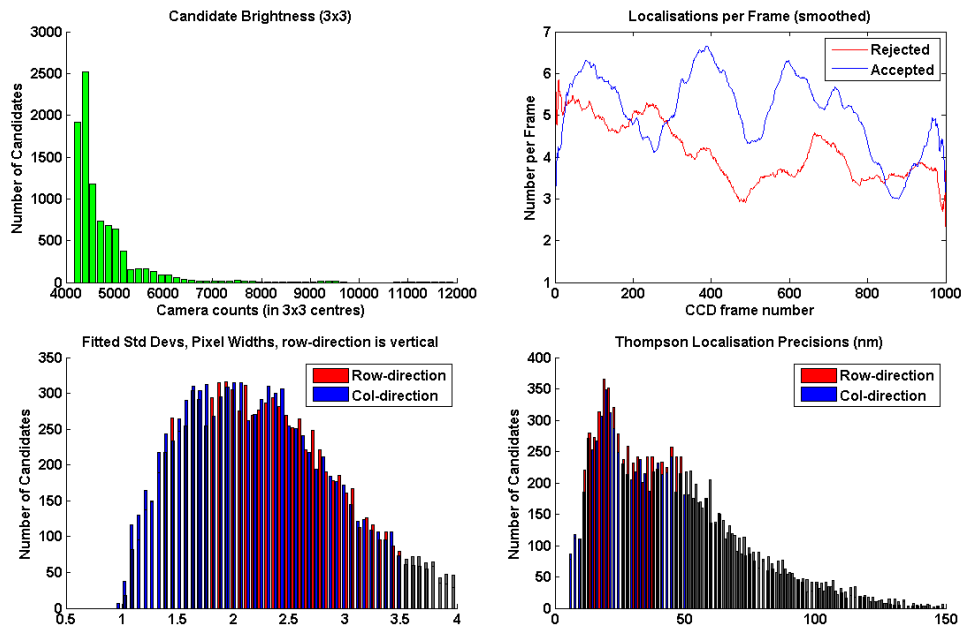
Figure 216: Histograms from **Figure 215** show that the number of candidates and the candidate brightness is relatively low and that about half the data is rejected.
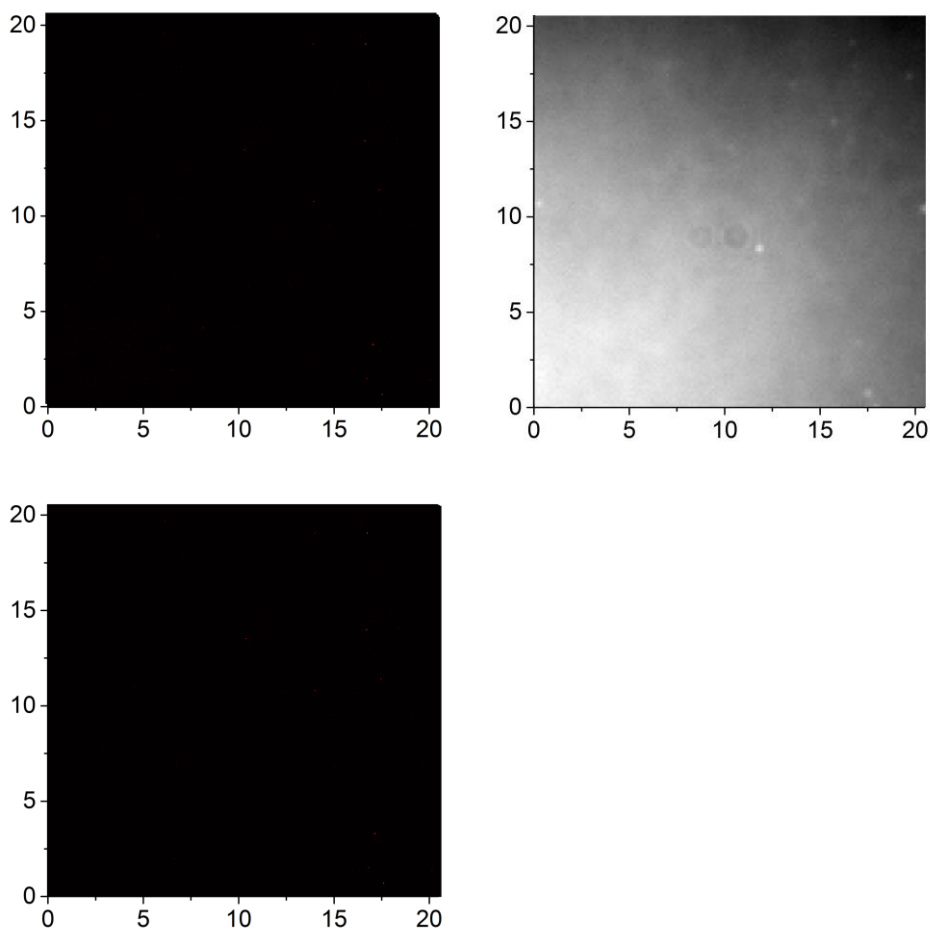
Figure 217: RainSTORM analysis of the 90 % power measurement (**Figure 214**). A localisation precision of 51 nm and 50 nm in *x* and *y* respectively was computed. Top left all localisations, top right the diffraction limited sum where it can be seen that the background noise is very high and bottom left the accepted localisations.
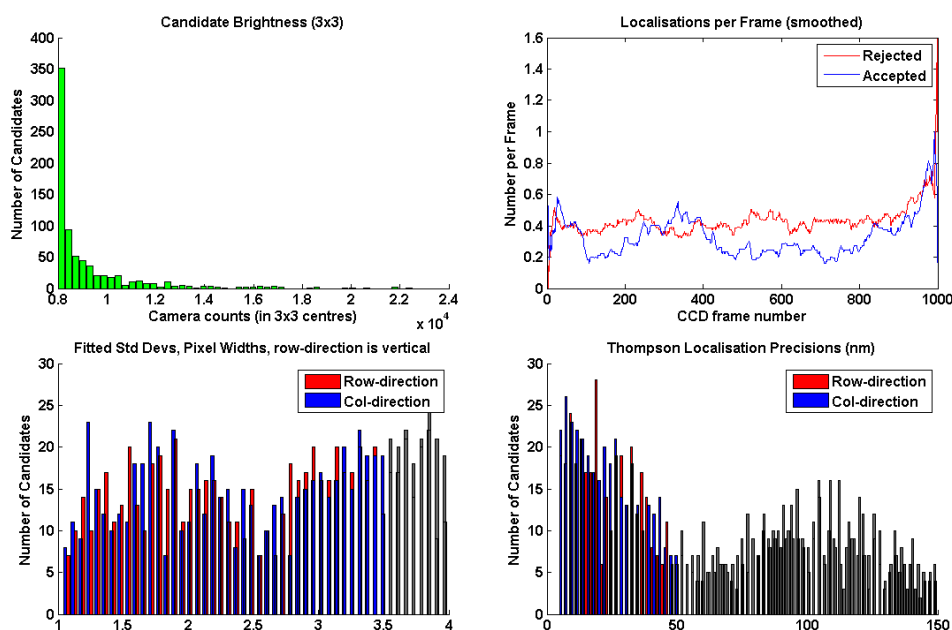
Figure 218: Histograms from **Figure 217** show that the number of candidates is extremely poor.

While the Au$_{25}$@BSA certainly showed very interesting blinking characteristics even without additional buffer and although they can clearly be seen as being very sensitive to buffer conditions they are not suitable as probes for dSTORM. The presence of multiple blink species makes data analysis too complex. The fact that they possess such a long blink time also unacceptably increases the acquisition time. It is possible the different blink durations have a relation to the multiple decay times observed in the fluorescence decays and relate to multiple sizes of Au species within BSA clusters but this is a poorly understood speculation. It is also possible the behaviour of the different blink types using single molecule microscopy may have acted as a spectroscopic tool for separating out different species of gold nanoclusters. It is difficult to investigate this problem further due to the inability to separate out different species of Au@BSA nanoclusters from each other and bulk BSA using conventional methods such as size-exclusion.

5.3 Au$_{25}$@GSH Nanoclusters as a dSTORM Probe?

BSA is a complicated reducing agent and protection protein for the Au$_{25}$ nanoclusters. In order to better understand them simpler Au$_{25}$@GSH nanoclusters were added to a LabTek chamber and then rinsed using PBS and imaged with PBS and STORM buffer respectively. The 561 nm laser was used with the BP600/37 nm filter. The blinking behaviour of the nanoclusters was compared with and without dSTORM buffer at varying laser powers.

255
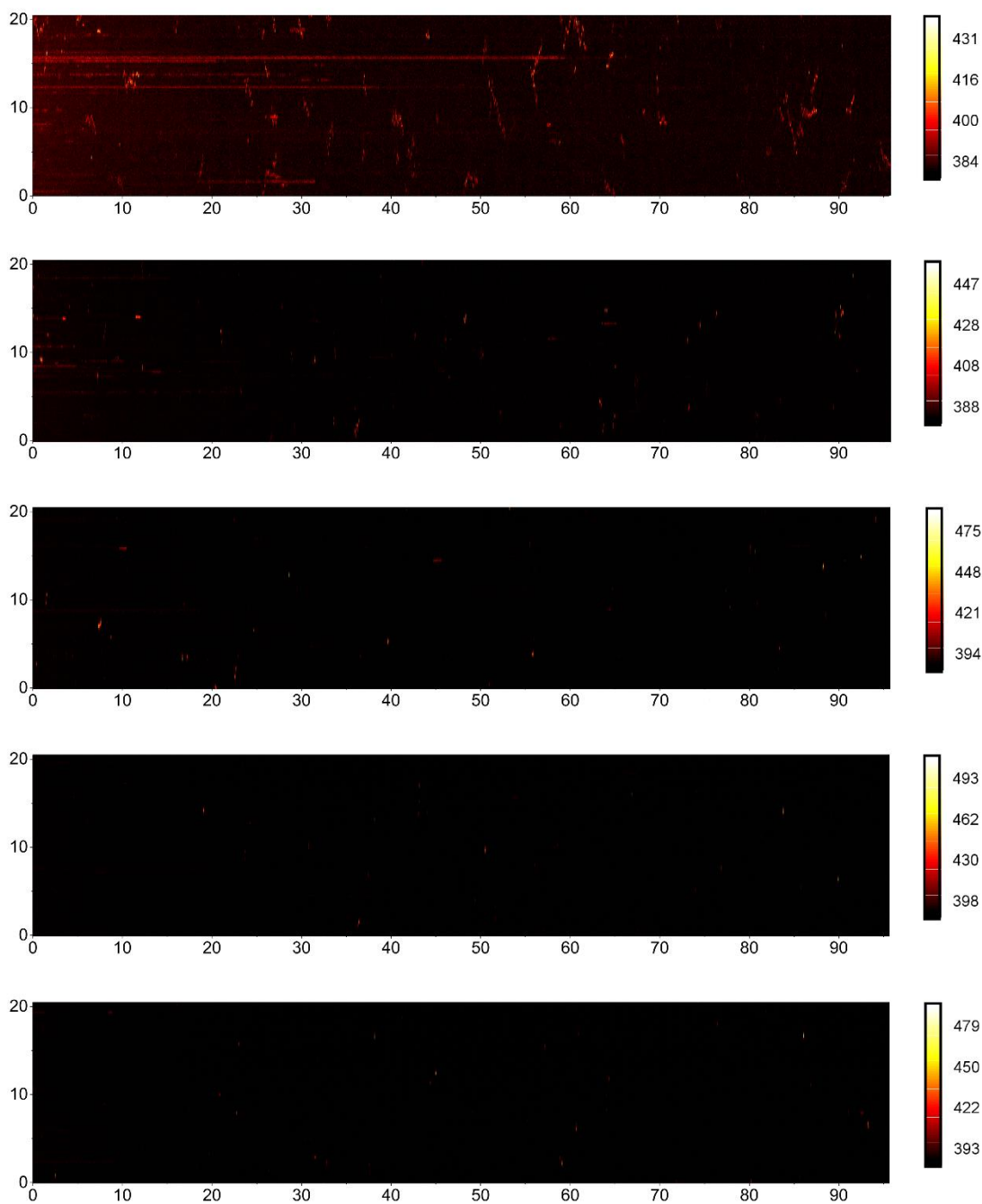
Figure 219: Reslice of blink data of Au$_{25}$@GSH nanoclusters measured in PBS at laser powers of 5 %, 19.06 %, 48.98 %, 71.26 % and 90 %. For low power the background fluorescence was relatively high and is observed to bleach with respect to time. Some long single molecule blinks can be observed. A large number of the single molecule blinks are not straight lines but are seen to drift. This is likely due to diffusion as the Au$_{25}$@GSH don't affix strongly to the slide. At higher powers the longer blinks are observed less frequently and there is significantly less background fluorescence. At higher powers, the shorter single molecule blinks become sparser. Each frame was 128×128 pixels and 5000 frames were recorded with a capture rate of 0.01 s (cycle time of 0.01912 s).
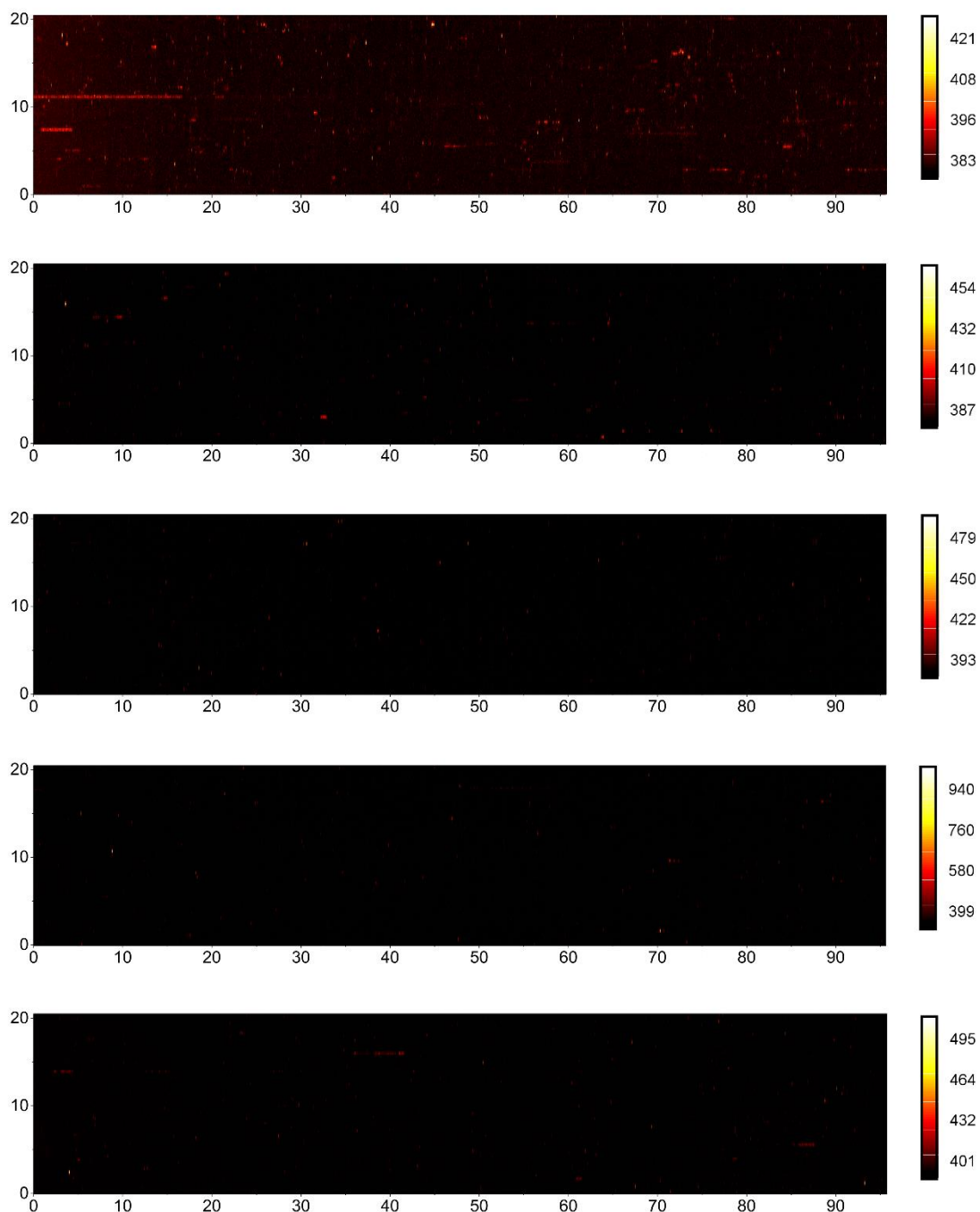
Figure 220: Usage of STORM buffer instead of PBS reduced the photobleaching at low power slightly and some longer lived blinks were observed at higher power. Each frame was 128×128 pixels and 5000 frames were recorded with a capture rate of 0.01 s (cycle time of 0.01912 s).

These nanoclusters also show complex blinking behaviour, dependant on the laser power and were more stable when the dSTORM buffer was used. The long-lived blinks seemed to only be visible at low power and appeared to suffer from photobleaching in this case the

high laser power may have cleaved the GSH from the nanoclusters breaking them up. These probes lack the blink duration and brightness required for dSTORM.

6. Conclusions

The work in this thesis looks at nanometrology using an assortment of fluorescence techniques. Time-resolved fluorescence anisotropy is a well-established technique which allows for measurement of nanoparticles providing it deals with more or less homogeneous samples and low concentrations. In this thesis time-resolved fluorescence anisotropy was demonstrated using both silica nanoparticles and proteins. Fluorescence anisotropy measurements have been carried out using a high throughput DeltaFlex TCSPC system significantly lowering the acquisition time and increasing the practicality of TRFA measurements. ADOTA, a long lived red photostable fluorophore with a high quantum yield was compared side by side to one of the traditional fluorophores Rhodamine 6G. Its longer lived emission will be a benefit for TRFA applications but care has to be taken with the data as it will report a lower particle size. Nanometrology measurements were also examined using dSTORM however unfortunately the ADOTA fluorophore did not yield bright enough single molecule blinks for this application. The fluorescence spectroscopy of gold nanoclusters was examined in detail. Gold nanoclusters show unique blinking characteristics and long decay times. Unfortunately, their decay is too complicated for successful TRFA applications and their single molecule blinks are not bright enough and are too long for dSTORM. These materials however possess single molecule blinks without the use of specialised buffer conditions and their refinement or the development of similar nanomaterials still hold great potential for fluorescence spectroscopy. The probes invested in this research didn't satisfy all categories in the stringent list of requirements necessary for a successful dSTORM application. In order to advance dSTORM new probes still need to be discovered in order to realise the full potential of dSTORM and photoswitchable mechanisms for fluorophores that are accessible at lower laser power would reduce photodamage of samples. Also new protocols for labelling i.e. to satisfy the Nyquist criterion at high resolution are desired.

The work in this thesis also looked into the use of fluorescence instruments in great detail and covered many of the current innovations regarding fluorescence instrumentation particularly in the area of nanometrology. The SUPA short term visit with HORIBA Scientific ISA Edison looked into the use of detector types such as CCDs and the traditional PMT in fluorescence spectroscopy. The industrial collaboration with HORIBA Scientific IBH Glasgow looked into the leading edge and next generation of timing electronics and

laser sources for time-resolved fluorescence spectroscopy. The work at NPL Biotechnology looked into developments within fluorescence microscopy pushing past the diffraction limit. Fluorescence instruments have moved from the photophysical labs and found a niche within the field of nanometrology especially within the vast area of the life-sciences. The demand of applications in the life sciences and significant advances in electronics such as timing electronics have made not only steady state excitation and emission fluorescence measurements standard but relatively more advanced fluorescence spectroscopy techniques such as the EEM, the fluorescence decay and steady state anisotropy easy to perform for the end user as well as fluorescence microscopy techniques such as steady state confocal microscopy and FLIM. The widespread use of fluorescence in these application areas and further demand has consequently led to the development of even more advanced techniques such as time-resolved fluorescence anisotropy, kinetic TCSPC, TRES, TREEM and even single molecule fluorescence techniques such as dSTORM. Fluorescence techniques still have a long way to go and undoubtedly will continue playing a key role in answering the vast number of questions within the life sciences. It has been a pleasure working on the leading edge of fluorescence instrumentation throughout the PhD. In the past there was much debate over time-domain vs frequency domain measurements however the rapid advances in hardware for time-domain measurements proved TCSPC the victor. These rapid developments are steadily continuing. With regards to hardware, the detector is still the main limitation. The awaited "multichannel detector with ps readout" [348–351] will revolutionise the field of fluorescence spectroscopy bringing time-resolved measurements to the frontier. Although all the super-resolution techniques will benefit from the advancement in hardware location microscopy should benefit the most. For dSTORM firstly a larger number of photons should be measured with a ns fast capture rate meaning more photons, less averaging single molecule counts with noise and hence a superior signal to noise ratio and enhanced localisation precision. It's also likely that ns blinks that cannot be resolved with the ms capture rate of the CCD will become measurable allowing utilisation of normal chemical systems which are currently inaccessible due to the slow capture rate of "fast" CCDs. This will remove undesirable perquisites to achieve super-resolution microscopy such as the high laser power and specialised dSTORM buffer which are currently a mandatory requirement when using a CCD. Measuring at laser powers comparable with standard steady-state and time-resolved measurements will result in less photodamage and hence more confidence with the widespread use of stochastic imaging.

If data is acquired fast enough it may also allow for kinetic 3D location microscopy with nanometre resolution which is of course the long term objective of fluorescence nanoscopy.

In closing the fluorescence research area is well-established but we have only seen the beginning of its applications on the nanoscale. The ease and automation of data analysis for large multi-dimensional datasets must come hand in hand with the above hardware improvements. With newer detectors it's possible that stochastic super-resolution microscopy becomes a widely applicable time-resolved measurement perhaps merging with FLIM to become something much greater… Fluorescence Lifetime Imaging Nanoscopy.

7. References

[1]   Ramanujam N 2000 Fluorescence spectroscopy in vivo *Encycl. Anal. Chem.* 20–56

[2]   Zhou Z, Guo L, Shiller A M, Lohrenz S E, Asper V L and Osburn C L 2013 Characterization of oil components from the Deepwater Horizon oil spill in the Gulf of Mexico using fluorescence EEM and PARAFAC techniques *Mar. Chem.* **148** 10–21

[3]   Henderson R K, Baker a., Murphy K R, Hambly a., Stuetz R M and Khan S J 2009 Fluorescence as a potential monitoring tool for recycled water systems: A review *Water Res.* **43** 863–81

[4]   Ludescher R D 2003 Phosphorescence Spectroscopy as Amorphous Solids *Characterisation of Cereals and Flours Properties, Analysis and Applications* ed G Kaletunc and K J Breslauer (Marcel Dekker, Inc) pp 437–72

[5]   You Y and Ludescher R D 2010 The effect of molecular size on molecular mobility in amorphous oligosaccharides *Food Biophys.* **5** 82–93

[6]   Nawrocka A and Lamorsk J 2013 Determination of Food Quality by Using Spectroscopic Methods *Advances in Agrophysical Research* (InTech) pp 347–68

[7]   Borisov S M, Mayr T, Karasyov A A, Klimant I, Chojnacki P, Moser C, Nagl S, Schaeferling M, Stich M I, Kocincova A S and Wolfbeis O S 2008 New Plastic Microparticles and Nanoparticles for Fluorescent Sensing and Encoding *Fluorescence of Supermolecules, Polymers, and Nanosystems* vol 4, ed M N Berberan-santos (Springer) pp 431–63

[8]   Hou X, Ke C, Bruns C J, McGonigal P R, Pettman R B and Stoddart J F 2015 Tunable solid-state fluorescent materials for supramolecular encryption. *Nat. Commun.* **6** 6884

[9]   Langhals H, Zgela D and Schlücker T 2014 High Performance Recycling of Polymers by Means of Their Fluorescence Lifetimes * 144–50

[10]   Langhals H, Zgela D and Schlücker T 2015 Improved High Performance Recycling of Polymers by Means of Bi-Exponential Analysis of Their Fluorescence Lifetimes 92–100

[11]   Shahzad A, Köhler G, Knapp M, Gaubitzer E, Puchinger M and Edetsberger M 2009 Emerging applications of fluorescence spectroscopy in medical microbiology field. *J. Transl. Med.* **7** 99

[12]   The I 2005 Lifetime based sensors / sensing *Topics in Fluorescence Spectroscopy Volume 10 Advanced Concepts in Fluorescence Sensing Part B: Macromolecular Sensing* vol 10, ed C D Geddes and J R Lakowicz (New York: Springer) pp 241–74

[13]   Paolesse R, Monti D, Dini F and Di Natale C 2010 Fluorescence Based Sensor Arrays *Luminescence Applied in Sensor Science* pp 139–74

[14]   Bosch L I and James T D 2006 Fluorescent Tict Sensors for Saccharides *Topics in Fluorescence Spectroscopy Volume 11 Glucose Sensing* vol 11, ed C D Geddes and J R Lakowicz (New York: Springer) pp 334–50

[15]   Cordes D B, Suri J T, Cappuccio F E, Jason N, Gamsey S, Sharrett Z, Thoniyot P, Wessling A and Singaram B 2006 Two-Component Optical Sugar Sensing Using Boronic Acid-Substituted Viologens with Anionic Fluorescent Dyes *Topics in*

Fluorescence Spectroscopy Volume 11 Glucose Sensing vol 11, ed C D Geddes and J R Lakowicz (New York: Springer) pp 47–87

[16]   Tolosa L and Rao G 2006 The Glucose Binding Protein as Glucose Sensor: Protein engineering for low-cost optical sensing of glucose *Topics in Fluorescence Spectroscopy Volume 11 Glucose Sensing* vol 11, ed C D Geddes and J R Lakowicz (New York: Springer) pp 323–31

[17]   Lakowicz J R 2002 Emerging Biomedical Applications of Time-Resolved Fluorescence Spectroscopy *Topics in Fluorescence Spectroscopy Volume 4 Probe Design and Chemical Sensing* vol 4, ed J R Lakowicz (New York, Boston, Dordrect, London, Moscow: Kluwer Academic Publishers) pp 1–19

[18]   Lee S H and Karim M M 2006 Recent Chemiluminescence Applications for Glucose Sensing *Topics in Fluorescence Spectroscopy Volume 11 Glucose Sensing* vol 11, ed C D Geddes and J R Lakowicz (New York: Springer) pp 311–22

[19]   Mcshane M J 2006 Microcapsules as "Smart Tattoo" Glucose Sensors: Engineering Systems with Enzymes and Glucose-Binding Sensing Elements *Topics in Fluorescence Spectroscopy Volume 11 Glucose Sensing* vol 11, ed C D Geddes and J R Lakowicz (New York: Springer) pp 131–63

[20]   Schultz J S 2006 Optically-Based Affinity Biosensors for Glucose *Topics in Fluorescence Spectroscopy Volume 11 Glucose Sensing* vol 11, ed C D Geddes and J R Lakowicz (New York: Springer) pp 283–310

[21]   Lualdi M, Colombo A, Leo E, Morelli D, Vannelli A, Battaglia L, Poiasina E and Marchesini R 2007 Natural Fluorescence Spectroscopy of Human Blood Plasma in the Diagnosis of Colorectal Cancer : Feasibility Study and Preliminary Results 567–71

[22]   Li B, Ryan P W, Shanahan M, Leister K J and Ryder A G 2011 Fluorescence excitation-emission matrix (EEM) spectroscopy for rapid identification and quality evaluation of cell culture media components *Appl. Spectrosc.* **65** 1240–9

[23]   Mills A and Hodgen S 2005 Fluorescent carbon dioxide indicators *Topics in Fluorescence Spectroscopy Volume 9 Advanced Concepts in Fluorescence Sensing Part A: Small Molecule Sensing* vol 9, ed C D Geddes and J R Lakowicz (New York: Springer) pp 119–61

[24]   Rao G, Bambot S B, Kwong S C W, Szmacinski H, Sipior J, Holavanahali R and Carter G 2002 Application of Fluorescence Sensing to Bioreactors *Topics in Fluorescence Spectroscopy Volume 4 Probe Design and Chemical Sensing* vol 4, ed J R Lakowicz (New York, Boston, Dordrect, London, Moscow: Kluwer Academic Publishers) pp 417–48

[25]   Prodi L, Montalti M, Zaccheroni N and Dolci L S 2005 Probes and sensors for cations *Topics in Fluorescence Spectroscopy Volume 9 Advanced Concepts in Fluorescence Sensing Part A: Small Molecule Sensing* vol 9, ed C D Geddes and J R Lakowicz (New York: Springer) pp 1–57

[26]   Valeur B 2002 Principles of Fluorescent Probe Design for Ion Recognition *Topics in Fluorescence Spectroscopy Volume 4 Probe Design and Chemical Sensing* vol 4, ed J R Lakowicz (New York, Boston, Dordrect, London, Moscow: Kluwer Academic Publishers) pp 21–48

[27]   Resch-genger U and Hennrich G 2005 Fluorescence Redox-Switchable Devices *Topics in Fluorescence Spectroscopy Volume 9 Advanced Concepts in Fluorescence*

Sensing Part A: Small Molecule Sensing vol 9, ed C D Geddes and J R Lakowicz (New York: Springer) pp 189–218

[28]   Banwell C N and McCash E M 1994 Introduction *Fundamentals of Molecular Spectroscopy* ed C N Banwell and E M McCash (McGraw Hill) pp 1–30

[29]   Borren M V A N, Brady N R, Ravelsloot J and Westerhoff H V 2002 Looking into a Living Cell *Fluorescence Spectroscopy, Imaging and Probes* ed O Wolfbeis, R Kraayenhof, A J W G Visser and G H C. (Springer) pp 361–72

[30]   Lopez-Duarte I, Vu T T, Izquierdo M A, Bull J a and Kuimova M K 2014 A molecular rotor for measuring viscosity in plasma membranes of live cells *Chem. Commun.* **50** 5282–4

[31]   Selvin P 2003 Lanthanide-labeled DNA *Topics in Fluorescence Spectroscopy Volume 7 DNA Technology* vol 7, ed J R Lakowicz (New York, Boston, Dordrect, London, Moscow: Kluwer Academic Publishers) pp 177–212

[32]   Gracie K, Smith W E, Yip P, Sutter J U, Birch D J S, Graham D and Faulds K 2014 Interaction of fluorescent dyes with DNA and spermine using fluorescence spectroscopy. *Analyst* **139** 3735–43

[33]   McGown L 2003 On-the-Fly Fluorescence Lifetime Detection in Capillary Electrophoresis for DNA Analysis *Topics in Fluorescence Spectroscopy Volume 7 DNA Technology* vol 7, ed J R Lakowicz (New York, Boston, Dordrect, London, Moscow: Kluwer Academic Publishers) pp 129–49

[34]   Piunno P and Krull U 2003 Fluorimetric DNA Biosensors *Topics in Fluorescence Spectroscopy Volume 7 DNA Technology* vol 7, ed J R Lakowicz (New York, Boston, Dordrect, London, Moscow: Kluwer Academic Publishers) pp 271–89

[35]   Sabato D, Rossi M, Malicka J, Gryczynski Z and Gryczynski I 2003 DNA arrays for genetic analyses and medical diagnosis *Topics in Fluorescence Spectroscopy Volume 7 DNA Technology* vol 7, ed J R Lakowicz (New York, Boston, Dordrect, London, Moscow: Kluwer Academic Publishers) pp 213–37

[36]   Schurr J M, Fujimoto B S, Wu P and Song L 2002 Fluorescence Studies of Nucleic Acids : Dynamics , Rigidities , and Structures *Topics in Fluorescence Spectroscopy Volume 3 Biochemical Applications* vol 3, ed J R Lakowicz (New York, Boston, Dordrect, London, Moscow: Kluwer Academic Publishers) pp 137–229

[37]   Demchenko A 2009 Opening New Horizons *Introduction to Fluorescence Sensing* (Springer) pp 507–44

[38]   Hattori M 2005 Finishing the euchromatic sequence of the human genome *Tanpakushitsu Kakusan Koso.* **50** 162–8

[39]   Nossal G J V 2003 The double helix and immunology. *Nature* **421** 440–4

[40]   Birch D J S 2011 Fluorescence detections and directions *Meas. Sci. Technol.* **22** 052002

[41]   Ozinskas A J 2002 Principles of Fluorescence Immunoassay *Topics in Fluorescence Spectroscopy Volume 4 Probe Design and Chemical Sensing* vol 4, ed J R Lakowicz (New York, Boston, Dordrect, London, Moscow: Kluwer Academic Publishers)

[42]   Chial H 2008 DNA sequencing technologies key to the Human Genome Project *Nat. Educ.* **1** 219

[43]   Yao J and Tjian R 2011 Sub-nuclear compartmentalization of core promoter factors

and target genes *Cell Cycle* **10** 2405–6

[44]   Frost N a., Shroff H, Kong H, Betzig E and Blanpied T a. 2010 Single-molecule discrimination of discrete perisynaptic and distributed sites of actin filament assembly within dendritic spines *Neuron* **67** 86–99

[45]   Chen B-C, Legant W R, Wang K, Shao L, Milkie D E, Davidson M W, Janetopoulos C, Wu X S, Hammer J a., Liu Z, English B P, Mimori-Kiyosue Y, Romero D P, Ritter A T, Lippincott-Schwartz J, Fritz-Laylin L, Mullins R D, Mitchell D M, Reymann a.-C, Bembenek J N, Bohme R, Grill S W, Wang J T, Seydoux G, Tulu U S, Kiehart D P and Betzig E 2014 Lattice light-sheet microscopy: Imaging molecules to embryos at high spatiotemporal resolution *Science (80-.).*

[46]   Liu Z, Legant W R, Chen B-C, Li L, Grimm J B, Lavis L D, Betzig E and Tjian R 2014 3D imaging of Sox2 enhancer clusters in embryonic stem cells *Elife* 1–29

[47]   Birch D J S, Chen Y and Rolinski O J 2015 David J. S. Birch, Yu Chen, and Olaf J. Rolinski *Biological and Medical Photonics, Spectroscopy and Microscopy Vol 4. Photonics* vol IV, ed E D L Andrews (Wiley) pp 1–56

[48]   Wehry E L 1997 Molecular Fluorescence and Phosphorescence Spectrometry *Handbook of Instrumental Techniques for Analytical Chemistry* ed F A Settle (Virginia: Prentice Hall PTR (ECS Professional)) pp 507–40

[49]   Limpouchová Z, Procházka K, Fidler V, Dvořák J and Bednář B 1993 Molecular Movements and Dynamics in Solutions Studied by Fluorescence Depolarization Measurement *Collect. Czechoslov. Chem. Commun.* **58** 213–33

[50]   Valeur B 2001 Absorption of UV – visible light *Molecular Fluorescence: Principles and Applications* ed B Valeur (Wiley-VCH) pp 20–33

[51]   O'Connor D V. and Phillips D 1984 Fluorescence, its Time Dependence and Applications *Time-Correlated Single Photon Counting* (London: Academic Press) pp 1–35

[52]   McGuinness C D 2006 *Glucose Sensing Based on the Intrinsic Time Dependent Fluorescence from Proteins: Applications of pulsed ultraviolet light emitting diodes and sol-gel derived matrices* (Strathclyde)

[53]   Birks J B 1969 Absorption *Photophysics of Aromatic Molecules* (Manchester: Wiley) pp 44–83

[54]   Lakowicz J R 2006 Introduction to Fluorescence *Principles of Fluorescence Spectroscopy* vol 32, ed J R Lakowicz (New York: Springer) pp 1–26

[55]   Birks J B 1969 Fluorescence *Photophysics of Aromatic Molecules* (Manchester: Wiley) pp 84–141

[56]   Gasiorowicz S 2003 Spin *Quantum Physics* ed S Gasiorowicz (John Wiley & Sons Inc.) pp 158–73

[57]   Birks J B 1969 Radiationless Transitions *Photophysics of Aromatic Molecules* (Manchester: Wiley) pp 142–92

[58]   Bogdanov V L 2002 Fluorescence and Multiwave Mixing Induced by Photon Absorption of Excited Molecules *Topics in Fluorescence Spectroscopy Volume 5 Nonlinear and Two-Photon-Induced Fluorescence* vol 5, ed J R Lakowicz (New York, Boston, Dordrect, London, Moscow: Kluwer Academic Publishers) pp 211–51

[59] Birch D J S and Imhof R E 2002 Time-Domain Fluorescence Spectroscopy Using Time-Correlated Single-Photon Counting *Topics in Fluorescence Spectroscopy Volume 1 Techniques* vol 1, ed J R Lakowicz (New York, Boston, Dordrect, London, Moscow: Kluwer Academic Publishers) pp 1–95

[60] Jenness J R 1929 Effect of Temperature Upon the Fluorescence of some Organic Solutions *Phys. Rev.* **34** 1275–85

[61] Sauer M, Hofkens J and Enderlein J 2011 Basic Principles of Fluorescence Spectroscopy *Handbook of Fluorescence Spectroscopy and Imaging from Ensemble to Single Molecules* (Wiley-VCH) pp 1–30

[62] Valeur B 2001 Characteristics of fluorescence emission *Molecular Fluorescence: Principles and Applications* vol 8, ed B Valeur (Wiley-VCH) pp 34–71

[63] Birks J B 1969 Delayed Luminescence *Photophysics of Aromatic Molecules* (Manchester: Wiley) pp 372–402

[64] Demchenko A 2009 Fluorescence Detection Techniques *Introduction to Fluorescence Sensing* (Springer) pp 65–118

[65] Eftink M R 2002 Fluorescence Quenching: Theory and Applications *Topics in Fluorescence Spectroscopy Volume 2 Principles* vol 2, ed J R Lakowicz (New York, Boston, Dordrect, London, Moscow: Kluwer Academic Publishers) pp 53–126

[66] Valeur B 2001 Effects of intermolecular photophysical processes on fluorescence emission *Molecular Fluorescence: Principles and Applications* vol 8, ed B Valeur (Wiley-VCH) pp 72–124

[67] Birks J B 1969 Interactions with Oxygen and Nitric Oxide *Photophysics of Aromatic Molecules* (Manchester: Wiley) pp 403–91

[68] Yip P, Karolin J and Birch D J S 2012 Fluorescence anisotropy metrology of electrostatically and covalently labelled silica nanoparticles *Meas. Sci. Technol.* **23** 084003

[69] Saito R and Dresselhaus M S 2014 Optical Properties of Carbon Nanotubes *Graphene Nanotubes and Graphene* (Elsevier) pp 77–98

[70] Lee S, Zhang S, McCamant D W, Kukura P and Mathies R A 2004 Theory of femtoseconf stimulated Raman spectroscopy *J. Chem. Phys.* **121** 3632–42

[71] Asher S a 1988 UV resonance Raman studies of molecular structure and dynamics: applications in physical and biophysical chemistry. *Annu. Rev. Phys. Chem.* **39** 537–88

[72] Greetham G M, Ronayne K L, Towrie M, Matousek P and Parker a W 2007 Femtosecond stimulated Raman scattering: development of a new facility for high temporal resolution Raman spectroscopy 2006–8

[73] Banwell C N and McCash E M 1994 Raman Spectroscopy *Fundamentals of Molecular Spectroscopy1* ed C N Banwell and E M McCash (McGraw Hill) pp 100–26

[74] Subramaniam V, Steel D G and Gafni A 2002 Room Temperature Tryptophan Phosphorescence as a Probe of Structural and Dynamic Properties of Proteins *Topics in Fluorescence Spectroscopy Volume 6 Protein Fluorescence* vol 6, ed J R Lakowicz (New York, Boston, Dordrect, London, Moscow: Kluwer Academic Publishers) pp 43–65

[75]   Birks J B 1969 Excited States of Aromatic Molecules *Photophysics of Aromatic Molecules* (Manchester: Wiley) pp 1–28

[76]   Boens N, Qin W and Basaric N 2007 Fluorescence lifetime standards for time and frequency domain fluorescence spectroscopy *Anal. ...* **79** 2137–49

[77]   Brackmann U Lambdachrome ® Laser Dyes

[78]   Invitrogen *The Molecular Probes® Handbook* (Invitrogen)

[79]   Demchenko A 2009 Design and Properties of Fluorescence Reporters *Introduction to Fluorescence Sensing* (Springer) pp 119–96

[80]   Haidekker M A, Nipper M, Mustafic A, Lichlyter D, Dakanali M and Theodorakis E A 2010 Dyes with Segmental Mobility: Molecular Rotors *Advanced Fluorescence Reporters in Chemistry and Biology I Fundamentals and Molecular Design* Springer Series on Fluorescence vol 8, ed A P Demchenko (Berlin, Heidelberg: Springer) pp 267–308

[81]   Han J and Burgess K 2010 Fluorescent indicators for intracellular pH. *Chem. Rev.* **110** 2709–28

[82]   Valeur B 2001 Fluorescent Molecular Sensors of Ions and Molecules *Molecular Fluorescence: Principles and Applications* ed B Valeur (Wiley-VCH) pp 273–350

[83]   Song L and Fayer M D 1991 Temperature dependent intersystem crossing and triplet-triplet absorption of rubrene in solid solution *J. Lumin.* **50** 75–81

[84]   Quinn P J 2010 A lipid matrix model of membrane raft structure. *Prog. Lipid Res.*

[85]   Kabouridis P S and Jury E C 2008 Lipid rafts and T-lymphocyte function: implications for autoimmunity. *FEBS Lett.* **582** 3711–8

[86]   Hosny N a, Mohamedi G, Rademeyer P, Owen J, Wu Y, Tang M-X, Eckersley R J, Stride E and Kuimova M K 2013 Mapping microbubble viscosity using fluorescence lifetime imaging of molecular rotors. *Proc. Natl. Acad. Sci. U. S. A.* **110** 9225–30

[87]   Valeur B 2001 Microviscosity, fluidity, molecular mobility. Estimations by means of fluorescence probes *Molecular Fluorescence: Principles and Applications* vol 8, ed B Valeur (Wiley-VCH) pp 226–46

[88]   Demchenko A P 2010 Comparative Analysis of Fluorescence Reporter Signals Based on Intensity, Anisotropy, Time-Resolution, and Wavelength-Ratiometry *Advanced Fluorescence Reporters in Chemistry and Biology I Fundamentals and Molecular Design* Springer Series on Fluorescence vol 8, ed A P Demchenko (Berlin, Heidelberg: Springer) pp 3–24

[89]   Hamatasu Photonics 2007 Basic Principles of Photomultiplier Tubes *Photomultiplier Tubes Basics and Applications* (Hamatsu) pp 27–34

[90]   Everett A J 1981 General Considerations on UV-visible spectrometry *Standards in Absorption Spectrometry* ed C Burgess and A Knowles (Chapman and Hall) pp 1–16

[91]   Desjardins P, Hansen J B and Allen M 2009 Microvolume protein concentration determination using the NanoDrop 2000c spectrophotometer. *J. Vis. Exp.* 3–5

[92]   Menges F 2014 Spekwin32 - optical spectroscopy software

[93]   Allen D W 2007 Holmium oxide glass wavelength standards *J. Res. Natl. Inst. Stand. Technol.* **112** 303

[94]   Weidner V R, Barnes P Y and Eckerle K L 1986 a Wavelength Standard for the Near Infrared Based on the Reflectance of Rare-Earth Oxides *J. Res. Natl. Bur. Stand. (1934).* **91** 243

[95]   Buist G J 1981 Wavelength Calibration *Standards in Absorption Spectrometry* ed C Burgess and A Knowles (Chapman and Hall) pp 111–20

[96]   Burgess C and Knowles A 1981 Recommended Procedures for Standardisation *Standards in Absorption Spectrometry1* ed C Bergess and A Knowless (Chapman and Hall) pp 130–6

[97]   ASTM International 2001 Standard Practice for Describing and Measuring Performance of Ultraviolet , *Annual Book of ASTM Standards* vol 03 (Pennsylvania) pp 1–10

[98]   McNeirney J and Slavin W 1962 A Wavelength Standard for Ultraviolet-Visible-Near Infrared Spectrophotometry *Appl. Opt.* **1** 365

[99]   Burke R W and Mavrodineanu R 1976 Acidic potassium dichromate solutions as ultraviolet absorbance standards *J. Res. Natl. Bur. Stand. Sect. A Phys. Chem.* **80A** 631

[100]   Vinter E 1981 Liquid absorbance standards *Standards in Absorption Spectrometry* ed C Burgess and A Knowles (Chapman and Hall) pp 48–82

[101]   Goncalves M S T 2010 Optimised UV/Visible Fluorescent Markers *Advanced Fluorescence Reporters in Chemistry and Biology I Fundamentals and Molecular Design* Springer Series on Fluorescence vol 8, ed A P Demchenko (Berlin, Heidelberg: Springer) pp 27–64

[102]   The Cell Working Party 1981 Tests of Cell Performance *Standards in Absorption Spectrometry* ed C Burgess and A Knowles (Chapman and Hall) pp 126–9

[103]   Perkin Elmer *UV WinLab Software User's Guide* (Perkin Elmer)

[104]   The Cell Working Party 1981 Cell Design and Construction *Standards in Absorption Spectrometry* ed C Burgess and A Knowles (Chapman and Hall) pp 17–41

[105]   Thompson R B 2002 Red and Near-Infrared Fluorometry *Topics in Fluorescence Spectroscopy Volume 4 Probe Design and Chemical Sensing* vol 4, ed J R Lakowicz (New York, Boston, Dordrect, London, Moscow: Kluwer Academic Publishers) pp 151–81

[106]   Carr B and Wright M 2013 *Nanoparticle tracking analysis—a review of applications and usage 2010–2012* (Nanosight)

[107]   Hole P, Sillence K, Hannell C, Maguire C M, Roesslein M, Suarez G, Capracotta S, Magdolenova Z, Horev-Azaria L, Dybowska A, Cooke L, Haase A, Contal S, Man?? S, Vennemann A, Sauvain J J, Staunton K C, Anguissola S, Luch A, Dusinska M, Korenstein R, Gutleb A C, Wiemann M, Prina-Mello A, Riediker M and Wick P 2013 Interlaboratory comparison of size measurements on nanoparticles using nanoparticle tracking analysis (NTA) *J. Nanoparticle Res.* **15**

[108]   Li Y, Yang G and Mei Z 2012 Spectroscopic and dynamic light scattering studies of the interaction between pterodontic acid and bovine serum albumin *Acta Pharm. Sin. B* **2** 53–9

[109]   Curiel D, Hayes E J and Beer P D 2005 Fluorescent Anion Complexation Agents *Topics in Fluorescence Spectroscopy Volume 9 Advanced Concepts in Fluorescence*

Sensing Part A: Small Molecule Sensing vol 9, ed C D Geddes and J R Lakowicz (New York: Springer) pp 59–118

[110] Zhao H, Mayer M L and Schuck P 2014 Analysis of Protein Interactions with Picomolar Binding A ffi nity by Fluorescence-Detected Sedimentation Velocity

[111] Johnson A R, Lee S J, Klein J and Kanicki J 2007 Absolute photoluminescence quantum efficiency measurement of light-emitting thin films *Rev. Sci. Instrum.* **78** 2007–9

[112] Gilmore A M A 2014 How to Collect National Institute of Standards and Technology (NIST) Traceable Fluorescence Excitation and Emission Spectra *Methods in Molecular Biology 1076 Fluorescence Spectroscopy and Microscopy Methods and Protocols* Methods in Molecular Biology vol 1076, ed Y Engelborghs and A J W G Visser (Totowa, NJ: Humana Press) pp 3–27

[113] Anon 1994 Light Sources *Guide for Spectroscopy* (Instruments S.A. Group Jobin Yvon Spex) pp 1–30

[114] Miller J N 1981 Monochromator Wavelength Calibration *Standards in Fluorescence Spectrometry Ultraviolet Spectrometry Group* ed J N Miller (Chapman and Hall) pp 8–14

[115] DeRose P C, Early E a. and Kramer G W 2007 Qualification of a fluorescence spectrometer for measuring true fluorescence spectra *Rev. Sci. Instrum.* **78**

[116] Sadler D a., Littlejohn D and Perkins C V. 1995 Automatic wavelength calibration procedure for use with an optical spectrometer and array detector *J. Anal. At. Spectrom.* **10** 253

[117] Miller J N 1981 Criteria for Fluorescence Spectrometer Sensitivity *Standards in Fluorescence Spectrometry Ultraviolet Spectrometry Group* ed J N Miller (Chapman and Hall) pp 20–6

[118] Lawaetz A J and Stedmon C A 2008 Fluorescence Intensity Calibration Using the Raman Scatter Peak of Water Fluorescence Intensity Calibration Using the Raman Scatter Peak of Water

[119] Matthews B J H, Jones a. C, Theodorou N K and Tudhope a. W 1996 Excitation-emission-matrix fluorescence spectroscopy applied to humic acid bands in coral reefs *Mar. Chem.* **55** 317–32

[120] Einhorn H D and Naudé D E H 1963 Stray Light in a Monochromator (Analysis and Prediction Based on Measurements by Means of Discharge Lamps and Filters) *J. Opt. Soc. Am.* **53** 721

[121] Barlier-Salsi A 2014 Stray light correction on array spectroradiometers for optical radiation risk assessment in the workplace *J. Radiol. Prot.* **34** 915–30

[122] Zong Y, Brown S W, Johnson B C, Lykke K R and Ohno Y 2006 Simple spectral stray light correction method for array spectroradiometers. *Appl. Opt.* **45** 1111–9

[123] Miller J N 1981 Stray Light in Fluorescence Spectrometers *Standards in Fluorescence Spectrometry Ultraviolet Spectrometry Group* (Chapman and Hall) pp 15–9

[124] Conmy R N, Coble P G and Del Castillo C E 2004 Calibration and performance of a new in situ multi-channel fluorometer for measurement of colored dissolved organic matter in the ocean *Cont. Shelf Res.* **24** 431–42

[125] Valeur B 2001 Principles of steady-state and time-resolved fluorometric techniques *Molecular Fluorescence: Principles and Applications* vol 8, ed B Valeur (Wiley-VCH) pp 155–99

[126] Birks J B 1976 Fluorescence quantum yield measurements *J. Res. Natl. Bur. Stand. Sect. A Phys. Chem.* **80A** 389

[127] Melhuish W H 1975 Modified technique for determining the wavelength-sensitivity curve of a spectrofluorimeter. *Appl. Opt.* **14** 26–7

[128] Eaton D F 1988 Reference Materials for Fluorescence Measurement *Pure Appl. Chem.* **60** 1107–14

[129] Nothnagel E A 1987 Quantum counter for correcting fluorescence excitation spectra at 320- to 800-nm wavelengths *Anal. Biochem.* **163** 224–37

[130] Melhuish W H 1962 Calibration of Spectrofluorimeters for Measuring Corrected Emission Spectra *J. Opt. Soc. Am.* **52** 1256

[131] Stair R and Smith W O 1943 A tungsten-in-quartz lamp and its applications in photoelectric radiometry *J. Res. Natl. Bur. Stand. (1934).* **30** 449

[132] Kosch M J, Sigernes F, Harang O, Systems C and Sciences P Absolute optical calibration using a simple tungsten light bulb: experiment **2** 50–4

[133] Derose P C, Gaigalas L W A K, Gaigalas A K, Kramer G W, Resch-genger U and Panne U 2008 Need for and Metrological Approaches Towards Standardization of Fluorescence Measurements from the View of National Metrology Institutes Fluorescence Standards : *Standardization and Quality Assurance in Fluorescence Measurements I* vol 5, ed U Resch-Genger (Springer) pp 33–62

[134] Ball C P, Levick A P, Woolliams E R, Green P D, Dury M R, Winkler R, Deadman A J, Fox N P and King M D 2013 Effect of polytetrafluoroethylene (PTFE) phase transition at 19°C on the use of Spectralon as a reference standard for reflectance. *Appl. Opt.* **52** 4806–12

[135] Stiegman A E, Bruegge C J and Springsteen A W 1993 Ultraviolet stability and contamination analysis of Spectralon diffuse reflectance material **32** 799–804

[136] Bruegge C J, Stiegman A E, Rainen R a. and Springsteen A W 1993 Use of Spectralon as a diffuse reflectance standard for in-flight calibration of earth-orbiting sensors **32** 805–14

[137] Hamamatsu Photonics 2007 *Photomultiplier Tubes Basics and Applications* (Hamatsu)

[138] DeRose P C, Smith M V., Mielenz K D, Blackburn D H and Kramer G W 2009 Characterization of Standard Reference Material 2940, Mn-ion-doped glass, spectral correction standard for fluorescence *J. Lumin.* **129** 349–55

[139] DeRose P C, Smith M V., Mielenz K D, Blackburn, Douglas H and Kramer G W 2008 Characterization of standard reference material 2941, uranyl-ion-doped glass, spectral correction standard for fluorescence *J. Lumin.* **128** 257–66

[140] Derose P C, Smith M V., Mielenz K D, Anderson J R and Kramer G W 2011 Characterization of Standard Reference Material 2942, Ce-ion-doped glass, spectral correction standard for UV fluorescence *J. Lumin.* **131** 1294–9

[141] Derose P C, Smith M V., Mielenz K D, Anderson J R and Kramer G W 2011 Characterization of Standard Reference Material 2943, Cu-ion-doped glass, spectral

correction standard for blue fluorescence *J. Lumin.* **131** 2509–14

[142] DeRose P C, Smith M V., Anderson J R and Kramer G W 2013 Characterization of standard reference material 2944, Bi-ion-doped glass, spectral correction standard for red fluorescence *J. Lumin.* **141** 9–14

[143] Goosh & Housego 2015 G&H OL 200, 220, 245 – Spectral irradiance standard 1000W, 200W, 45W

[144] NIST 2012 Relative Intensity Correction Standards for Fluorescence and Raman Spectroscopy

[145] Kessel D 1991 Artifacts in fluorescence emission spectroscopy related to Wood's anomaly. *Photochem. Photobiol.* **54** 481–3

[146] Maystre D 2012 Theory of Wood's Anomalies *Plasmonics* vol 167 pp 39–83

[147] Lawaetz a. J and Stedmon C a. 2009 Fluorescence intensity calibration using the Raman scatter peak of water *Appl. Spectrosc.* **63** 936–40

[148] Mostofa K M G, Liu C, Yoshioka T, Vione D, Zhang Y and Sakugawa H 2013 Fluorescence Dissolved Organic Matter in Natural Waters *Photobiogeochemistry of Organic Matter: Principles and Practices in Water Environments* ed K M Mostofa, T Yoshioka, M A Mottaleb and D Vione (Springer) pp 429–560

[149] Murphy K R, Butler K D, Spencer R G M, Stedmon C a, Boehme J R and Aiken G R 2010 Measurement of Dissolved Organic Matter Fluorescence in Aquatic Environments: An Interlaboratory Comparison RID B-8217-2009 RID B-5841-2008 *Environ. Sci. Technol.* **44** 9405–12

[150] Mccreery R L, Chalmers J M and Editors P R G 2002 Photometric Standards for Raman Spectroscopy Photometric Standards for Raman Spectroscopy *Handb. Vib. Spectrosc.* 1–14

[151] Anon 1994 Detectors *Guide for Spectroscopy* (Instruments S.A. Group Jobin Yvon Spex) pp 181–236

[152] Birch D J S and Hungerford G 2002 Instrumentation for Red / Near-Infrared Fluorescence *Topics in Fluorescence Spectroscopy Volume 4 Probe Design and Chemical Sensing* vol 4, ed J R Lakowicz (New York, Boston, Dordrect, London, Moscow: Kluwer Academic Publishers) pp 377–416

[153] Patra D and Barakat C 2011 Synchronous fluorescence spectroscopic study of solvatochromic curcumin dye. *Spectrochim. Acta. A. Mol. Biomol. Spectrosc.* **79** 1034–41

[154] Dankowska a., Małecka M and Kowalewski W 2013 Discrimination of edible olive oils by means of synchronous fluorescence spectroscopy with multivariate data analysis *Grasas y Aceites* **64** 425–31

[155] Rei A, Ferreira M I C and Hungerford G 2008 Nile red synchronous scan fluorescence spectroscopy to follow matrix modification in sol-gel derived media and its effect on the peroxidase activity of cytochrome c. *J. Fluoresc.* **18** 1083–91

[156] Spectrometry L and Vo-dinh T 1978 Multicomponent Analysis by Synchronous Spectrometry *Anal. Chem.* **50** 396–401

[157] Anon 1994 Monochromators *Guide for Spectroscopy* (Instruments S.A. Group Jobin Yvon Spex) pp 31–172

[158] Bahram M, Bro R, Stedmon C, Afkhami A and Roskilde D- 2007 Handling of

Rayleigh and Raman scatter for PARAFAC modeling of fluorescence data using interpolation

[159] The Cell Working Party 1981 Cell Handling *Standards in Absorption Spectrometry* ed C Burgess and A Knowles (Chapman and Hall) pp 121–5

[160] MacDonald B C, Lvin S J and Patterson H 1997 Correction of fluorescence inner filter effects and the partitioning of pyrene to dissolved organic carbon *Anal. Chim. Acta* **338** 155–62

[161] Borissevitch I E 1999 More about the inner filter effect: Corrections of Stern-Volmer fluorescence quenching constants are necessary at very low optical absorption of the quencher *J. Lumin.* **81** 219–24

[162] Luciani X, Mounier S, Redon R and Bois A 2009 A simple correction method of inner filter effects affecting FEEM and its application to the PARAFAC decomposition *Chemom. Intell. Lab. Syst.* **96** 227–38

[163] Gilmore A, Hurteaux R, FitzGerald S and Knowles A 2012 Moving towards a technical specification for fluorescence excitation-emission mapping and absorbance analysis of colored dissolved organic matter *WIT Trans. Ecol. Environ.* **160** 295–306

[164] Christmann D R, Crouch S R and Timnick A 1981 Automated instrument for absorption-corrected molecular fluorescence measurements by the cell shift method *Anal. Chem.* **53** 276–80

[165] Larsson T, Wedborg M and Turner D 2007 Correction of inner-filter effect in fluorescence excitation-emission matrix spectrometry using Raman scatter *Anal. Chim. Acta* **583** 357–63

[166] Bro R and Gallagher N B PARAFAC for Analysis of Fluorescence EEM Data 1–2

[167] Murphy K R, Stedmon C a., Graeber D and Bro R 2013 Fluorescence spectroscopy and multi-way techniques. PARAFAC *Anal. Methods* **5** 6557

[168] Cui H, Shi J, Qiu L, Zhao Y, Wei Z, Wang X, Jia L and Li J 2016 Characterization of chromophoric dissolved organic matter and relationships among PARAFAC components and water quality parameters in Heilongjiang, China *Environ. Sci. Pollut. Res.*

[169] Lester Y, Ferrer I, Thurman E M, Sitterley K a, Korak J a, Aiken G and Linden K G 2015 Characterization of hydraulic fracturing flowback water in Colorado: Implications for water treatment. *Sci. Total Environ.* **512-513** 637–44

[170] Lloyd J B F 1981 Inner filter Effects, Sample Cells and their Geometry in Fluorescence Spectrometry *Standards in Fluorescence Spectrometry Ultraviolet Spectrometry Group* ed J N Miller (Chapman and Hall) pp 27–43

[171] Lakowicz J R 2006 Fluorescence Anisotropy *Principles of Fluorescence Spectroscopy* vol 64, ed J R Lakowicz (New York: Springer) pp 353–82

[172] Steiner R F 2002 Fluorescence Anisotropy: Theory and Applications *Topics in Fluorescence Spectroscopy Volume 2 Principles* vol 2, ed J R Lakowicz (New York, Boston, Dordrect, London, Moscow: Kluwer Academic Publishers) pp 1–52

[173] Becker W 2005 Practice of TCSPC Experiments *Advanced Time-Correlated Single photon Counting* (Springer)

[174] Roberts G C K 1981 Correction of Excitation and Emission Spectra *Standards in*

Fluorescence Spectrometry Ultraviolet Spectrometry Group ed J N Miller (Chapman and Hall) pp 49–67

[175] Ghosh S, Saha S, Goswami D, Bilgrami S and Mayor S 2012 *Dynamic imaging of homo-FRET in live cells by fluorescence anisotropy microscopy* vol 505 (Elsevier Inc.)

[176] Groza R C, Li B and Ryder A G 2015 Anisotropy resolved multidimensional emission spectroscopy (ARMES): A new tool for protein analysis *Anal. Chim. Acta* **886** 133–42

[177] Groza R C, Calvet A and Ryder A G 2014 A fluorescence anisotropy method for measuring protein concentration in complex cell culture media *Anal. Chim. Acta* **821** 54–61

[178] Szmacinski H and Lakowicz J R 2002 Lifetime-Based Sensing *Topics in Fluorescence Spectroscopy Volume 4 Probe Design and Chemical Sensing* vol 4, ed J R Lakowicz (New York, Boston, Dordrect, London, Moscow: Kluwer Academic Publishers) pp 295–334

[179] O'Hagan W J, McKenna M, Sherrington D C, Rolinski O J and Birch D J S 2002 MHz LED source for nanosecond fluorescence sensing *Meas. Sci. Technol.* **13** 84–91

[180] G J-C, Bunzil G and Eliseeva S V 2011 Basics of Lanthanide Photophysics *Lanthanide Luminescence Photophysical, Analytical and Biological Aspects* vol 7, ed P Hanninen and H Harma (Springer)

[181] Tanaka F and Yamashita S 1984 Luminescence Lifetimes of Aqueous Europium Chloride, Nitrate, Sulfate, and Perchlorate Solutions. Studies on the Nature of the Inner Coordination Sphere of the Europium(III) Ion *Inorg. Chem.* **23** 2044–6

[182] Jinno M, Kurokawa H, Aono M and Ninomiya H 2000 The afterglow characteristics of xenon pulsed plasma for mercury-free fluorescent lamps *Czechoslov. J. Phys.* **50** 433–6

[183] Becker W 2005 Overview of Photon Counting Techniques *Advanced Time-Correlated Single photon Counting* (Springer)

[184] Lakowicz J R 2006 Time-Domain Lifetime Measurements *Principles of Fluorescence Spectroscopy* ed J R Lakowicz (New York: Springer) pp 97–155

[185] O'Connor D V. and Phillips D 1984 Electronics *Time-Correlated Single Photon Counting* (London: Academic Press) pp 132–57

[186] Hamatasu Photonics 2007 Characteristics of Photomultiplier Tubes *Photomultiplier Tubes Basics and Applications* (Hamatsu) pp 43–96

[187] Hamatasu Photonics 2007 MCP-PMT *Photomultiplier Tubes Basics and Applications* (Hamatsu) pp 201–22

[188] Becker W 2005 Detectors for Photon Counting *Advanced Time-Correlated Single photon Counting* (Springer)

[189] Gmür A 2013 *Photomultiplier Tube Tests in Liquid Xenon for Direct Dark Matter Detection Experiments* (Swizz University Zurich)

[190] Akgun U, Ayan A S, Aydin G, Duru F, Olson J and Onel Y 2008 Afterpulse timing and rate investigation of three different Hamamatsu Photomultiplier Tubes *J. Instrum.* **3** T01001

[191] Small E W 2002 Laser Sources and Microchannel Plate Detectors for Pulse Fluorometry *Topics in Fluorescence Spectroscopy Volume 1 Techniques* Topics in Fluorescence Spectroscopy vol 1, ed J R Lakowicz (New York, Boston, Dordrect, London, Moscow: Kluwer Academic Publishers) pp 97–182

[192] Straume M, Frasier-cadoret S G and Johnson M L 2002 Least-Squares Analysis of Fluorescence Data *Topics in Fluorescence Spectroscopy Volume 2 Principles* vol 2, ed J R Lakowicz (New York, Boston, Dordrect, London, Moscow: Kluwer Academic Publishers) pp 177–240

[193] Kierdaszuk B 2010 From discrete multi-exponential model to lifetime distribution model and power law fluorescence decay function *Spectroscopy* **24** 399–407

[194] Večeř J, Kowalczyk a. a., Davenport L and Dale R E 1993 Reconvolution analysis in time-resolved fluorescence experiments—an alternative approach: Reference-to-excitation-to-fluorescence reconvolution *Rev. Sci. Instrum.* **64** 3413

[195] O'Connor D V. and Phillips D 1984 Data Analysis *Time-Correlated Single Photon Counting* vol 1 (London: Academic Press) pp 158–210

[196] Lakowicz J 2000 On Spectral Relaxation in Proteins†¶‖ *Photochem. Photobiol.* **72** 421–37

[197] Boens N, Ameloot M and Valeur B 2008 Practical Time-Resolved Fluorescence Spectroscopy: Avoiding Artifacts and Using Lifetime Standards *Standardization and Quality Assurance in Fluorescence Measurements I* vol 5, ed U Resch-Genger (Springer) pp 215–32

[198] Rolinski O J, Martin A and Birch D J S 2008 Human serum albumin and quercetin interactions monitored by time-resolved fluorescence: evidence for enhanced discrete rotamer conformations. *J. Biomed. Opt.* **12** 034013

[199] Rolinski O J, Martin A and Birch D J S 2008 Human serum albumin-flavonoid interactions monitored by means of tryptophan kinetics. *Ann. N. Y. Acad. Sci.* **1130** 314–9

[200] McLoskey D, Birch D J S, Sanderson A, Suhling K, Welch E and Hicks P J 1996 Multiplexed single-photon counting. I. A time-correlated fluorescence lifetime camera *Rev. Sci. Instrum.* **67** 2228

[201] Birch D J S, McLoskey D, Sanderson a., Suhling K and Holmes a. S 1994 Multiplexed time-correlated single-photon counting *J. Fluoresc.* **4** 91–102

[202] Valeur B 2001 Fluorescence polarization. Emission anisotropy *Molecular Fluorescence: Principles and Applications* vol 8, ed B Valeur (Wiley-VCH) pp 125–54

[203] Kawski A 1993 Fluorescence Anisotropy: Theory and Applications of Rotational Depolarization *Crit. Rev. Anal. Chem.* **23** 459–529

[204] Szabo A 1984 Theory of fluorescence depolarization in macromolecules and membranes *J. Chem. Phys.* **81** 150

[205] Anon 2005 2.2.3 Viscosities *Kaye & Laby Tables of Physical & Chemical Contents* (National Physical Laboratory)

[206] Yang C, Ma P, Jing F and Tang D 2003 Excess Molar Volumes , Viscosities , and Heat Capacities for the Mixtures of Ethylene Glycol + Water from 273 . 15 K to 353 . 15 K 836–40

[207] Ge M, Ma J and Chu B 2010 Densities and Viscosities of Propane-1,2,3-triol + Ethane-1,2-diol at T = (298.15 to 338.15) K *J. Chem. Eng. Data* **55** 2649–51

[208] Karolin J and Geddes C D 2015 Silica nanoparticle metrology using Ursa Blue™ and colloidal Ludox solutions *Dye. Pigment.* **112** 50–3

[209] Smith T a and Ghiggino K P 2015 A review of the analysis of complex time-resolved fluorescence anisotropy data *Methods Appl. Fluoresc.* **3** 022001

[210] Glycerin Producers' Association 1963 *Physical Properties of Glycerine and Its Solutions*

[211] Anfinrud P a, Hart D E, Hedstrom J F and Struve W S 1986 Fluorescence depolarization of rhodamine 6G in glycerol: A photon-counting test of three-dimensional excitation transport theory *J.Phys.Chem.* **90** 2374–9

[212] Strickler S J and Berg R a. 1962 Relationship between Absorption Intensity and Fluorescence Lifetime of Molecules *J. Chem. Phys.* **37** 814

[213] Hungerford G, Allison A, McLoskey D, Kuimova M K, Yahioglu G and Suhling K 2009 Monitoring sol-to-gel transitions via fluorescence lifetime determination using viscosity sensitive fluorescent probes. *J. Phys. Chem. B* **113** 12067–74

[214] Sørensen T J, Thyrhaug E, Szabelski M, Luchowski R, Gryczynski I, Gryczynski Z and Laursen B W 2013 Azadioxatriangulenium (ADOTA(+)): A long fluorescence lifetime fluorophore for large biomolecule binding assay. *Methods Appl. Fluoresc.* **1** 25001

[215] Lettinga M P, Van Kats C M and Philipse A P 2000 Rotational diffusion of tracer spheres in packings and dispersions of colloidal spheres studied with time-resolved phosphorescence anisotropy *Langmuir* **16** 6166–72

[216] Lettinga P 1999 *Phosphorescence spectroscopy and its application to the study of colloidal dynamics* (Utrecht University)

[217] Excitation T, Johnson C K and Wan C 2002 Anisotropy Decays Induced by Two-Photon Excitation *Topics in Fluorescence Spectroscopy Volume 5 Nonlinear and Two-Photon-Induced Fluorescence* vol 5, ed J R Lakowicz (New York, Boston, Dordrect, London, Moscow: Kluwer Academic Publishers) pp 43–85

[218] Garcia Sanchez F, Navas Diaz a., Carnero Ruiz C and Lopez Guerrero M M 2010 Fluid viscosity determination based on frequency domain time-resolved fluorescence anisotropy *J. Mol. Liq.* **155** 121–6

[219] Pramanik R, Kumar Das P and Bagchi S 2000 Fluorescence anisotropy of ketocyanine dyes in homogeneous and heterogeneous media. Estimation of micellar microviscosity *Phys. Chem. Chem. Phys.* **2** 4307–11

[220] Khara D C and Samanta A 2010 Rotational dynamics of positively and negatively charged solutes in ionic liquid and viscous molecular solvent studied by time-resolved fluorescence anisotropy measurements. *Phys. Chem. Chem. Phys.* **12** 7671–7

[221] Kostamovaara J, Tenhunen J, Kögler M, Nissinen I, Nissinen J and Keränen P 2013 Fluorescence suppression in Raman spectroscopy using a time-gated CMOS SPAD. *Opt. Express* **21** 31632–45

[222] Lemos M, Sárniková K, Bot F, Anese M and Hungerford G 2015 Use of Time-Resolved Fluorescence to Monitor Bioactive Compounds in Plant Based Foodstuffs *Biosensors* **5** 367–97

[223] Barakat C and Patra D 2013 Combining time-resolved fluorescence with synchronous fluorescence spectroscopy to study bovine serum albumin-curcumin complex during unfolding and refolding processes *Luminescence* **28** 149–55

[224] Kumaran R and Ramamurthy P 2011 Denaturation mechanism of BSA by urea derivatives: evidence for hydrogen-bonding mode from fluorescence tools. *J. Fluoresc.* **21** 1499–508

[225] Albani J R 2009 Fluorescence lifetimes of tryptophan: structural origin and relation with So --> 1Lb and So --> 1La transitions. *J. Fluoresc.* **19** 1061–71

[226] Albani J R 2011 Relation between proteins tertiary structure, tryptophan fluorescence lifetimes and tryptophan S(o)→(1)L(b) and S(o)→(1)L(a) transitions. Studies on α1-acid glycoprotein and β-lactoglobulin. *J. Fluoresc.* **21** 1301–9

[227] Moriyama Y, Ohta D, Hachiya K, Mitsui Y and Takeda K 1996 Fluorescence behavior of tryptophan residues of bovine and human serum albumins in ionic surfactant solutions: A comparative study of the two and one tryptophan(s) of bovine and human albumins *J. Protein Chem.* **15** 265–72

[228] Hungerford G, Kulwinder S and McLoskey D 2014 Time Domain Luminescence Instrumentation *Luminescence The Instrumental Key to the Future of Nanotechnology* ed A M Gilmore (Pan Stanford Publishing) pp 203–28

[229] Tokunaga J 1975 Oxygen, Nitrogen, and Carbon Dioxide in Aqueous *J. Chem Engin Data* **20** 41–6

[230] Wollman A J M, Nudd R, Hedlund E G and Leake M C 2015 From Animaculum to single molecules: 300 years of the light microscope *Open Biol.* **5** 150019–150019

[231] Thompson R B 2002 Fluorescence- Based Fiber-Optic Sensors *Topics in Fluorescence Spectroscopy Volume 2 Principles* vol 2, ed J R Lakowicz (New York, Boston, Dordrect, London, Moscow: Kluwer Academic Publishers) pp 345–65

[232] Gerritsen H C, Draaijer A, Heuvel D J Van Den and Agronskaia A V 2006 Fluorescence Lifetime Imaging in Scanning Microscopy *Handbook of Biological Confocal Microscopy* ed J B Pawley (Springer) pp 516–34

[233] Centonze V and Pawley J B 2006 Tutorial on Practical Confocal Microscopy and Use of the Confocal Test Specimen *Handbook of Biological Confocal Microscopy* ed J B Pawley (Springer) pp 627–49

[234] Ulbrich M H 2015 Counting Molecules: Towards Quantitative Imaging *Springer Series on Fluorescence* Springer Series on Fluorescence vol 14, ed P Tinnefeld, C Eggeling and S W Hell (Berlin, Heidelberg: Springer Berlin Heidelberg) pp 263–91

[235] Pawley J B 2006 Points , Pixels , and Gray Levels : Digitizing Image Data *Handbook of Biological Confocal Microscopy* ed J B Pawley (Springer) pp 59–79

[236] Inoué S 2006 Foundations of Confocal Scanned Imaging in Light Microscopy *Handbook of Biological Confocal Microscopy* ed J B Pawley (Springer) pp 1–19

[237] White R A, Kutz K J and Wampler J E 2002 Fundamentals of Fluorescence Microscopy *Topics in Fluorescence Spectroscopy Volume 1 Techniques* vol 1, ed J R Lakowicz (New York, Boston, Dordrect, London, Moscow: Kluwer Academic Publishers) pp 379–410

[238] Shroff H, Galbraith C G, Galbraith J a, White H, Gillette J, Olenych S, Davidson M W and Betzig E 2007 Dual-color superresolution imaging of genetically expressed probes within individual adhesion complexes *Proc. Natl. Acad. Sci.* **104** 20308–13

[239] Wu Y, Stefl M, Olzyńska A, Hof M, Yahioglu G, Yip P, Casey D R, Ces O, Humpolíčková J and Kuimova M K 2013 Molecular rheometry: direct determination of viscosity in Lo and Ld lipid phases via fluorescence lifetime imaging. *Phys. Chem. Chem. Phys.* **15** 14986–93

[240] Wu Y, Stefl M, Olzyńska A, Hof M, Yahioglu G, Yip P, Casey D R, Ces O, Humpolíčková J and Kuimova M K 2013 Supporting Information Molecular rheometry: direct determination of viscosity in Lo and Ld lipid phases via fluorescence lifetime imaging. *Phys. Chem. Chem. Phys.* **15** 14986–93

[241] Thompson N L 2002 Fluorescence Correlation Spectroscopy *Topics in Fluorescence Spectroscopy Volume 1 Techniques* Topics in Fluorescence Spectroscopy vol 1, ed J R Lakowicz (New York, Boston, Dordrect, London, Moscow: Kluwer Academic Publishers) pp 337–78

[242] Schmidt T, Schotz G J and Schutz G J 2009 Single-Molecule Analysis of Biomembranes *Handbook of Single-Molecule Biophysics* ed P Hinterdorfer and A Van Oijen (Springer) pp 19–42

[243] Visser N V, Hink M A, Hoek A Van and Visser A J W G 1999 Comparison Between Fluorescence Correlation Spectroscopy and Time-Resolved Fluorescence Anisotropy as Illustrated with a Fluorescent Dextran Conjugate **9** 251–5

[244] Bates M, Huang B, Dempsey G T and Zhuang X 2007 Multicolor super-resolution imaging with photo-switchable fluorescent probes. *Science (80-.).* **317** 1749–53

[245] Schermelleh L, Heintzmann R and Leonhardt H 2010 A guide to super-resolution fluorescence microscopy *J. Cell Biol.* **190** 165–75

[246] Betzig E 1995 Proposed method for molecular optical imaging. *Opt. Lett.* **20** 237–9

[247] Demchenko A 2009 Sensing Inside Living Cells and Tissues *Introduction to Fluorescence Sensing* (Springer) pp 455–506

[248] Kaminski Schierle G S, Van De Linde S, Erdelyi M, Esbjörner E K, Klein T, Rees E, Bertoncini C W, Dobson C M, Sauer M and Kaminski C F 2011 In situ measurements of the formation and morphology of intracellular β-amyloid fibrils by super-resolution fluorescence imaging *J. Am. Chem. Soc.* **133** 12902–5

[249] Jost A and Heintzmann R 2013 Superresolution Multidimensional Imaging with Structured Illumination Microscopy *Annu. Rev. Mater. Res.* **43** 261–82

[250] Creath K and Wyant J 1992 Optical Metrology of Diffuse Surfaces *Optical shop testing* ed D Malacara (John Wiley & Sons Inc.) pp 756–807

[251] Qian J, Lei M, Dan D, Yao B, Zhou X, Yang Y, Yan S, Min J and Yu X 2015 Full-color structured illumination optical sectioning microscopy. *Sci. Rep.* **5** 14513

[252] Gustafsson M G 2000 Surpassing the lateral resolution limit by a factor of two using structured illumination microscopy. *J. Microsc.* **198** 82–7

[253] Rego E H, Shao L, Macklin J J, Winoto L, Johansson G a., Kamps-Hughes N, Davidson M W and Gustafsson M G L 2012 PNAS Plus: Nonlinear structured-illumination microscopy with a photoswitchable protein reveals cellular structures at 50-nm resolution *Proc. Natl. Acad. Sci.* **109** E135–43

[254] Neil M a, Juskaitis R and Wilson T 1997 Method of obtaining optical sectioning by using structured light in a conventional microscope. *Opt. Lett.* **22** 1905–7

[255] Gustafsson M G L 2005 Nonlinear structured-illumination microscopy: wide-field fluorescence imaging with theoretically unlimited resolution. *Proc. Natl. Acad. Sci. U. S. A.* **102** 13081–6

[256] Eggeling C and Hell S W 2015 STED Fluorescence Nanoscopy *Springer Series on Fluorescence Far-Field Optical nanoscopy* Springer Series on Fluorescence vol 14, ed P Tinnefeld, C Eggeling and S W Hell (Berlin, Heidelberg: Springer Berlin Heidelberg) pp 3–25

[257] Huang B, Bates M and Zhuang X 2010 Super resolution fluorescence microscopy *Annu. Rev. Biochem.* **78** 993–1016

[258] Betzig E 2005 Sparse and composite coherent lattices *Phys. Rev. A - At. Mol. Opt. Phys.* **71** 3–7

[259] Betzig E 2005 Excitation strategies for optical lattice microscopy. *Opt. Express* **13** 3021–36

[260] Chozinski T J, Gagnon L A and Vaughan J C 2014 Twinkle, twinkle little star: Photoswitchable fluorophores for super-resolution imaging *FEBS Lett.* **588** 3603–12

[261] Fernández-Suárez M and Ting A Y 2008 Fluorescent probes for super-resolution imaging in living cells. *Nat. Rev. Mol. Cell Biol.* **9** 929–43

[262] Harke B, Keller J, Ullal C K, Westphal V, Schönle A and Hell S W 2008 Resolution scaling in STED microscopy. *Opt. Express* **16** 4154–62

[263] Hell S W, Dyba M and Jakobs S 2004 Concepts for nanoscale resolution in fluorescence microscopy *Curr. Opin. Neurobiol.* **14** 599–609

[264] Patterson G H 2002 A Photoactivatable GFP for Selective Photolabeling of Proteins and Cells *Science (80-.).* **297** 1873–7

[265] Couzin J 2003 New Optics Strategies Cut Through Diffraction Barrier NSF Wants PIs to Mentor Their Postdocs Do Gamma Ray Bursts Always Line Up With Galaxies ? *Science* **313**

[266] Betzig E, Patterson G H, Sougrat R, Lindwasser O W, Olenych S, Bonifacino J S, Davidson M W, Lippincott-Schwartz J and Hess H F 2006 Imaging intracellular fluorescent proteins at nanometer resolution. *Science* **313** 1642–5

[267] Nobelprize.org. 2014 The Nobel Prize in Chemistry 2014 *Nobel Media AB 2014. Web.*

[268] Sauer M 2015 A Practical Guide to dSTORM: Super-Resolution Imaging with Standard Fluorescence Probes *Springer Series on Fluorescence Far-Field Optical nanoscopy* Springer Series on Fluorescence vol 14, ed P Tinnefeld, C Eggeling and S W Hell (Berlin, Heidelberg: Springer Berlin Heidelberg) pp 65–84

[269] Xiao J 2009 Single-Molecule Imaging in Live Cells *Handbook of Single-Molecule Biophysics* ed P Hinterdorfer and A Van Oijen (Springer)

[270] Xu K, Shim S-H and Zhuang X 2015 Super-Resolution Imaging Through Stochastic Switching and Localization of Single Molecules: An overview *Springer Series on Fluorescence Far-Field Optical nanoscopy* Springer Series on Fluorescence vol 14, ed P Tinnefeld, C Eggeling and S W Hell (Berlin, Heidelberg: Springer Berlin Heidelberg) pp 27–64

[271] Thompson R E, Larson D R and Webb W W 2002 Precise nanometer localization

analysis for individual fluorescent probes. *Biophys. J.* **82** 2775–83

[272] Dertinger T, Xu J, Naini O F, Vogel R and Weiss S 2012 SOFI-based 3D superresolution sectioning with a widefield microscope. *Opt. nanoscopy* **1** 2

[273] Rees E J, Erdelyi M, Schierle G S K, Knight A and Kaminski C F 2013 Elements of image processing in localization microscopy *J. Opt.* **15** 094012

[274] Lew M D, Lee S F, Thompson M A, Lee H D and Moerner W E 2015 Single-Molecule Photocontrol and Nanoscopy *Springer Series on Fluorescence Far-Field Optical nanoscopy* Springer Series on Fluorescence vol 14, ed P Tinnefeld, C Eggeling and S W Hell (Berlin, Heidelberg: Springer Berlin Heidelberg) pp 87–110

[275] Aramendia P F and Bossi M L 2015 Probes for Nanoscopy: Photoswitchable Fluorophores *Springer Series on Fluorescence Far-Field Optical nanoscopy* Springer Series on Fluorescence vol 14, ed P Tinnefeld, C Eggeling and S W Hell (Berlin, Heidelberg: Springer Berlin Heidelberg) pp 189–2013

[276] Hernández I C, Buttafava M, Boso G, Diaspro A, Tosi A and Vicidomini G 2015 Gated STED microscopy with time-gated single-photon avalanche diode *Biomed. Opt. Express* **6** 2258

[277] Olivier N, Keller D, Rajan V S, Gönczy P and Manley S 2013 Simple buffers for 3D STORM microscopy. *Biomed. Opt. Express* **4** 885–99

[278] Heilemann M, Van De Linde S, Schüttpelz M, Kasper R, Seefeldt B, Mukherjee A, Tinnefeld P and Sauer M 2008 Subdiffraction-resolution fluorescence imaging with conventional fluorescent probes *Angew. Chemie - Int. Ed.* **47** 6172–6

[279] Michel C H, Kumar S, Pinotsi D, Tunnacliffe A, George-Hyslop P S, Mandelkow E, Mandelkow E M, Kaminski C F and Schierle G S K 2014 Extracellular monomeric tau protein is sufficient to initiate the spread of tau protein pathology *J. Biol. Chem.* **289** 956–67

[280] van de Linde S, Krstić I, Prisner T, Doose S, Heilemann M and Sauer M 2011 Photoinduced formation of reversible dye radicals and their impact on super-resolution imaging. *Photochem. Photobiol. Sci.* **10** 499–506

[281] Vogelsang J, Cordes T, Forthmann C, Steinhauer C and Tinnefeld P 2009 Controlling the fluorescence of ordinary oxazine dyes for single-molecule switching and superresolution microscopy. *Proc. Natl. Acad. Sci. U. S. A.* **106** 8107–12

[282] Webb D J and Brown C M 2013 Cell Imaging Techniques *Cell Imaging Techniques* vol 931, ed S Meding and A Walch (Springer) pp 29–57

[283] Metcalf D J, Edwards R, Kumarswami N and Knight A E 2013 Test samples for optimizing STORM super-resolution microscopy. *J. Vis. Exp.* 1–17

[284] Ströhl F and Kaminski C F 2015 A joint Richardson—Lucy deconvolution algorithm for the reconstruction of multifocal structured illumination microscopy data *Methods Appl. Fluoresc.* **3** 014002

[285] Lampe A, Haucke V, Sigrist S J, Heilemann M and Schmoranzer J 2012 Multi-colour direct STORM with red emitting carbocyanines *Biol. Cell* **104** 229–37

[286] Dempsey G T, Vaughan J C, Chen K H, Bates M and Zhuang X 2011 Evaluation of fluorophores for optimal performance in localization-based super-resolution imaging *Nat. Methods* **8** 1027–36

[287] Nakatani H, Haga M and Hiromi K 1974 Kinetic studies on binding of bovine serum

albumin with 1-anilino-8-naphthalene sulfonate *FEBS Lett.* **43** 293–6

[288] Takeda K and Yamamoto K 1990 Fluorescence lifetime and rotational correlation time of bovine serum albumin-sodium dodecyl sulfate complex labeled with 1-dimethylaminonaphthalene-5-sulfonyl chloride: effect of disulfide bridges in the protein on these fluorescence parameters. *J. Protein Chem.* **9** 17–22

[289] Gonza F L and Levi V 2003 Determination of the Molecular Size of BSA by Fluorescence Anisotropy * **31** 319–22

[290] Hungerford G, Benesch J, Mano J F and Reis R L 2007 Effect of the labelling ratio on the photophysics of fluorescein isothiocyanate (FITC) conjugated to bovine serum albumin. *Photochem. Photobiol. Sci.* **6** 152–8

[291] Thompson R B 2005 Protein-based Biosensors with Polarization Transduction *Topics in Fluorescence Spectroscopy Volume 10 Advanced Concepts in Fluorescence Sensing Part B: Macromolecular Sensing* vol 10, ed C D Geddes and J R Lakowicz (New York: Springer) pp 1–19

[292] GE Healthcare *Gel filtration principles and methods*

[293] Chiu K, Agoubi L L, Lee I, Limpar M T, Lowe J W and Goh S L 2010 Effects of Polymer Molecular Weight on the Size, Activity, and Stability of PEG-Functionalized Trypsin *Biomacromolecules* **11** 3688–92

[294] James N G and Jameson D M 2014 Steady-State Fluorescence Polarization/Anisotropy for the Study of Protein Interactions *Fluorescence Spectroscopy and Microscopy: Methods and Protocols* Methods in Molecular Biology vol 1076, ed Y Engelborghs and A J W G Visser (Totowa, NJ: Humana Press) pp 29–42

[295] Grace Davison 2011 *Ludox® SM-30 Colloidal Silica Product Information*

[296] Grace Davison 2010 *Ludox® AM Colloidal Silica Product Information*

[297] Grace Davison 2010 *Ludox® AS-40 Colloidal Silica Product Information*

[298] Apperson K, Karolin J, Martin R W and Birch D J S 2009 Nanoparticle metrology standards based on the time-resolved fluorescence anisotropy of silica colloids *Meas. Sci. Technol.* **20** 025310

[299] Apperson K 2003 *A Fluorescence Study of Beer* (University of Strathclyde)

[300] Green D L, Lin J S, Lam Y-F, Hu M Z-C, Schaefer D W and Harris M T 2003 Size, volume fraction, and nucleation of Stober silica nanoparticles *J. Colloid Interface Sci.* **266** 346–58

[301] Rahman I a., Vejayakumaran P, Sipaut C S, Ismail J, Bakar M A, Adnan R and Chee C K 2007 An optimized sol–gel synthesis of stable primary equivalent silica particles *Colloids Surfaces A Physicochem. Eng. Asp.* **294** 102–10

[302] Liang S, John C L, Xu S, Chen J, Jin Y, Yuan Q, Tan W and Zhao J X 2010 Silica-Based Nanoparticles: Design and Properties *Advanced Fluorescence Reporters in Chemistry and Biology II Molecular Constructions, Polymers and Nanoparticles* Springer Series on Fluorescence vol 9, ed A P Demchenko (Berlin, Heidelberg: Springer Berlin Heidelberg) pp 229–51

[303] Rahman I A and Padavettan V 2012 Synthesis of Silica Nanoparticles by Sol-Gel: Size-Dependent Properties, Surface Modification, and Applications in Silica-Polymer Nanocomposites—A Review *J. Nanomater.* **2012** 1–15

[304] Smith E A and Chen W 2008 How to prevent the loss of surface functionality derived from aminosilanes. *Langmuir* **24** 12405–9

[305] Hench L L and West J K 1990 The sol-gel process *Chem. Rev.* **90** 33–72

[306] Birch D J S, Geddes C D, Leishman J K R and Rolinski O J 2002 Fluorescence Nanometrology in Sol-Gels *Fluorescence Spectroscopy, Imaging and Probes* ed O Wolfbeis, R Kraayenhof, A J W G Visser and G H C. (Springer) pp 69–85

[307] Karolin J, Geddes C D, Wynne K and Birch D J S 2002 Nanoparticle metrology in sol-gels using multiphoton excited fluorescence *Meas. Sci. Technol.* **13** 21–7

[308] Birch D and Geddes C 2000 Sol-gel particle growth studied using fluorescence anisotropy: An alternative to scattering techniques *Phys. Rev. E* **62** 2977–80

[309] Cleary A, Karolin J and Birch D J S 2006 pH tracking of silica hydrogel nanoparticle growth *Appl. Phys. Lett.* **89** 113125

[310] Leishman R 2003 *The Study of Silica Particle Formation and Growth in Alkaline Silica-Sols Using Fluorescence Anisotropy* (University of Strathclyde)

[311] Rich R M, Mummert M, Gryczynski Z, Borejdo J, Sorensen T J, Laursen B, Foldes-Papp Z, Gryczynski I and Fudala R 2013 Elimination of autofluorescence in fluorescence correlation spectroscopy using the AzaDiOxaTriAngulenium (ADOTA) fluorophore in combination with time-correlated single-photon counting (TCSPC) *Anal. Bioanal. Chem.* **405** 4887–94

[312] Rich R M, Stankowska D L, Maliwal B P, Sørensen T J, Laursen B W, Krishnamoorthy R R, Gryczynski Z, Borejdo J, Gryczynski I and Fudala R 2013 Elimination of autofluorescence background from fluorescence tissue images by use of time-gated detection and the AzaDiOxaTriAngulenium (ADOTA) fluorophore. *Anal. Bioanal. Chem.* **405** 2065–75

[313] Thyrhaug E, Sørensen T J, Gryczynski I, Gryczynski Z and Laursen B W 2013 Polarization and symmetry of electronic transitions in long fluorescence lifetime triangulenium dyes *J. Phys. Chem. A* **117** 2160–8

[314] Sørensen T J, Thyrhaug E, Szabelski M, Luchowski R, Gryczynski I, Gryczynski Z and Laursen B W 2013 Azadioxatriangulenium: a long fluorescence lifetime fluorophore for large biomolecule binding assay *Methods Appl. Fluoresc.* **1** 025001

[315] Chib R, Raut S, Shah S, Grobelna B, Akopova I, Rich R, Sørensen T J, Laursen B W, Grajek H, Gryczynski Z and Gryczynski I 2015 Steady state and time resolved fluorescence studies of azadioxatriangulenium (ADOTA) fluorophore in silica and PVA thin films *Dye. Pigment.* **117** 16–23

[316] Bogh S a, Bora I, Rosenberg M, Thyrhaug E, Laursen B W and Just T Azadioxatriangulenium : exploring the effect of a 20 ns fluorescence lifetime in fluorescence anisotropy measurements **045001**

[317] Stewart H L, Yip P, Rosenberg M, Sørensen T J, Laursen B W, Knight A E and Birch D J S 2016 Nanoparticle metrology of silica colloids and super-resolution studies using the ADOTA fluorophore *Meas. Sci. Technol.* **27** 045007

[318] Lu Y and Chen W 2012 Sub-nanometre sized metal clusters: from synthetic challenges to the unique property discoveries *Chem. Soc. Rev.* **41** 3594

[319] Rosenberg H M 1995 *The Solid State* (Oxford Physics)

[320] Zheng J, Zhang C and Dickson R M 2004 Highly fluorescent, water-soluble, size-

tunable gold quantum dots *Phys. Rev. Lett.* **93** 5–8

[321] Haruta M 2003 When gold is not noble: Catalysis by nanoparticles *Chem. Rec.* **3** 75–87

[322] Xu H and Suslick K S 2010 Water-soluble fluorescent silver nanoclusters *Adv. Mater.* **22** 1078–82

[323] Lin C A J, Lee C H, Hsieh J T, Wang H H, Li J K, Shen J L, Chan W H, Yeh H I and Chang W H 2009 Synthesis of fluorescent metallic nanoclusters toward biomedical application: Recent progress and present challenges *J. Med. Biol. Eng.* **29** 276–83

[324] Carotenuto G, Longo a., De Petrocellis L, De Nicola S, Repetto P, Perlo P and Ambrosio L 2007 Synthesis of Molecular Gold Clusters With Luminescence Properties By Mercaptide Thermolysis in Polymer Matrices *Int. J. Nanosci.* **06** 65–9

[325] Hammer B and Norskov J K 1995 Why gold is the noblest of all the metals *Nature* **376** 238–40

[326] Häkkinen H 2012 The gold–sulfur interface at the nanoscale *Nat. Chem.* **4** 443–55

[327] Newman J D S and Blanchard G J 2006 Formation of gold nanoparticles using amine reducing agents. *Langmuir* **22** 5882–7

[328] Chen Y, Zeng C, Kauffman D R and Jin R 2015 Tuning the Magic Size of Atomically Precise Gold Nanoclusters via Isomeric Methylbenzenethiols *Nano Lett.* 150427145900005

[329] Krommenhoek P J, Wang J, Hentz N, Johnston-Peck A C, Kozek K a., Kalyuzhny G and Tracy J B 2012 Bulky adamantanethiolate and cyclohexanethiolate ligands favor smaller gold nanoparticles with altered discrete sizes *ACS Nano* **6** 4903–11

[330] Nishigaki J I, Tsunoyama R, Tsunoyama H, Ichikuni N, Yamazoe S, Negishi Y, Ito M, Matsuo T, Tamao K and Tsukuda T 2012 A new binding motif of sterically demanding thiolates on a gold cluster *J. Am. Chem. Soc.* **134** 14295–7

[331] Shichibu Y and Konishi K 2010 HCl-Induced Nuclearity Convergence in Diphosphine-Protected Ultrasmall Gold Clusters: A Novel Synthetic Route to "Magic-Number" Au13 Clusters *Small* **6** 1216–20

[332] Chaudhari K, Xavier P L and Pradeep T 2011 Understanding the evolution of luminescent gold quantum clusters in protein templates. *ACS Nano* **5** 8816–27

[333] Xie J, Zheng Y and Ying J Y 2009 Protein-directed synthesis of highly fluorescent gold nanoclusters. *J. Am. Chem. Soc.* **131** 888–9

[334] Xie J, Zheng Y and Ying J Y Supporting Information Protein-Directed Synthesis of Highly Fluorescent Gold Nanoclusters 1–6

[335] Li C, Sutter J U, Birch D J S and Chen Y 2012 Fluorescence anisotropy of protein - Gold nanoclusters *Proceedings of the IEEE Conference on Nanotechnology* pp 23–6

[336] Watkins H C 2013 *Investigation of Reshaping and Nanocluster Formation in Gold Nanostars* (Imperial College London)

[337] Raut S, Chib R, Rich R, Shumilov D, Gryczynski Z and Gryczynski I 2013 Polarization properties of fluorescent BSA protected Au25 nanoclusters. *Nanoscale* **5** 3441–6

[338] Cao X-L, Li H-W, Yue Y and Wu Y 2013 pH-Induced conformational changes of BSA in fluorescent AuNCs@BSA and its effects on NCs emission *Vib. Spectrosc.* **65** 186–92

[339] Eftink M R 2002 Intrinsic Fluorescence of Proteins *Topics in Fluorescence Spectroscopy Volume 6 Protein Fluorescence* vol 6, ed J R Lakowicz (New York, Boston, Dordrect, London, Moscow: Kluwer Academic Publishers) pp 1–15

[340] Ding S-N and Guo Y-X 2015 One-pot synthesis of dual-emitting BSA–Pt–Au bimetallic nanoclusters for fluorescence ratiometric detection of mercury ions and cysteine *Anal. Methods* **7** 5787–93

[341] Friedli G-L 1996 *Interaction of Seamidated Soluable Wheat Protein (SWP) with other Food Proteins and Metals* (University of Surrey)

[342] Babcock J J and Brancaleon L 2013 Bovine serum albumin oligomers in the E- and B-forms at low protein concentration and ionic strength *Int. J. Biol. Macromol.* **53** 42–53

[343] Durgadas C V, Sharma C P and Sreenivasan K 2011 Fluorescent gold clusters as nanosensors for copper ions in live cells. *Analyst* **136** 933–40

[344] Guo Y, Wang Z, Shao H and Jiang X 2012 Stable fluorescent gold nanoparticles for detection of Cu2+ with good sensitivity and selectivity. *Analyst* **137** 301–4

[345] Sahu K, Mondal S K, Ghosh S, Roy D and Bhattacharyya K 2006 Temperature dependence of solvation dynamics and anisotropy decay in a protein: ANS in bovine serum albumin. *J. Chem. Phys.* **124** 124909

[346] Russell B A, Kubiak-Ossowska K, Mulheran P A, Birch D J S and Chen Y 2015 Locating the Nucleation Sites for Protein Encapsulated Gold Nanoclusters: A Molecular Dynamics and Fluorescence Study *Phys. Chem. Chem. Phys.* In Press

[347] Shang L, Azadfar N, Stockmar F, Send W, Trouillet V, Bruns M, Gerthsen D and Nienhaus G U 2011 One-Pot Synthesis of Near-Infrared Fluorescent Gold Clusters for Cellular Fluorescence Lifetime Imaging. *Small* 2614–20

[348] Tyndall D, Rae B, Li D, Richardson J, Arlt J and Henderson R 2012 A 100Mphoton/s time-resolved mini-silicon photomultiplier with on-chip fluorescence lifetime estimation in 0.13??m CMOS imaging technology *Dig. Tech. Pap. - IEEE Int. Solid-State Circuits Conf.* **55** 122–3

[349] Gersbach M, Richardson J, Mazaleyrat E, Hardillier S, Niclass C, Henderson R, Grant L and Charbon E 2009 A low-noise single-photon detector implemented in a 130nm CMOS imaging process *Solid. State. Electron.* **53** 803–8

[350] Search H, Journals C, Contact A, Iopscience M, Address I P, Agronskaia A V, Tertoolen L and Gerritsen H C 2003 High frame rate fluorescence lifetime *J. Appl. Phys.* **36** 1655–62

[351] Gersbach M, Maruyama Y, Trimananda R, Fishburn M W, Stoppa D, Richardson J A, Walker R, Henderson R and Charbon E 2012 A time-resolved, low-noise single-photon image sensor fabricated in deep-submicron CMOS technology *IEEE J. Solid-State Circuits* **47** 1394–407